THE UNIVERSITY OF QUEENSLAND

AUSTRALIA

An Experimental Investigation of an Airframe Integrated Three-Dimensional Scramjet Engine at a Mach 10 Flight Condition

Luke James Doherty

Bachelor of Engineering (Hons. I)
Bachelor of Science

A thesis submitted for the degree of Doctor of Philosophy at The University of Queensland in 2014

SCHOOL OF MECHANICAL AND MINING ENGINEERING
CENTRE FOR HYPERSONICS

ABSTRACT

Realisation of the dream of airbreathing access-to-space requires the development of a scramjet engine that produces sufficient net thrust to enable acceleration over a wide Mach number range. With engines that are highly integrated with the airframe, the net performance of a scramjet powered vehicle is closely coupled with the vehicle attitude and is difficult to determine only from component level studies. This work investigates the influence of airframe integration on the performance of an airframe integrated scramjet through the measurement of internal pressure distribution and the direct measurement of the net lift, thrust and pitching moment using a three-component stress wave force balance.

The engine chosen as the basis for this study was the Mach 12 rectangular-to-elliptical shape-transition (M12REST) scramjet that was developed by Suraweera and Smart (2009) as a research engine for access-to-space applications. The inlet and combustor flowpath were integrated with a slender 6° wedge forebody, streamlined external geometry and three dimensional thrust nozzle. The scale of the engine was chosen so that the entire engine would fit within the core-flow diamond (bi-conic) produced by a Mach 10 facility nozzle. The Mach 10B facility nozzle was chosen because it is the largest nozzle current in use with the T4 Stalker Tube and because the off-design performance of a scramjet engine is of interest for access-to-space vehicles that must accelerate over a range of Mach numbers.

Freejet experiments were conducted within the T4 Stalker Tube. Two true-flight Mach 10 test conditions were used: a high pressure test condition that replicated flight at a dynamic pressure of 48 kPa and a low pressure test condition that replicated flight at a dynamic pressure of 28 kPa. Scaling of the test conditions according to the established binary scaling law was not completed due to facility operational limits.

The engine featured two fuel injection stations from which gaseous hydrogen was injected. The first injection station was partway along the length of the inlet while the second injection station was at the start of the combustor behind a rearward facing circumferential step. In addition to investigating inlet-only and step-only injection, a combined scheme where 68 % of the fuel was injected from the step station and 32 % from the inlet station was also investigated.

To support the analysis of the experimental results, numerical simulations of the engine with no fuel injection were conducted using the NASA code VULCAN. Analysis of the simulations show that the mass capture ratio with respect to the projected inlet area is approximately 60 % at each test condition. The simulations also show that spillage of flow from the slender forebody accounts for just 12 % of the flow through the projected

inlet area, a small but non-negligible fraction. By integrating the engine surface forces, the drag coefficient with respect to the projected frontal area of the engine is calculated to be 0.219 at the high pressure test condition and 0.243 at the low pressure test condition. A breakdown of the total drag shows that the internal and external drag are approximately equal and approximately double that of the forebody. With respect to the planform area of the engine, the lift coefficient is calculated to be 0.038 at both test conditions. The centre of force is located at 36 % of the model length.

Pressure measurements along the internal bodyside wall of the engine were used to assess inlet starting and the presence of combustion. The results show unequivocally that fuel injected from the inlet injection station acts as a pilot for fuel injected from the step injection station. For both the inlet and combined injection schemes significant combustion was obtained over a range of fuel equivalence ratios at each test condition. In comparison, negligible combustion-induced pressure rise was measured for the step injection scheme, a consequence of the reaction length being greater than the combustor length for this engine and test condition.

Using a three-component force balance, the drag was successfully measured for both fuel-on and fuel-off tests. At the high pressure test condition the average fuel-off drag coefficient of the engine was measured to be 0.246 ± 0.025, a value that is within 12 % of numerical simulation. At the low pressure test condition the drag coefficient was measured to be 0.312 ± 0.032, a value that is within 28 % of numerical simulation. When gaseous hydrogen fuel was injected from the inlet injection station at an equivalence ratio of 0.75, the measured drag coefficient reduced to 0.218 ± 0.062, corresponding to a specific impulse increment of 2180 s and a specific thrust increment of 470 N s/kg. For the combined injection scheme, a drag coefficient of 0.118 ± 0.034 was measured for a fuel equivalence ratio of 1.20, corresponding to a specific impulse increment of 2160 s and a specific thrust increment of 740 N s/kg. Net positive thrust was not achieved, due in part to a low performance three-dimensional nozzle. Also, an interaction of the force balance shielding and facility nozzle was observed. This interaction adversely affected the size of the core-flow diamond and the measured lift and centre of force.

This thesis represents the first time that force data have been measured for a hydrogen fuelled scramjet engine at true-flight Mach 10 test conditions. This work demonstrates that, although difficult, the direct measurement of the aerodynamic performance of a geometrically and mechanically complex, airframe integrated, fuelled scramjet engine module at a high Mach number flight condition is possible within the T4 Stalker Tube. Finally, airframe integration did not significantly alter the characteristics of the M12REST engine, indicating that this class of engine is suitable for use in an airframe integrated, access-to-space system.

DECLARATION BY AUTHOR

This thesis is composed of my original work, and contains no material previously published or written by another person except where due reference has been made in the text. I have clearly stated the contribution by others to jointly-authored works that I have included in my thesis.

I have clearly stated the contribution of others to my thesis as a whole, including statistical assistance, survey design, data analysis, significant technical procedures, professional editorial advice, and any other original research work used or reported in my thesis. The content of my thesis is the result of work I have carried out since the commencement of my research higher qualifications candidature and does not include a substantial part of work that has been submitted to qualify for the award of any other qualifications or diploma in any university or other tertiary institution. I have clearly stated which parts of my thesis, if any, have been submitted to qualify for another award.

I acknowledge that an electronic copy of my thesis must be lodged with the University Library and, subject to the General Award Rules of The University of Queensland, immediately made available for research and study in accordance with the Copyright Act 1968.

I acknowledge that copyright of all material contained in my thesis resides with the copyright holder(s) of that material. Where appropriate I have obtained copyright permission from the copyright holder to reproduce material in this thesis.

Luke James Doherty
August, 2014

PUBLICATIONS DURING CANDIDATURE

DOHERTY, LJ (2009). *Guide to Creating* REST *Inlet Models in* CATIA. Research Report 2009/10. Brisbane, Australia: School of Mechanical and Mining Engineering, The University of Queensland.

– (2013a). *Simulation and Uncertainty Analysis of the T4 Mach 10 Nozzle Flow using* NENZFR. Research Report 2013/16. Brisbane, Australia: School of Mechanical and Mining Engineering, The University of Queensland (cited on pages 38, 42, 43, 64, 144, 293–296).

– (2013b). *Thesis Supplement I: Design and Assembly of the Mach 12* REST *Three-Component Force Balance Model*. Research Report 2013/14. Brisbane, Australia: School of Mechanical and Mining Engineering, The University of Queensland (cited on pages 50, 51, 55, 57, 64, 80, 98, 99, 161, 164, 205, 266, 315, 333).

– (2013c). *Thesis Supplement II: Three-Component Force Balance Calibration Data for the Mach 12* REST *Engine*. Research Report 2013/15. Brisbane, Australia: School of Mechanical and Mining Engineering, The University of Queensland (cited on pages 90, 92, 93, 251, 254, 266).

DOHERTY, LJ, CHAN, WYK, ZANDER, F, JACOBS, PA, GOLLAN, RJ, and KIRCHHARTZ, RM (2012). NENZFR*: Non-Equlibrium Nozzle Flow, Reloaded*. Research Report 2012/08. Brisbane, Australia: School of Mechanical and Mining Engineering, The University of Queensland (cited on pages 41, 43, 290, 293).

DOHERTY, LJ, SMART, MK, and MEE, DJ (2012). "Design of an Airframe Integrated 3-D Scramjet and Experimental Results at a Mach 10 Flight Condition". In: *18th* AIAA/3AF *International Space Planes and Hypersonic Systems and Technologies Conference*. Tours, France: AIAA-2012-5910. DOI: 10.2514/6.2012-5910.

DOHERTY, LJ and WISE, DJ (2013). *Pitot Survey Data for the* T4 *Mach 10 Nozzle*. Research Report 2013/07. Brisbane, Australia: School of Mechanical and Mining Engineering, The University of Queensland (cited on pages 38, 39).

PUBLICATIONS INCLUDED IN THIS THESIS

DOHERTY, LJ, SMART, MK, and MEE, DJ (2012). "Design of an Airframe Integrated 3-D Scramjet and Experimental Results at a Mach 10 Flight Condition". In: *18th* AIAA/3AF *International Space Planes and Hypersonic Systems and Technologies Conference*. Tours, France: AIAA-2012-5910. DOI: 10.2514/6.2012-5910.

Parts of this paper are included in Chapters 3, 5 and 6. Doherty was responsible for 95 % of the analysis, 90 % of the interpretation of the data and 85 % of the drafting and writing. Smart was responsible for 5 % of the analysis, 10 % of the interpretation of the data and 5 % of the drafting and writing. Mee was responsible for 5 % of the interpretation of the data and 5 % of the drafting and writing.

CONTRIBUTIONS BY OTHERS TO THIS THESIS

Prof. Michael Smart provided substantial input into the conception of the project. He also contributed the numerical simulations that are presented in Chapter 5, being responsible for the preparation of the computational grid and running of the simulations. The author was responsible for all subsequent analysis of the simulation results.

STATEMENT OF PARTS OF THE THESIS SUBMITTED TO QUALIFY FOR THE AWARD OF ANOTHER DEGREE

None.

ACKNOWLEDGEMENTS

And so it ends. The final curtain call, the last words that I will write for my thesis (but certainly not the least). I sit here, in a bean bag on the verandah at the front door, a location where so much of my thesis has been written. I am enjoying this moment of reflection. As much as a thesis is an individual pursuit, no thesis could be finished without the support of many people and so I take pleasure in acknowledging the following:

First and foremost my sincere thanks goes to my supervisor Prof. Michael Smart. Thank you for conceiving the project and for your continual support, encouragement and guidance throughout my long candidature. Thank you for sharing your enthusiasm and expertise in the field with me, for letting me do my own thing and helping me see the bigger picture, even when I was buried in the details.

My sincere thanks also goes to my associate supervisor Prof. David Mee. Thank you for sharing your expertise in the stress wave force measurement technique and for always being willing to stay late to discuss my calibration results. Your knowledge of the inner workings of the force balance continues to amaze me. Throughout my candidature your questions, comments and advice always made me think more carefully about my work.

To Mr. Keith Hitchock, thank you for your support, both technical and otherwise, throughout the duration of my two test campaigns. Your willingness to stay late to fix what I broke and ensure that everything was ready for the next day was always appreciated; it was a pleasure working with you. To the T4 operators Dylan, Philippe, Arman and Dan, thank you for the effort you put into operating the facility and the patience you displayed when faced with cleaning the nozzle throat after every shot.

To the original room 310 crew, Rainer Kirchhartz, Sarah Razzaqi, Tom Jazra, Wilson Chan and Drew Ridings, thanks for showing me 'the way of the PhD', for the advice you gave, the conversations we had and the laughs we shared. To Wilson, thanks for being such a good mate over the years, for your continual encouragement and for your critique of my thesis. To Rainer and the original post-docs, James Turner and Mel Suraweera, thank you for being such great mentors in all things T4 and REST engine related.

To Dr. Rowan Gollan and Dr. Peter Jacobs, thank you for sharing your expertise in Eilmer and CFD generally and for always answering my simple computational-related questions. To the current and almost finished post-grads, Dylan Wise, Philippe Lorrain, Rolf Gehre, Dave Petty, James Barth, Dawid Preller and Matt Bricalli, thank you for making the top level of the mechanical engineering building a slightly more bearable place to work.

Particular thanks to Rolf and Dave for reading my thesis and offering insightful and worthwhile criticism.

To Prof. Russell Boyce and the SCRAMSPACE project, thank you for paying for the manufacture of the engine and for both experimental test campaigns. To Prof. Ross McAree and Miss Brianne Mackinnon, thank you for shielding me from the wrath of the graduate school in the final months of my candidature after I missed yet another deadline. You prevented the graduate school from terminating my candiature, a feat for which I will always be grateful.

To all the other academics, post-docs and post-grads within the Centre for Hypersonics and School of Mechanical and Mining Engineering, more than anything, the quality of the people I've met and worked alongside has made completing my studies at UQ a pleasure.

To my best mates, Kev, Ross and Borika, you have each been a constant source of encouragement and support throughout both my undergraduate and postgraduate degrees. Thank you for the laughs we've shared, the trips we've taken, for putting up with my various moods and for always listening when I complained to you about my work. I can't wait to see what the future brings for us each.

To Rob, Issy, Wayne and all my other climbing mates, thank you for turning me into a climber-for-life and for keeping me sane these past few years. I look forward to many future climbing trips with you all.

To my parents, thank you for providing such a loving and supportative environment throughout the entirety of my life so far. This thesis would not have been finished if you hadn't been willing and happy to let me live under your roof for so long.

Finally, to my brother Kurt, thank you being my regular climbing partner over the years and for always being willing to help me out whenever and with whatever I ask. Thank you also for spending hours developing the LaTeX class file used for this thesis.

KEYWORDS

scramjet engine, hypersonics, airbreathing propulsion, three-dimensional inlet, experimental, stress wave force balance, shock tunnel, short duration ground testing

AUSTRALIAN AND NEW ZEALAND STANDARD RESEARCH CLASSIFICATIONS (ANZSRC)

090107, Hypersonic Propulsion and Hypersonic Aerodynamics, 100 %

FIELDS OF RESEARCH (FoR) CLASSIFICATION

0901, Aerospace Engineering, 100 %

An Experimental Investigation of an Airframe Integrated Three-Dimensional Scramjet Engine at a Mach 10 Flight Condition

A Thesis

by

Luke James Doherty

December, 2013

Supervisor: Prof. Michael Smart
Associate Supervisor: Prof. David Mee

Commenced: 21st July 2008
First Submission: 25th December 2013
Revised: 30th April – 19th August 2014

THE UNIVERSITY OF QUEENSLAND

For my parents and brother,
and their never-ending support.

"...when you can measure what you are speaking about, and express it in numbers, you know something about it; but when you cannot measure it, when you cannot express it in numbers, your knowledge is of a meagre and unsatisfactory kind; it may be the beginning of knowledge, but you have scarcely in your thoughts advanced to the state of Science ..."

– William Thomson (Lord Kelvin), 1883

"Measurement is the first step that leads to control and eventually to improvement. If you can't measure something, you can't understand it. If you can't understand it, you can't control it. If you can't control it, you can't improve it."

– H. James Harrington, 1987

"It is not the critic who counts; not the man who points out how the strong man stumbles, or where the doer of deeds could have done them better. The credit belongs to the man who is actually in the arena, whose face is marred by dust and sweat and blood; who strives valiantly; who errs, who comes short again and again, because there is no effort without error and shortcoming; but who does actually strive to do the deeds; who knows great enthusiasms, the great devotions; who spends himself in a worthy cause; who at the best knows in the end the triumph of high achievement, and who at the worst, if he fails, at least fails while daring greatly, so that his place shall never be with those cold and timid souls who neither know victory nor defeat."

– Theodore Roosevelt, 1910

SHORT CONTENTS

CONTENTS

LIST OF FIGURES

LIST OF TABLES

NOMENCLATURE

ACRONYMS

3CFB	Three-Component Force Balance
CAD	Computer Aided Design
CFD	Computational Fluid Dynamics
CfH	Centre for Hypersonics
DLR	German Aerospace Center
GIRF	Global Impulse Response Function
HEG	High Enthalpy Shock Tunnel, Göttingen
HIEST	High Enthalpy Shock Tunnel
HP	High Pressure (Test Condition)
HXFE	Hyper-X Flight Engine
IRF	Impulse Response Function
JAXA	Japan Aerospace Exploration Agency
KRC	Kakuda Research Center
LaRC	Langley Research Center
LP	Low Pressure (Test Condition)
NASA	National Aeronautical and Space Administration
NATO	North Atlantic Treaty Organisation
NENZF	Non-Equilibrium Nozzle Flow
NENZFR	Non-Equilibrium Nozzle Flow, Reloaded
RANS	Reynolds Averaged Navier Stokes
REST	Rectangular-to-Elliptical Shape Transition
RJTF	Ramjet Engine Test Facility
SWFMT	Stress Wave Force Measurement Technique
UQ	The University of Queensland

ROMAN LETTERS

A	area, m^2
A	axial direction, m, introduced in Section 4.4
a	axial coordinate, m or speed of sound, m/s

A_p	projected planar or planform area, m^2, introduced in Section 4.7
A_1	projected engine capture area, m^2, introduced in Section 5.4
A_2	theoretical engine capture area, m^2, introduced in Section 5.4
A_F	projected frontal area, m^2, introduced in Section 5.4
A_o	output specification matrix, introduced in Section 4.4
a_{vi}	element of output specification relating strain output v to stress bar i output
B_ψ	absolute bias uncertainty in measurement ψ, introduced in Appendix C
C_D	drag coefficient, introduced in Section 4.7
CF	normalised centre of force location, introduced in Section 4.7
C_L	lift coefficient, introduced in Section 4.7
C_M	moment coefficient, introduced in Section 4.7
d_j^k	moment arm for calibration hit in direction k at calibration location j, m, introduced in Section 4.5
e	specific internal energy, J/kg
F	force, N
$\mathbf{G}$	global impulse response function, introduced in Section 4.3
G	impulse response function, introduced in Section 4.3
g	acceleration due to gravity, $9.81\,m/s^2$
G_k^i	overall impulse response for bar i due to a distributed load in direction k, introduced in Section 4.4
G_k^{ij}	individual impulse response function for stress bar i due to a force at calibration location j in direction k, introduced in Section 4.4
G_{vl}	sub-matrix of global impulse response function that relates output v to a distributed load in direction l
H	total enthalpy, J/kg
h	enthalpy, J/kg
I_{sp}	specific impulse, s, introduced in Section 7.6
k	coefficient of thermal conductivity, $W/(K\,m^2)$
L	(engine) length, m
$\dot{m}$	mass flow rate, kg/s
M	Mach number or moment, N m
$m_{c,i}$	mass capture ratio with respect to reference area A_i, $i \in \{F, 1, 2\}$, introduced in Section 5.4

$m_{sp,i}$	forebody mass spillage fraction with respect to reference area A_i, $i \in \{F, 1, 2\}$, introduced in Section 5.4
N	normal direction, m, introduced in Section 4.4
n	normal coordinate, m
p	pressure, Pa
p/p_1	normalised pressure ratio, introduced in Section 3.5.2
P_ψ	absolute precision uncertainty in measurement ψ, introduced in Appendix C
q	dynamic pressure, Pa or heat addition per unit mass, J/kg
Re_u	unit Reynolds number, 1/m
T	temperature, K
t	time, s
T_{sp}	specific thrust, N s/kg, introduced in Section 7.6
tke	turbulent kinetic energy, J/kg
u	velocity, m/s or input force signal, N
U_ψ	total absolute uncertainty in measurement ψ, introduced in Appendix C
w	(engine) width, m
w_{jk}	weighting factor for a force at location j in direction k, introduced in Section 4.4
x	streamwise/longitudinal coordinate, m
X_ψ	total relative uncertainty in measurement ψ, introduced in Appendix C
X_ψ^B	relative bias uncertainty in measurement ψ, introduced in Appendix C
X_ψ^P	relative precision uncertainty in measurement ψ, introduced in Appendix C
y	strain output signal, V or transverse/vertical coordinate, m
Y_i	mass fraction of chemical species *i*
z	lateral coordinate, m

GREEK LETTERS

α	fuel calibration constant, introduced in Section 3.4.5
Δh_c	heat of formation/combustion, J/kg
δ	boundary layer thickness, m
η_o	overall thermodynamic efficiency, introduced in Section 7.6

$\eta_{o,c}$	corrected overall thermodynamic efficiency, introduced in Section 7.6
γ	specific heat ratio
λ	stoichiometric fuel-air ratio
μ	static viscosity, s Pa
ϕ	fuel equivalence ratio, introduced in Section 3.4.5
Π	fuel-on pressure increment per unit mass of fuel, defined by Equation (6.1)
ψ_f	fuel specific exergy, J/kg, introduced in Section 7.6
ρ	density, kg/m^3
τ	dummy (time) variable, s
ξ	fuel split parameter, introduced in Section 3.4.5
β	(oblique) shock angle, °
θ	flow deflection angle, °
ω	specific dissipation rate

SUBSCRIPT AND SUPERSCRIPT

A	air
BC	balance centre
c	corrected (force) or captured (air)
CT	compression tube
D	drag
f	fill or fuel
$f,1$	inlet fuel injection
$f,2$	step fuel injection
f,c	combined fuel injection
I	inlet (coordinate system)
i	stress bar index $\{1,2,3,4\}$
j	fuel plenum index or force balance calibration lug location
k	calibration hit direction $\{N, A\}$
L	lift
l	distributed force direction index $\{N, A, M\}$
LE	leading edge (location)
M	moment
NOM	nominal
$\parallel$	parallel direction

p	plenum
RES	reservior
s	nozzle supply
SS	shock speed
ST	shock tube
th	inlet throat
T	thrust
t	total or turbulent or transition
TOT	total
Tf	tank final
Ti	tank initial
ν	strain output signal direction index $\{N, A, M\}$

INTRODUCTION

The first chapter, in which the thesis is introduced, the motivation established, the aims defined and the report structure explained, thus beginning the story.

1

1.1 ANATOMY OF A SCRAMJET ENGINE

Conceptually simple, practically complex. Supersonic combustion ramjet engines, aka scramjet engines, are a class of hypersonic[1] airbreathing engine that have been subject to continuous study since first being documentated in the open literature by Antonio Ferri in 1961 (see the introductory paragraphs of Ferri (1973) and Chapter 4 of Heppenheimer (2007)). Scramjet engines are in essence a carefully contoured, hollow tube. Operating on the Brayton cycle, the basis for almost all airbreathing propulsion systems, scramjet engines rely on ram compression of air through the engine inlet to produce conditions suitable for combustion of fuel.

Figure 1.1 provides a schematic of a generic airframe integrated scramjet engine alongside a Mollier diagram of the ideal Brayton cycle. The Brayton cycle is characterised by adiabatic compression, constant pressure heat addition, adiabatic expansion and constant pressure heat rejection. Reference stations through the engine are labelled according to the convention of Heiser and Pratt (1994). Station 0 is the undisturbed freestream ahead of the vehicle. Flow is compressed from station 0 to station 2, the inlet throat. This compression process may be achieved via external compression, in which the compression process occurs on the external surfaces of the forebody only, via internal compression, in which converging side walls completely enclose the flow, or via a mixture of both external and internal compression (Heiser and Pratt, 1994, Chapter 5). A mixed compression process is typical for airframe integrated scramjet engines and for this type of process, station 1 is an intermediary station that is just upstream of the inlet.

The region between stations 2 and 3 is called the isolator. Though not required thermodynamically, the isolator is important for the practical operation of a scramjet engine, particularly for flight below approximately Mach 8, as it prevents the pressure rise in the combustion chamber from affecting the inlet flow (see, for example, Billig et al., 1990). The combustion chamber lies between stations 3 and 4. This is where fuel is (typically) injected and burnt. Finally, to generate thrust the flow must be expanded.

1 For a concise discussion of the distinguishing phenomena of hypersonic flows see Section 1.3 in Anderson (2006).

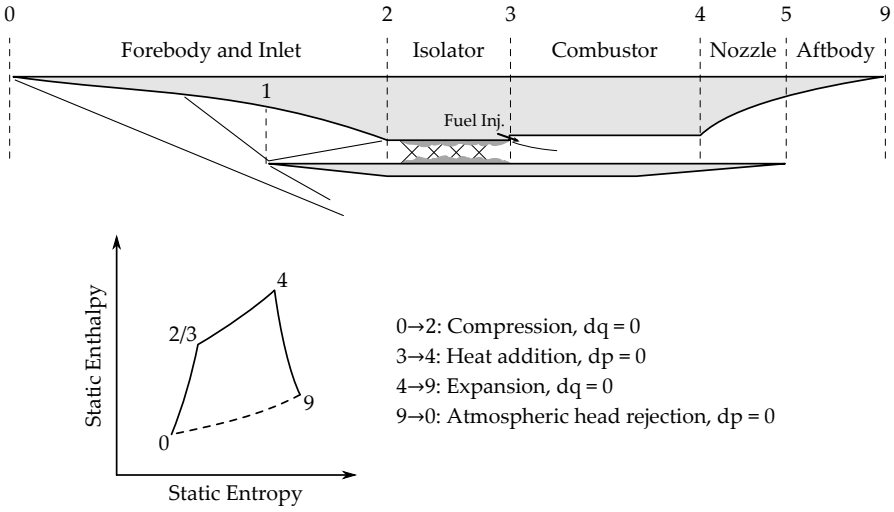

Figure 1.1 – Schematic of an airframe integrated scramjet engine and the theromdynamic operating cycle, the Brayton cycle. Adapted from Billig et al. (1990), Builder (1964), and Rogers et al. (1998).

Similar to the inlet, for airframe integrated scramjets, the expansion of the flow is achieved by an initial internal expansion (stations 5 to 9) and then by further expansion on the vehicle aftbody (stations 9 to 10). The jump in station numbering from 5 to 9 across the internal nozzle ensures consistency with the convention used for jet turbine engines (Oates, 1997).

As noted above, the Brayton cycle is the basic thermodynamic operating cycle for jet turbine engines, ramjet engines and scramjet engines. Given that both jet turbine and (to a slightly lesser extent) ramjet engine technologies are mature, it is important to consider why scramjets become necessary as the flight speed increases. Referring to Figure 1.1, the compression ratio for the Brayton cycle is defined as the static enthalpy ratio across the inlet (and forebody, i.e. h_2/h_0). The optimum compression ratio is that ratio which maximises the thrust for a given heat input (Builder, 1964). Czysz (1988) compared the optimum compression ratio with the kinetic (ram) compression ratio across a range of flight speeds. Three different regimes were identified. At flight velocities below approximately 1500 m/s the maximum attainable ram compression is less than the optimum. Some form of mechanical compression is therefore required to make up the difference. This is achieved in jet turbines through the use of multistage radial compressors (Oates, 1997). For flight between approximately 1200 and 1800 m/s, the maximum attainable ram compression is comparable with the optimum compression ratio, implying that the inlet should decelerate the flow to a subsonic velocity. This is achieved in ramjet engines by terminating the compression process with a normal shock (Heiser and Pratt, 1994). Finally, as the flight speed increases above 1800 m/s the maximum attainable ram compression becomes increasingly

larger than the optimum compression ratio. It is therefore desirable to limit the compression process such that the main flow through the engine remains supersonic, thus resulting in the supersonic compression ramjet engine.

1.2 RESEARCH CONTEXT

As evidenced throughout the last 50 years of research, the conceptual simplicity of a scramjet engine belies the practical complexities associated with achieving sustained hypersonic flight through supersonic combustion of fuel. Numerous scramjet powered vehicle concepts have been proposed over the years (Curran, 2001) and they generally fall into one of two categories; they are either designed for cruise or designed for acceleration (Hirschel and Weiland, 2009). Cruise vehicles typically take the form of either cruise weapons systems, interceptor/first-strike systems, or global transport systems. Examples of this category include Boeing's X-51 waverider flight demonstrator vehicle and the missile designs discussed by Billig (1995). In comparison, accelerator vehicles are typically focussed on access-to-space and include single-, two- or multiple-stage-to-orbit concepts (SSTO, TSTO, MSTO respectively). Examples of this category include the United States National Aero-Space Plane SSTO concept (Barthelemy, 1989; Rogers et al., 1998), the German Sänger TSTO concept (Högenauer and Koelle, 1989) and more recently the TSTO concepts proposed by Bowcutt et al. (2011) and Bradford et al. (2004). This thesis is being conducted within a broad project at The University of Queensland examining the applicability of using scramjet engines for access-to-space. The ultimate goal is to provide Australia with a capability of launching small payloads, around 200 kg mass, to low Earth orbit. The specific vehicle concept is a three-stage, rocket-scramjet-rocket system (Jazra, 2010; Jazra et al., 2013; Smart and Tetlow, 2009).

While often postulated as forming the basis for an efficient access-to-space system, scramjet powered vehicles have yet to travel through Earth's atmosphere as anything other than fundamental flight experiments. One key requirement for an airbreathing access-to-space system is that the engines produce sufficient net thrust to enable acceleration over a wide Mach number range (Sacher, 2010). Although scramjets are more efficient than rocket engines in terms of the specific impulse,[2] both the net thrust and thrust-to-weight ratio are small due to the large vehicle drag that is dominated by internal viscous drag (Stalker, 2006b), and increased vehicle complexity.

2 That is, thrust-per-unit-fuel-mass basis. The improved efficiency of a scramjet is a consequence of scramjet engines using the oxygen in the captured air mass to burn the fuel. This oxygen does not enter the efficiency calculation. In contrast, for rockets the per-unit-fuel-mass is actually a per-unit-propellant-mass which includes the oxidiser mass flow.

Despite net thrust being a key requirement, a survey of the open literature quickly reveals a distinct lack of experimental results demonstrating net thrust production of complete scramjet engine modules. The literature may be broadly divided into two categories. The first includes those studies that examine fundamental flow or aerothermochemical phenomena at a component level. Examples include boundary layer transition on cones and flat plates (Mee, 2002; Simeonides, 2003), inlet design studies (Gollan and Jacobs, 2013; Tan et al., 2011), fuel injector studies examining mixing performance (Ben-Yakar et al., 2006; Kawai and Lele, 2010), direct connect studies of combustion efficiency (Kobayashi et al., 2006; Tomioka et al., 2006), studies of shock-boundary layer or shock-shock interactions (Burtschell and Zeitoun, 2003; Dann and Morgan, 2011) and studies of single-expansion ramp nozzles (Hirschen et al., 2009; Tanimizu et al., 2011). The second broad category includes numerical studies that examine the design, optimisation and ascent trajectories of scramjet powered vehicles at a global system level (see for e.g. Bilardo et al., 2003; Bowcutt et al., 2002; Flaherty et al., 2010; Hunt, 1987; Jazra et al., 2013). Studies of this sort are often based on simplified analyses of the engine performance. Few papers exist in the open literature that bridge the gap between these two categories and establish experimentally the net performance of a complete scramjet engine module. While such studies must have been completed in the past as part of both NASA's X-43 and Boeing's X-51 flight experiments, the experimental and computational vehicle performance data remains largely classified.

A second key requirement for airbreathing access-to-space systems is that the engines must be highly integrated with the vehicle. Known as propulsion-airframe integration or simply airframe integration, the entire underside surface[3] of the vehicle becomes part of the propulsion system, typically to such an extent that hypersonic airbreathing vehicles may be considered 'flying engines'. The primary rationale for airframe integration is that it takes advantage of the gas that has been partially compressed by the vehicle bow-shock, simultaneously reducing the required compression ratio of the engine inlet and significantly increasing the freestream capture area (Hirschel and Weiland, 2009, Section 4.5). Disadvantages of airframe integration are generally related to the increased interdependency of the airframe and propulsion system and include the ingestion of the forebody boundary layer by the inlet, non-uniformities arising from forebody flow spillage, and a strong coupling of the engine operation and vehicles dynamics through the vehicle attitude (Hunt et al., 1997; Lewis, 2003; McRuer, 1991).

Despite the prevalence of the idea and need for airframe integration, experimental data is not often reported, with most studies instead focussing

3 Depending on the vehicle and engine geometry the engines may not necessarily be integrated with the underside surface, see for example Bowcutt et al. (2011).

on overall design issues and numerical analysis (Lewis, 2003; Sacher, 2010). The NATO (2006, Section 1.4.6) report *Technologies for Propelled Hypersonic Flight* states that:

> " Airframe-propulsion integration has been studied extensively in France and Germany, but only using computations of different levels. Testing demonstration and associated methodology has been prepared, . . . no specific experimental work has yet been conducted in Western Europe."

Whilst a highly integrated vehicle was developed for NASA's X-43 flight experiment, little experimental data is available for this vehicle. As an example, Witte et al. (2003) discusses airframe integration issues and test methodologies but does not present details of the experimental results and conclusions.

In summary, a requirement to experimentally investigate net thrust production and airframe integration of scramjet engines clearly exists as each of these technologies are important for enabling hypersonic airbreathing access-to-space.

1.3 THESIS MOTIVATION

Over the past decade one portion of the research conducted within the Centre for Hypersonics (CFH) at The University of Queensland has focussed on three-dimensional fixed geometry scramjet engines designed using the rectangular-to-elliptical-shape-transition (REST) methodology of Smart (1999). Taking advantage of the structural and flow benefits of an elliptical combustor (Beckel et al., 2006) while allowing efficient integration with a planar vehicle forebody, REST scramjet engines have demonstrated good performance with respect to inlet starting and compression efficiency and robust combustion of fuel (Smart, 2001; Turner and Smart, 2010). The design methodology has recently been extended to allow inlet integration with conical vehicle forebodies (Gollan and Smart, 2013).

To examine the applicability of this class of engine for access-to-space applications, Suraweera and Smart (2009) developed a REST engine that was designed for flight from Mach 6 to 12. Tested in semi-freejet mode[4] at an off-design Mach number, this engine demonstrated good thrust potential. The engine has also served as the basis for a vehicle-optimisation study (Jazra et al., 2013), a study that relied on quasi-one-dimensional cycle analysis for the prediction of the engine performance across the required Mach number range.

This thesis is motivated by the desire to investigate the influence of airframe integration on engine operation and to investigate net thrust

4 That is the test facility delivered conditions equivalent to those behind an assumed vehicle forebody shock.

performance at high Mach numbers. It uses the Mach 12 REST engine as an example of the three-dimensional fixed-geometry scramjet engines that are currently under investigation within the Centre for Hypersonics at The University of Queensland.

1.4 THESIS AIM AND METHODOLOGY

On the basis of the preceding discussion, the aim of this thesis is to, for the first time,

experimentally investigate the performance of an airframe integrated REST*-based scramjet engine module at a true Mach 10 flight condition.*

This will be achieved through

1. integration of an existing engine with a forebody and streamlined external geometry;

2. quantification of the forebody mass flow spillage;

3. the experimental measurement of internal pressure with and without injection of gaseous hydrogen fuel;

4. the experimental demonstration of inlet starting with ingestion of a thick boundary layer; and,

5. characterisation of the aerodynamic performance of the engine module for a range of fuel equivalence ratios and fuelling schemes through the direct measurement of the net lift, thrust and pitching moment in an impulse facility.

As stated above, the methodology of this thesis was primarily experimental, with analytical and computational studies completed in support of the experiments. A new airframe integrated experimental model was developed and tested within the T4 Stalker Tube at The University of Queensland, a facility that has a long history of being used for scramjet-based experimental investigations (Stalker et al., 2005) and a three-component stress wave force balance (Robinson et al., 2006; Simmons et al., 1993) was used to directly measure the lift, thrust and pitching moment of the engine module.

The engine developed in this thesis was not optimised for maximum thrust as this would have required detailed design, analysis and optimisation of a three-dimensional engine nozzle, an investigation requiring a separate project. Rather, the focus of this work was to investigate the influence of airframe integration on engine operation and directly measure the net aerodynamic forces.

1.5 THESIS STRUCTURE

This report is organised into eight chapters, including the Introduction and a set of twelve supporting appendices. The remaining chapters are

Chapter 2 Literature Review

This chapter provides a review of the pertinent literature, focussing on previous REST engine tests and past force balance tests of complete scramjet engines.

Chapter 3 Facility, Model and Test Flow Conditions

The first of two chapters that concentrate on the experimental apparatus. This chapter details the T4 Stalker Tube facility and its instrumentation, the calculation of the test flow conditions and the M12REST engine that was developed for this work. Details of the instrumentation of the engine and fuel injection system are provided. Finally, the chapter ends with an explanation of the selection of an appropriate test time and the data reduction methods used for the internal engine pressure measurements.

Chapter 4 Force Balance Theory and Calibration

The second chapter focussed on the experimental apparatus. This chapter provides a succinct yet complete description of the force balance technique and calibration method. Relevant calibration results are shown and discussed, and the data reduction methods for the engine force data are explained.

Chapter 5 Engine Flow Field Analysis

This chapter provides an analysis of the fuel-off numerical simulations of the M12REST engine that were completed in support of the experiments. The analysis examines the dominant internal flow structures, the engine mass capture performance and flow spillage from the forebody. The predicted net forces of the engine for the case of no fuel injection are also provided and discussed in the context of developing an airbreathing access-to-space system that generates net thrust at high Mach numbers.

Chapter 6 Pressure Results

The first of two results chapters, this chapter presents the internal engine pressure data. Data for three different fuel injection configurations at a range of fuel equivalence ratios are provided. The influence of flight dynamic pressure is examined and the current data are compared with that of an un-installed engine.

Chapter 7 Force Balance Results

The second experimental results chapter, this chapter presents the engine force data for no fuel injection and two different injection configurations. Engine performance metrics are calculated and discussed.

Chapter 8 Conclusions and Recommendations

The final chapter of the thesis, this chapter summarises the significant findings from Chapters 6 and 7, differentiating between those of a technical nature and those of a scientific nature. Recommendations for future work are also provided in this chapter.

A final introductory note: two test campaigns were conducted as a part of this thesis within the T4 Stalker Tube. The first attempted to simultaneously measure the internal pressure distribution and the net lift, thrust and pitching moment using a three component force balance. This campaign, which occurred from November 2010 to May 2011, encounted unforeseen technical difficulties, difficulties that were caused by an adverse interaction of the force balance shielding and facility nozzle flow. The second test campaign, which occurred from December 2011 to February 2012, measured only the internal pressure distribution of the engine. The force balance was not used and was instead replaced by a streamlined rigid mount. The primary goal of the second test campaign was to confirm the engine and facility operation. The data presented in Chapter 6 are taken exclusively from the second test campaign while the data presented in Chapter 7 are taken exclusively from the first test campaign. Throughout this report the terms 'Campaign 1' and 'force balance campaign' will be used synonymously, as will the terms 'Campaign 2' and 'rigid-mount test campaign'.

LITERATURE REVIEW

The second chapter, in which we concern ourselves with a review of the literature, with particular attention paid to REST *scramjets and scramjet engine force balance experiments, thereby laying the first foundations of the thesis.*

2

2.1 INTRODUCTION

In this chapter a review of the pertinent literature is provided. The first half of the chapter, Section 2.2, summarises past experimental work relating to REST inlets and REST-based scramjets, with particular focus on the M12REST access-to-space engine. The second half of the chapter, Section 2.3, then reviews the past force balance experiments that have been conducted using complete scramjet engines at the National Aeronautical and Space Administration (NASA), the Japan Aerospace Exploration Agency (JAXA) and The University of Queensland (UQ). This literature review is very focussed; readers requiring a more general review and introduction to hypersonic flow theory are referred to the classic textbook by Anderson (2000). For further background on scramjet engine technology readers are referred to the textbook by Heiser and Pratt (1994), the collection by Murthy and Curran (2001) and the review by Curran (2001).

2.2 REST ENGINE DESIGN AND TESTING

The rectangular-to-elliptical-shape-transition (REST) methodology was developed by Smart (1999) as a means of generating three-dimensional, fixed-geometry inlets that feature no boundary-layer bleeds. Provided they are able to self-start and operate over a wide Mach number range, these types of inlets are favourable as they reduce structural complexity (Beckel et al., 2006). The methodology, reported in detail in Smart (1999), is based on a quasi-streamline-tracing technique in which the inlet capture and throat geometry are specified a priori.

The design of all REST inlets begins by defining an axisymmetric compression flow field that provides the desired pressure rise at the design operating condition. The quasi-rectangular inlet capture and elliptical throat are then superimposed on this flow field as shown in Figure 2.1. Streamlines which intersect these cross-sections are traced through the flow field and merged using a lofting procedure to create the inviscid inlet shape (Figure 2.2). A viscous correction is then made to the geometry to account for boundary layer growth and the overall length of the

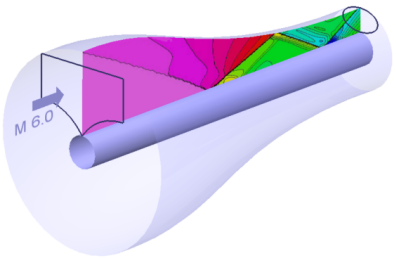

Figure 2.1 – Compression flow field and corresponding Mach number contours used during the design of the M8-radical farming REST engine (Turner and Smart, 2008).

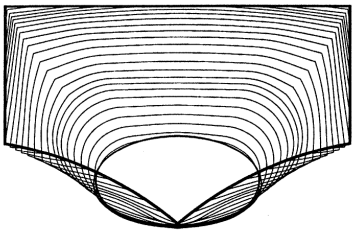

Figure 2.2 – Cross-sections defining a REST inlet (Smart, 1999)

compression flow field is adjusted until boundary layer separtion criteria for the viscous-corrected shape are satisfied (Smart, 1999). The result is a relatively slender three-dimensional inlet that smoothly transitions from a quasi-rectangular capture area to an elliptical throat and features highly swept leading edges and a notched cowl.

Since developing the method, a total of four inlets have been designed, built and tested in several different facilities. These inlets are shown in Figure 2.3 and summarised in Table 2.1. Each inlet was designed with the assumption that it would be installed on a vehicle with a forebody equivalent to a 6° wedge. The first experimental results for a REST inlet are reported in Smart (2001). Shown in Figure 2.3a, this inlet was designed for installation on a vehicle cruising at Mach 7.1 with freestream dynamic pressure of 50 kPa. Designated as M7REST in this thesis, the design Mach number of this inlet was 6. Experiments were conducted in the NASA Langley Research Center (LaRC) Arc heated Scramjet Test Facility (AHSTF) at Mach 6.2 with the goal of validating the design methodology. Smart (2001) reported that the inlet was self-starting and exhibited good performance, with a mass capture ratio of approximately 96 %, a kinetic energy efficiency of approximately 96.6 % and a compression ratio of approximately 15.8.

The second REST inlet to be designed and tested is shown in Figure 2.3b. Designated as M7(V2)REST, Smart and Trexler (2004) report that this inlet was an improved version of the M7REST inlet, being designed for installation on the same vehicle but with an inlet design Mach number of 5.7, a 20 % reduction in inlet length and a reduced internal contraction ratio.[1] The purpose of these changes was to permit the M7(V2)REST inlet to self-start at Mach 4 (Smart and Trexler, 2004). Experiments were conducted in the NASA LaRC Mach 4 Blown Down Facility (M4BDF) with the goal of examining the self-starting capability and performance of the inlet at

1 The internal contraction ratios of the M7REST and M7(V2)REST inlets were 2.15 and 1.77, respectively (Smart, 2001; Smart and Trexler, 2004).

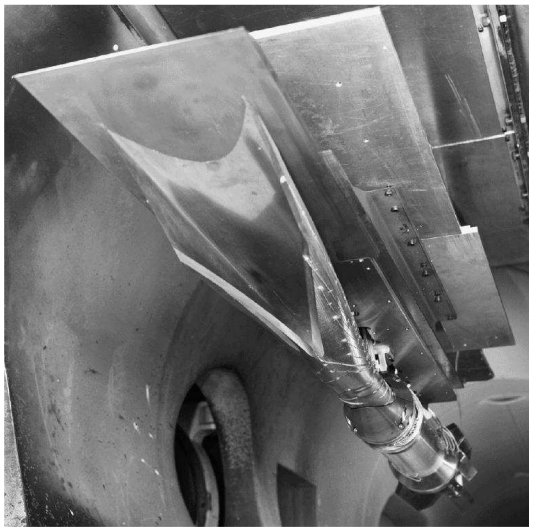

(a) M7REST inlet in the LARC AHSTF

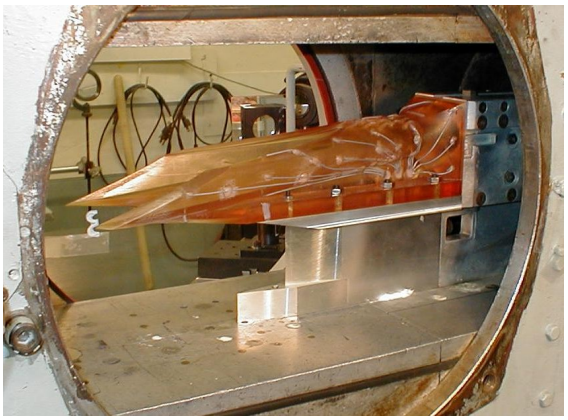

(b) M7(V2)REST inlet in the LARC M4BDF

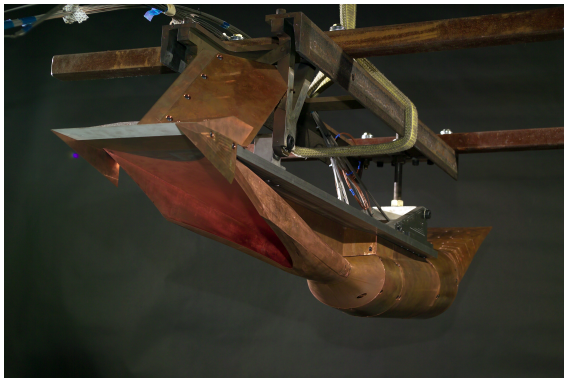

(c) M7(V2)REST engine at LARC

(d) M8REST-RF engine at UQ

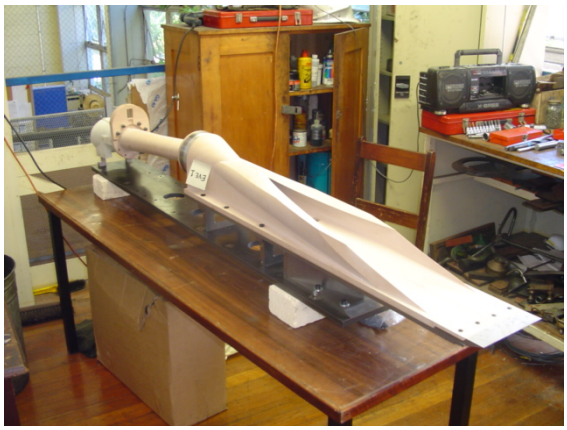

(e) Design-scale M12REST engine at UQ

Figure 2.3 – Various REST inlets and engines that have been designed and tested over the period 1999-current at NASA Langley Research Center and The University of Queensland

Table 2.1 – Summary of REST inlets

Inlet Name	Design Point		Test Facility: Condition	Instumentation	Reference	Notes
	Vehicle[a]	Inlet				
M7	$M_f = 7.1$, $q_f =$ 50 kPa	$M = 6$	NASA Langley Research Center (LARC) Arc Heated Scramjet Test Facility (AHSTF): $M_e = 6.18$, inlet only	Mass capture, static and pitot pressure profiles at inlet throat, static pressure in the inlet, some thermocouples.	Smart (2001)	First experimental testing of a REST inlet.
M7(V2)	$M_f = 7.1$, $q_f =$ 50 kPa	$M = 5.7$	NASA LARC Mach 4 Blown Down Facility (M4BDF): $M_e = 4$, inlet only	Mass capture, pitot rake at inlet throat, static pressure in the inlet, some thermocouples.	Smart and Trexler (2004)	Study of low Mach number self-starting capability of a REST inlet.
			NASA LARC Combustion Heated Scramjet Test Facility (CHSTF): $M_e =$ 4.46, semi-freejet testing	Static pressure and surface thermocouples, six-component force balance.	Smart and Ruf (2006)	First complete engine testing of a REST-based scramjet.
M8-RF[b]	$M_f = 8$, $q_f =$ 50 kPa	$M = 6$	The University of Queensland's T4 Stalker Tube (UQ T4): $M_e = 6.6$, semi-freejet	Static pressure	Turner (2010) and Turner and Smart (2008, 2010, 2013)	Application of radical farming to REST-based engine. First use of inlet injection.
M12	$M_f = 12$, $q_f =$ 50 kPa	$M = 9.1$	UQ T4: $M_e = 7.15$, semi-freejet	Static pressure	Moule and Smart (2013) and Suraweera and Smart (2009)	Exploratory engine for access-to-space applications.

[a] All inlets are designed with the assumption that they will be installed on a vehicle with a forebody equivalent to a 6° wedge.
[b] This inlet was deliberately designed to be "over-sped", thus the design compression field used a $M = 6$ inflow rather than a $M = 6.7$ inflow (which corresponds to the vehicle design flight speed).

an off-design Mach number (Smart and Trexler, 2004). Despite the design changes, Smart and Trexler (2004) reported that the M7(V2)REST inlet did not self-start at the Mach 4 test condition, a limitation that was overcome by adding 8 boundary layer bleed holes to each side of the inlet. In this configuration, the inlet self-started with a mass capture ratio of 79.7 % and compression ratio 12.6.

Following on from the successful off-design tests, Smart and Ruf (2006) mated the M7(V2)REST with an isolator, divergent combustor and thrust nozzle, thus forming the first complete REST scramjet engine. Shown in Figure 2.3c, the complete engine was tested in the NASA LaRC Combustion Heated Scramjet Test Facility (CHSTF) at Mach 4.5. Gaseous hydrogen fuel was used in conjunction with a silane-hydrogen pilot. Instrumentation consisted primarily of static pressure transducers and surface thermocouples. A six-component force balance was also used but facility-model interactions in the LaRC CHSTF prevented net force data from being measured; only the force increment due to combustion could be quantified. Furthermore, Smart and Ruf (2006) did not provide any details concerning the geometry of the isolator, combustor, nozzle or fuel injection station and all plots were shown in the paper without axis limits.

Shown in Figure 2.3d, the M8REST-RF engine was developed by Turner and Smart (2010) for the purpose of evaluating the application of inlet fuel injection and the radical-farming concept (Gardner et al., 2002; Odam, 2004; Odam and Paull, 2007) to a three-dimensional engine. This engine was the first REST engine to be designed at The University of Queensland and was the third engine overall. Experiments were conducted in the T4 Stalker Tube at Mach 6.6, corresponding to flight at Mach 8 with a vehicle forebody equivalent to a 6° wedge. Instrumented with surface static pressure transducers in the engine symmetry plane, experimental results reported by Turner and Smart (2010) demonstrated the first successful use of inlet fuel injection in a REST scramjet. No evidence of combustion within the inlet was observed and the inlet remained started up to an equivalence ratio of 0.92. Compared with fuel injection in the combustor, inlet injection produced substantial pressure rise within the engine (Turner and Smart, 2008).

The fourth and most current REST engine to be developed is the M12REST engine which is shown in Figure 2.3e. Unlike the other REST inlets, which have been designed for vehicles flying below Mach 8, the M12REST engine was developed by Suraweera and Smart (2009) as an exploratory engine for examining the applicability of the REST design methodology for access-to-space applications. This engine is of particular interest for this thesis and so its performance and design are discussed in detail in Section 2.2.1.

The set of experimental data amassed so far for the REST family of inlets indicates that these inlets are a viable fixed-geometry, three-dimensional design. The inlets have shown an ability to self-start and operate over a large Mach number range below the design point. Results have also shown

that these inlets are able to accept inlet injection of fuel, a feature that is expected to be important at higher flight speeds where the required mixing length is large. However, surveying the information in Table 2.1 and photographs of Figure 2.3 it can be seen that

1. Each engine has featured a short forebody. No REST inlet has yet been tested with a forebody sized by the shock-on-lip criterion at the design flight Mach number.
2. Each engine has been tested in semi-freejet mode with the facility nozzle delivering flow equivalent to post-forebody shock conditions. No REST inlet has been tested with the presence of the vehicle forebody shock and forebody flow spillage.
3. Instrumentation of the engines has typically consisted of surface pressure measurements and thermocouples.

Hence, although each REST engine has been designed to be integrated with a vehicle, the effects of airframe integration, and in particular the ingestion of a thick forebody boundary layer by the inlet and flow non-uniformity due to forebody flow spillage, have not been examined to date. Similarly, the net aerodynamic performance of an airframe integrated REST engine module has also not yet been quantified.

2.2.1 M12REST *engine*

The M12REST engine was designed in 2006 by Prof. Michael Smart and Dr. Milinda Suraweera as a research engine to examine the operation of a hydrogen fuelled scramjet at speeds relevant to access-to-space. Assuming installation on a vehicle with a forebody equivalent to a 6° wedge, the inlet was developed for flight at Mach 12 with operation down to Mach 6 at a freestream dynamic pressure of 50 kPa. To complete the engine, the inlet was combined with a short forebody plate, an elliptical combustor and a generic conical nozzle as shown in Figure 2.4.

Fuel was supplied to the engine through two injection stations, one part-way along the inlet and one at a 2.5 mm circumferential step that served as the start of the combustor (Figure 2.5). The inlet injection station consisted of 3 portholes, 4 mm in diameter and angled at 45° to the local flow. The step injection station consisted of 48 portholes, 1.5 mm in diameter, positioned at the mid-height of the step and angled at 10° to the axis of the inlet. Sonic injection of hydrogen fuel from either or both fuelling stations could be achieved and it was found that the fuelling configuration had a significant effect on the engine performance. Further details pertaining to the engine design and experimental model may be found in Suraweera and Smart (2009).

The assembled engine was tested by Suraweera and Smart (2009) in semi-freejet mode in the T4 Stalker Tube at conditions equivalent to flight

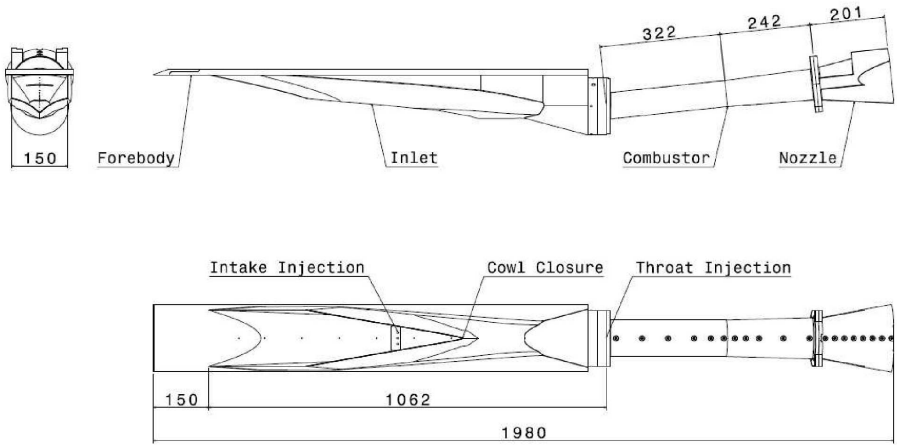

Figure 2.4 – Schematic of the design-scale M12REST engine (Suraweera and Smart, 2009)

at Mach 8.7. Four different fuelling configurations were examined: inlet injection, step injection and two combined injection schemes. The ratio of fuel mass flow injected through the inlet station to fuel mass flow injected through the step station was 9:11 for the first combined injection scheme and 1:2 for the second combined injection scheme.

The pressure profiles obtained for each configuration at various total fuel equivalence ratios are discussed in detail by Suraweera and Smart (2009) and so will not be repeated here. Quasi-one dimensional cycle analysis results are reported by Moule and Smart (2013). In all cases, significant pressure rise due to sustained supersonic combustion was observed. Figure 2.6 shows the estimated thrust coefficient for each fuelling scheme and total fuel equivalence ratio from which it can be seen that intake injection performed best at low fuel equivalence ratios ($\phi < 0.5$), step injection performed best in the midrange ($0.6 < \phi < 0.8$) before leveling off, and the two combined fuelling schemes produced the same thrust as each other and out-performed injection from the step for high fuel equivalence ratios ($\phi > 0.8$).

Plateauing of the step injection results with increasing fuel equivalence ratio is indicative of mixing-limited combustion.[2] Increasing the available mixing length, which is achieved in this engine by injection of fuel from the inlet station, is expected to increase the thrust levels obtained. However, increasing pressure in the inlet and isolator resulted in inlet unstart at $\phi = 0.62$ for inlet-only injection. Steady pressure levels were maintained at $\phi =$

2 In this thesis mixing-limited combustion is distinguished from mixing-controlled combustion. Mixing-limited combustion refers to the case where, for a particular cross-section, the combustion induced pressure rise does not increase with fuel equivalence ratio. Mixing-controlled combustion refers to the case where the distribution of combustion induced pressure rise along a duct is governed by the rate at which fuel and air are mixed.

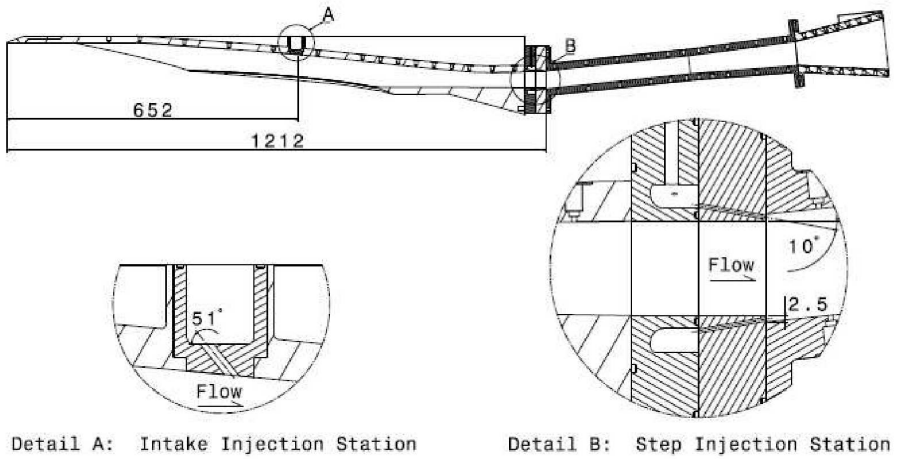

Figure 2.5 – Schematic of the fuelling stations of the design-scale M12REST engine (Suraweera and Smart, 2009)

0.40. Thus, inlet-only injection is limited in its useability. In comparison, by injecting the majority of fuel at the step, the combined injection schemes utilise the longer mixing length available from intake injection while ensuring that the inlet remains started at high total fuel equivalence ratios. In terms of both the combustion induced pressure rise within the engine and the estimated thrust coefficient (Figure 2.6), the two combined injection schemes were observed by Suraweera and Smart (2009) to give the best performance.

So far in this section the performance characteristics of the internal M12REST flowpath have been discussed in terms of the thrust coefficient while no mention has been made on how the thrust was calculated. Following the explanation given by Suraweera and Smart (2009), the thrust coefficient was calculated from the combination of the experimental pressure distribution in the combustor and nozzle, a computational fluid dynamics (CFD) pressure distribution in the inlet and a CFD fuel-off skin friction distribution thoughout the engine. This methodology is a limitation of this style of engine test. Though performance comparisons at different flight conditions, fuelling configurations or injectors may be made, the actual performance can only be approximately determined due to the lack of experimental skin friction data and the coarse resolution of the pressure data. This situation is most directly resolved by utilisation of a force balance which directly measures the total integrated forces acting on the engine, and so accounts for the many complex interactions and flow features.

Two important points must be noted regarding the thrust coefficient data plotted in Figure 2.6. Firstly, the estimated thrust coefficients calculated for each fuelling configuration do not include any effects of skin friction

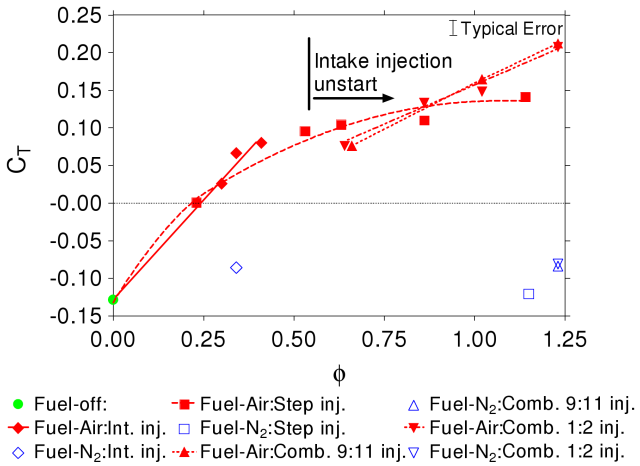

Figure 2.6 – Internal thrust coefficient for the M12REST engine at conditions equivalent to Mach 8.7 flight (Suraweera and Smart, 2009)

reduction due to combustion of fuel within the boundary layer (Kirchhartz et al., 2012; Stalker, 2005). Suraweera and Smart (2009) estimate that these effects could increase the thrust levels by *at least* 50 % and 35 % for the step and combined injection schemes, respectively. This is a significant increase. Secondly, the thrust nozzle used was a generic conical nozzle with an area ratio of 8 with respect to the inlet throat. For an idealized axisymmetric engine, Stalker et al. (2005, Figure 7) demonstrated that increasing the nozzle area ratio from 5 to 10 resulted in a thrust increase of approximately 20 %. Therefore, the thrust coefficient values calculated by Suraweera and Smart (2009) for the M12REST engine are not expected to change significantly if a larger area ratio nozzle was fitted. However, while not strongly dependent on the area ratio, the nozzle thrust is strongly influenced by the overall design and integration of the nozzle with the engine and airframe (Hirschen et al., 2009; Tanimizu et al., 2009). When multiple REST engines are integrated with a notionally two-dimensional vehicle, the thrust nozzle for each engine will need to undergo shape transition from the elliptical combustor to a two-dimensional single-expansion ramp. Similarly, for axisymmetric vehicles like that studied by Jazra et al. (2013), the thrust nozzle will need to transition from the elliptical combustor to match the circular aftbody of the vehicle (which has a curvature that is negative with respect to the upper half of the combustor ellipse). The optimal design of shape-transitioning, three-dimensional, thrust nozzles is a complex design problem that has implications for both the engine and vehicle performance. Thus, although the M12REST flowpath results of Suraweera and Smart (2009) are encouraging and demonstrate the potential performance of the flowpath, further work is required, particularly in terms of the development of a suitable thrust nozzle and the determination of the integrated

performance of a single engine module.

2.3 Force balance testing of scramjets

Force balance testing of scramjet engines and vehicles is difficult in general and becomes more difficult as the flight speed moves beyond Mach 8. This section provides an overview of previous scramjet force balance testing. It will be seen that the majority of tests have been conducted in continuous facilities that have test times of tens of seconds or longer. Furthermore, most experiments involving force balances focus on determining force-increments rather than the net aerodynamic forces.

2.3.1 *National Aeronautics and Space Administration*

Hyper-X, shown in Figure 2.7, was nasa's experimental hypersonic flight vehicle. In comparison with the goals of the much larger nasp program of the 1980s and early 1990s, the Hyper-X program aimed to fly a relatively small-scaled airframe-integrated, scramjet powered vechicle in an effort to demonstrate the associated family of technologies and design methodologies. Two Mach 7 flights and one Mach 10 flight were planned and of these, one Mach 7 flight and the Mach 10 flight were successful.

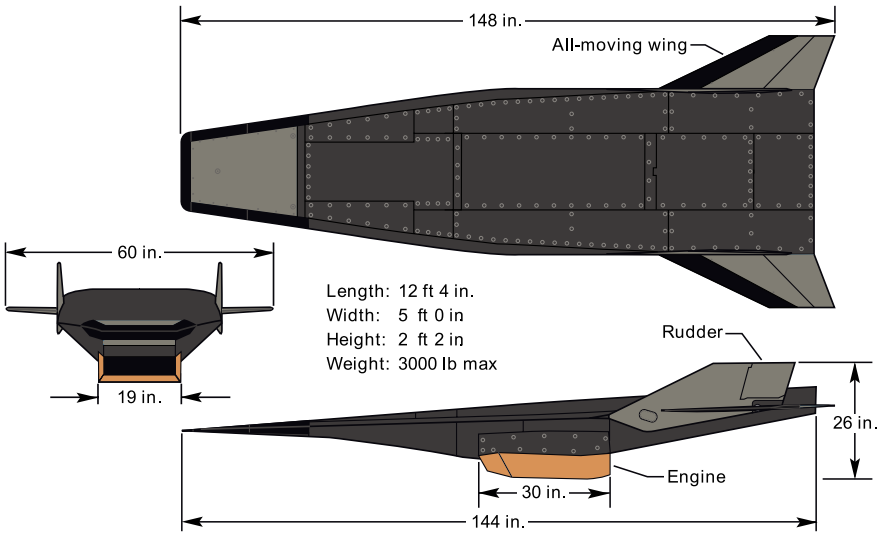

Figure 2.7 – nasa's Hyper-X flight vehicle (Marshall and Corpening, 2005)

The aerodynamic and propulsive database amassed over the course of the Hyper-X program was perhaps the most comprehensive ever developed for a hypersonic vehicle (Voland et al., 2006), and it relied heavily

on the consolidation of computational predictions and experimental data. The backbone of the database was high-quality experimental aerodynamic data obtained for the inlet-closed vehicle using small-scale models ($< 20\,\%$ full-scale), tested in continuous facilities (Engelund et al., 2001; Holland et al., 2001).

Force and moment increments associated with opening the inlet cowl and engine operation were primarily determined through validated analytical and CFD analyses (Cockrell et al., 2001). In essence, a two-step process was used: First, the computational tools were benchmarked against the inlet-closed aerodynamic data. Next, the tools were used to calculate the inlet-open and fuel-on force and moment increments. For the Mach 7 flight condition, the predicted force and moment were experimentally verified by full-scale propulsion flowpath tests that were conducted in the NASA Langley Research Center (LaRC) 8-ft High Temperature Tunnel (8-ft HTT; Engelund et al., 2001). The results of these validation processes are shown in Figure 2.8a and Figure 2.8b and, as is typical with most Hyper-X associated publications, the scale of the vertical axes has not been given. Overall the authors claim very good agreement between the various results.

The model used for the full-scale propulsion flowpath tests is shown in Figure 2.9. It consisted of the Hyper-X Flight Engine (HXFE) mounted to the Vehicle Flowpath Simulator (VFS), which together provided a complete tip-to-tail replication of the lower flowpath surfaces of the flight vehicle. The incomplete representation of the entire vehicle and interference from the pedestal mount restricted the force measurement to incremental data only.

Ground testing at speeds beyond Mach 8 is limited to impulse facilities such as reflected-shock and shock-expansion tunnels. The influence of this fact on the Hyper-X program is very obvious. Unlike the numerous long duration full-scale propulsion tests conducted for the Mach 7 flight, a much smaller set of experiments, conducted using the HyPulse and LENS reflected-shock tunnels were completed for the Mach 10 flight condition (Ferlemann, 2005; Rogers et al., 2001). The model tested in the HyPulse facility was a full-scale height, partial width and truncated length engine. The experiments were conducted in semi-direct-connect mode. In constrast, the model tested in the LENS facility was a full-scale replica of the Mach 10 engine, though, with the exception of a single paragraph in the paper by Ferlemann (2005), there is very little mention of the LENS Hyper-X tests in the literature.

Furthermore, in comparison with the Mach 7 ground tests, there were no direct measurements of the propulsive aerodynamic coefficients at the Mach 10 flight condition.[3] This is despite the necessary tools existing (see

3 This statement is based on the lack of any force data in the papers of Bakos et al. (1999), Ferlemann (2005), and Rogers et al. (2005, 2001). It is quite possible that force measurements were taken; however, they have not been published.

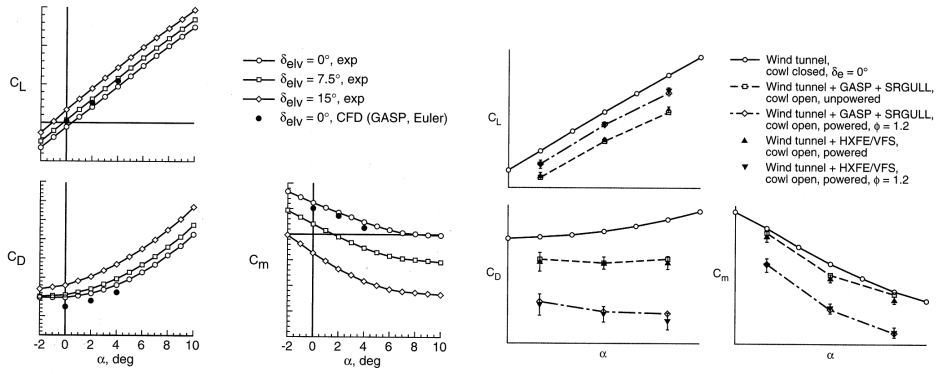

(a) Mach 6 aerodynamic coefficients for various elevator deflections.

(b) Aerodynamic coefficients for inlet-open unpowered and powered modes.

Figure 2.8 – Comparison of computational predictions and combined wind tunnel data (Engelund et al., 2001)

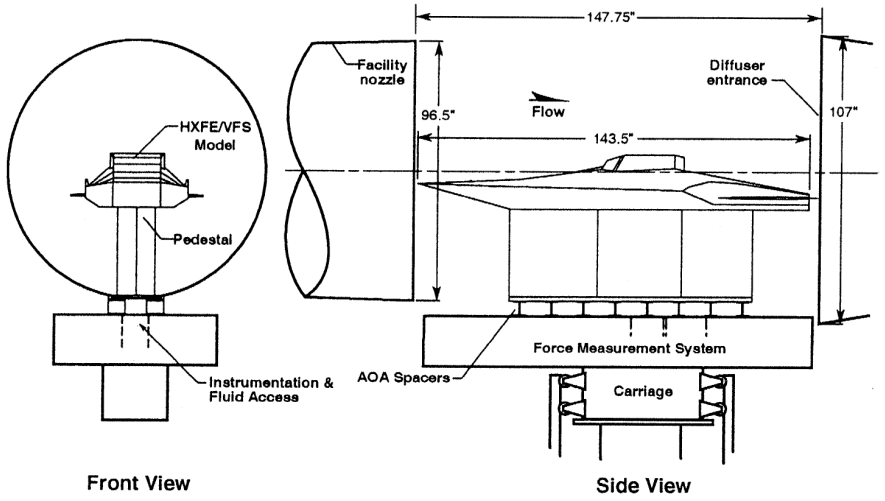

Figure 2.9 – Hyper-X vfs and hxfe installation in the nasa larc 8-ft htt (Cockrell et al., 2001)

for e.g. Takahashi et al., 1999). The engine data recorded at the Mach 10 condition consisted of surface static pressure measurements, thin-film heat flux gauges and a Pitot pressure rake that was used to survey the forebody flow (Bakos et al., 1999). The forebody flow was also visualised using a high-speed Schlieren system. The pressure measurements were compared with and used to validate the computational tools. Furthermore, to increase confidence in the Mach 10 results, the Mach 7 flowpath was tested at its design condition in HyPulse, thus allowing comparison with the experimental data obtained from long-duration tests (Bakos et al., 1999; Rogers et al., 2001).

The HYPER-X program completed two successful flights, one at Mach 7[4] and one at Mach 10. For each flight, the measured data reasonably matched the design predictions (Ferlemann, 2005; Ferlemann et al., 2005). Despite its complexity, the design methodology used during the HYPER-X program was ultimately validated by the success of the flights.

2.3.2 *Japan Aerospace Exploration Agency*

The Japan Aerospace Exploration Agency (JAXA) has been an active contributor to the field of supersonic combustion research for many years and, in comparison with NASA, more freely publishes their scramjet engine data (Kanda et al., 2001). As with any research organisation, the available facilites have influenced the research undertaken at JAXA. The two primary scramjet research facilities operated by JAXA at the Kakuda Research Center (KRC) are the HIEST Stalker Tube (high-enthalpy, reflected shock tunnel) and the vitiated blowdown Ramjet Engine Test Facility (RJTF). Force balance experiments that have been conducted in each of these facilities are briefly reviewed in this section.

The RJTF is able to generate test flows up to Mach 8 at an altitude of 35 km (Yatsuyanagi et al., 1998). Consequently a significant proportion of the research at JAXA has focussed on scramjet and dual-mode scramjet combustion up to Mach 8. As a part of its infrastructure, the RJTF includes a three-component force balance which permits the determination of the thrust/drag, lift and pitching moment of large scale scramjet engines ($\approx 2\,\text{m}$ in length and $\approx 0.2\,\text{m}$ in width and height). Shown in Figure 2.10a, this balance is based on a floating frame arrangement in which four load cells are used to determine the aerodynamic forces acting on the model (Shimura et al., 2001). Kanda et al. (2002) states that the balance is able to resolve forces to within $\pm 50\,\text{N}$, corresponding approximately to $\pm 7.5\,\%$ and $\pm 5\,\%$ of the fuel-off lift and drag, respectively. The standard configuration for the scramjet engine studied at JAXA is shown in Figure 2.10b.

4 This was the second flight at Mach 7. Although the first Mach 7 flight failed, the failure was due to the rocket booster and not the X-43A scramjet vehicle (Marshall and Corpening, 2005).

The engine has a relatively simple shape, featuring a 6° (half-angle) wedge sidewall compression inlet with sweptback leading edges and a central strut.

Shimura et al. (2001) studied the thrust, lift and pitching moment for different configurations at Mach 4, 6 and 8 flight conditions, finding that thrust increased linearly with fuel mass flow until engine unstart occurred, at which point the thrust significantly decreased and the lift significantly increased. Net thrust was observed at the Mach 6 condition but not at the Mach 4 or 8 conditions (at each condition the strut configuration was different), a result that was due to the installation drag of the supporting structure. Mitani et al. (2003) provide a good overview of the various configurations that have been studied and indicate that net internal thrust has been demonstrated at Mach 4, 6 and 8 conditions for the internal flowpath, with the magnitude decreasing with increasing flight speed (as expected).

Similar to the strategy used by NASA during the HYPER-X program, JAXA researchers regularly discuss and compare engine configurations based on the internal thrust increment due to combustion. The focus on internal performance is justified by Mitani et al. (2003) who state that internal drag is intrinsically related to irreversible processes through the engine but that external drag is dependent on integration of the engine with the vehicle and, on a per-engine basis, decreases when engines are stacked side-by-side. Despite this justification for focussing on the internal performance of an engine, JAXA researchers have also reported, albeit briefly, on the external and installation drag of the engine. Consequently a number of interesting results have been obtained including, (1) agreement to within 5 % for the drag obtained from the force balance and that obtained from integration of the measured pressure distribution and estimated skin friction distribution (see Figure 2.11 and Mitani et al., 2002, 1999); (2) experimental demonstration that the external drag and total fuel-off internal drag are comparable (Mitani et al., 1999), and (3) demonstration that the internal viscous drag accounts for significantly more than 50 % of the total internal drag (Mitani et al., 2002).

The HIEST Stalker Tube has been in operation since 1997 and is capable of generating nozzle supply enthalpies up to 25 MJ/kg and nozzle supply pressures up to 150 MPa. As a part of its infastructure, JAXA have developed a free-flight accelerometer-based force balance (Takahashi et al., 1999; Tanno et al., 2005). Shown in Figure 2.12, this balance is a single-component force balance that has been used with engine models up to 3 m in length (Itoh, 2005). Since 2005 JAXA has regularly used this balance to study scramjet engine performance at enthalpies in the range of 4 to 9 MJ/kg. Initially, JAXA examined the single wedge engine configuration shown in Figure 2.13a. However, difficulty in maintaining intensive combustion (Takahashi et al., 2005) and high viscous drag in the long combustor (Rowan et al., 2005) have seen JAXA shift to the three-ramp design shown

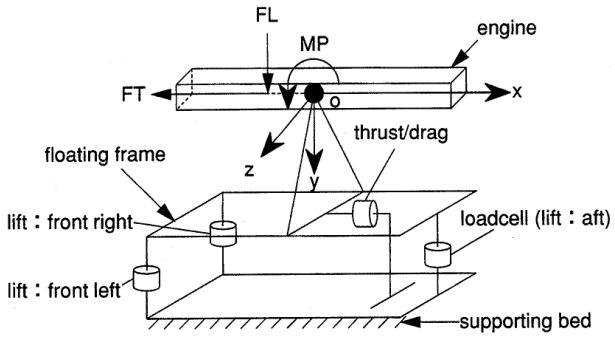

(a) Schematic of the force balance used in the RJTF (Shimura et al., 2001).

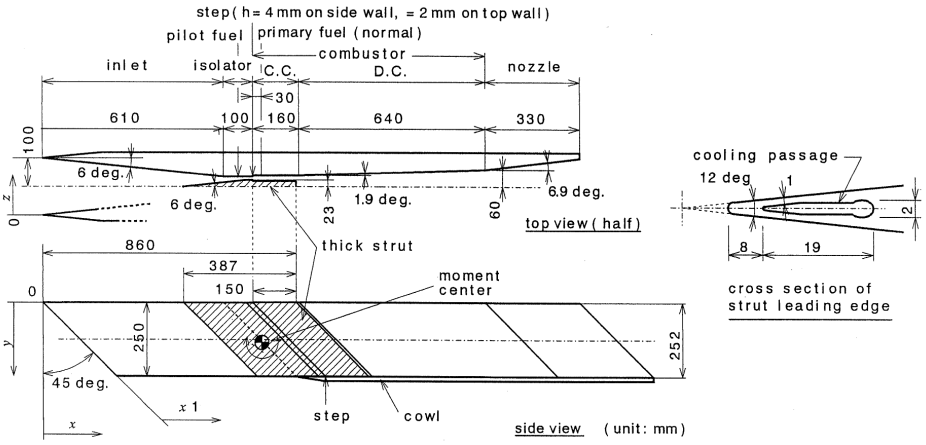

(b) Sidewall compression, water-cooled scramjet engine (Kanda et al., 2001).

Figure 2.10 – Scramjet model and force balance studied and used in RJTF

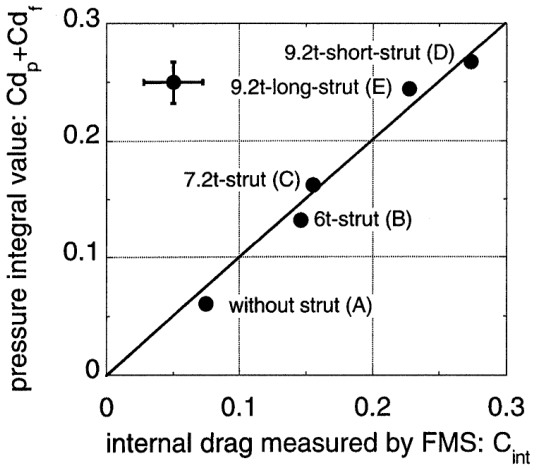

Figure 2.11 – Comparison of the measured internal drag and that calculated from the measured pressure distribution (Mitani et al., 2002)

in Figure 2.13b. This engine was designed so that the combustor entrance pressure was double that of the previous engines, resulting in increased combustion pressures despite the decreased combustor length (Takahashi et al., 2006).

Experimental thrust coefficient and specific impulse data measured by JAXA for various Mach 12 scramjet engines are plotted in Figure 2.14. To date, JAXA has yet to demonstrate net thrust with its Mach 12 engines (Figure 2.14b), though the specific impulse increment has improved with each design iteration (Figure 2.14c). The dominance of the viscous drag in Figure 2.14a is reflective of the very long combustor used for the M12-02 design and is consistent with the assertion of Stalker (2006b) that viscous drag is a significant portion of the total drag at sub-orbital velocities. Furthermore, it is interesting to note that for the M12-02 engine, the simple backward-facing step injector performed the best, demonstrating that complex injector configurations may not be required for scramjets operating at flight enthalpies above 4 MJ/kg.

Table 2.2 – Typical HIEST Test Conditions used for the JAXA Mach 12 Engine Experiments

		Condition			
Quantity	Units	A	B	C	D
M_f		9	10	12	14
$p_{0,f}$	MPa	30	30	30	30
$H_{0,f}$	MJ/kg	4	5	7	9
T_e	K	330	440	630	950
p_e	kPa	3.0	2.8	3.5	3.8
M_e		7.5	7.2	6.8	6.4

Despite the interesting results obtained by JAXA for the Mach 12 engines, they are not representative of what could be expected in flight. Table 2.2, adapted from Takahashi et al. (2006), shows the conditions at which the JAXA Mach 12 engines are typically tested. Despite the enthalpy being matched to various flight Mach numbers, neither the freestream temperature nor the freestream Mach number are matched and thus the test conditions do not replicate a flight condition. With no mention of an assumed vehicle forebody in any of the relevant papers, it may be concluded that the motivation for the experiments must be to either gather data for the validation of numerical simulations or to examine fundamental combustion performance over a range of enthalpies.

Finally, it may be said that the regularity and consistency with which force data are presented and used by the JAXA researchers is something to which other institutes can aspire. In combination with internal pressure measurements, force data greatly assists with understanding and comparing various engine designs.

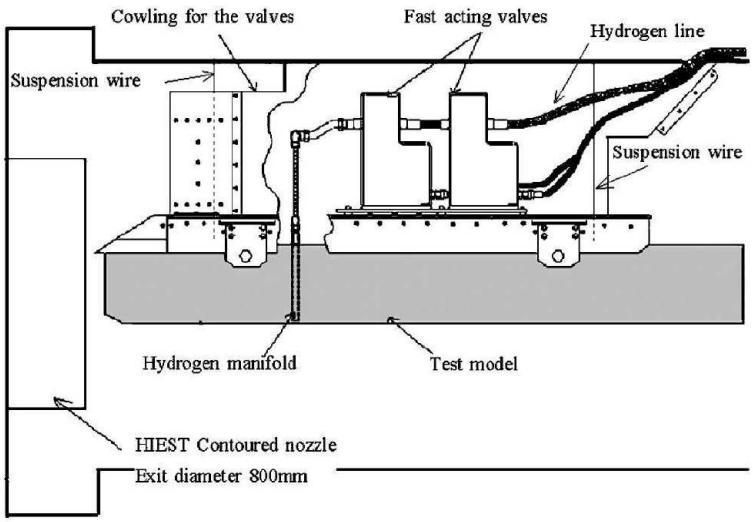

Figure 2.12 – Single-component free-flight force balance used in HIEST (Tanno et al., 2005)

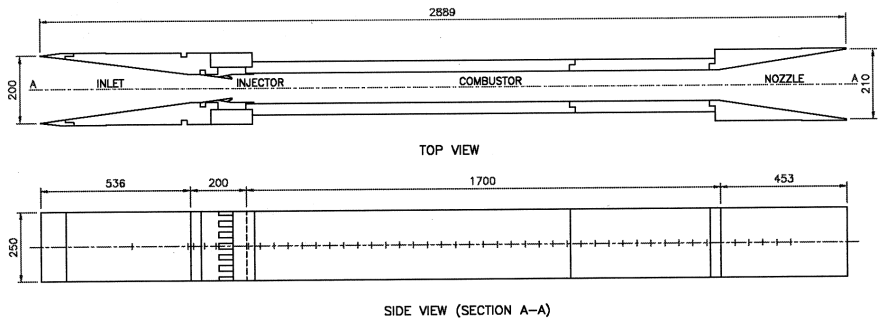

(a) M12-02 engine configuration (Rowan et al., 2005)

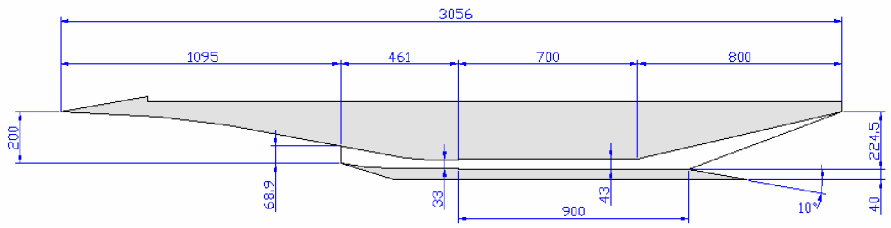

(b) M12-03 engine configuration (Takahashi et al., 2006)

Figure 2.13 – Basic Mach 12 scramjet engine configurations studied by JAXA since 2005

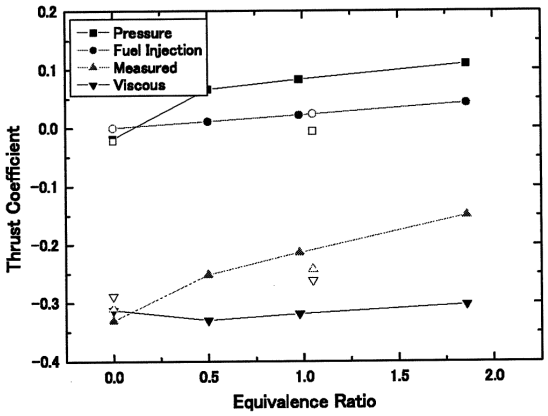

(a) Thrust coefficient for the M12-02 engine at a 7 MJ/kg test condition. The injection configuration was 40 % hyper-mixer, 60 % slot injection with $\phi_T = 1$ (Rowan et al., 2005).

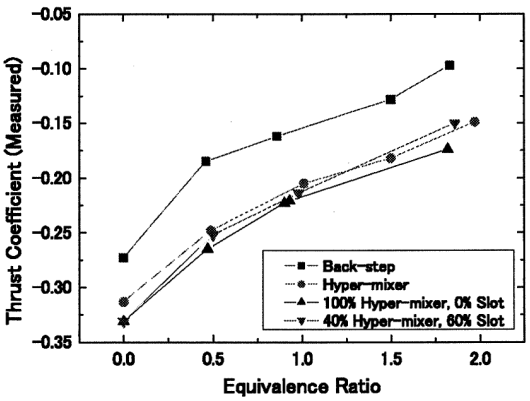

(b) Comparison of the thrust coefficient for different injection configurations for the M12-02 engine at a 7 MJ/kg test condition and with $\phi = 1$ (Rowan et al., 2005)

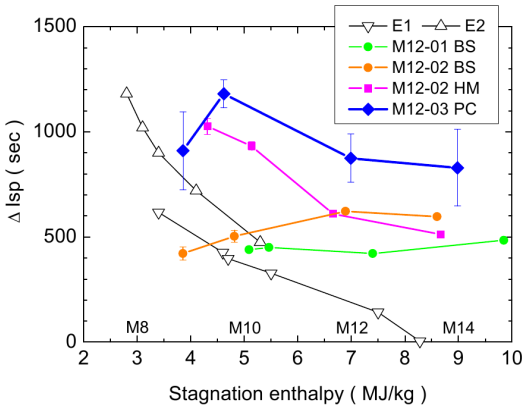

(c) Specific impulse increment for various designs (Takahashi et al., 2006). Note that engines E1 and E2 are Mach 8 engines like that shown in Figure 2.10b. BS=Backward facing step injector, HM=Hyper-mixer injector, PC=Parallel combustor with swept ramp injector.

Figure 2.14 – Experimental thrust coefficient and specific impulse increment measured by JAXA for various Mach 12 engines

2.3.3 *The University of Queensland*

In comparison with the blowdown hypersonic facilities available at NASA and JAXA, the primary scramjet facility at The University of Queensland (UQ) is the T4 Stalker Tube, a free-piston driven reflected-shock tunnel. This impulse facility generates steady test times of several milliseconds or less and so the measurement of aerodynamic force cannot be accomplished with standard load-cell based balances like that of the NASA 8-ft HTT (Figure 2.9) or the JAXA RJTF (Figure 2.10a).

A method pioneered and developed by researchers at UQ for the measurement of aerodynamic forces within impulse facilities is known as the stress wave force measurement technique (SWFMT). First proposed by Sanderson and Simmons (1991), the SWFMT is based on the principle that when the test time becomes very small, the model and its support structure do not reach equilibrium and, by measuring the propagation of stress waves in a properly designed support, the forces on the model may be inferred.

Initially used to examine drag on axisymmetric models (see, for example, Porter et al., 1994; Smith and Mee, 1996a; Tuttle et al., 1995), the technique was quickly extended to allow investigation of non-axisymmetric geometries and multiple force components (see, for example, Simmons et al., 1993). Tuttle et al. (1994) attempted to measure the thrust generated by a two-dimensional scramjet nozzle[5] but asymmetric loading adversely affected the quality of the results (Tuttle, 1996). The first complete scramjet engine to be tested on a stress wave force balance was a quasi-axisymmetric engine (Paull et al., 1995a,b). A modified version of this engine was later used by Tanimizu et al. (2009, 2011) as the basis for a nozzle optimization study. The quasi-axisymmetric engine was followed by a symmetric engine consisting of two scramjets back-to-back (Stalker and Paull, 1998). Finally, the development of a three-component force balance by Robinson (2003d) allowed the thrust/drag, lift and pitching moment of a single scramjet engine to be experimentally measured within an impulsive hypersonic facility. These engines are briefly discussed in the following paragraphs.

The quasi-axisymmetric scramjet studied by Paull et al. (1995a,b) is shown in Figure 2.15. Note that the entire engine and fuel system were mounted to the force balance. This engine was tested at a nominal Mach number of 6 with the nozzle supply enthalpy varied between 2.8 MJ/kg and 8.5 MJ/kg. Hydrogen fuel alone did not combust and so a 13 % silane, 87 % hydrogen mixture was used at fuel equivalence ratios up to 0.8. The performance of this engine is compared with analytical predictions in Figure 2.16. The analytical predictions were obtained by using established theories to estimate the pressure and shear stress distributions. Overall, the experimental trends were well matched by the analytical predictions.

5 Only the nozzle was attached to the force balance.

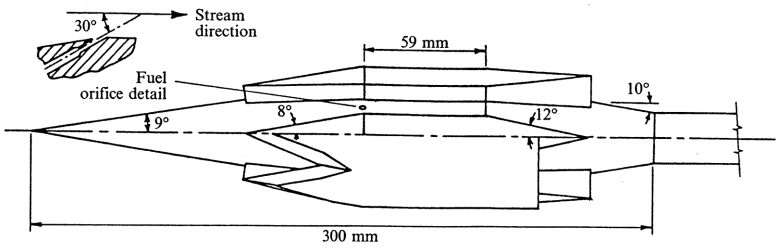

(a) The scramjet model

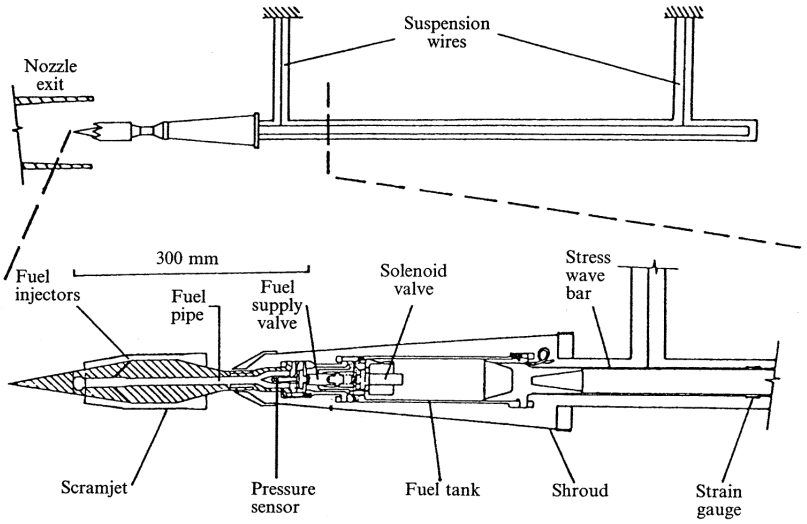

(b) Model and force balance

Figure 2.15 – The axisymmetric scramjet and force balance arrangement studied by Paull et al. (1995a)

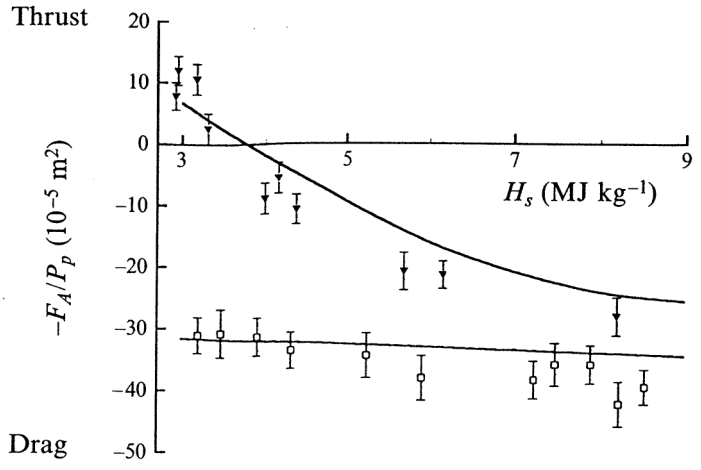

Figure 2.16 – Resultant axial force measured for a quasi-axisymmetric scramjet for fuel-on (solid symbols) and fuel-off (open symbols) (Paull et al., 1995a)

Although the performance of the quasi-axisymmetric engine was quite poor, with net thrust being produced over a very limited range of nozzle supply enthalpies, the results plotted in Figure 2.16 represent the first experimental demonstration of net thrust production for a scramjet engine. Paull et al. (1995a) and further discussions by Stalker et al. (2005) postulate a number of reasons for this poor performance including the need to use a silane-hydrogen mixture, an inability to fuel at stoichoimetric equivalence ratios (due to thermal choking), poor thrust nozzle design, and high inviscid and viscous drag levels. Some but not all of these factors may be mitigated by improving the design of the engine. Paull et al. (1995a) state clearly that the engine was designed to allow for ease of analysis and manufacturing, and not for optimum performance. The research was focussed on the validation of the SWFMT technique for high velocity testing of scramjet engines and in this respect was successful.

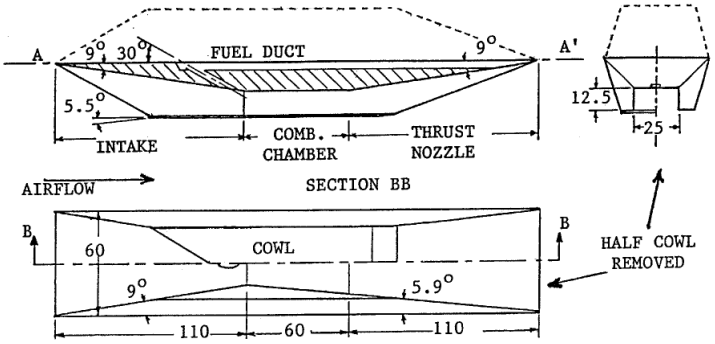

Figure 2.17 – Hydrogen fuelled cruise scramjet model (Stalker and Paull, 1998)

The second scramjet engine to be examined at UQ using the SWFMT is shown in Figure 2.17. Although the model is not axisymmetric, two engines placed back-to-back were used to ensure that only axial forces were generated. Once again, the design of the engine focussed on ease of manufacture and analysis rather than outright performance (Stalker and Paull, 1998). Despite this, the engine achieved cruise (i.e. thrust equal drag) at a Mach number of 6.4, total enthalpy of 3.5 MJ/kg and hydrogen fuel equivalence ratio of $\phi = 1$ without the use any ignition aids. Simple analysis was again able to predict the fuel-off drag reasonably well, but not the fuel-on performance.

The next scramjet engine to be discussed is shown in Figure 2.18a. Continued development of the SWFMT eventually made it possible to measure three components of force on a two-dimensional scramjet engine that was 0.6 m in length. The three-component force balance is discussed in detail in Chapter 4 and so only the scramjet engine results will be covered here. As with previous force balance scramjet models at UQ, the engine shown in Figure 2.18a was designed primarily for the evaluation

of the force balance (Robinson, 2003d).

The thrust, lift and pitching moment coefficients measured for the engine are shown in Figures 2.18b to 2.18d for tests at a Mach number of 6.6, a stagnation enthalpy of 3.3 MJ/kg and a freestream static pressure of 7.0 kPa (Robinson, 2003d). Good comparison with predictions was obtained for the thrust and lift forces with both increasing linearly with fuel mass flow rate. The poor prediction of the pitching moment was attributed by Robinson et al. (2006) to inaccurate estimation of the pressure distribution on the latter part of the thrust surface. In comparison with the purely analytical method used by Paull et al. (1995a) (for example), Robinson (2003d) made use of simple CFD simulations and some of the measured pressure data to determine the theoretical forces. The increase in lift and pitch-down moment are both attributed to increased pressure on the thrust surface arising from combustion of the fuel.

Examining Figure 2.18b it can be seen that the engine was approaching cruise at a fuel equivalence ratio of 1.4. This result suggests that incomplete combustion occured (Stalker et al., 2005). Furthermore, it is likely that this result is a consequence of the simple design of the engine. Overall however, the results of the experiments of (Robinson et al., 2006) demonstrate that it is possible to accurately measure the thrust, lift and pitching moment of a single scramjet engine in a shock tunnel.

Any scramjet engine that is used as a part of an access-to-space system will be required to operate over a large Mach number range. Recognizing this fact, Tanimizu et al. (2009, 2011) have recently revisited the quasi-axisymmetric engine design of Paull et al. (1995a). Two new models were developed by Tanimizu (2008). These are compared with the engine of Paull et al. (1995a) in Figure 2.19a. Model 1 featured an identical intake to model 0 but was fitted with a larger area ratio nozzle (8.65 compared with 5.8). Model 2 was designed for flight at Mach 8 and featured a shorter, divergent combustor than either model 0 or 1.

Models 1 and 2 were tested in the T4 Stalker Tube across a range of nozzle supply using three different facility nozzles – the Mach 6 nozzle, the Mach 8B nozzle and the Mach 10B nozzle. Measured drag coefficient data for model 1 are compared with a theorectical prediction in Figure 2.19b. The theoretical prediction compares well with the experimental results over the full range of test conditions examined. The variation in drag is dominated by the variation in the unit Reynolds number of the test flow[6] which affects the surface viscous force. With the force prediction methodology validated, Tanimizu et al. (2011) used model 2 as the basis for a nozzle optimization study, finding that for this type of engine, the benefit of increasing the nozzle area ratio by deflecting the external cowl surfaces was counteracted by an increase in inviscid drag on the external cowl.

6 For fixed facility nozzle, increasing the nozzle supply enthalpy decreases the Mach number and unit Reynolds number of the test flow.

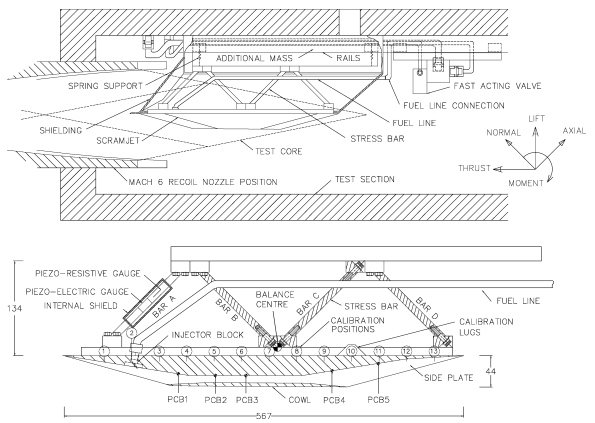

(a) Scramjet model

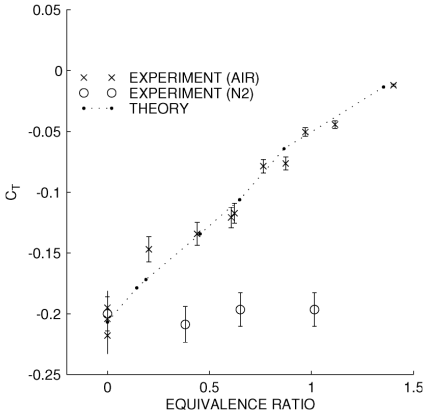

(b) Thrust coefficient data

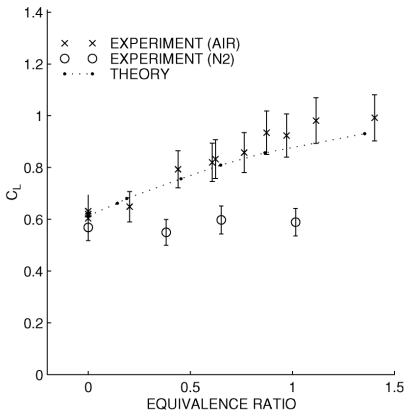

(c) Lift coefficient data

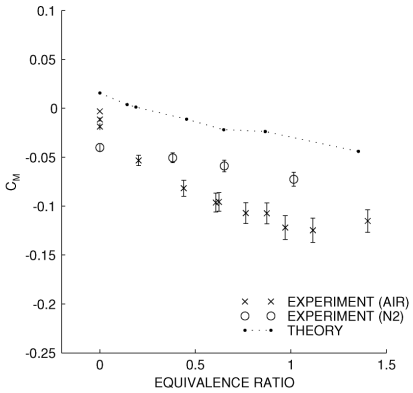

(d) Pitching moment coefficient data

Figure 2.18 – The three-component force balance and resulting measured scramjet engine data produced by Robinson et al. (2006)

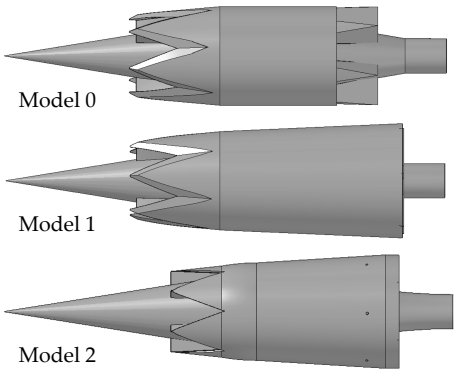

(a) Quasi-axisymmetric scramjet engines

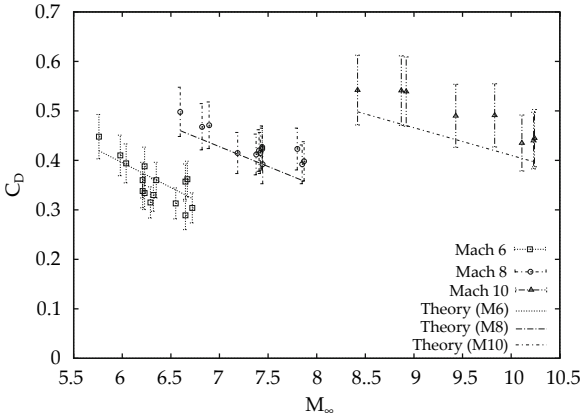

(b) Variation in drag coefficient for model 1

Figure 2.19 – Quasi-axisymmetric engines investigated by Tanimizu et al. (2009, 2011)

The basic geometry therefore limits the maximum attainable performance. Tanimizu et al. (2009) estimate that this type of engine is likely to be limited to flight below Mach 8.

2.4 SUMMARY

The preceeding literature review has established that the majority of scramjet engine force balance tests have been conducted in intermitent or continous flow facilities using quite large engine models. Furthermore, the majority of these tests have focussed on the internal thrust increment associated with the injection and combustion of fuel rather than the net aerodynamic forces. Though some force balance testing has been conducted at UQ in an impulse facility, these tests have mostly focussed on small-scale, simple geometry models that have been designed to evaluate the stress wave force measurement technique rather than being designed for good net performance.

The review has also shown that three-dimensional, fixed-geometry inlets, which smoothly transition from a quasi-rectangular capture area to an elliptical throat, offer promising performance attributes compared with relatively simple two-dimensional geometries. However, no force balance testing of a REST-based engine has been completed and so the true aerodynamic characteristics of this class of engine are still unknown.

FACILITY, MODEL AND TEST FLOW CONDITIONS

The third chapter, in which we describe the wind tunnel facility, discuss the test flow conditions and concern ourselves with details of the experimental model, thereby laying the second foundations of the thesis.

3

3.1 INTRODUCTION

The methodology of this thesis was primarily experimental and, as such, the goals of this chapter and the next are to provide descriptions of the apparatus that was used. The three pillars that underlie this thesis are:

1. the T4 Stalker Tube developed by Stalker (1966, 1967, 1989);
2. the internal flowpath of the M12REST scramjet engine developed by Suraweera and Smart (2009); and,
3. the three-component force balance developed by Robinson (2003d).

The first two are described in dedicated sections of this chapter while the force balance, due to its complexity, is described separately in Chapter 4. We begin the current chapter with a brief overview of the test facility, the T4 Stalker Tube, in Section 3.2. The Mach 10B contoured nozzle is also described in this section prior to a summary of the facility instrumentation and data acquisition system. Section 3.3 discusses the calculation of the nozzle supply and test flow properties as well as presenting equivalent flight conditions. Section 3.4 focusses on the M12REST engine. An overview of the design of the airframe integrated engine is given first, followed by summaries of the instrumentation, hydrogen fuel delivery system and the mounting and positioning of the engine within the test section. The final section of this chapter, Section 3.5, focusses on the data reduction methods that have been used in this thesis. Flow establishment over the model and the selection of an appropriate test time are discussed, and the calculation of normalised pressure detailed.

3.2 TEST FACILITY

3.2.1 *The T4 Stalker Tube*

The experiments reported in this thesis were carried out in The University of Queensland's T4 Stalker Tube (Stalker, 1966, 1967, 1989). Shown schematically in Figure 3.1, this facility is a free-piston driven reflected

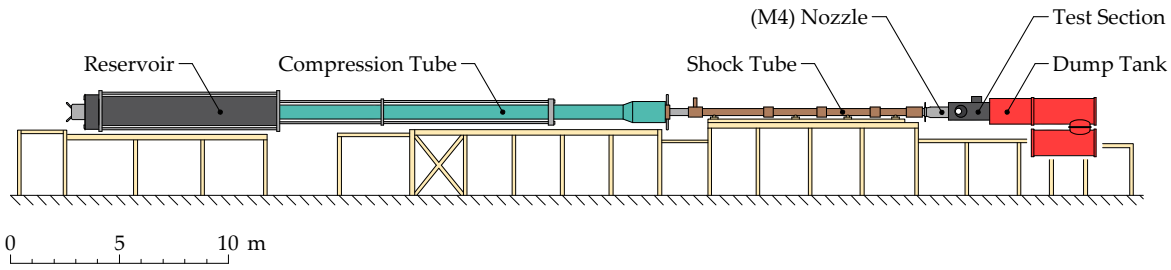

Figure 3.1 – Schematic of The University of Queensland's T4 Stalker Tube. Adapted from Suraweera (2006).

shock tunnel that was commissioned in 1987 and has been in continual use and development ever since (Stalker, 2006b; Stalker et al., 2005). Falling into the class of wind tunnels known as impulse facilities (Lu and Marren, 2002), the T4 Stalker Tube is capable of generating flows with enthalpies in the range 3 to 15 MJ/kg and total pressures up to 90 MPa. Although somewhat dependent on the facility dimensions and driver mechanism, the ability to produce high total pressure flows with enthalpies above 3 MJ/kg comes at a cost of the available flow duration. Steady test times are typically limited to a few milliseconds[1] within the T4 Stalker Tube.

The facility is comprised of six main sections: a reservoir, compression tube, shock tube, contoured convergent-divergent nozzle, test section and dump tank. The compression tube has a length of 26 m and an internal diameter of 230 mm. The shock tube has a length of 10 m and an internal diameter of 76 mm (Stalker and Morgan, 1988). The reservoir and compression tube are separated by a 90.4 kg free piston.[2] A steel plate, known as the primary diaphram, separates the shock tube from the compression tube and a secondary mylar diaphram separates the shock tube from the nozzle, test section and dump tank.

Prior to an experiment, otherwise known as a shot, and in preparation for filling each section of the tunnel with the required gas, the facility is evacuated to a pressure less than 133 Pa (1 torr). The shock tube is then filled with the test gas, either dry air or nitrogen, the compression tube is filled with the driver gas, either argon, helium or a mixture of the two, and the reservior is filled with high pressure air. The dump tank and test section remain evacuated. The filling pressure of each section of the facility, driver gas mixture, thickness of the primary diaphragm and nozzle area ratio dictate the resulting test flow properties. For this thesis the T4 Stalker Tube was operated at two different Mach 10 test conditions: a high

1 A discussion of flow establishment and selection of the test period is provided in Section 3.5.1.

2 The piston mass was measured in early 2013 by Mr. Philippe Lorrain and Dr. Stefan Brieschenk. This mass includes all o-rings and brakes.

pressure test condition representing flight at a dynamic pressure of 48 kPa and a low pressure test condition representing flight at a dynamic pressure of 28 kPa. The filling requirements for each test condition are provided in Table 3.1.

Table 3.1 – Filling Conditions

		Units	Low Pressure	High Pressure
Reservoir	$p_{RES,f}$	MPa	6.5	12.5
Compression Tube	$p_{CT,f}$	kPa	80.5	156
	%Ar	—	60	45
	%He	—	40	55
Shock Tube	$p_{ST,f}$	kPa	160	250
Primary Diaphragm		mm	6	6

Once each section of the facility is filled, the experiment is initiated by allowing the piston to be accelerated by the high pressure gas in the reservoir. The single stroke of the piston occurs sufficiently fast that the driver gas is compressed almost adiabatically to the rupture pressure of the primary diaphragm. Upon rupture, the hot, high pressure driver gas expands into the shock tube driving a normal shock along the length of the tube. This primary shock processes the gas in the shock tube, increasing its temperature and pressure and accelerating it in the laboratory reference frame. The velocity of the piston is tuned so that when the primary diaphragm ruptures the volume of driver gas displaced by the piston matches the volume of driver gas entering the shock tube (Stalker, 1967).

At the downstream end of the shock tube, the secondary diaphragm is located at the throat of a convergent-divergent nozzle. When the primary shock reaches the downstream end of the shock tube, the wall boundary condition (see section 7.3 in Anderson, 2003) requires the formation of a reflected shock. This reflected shock travels back upstream and processes the oncoming test gas, further increasing the temperature and pressure and reducing the axial velocity of the gas to (near) zero.[3] The post-reflected shock, quasi-steady conditions of the test gas at the downstream end of the shock tube are known as the nozzle supply conditions. This very hot, high pressure gas ruptures the secondary diaphragm and expands through the converging-diverging nozzle to produce the test flow. These major wave processes are depicted in Figure 3.2 in the form of an x–t diagram. Further discussion and analysis of free-piston driven reflected shock tunnels and expansion tunnels may be found in the work of Stalker (1966, 1967, 1989, 2006a) and Gildfind et al. (2011).

Nominal nozzle supply conditions for each test condition are provided

3 The actual gas dynamic processes occuring in this region of the shock tube are far more complex than the simple, one-dimensional and idealised explanation given here. Interested readers are referred to the computational study by Goozée et al. (2006).

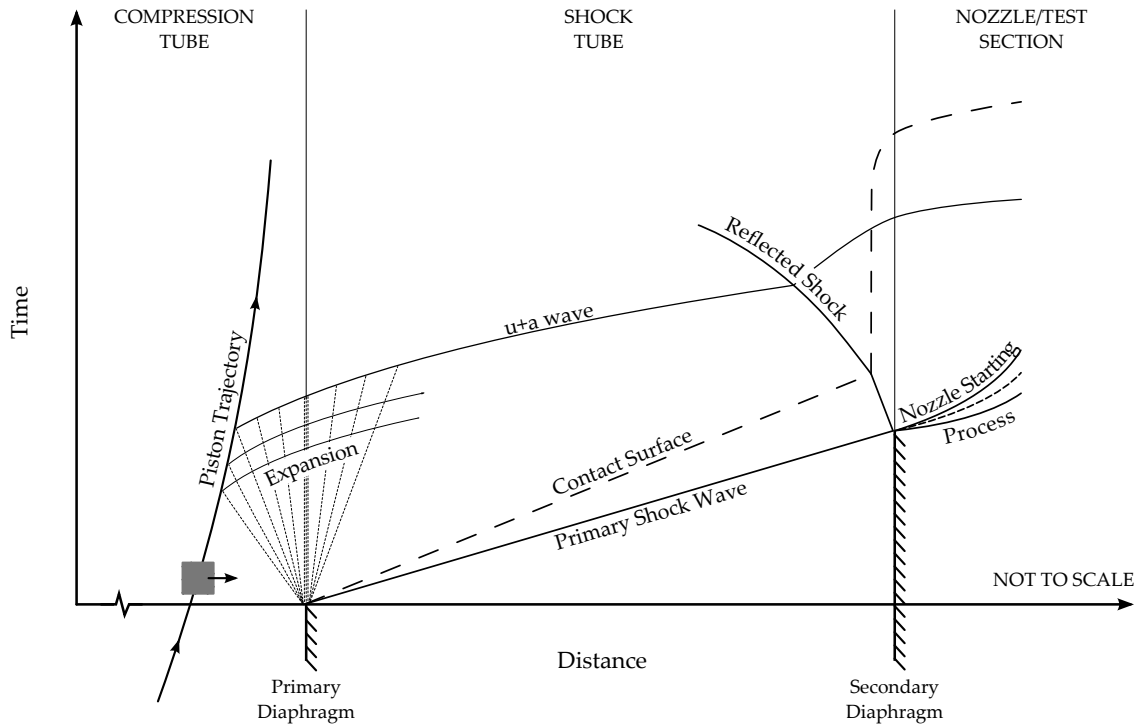

Figure 3.2 – Distance-Time diagram depicting the basic wave processes of a generic Stalker Tube. Adapted from Gildfind et al. (2011), Hess (2009), and Stalker (1967).

in Table 3.2 along with the experimental uncertainty for a single shot. Calculation of the uncertainty is detailed in Appendix C. The measured shock speed and nozzle supply pressure for each shot conducted for this thesis are plotted in Figure 3.3. For comparison the nominal values and experimental uncertainty are also plotted. Nozzle supply conditions for each individual shot are listed in Table L.1.

Figure 3.3 provides a good visual representation of the repeatability of each condition. Throughout a test campaign, the shot-to-shot variation of the nozzle supply and test flow properties was described using second-order polynomial response surfaces. The domain size of each response surface was chosen to be $\pm 6\,\%$ and $\pm 15\,\%$ of the nominal shock speed and nozzle supply pressure, respectively, and are indicated in Figure 3.3 by rectangular boxes. Clearly this range proved sufficient to cover the majority of shots conducted for this thesis. Finally, note that the nozzle supply density, temperature and enthalpy are not measured directly during an experiment but are inferred from a reflected shock calculation using the measured (primary) shock speed and nozzle supply pressure and assuming that the compressed and heated test gas remains in chemical and thermal equilibrium. Calculation of the supply conditions and the response surface methodology are discussed further in Section 3.3.

Table 3.2 – Nominal Shock Speed and Nozzle Supply Conditions. The quoted experimental uncertainties are for a single shot.

	Units	Low Pressure[a]		High Pressure[b]	
u_{ss}	m/s	2300	$\pm$ 115	2195	$\pm$ 110
p_s	MPa	40.1	$\pm$ 1.4	71.5	$\pm$ 2.6
T_s	K	3909	$\pm$ 195	3837	$\pm$ 196
ρ_s	kg/m^3	35.1	$\pm$ 2.2	64.2	$\pm$ 3.9
H_s	MJ/kg	4.96	$\pm$ 0.37	4.78	$\pm$ 0.35

[a] Based on all campaign 2 low pressure shots.
[b] Based on campaign 2 shots 10954, 10955, 10960, 10962, 10973, 10974 and 10975.

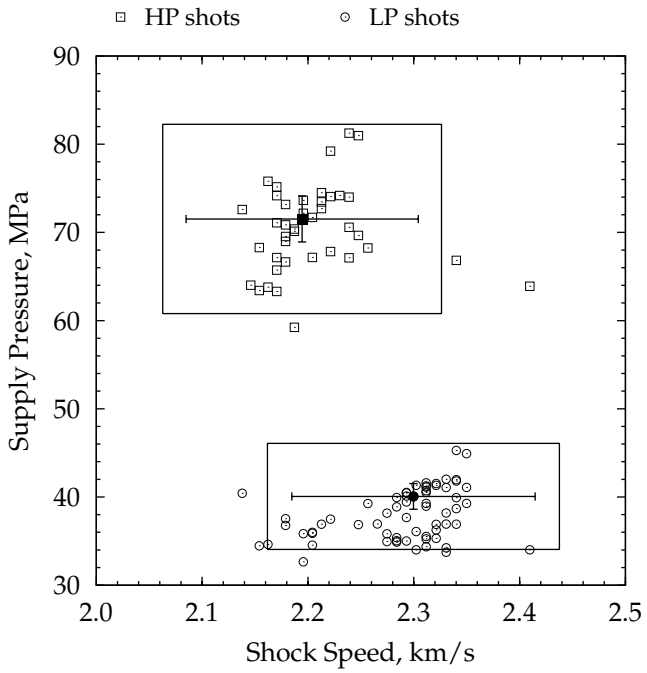

Figure 3.3 – Repeatability of the Mach 10 test conditions. Individual shots are plotted as open symbols. The nominal conditions, as given in Table 3.2, are plotted as solid symbols along with the experimental uncertainty. The boxes indicate the design domain of the response surface for each condition.

3.2.2 *Mach 10B Contoured Nozzle*

A Mach 10 contoured nozzle was used for these experiments. It has a throat diameter of 9.52 mm and an exit diameter of 378.6 mm, giving a total geometric area ratio of 1580. Measuring from the throat, the nozzle has a total length of 1640 mm. Bezier control points that define the nozzle contour may be found in Doherty (2013a).

The Mach 10B nozzle is the largest nozzle currently in use with the T4 Stalker Tube and its size brings with it both advantages and disadvantages. As shown in Figure 3.18 the large exit diameter and contoured geometry of the nozzle produce a large core flow diamond that extends well upstream and downstream of the nozzle exit plane and exhibits good uniformity. Experimental Pitot pressure profiles plotted in Figure 3.4 indicate a core flow radius greater than 130 mm at approximately 150 mm downstream of the nozzle exit. Furthermore, the reasonable comparison between numerical and experimental results displayed in Figure 3.4 provides confidence in the nozzle flow field computations.[4]

Although the large core makes the Mach 10 nozzle suitable for freejet testing of moderately sized scramjets at close to true flight conditions, the high Mach number, low freestream static pressure and overall length of the nozzle adversely affect the starting time and subsequently the available test time (see Doherty and Wise, 2013, and Section 3.5.1 of this report). Ensuring that the pressure in the facility nozzle and test section was less than 66 Pa (0.5 Torr) prior to flow onset and late injection of fuel in the scramjet (Section 3.4.5 and Appendix H.3) were each found to be important for minimising the flow establishment time of the nozzle and engine flow fields.

Additionally, the nozzle throat is subject to very high thermal loads that have in the past caused significant erosion of material despite the short flow duration. Previously, the nozzle throat was made from a copper alloy that would last approximately 10 shots. Initial attempts at replacing the copper throat with one machined from a titanium-zirconium-molybdenum (TZM) alloy were unsuccessful. The TZM throat component failed by chipping at the interface with the downstream supersonic expansion component (Suraweera and Smart, 2008). Thermal-structural analysis completed by Williams (2010) indicated that this failure was caused by a thermally induced stress concentration resulting from the different thermal expansion of the TZM throat component and copper supersonic expansion component. Williams (2010) analysis showed that using TZM for both the nozzle throat and supersonic expansion would alleviate the stress concentration.

4 Note however, that the usefulness of Pitot pressure as a validation measurement for nozzle flow field simulations is limited for two reasons. Firstly, the experimental measurement is inherently noisy (McGilvray et al., 2009). Secondly, once downstream of the nozzle exit plane the Pitot pressure profile is relatively insensitive (when compared with static pressure, temperature or velocity) to changes in the computational inputs (Doherty, 2013a).

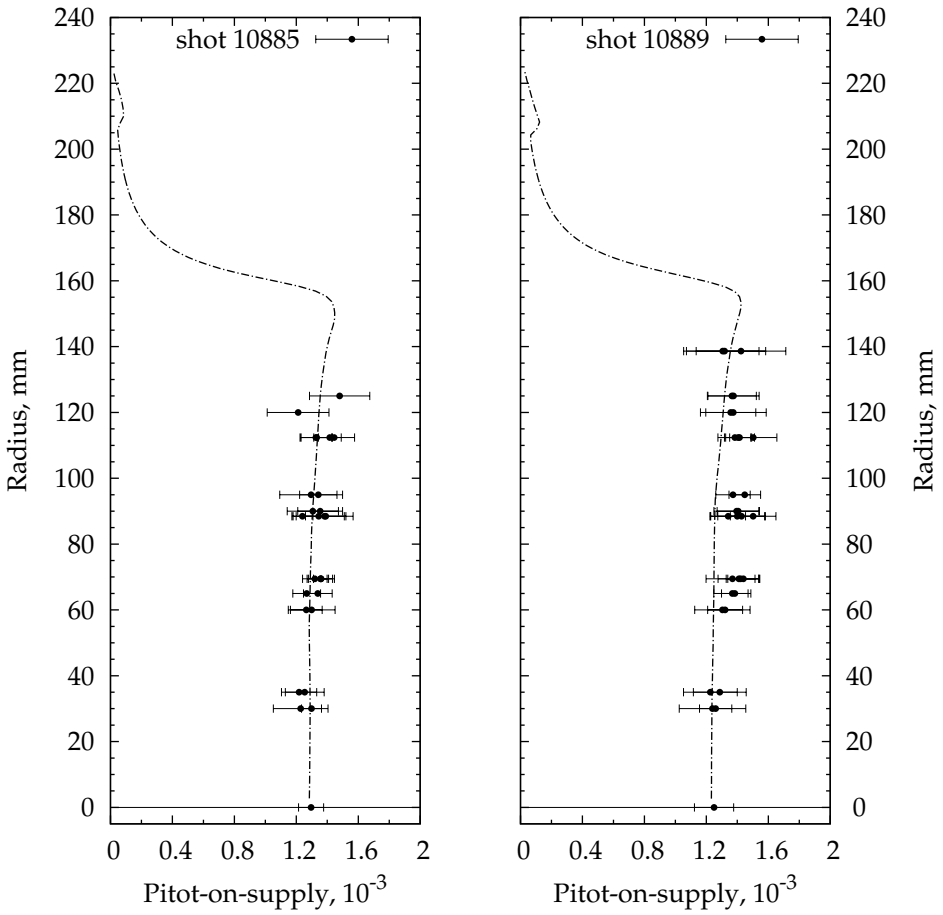

(a) Low pressure test condition (b) High pressure test condition

Figure 3.4 – Comparison of experimental and computational Pitot-on-supply pressure ratio for each test condition. The Pitot rake was located (135 ± 2) mm downstream of the nozzle exit plane for the low pressure condition and (165 ± 2) mm for the high pressure condition. The error bars indicate one standard deviation of the variation during the test time. Adapted from Doherty and Wise (2013).

(a) New TZM throat fitted prior to the start of campaign 1.

(b) TZM throat directly after shot 10762. This was the 22nd shot of campaign 1.

Figure 3.5 – Comparison of the nozzle throat insert component before and after a high pressure Mach 10 shot

Prior to the first shot conducted for this thesis, a new TZM supersonic expansion and nozzle throat insert were fitted to the nozzle. This configuration subsequently completed 60 successive shots without incurring damage due to erosion or chipping. Photographs of the throat component before and after a high pressure shot are shown in Figure 3.5. Material, clearly seen in Figure 3.5b and hypothesised to originate from the walls of the shock tube, was deposited and baked onto the surface of the throat during each shot. A similar fine dust was also deposited on the inner surface of the supersonic expansion and contoured sections of the nozzle. After each shot this dust cleaned from the nozzle throat and expansion surfaces.

3.2.3 *Instrumentation*

Minimal instrumentation was used on the facility itself however, each measurement was crucial for the analysis of the test conditions (described in Section 3.3). The speed of the primary shock wave was measured using three uncalibrated Kistler Type 601H gauges that were linked in series and spaced at intervals of 2.003 m.

The nozzle supply pressure was measured using two PCB® model 101M91 transducers, each of which feature a ceramic coating to thermally protect the transducer. Labelled as SPA and SPB, the measurement uncertainty of these gauges was $\pm 3.7\,\%$ and $\pm 3.6\,\%$, respectively (Appendix C.3). Typically the average of the two measurements would be used when calculating the nozzle supply conditions however, as shown in Figure 3.6, at some point prior to this work the ceramic coating on the head of gauge SPA was chipped. Consequently, only gauge SPB was used for data processing in this thesis. Appendix A describes the calibration of these transducers using a hydraulic rig and provides sample calibration data.

The movement of the facility during a shot was measured using a Mea-

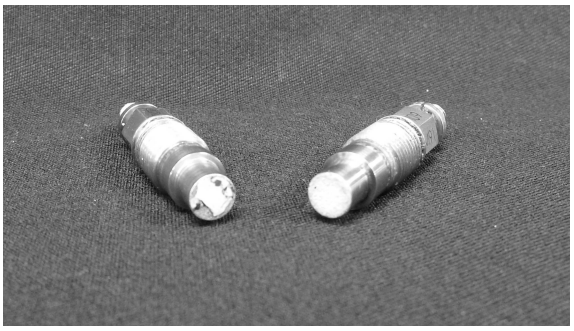

Figure 3.6 – Nozzle supply pressure transducers. Gauge SPA is shown on the left, gauge SPB on the right.

surement Specialties™ model DC-EC 5000(MC) linear voltage displacement transducer (LVDT). The maximum recoil was (161 ± 3) mm for a high pressure shot and (134 ± 3) mm for a low pressure shot.[5] The facility movement was measured for two reasons. Firstly, the recoil measurement was used to trigger the fuel solenoid valve and initiate flow to the fuel plenums prior to flow arrival at the model (Section 3.4.5). Secondly, determination of the model postion with respect to the nozzle exit plane is important and requires knowledge of the facility movement during a shot.

Finally, all data were recorded using National Instruments™ PXI-6133 14-bit cards connected to a PXI-8196 controller (Ridings, 2012). BNC-2090A adapters were also employed to ensure ease of use with Kulite® and PCB® transducers. The engine and nozzle supply pressure data were recorded using a 1 MHz sampling rate (1 µs timebase). Fuel plenum pressure and force balance strain data were recorded using a 200 kHz sampling rate (5 µs timebase) and the tunnel recoil was recorded using a 2.5 kHz sampling rate (400 µs timebase).[6]

3.3 TEST FLOW CONDITIONS

3.3.1 *Calculation of Test Flow Properties*

The nozzle exit conditions obtained during a test were calculated using the Centre for Hypersonics (CfH) in-house program NENZFR[7] (Doherty, Chan, et al., 2012). This program was developed to provide a relatively rapid cal-

5 The uncertainty quoted for the recoil represents one standard deviation of the shot-to-shot repeatability across both test campaigns that were completed for this thesis.

6 Discussed in Appendix H.3, the operation of the engine was found to be sensitive to timing of fuel injection. The large timebase used for the facility recoil (which in turn triggers the fuel valve) adversely affected the repeatability of fuel injection. For future experiments with this engine it is recommended that the facility recoil be measured on a 5 µs timebase, consistent with the fuel plenum pressure transducers.

7 Non-Equilibrium Nozzle Flow Reloaded

culation of the nozzle flow while still accounting for the multi-dimensional expansion of the test gas, including non-equilibrium chemistry and viscous effects. NENZFR was thus intended to become a replacement for the legacy Fortran code, NENZF (Lordi et al., 1966). NENZFR consists of a set of Python programs that couple the calculation of the nozzle supply conditions using ESTCj (Jacobs et al., 2011) with a 2-D axisymmetric compressible Reynolds averaged Navier-Stokes (RANS) calculation of the nozzle flow using Eilmer. Eilmer is the CfH in-house CFD code that solves the three-dimensional Navier-Stokes equations for turbulent, chemically reacting, compressible flows; its formulation, verification and validation is described by Gollan and Jacobs (2013) and its user manual and theory book by Jacobs and Gollan (2008) and Jacobs et al. (2010), respectively.

The overall calculation procedure implemented in NENZFR is as follows: Taking the measured primary shock speed, initial filling conditions of the shock tube, and measured nozzle supply pressure as inputs, ESTCj completes a one-dimensional reflected shock calculation assuming chemical and thermal equilibrium. The equilibrium gas properties are taken from the NASA CEA2 database (McBride et al., 2002). The conditions calculated behind the reflected shock are then isentropically expanded to the measured nozzle supply pressure in order to provide an estimate for the nozzle supply conditions. A further isentropic expansion to Mach 1 provides inflow properties for the Eilmer nozzle calculation.

Using the calculated inflow properties and additional user-defined simulation parameters discussed below, NENZFR generates an Eilmer input for the calculation of the nozzle flow. For this thesis, the calculations were performed using a thermally perfect mixture of N_2, O_2, N, O and NO, the reaction scheme of Gupta et al. (1990) and the 2006 Wilcox $k-\omega$ turbulence model. Implementation of this turbulence model within Eilmer was validated by Chan et al. (2012) for several hypersonic test cases.

The boundary layers were solved to the wall assuming the first 100 mm of the nozzle to be laminar. Good comparison between the measured and predicted engine forebody pressure throughout each experimental campaign provided confidence in the appropriateness[8] of this value (see Figure 7.3 and Doherty, 2013a). The laminar-to-turbulent viscosity ratio and turbulence intensity at the throat were taken to be 100 and 5 % respectively.[9] An isothermal wall temperature of 300 K was used for the nozzle

8 No experimental data examining the location of transition exist for the T4 Mach 10B nozzle. Data recorded by Riedmüller (2008) for the T4 Mach 6 nozzle indicated that the boudnary layer was fully turbulent by the first measurement location, 230 mm downstream of the nozzle throat plane.

9 The uncertainty analysis presented in Appendix C indicates that the nozzle exit properties are not very sensitive to these inputs. Although for a different geometry, this is consistent with Chan et al. (2012) who found that changes in the dimensionless velocity profile and skin friction coefficient of a flat plate were small relative to the experimental uncertainty even when the turbulence intensity and viscosity ratio were varied over several orders of magnitude.

walls as this is a good assumption for the test times of several milliseconds in T4.

Once the Eilmer calculation of the nozzle is complete, NENZFR computes averaged test flow properties by conserving the mass, momentum and energy fluxes (Baurle and Gaffney, 2008) at the nozzle exit over a nominated core radius.[10] The frontal area of the scramjet engine used in this work required a core radius of 60 mm (Figure 3.18). The resulting values for each test condition are given in Table 3.3. The quoted uncertainties represent the total uncertainty due to the inputs to NENZFR, the grid convergence error and the spatial variation over the core radius (Appendix C). The predicted nozzle exit properties and flow composition for each shot are provided in Tables L.2 and L.3.

Compared with the inviscid, quasi-one-dimensional method implemented in the legacy code NENZF, NENZFR represents an increase in fidelity for the calculation of test flow properties for the T4 Stalker Tube. The improvement however comes at the cost of computational time, with a typical NENZFR simulation taking on the order of hours to finish[11] rather than the few minutes required by NENZF. To overcome this limitation for test campaigns in which a large number of shots are to be completed, and because it is useful to know the test flow conditions immediately following a shot, a response surface methodology has been implemented in NENZFR whereby the shot-to-shot variation of each nozzle exit property is described using a second-order polynomial function of the shock speed and nozzle supply pressure (Doherty, Chan, et al., 2012). During an experimental campaign, the prepared response surfaces[12] are used to rapidly calculate the nozzle exit conditions for each shot with little loss in accuracy compared with a full NENZFR simulation (Doherty, 2013a).

3.3.2 *Equivalent Flight Conditions*

When conducting sub-scale scramjet engine tests, similitude of the test to flight is typically achieved by keeping the binary scaling parameter ρL constant and simultaneously matching the velocity, temperature, gas composition and fuel equivalence ratio.[13] This technique ensures that the total enthalpy, Mach number, Reynolds number and binary reaction length are matched between full- and sub-scale (Hornung, 1988; Stalker and Pulsonetti, 2004). Because the high pressure condition listed in Table 3.3 represents the upper operational limit of the T4 Stalker Tube, no scaling

10 The nominated core radius should be less than the nominal core radius of the nozzle. Based on the data plotted in Figure 3.4, the T4 Mach 10 nozzle has a nominal core flow radius of approximately 145 mm.

11 Typically, a single NENZFR simulation was run on 8 Intel L5520 2.26 GHz cpus.

12 Individual response surfaces are found *for each* exit flow property and *each* nominal test condition.

13 Other parameters to match include freestream turbulence and acoustic noise level.

Table 3.3 – Nominal Test Flow computed using NENZFR

(a) Flow properties

	Units	Low Pressure		High Pressure	
H	MJ/kg	4.96	± 0.37	4.78	± 0.35
p	Pa	380	± 22	638	± 37
T	K	225	± 22	213	± 20
ρ	kg/m^3	0.005 85	$\pm 0.000\,37$	0.010 37	$\pm 0.000\,64$
u_x	m/s	3089	± 104	3044	± 100
M		10.24	± 0.16	10.38	± 0.16
q	kPa	27.9	± 1.1	48.0	± 1.9
Re_u	$10^6/m$	1.23	± 0.13	2.25	± 0.24
ρu_x	$kg/(s\,m^2)$	18.1	± 0.7	31.5	± 1.3

(b) Flow composition

Species	Low Pressure		High Pressure	
Y_{N2}	0.7322	± 0.0023	0.7336	± 0.0026
Y_{O2}	0.1912	± 0.0033	0.1940	± 0.0032
Y_N	0	± 0	0	± 0
Y_O	0.0020	± 0.0008	0.0008	± 0.0003
Y_{NO}	0.0746	± 0.0048	0.0716	± 0.0054

Table 3.4 – Equivalent Flight Conditions

	Units	Low Pressure	High Pressure
Altitude	km	37.4	33.7
H	MJ/kg	5.01	4.87
p	Pa	408	693
T	K	243	233
ρ	kg/m^3	0.005 85	0.010 37
u_x	m/s	3089	3044
M		9.88	9.95
q	kPa	27.9	48.0
Re_u	$10^6/m$	1.15	2.09
ρu_x	$kg/(s\,m^2)$	18.1	31.6

of the test condition was possible for this thesis despite the M12REST engine being a sub-scale model. Taking account of the free-jet nature of the experiments, equivalent flight conditions are thus defined by matching the experimental density and velocity and using the NASA (1976) atmospheric standard to fix the flight altitude, pressure and temperature. The resulting flight condition data are provided in Table 3.4.

Comparing the values in Tables 3.3 and 3.4, the temperature achieved in the experiment was approximately 20 K lower than the estimated flight value. This difference is within the variation of experimental atmospheric data (NASA, 1976, Figure 25). As a consequence of the static temperature being smaller, the experimental values of total enthalpy, unit Reynolds number and static pressure are also smaller than flight values, whilst the Mach number was slightly larger. The dynamic pressure and mass flux were matched between the experiment and flight. One difference between the test flow and flight conditions is the gas composition – atomic oxygen and nitrous oxide are both present in the test flow but neither are predicted to be present for flight below 80 km altitude (NASA, 1976, Section 1.3.2). These species occur in the test flow because rapid expansion of the nozzle supply gas through the facility nozzle freezes the chemical composition. The test flow composition predicted by NENZFR is consistent with the experimental mass spectrometer measurements made by Boyce et al. (2005b) for the T4 Stalker Tube.

Nozzle exit data for each shot are plotted on velocity-, pressure-, and temperature-altitude maps in Figure 3.7. Constant dynamic pressure and constant Mach number trajectories are indicated on the velocity-altitude map and the variation of atmospheric pressure and temperature, as defined by NASA (1976), are provided on the respective pressure- and temperature-altitude maps. Figure 3.7 clearly shows the differences between the experiment and flight conditions and the effect of shot-to-shot variability on the test flow properties. Nonetheless, the experimental conditions used in this thesis are sufficiently close the respective flight conditions to be considered as true-flight test conditions.

3.3.3 *Forebody Flow Conditions*

The engine studied in this thesis, and which is introduced in Section 3.4, featured a 6° wedge forebody. Post-forebody shock flow conditions are provided in Table 3.5. These are calculated by processing the nozzle exit properties given in Table 3.3 though a 2-D oblique shock assuming a frozen mixture composition. The quoted uncertainties represent the propagated uncertainties of the inputs to NENZFR as explained in Appendix C.5. Forebody flow conditions calculated for each shot are provided in Table L.5.

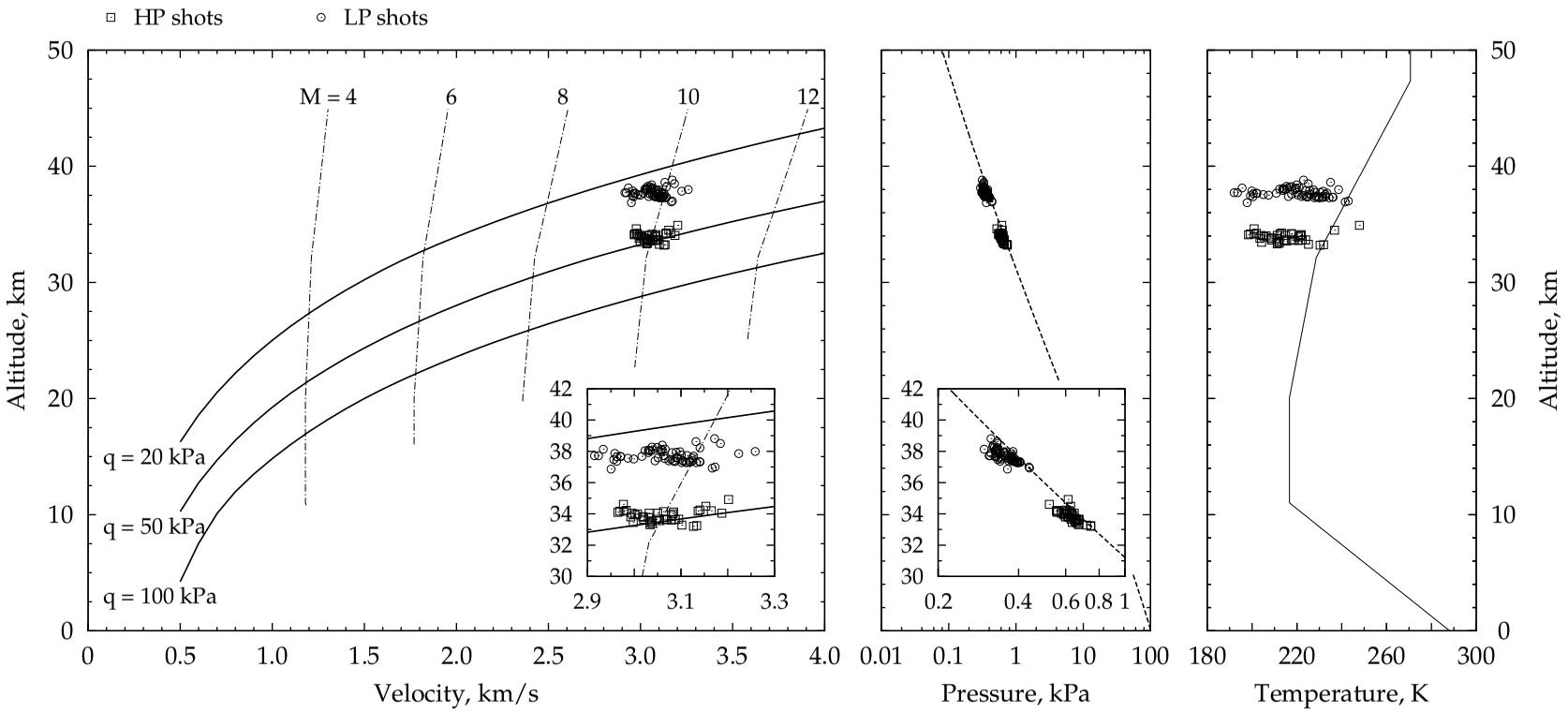

Figure 3.7 – Velocity-altitude, pressure-altitude and temperature-altitude maps of the nozzle exit conditions for each shot. The atmospheric data were calculated using the NASA (1976) standard.

Table 3.5 – Forebody Flow Properties

	Units	Low Pressure		High Pressure	
p	Pa	1427	± 69	2429	± 118
T	K	350	± 31	334	± 29
ρ	kg/m^3	0.0141	± 0.0010	0.0252	± 0.0018
u_x	m/s	3031	± 101	2987	± 98
u_y	m/s	-319	± 12	-314	± 11
M		8.1	± 0.1	8.2	± 0.1
q	kPa	65.6	± 2.6	113.8	± 4.4
Re_u	$10^6/m$	2.07	± 0.20	3.77	± 0.38
$\rho u_{\parallel}$	$kg/(s\,m^2)$	43.0	± 2.1	75.8	± 3.5

3.3.4 *Limitations of Shock Tunnel Testing*

Impulse facilities, of which shock tunnels are one type, are a class of facility capable of generating test flows with total enthalpy and pressure corresponding to flight above Mach 8 (Lu and Marren, 2002). There are however, several limitations of shock tunnel testing, including a short test time, contamination of the test flow with driver gas and the presence of dissociated species in the test flow. These limitations and the suitability of using the T4 Stalker Tube for this thesis are discussed briefly in this section.

The duration of steady flow produced by shock tunnels is typically only a few milliseconds in length. This short duration is a disadvantage because the flow around the model takes time to establish. It is important to ensure that the test time is sufficiently long for the model flow field to achieve a steady state. Davies and Bernstein (1969), among others, studied the establishment of laminar and turbulent boundary layers on a flat plate in a shock tube, correlating the establishment time with the number of flow lengths that pass over the model. Early research conducted at the Centre for Hypersonics also demonstrated that, in the absence of large scale flow separations or wake flow regions, hypersonic duct flows with pressure gradients achieved steady state in the short test time generated by the T4 Stalker Tube (Stalker et al., 2005).

Other disadvantages resulting from a short flow duration include the need for specialised high speed instrumentation (Simmons, 1995), such as the force balance used in this thesis, and the ability to conduct only performance orientated tests. Operational tests, which examine longer duration unsteady flow phenomena such as scramjet inlet starting, and material durability tests, which examine thermal load management, cannot be undertaken in impulse facilities as they require test times on the order of several seconds and minutes or hours, respectively (Marren et al., 2001). In the context of performance, operational and durability tests, a short test

time is also an advantage as it allows fundamental hypersonic phenomena to be investigated in isolation of the difficulties associated with thermal management of the model.

The remaining two limitations to be discussed are contamination of the test flow by driver gas and the presence of dissociated species in the test gas. Depending on the test condition enthalpy, driver gas contamination can limit the available test time (Boyce et al., 2005a). Simple numerical simulations completed by Chan (2012, Appendix G) demonstrate that a level of 10 % (by volume) driver gas delays the ignition process by tens of microseconds but does not affect the other combustion processes, thereby justifying the limit of 10 % contamination for combustion studies in the T4 Stalker Tube. Discussed further in Section 3.5.1, for the test conditions used in this thesis, driver gas contamination of the test flow occurs well after the steady test flow period. As noted in Section 3.3.2, dissociated species such as O, N, and NO may be present in the test gas as a result of rapid expansion of the test gas from the nozzle supply region. The presence of these species affects ignition and reaction of fuel (Han et al., 2004; Pellett et al., 2002). The importance of this influence depends on the goals of the experiment and can be assessed using numerical simulation.

Through careful selection of the test time interval (discussed further in Section 3.5.1), using an appropriately sized experimental model and combining theoretical analysis and numerical simulation with experimental data, each of the limitations identified above can be managed. Since being commissioned in 1987, experiments conducted in the T4 Stalker Tube have produced significant contributions in the field of supersonic combustion research. Stalker et al. (2005) provide an detailed summary covering the period up to 2005. Furthermore, results from the HyShot II flight experiment were found to match results from experiments conducted in the T4 Stalker Tube (Smart, 2006), providing further evidence of the validity and usefulness of shock tunnel testing for the development of scramjet engines.

Finally, it was noted in Section 3.3.2 that although the current experimental model is sub-design-scale, facility operational limits prevented the test condition from being scaled according to the binary scaling methodology $\rho L = \text{constant}$. Noting that the design-scale was chosen somewhat arbitarily, and that the current test conditions are true-flight test conditions (i.e. matched static temperature, pressure and velocity), it is argued here that the inability to scale the test condition does not matter. The experiments reported in this thesis demonstrate how the small-scale airframe integrated M12REST engine operates at the current test condition. This in of itself is useful and interesting, particularly given the airframe integrated nature of the engine and the measurement of aerodynamic forces.

3.4 SMALL-SCALE MACH 12 REST ENGINE

3.4.1 *Scramjet Model*

The scramjet model developed for the current work is shown in Figures 3.8 and 3.9. The internal geometry of the inlet and combustor of this engine were based on the Mach 12 REST engine described in Suraweera and Smart (2009). These were integrated with a forebody and quasi-elliptical nozzle, and the external shape was streamlined to minimise the overall frontal area. The inlet was designed using the methodologies of Smart (1999) with a flight Mach number of 12 and assuming the forebody precompression of the vehicle was equivalent to a six degree wedge. While designed for Mach 12 flight, Suraweera and Smart were also interested in evaluating the engine operation at off-design Mach numbers. Consequently, they chose a design scale that maximised the inlet capture area subject to the size constraint imposed by the core flow diameter produced by the T4 Stalker Tube Mach 8 nozzle. The inlet contraction ratio was determined by the requirement that both the flight dynamic pressure and combustor entrance static pressure should be 0.5 atm. The resulting inlet had a total geometric contraction ratio of 6.61, an internal contraction ratio of 2.26 and a short isolator downstream of the throat.[14]

For the current work, the overall size of the engine was defined by the requirement that the *entire* model fit within the core-flow diamond[15] produced by the Mach 10B nozzle of the test facility as this would be necessary for force balance testing. This resulted in an engine that was 0.32 of the design scale, i.e. approximately one-third scale. The model was 914.8 mm in length, 57.6 mm in width and 102.5 mm in height. The inlet was 339.8 mm in length (excluding the forebody) with a capture area width of 48 mm and a projected area of 3308 mm^2. The projected frontal area of the engine was 5552 mm^2. The inlet leading edges were half-blunt[16] with a radius of of 0.7 mm; this radius was equal to that of the design-scale engine. The forebody leading edge was fully-blunt[16] with a radius of 0.5 mm.

Two fuel injection stations were used on this model. The inlet injection station consisted of three portholes, each 1.3 mm in diameter and angled at 45° to the local surface. As shown in Figure 3.8, this injection station was located 163 mm from the start of the inlet. Scaled directly from the engine developed by Suraweera and Smart (2009), the inlet injectors were sized to enable the fuel jets to penetrate through the inlet boundary layer, thereby

14 The total geometric contraction ratio is calculated with respect to the post-forebody shock inlet capture area, i.e a capture area that is defined by projecting the inlet leading edges parallel to the engine forebody.

15 Note that as the facility nozzle is axisymmetric, the core-flow diamond is actually bi-conic in shape.

16 A half-blunted leading edge has the form  while a fully-blunted leading edge has the form 

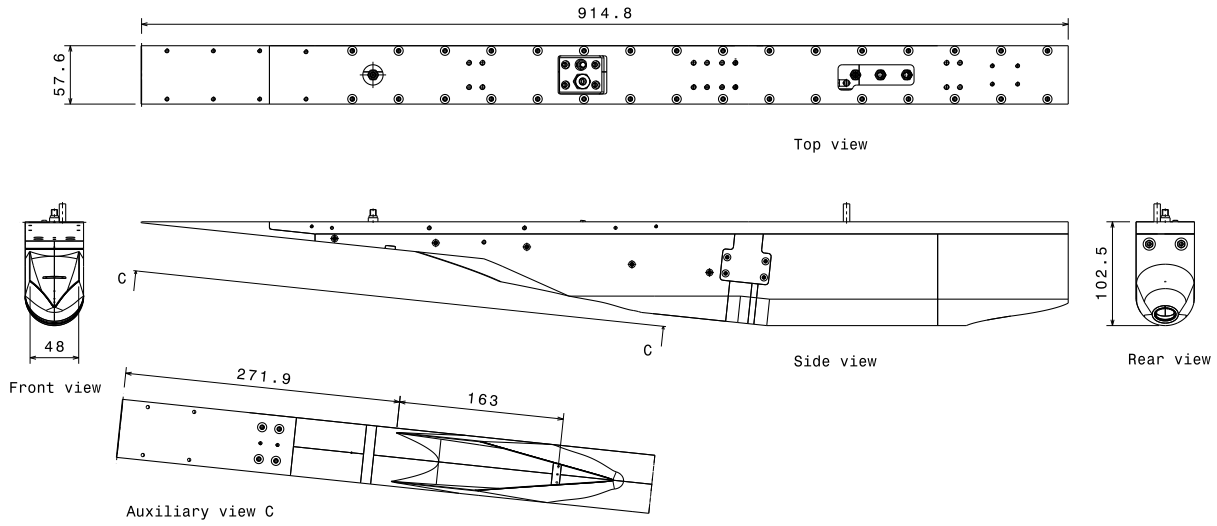

Figure 3.8 – The small-scale Mach 12 REST engine model

facilitating the mixing of fuel with the mainstream flow through the engine. Recent simulations by Barth et al. (2014) however, have demonstrated that when the forebody boundary layer is accounted for, the inlet injected fuel remains entrained in the bodyside boundary layer of the inlet.

The second injection station was located at the combustor entrance behind a rearward facing circumferential step of height 0.8 mm. This step injection station consisted of 24 portholes, each 0.65 mm in diameter and angled at 15° to the axis of the isolator. These injectors were designed to entrain fuel in the engine boundary layer (Doherty, 2013b; Suraweera and Smart, 2009), thereby benefitting from skin friction reduction through boundary layer combustion (Goyne et al., 2000; Stalker, 2005).

The elliptical cross-section at the end of the inlet had a major axis of 19.85 mm and a minor axis of 11.29 mm (aspect ratio of 1.76). The entrance height of the combustor immediately downstream of the step was $H = 12.89$ mm and its axis was angled at 6° to the inlet axis in order to realign the flow with the nominal flight direction. The combustor consisted of a constant area section 103.0 mm in length (L/H = 8.0) and a diverging section 77.4 mm in length (L/H = 6.0). The area ratio of the combustor exit relative to the inlet throat was 2.0 and the divergence angle was kept approximately constant around the circumference.

A three-dimensional quasi-elliptical nozzle completed the engine flowpath. Although crucial to the overall vehicle performance, the design of an optimum three-dimensional nozzle was not considered within the scope of the current work. The nozzle developed for this engine was 128.9 mm in length (L/H = 10.0). It had a projected exit area of 2869 mm^2, corre-

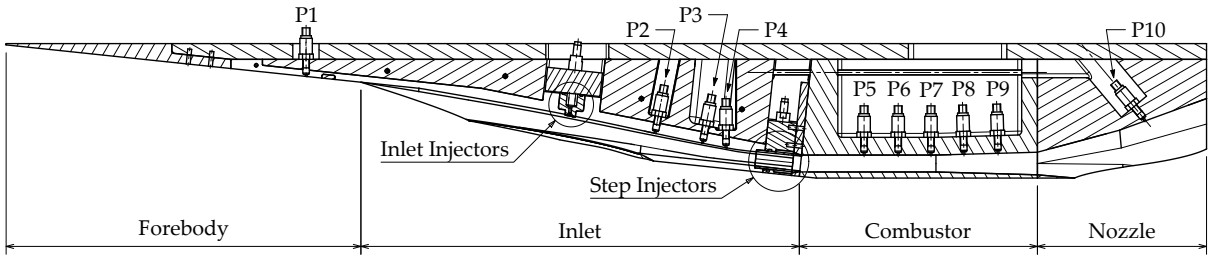

Figure 3.9 – A cross-section through the symmetry plane showing the internal geometry and locations of the internal pressure taps

sponding to an area ratio of 16.5 relative to the inlet throat. The expansion angle in the vertical symmetry plane was 20° for the first half and 30° for the second half of the nozzle. In the horizontal plane the expansion angle was constant at 13.5° such that the side wall thickness at the nozzle exit was 0.45 mm. To increase usage of the available area, and because of the thin wall on the cowlside, the axis of the nozzle was rotated 5° relative to the combustor axis. The resulting geometry underwent a shape transition from an ellipse at the entrance to a rectangle with rounded corners at the exit. On the cowlside, the intersection of the expanding internal surface with the external engine surface defined the trailing edge of the nozzle and resulted in a sweeping three-dimensional curve.

Figure 3.10 shows the engine components prior to assembly and installation into the facility test section. The total mass of the model, excluding the instrumentation and fuel system, was 9.6 kg. Further details of the design and assembly of the engine are reported in Doherty (2013b).

3.4.2 *Forebody Integration*

Consistent with the assumptions of the inlet design, the forebody used for this model was a simple 6° wedge. The forebody length was defined by ensuring that the inlet cowl closure point is intersected by an inviscid two-dimensional (2-D) shock originating from a sharp leading edge at the Mach 12 design condition. This criterion is equivalent to the classical shock-on-lip requirement used for 2-D inlet design.

In general however, the shock-on-lip requirement is not as well defined for 3-D inlets with swept leading edges as it is for 2-D inlets. Depending on the inlet and forebody design, the shock surface may intersect the leading edges along some distance and not just at the cowl closure location. For the REST family of inlets this tends not to be the case, although it is possible that at the design condition the forebody shock impinges on the external leading edge surfaces. Such a situation should be avoided due to the adverse heating loads and flow features that may be generated.

Noting that heating loads preclude the use of sharp leading edges

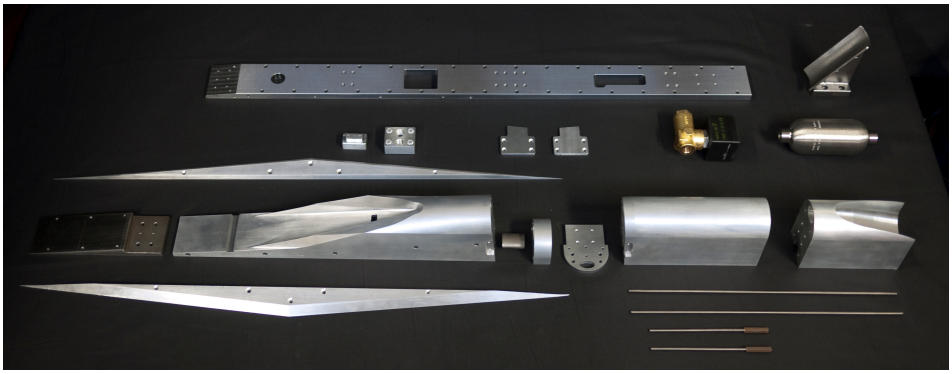

(a) The individual components of the small-scale Mach 12 REST engine

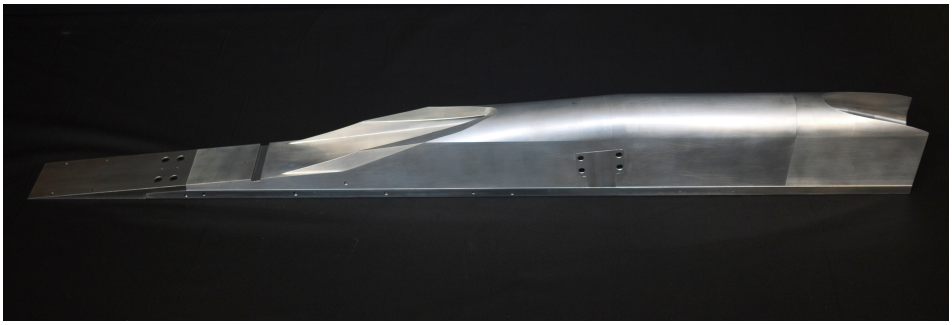

(b) A cowlside view of the assembled engine

Figure 3.10 – Photographs of the small-scale Mach 12 REST engine model

in flight (Anderson, 2006, Section 6.5.2), the forebody leading edge was blunted to a radius of 0.5 mm. In combination with viscous interaction, the leading edge bluntness causes an increase in the forebody shock standoff, thereby providing a conservative design for the forebody length. To allow for replacement due to damage or for future studies examining the influence of forebody length and leading edge bluntness on the engine, the front portion of the forebody was designed as a separate component (Figure 3.10).

Flow uniformity and the state of the boundary layer are two other factors that need to be considered when integrating an engine with an airframe. The adverse pressure gradients and shock-boundary layer interactions that exist within the inlet are sufficiently strong to induce separation of a laminar boundary layer (Dann and Morgan, 2011; Smart, 1999). Therefore, ensuring that the boundary layer transitions to turbulence on the vehicle forebody is important for the correct operation of the engine. Furthermore, both surface heating and skin friction increase downstream of the transition location (Hirschel and Weiland, 2009; van Driest, 1956) and so the state of the boundary layer has a significant influence on the overall vehicle performance (see for e.g. Bowcutt et al., 1987; Hirschel, 2005, Section 7.3). Despite this importance, accurate prediction of the transition location on

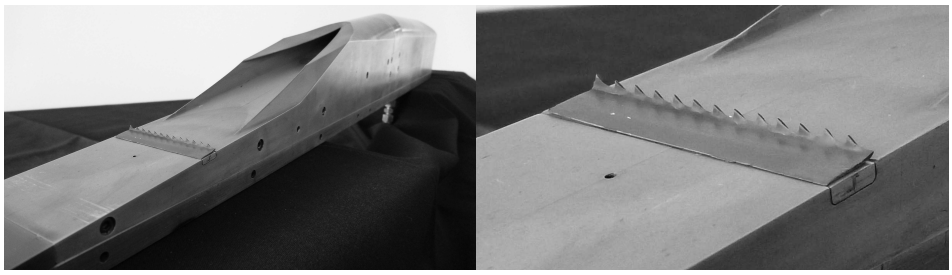

Figure 3.11 – Sawtooth boundary layer trip. The teeth were approximately 3 mm in height and 90° to the surface of the forebody. The 0.5 mm diameter forebody pressure tap is visible in the right hand photograph.

the forebody was not a focus of this thesis as it remains a state-of-the-art research area (Johnson et al., 2008; Simeonides, 2003; Wise and Smart, 2012).

Irrespective of the points raised in the preceeding paragraph, a rough estimate of the transition length may be calculated using the work of He and Morgan (1994) who found that within the T4 Stalker Tube, transition on a flat plate at Mach 6.6 was given by:

$$L_{tr} = \frac{2487}{Re_u^{0.6}} \tag{3.1}$$

From Table 3.5, the unit Reynolds number behind the forebody shock was $(3.77 \pm 0.40) \times 10^6$/m and $(2.07 \pm 0.21) \times 10^6$/m for the high and low pressure conditions respectively. The transition length is thus estimated to be 300 mm for the high pressure condition and 440 mm for the low pressure condition. Examining Figure 3.8, it can be seen that the transition length is comparable to the forebody length at the high pressure condition and is comparable to the total distance from the forebody leading edge to the inlet injection station at the low pressure condition.

To provide a means of forcing transition to turbulence during the experiments, a slot in which a boundary layer trip could be fitted was incorporated into the forebody 20 mm upstream of the start of the inlet (Figure 3.8). The saw-tooth trip that was fitted for some shots is shown in Figure 3.11. Comparative fuel-off shots with and without the trip fitted are presented in Chapter 6 and demonstrate that no trip was necessary at either test condition. Thus, the forebody length was sufficient for the Mach 10 flow produced by the T4 Stalker Tube.

Nonuniformity of the flow entering the inlet as a result of spillage from the forebody is expected to be larger on single engine vehicles than on multi-engine vehicles (Hirschel and Weiland, 2009). For any vehicle design there is a trade-off between improving uniformity of the inlet inflow (and thus mass-capture) through altering the width and shape of the forebody, and minimising the overall frontal area and associated drag. The small-

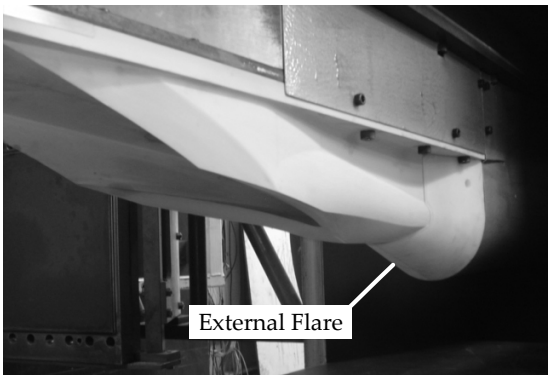

(a) The external flare present on the Mach 8 REST model tested by Turner and Smart (2008)

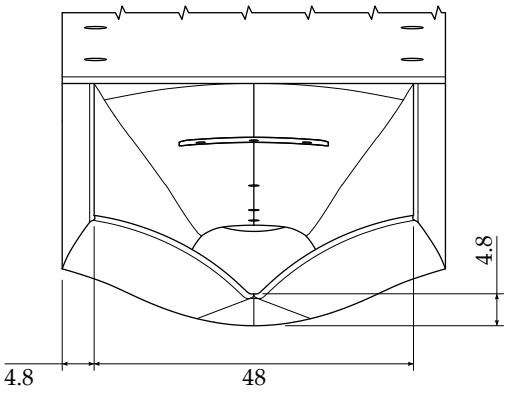

(b) Definition of the inlet wall thickness for the current engine

Figure 3.12 – Previous REST models featured a large flare downstream of the cowl closure point as seen on the left. This was eliminated in the current design given on the right.

scale Mach 12 REST engine represents the first time that a REST-based scramjet has been integrated with an airframe and tested in freejet mode. Consequently, baseline data for a simple wedge forebody were desired and optimisation studies of the forebody design were not considered within the scope of this thesis. Fuel-off numerical simulations, presented in Chapter 5, were used to examine the mass capture performance of the airframe integrated engine.

3.4.3 *External Vehicle Design Considerations*

A significant and original difference between the current engine and previous REST-based scramjets tested at The University of Queensland is the external geometry. The engine developed in this thesis represents the *first* time that a REST-based scramjet engine has been designed with streamlined external aerodynamics. Previous engine tests were focused solely on the performance of the internal flowpath and little attention was given to the external aerodynamics beyond ensuring that the model was easy to manufacture and assemble, and that the external shape did not affect the internal flow. To this end, all previous models featured a large flaring of the external geometry downstream of the inlet cowl closure point. This flare, seen in Figure 3.12a for the engine tested by Turner and Smart (2008), allowed the inlet, plenum chamber, and combustor to be connected by a flange joint with the internal flowpath sealed by an o-ring at each interface.

The drag penalty incurred by this flare is large and undesirable for

a flight engine. Since the current model was developed for testing on a force balance, a flare was not included in the design. Instead, the wall thickness of the inlet was specified to be 10 % of the capture width when viewed parallel to the forebody. This is shown in Figure 3.12b and resulted in a wall thickness of 4.8 mm for the current model; a thickness that was considered reasonable. The resulting streamlined external geometry becomes apparent when comparing photographs of the current engine (Figures 3.10 and 3.11) with those of previous REST engine (Figure 2.3). Clearly, the M12REST engine designed for this thesis provides the first indication for the shape of a REST-based flight engine.

The streamlined external geometry did however, introduce some design difficulties. Due to the elliptical cross-sectional shape and contraction of the internal flowpath, the minimum engine wall thickness occurs in the symmetry plane, on the cowlside of the inlet. This thin cowl wall placed significant limitations on the design of the step injector plenum and was the major design challenge for this experimental model. While it could be expected that increasing the engine size to flight-scale would partially mitigate these design limitations, the requirement for minimum frontal area will cause a decrease in the proportional wall thickness.[17] Thus, similar design limitations are anticipated to exist for all engines, particularly given that a thin combustor wall on the cowlside may be of benefit for radiation cooling of the structure (Zander and Morgan, 2009). Details of the final design of the step injector plenum, including finite element analysis, are provided in Doherty (2013b).

3.4.4 *Instrumentation*

In addition to the three-component force balance, the model was instrumented with several static pressure transducers that were located along the internal bodyside surface of the engine. The number and locations of the pressure taps[18] were restricted by the small scale of the model, the size of the available sensors and the streamlined external aerodynamics. Pressure measurements on the internal cowlside surface or of the external flow (with the exception of the forebody) were not feasible.

Figure 3.9 shows the configuration of the pressure transducers used for the second test campaign. Throughout this report these transducers are numbered consecutively from P1 through to P10, with P1 being the forebody tap, P2 through P4 the inlet taps, P5 through P9 the combustor taps and P10 the nozzle tap. The initial configuration used for the entirety of the first test campaign did not include inlet taps P2 and P4 or combustor tap P7. There are two reasons why these transducers were not included in the original engine design. Firstly, in an effort to reduce the complexity of

17 Defined as the ratio of inlet wall thickness to inlet capture width.
18 That is, the pressure measurement hole.

the model the number of engine pressure taps was kept to a minimum. Secondly, because this model was to be tested on a force balance, there was the requirement that the mechanical design of the inlet and nozzle provide sufficient force transmission pathways to the force balance stress bars. As will be shown in Chapter 7, interpreting whether or not the inlet flow was started was difficult with only a single transducer in the inlet. It was for this reason that additional transducers upstream and downstream of P3 were added for the second campaign. An extra transducer (P7) was also added to the middle of the combustor in order to provide additional combustion pressure data for fuel-on experiments.

Three different ranges of Kulite® series XTEL-190M absolute pressure transducers were used in the model: 0 to 68.9 kPa (0 to 10 psi) for the forebody and nozzle, 0 to 172.4 kPa (0 to 25 psi) for the inlet, and 0 to 689.5 kPa (0 to 100 psi) for the combustor. The measurement uncertainty of these transducers was at most $\pm 1.6\,\%$ (Appendices A.3 and C.3).

A Pitot probe was installed on the model during the experiments to monitor the test flow entering the engine. As detailed in Appendix D the design of the probe followed that of McGilvray et al. (2009) and was instrumented with a PCB® model 111A22 piezoelectric pressure transducer of range 0 to 344.8 kPa (0 to 50 psi). During the first test campaign the Pitot probe was located 15 mm off the symmetry plane, 20 mm behind the leading edge and 20 mm above[19] the top surface of the engine. For the second test campaign the probe was located on the symmetry plane 10 mm behind the leading edge of the engine and 12 mm above the top surface of the engine, ensuring that it did not influence the flow entering the engine. The change in location of the engine Pitot probe was a consequence of the alteration of the engine mounting and associated shielding between the two test campaigns (see Sections 3.4.6 and 4.2).

To allow determination of the fuel mass flow rate, each fuel plenum was instrumented with a single PCB® model 111A26 piezoelectric pressure transducer of range 0 to 3448 kPa (0 to 500 psi). The measurement uncertainty of these transducers was $\pm 2.9\,\%$ (Appendices A.3 and C.3).

Calibration methods for each transducer and sample results are presented in Appendix A and the transducer mountings are detailed in Appendix D. Details of the fuel system and the calculation of the fuel mass flow are provided next.

3.4.5 *Fuel Supply System*

The scramjet engine was fuelled using gaseous hydrogen over a range of equivalence ratios for three different fuelling configurations: (1) inlet-only injection, (2) step-only injection and, (3) a combined scheme using both

19 This height includes a 4 mm spacing between the engine top surface and shielding bottom surface (Section 4.2).

the inlet and step injectors. At high Mach numbers the thrust gained from the injection of fuel becomes an increasing fraction of the total thrust (Czysz, 1988; Vandenkerckhove and Barrére, 1997) and it is important that this contribution is not neglected when testing scramjet engines on force balances. For the current model, this was achieved by using an on-board fuel tank similar to that of Paull et al. (1995b) rather than a Ludwieg tube that is external to the test section and connected to the model with rigid fuel piping (see, for example, Robinson, 2003d; Turner, 2010).

A schematic of the fuel supply system used for the force balance tests (campaign 1) is given in Figure 3.13. The on-board system consisted of a Swagelok® stainless steel sampling cylinder with a volume of 150 cm^3 (part number 316L-HDF4-150) and a fast acting Asco Joucomatic® solenoid valve (model SC B223A125). The fuel tank, solenoid valve and injector plenums were connected using 1/4 inch stainless steel tubing that had an internal diameter of 0.180 inch (4.572 mm). The cross-sectional area of the tube and the minimum area within the solenoid valve were both larger than the total area of the step and inlet injector holes,[20] thus ensuring that the fuel flow would be choked at the exit of the injectors.

The fuel tank was connected to the external system via a length of 1/8 inch stainless steel tubing (Figure 3.13). To minimise the forces imparted to the model by this filling line, the tubing was formed into a flexible coil as shown in Figure 3.14b. During a test this coil acted as a very weak spring with an estimated spring constant of approximately 0.7 N/mm (Doherty, 2013b). Additionally, the use of small diameter tubing and the inclusion of a manual isolation valve ensured that the volume of the filling line was only 8 % of the volume of the on-board tank,[21] thereby limiting the fuel mass flow through the filling line during a test and reducing the magnitude of the reaction force imparted to the model by the filling line. The fuel tank pressure was monitored using a GE® Druck pressure transmitter (model PTX7517-3257) that was mounted external to the test section and connected to a Gefran digital display unit (model 2400). Photographs of the on-board fuel system are provided in Figure 3.14.

For the streamlined-mount engine tests (campaign 2) the fuel system was configured almost identically to that shown in Figures 3.13 and 3.14. The only difference was the replacement of the 1/8 inch flexible coil with a short length of 1/4 inch tubing. This change was possible because the force balance was not used in the second set of tests. The volume of the filling line decreased slighty to 7 % of the tank volume. As discussed in Section 3.4.6, the removal of the coil permitted the model shielding to be streamlined.

20 The total area of the injectors was 11.95 mm^2, equivalent to a single injector of diameter 3.9 mm. The cross-sectional area of 1/4 inch tubing was 16.42 mm^2. The minimum orifice diameter of the solenoid valve was 9 mm.

21 For comparison, the volume of the filling line would have been 68 % of the tank volume if 1/4 inch tubing had been used instead of 1/8 inch tubing for the first test campaign setup.

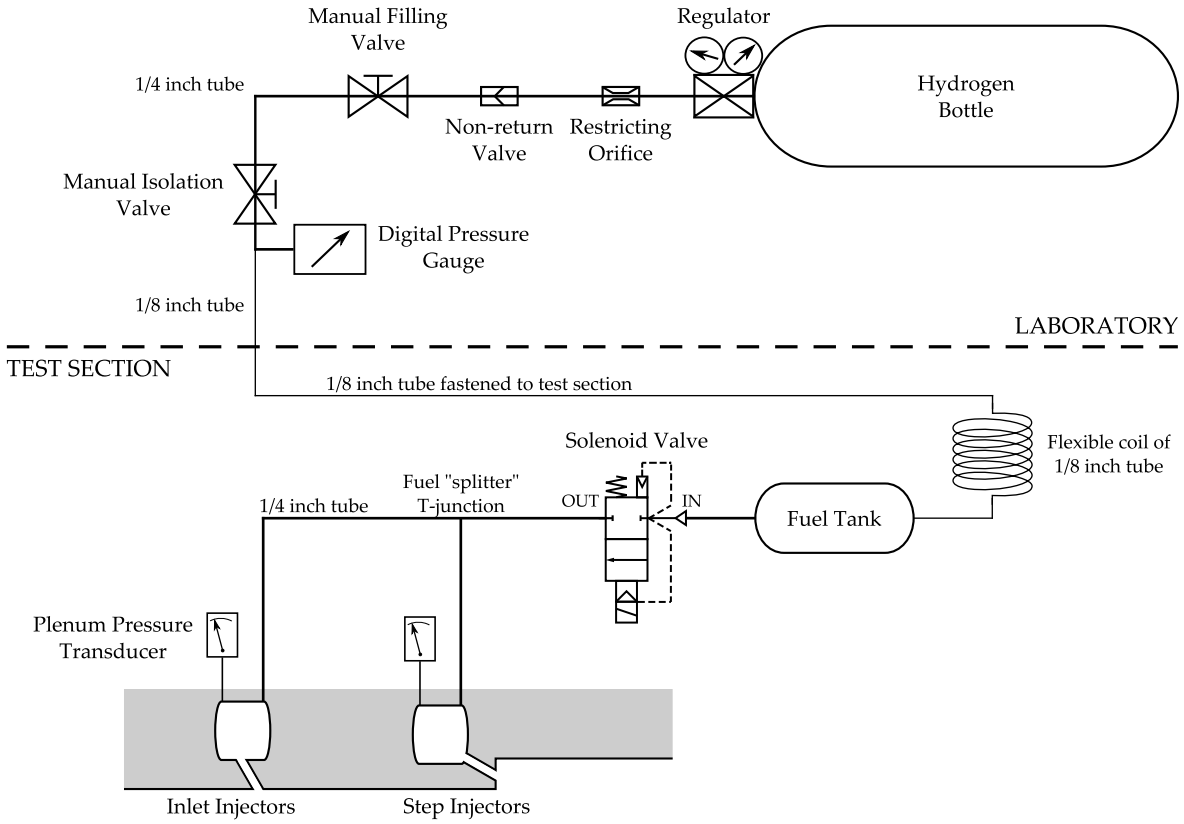

Figure 3.13 – Schematic of the T4 Stalker Tube fuel system configured for the current experiments

The Asco Joucomatic® valve used to initiate flow of fuel to the injectors had an opening delay of approximately 8 ms. As this delay was longer than the steady flow duration of the facility, the valve was triggered prior to flow arrival at the model. The trigger signal was generated based on the recoil motion of the facility. Typical time-histories of the trigger signal and fuel plenum pressures are given in Figure 3.15. For comparison, the Pitot pressure trace and fuel split parameter defined by Equation (3.7) are also plotted and the test time is indicated. The delay between valve trigger and the rise of the plenum pressure is obvious.

In the current experiments the solenoid valve was held open for a duration of 100 ms allowing the fuel tank to almost completely empty. Due to the small volume of the on-board tank, the fuel system delivered a steady plenum pressure for only ≈2.5 ms. Although similar in length to the test time, this period was considered to be sufficiently long for the current experiments. During the second set of tests, the timing of fuel injection was found to influence the establishment of steady flow within the engine. Discussed further in Appendix H.3, this required late

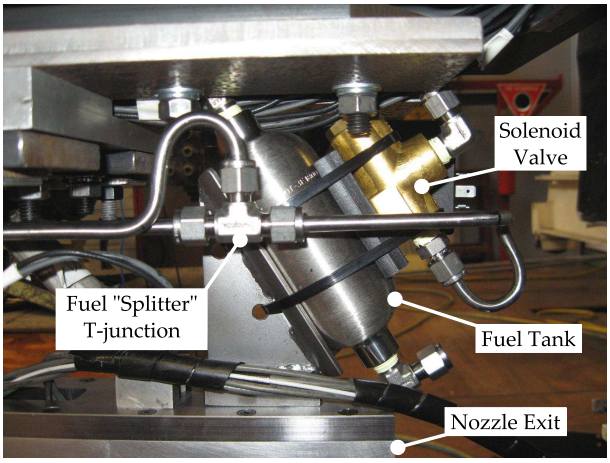

(a) The fuel tank and solenoid mounted at the rear of the engine. Note that the flexible coil has not been fitted in this image.

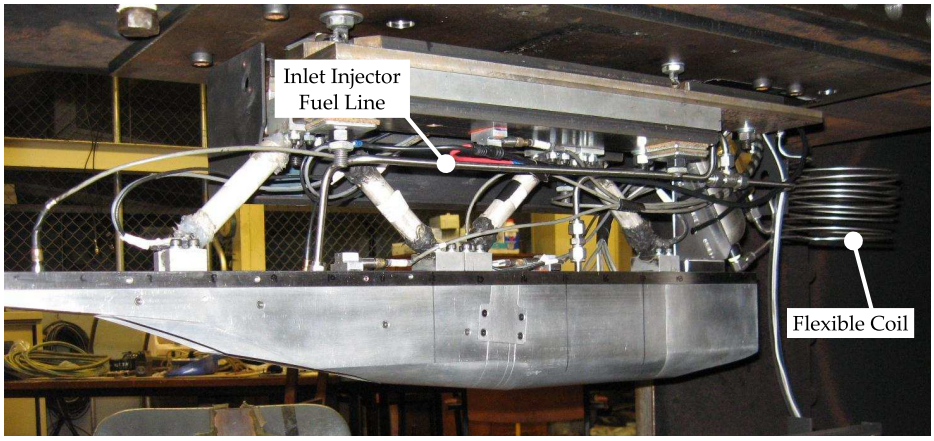

(b) The completed installation of the engine model prior to the first test campaign. Both the inlet and step injector fuel lines are visible as is the flexible coil of 1/8 inch tubing at the rear of the engine.

Figure 3.14 – Photographs of the on-board fuel system used for the small-scale M12REST engine

triggering of the fuel valve and consequently the fuel plenum pressures were rising during the test time (Figure 3.15). Furthermore, the rate at which each plenum pressure approached the steady value was different due to the differing volumes of the plenums and the differing lengths of tubing between the fuel splitter and plenum chamber (Figures 3.13 and 3.14b). As a consequence, the fuel split parameter varied throughout the test time for the combined fuel injection scheme. Calculation of the fuel mass flow rate from the measured plenum pressure, the fuel equivalence ratio and the fuel split parameter are discussed next.

Prior to the experiments each fuelling configuration was calibrated to

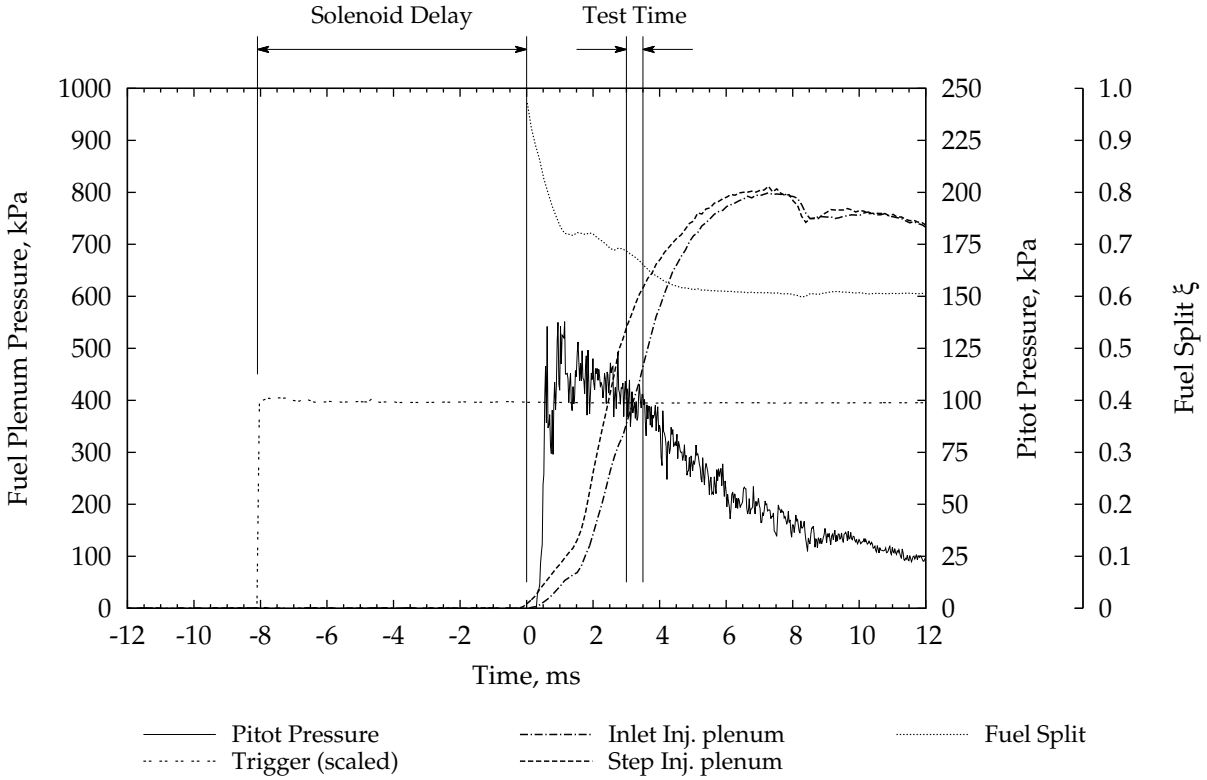

Figure 3.15 – Time histories of the fuel trigger, Pitot pressure and fuel plenum pressure signals during shot 10960. The computed fuel split parameter is also shown. Note that the time axis is shifted so that zero corresponds to the trigger time of the nozzle supply pressure transducers.

determine the mass flow rate of hydrogen as a function of the plenum pressure and initial tank fill pressure. The theoretical basis for the calibration procedure is provided in full in Appendix A.4 along with sample results. An overview is provided here.

With the assumption of sonic injection and a near stagnated gas in the plenum chamber, the fuel mass flow rate becomes a function of the stagnation conditions within the plenum and the gas properties. Since the plenum temperature was not measured directly, the gas in the tank is assumed to undergo an initial isentropic expansion and then flow adiabatically and with a loss of total pressure through the rest of the system to the plenum.[22] These assumptions allow the mass flow rate for a

22 Gangurde et al. (2007) confirmed the validity of these assumptions by comparing numerical simulations of the T4 fuel delivery system with experimental data (see also Gangurde, 2007). The simulations were completed using the one-dimensional Lagrangian computer code, L1D (Jacobs, 1994, 1998).

single plenum to be written as

$$\dot{m}_{f,j} = \alpha_j p_{Ti}^{\frac{\gamma-1}{2\gamma}} p_{p,j}^{\frac{\gamma+1}{2\gamma}} \tag{3.2}$$

where α_j is a constant that is similar to a discharge coefficient, p_{Ti} is the intial fill pressure of the tank and $P_{p,j}$ is the measured pressure of plenum where $j = 1$ corresponds to the inlet plenum and $j = 2$ corresponds to the step plenum.

As detailed in Appendix A.4, the constant α_j is determined experimentally and is *unique* to the system configuration used during the calibration. For combined fuelling schemes a third calibration constant, α_C, is introduced such that

$$\dot{m}_{f,t} = \alpha_c \sum_j \dot{m}_{f,j} = \alpha_c p_{Ti}^{\frac{\gamma-1}{2\gamma}} \left(\alpha_1 p_{p,1}^{\frac{\gamma+1}{2\gamma}} + \alpha_2 p_{p,2}^{\frac{\gamma+1}{2\gamma}} \right) \tag{3.3}$$

This constant is also determined experimentally using the same methodology as the individual calibration constants (Appendix A.4).

In this thesis the mass flow of fuel is quoted in the form of the global fuel equivalence ratio. Denoted by ϕ and defined by

$$\phi = \frac{1}{\lambda} \frac{\dot{m}_f}{\dot{m}_A} \tag{3.4}$$

the equivalence ratio is the ratio of actual fuel mass flow to that theoretically required to burn all available oxygen in the air that flows through the engine. In Equation (3.4), λ is the stoichiometric fuel-air ratio and $\dot{m}_f$ and $\dot{m}_A$ are the mass flow rates of fuel and air respectively. The case of $\phi = 1$ is stoichiometric while $\phi > 1$ represents a fuel-rich mixture and $\phi < 1$ a fuel-lean (or air-rich) mixture. For experiments using nitrogen as the test gas the quoted equivalence ratio is an equivalent value calculated by assuming that the captured mass flow of nitrogen is replaced by an equal mass flow of air.

The stoichiometric fuel-air ratio used in Equation (3.4) is dependent on the type of fuel being burnt and the (assumed) composition of air. In this thesis, gaseous hydrogen is used as the fuel and, to ensure consistency with the gas model used for the calculation of the facility nozzle flow (Section 3.3.1), air is taken to be formed from 21 % oxygen and 79 % nitrogen (by mole) with a molar mass of 28.85 kg/kmol. The complete reaction for hydrogen and air, neglecting the intermediary reactions and species is given by

$$2H_2 + \left(O_2 + \frac{79}{21} N_2 \right) \longrightarrow 2H_2O + \frac{79}{21} N_2 + \Delta h_c \tag{3.5}$$

where Δh_c is the heat of formation of the fuel and is taken to be 120 MJ/kg-

of-H_2 in this thesis. Taking the molar weights of H_2, O_2 and N_2 to be 2.016 kg/kmol, 31.999 kg/kmol and 28.013 kg/kmol respectively, the stoichoimetric fuel-air ratio for hydrogen is $\lambda = 0.029\,35$.

The mass flow of air through the engine is a function of both the facility nozzle exit flow properties and the engine mass capture ratio. Following Smart (2001), the engine mass capture was not directly measured in this thesis but was instead determined from fuel-off numerical simulations of the engine. These simulations are presented and discussed in Chapter 5. Defined with respect to the projected frontal area of the inlet $A_1 = 3308\,mm^2$ (Figure 5.5), the mass capture ratio $m_{c,1}$ is calculated from the simulations to be 60.7 % at the high pressure test condition and 58.2 % at the low pressure test condition. Thus, for each experiment the captured mass flow of air is calculated using

$$\dot{m}_A = m_{c,1} A_1 \rho u_x \tag{3.6}$$

where ρ and u_x are the *shot-specific* static density and axial velocity of the facility nozzle exit flow. These properties are calculated using NENZFR as described in Section 3.3.1. Further discussion of the mass capture performance of the M12REST engine is provided in Section 5.4.

Finally, for combined fuel configurations it is useful to know what fraction of the total fuel is injected from each plenum. This is accomplished by defining the fuel split parameter as

$$\xi = \frac{\dot{m}_{f,2}}{\dot{m}_{f,t}} = 1 - \frac{\dot{m}_{f,1}}{\dot{m}_{f,t}} \tag{3.7}$$

The fuel split has a range between 0, for the inlet injection scheme and 1 for the step injection scheme. A typical time history for the fuel split is provided in Figure 3.15. Due to the necessarily late timing of fuel injection and the different filling rates of each plenum, the fuel split varied approximately linearly during the nominal test time.

3.4.6 *Model Mounting within the Test Section*

Two different methods for mounting the engine within the test section were used in this work. The three-component force balance designed by Robinson (2003d) was used during the first test campaign and a streamlined rigid mount was used during the second campaign. Figure 3.16 provides a side-by-side comparison of the two systems, with each shown as an exploded assembly. The three-component force balance is depicted on the left and the rigid mount on the right.

The force balance consists of four bars orientated at 45° to the horizontal. These connect the top of the model and to the underside of the (so-called) top plate. During the initial development of the balance, Robinson

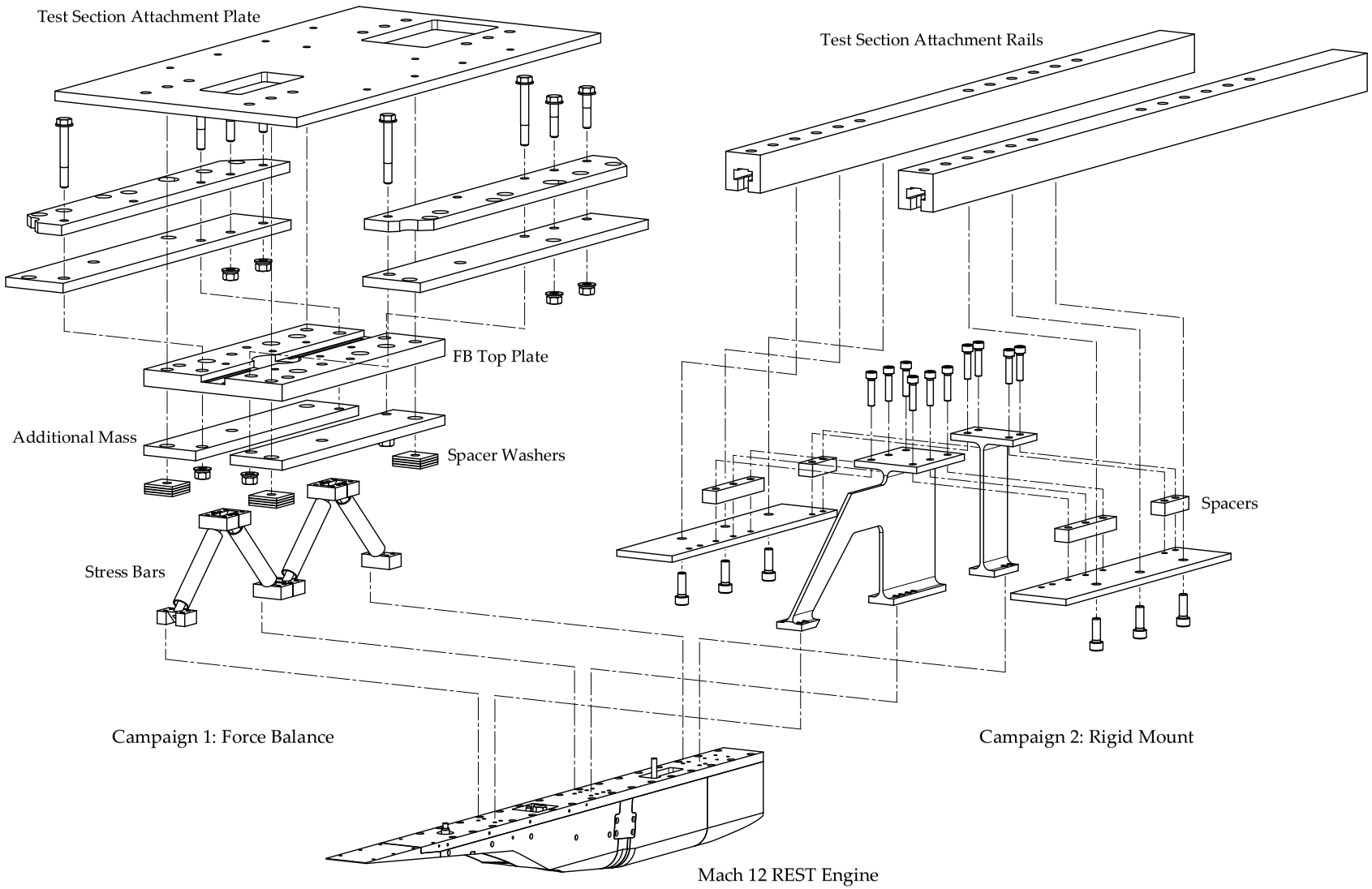

Figure 3.16 – Exploded view of the engine-test section attachment structures. The three-component force balance is shown on the left; the rigid structure on the right. For clarity only selected fastners have been shown.

(2003d) found that the quality of the measured strain signals was improved by vibrationally isolating the model-force balance assembly from the facility. He accomplished this by adding 20 kg of mass to the top plate and suspending the assembly from the test section roof using 5 kN/m springs thus forming a two-degree-of-freedom vibration isolation system for the model (Rao, 2004; Robinson, 2003b). The same mounting arrangement was used for the current work, however, the additional mass was modified to allow the model to be positioned higher in the test section (Doherty, 2013b). Photographs of the force balance assembly and spring attachment are provided in Figures 3.17a and 3.17b. Typical strain signals plotted in Figure 4.14 are nominally zero prior to flow arrival, indicating that the model-force balance assembly was sufficiently isolated from facility vibrations.[23]

A photograph of the rigid mount developed and used during the second test campaign is provided in Figure 3.17c. This mount was designed to use the standard T4 attachment rails and to position the model at the same location in the test section as the force balance mounting. Furthermore, the mount and its associated shielding (Figure 4.1b) were designed to provide minimal blockage of the facility nozzle, ensuring that the flow entering the engine and the starting process of the nozzle were not adversely affected.

3.4.7 *Model Position within the Test Section*

The size and position of the engine were constrained by the requirement that the entire model fit within the core flow diamond produced by the facility nozzle. Figure 3.18 provides a schematic of the model, test section and Mach 10B nozzle. Overlayed on the schematic are contours of Mach number (Figure 3.18a) and static-on-supply pressure ratio (Figure 3.18b). Note that the engine was *not* included in the nozzle flow field simulation (Section 3.3.1). Contour lines for the high pressure test condition are shown in the top half of each image; those for the low pressure condition are shown in the lower half. For clarity the engine mounting and shielding have not been drawn. Figure 3.18 clearly indicates

1. the relative size of the model and core flow diamond,
2. the flow uniformity over the core and,
3. the location of the model with respect to the core and nozzle exit plane.

Further discussion of the nozzle flow is provided in Section 3.2.2 and Doherty (2013a). The engine was mounted at an angle-of-attack (AOA)

23 The speed of sound of longitudinal vibrations in steel is approximately 5900 m/s (Haynes, 2013, Section 14). This is substantially faster than the speed of the primary shock ($\approx$ 2200 m/s); thus, vibrations caused by the launch of the piston, facility recoil and rupturing of the primary diaphragm reach the test section earlier than the flow.

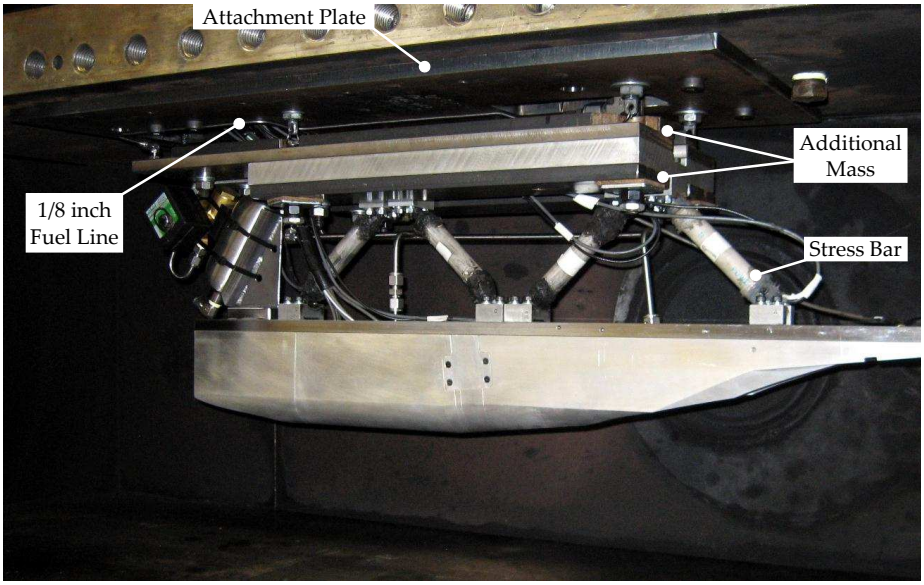

(a) Three-component force balance (campaign 1)

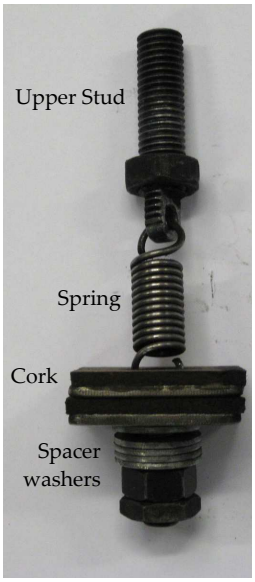

(b) Spring attachment

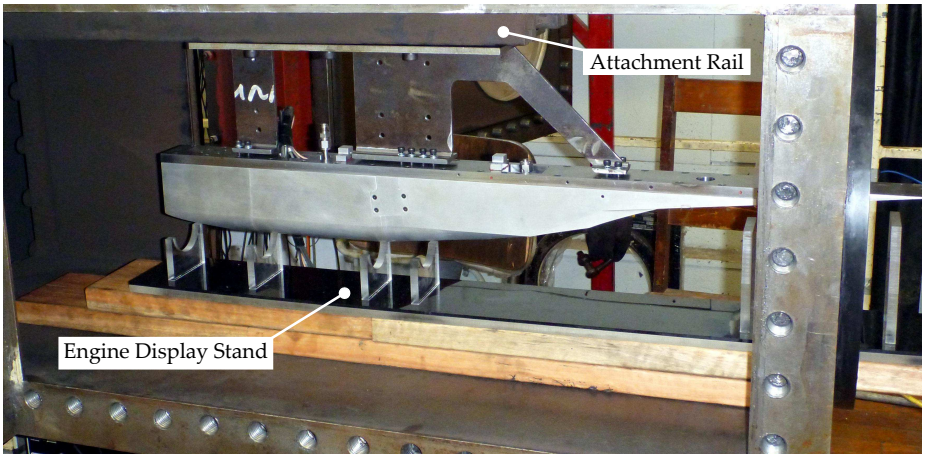

(c) Rigid structure (campaign 2)

Figure 3.17 – Engine-test section attachment

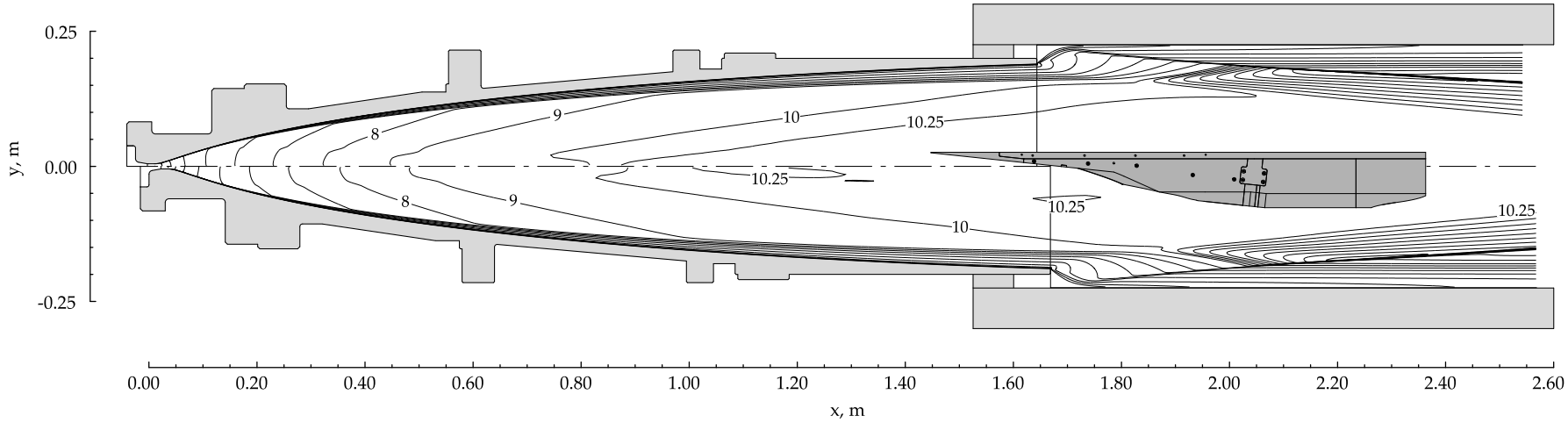

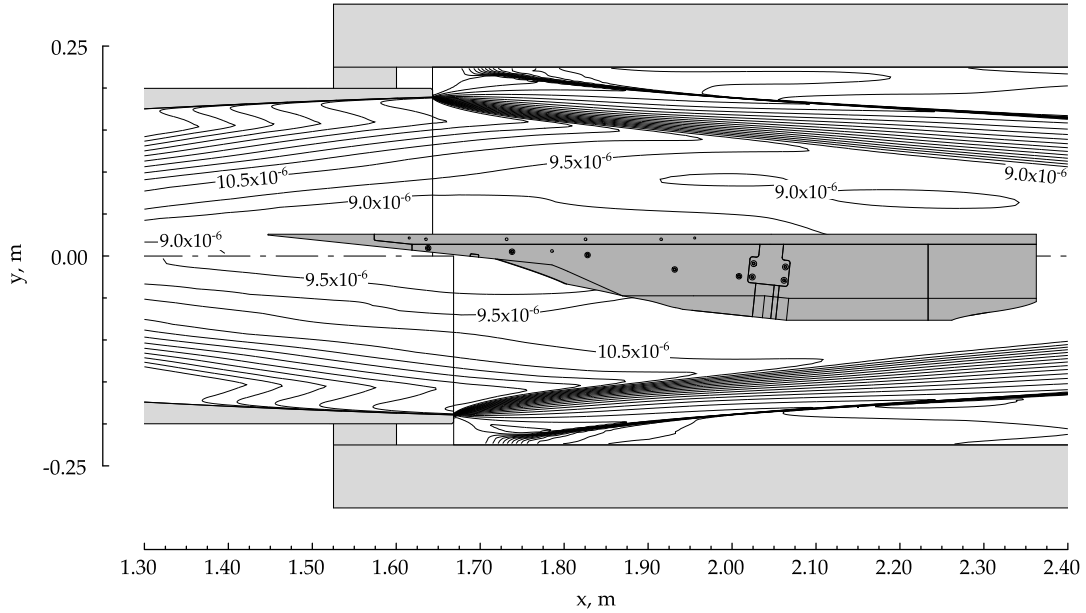

Figure 3.18 – Nozzle flow field computations overlayed on a schematic of the engine, test section and nozzle. The engine was *not* included in the computations. For each figure the high pressure test condition is given in the upper half, the low pressure test condition in the lower half. For clarity the engine mounting, fuel system and shielding are not shown.

(a, above) Contours of Mach number, shown at increments of 1 between 3 and 10 and increments of 0.25 between 10.25 and 12.5.

(b, left) Contours of static-on-supply pressure ratio, shown at increments of 0.5×10^{-6} between 0 and 15×10^{-6}. This increment is equivalent to 35.8 Pa for the high pressure condition and 20.0 Pa for the low pressure condition.

of $(0.0 \pm 0.1)^\circ$ and angle-of-yaw (AOY) of $(0.0 \pm 0.1)^\circ$ with respect to the nozzle centerline. To ensure that the expansion emanating from the nozzle exit corner did not impact the rear of the engine, the model was positioned such that the leading edge was (197 ± 3) mm upstream of the nozzle exit plane for the high pressure condition and (224 ± 3) mm upstream for the low pressure condition.[24] This difference in axial position did not influence the operation of the engine. Finally, the vertical position of the model was such that the top surface of the engine was approximately 26 mm above the centreline of the nozzle.

3.5 DATA REDUCTION: TEST TIME AND NORMALISED PRESSURE

3.5.1 *Test Time Determination*

The test time is defined as the period over which the experimental data accurately represent that which would be obtained during an equivalent flight. Due to the inherently transient nature of flow produced by shock tunnel facilities, selection of an appropriate test time is important. Figure 3.19 shows the time histories of the nozzle supply, Pitot, and selected engine pressure tranducers during a typical experiment and defines the test time used for the current work. The Pitot and engine pressures have been normalised by the nozzle supply pressure using a time offset that accounts for the flow transit time from the nozzle supply region to the pressure transducer. The time axis has been shifted so that time zero corresponds to the trigger of the nozzle supply pressure.

Within shock tunnel facilities the start of test time occurs once quasi-steady flow has been established in the facility nozzle and over the model.[25] The facility nozzle flow is considered started once the initial unsteady expansion has been swept out of the nozzle (Smith, 1966) and is indicated by a steady Pitot-to-supply pressure ratio. For the Mach 10B nozzle used in this work the starting process typically took around 1 ms from flow arrival at the Pitot pressure (Figure 3.19). The flow transit time from the nozzle supply region to the Pitot pressure location was approximately 0.5 ms.

The flow over the model also takes time to develop. In previous studies the model establishment time after the passing of the starting pulse of gas has been correlated with the required number of flow lengths based on a characteristic length and velocity (see, for example, Davies and Bernstein, 1969; East et al., 1980; Jacobs et al., 1992; Lee and Lewis, 1993). For the current work an additional constraint was the requirement that

24 Height restictions imposed by the force balance prevented the model from being raised higher than shown in Figure 3.18.

25 It should be noted that even with steady facility flow the phenomena of interest may be inherently unsteady. See for example Kleine et al. (2005), who visualise the unsteady flow around a double cone geometry using high-speed colour schlieren.

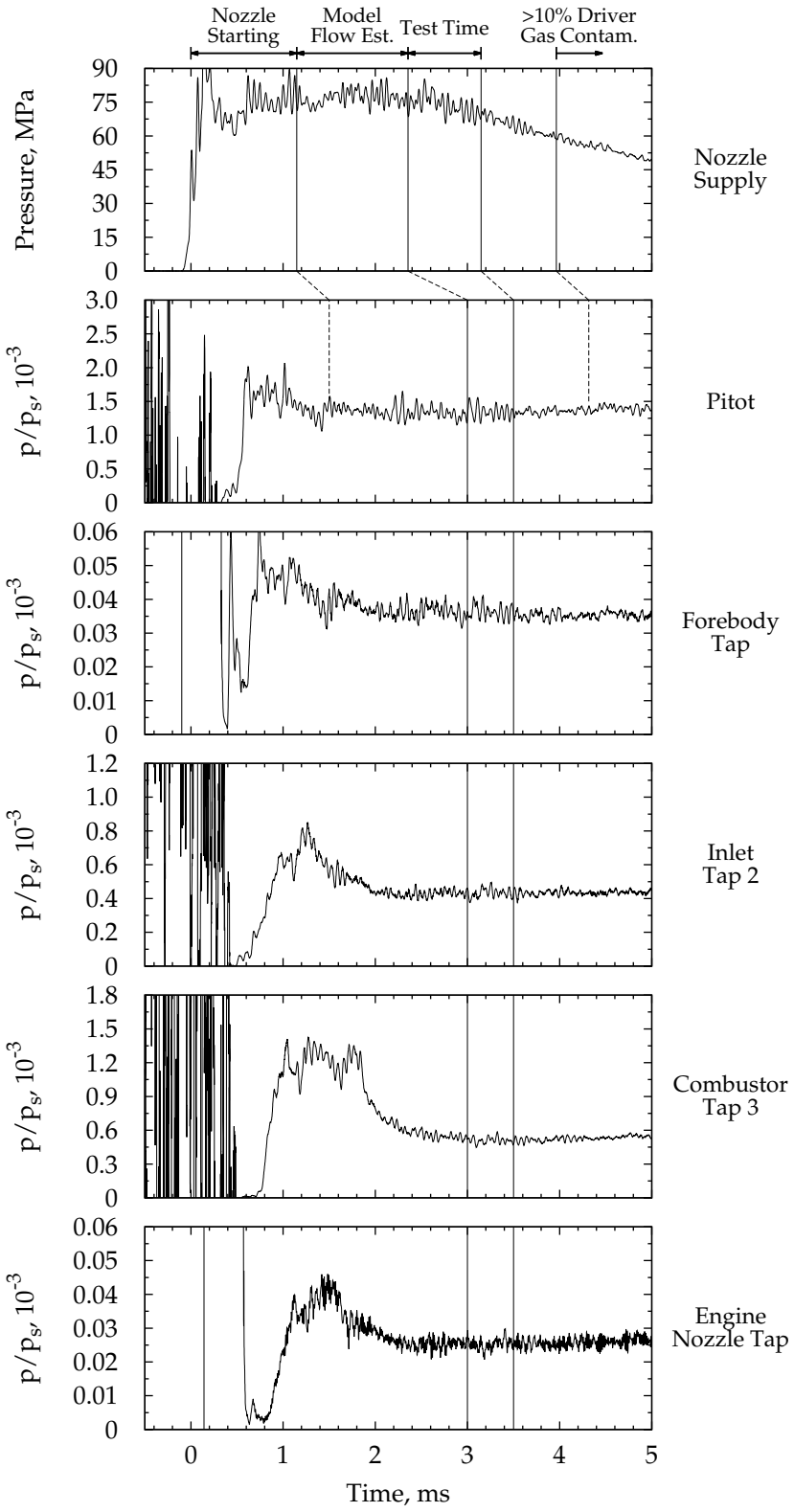

Figure 3.19 – Time histories of the nozzle supply, Pitot, and selected engine pressure transducers during shot 10975. All signals have been filtered by a 20 µs moving average filter. The time axis has been shifted so that zero corresponds to the trigger of the nozzle supply pressure. The Pitot and engine pressures have been normalised by the nozzle supply pressure using a time offset that accounts for the flow transit time.

the entire model flow be established during the test time as this would be appropriate for force balance tests. The normalised engine forebody and nozzle pressures were used to assess the overall starting time. Referring to Figure 3.19, the engine nozzle pressure takes approximately 1 ms to reach a steady normalised value after the peak value.[26] This time period corresponds to approximately 3 flow lengths based on the freestream velocity and model length and is consistent with previous studies (Jacobs et al., 1992; Rogers and Weidner, 1993).

A consequence of using an identical test window for the entire engine is that different segments of the nozzle supply pressure trace are used to normalise each engine pressure data during the test time. For example, for shot 10975 plotted in Figure 3.19, the portion of the nozzle supply trace between 2.36 ms $\leqslant t \leqslant$ 2.86 ms is used to normalise the engine nozzle pressure during the test time, whilst the portion between 2.65 ms $\leqslant t \leqslant$ 3.15 ms is used to normalise the Pitot pressure trace. The segments of the nozzle supply trace are different because of the different flow transit times between the nozzle supply region and each engine pressure measurement. In this work, the mean nozzle supply pressure for a single shot was calculated using an overall test time that was defined by

$$\overline{p}_s = \langle p_s(t) \rangle_{t_{start}-\tau_{10}}^{t_{end}-\tau_{PP}} \tag{3.8}$$

where (t_{start}, t_{end}) is the test time for the engine and τ_{PP} and τ_{10} are the flow transit times from the nozzle supply region to the model Pitot probe and engine nozzle transducer locations, respectively. In this context τ_{PP} serves as an approximation for flow arrival at the model leading edge and τ_{10} serves as an approximation for flow arrival at the engine nozzle exit plane.

The end of test time is determined by either contamination of the test gas with driver gas or by a change in the nozzle supply pressure greater than a predefined threshold. Due to the long flow establishment time of these experiments and a slightly undertailored test condition, the test time typically occurred on the relaxing portion of the nozzle supply pressure trace. The total variation in pressure during the test time was approximately $\pm 10\,\%$ of the mean. This variation was considered acceptable.

Previous experiments by Boyce et al. (2005a), Paull (1996), and Skinner (1994) have demonstrated that the time of arrival of driver gas in the test section decreases as the nozzle supply enthalpy increases. Using mass spectrometry measurements conducted in the T4 Stalker Tube, Boyce et al. (2005a) derived the following correlation for the arrival of the driver gas in the test section:

$$t = 62.1 H_s^{-1.7} \pm 38\,\% \tag{3.9}$$

26 The peak is the head of the unsteady expansion formed during the nozzle starting process.

where h_s is the supply enthalpy in units of MJ/kg and t is the contamination time after flow arrival at the model in units of milliseconds. This correlation is based on the data sets of Boyce et al. (2005a) and Skinner (1994) assuming a driver gas contamination level of 10 %. This level of contamination was confirmed by Chan (2012, Appendix G) as being suitable for combustion experiments within shock tunnel facilities.

Reproduced from Boyce et al. (2005a), Figure 3.20 compares Equation (3.9) with experimental data. The uncertainty bands of the correlation are also depicted. Examining Figure 3.20, it is clear that the uncertainty of the correlation results from the scatter of the experimental results. This scatter must be taken into account when using the correlation to estimate the time of arrival of driver gas in the test section. Noting that in this thesis the nominal enthalpy of each test condition is slightly less than 5 MJ/kg (Table 3.2), and that at this enthalpy the experimental data lie above the correlation (Figure 3.20), then Equation (3.9) provides a slightly conservative estimate for the driver gas contamination time for both test conditions used in this thesis. The calculated contamination time is shown in Figure 3.19 for the nominal low pressure test condition.

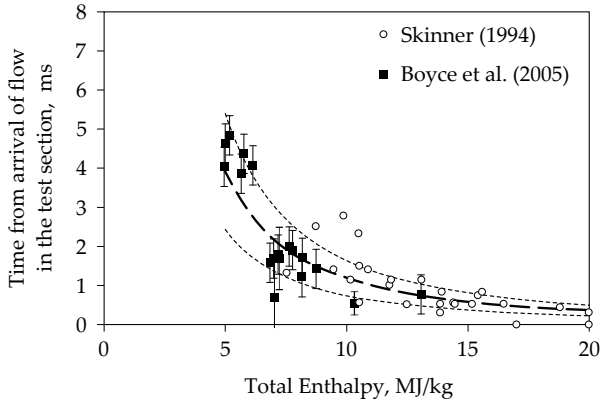

Figure 3.20 – Variation of driver gas contamination time with nozzle supply enthalpy. Reproduced from Boyce et al. (2005a).

The normalised engine traces shown in Figure 3.19 represent an exemplary fuel-off shot for which the model establishment time was shorter than that indicated. Over the course of the two test campaigns, the engine pressures were observed to attain a steady level sometime between 2.5 and 3.0 ms, with fuel-off shots generally, but not always, establishing earlier than fuel-on shots. During the force balance test campaign, the recovered forces were observed to establish slower than the internal pressure measurements, typically requiring a total establishment time of 3.5 ms (after trigger of the nozzle supply pressure). This increased establishment time is hypothesised to be related to the surface shear stress which was found by Jacobs et al. (1992) to take longer to establish than the surface

pressure. Calibration results for the force balance presented in Chapter 4 and Appendix B demonstrate that although the balance provides a realistic measurement of slow force establishment, the recovered forces may be slightly oscillatory compared with the input force and therefore requires a longer test time. Thus, the test time was typically taken to be from 3.0 to 3.5 ms for pressure-only shots and from 3.5 to 4.5 ms for force balance shots.

3.5.2 *Normalised Pressure*

Engine pressure data are presented in Chapters 6 and 7 in the form of a pressure ratio[27] relative to the forebody pressure. Each measurement represents the mean of the transient normalised data over the nominated test time. The transient normalisation is defined by

$$\frac{p}{p_1} = \frac{p(t)}{p_s(t-\tau)}\left(\frac{p_s}{p_1}\right)_{nom} \tag{3.10}$$

where $p(t)$ is the measured engine pressure, $p_s(t)$ is the measured nozzle supply pressure and τ accounts for the transit time from the supply region to the transducer location of interest. The nominal supply pressure ($p_{s,nom}$) and forebody pressure ($p_{1,nom}$) are taken from Table 3.2 and Table 3.5 respectively. Computing the pressure ratio in this way removes the shot-to-shot variation and presents the data relative to the nominal forebody conditions. The label p/p_1 is used throughout this thesis for the mean pressure ratio. The total experimental uncertainty of the pressure ratio is $\pm 5.5\,\%$. Calculation of this uncertainty is detailed in Appendix C.6.

27 This is consistent with the typical formulation used for the analysis of gas turbine engines, see for example Oates (1997). Also, it is trivial to show that for fixed Mach number the pressure coefficient (C_p) is a linear transformation of the pressure ratio.

FORCE BALANCE THEORY AND CALIBRATION

The fourth chapter, in which we concern ourselves with a three-component force balance, describing the theory and calibration methodology, as well as presenting selected calibration results, thus completing the foundations of the thesis.

4

4.1 INTRODUCTION

This chapter describes the three-component force balance (3CFB) that was used for this thesis. In conjunction with Chapter 3, this is the second and final chapter that focusses on the experimental apparatus. The 3CFB used in this thesis was designed by Robinson (2003d) to recover three components of force (lift, thrust/drag and pitching moment) acting on a moderate scale, fuelled scramjet engine. The balance is based on the stress wave force measurement technique (SWFMT) that was proposed by Sanderson and Simmons (1991) for the measurement of aerodynamic drag within test flows of a few milliseconds. This technique has been under continual development within the Centre for Hypersonics and has been extended to the measurement of three and six components of force (see for e.g. Mee et al., 1996; Smith et al., 2001). The balance used in this thesis was not designed specifically for the M12REST engine.

The goal of this chapter is to provide a succinct yet complete explanation of the calibration theory and methodology of the 3CFB. In fact, the explanation provided in this chapter of the calibration of a multi-component stress wave force balance is the most comprehensive and detailed to date. The introduction continues with a discussion of the philosophy underlying the measurement technique and the calibration of stress wave force balances. A chronological list of papers that track the development and application of stress wave force balances is also provided. Section 4.2 describes the balance instrumentation and shielding while the basic theory for both single- and multi-component balances is given in Section 4.3. The formation of the global response function of a multi-component balance from a set of point-load calibrations is detailed in Section 4.4. Calibration weighting factors for the M12REST-3CFB assembly are then defined in Section 4.5. Section 4.6 summarises the methods used to evaluate the quality of the calibration data and the global response function. Sample calibration results are also provided. Section 4.7 outlines the data reduction methods used in this thesis for the force balance data and the final section of the chapter, Section 4.8, presents an assessment of the experimental uncertainty.

4.1.1 *Measurement and Calibration Philosophy*

Before considering the details of the stress wave force measurement technique and balance calibration, it is useful to first understand the underlying philosophy of the method as this provides the context for the remainder of the chapter. Consider a typical reflected shock tunnel experiment of an aerodynamic body. The test gas expands transiently from the facility nozzle, arriving first at the model leading edge before sweeping through and around the model. At each instance in time the flow of gas interacts with the model surfaces, imparting transient forces through the action of the surface pressure and skin friction. These surface forces in turn create stress waves that propagate through the model structure. At the interfaces of the model components the stress waves are transmitted and reflected, leading to a complex superposition of waves within the model. Although the aerodynamic forces acting on the model may attain a steady or quasi-steady level, internal force equilibrium between the model and support structure is not achieved during the short flow period generated by a typical reflected shock tunnel.

Under the assumption of a causal, time-invariant and linear system, the time-evolution of the pattern of stress waves within the model is uniquely determined by the time-evolution of the distributed aerodynamic load acting on the model surfaces. In theory, knowledge of the impulse response function of the model and sufficient characterisation of the stress wave pattern permits the load distribution to be spatially and time-accurately resolved. However, in practice, the primary interest is to measure the net aerodynamic forces, not the specific distribution. This is achieved by coupling the model with an appropriately designed supporting structure consisting of one or more stress bars, each of which is instrumented with at least one strain gauge.[1] During an experiment, some fraction of the stress waves that propagate through the model pass into the force balance and are recorded by strain gauges. The implicit function of each stress bar is to act as a filter for the complex stress wave pattern within the model. With a well designed balance, the response of a single stress bar depends only on the magnitude of a single force component.[2] Designing a balance that behaves in this way is relatively easy to achieve for single-component force measurement when the net force on the model acts only in the direction of the stress bar (see for e.g. Paull et al., 1995a; Porter et al., 1994) and more difficult to achieve for multi-component force measurement (see for e.g. Robinson et al., 2007).

The calibration method for stress wave force balances is based on the recognition that, subject to the assumptions of a causal, linear and time-

1 Multiple gauges are used to provide redundancy and repeatability.

2 That is, in theory, a stress bar designed to respond to drag should not respond when a pure distributed lift is applied to the model. Ideally, the response is also independent of the distribution of drag (see for e.g. Robinson et al., 2011).

invariant system, a distributed aerodynamic load acting on the model may be formed from a superposition of an infinite number of point loads. Similarly, the net strain response of the balance is a superposition of the individual strain responses for each point load. The overall calibration procedure involves imparting a series of point loads at different locations on the model using an instrumented impact hammer (Mee, 2003). The measured strain response and hammer signals are used to form a point-load impulse response function (IRF) for each calibration hit. Using a reference force distribution for the model, the individual point-load impulse responses may be combined to form the global impulse response function (GIRF) of the balance. During an experiment the net applied aerodynamic load is recovered by using the global impulse response function to deconvolve the measured strain signals.

Requiring knowledge of a reference force distribution does not invalidate the calibration methodology. In fact, requiring knowledge of a reference input is the basis for the calibration of any measurement device. Consider for example the calibration of a pressure transducer as described in Appendix A.3. The basic calibration procedure is to apply a known pressure, which is measured with a reference transducer, and measure the corresponding output of the transducer to be calibrated. During an experiment, the measured transducer output is used to infer that the same pressure is acting on the transducer as was applied during the calibration. In comparison with the calibration of a pressure transducer, the calibration of a multi-component stress wave force balance is significantly more complex. This complexity arises because the strain responses may be coupled with different input forces, both the magnitude and distribution of the applied load can change and a finite number of calibration hits are used to infer the response of the balance to an distributed load.

The extent of coupling between the strain responses and force inputs and sensitivity of the strain outputs to variations in the distribution of force are both dependent on the design of the balance (see for e.g. Robinson et al., 2007, 2011). As already noted, an ideal balance is one for which no coupling exists between non-corresponding inputs and outputs, and for which the strain output is dependent only on the net applied force and not the force distribution. Consequently, any reference load distribution could be used to calibrate an ideal balance. In practice however, some coupling exists and the strain outputs are somewhat dependent on the distribution of load. The calibration process therefore 'tunes' the balance response to the reference load distribution. The sensitivity of the quality of the recovered forces to the shape of the applied load distribution is carefully evaluated as a part of the calibration process.

The determination of the system response from individual calibration point loads becomes increasingly complex as the number of force components to be resolved increases. A complete and detailed explanation of the calibration methodology for multi-component stress wave force balances

is provided in the remainder of this chapter. Although the nomenclature is somewhat specific to the 3CFB and M12REST engine used in this thesis, the equations and analysis methods presented here are easily adapted to other configurations. It is expected that this chapter will be useful for anyone who is interested in conducting experiments with a multi-component stress wave force balance.

4.1.2 *Background Reading*

While this chapter was written to be self-contained, readers unfamiliar with the stress wave force measurement technique and who desire further material on the development and application of the method are referred to the following papers:

1. Sanderson and Simmons (1991): this was the first paper to present the stress wave force measurement technique as a method by which the drag force acting on an axisymmetric body could be measured in a test flow with duration of approximately 1 ms.
2. Simmons et al. (1993): this paper reports on early attempts to extend the technique to multiple-components of force measurement on a sharp cone at angle of attack and to the measurement of thrust on a two-dimensional scramjet nozzle. See also Mee et al. (1992), Tuttle et al. (1994), and Tuttle and Simmons (1992).
3. Porter et al. (1994) and Tuttle et al. (1995): these papers apply the method to (axially) non-uniform load distributions and larger models.
4. Paull et al. (1995a): this paper applies the method to the measurement of thrust for a quasi-axisymmetric, hydrogen-fuelled scramjet engine. The data reported in this paper represent the first experimental demonstration of net thrust production for a scramjet engine.
5. Daniel and Mee (1995) and Mee et al. (1996): through a combination of finite-element analysis and experiments, these papers demonstrate that the technique can be used to recover multiple force components for a sharp cone.
6. Smith and Mee (1996a): this paper presents the results of an investigation into the suitability of the technique for use in expansion tubes facilities that have test times on the order of 50 µs.
7. Smith and Mee (1996b): this technical note demonstrates the suitability of using piezo-electric film for the dynamic measurement of axial stress waves.
8. Smith et al. (2001): using finite-element analysis, this paper presents the design and analysis of an internal six-component balance for

aerodynamic force measurement on a small-scale, blunt-nosed vehicle.

9. Tanno et al. (2001): this paper documents the development and use of a single component balance to measure the internal skin friction drag acting on an axisymmetric scramjet combustor. See also Chan (2012), Kirchhartz et al. (2012), and Rowan and Paull (2006).

10. Mee (2002, 2003): this report and paper describe the dynamic calibration of a single component balance using an instrumented impact hammer. The results and techniques described in these documents serve as a key foundation for the calibration method presented in this thesis.

11. Abdel-Jawad (2004) and Abdel-Jawad et al. (2001): this thesis and paper present the results of a study examining the stability of a reentry vehicle using a three component force balance in an expansion tube facility.

12. Robinson (2003d) and Robinson et al. (2006, 2004): this thesis and associated papers document the development of a three component balance for the measurement of lift, thrust and pitching moment of moderately sized scramjet engines. See also Robinson (2003a,b,c).

13. Sahoo et al. (2005): this paper compares a stress wave force balance with an accelerometer based balance for the measurement of drag on a blunted cone. The two measurement techniques were found to give comparable results.

14. Abdel-Jawad et al. (2007): this paper describes a methodology for the determination of calibration weighting factors for a three-component force balance but lacks details regarding the formation of the GIRF.

15. Robinson et al. (2007): using finite-element analysis, this paper briefly examines how the design of a multi-component balance affects the quality of the recovered forces. Both an external and internal balance are compared. It was found that the external balance gave improved recovery of the applied load compared with the internal balance.

16. Tanimizu et al. (2009): this paper presents the results of a scramjet engine nozzle optimisation study. A single component balance was used to examine the influence of the nozzle on the fuel-off drag of a quasi-axisymmetric scramjet engine.

17. Robinson et al. (2011): this paper presents the measurement of three components of force on a large blunted cone at angle-of-attack within the DLR HEG shock tunnel facility.

4.2 INSTRUMENTATION AND SHIELDING

Shown in Figures 3.16 and 4.3, the 3CFB was designed specifically to measure three components of force (lift, thrust/drag, pitching moment) on moderate scale scramjet engines within the T4 Stalker Tube (Robinson, 2003d). The balance consists of four stress bars mounted in a symmetric pattern at 45° to the top surface of the scramjet model. Each bar is instrumented with piezo-electric and, as a backup, piezo-resistive strain gauges. For completeness, a summary of the application of gauges, taken from Robinson (2003d) pages 106-107, is provided in the following paragraph:

"The piezo-electric film was cut into strips measuring 25 mm by 31 mm and glued to each bar using M-BOND AE-15 adhesive. Each piezo-electric gauge was physically and electrically shielded using insulated copper sheeting. In addition to the piezo-electric film, each stress bar was instrumented with two Kulite® ACP-120 semi-conductor piezo-resistive strain gauges. These were connected in a bending-compensation half Wheatstone bridge arrangement and, to further reduce bending effects, positioned on the side of each stress bar.[3] The entire instrumented region of each bar was further shielded using a section of PVC pipe that was sealed with RTV silicone adhesive." [foonote added]

The instrumentation of the bars was left un-touched for the current work; however, prior to the first experiment, gauge operation was confirmed using a test model (Figure B.1). The signal-to-noise ratio of the piezo-electic film was found to be higher than that of the Kulite® piezo-resistive gauges. Consequently, and following Robinson (2003d), the piezo-electric film gauges were considered to be the primary strain measurement sensor in this thesis. The Kulite® piezo-resistive gauges were used as a secondary measurement. Of the eight gauges, only the piezo-resistive gauge on bar 1 was found to be faulty. Since the piezo-resistive gauges were to be used only as a redundant system, reinstrumentation of the bars for this thesis was considered unnecessary. The primary gauges were labelled *a* through *d* corresponding to bars 1 through 4; the secondary gauges were labelled *e* through *h*.

To ensure that only the model surfaces were exposed to the test flow, the entire force balance mount was aerodynamically shielded from the test flow. Shown and compared with the streamlined mount shielding in Figure 4.1, the force balance shielding for the M12REST engine was heavily inspired by the final shielding design used by Robinson (2003d, Section 7.5.2). The shielding featured an upper box that surrounded the top plate and additional inertial mass that was attached to the top plate (Figure 3.16), a swept nose piece and narrow sides to protect the forebody

3 Bending may be induced in the bars by a rolling or yawing moment caused by asymmetric engine operation or non-perfect alignment of the model within the test section. Each piezo-electric gauge was bending-compensated by being wrapped around the circumference of each bar.

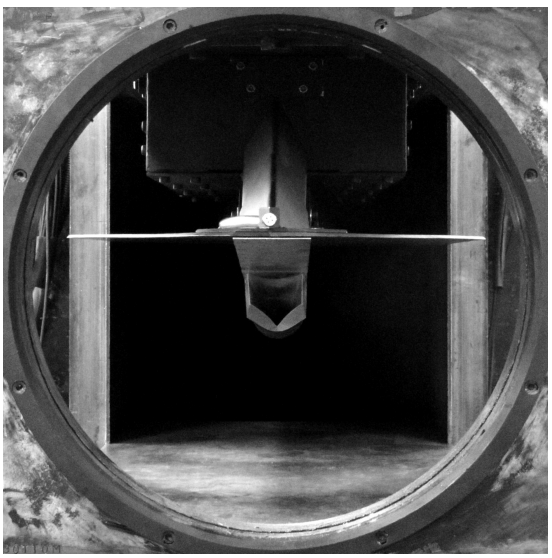

(a) Force balance shielding

(b) Streamlined shielding for the rigid mount used in the second test campaign (Section 3.4.6).

Figure 4.1 – Force-balance and streamlined mount shielding comparison

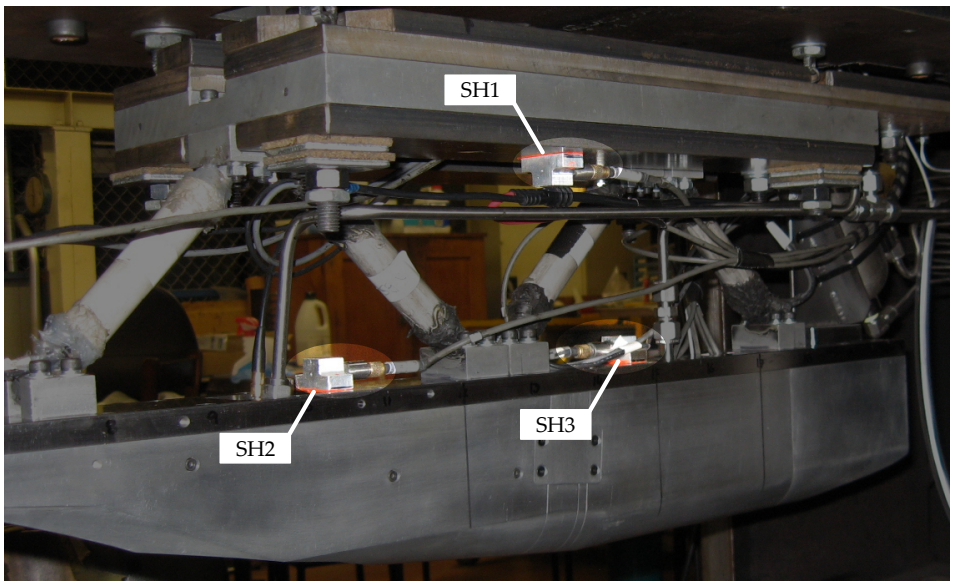

Figure 4.2 – Location of the inner shielding pressure measurements. The fourth measurement (not shown) was located on the left hand side and to the rear of the force balance top plate.

pressure transducer and stress bars, and swept 'wings' to prevent flow disturbances from the upper box shielding from interacting with the flow around the model. Technical drawings for the shielding are provided in Doherty (2013b).

The force balance shielding was designed to allow the model and balance to move approximately 2 mm in any direction without contacting the shielding. The resulting gap between the shielding 'wings' and top surface of the engine allowed gas to enter and fill the inner shielding cavity during a test. This internal shielding pressure was measured using four Kulite® series XTEL-190M absolute pressure transducers. These were labelled SH1, SH2, SH3 and SH4. The locations of SH1, SH2 and SH3 are shown in Figure 4.2. Gauges of range 0 to 68.9 kPa (0 to 10 psi) were mounted in locations SH1 and SH2 and gauges of range 0 to 172.4 kPa (0 to 25 psi) were mounted in locations SH3 and SH4. The design of the mounting block for the shielding pressure transducers is provided in Appendix D. Correction of the force data using the internal shielding pressure data is discussed in Section 4.7.

4.3 BASIC THEORY

This section outlines the basic theory of the SWFMT for both single and multi-component balances and is based on the introductory sections of Robinson (2003a) and Mee (2003).

4.3.1 *Single component balance*

The fundamental assumptions of the SWFMT are that the model and balance assembly behave as a linear, causal and time-invariant dynamic system (Sanderson and Simmons, 1991). For a single component balance (typically measuring drag), these assumptions allow the applied load $u(t)$ to be related to the measured strain response $y(t)$ via a convolution integral:[4]

$$y(t) = \int_0^t g(t-\tau)u(\tau)d\tau \tag{4.1}$$

where $g(t)$ is the system impulse response function that is determined from a calibration (Mee, 2003). For discretized data, $u(t)$, $y(t)$ and $g(t)$ are replaced by u_r, y_r and g_r, respectively and Equation (4.1) is rewritten as

$$y_r = \sum_{s=0}^{r} g_{r-s}u_s\delta t \tag{4.2}$$

4 An alternate, but equivalent form of the convolution integral is $y(t) = \int_0^t g(\tau)u(t-\tau)d\tau$.

where $r \in \{0, 1, 2, 3, \ldots, k\}$, the sampling interval is δt and $t_r = r\delta t$. Expressing this in matrix form, we write

$$\mathbf{y} = G\mathbf{u}\delta t \tag{4.3}$$

where $\mathbf{y}$ is the time-series output vector (strain), $\mathbf{u}$ is the time-series input vector (aerodynamic load) and G is the discretised impulse response function (IRF) with form

$$G = \begin{bmatrix} g_0 & 0 & \ldots & 0 \\ g_1 & g_0 & \ldots & 0 \\ \vdots & \vdots & \ddots & \vdots \\ g_n & g_{n-1} & \cdots & g_0 \end{bmatrix} \tag{4.4}$$

With a known IRF and measured strain response, the solution of Equation (4.3) defines the unknown load that was applied to the model during an experiment. This calculation, known as deconvolution, was completed in the time domain using the Fortran computer program HYFORCE (Mee, 2007). The program implements the constrained iterative algorithm proposed by Prost and Goutte (1984).

4.3.2 *Multi-component balance*

Generalising Equation (4.3) to a multi-component system gives

$$\begin{pmatrix} \mathbf{y_1} \\ \mathbf{y_2} \\ \vdots \\ \mathbf{y_n} \end{pmatrix} = \begin{bmatrix} G_{11} & G_{12} & \ldots & G_{1n} \\ G_{21} & G_{22} & \ldots & G_{2n} \\ \vdots & \vdots & \ddots & \vdots \\ G_{n1} & G_{n2} & \ldots & G_{nn} \end{bmatrix} \begin{pmatrix} \mathbf{u_1} \\ \mathbf{u_2} \\ \vdots \\ \mathbf{u_n} \end{pmatrix} \delta t \tag{4.5}$$

where n is the number of force components to be recovered, $\mathbf{y_n}$ are output vectors, $\mathbf{u_m}$ are input vectors and G_{nm} are impulse response matrices that relate output $\mathbf{y_n}$ to input $\mathbf{u_m}$ and are of the form of Equation (4.4). The matrix

$$\mathbf{G} = \begin{bmatrix} G_{11} & G_{12} & \ldots & G_{1n} \\ G_{21} & G_{22} & \ldots & G_{2n} \\ \vdots & \vdots & \ddots & \vdots \\ G_{n1} & G_{n2} & \ldots & G_{nn} \end{bmatrix} \tag{4.6}$$

is known as the global impulse response function (GIRF). As described in Section 4.1.1, the perfect force balance is one for which each strain output ($\mathbf{y}_n$) is uniquely dependent on the corresponding force input ($\mathbf{u}_n$), meaning that each off-diagonal sub-matrix of the GIRF is a null-matrix. In practice some coupling between the individual components is always

present, with the extent of coupling depending on the model and balance arrangement. For a coupled balance, accurate recovery of the input load requires that the system response be sufficiently characterised. Hence, each element of the GIRF must be carefully determined via a calibration process.

4.4 FORMATION OF THE GLOBAL IMPULSE RESPONSE FUNCTION

Depicted in Figure 4.3, the calibration of the M12REST-3CFB assembly involves using an instrumented impact hammer to apply an impulsive force to the model at various locations in two orthogonal directions. The number of possible locations for the calibration lug is dictated by the model design. The M12REST engine featured twenty calibration stations distributed uniformly along the top surface of the model. At every calibration station the lug could be placed on either the left or right side of the engine. Due to access restrictions (compare Figure 3.14 with Figure 4.3) and a narrow model width, calibration locations in the engine symmetry plane were not considered necessary. Strain signals recorded for hits on the left and right sides of the engine displayed good symmetry (Appendix B.9). The coordinates of each calibration station are provided in Appendix E.4.

Two coordinate systems are defined in Figure 4.3, the lift-drag coordinate system and the normal-axial coordinate system. Although the lift-drag force components are of primary interest in this work, the calibration of the balance was completed using the normal-axial coordinate system that is aligned with the stress bars. The reason for working in this coordinate system was so that each calibration hammer hit was parallel to the orientation of the force balance stress bars. Appropriately combining the individual calibration hits permits the response of each bar to a distributed pure normal, pure axial or pure moment load to be determined. Additionally, the form of the calibration lug ensured that the line of action of each hammer hit intersected with the top surface of the engine. This would not have been the case had a square calibration lug been used and the hammer hits conducted in the lift and drag directions. Finally, the calibration lug was necessary because the complex geometry of the engine prevented orthogonal hammer hits from being completed on the engine surfaces.

Each hammer hit generates stress waves in each bar. Performing single-component deconvolution produces a set of individual impulse response functions.[5] Denoted by G_k^{ij}, these individual IRF describe how bar $i \in \{1,2,3,4\}$ responds to a force input at station $j \in \{1,2,\ldots,20\}$ in direction $k \in \{N,A\}$. For clarity, indices for the left and right sides and multiple hits

5 Hammer hits on the top surface of the model are in the *negative* normal and axial directions. To ensure that the individual IRF have the correct sign (relative to the assumed coordinate system), each recorded strain signal is inverted prior to deconvolution with the recorded hammer pulse.

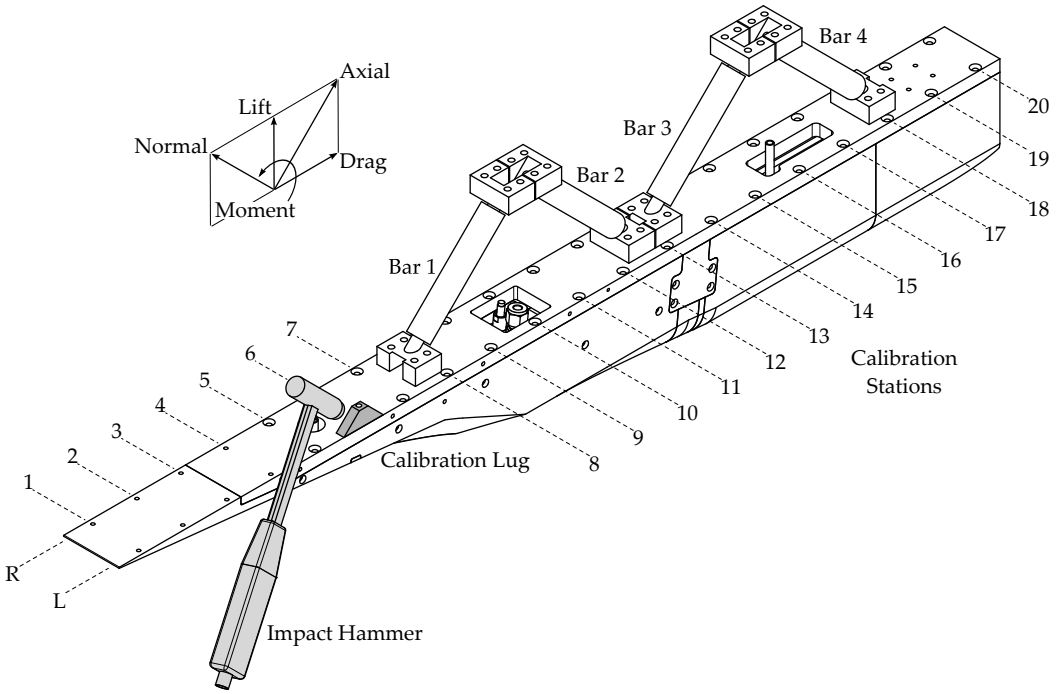

Figure 4.3 – Calibration of the 3CFB using an instrumented impact hammer and calibration lug. The calibration lug and impact hammer are shown in position for hit LUN06 (the hit naming convention is defined in Appendix B.2). For clarity the fuel system, force balance top plate and additional mass have not been drawn.

---

are not explicitly stated in the following paragraphs, with the understanding that G_k^{ij} actually represents the transient average of two hits on both the left and right sides for the jth axial location.[6] A third hit set was used to provide an independent evaluation of the balance calibration, thereby permitting an assessment of the sensitivity of the GIRF to small changes in the component strains. This is explained further in Section 4.6. With four stress bars and 240 hammer hits, a total of 960 individual IRF were produced. Combination of these individual IRF to form the GIRF of the balance is the subject of the remainder of this section.

During an experiment a distributed aerodynamic load acts over the entire surface of the model. Since the system is assumed to be linear, this load can be written as the weighted superposition of a set of unit loads where the time history of the unit load matches that of the distributed load. The resultant strains are also a weighted superposition of the strain responses to each unit load. Defining G_l^i as the overall impulse response

6 That is, G_k^{ij} is the average IRF for left hit 1, left hit 2, right hit 1 and right hit 2.

of bar i due to a distributed load in direction $l \in \{N, A, M\}$ then

$$G_l^i = \sum_{jk} w_{jl}^k G_k^{ij} \tag{4.7}$$

where w_{jl}^k are weighting factors that describe the contribution of a calibration hit in direction $k \in \{N, A\}$ to the loading distribution in direction-l at the jth axial station and G_k^{ij} are the individual IRF computed from the calibration hits. Once again, note that in this thesis G_k^{ij} represents the average of two hits on the left side and two hits on the right side of the model for the jth axial station.

The weighting factors w_{jl}^k in Equation (4.7) cannot be chosen arbitarily but must conform to a number of constraints and reflect the physical design of the balance and the hit directions. Firstly, the normal and axial coordinates are orthogonal;[7] a calibration hit in the axial direction has no component of *force* in the normal direction and so $w_{jA}^N = 0$. Similarly, a calibration hit in the normal direction has no axial force component and so $w_{jN}^A = 0$. Secondly, noting that calibration hits in either direction each contribute a moment about the balance centre[8] then $w_{jM}^N \neq 0$ and $w_{jM}^A \neq 0$. Finally, Mee (2007) states that the weighting factors should satisfy the following constraints:

$$\text{Constraint 1:} \quad \sum_j w_{jk}^k = 1 \quad \forall\, k \tag{4.8}$$

$$\text{Constraint 2:} \quad \sum_j w_{jk}^k d_j^k = 0 \quad \forall\, k \tag{4.9}$$

$$\text{Constraint 3:} \quad \sum_{jk} w_{jM}^k = 0 \tag{4.10}$$

$$\text{Constraint 4:} \quad \sum_{jk} w_{jM}^k d_j^k = 1 \tag{4.11}$$

where d_j^k is the moment arm relative to the balance centre. Constraints 1 and 2 require that for each orthogonal force direction the calibration point loads are combined to produce a unit load with no moment about the balance centre. Similarly, constraints 3 and 4 require that when added together the moment weighting factors for each calibration hit produce no net force and a unit moment about the balance centre. These four constraints are equivalent to the methodology described by Abdel-Jawad

7 This orthogonality should not be confused with the fact that each calibration hit produces a response in all four stress bars. As each bar responds to each hit, the force balance outputs are coupled and the off-diagonal terms in Equation (4.6) are non-zero.

8 Although each individual hit generates a moment about the balance centre in two planes (M_x and M_z), hits on the left and right side of the model (Figure 4.3) are averaged, thereby eliminating the out-of-plane moment M_x. The weighting factor w_{jl}^k is for the averaged hit.

et al. (2007). Calculation of the weighting factors and the definition of the balance centre is detailed in Section 4.5 for the M12REST engine.

Using the overall impulse responses for each bar we may write

$$\begin{pmatrix} y_1 \\ y_2 \\ y_3 \\ y_4 \end{pmatrix} = \begin{bmatrix} G_N^1 & G_A^1 & G_M^1 \\ G_N^2 & G_A^2 & G_M^2 \\ G_N^3 & G_A^3 & G_M^3 \\ G_N^4 & G_A^4 & G_M^4 \end{bmatrix} \begin{pmatrix} u_N \\ u_A \\ u_M \end{pmatrix} \delta t \tag{4.12}$$

The final step in the formation of the GIRF involves the combination of the signals so that that the number of outputs matches the number of force components to be recovered. There are two reasons for this reduction: Firstly, the iterative deconvolution algorithm of Prost and Goutte (1984) was implemented in the Fortran program HYFORCE (Mee, 2007) for square systems. Secondly, the signals are combined in such a way as to enhance the diagonal dominance of the GIRF matrix and improve the ability of the balance to recover an input load. The reduction of signals is achieved using an output specification matrix A_o as follows

$$\begin{pmatrix} y_N \\ y_A \\ y_M \end{pmatrix} = A_o \begin{pmatrix} y_1 \\ y_2 \\ y_3 \\ y_4 \end{pmatrix} \tag{4.13}$$

$$= \begin{bmatrix} a_{N1} & a_{N2} & a_{N3} & a_{N4} \\ a_{A1} & a_{A2} & a_{A3} & a_{A4} \\ a_{M1} & a_{M2} & a_{M3} & a_{M4} \end{bmatrix} \begin{pmatrix} y_1 \\ y_2 \\ y_3 \\ y_4 \end{pmatrix} \tag{4.14}$$

$$= \begin{bmatrix} G_{NN} & G_{NA} & G_{NM} \\ G_{AN} & G_{AA} & G_{AM} \\ G_{MN} & G_{MA} & G_{MM} \end{bmatrix} \begin{pmatrix} u_N \\ u_A \\ u_M \end{pmatrix} \delta t \tag{4.15}$$

Note that Equation (4.15) has the same form as Equation (4.5). The output specification matrix used in this thesis for the primary gauges ($A_{o,p}$) was

$$A_{o,p} = \begin{array}{c} \\ N \\ A \\ M \end{array} \begin{array}{c} \begin{array}{cccc} 1 & 2 & 3 & 4 \end{array} \\ \begin{bmatrix} 0 & -0.5 & 0 & 0.5 \\ 0.5 & 0 & 0.5 & 0 \\ -0.25 & 0.25 & 0.25 & 0.25 \end{bmatrix} \end{array} \tag{4.16}$$

The selection of these factors is a choice in the design of the force balance calibration and depends on the relative sensitivities and polarities of the individual gauges and on the arrangement of the stress bars. The values should be chosen to reduce the cross-coupling of the balance. For the current work, the rationale behind Equation (4.16) is as follows: the signals

from bars 1 and 3, being parallel to the axial direction were averaged to give the axial strain. Similarly, the signals from bars 2 and 4, being parallel to the normal direction, were averaged to give the normal strain. The difference between the signals from bars 1 and 3 and the difference between the signals from bars 2 and 4 were averaged to give the moment strain. Finally, bar 2 was inversed in order to account for the opposite polarity of this gauge relative to the other primary gauges (Appendix B.4).

Using the notation of Equation (4.7), the GIRF sub-matrix that relates output $\nu \in \{N, A, M\}$ to a distributed load in direction-l may be written as

$$G_{\nu l} = \sum_{ijk} a_{\nu i} w_{jl}^{k} G_{k}^{ij} \tag{4.17}$$

where $a_{\nu i}$ are elements of the output specification matrix A_o. Equation (4.17) is a general equation that describes the formation of a global impulse response function from a set of calibration point loads.

4.5 CALIBRATION WEIGHTING FACTORS

In the previous section it was shown how the individual IRF may be combined to form a GIRF using a set of weightings and an output specification matrix. Defining appropriate weighting factors is perhaps the most important aspect of the calibration process. The methodology used in this thesis is described in this section. Although the nomenclature is specific to the 3CFB and M12REST engine, the methodology described here may be easily adapted to other multi-component force balances and experimental models.

For the M12REST-3CFB assembly, the calibration weighting factors w_{jl}^{k} are defined using the reference load distribution shown in Figure 4.4 for both the lift-drag and normal-axial coordinate systems. The origin of this load distribution is explained later in this section. Each column in Figure 4.4 represents the total force acting on a matching slice of the engine, with each slice corresponding to an interval centred on an axial calibration station (Figure 4.3). This load distribution is assumed to artificially act on the top surface of the engine because this is where the calibration hits are performed. As introduced in Section 4.4, the calibration weighting factors must satisfy the four constraints encapsulated by Equations (4.8) to (4.11). To ensure that constraints 2 and 3 are satisfied, the balance centre is defined as coinciding with the centre of force location of the artificial normal-axial load distribution. With respect to the engine coordinate system, the centre of force is given by

$$a_{BC} = \frac{1}{F_{N,TOT}} \sum_{j=2}^{20} F_{jN} a_j \tag{4.18}$$

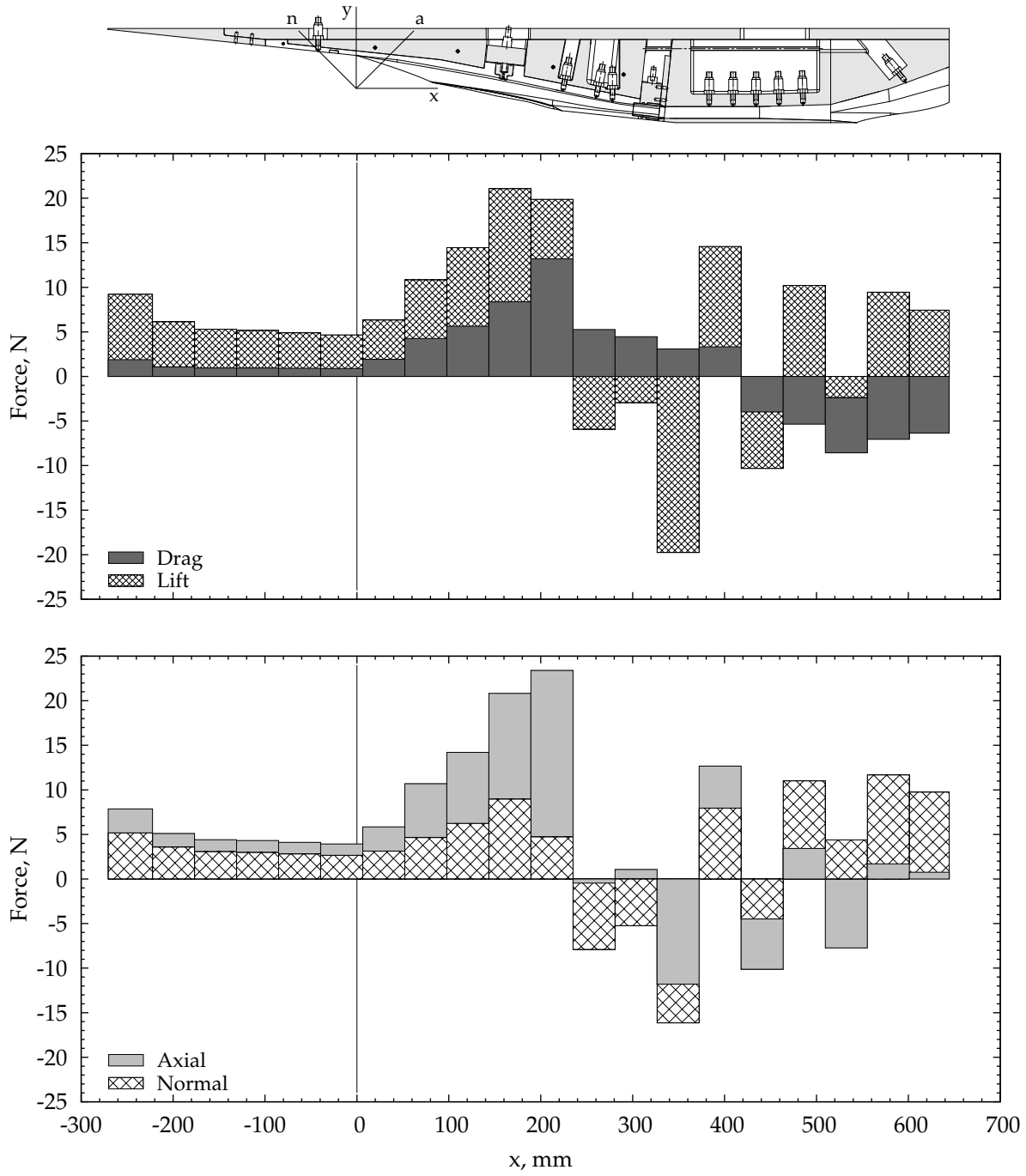

Figure 4.4 – Reference load distribution used for the formation of the GIRF of the balance. Each column represents the total forces acting on a slice of the engine. This distribution corresponds approximately to a fuel-on load distribution for the M12REST engine. It was created from the fuel-off load distribution given in Figure 4.5.

$$n_{BC} = \frac{1}{F_{A,TOT}} \sum_{j=2}^{20} F_{jA} n_j \tag{4.19}$$

where (a_j, n_j) are the coordinates of the jth axial station (Figure 4.4 and Appendix E), F_{jk} with $k \in \{N, A\}$ is the total force acting on a slice of the engine and $F_{k,TOT}$ is the net force. Note that due to difficulty in obtaining a single clean hit at the first calibration station ($j = 1$), only calibration stations 2 to 20 were used to form the GIRF. With the centre of the balance known, the moment arm for each calibration hit is

$$d_j^k = k_j - k_{BC} \tag{4.20}$$

To ensure that constraints 1 and 4 are satisfied, the weighting factors are defined as follows

$$w_{jk}^k = \frac{F_{jk}}{F_{k,TOT}} \tag{4.21}$$

$$w_{jM}^k = \frac{M_{jk}}{\sum_{jk} \delta_k M_{jk} d_j^k} = \frac{\delta_k F_{jk} d_j^k}{\sum_{jk} F_{jk} d_j^k d_j^k} \tag{4.22}$$

$$\delta_k = \begin{cases} 1 & \text{for } k = N \\ -1 & \text{for } k = A \end{cases}$$

where M_{jk} is the moment about the balance centre due to force F_{jk}. The factor δ_k enforces a right-hand sign convention for the moment. The complete set of weighting factors is provided in Appendix B.6.

The load distribution depicted in Figure 4.4 is one of three reference load distributions that were investigated for this thesis and corresponds approximately to a fuel-on load distribution for the M12REST engine. The other two load distributions were

(1) a fuel-off load distribution and,

(2) a uniform load distribution.

The fuel-off load distribution is provided in Figure 4.5. This distribution was computed from the fuel-off numerical simulation presented in Chapter 5 by integrating the surface pressure and viscous forces. Since no fuel-on computational data was available for this thesis, the fuel-on load distribution provided in Figure 4.4 was artificially created from the fuel-off load distribution. The modifications to the fuel-off distribution consisted of adding a drag increment of $-6\,N$ to each distribution slice in the divergent protion of the combustor and engine nozzle (stations $j \geqslant 16$) and adding a lift increment of $5\,N$ to each distribution slice in the open portion of the engine nozzle (stations $j \geqslant 18$). Due to its simplicity, no figure depicting the uniform load distribution is provided in this thesis.

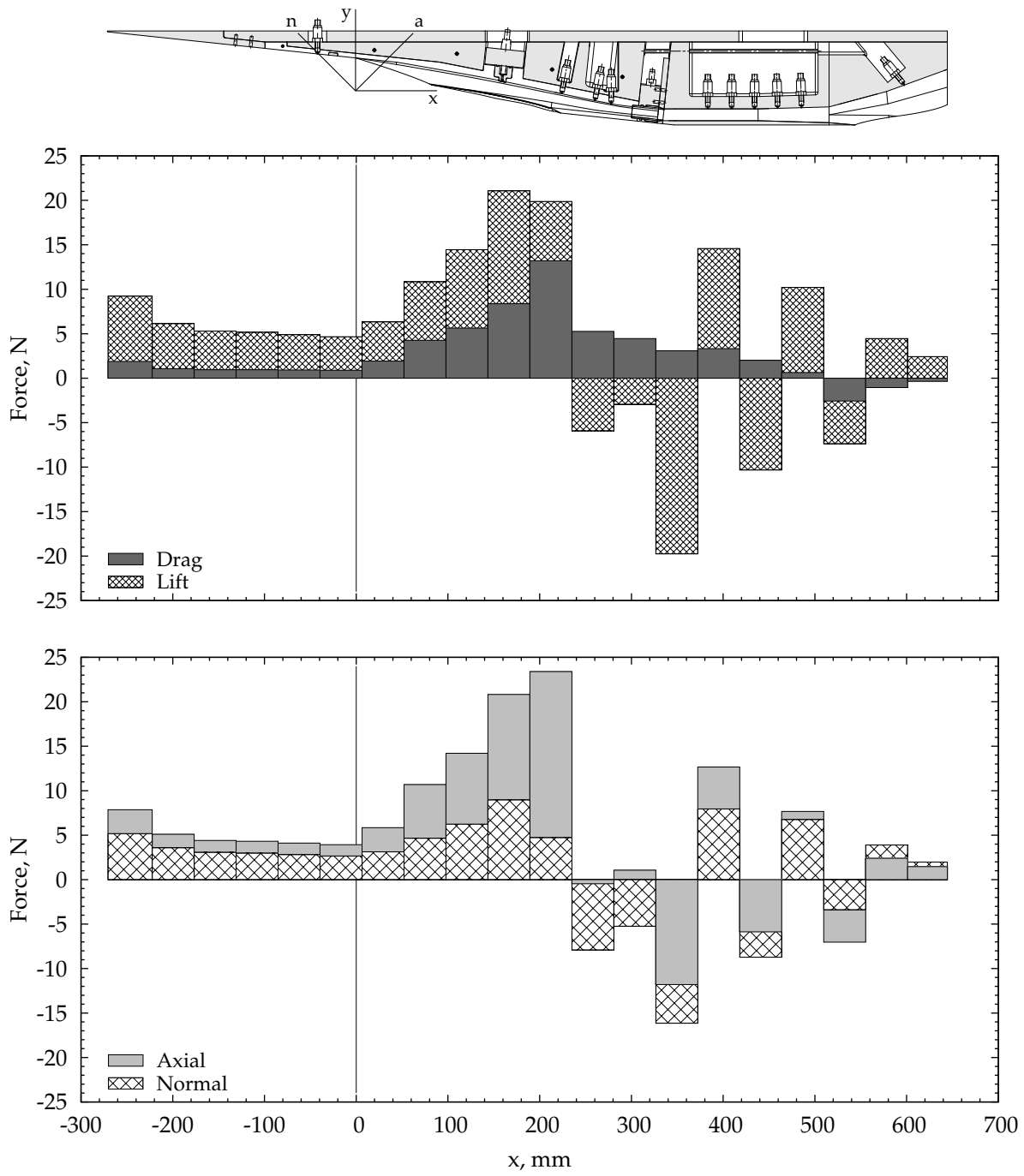

Figure 4.5 – Fuel-off load distribution for the high pressure test condition. Each column shows the total forces acting on a slice of the engine.

Studying the fuel-off load distribution provided in Figure 4.5 it can be seen that, moving downstream, both the lift and drag initially decrease due to a reduction in surface pressure caused by flow spillage from the slender forebody (Section 5.3). In the inlet, the lift and drag increase in magnitude as the flow is compressed, with the largest forces occurring at the cowl closure location ($x \approx 215\,\text{mm}$) where flow is spilled from the inlet and the inlet shocks interact with the forebody shock (Figure 5.3). Unsteadiness in the flow spilled from the inlet and forebody would result in a time-varying force being imparted to the model and although schlieren visualisation of the cowl closure location would provide a good indication of this unsteadiness, the relative position of the model and test section windows prevented any such visualisation from being completed in this thesis (see Figure 7.2 and Appendix K). Once downstream of the cowl closure location, the inlet surfaces begin to turn and become aligned with the flight direction causing the drag distribution to decrease while the lift alternates between positive and negative according to the shock impingement locations (Figure 5.4). Within the divergent portion of the combustor the drag drops sharply and decreases further in the nozzle such that some thrust is generated. Figure 4.4 clearly shows that drag accumulated in the front three-quarters of the engine is not counteracted by the nozzle thrust; a result that is expected for a fuel-off simulation.

Of the three load distributions, a GIRF formed using the approximate fuel-on load distribution (Figure 4.4) was found to most accurately recover different input loads. Evaluation of the GIRF is discussed in Section 4.6. The dependency of the quality of a GIRF on the form of the reference load distribution is due to changes in the balance centre location. As described above, the balance centre is defined as coinciding with the centre of force for the normal-axial reference load distribution. Defining the balance centre in this way ensures that the weighting factors satisfy constraints 2 and 3 as given by Equations (4.9) and (4.10). The consequence of this definition is that the balance centre is not unique, but is dependent on the form of the reference load distribution. In turn, the location of the balance centre affects the extent of coupling between the normal and axial strain outputs and the moment input. A GIRF formed using the fuel-on load distribution was found to be less coupled than one formed from either the fuel-off or uniform load distributions and so was better able to recover different input loads (Doherty, 2013c).

4.6 Evaluation of the Calibration Data and GIRF

The creation of a GIRF from a set of hammer hits represents only half of the calibration procedure. Once formed, the GIRF must be assessed to determine how well it characterises the true response of the balance. For a well-designed balance, a GIRF that sufficiently characterises the

true response will accurately recover arbitrary load distributions that are applied to the model with arbitrary time history. Hence, the GIRF is assessed by examining its ability to recover various input loads. This assessment is accomplished via a convolution-deconvolution cycle: Each individual IRF is convolved with a unit-load that has a prescribed time history.[9] The output of the convolution is a set of expected unit-load strain responses. A weighted summation of these unit responses according to a specified loading distribution and the output specification matrix[10] gives the *expected* net-strain response of the balance. Deconvolving the expected net-strain with the GIRF recovers the input forces which may then be compared with the known inputs.[11] The unit-load used in thesis for evaluation of the GIRF is shown in Figure 4.6. The time history of this load approximately matches that expected during a typical test in the T4 Stalker Tube (cf. Figure 3.19), albeit shifted in time.

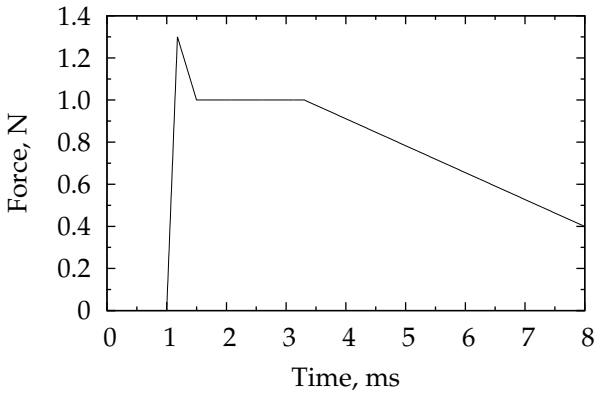

Figure 4.6 – Time history for a unit, tunnel-type input load

The convolution-deconvolution process described above allows the sensitivity of the GIRF to variations in the input load distribution and to different combinations of the calibration hits to be quantified, thereby allowing the quality of the balance design and the calibration to be assessed. For this thesis a total of eight different evaluation criteria of the calibration data and GIRF were used. These are listed below in the order of completion. Items 1 and 2 assess the quality of the individual calibration hits and the individual IRF while items 3 to 7 assess the quality of the GIRF by examining its ability to recover various distributed and point loads.

Two calibrations of the force balance were completed; one prior to the

9 Note that in this thesis the term 'unit-load' is used to refer to an input that has unit magnitude and is constant during a prescribed test time. Outside of the prescribed test time the load magnitude can vary and may be larger than or smaller than unity.

10 The output specification matrix used to combine the unit strain responses must be consistent with that used to form the GIRF, cf. Equation (4.13).

11 The net input force signal is calculated by simply scaling the unit-load by the net force of the specified loading distribution.

test campaign and one after the test campaign. These are referred to as the *pre-* and *post*-campaign calibrations. Differences between these calibrations provides an indication of the extent of change that occured to the model joints over the course of the test campaign. For each calibration two GIRF were formed; one from the primary strain gauges and one from the secondary strain gauges (Section 4.4). These are referred to as the *primary* and *secondary* GIRF. Calibration results for the pre- and post-campaign primary GIRF are presented and discussed in the remaining sections of this chapter. Similar results were attained for the secondary GIRF; these may be found in Doherty (2013c).

Three hammer hits were completed at each location for each calibration. Hit sets 1 and 2 were used to form the GIRF while hit set 3 was used to form the expected net-strain response for a nominated load distribution. Experimental engine force data presented in this thesis represent the average recovered force based on the pre- and post-campaign GIRF. The eight evaluations are as follows:

1. Hammer pulse quality:
   A perfect impulse, convolved with a step should return a step. This principle allows the quality of each hammer hit to be assessed (Mee, 2002). Further discussion and sample results are provided in Appendix B.8.
2. Strain repeatability:
   Repeatability of strain responses for multiple hits and for hits on the left and right sides may be examined by comparing normalised strain signals where the area under the associated hammer pulse is used as the normalising factor. Alternatively, unit-load strain responses may be compared. Sample results for the current work are provided in Appendix B.9.
3. Point-load recovery using the GIRF:
   The normal, axial and moment strains for a unit point load were computed for every calibration hit using Equation (4.14) and the individual expected unit-strain responses for each bar.[12] These combined strains were then deconvolved using the GIRF and the recovered forces compared with the true input point load. Sample results for the current work are provided in Appendix B.10.
4. Recovery of the reference load distribution:
   The third set of individual unit-load strain responses were combined according to the reference load distribution given in Figure 4.4. The resulting normal, axial and moment strain signals, known as the *expected* strain signals, were then decovolved using the GIRF and the recovered forces compared with the known input forces. Since the

12 In this thesis the expected strains for the left and right hits were averaged prior to formation of the expected normal, axial and moment strains.

GIRF was formed using the same load distribution but from hit sets 1 and 2, this evaluation provides both a check on the formation of the GIRF and allows the sensitivity of the GIRF to small changes in the component strains to be assessed. Results are given in Figure 4.7 and are discussed in Section 4.6.1.

5. Fuel-off distributed load recovery:
   The sensitivity of the GIRF to the shape of the load distribution was assessed by examining the ability of the GIRF to recover the fuel-off distributed load provided in Figure 4.5. Following a similar methodology to item 4, the normal, axial and moment strains corresponding to this force distribution were computed and deconvolved using the GIRF. Results are given in Figure 4.10 and are discussed in Section 4.6.2.

6. Fuel-off lower distributed load recovery:
   The sensitivity of the GIRF to the location of the load distribution was assessed by completing additional calibration hits to the lower and rear surfaces of the M12REST engine. Individual IRF for these hits were generated and convolved with the input load given in Figure 4.6 to generate the expected unit-load strain responses.

   Following the methodology of item 4, the strains from both the lower and upper hits were combined according to the fuel-off load distribution given in Figure 4.5. The resulting normal, axial and moment strains were then deconvolved using the GIRF and the recovered forces compared with the known inputs. Results are given in Figure 4.12 and are discussed in Section 4.6.3.

7. Distributed side load recovery:
   Additional calibration hits perpendicular to the side of the M12REST engine were conducted. These hits permitted an assessment of the sensitivity of the GIRF to asymmetric out-of-plane forces. For each side hit, individual IRF were generated and convolved with the unit tunnel-type load of Figure 4.6. The resulting unit-strain responses were combined assuming a uniform pressure acted on the side of the engine. The normal, axial and moment strains were then deconvolved using the GIRF. Results are provided in Appendix B.12.

The following three sections discuss items 4 to 6 in further detail. Only calibration results for the primary GIRF are discussed in this thesis. Results for the secondary GIRF were found to be comparable with those of the primary GIRF and are presented in full in Doherty (2013c).

4.6.1 *Recovery of the Reference Load Distribution*

The ability of the pre- and post-campaign GIRF to recover the net forces of the reference (fuel-on) load distribution are shown in Figure 4.7 for both

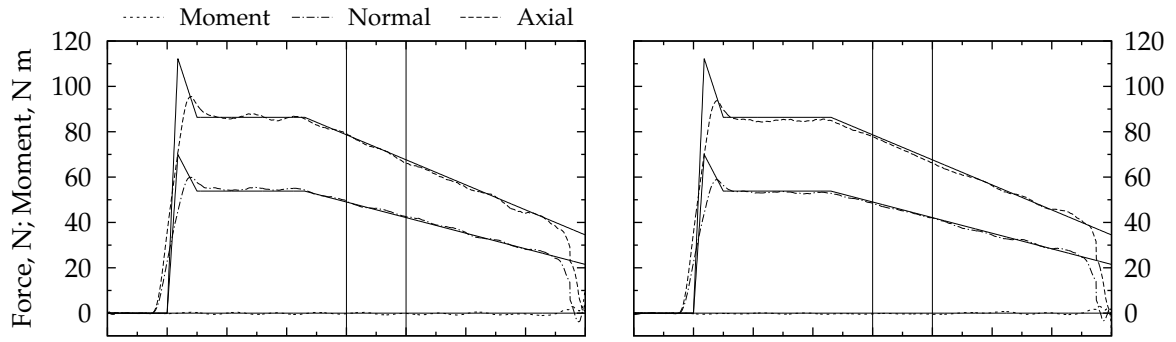

(a) Recovered normal, axial and moment force components.

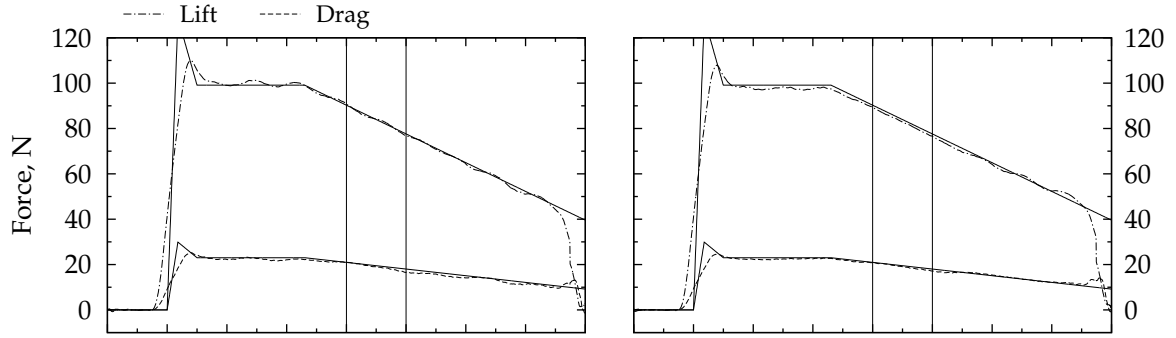

(b) Recovered lift and drag force components. These are computed via a coordinate transformation from the recovered Normal and Axial forces (Appendix E).

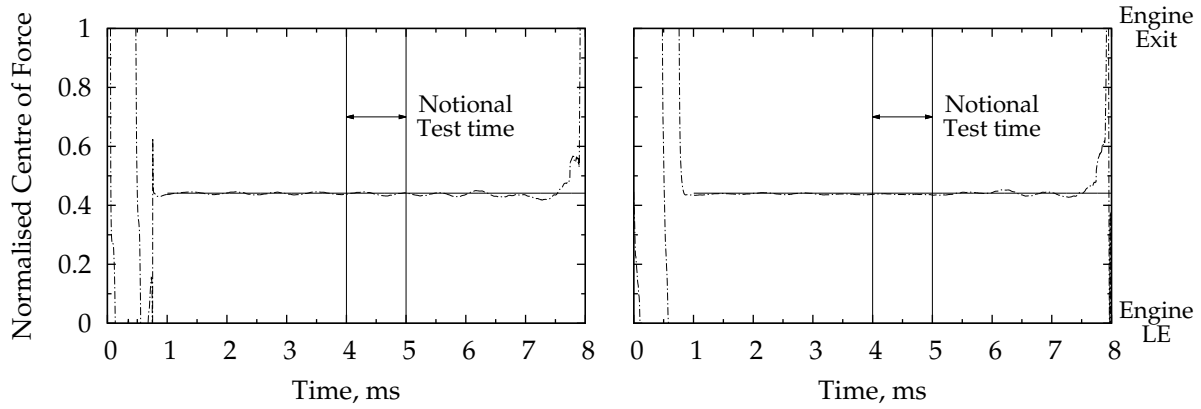

(c) Recovered normalised centre of force. This is computed from the recovered lift, drag and moment using knowledge of the balance centre and leading edge locations (Section 4.7).

Figure 4.7 – Reference (fuel-on) distributed load recovery using the GIRF formed from the *primary* gauges. *Pre*-campaign calibration data is given in the left hand column, *post*-campaign calibration data is given in the right hand column. The recovered forces have been filtered by a 500 µs moving average.

the normal-axial-moment and lift-drag coordinate frames. The recovered centre of force, computed from the lift and drag using knowledge of the balance centre and leading edge locations has also been plotted.[13] Pre-campaign calibration data are shown in the left column; post-campaign calibration data are shown in the right column. For each force component the actual input load has been drawn as a solid line for comparison.

Examining Figure 4.7 it is clear that both the time history and magnitude of the input load are well recovered by each GIRF. Taking an average[14] between 4 and 5 ms, the drag was recovered to within −2.8 % of the input, the lift to within −0.1 % and the centre of force to within −0.4 % for the pre-campaign GIRF. For the post-campaign GIRF, the drag, lift and centre of force were recovered to within −2.2 %, −1.3 % and −0.8 % of the inputs respectively. Note that a negative sign indicates that the recovered force was smaller than the input force. Average forces are given in Table 4.1 for the input signals.

Table 4.1 – Nominal Forces for each Distributed Load for a Test Time between 4 and 5 ms

	Units	Reference[a]	Fuel-off	Lower Fuel-off
Lift	N	83.9	71.2	79.0
Drag	N	19.5	44.9	44.9
Centre of Force	mm	403.5	324.1	336.6

[a] aka Fuel-on

The lack of perfect recovery of the input forces is a consequence of using a finite number of deconvolution iterations[15] and the imperfect repeatability of the individual strain responses; hit sets 1 and 2 were used to form the GIRF while hit set 3 was used to form the strain signals that were deconvolved. Noting that both the GIRF and expected strain signals were formed using the upper calibration hit data and the same reference load distribution, the GIRF was expected to recover the input forces. The good match between the input and recovered time histories thus indicates the correct implementation of the methodology detailed in Sections 4.3 to 4.5.

Studying the results in Figure 4.7 it can be seen that the recovered forces rise earlier and more slowly than the input forces and that the recovered

13 See Section 4.7 for details of this calculation.

14 This period is equivalent to a test time between 3.5 and 4.5 ms in Figure 3.19 and is consistent with the test time used to process the experimental force data. Note that, compared with the test time shown in Figure 3.19 for the engine pressures, a later test time was used to process force balance experiments because the engine forces were observed to establish more slowly than the engine pressures (see Sections 3.5.1 and 7.3). A longer test time was used for engine force tests in order to average over the low frequency oscillation present in Figures 4.8, 4.12, B.12 and B.13.

15 Unless otherwise states, all force results presented in this work were generated using 1500 deconvolution iterations.

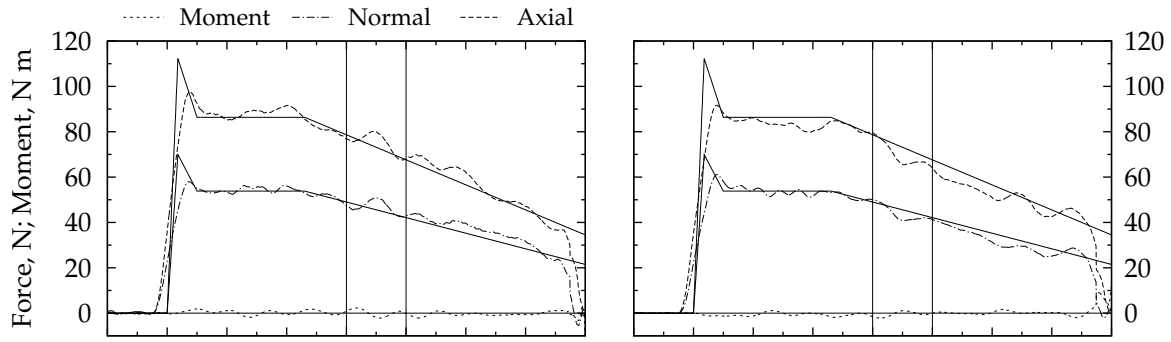

(a) Recovered normal, axial and moment force components.

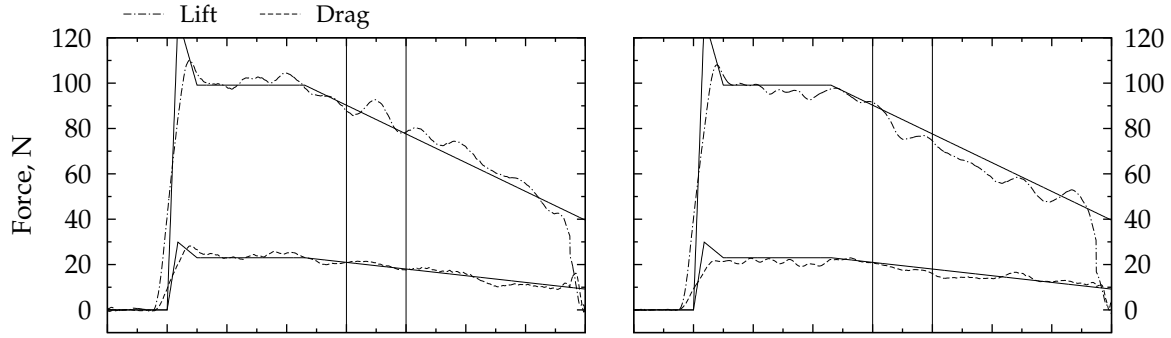

(b) Recovered lift and drag force components. These are computed via a coordinate transformation from the recovered Normal and Axial forces (Appendix E).

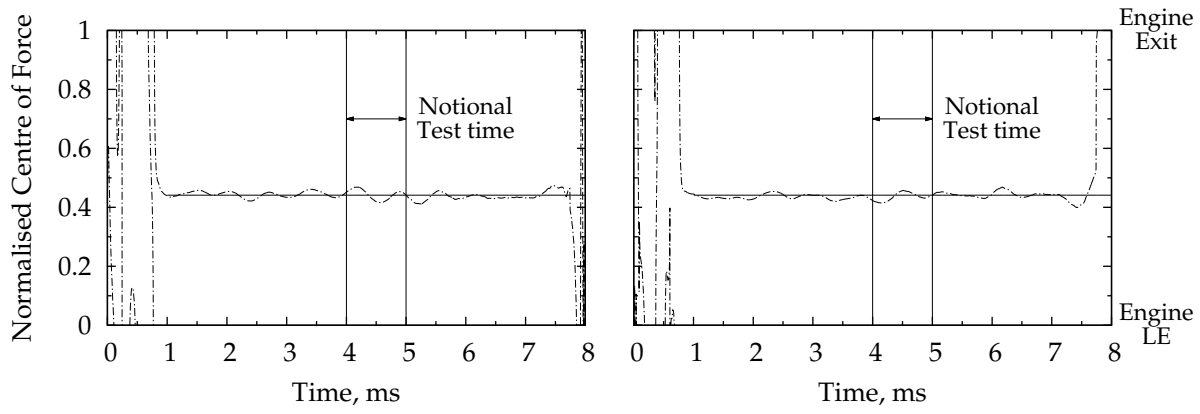

(c) Recovered normalised centre of force. This is computed from the recovered lift, drag and moment using knowledge of the balance centre and leading edge locations (Section 4.7).

Figure 4.8 – Cross-deconvolved recovered forces for the reference (fuel-on) distributed load formed from the *primary* gauges. *Pre*-campaign strain data deconvolved using the *post*-campaign GIRF is given in the left hand column, *post*-campaign strain data deconvolved using the *pre*-campaign GIRF is given in the right hand column. The recovered forces have been filtered by a 500 µs moving average.

forces do not match the peak force. These differences are primarily a consequence of filtering the recovered forces by a 500 µs moving average which was used to decrease the noise in the recovered signals.[16] It can also be seen that the post-campaign recovered forces are consistently, albeit slightly, smaller than the pre-campaign recovered forces. This suggests that the individual component strains may have changed between the two calibrations (i.e. over the course of the experimental campaign). To investigate these results further, the *pre*-campaign expected strain[17] was deconvolved using the *post*-campaign GIRF and, similarly, the *post*-campaign expected strain was deconvolved using the *pre*-campaign GIRF. This process is referred to in this thesis as cross-deconvolution, where the prefix 'cross' is added to emphasise that the expected strain and GIRF are taken from different calibrations. The forces recovered from cross-deconvolution are provided in Figure 4.8.

Comparing the results in Figure 4.8 with those in Figure 4.7, it is clear that the forces recovered from cross-deconvolution do not match the input loads as well as the forces recovered from self-deconvolution. The magnitude of the recovered signals are different from the input loads and an oscillation with period approximately 0.8 ms is present. This oscillation is particularly noticeable in the recovered centre of force signal. These results confirm that the calibration strains were different in the pre- and post-campaign calibrations. The degradation in quality of the recovered forces is a consequence of the expected net-strain signals being inconsistent with the GIRF. Even so, the degradation is not too significant. When averaged over the test time, the drag, lift and centre of force are recovered to within 2.9 %, 2.8 % and 0.6 % for the pre-campaign strain deconvolved with the post-campaign GIRF (i.e. the left hand column in Figure 4.8). Similarly, when the post-campaign strain is deconvolved with the pre-campaign GIRF, the drag, lift and centre of force are recovered to within −6.1 %, −4.5 % and −1.2 % respectively. These errors are considered acceptable for this thesis, particularly given that the experimental forces presented in Chapter 7 actually represent the average of the forces recovered using both the pre- and post-campaign GIRF.[18]

Further confirmation that the calibration strains changed over the course of the experimental campaign is provided by Figure 4.9 in which nor-

16 The deconvolution process amplifies noise on the signals (Sanderson and Simmons, 1991), so some form of filtering is usually required.

17 Explained earlier in Section 4.6, the expected strains are formed by combining the individual strains responses of each calibration location according to the defined loading distribution and output specification matrix. Only data from the third calibration hit set were used to form the expected strain in this thesis.

18 Taking the average of the pre- and post-campaign recovered forces plotted in Figure 4.8, the drag, lift and centre of force are recovered to within −1.6 %, −0.9 % and −0.3 % of the input force during the notional test time. These differences are comparable with the self-deconvolved results.

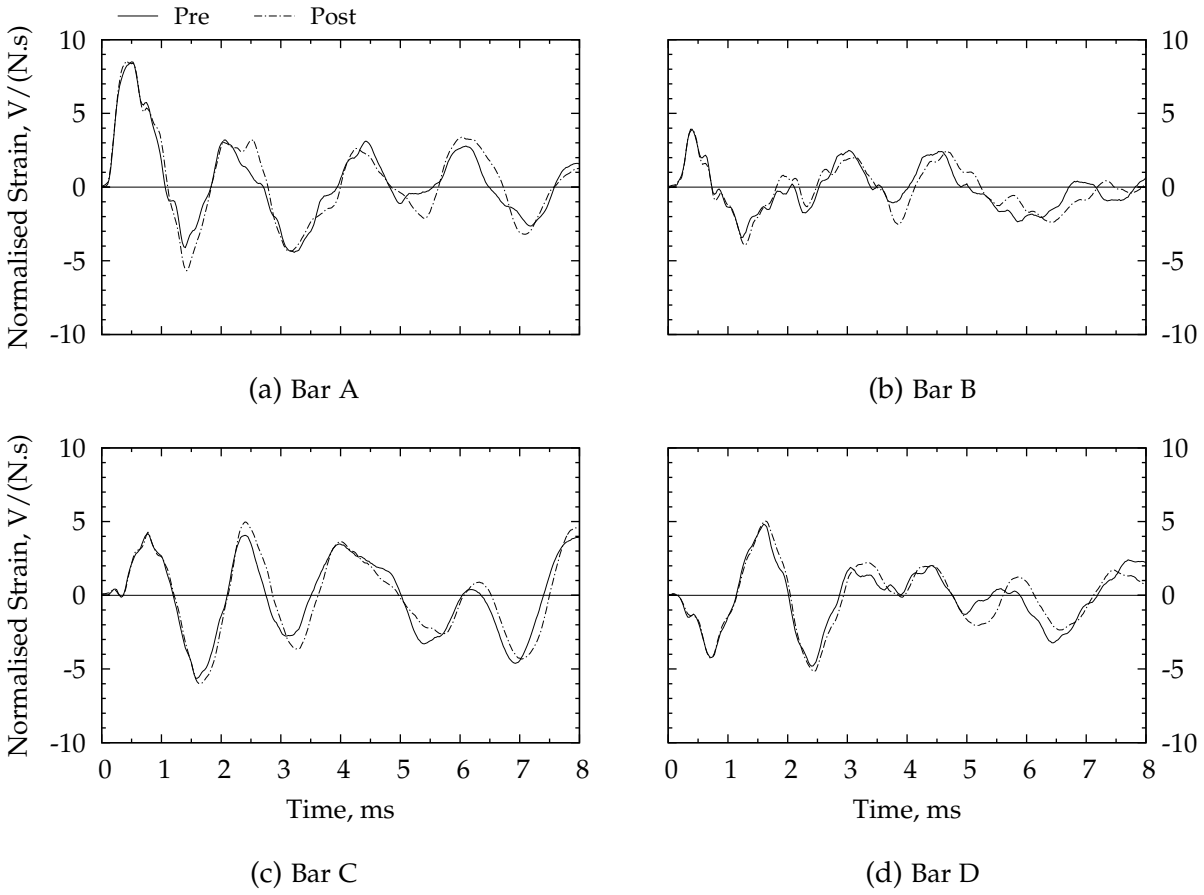

Figure 4.9 – Comparison of the pre- and post-campaign normalised strain signals for hit LUA052. *Primary* strain data.

malised strain signals[19] from the pre- and post-campaign calibration are compared for upper calibration hit LUA05_2. The most notable difference is that the higher frequency content that was present in the pre-campaign data is suppressed in the post-campaign data. The signal peaks are also affected and at later times the post-campaign signals are shifted in time relative to the pre-campaign signals. Comparisons of the calibration data at other locations show similar changes. A loss of high frequency content from the waves transmitted across an interface indicates that the interface joint was not sufficiently rigid or that insufficient grease was used.[20] Throughout the development of the M12REST engine careful attention was paid to the mechanical design to ensure that each joint would be under a compressive load once assembled (Doherty, 2013b). Futhermore,

19 See item 2 on page 92.

20 Typically a grease is used at each interface to povide a transmission medium for the stress waves. Using the test model shown in Figure B.1, Robinson (2003a, Section 5.4.3) found that neglecting to use grease at each interface adversely affected the repeatability, symmetry and form of the calibration strains.

during assembly Loctite® 515™ Master Gasket was applied to each sealing interface and Molykote® 111 compound grease[21] was applied to each non-sealing interface (Doherty, 2013b). A transmission medium for the stress waves was thus present at every joint of the model. Finally, when the model was disassembled at the end of the test campaign no loose screws were identified. Hence, exactly what changed with the model, or when the change occurred remains unresolved. Prior to future experiments with the 3CFB and M12REST engine it is recommended that the long term stability of Loctite® 515™ as a stress wave transmission medium be investigated.[22] It is also recommended that regular calibrations of the force balance be completed throughout the duration of any future experimental campaigns.

4.6.2 *Fuel-off Distributed Load Recovery*

The ability of the pre- and post-campaign GIRF to recover the net forces of the M12REST fuel-off distributed load are shown in Figure 4.10 for both the normal-axial-moment and lift-drag coordinate frames. Again the computed centre of force and the actual input loads have been plotted. Examining Figure 4.10 it is clear that both the time history and magnitude of the input load are well recovered by each GIRF. The quality of the recovered force signals is comparable with that obtained in Figure 4.7 for recovery of the reference load distribution. The slight differences that exist between the recovered and input force signals are attributed to small changes in the component strains. Taking an average between 4 and 5 ms, the drag, lift and centre of force were recovered to within −1.3 %, −1.4 % and −1.3 % of the input for the pre-campaign GIRF and were recovered to within −1.3 %, −1.6 % and −1.7 % of the input for the post-campaign GIRF. These results demonstrate that a GIRF formed using the reference, fuel-on, load distribution is able to accurately recover a fuel-off distributed load.

Cross-deconvolved results, in which the pre-campaign strain is deconvolved with the post-campaign GIRF and vice versa, are provided in Figure B.12. Comparing Figures 4.10 and B.12 it can be seen that the forces recovered from cross-deconvolution do not match the input loads as closely as forces recovered from self-deconvolution. This is consistent with the results presented and discussed in Section 4.6.1 for the reference load distribution. The extent to which the cross-deconvolved forces are different from the self-deconvolved forces is comparable with that obtained for the reference load distribution. Therefore, as discussed in detail in Section 4.6.1, the reduced quality of the cross-deconvolved recovered forces is taken to be a consequence of differences in the measured strain signals for the pre- and post-campaign calibrations as shown in Figure 4.9.

21 Otherwise known as o-ring or vacuum grease.

22 Robinson (2003a) previously investigated the use of Molykote® 111 as a stress wave transmission medium and found that strain signals measured several weeks apart were repeatable.

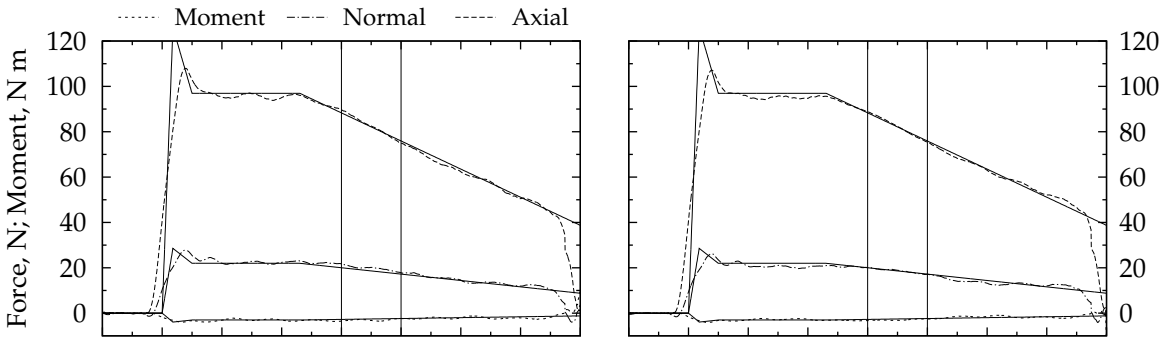

(a) Recovered normal, axial and moment force components.

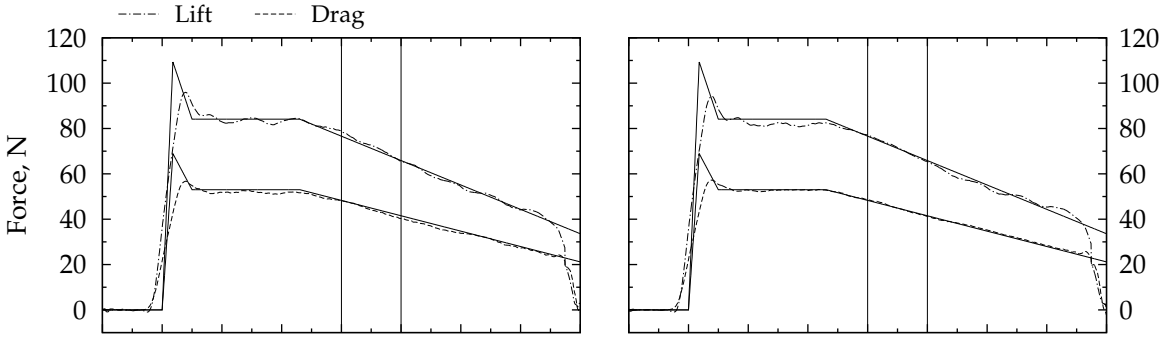

(b) Recovered lift and drag force components. These are computed via a coordinate transformation from the recovered Normal and Axial forces (Appendix E).

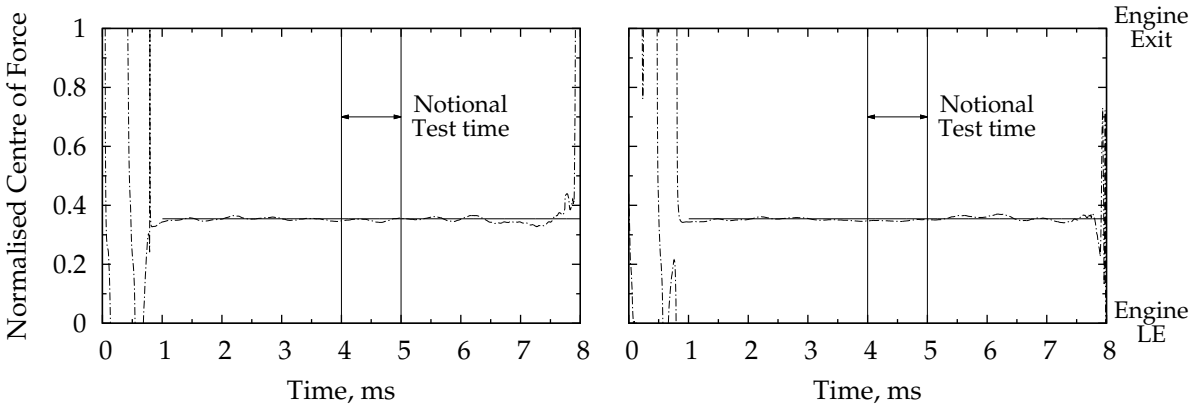

(c) Recovered normalised centre of force. This is computed from the recovered lift, drag and moment using knowledge of the balance centre and leading edge locations (Section 4.7).

Figure 4.10 – Fuel-off distributed load recovery using the GIRF formed from the *primary* gauges. *Pre*-campaign calibration data is given in the left hand column, *post*-campaign calibration data is given in the right hand column. The recovered forces have been filtered by a 500 µs moving average.

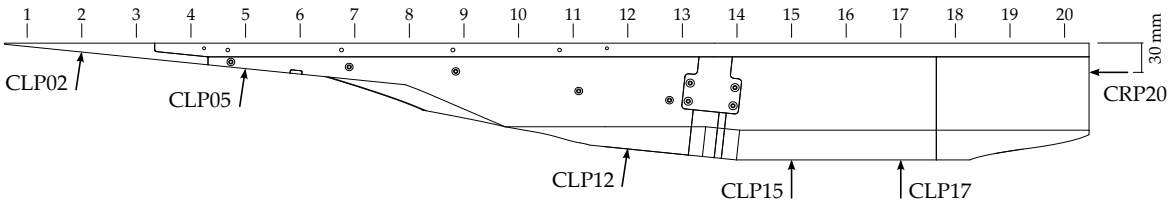

Figure 4.11 – Lower calibration hit locations

4.6.3 *Fuel-off Distributed Lower Load Recovery*

The third evaluation of the GIRF required additional calibration hits to be completed on the lower and rear surfaces of the model. Depicted in Figure 4.11, these hits were performed at six locations on the symmetry plane of the engine and perpendicular to the local surface. Two hits were performed at each location. Unit-strain responses of the five lower locations were combined according to the fuel-off lift distribution of Figure 4.5. The unit-strain response of the rear hit (CRP20) was combined with strain responses for the upper calibration locations according to the fuel-off drag distribution of Figure 4.5. Details of the calibration coordinates and weighting factors are provided in Appendix B.7. The expected strain signals were deconvolved using the associated pre- and post-campaign GIRF. The resultant recovered loads are plotted in Figure 4.12 for both the normal-axial-moment and lift-drag coordinate systems. Again, the recovered centre of force location and true input loads have been plotted.

Comparing the data of Figures 4.7, 4.10 and 4.12 it is clear the ability of the GIRF to recover the input load has been degraded through the use of the lower calibration hit data. The recovered force signals feature a higher frequency oscillation superimposed on a lower frequency oscillation. The higher frequency oscillation has a period of approximately 0.8 ms which is similar to the oscillation present in the forces recovered for the reference load distribution via cross-deconvolution (Figure 4.8). The lower frequency oscillation has a period of approximately 3.2 ms and is dominant in the recovered normal, axial and moment components. Due to the transformation to the lift-drag coordinate system, this oscillation remains in the recovered lift and centre of force but is eliminated from the recovered drag.

In comparison with the results obtained for the reference and fuel-off load distributions (Sections 4.6.1 and 4.6.2), noticeable differences exist between the forces recovered for the pre-campaign calibration data and those recovered for the post-campaign calibration data; the low frequency oscillation is more significant in the post-campaign recovered forces than in the pre-campaign recovered forces. Cross-deconvolved results for the

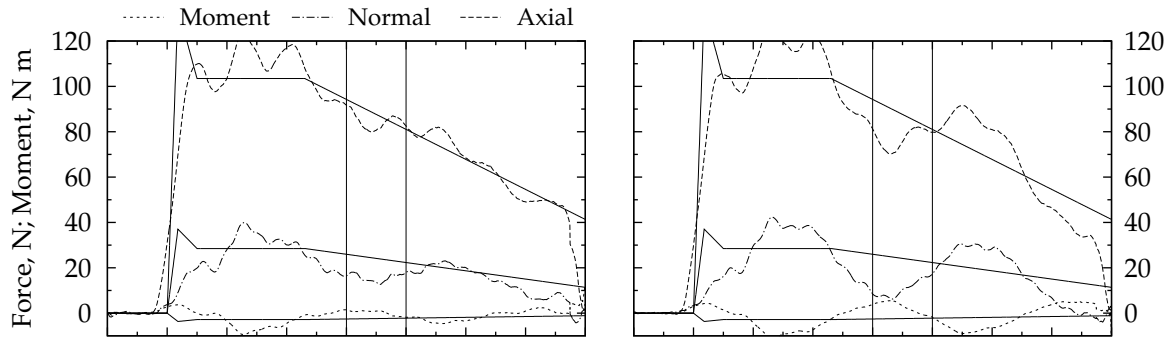

(a) Recovered normal, axial and moment force components

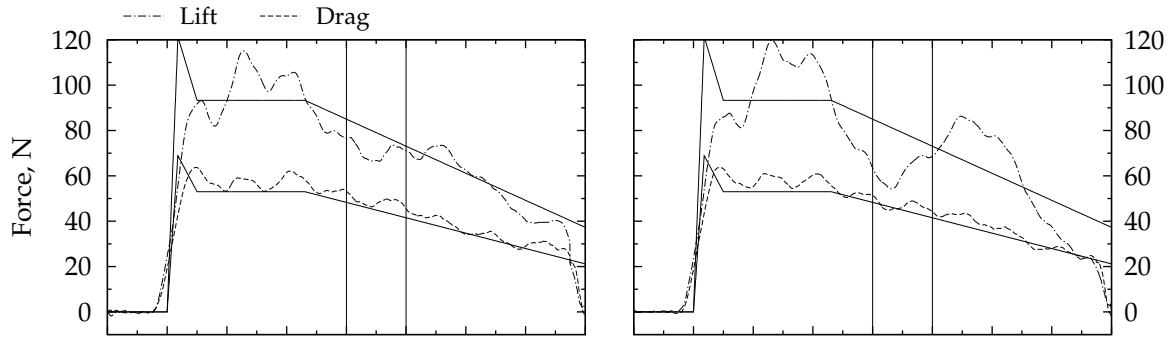

(b) Recovered lift and drag force components. These are computed via a coordinate transformation from the recovered Normal and Axial forces (Appendix E).

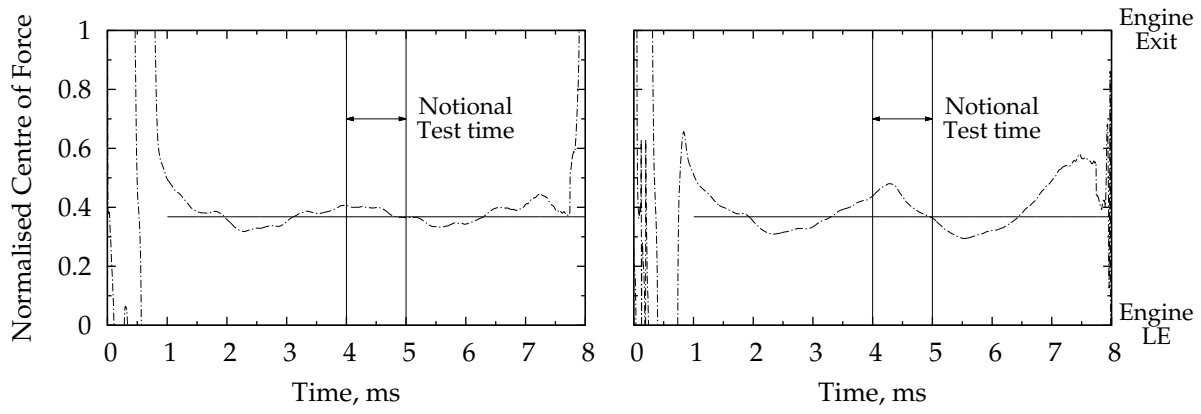

(c) Recovered normalised centre of force. This is computed from the recovered lift, drag and moment using knowledge of the balance centre and leading edge locations (Section 4.7).

Figure 4.12 – Recovered forces for the fuel-off distributed load formed from both the lower and upper calibration hits using the *primary* gauges. *Pre*-campaign calibration data is given in the left hand column, *post*-campaign calibration data is given in the right hand column. The recovered forces have been filtered by a 500 µs moving average.

lower distributed load are provided in Figure B.13 and are comparable with the self-deconvolved results presented in Figure 4.12. Such a similarity between the cross- and self-deconvolved forces was not obtained for either the reference or fuel-off load distributions (see Sections 4.6.1 and 4.6.2). These results indicate that the difference between the upper and lower distributed load strain signals is more significant than any differences in the calibration strains of the pre- and post-campaign calibrations.

There are two inter-related reasons why the pre- and post-campaign GIRF do not recover the lower distributed load very well. Firstly, hits to the lower surfaces of the engine induce a different stress wave pattern within the model than hits to the upper surface. This difference is shown in Figure 4.13 in which the normal, axial and moment unit-load strain responses for lower hits CLP12 and CLP15 are compared with the normal, axial and moment unit-load responses of equivalent hits to the upper surface of the model. Secondly, the GIRF was formed using 19 of the 20 available calibration stations (Section 4.5) whereas the lower lift strain signal was based on only five lower calibration locations (Figure 4.11). For a specified net force, the stress wave pattern induced within the model by a distributed load is different from that induced by an equivalent point load. For an ideal balance this difference would not matter. However, because the stress bars of the 3CFB used in this thesis attach to the top surface of the M12REST engine at an angle of 45°, the response of each bar is, to some extent, dependent on the distribution of load. The effect of this dependency is clearly seen in the recovered point-load forces presented in Appendix B.10. The quality of the recovered point-forces varies according to the location at which the point-load was applied. If the strain response of the balance was independent of the distribution of load, each point-load would be recovered equally well. This dependency of the response of the balance on the form of the load distribution is an inherent deficiency in the design of the 3CFB used in this thesis.

Noting that the lower unit-load strain responses plotted in Figure 4.13 are very similar to the equivalent upper unit-load responses, and that the recovered point-loads for stations 2 and 5 exhibit the same large scale, low frequency oscillation as the recovered lower distributed load (cf. Figures 4.12 and B.11), it is therefore expected that the inability of the GIRF to recover the distributed lower load is primarily related to the limited number of lower calibration hits that were used to form the expected strain signal. If additional lower calibration hits were included, it is expected that the recovered forces would more closely match the true input loads than those plotted in Figure 4.12. In this thesis the lower calibration hit data was not analysed until after the test campaign and the model and balance had been disassembled. Additional lower calibration hits were therefore unable to be completed. It is recommended that prior to future test campaigns the ability of the GIRF to recover a load formed from a full set of lower calibration hits be investigated.

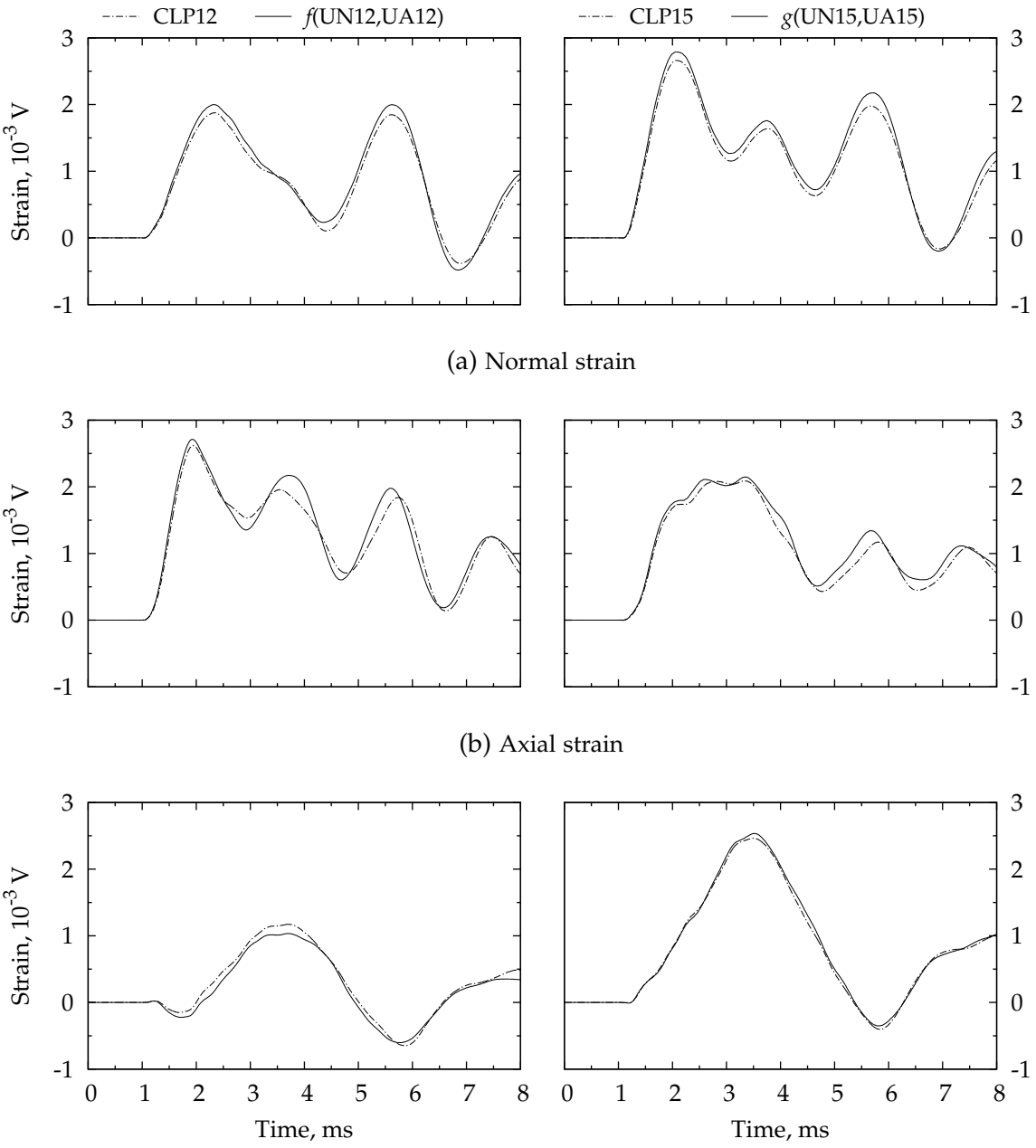

(a) Normal strain

(b) Axial strain

(c) Moment strain

Figure 4.13 – Comparison of unit-load strain responses for lower hit locations CLP12 and CLP15 with equivalent upper hit unit-load responses. Data for hit CLP12 are given in the left hand column, data for hit CLP15 are given in the right hand column. The upper hit strain responses were combined according to the following functions: $f(n, a) = ((n + a)\cos 6° + (-n + a)\sin 6°)/\sqrt{2}$ and $g(n, a) = (n + a)/\sqrt{2}$. Note that the data for CLP12 and CLP15 each represent the average of hits 1 and 2 at these locations. Similarly, the data for UN12, UA12, UN15 and UA15 each represent the average of hits 1 and 2 on the left and right sides of the model. *Pre*-campaign calibration data.

The large scale, low-frequency oscillation present in the recovered lift and centre of force plotted in Figure 4.12 means that the error for these force components is strongly dependent on the chosen test window. Even so, the relative errors for an averaging window between 4 and 5 ms are as follows: For the pre-campaign GIRF the drag, lift and centre of force were recovered to within 8.4 %, −10.4 % and 5.9 % of the input. For the post-campaign GIRF the drag, lift and centre of force were recovered to within 4.3 %, −21.5 % and 16.3 % of the input.

4.7 DATA REDUCTION: FORCE COEFFICIENTS

Engine force data are presented in this thesis in both dimensional form and also as non-dimensional force coefficients and a centre of force location. The steps required to calculate these coefficients are

1. Combine the measured strain signals using the output specification matrix defined by Equation (4.16) to give the experimental normal, axial and moment strains. Example raw and combined strain signals for a fuel-off shot are provided in Figure 4.14.
2. Deconvolve the primary combined strains using the pre- and post-campaign GIRF. This gives the *uncorrected* normal, axial and moment forces, where the recovered moment is relative to the centre of the balance.
3. Combine the normal and axial forces to give the recovered lift and drag forces (Appendix E.4).
4. Remove the lift and moment induced by the build up of pressure inside the shielding. This gives the *corrected* lift and moment. This calculation, including sample results is detailed below.
5. Calculate the net (corrected) moment about the leading edge of the engine.
6. Filter the corrected forces using a 500 µs moving average.
7. Calculate the force coefficients and centre of force location (details below).
8. Average the corrected force coefficients over a nominated test time.

The drag coeffient is defined by

$$C_D(t) = \frac{1}{A_f} \frac{F_D(t)}{q(t)} \tag{4.23}$$

where $A_f = 5552 \times 10^{-6}\,m^2$ is the projected frontal area of the M12REST engine; $F_D(t)$ is the drag force and $q(t)$ is the nozzle exit or freestream

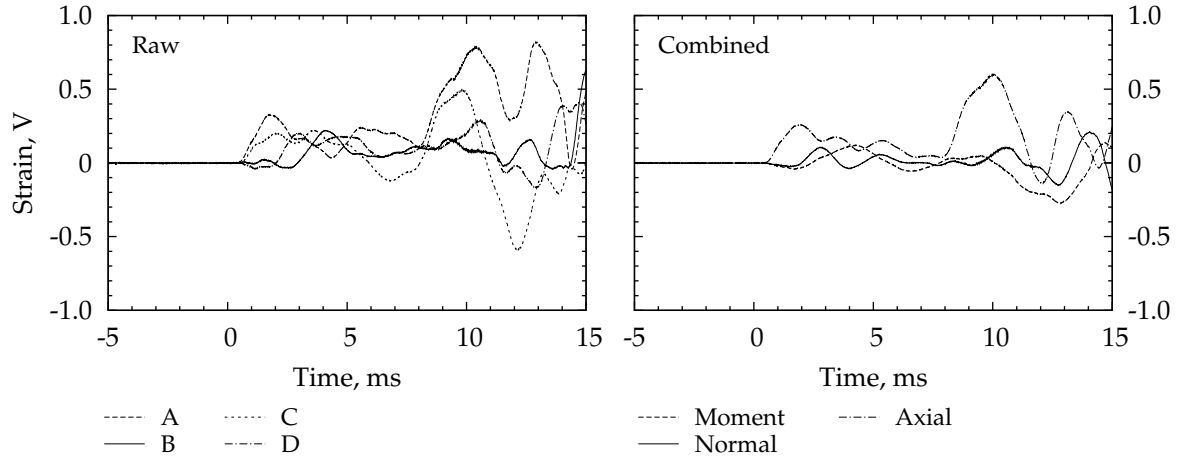

Figure 4.14 – Typical raw and combined *primary* strain signals. The data are from shot 10770. The time axis has been shifted so that zero corresponds to the trigger of the nozzle supply pressure.

---

dynamic pressure. The dynamic pressure is not directly measured for experiments conducted within the T4 Stalker Tube and so it must be inferred. Assuming that the dynamic pressure is a constant fraction of the nozzle supply pressure once the facility nozzle flow is started, then Equation (4.23) may be rewritten as

$$C_D(t) = \frac{1}{A_f} \frac{F_D(t)}{p_s(t-\tau_{PP})} \left(\frac{p_s}{q}\right)_{nom} \tag{4.24}$$

where $p_s(t)$ is the measured nozzle supply pressure and τ_{PP} accounts for the transit time from the nozzle supply region to the location of the Pitot pressure transducer and provides a good indication of flow arrival at the model leading edge. The nominal nozzle supply pressure $p_{s,nom}$ and dynamic pressure q_{nom} are taken from Table 3.2 and Table 3.5, respectively and are based on a NENZFR simulation of the facility nozzle flow. Using Equation (4.24) to calculate the drag coefficient removes the shot-to-shot variation and presents the data relative to the nominal freestream dynamic pressure. This definition is consistent with the Pitot pressure based definition used by Chan (2012) and Mee (2003) and with the normalisation method used in this thesis for the engine pressure data (Section 3.5.2). In a similar way the lift and moment coefficients are defined by

$$C_L(t) = \frac{1}{A_p} \frac{F_{L,c}(t)}{p_s(t-\tau_{PP})} \left(\frac{p_s}{q}\right)_{nom} \tag{4.25}$$

$$C_M(t) = \frac{1}{A_p L} \frac{M_{BC,c}(t)}{p_s(t-\tau_{PP})} \left(\frac{p_s}{q}\right)_{nom} \tag{4.26}$$

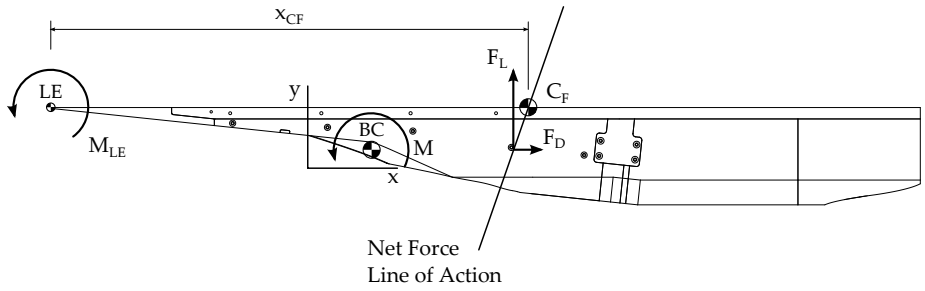

Figure 4.15 – Calculation of the experimental centre of force

where $F_{L,c}(t)$ and $M_{BC,c}(t)$ are the *corrected* lift and moment, $L = 0.915\,m$ is the overall length and $A_p = 52\,704 \times 10^{-6}\,m^2$ is the projected planar area[23] of the M12REST engine.

The moment coefficient defined by Equation (4.26) is relative to the centre of the balance. As the definition of the balance centre is somewhat arbitary (Appendix E.4), it is more physically meaningful to present either the moment about the model leading edge or a centre of force location. The corrected moment about the model leading edge is given by

$$M_{LE,c}(t) = M_{BC,c}(t) + F_{L,c}(t)(x_{BC} - x_{LE}) - F_D(t)(y_{BC} - y_{LE}) \qquad (4.27)$$

where F_D, $F_{L,c}$ and $M_{BC,c}$ are the corrected drag, lift and moment about the balance centre, and (x_{BC}, y_{BC}) and (x_{LE}, y_{LE}) are the locations of the balance centre and model leading edge in the engine coordinate system and are defined in Appendix E.4. During an experiment only the net moment about the balance centre is recovered, the individual moment contributions due to the lift and drag force distributions cannot be individually resolved. Consequently, the unique centre of force location cannot be determined experimentally, only the line of action of the net force is resolved.[24] Referring to Figure 4.15, the net force line of action is converted to a normalised centre of force location using

$$CF(t) = \frac{x_{CF}(t)}{L} = \frac{1}{L}\frac{M_{LE,c}(t)}{F_{L,c}(t)} \qquad (4.28)$$

where the vertical location of the centre of force has been chosen *a priori* to correspond to the top surface of the model, i.e. $y_{CF} = y_{LE}$.

Force Corrections

During an experiment the inner shielding cavity fills with gas. This gas exerts a moment and a negative lift on the model. Typical pressure traces

23 $A_p = L \times w$ where $L = 0.915\,m$ is the model length and $w = 0.0576\,m$ is the model width. See Figure 3.8 and Appendix E.4.

24 See Appendix F for further discussion.

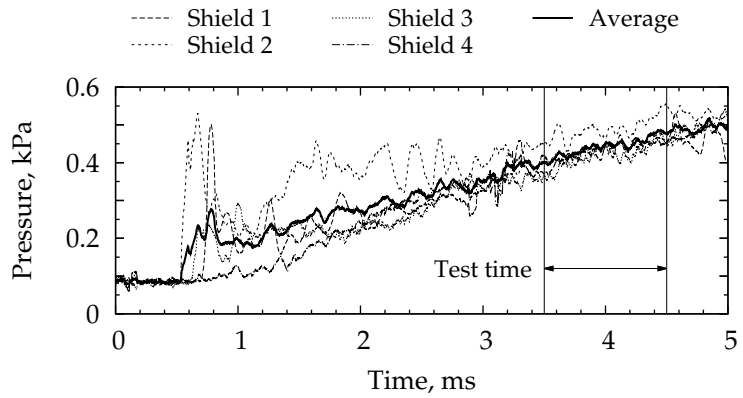

Figure 4.16 – Typical inner shielding pressure for a shot at the lower pressure test condition. These data are for shot 10770 and have been filtered by a 60 µs moving average. The time axis has been shifted so that zero corresponds to the trigger of the nozzle supply pressure.

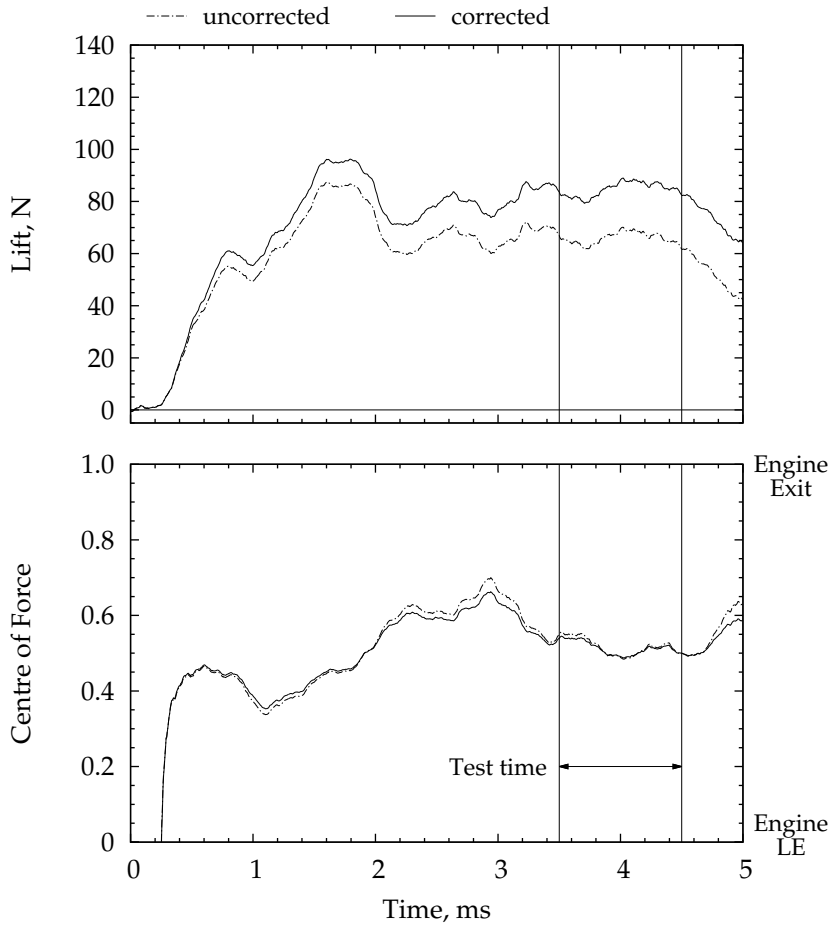

Figure 4.17 – Influence of shielding pressure build-up on the recovered lift and centre of force. These data are for shot 10770 and have been filtered using a 500 µs moving average. The time axis has been shifted so that zero corresponds to the trigger of the nozzle supply pressure.

for a shot at the low pressure test condition are provided in Figure 4.16. Reasonable agreement between the four measurements was usual which, due to the different locations of the measurements (Figure 4.2), indicates that the pressure within the shielding cavity was relatively uniform. During the test time, the inner shielding pressures were comparable to the freestream static pressure (cf. Table 3.3). The lift and moment induced by the pressure build-up were calculated assuming that the averaged pressure acts uniformly on the top surface of the M12REST engine. These forces were then subtracted from the recovered lift and moment to give the corrected lift and moment, as follows

$$F_{L,c}(t) = F_L(t) + A_p p_{sh}(t) \tag{4.29}$$

$$M_{BC,c}(t) = M_{BC}(t) - p_{sh}(t)\frac{A_p}{2}\left(2(x_{BC} - x_{LE}) - L\right) \tag{4.30}$$

where $p_{sh}(t)$ is the average inner shielding pressure. The corrected lift and moment are used to define the centre of force as per Equation (4.28). A comparison of the raw and corrected lift and centre of force signals is provided in Figure 4.17. The results indicate that the centre of force was relatively unaffected and that negative lift induced by the pressure build-up within the shielding was approximately 25 % of the corrected signal.[25]

4.8 UNCERTAINTY ANALYSIS

This section presents an analysis of the uncertainty in the recovered forces, force coefficients and centre of force location. The analysis is based on the theory presented in Appendix C.2. Table 4.2 summarises the absolute errors in the recovered forces for each load distribution for various combinations of the primary pre- and post-campaign calibration data. Before analysing these errors it is useful to define some notation. For each load distribution, let $U^k_{f,j}$ designate the absolute error in force component $f \in \{F_L, F_D, M_{BC}, CF\}$ when GIRF $j \in \{\text{Pre}, \text{Post}\}$ is used to deconvolve strain $k \in \{\text{Pre}, \text{Post}\}$. For example, for the fuel-off load distribution, $U^{\text{Post}}_{F_D,\text{Pre}} = -1.7\,\text{N}$ is the error in the recovered drag signal generated by deconvolving the post-campaign strain with the pre-campaign GIRF.

As explained in Section 4.6, calibration hit sets 1 and 2 were used to form the GIRF, while calibration hit set 3 was used to form the strain signals to be deconvolved. The advantage of this method is that the strain signals are independent of the GIRF and so the overall calibration error of

25 Robinson (2003d, Figures 7.14 and B.1) also found that lift due to pressure build-up within the shielding was 25 to 30 % of the corrected lift value for no fuel injection.

a *particular* GIRF is given by[26]

$$(u_{f,j})^2 = \sum_k (u_{f,j}^k)^2 \tag{4.31}$$

The experimental force data presented in Chapter 7 of this thesis represent the average of the forces recovered using both the pre- and post-campaign GIRF. Since these two GIRF are independent of one another, the overall calibration error in each force component is

$$(u_f)^2 = \sum_j \left(\frac{1}{2}\right)^2 (u_{f,j})^2 = \frac{1}{4} \sum_{jk} (u_{f,j}^k)^2 \tag{4.32}$$

where Equation (4.31) has been used. Using the individual calibration errors listed Table 4.2 to evaluate Equation (4.32), the overall calibration uncertainty for each load distribution can be found. The results are provided in Table 4.3a.

Two additional uncertainties exist for the forces recovered during a shot. These are summarised in Table 4.3b. The first additional uncertainty is due to an unbalanced side force that may exist as a consequence of misalignment of the M12REST engine with respect to the nozzle flow. This uncertainty is present for both fuel-off and fuel-on experiments and, based on the analysis presented in Appendix B.12, has a magnitude of $\pm 1\,\mathrm{N}$ for the recovered lift and drag and a magnitude of $\pm 1\,\mathrm{N\,m}$ for the recovered moment about the balance centre. The second additional uncertainty is only present for fuel-on experiments and is due to the opening of the fuel solenoid valve. The magnitude of this uncertainty is $\pm 6\,\mathrm{N}$ for the recovered lift and drag and $\pm 6\,\mathrm{N\,m}$ for the recovered moment about the balance centre. These uncertainties were determined by triggering the fuel solenoid valve with no fuel in the tank and deconvolving the resulting strain signals using the GIRF. Comparing the uncertainty values in Tables 4.3a and 4.3b it can be seen that the uncertainty due to triggering of the fuel valve is significant compared with the calibration uncertainties. Therefore, for future experiments it is recommended that the on-board fuel tank and fuel solenoid valve be vibrationally insulated from the model.[27]

The total experimental uncertainty for the recovered forces are listed in Table 4.3c for both fuel-off and fuel-on experiments. For fuel-off experiments the total experimental uncertainty is calculated as the root-sum-square of the experimental misalignment uncertainty and the calibration uncertainties for the fuel-off and lower fuel-off distributed loads. For fuel-on experiments the total uncertainty is calculated as the root-sum-square of the experimental misalignment and solenoid valve uncertainties and

26 See Section 4-2.3 of Coleman and Steele (1999), in particular Example 4.2.

27 A soft gasket material such as that used for the spring attachment shown in Figure 3.17b may be suitable.

Table 4.2 – Absolute Errors in the Forces Recovered using the *Primary* GIRF for Various Combinations of the *Pre*- and *Post*-campaign Calibration Data

Strain GIRF		Pre Pre	Pre Post	Post Pre	Post Post
		Reference (Fuel-on)			
Lift	N	−0.1	2.3	−3.8	−1.1
Drag	N	−0.5	0.6	−1.2	−0.4
Moment	N m	−0.2	0.2	−0.5	−0.3
Centre of Force	mm	−1.6	2.4	−4.9	−3.4
		Fuel-off			
Lift	N	1.0	4.1	−3.0	0.1
Drag	N	−0.6	1.5	−1.7	0.1
Moment	N m	−0.5	−0.6	−0.1	−0.4
Centre of Force	mm	−4.1	−4.5	−2.6	−5.4
		Lower Fuel-off			
Lift	N	−8.2	−6.1	−18.6	−17.0
Drag	N	3.8	6.6	−0.5	1.9
Moment	N m	2.6	3.0	4.4	5.0
Centre of Force	mm	19.9	23.7	47.4	54.7

Table 4.3 – Calibration and Experimental Errors in the *Uncorrected* Recovered Forces. Force unit – N; Moment unit – N m; Centre of Force unit – mm

(a) Overall Calibration Errors

Load Distribution	u_{F_D}	u_{F_L}	$u_{M_{BC}}$	u_{CF}
Reference (Fuel-on)	0.7	2.6	0.3	3.3
Fuel-off	1.2	2.3	0.4	4.3
Lower Fuel-off	3.9	13.6	3.9	39.4

(b) Additional Experimental Errors

Error Source	u_{F_D}	u_{F_L}	$u_{M_{BC}}$
Misalignment side force	1.0	1.0	1.0
Fuel solenoid valve	6.0	6.0	6.0

(c) Total Experimental Error

Experiment Type	u_{F_D}	u_{F_L}	$u_{M_{BC}}$
Fuel-off	4.2	13.9	4.0
Fuel-on	7.4	15.3	7.2

the calibration uncertainties for all three load distributions.

Examining the values in Table 4.3c it can be seen that the total experimental uncertainty in fuel-off drag is 4.2 N, or 9.4 % of the nominal fuel-off value listed in Table 4.1. Similarly, the total experimental uncertainty in fuel-on drag is 7.4 N, or 37.9 % of the nominal fuel-on value listed in Table 4.1. Note that the relative uncertainty for the fuel-on drag force is very high because the nominal value is small. For the recovered lift, the experimental uncertainty for a fuel-on experiment is comparable with that of a fuel-off experiment and each is dominated by the calibration error for the lower distributed load. Note that the values listed in Table 4.3c are the uncertainties for the *uncorrected* forces. Uncertainties for the corrected force coefficients and centre of force location are defined next.

Experimental engine drag data are presented in this thesis in the form of a drag coefficient as defined by Equation (4.24). The total relative uncertainty of the drag coefficient is

$$X_{C_D} = \sqrt{\left(\frac{U_{F_D}}{F_D}\right)^2 + X_{q_{nom}}^2} \tag{4.33}$$

where U_{F_D} is the absolute uncertainty in the drag as given in Table 4.3c, F_D is the recovered drag force and $X_{q_{nom}}$ is the relative uncertainty in the nozzle exit dynamic pressure and is taken from either Table C.4 or Table C.3 depending on the test condition. The derivation of Equation (4.33) is presented in Appendix C.7.

Similarly, engine lift data are presented in the form of the corrected lift coefficient as defined by Equations (4.25) and (4.29). The total relative uncertainty of the corrected lift coefficient is

$$X_{C_{L,c}} = \sqrt{\left(\frac{1}{F_{L,c}}\right)^2 \left(U_{F_L}^2 + A_p^2 U_{p_{sh}}^2\right) + X_{q_{nom}}^2} \tag{4.34}$$

where U_{F_L} is the absolute uncertainty in the uncorrected lift as given in Table 4.3c, $F_{L,c}$ is the corrected lift force and $U_{p_{sh}}$ is the absolute uncertainty of the inner shielding pressure measurement. Derivation of Equation (4.34) is presented in Appendix C.7.2 and calculation of $U_{p_{sh}}$ is discussed in Appendix C.7.5

It was noted in Section 4.7 that the definition of the balance centre is arbitary and that, as such, the recovered engine moment data are presented in the form of either the moment about the model leading edge (defined by Equation (4.27)) or as the centre of force location (defined by Equation (4.28)). The uncertainty expressions for each of these quantities are derived in Appendix C.7 and reproduced as follows

$$U_{M_{LE,c}} = \Bigg(U_{M_{BC}}^2 + (x_{BC} - x_{LE})^2 U_{F_L}^2 + (y_{BC} - y_{LE})^2 U_{F_D}^2$$

$$+\left(\frac{L}{2}A_p\right)^2 u_{p_{sh}}^2\Bigg)^{\frac{1}{2}} \quad (4.35)$$

$$u_{CF} = \frac{1}{LF_{L,c}}\Bigg(u_{M_{LE,c}}^2 + L^2 CF\left(CF - \frac{2(x_{BC} - x_{LE})}{L}\right)u_{F_L}^2 + (LA_p)^2\left(CF^2 - CF\right)u_{p_{sh}}^2\Bigg)^{\frac{1}{2}} \quad (4.36)$$

where each term has been defined previously in this chapter.

ENGINE FLOW FIELD ANALYSIS

The fifth chapter, in which fuel-off numerical simulations of the engine are presented, the engine mass capture performance is examined, the net forces are quantified and we consider the question of how much drag is too much?

5

5.1 INTRODUCTION

This chapter presents an analysis of the M12REST engine flow field for the case of no fuel injection. The analysis is based on Navier-Stokes CFD simulations of the engine using the NASA code VULCAN (White and Morrison, 1999). These simulations were completed in support of the experiments with the goals of (1) providing a numerical pressure distribution with which the experimental data could be compared, (2) quantifying flow spillage from the slender forebody and the overall engine mass capture ratio, (3) providing an estimate for the net lift, drag and pitching moment of the M12REST engine, and (4) providing a force distribution for use with the calibration of the three-component force balance (Chapter 4).

Section 5.2 summarises the NASA code VULCAN that was used to perform the simulations and the computational grid. In Section 5.3 several figures are presented which document the internal and external flow fields of the M12REST engine. The significant flow features are identified and discussed. The engine mass capture performance is then discussed in Section 5.4 in the context of airframe integration of scramjet engines. Section 5.5 presents an analysis of the net forces of the M12REST engine and finally, Section 5.6 concludes the chapter with a discussion of the thrust generation capability of the M12REST engine.

5.2 NUMERICAL SCHEME AND COMPUTATIONAL GRID

Developed at the NASA Langley Research Centre, the VULCAN code (Baurle, 2012; White and Morrison, 1999) was used in this thesis for the numerical simulation of the M12REST engine. This code solves the three-dimensional Navier-Stokes equations for turbulent, chemically reacting flows using structured grids.

A schematic of the computational domain is shown in Figure 5.1. The geometry modelled in the simulations closely matched the experimental M12REST engine. Flow spillage from the forebody and engine inlet were accounted for and the external flow along the sides and lower surfaces of the engine were also modelled. Flow along the upper external surface

was not included in the simulation as this surface was shielded during the experiments (cf. Figure 4.1). The modelled forebody featured a fully-blunted leading edge of radius 0.5 mm, consistent with the design of the M12REST engine (Section 3.4.1), while, to simplify the computational grid, the half-blunted[1] inlet leading edges were modelled as perfectly sharp.

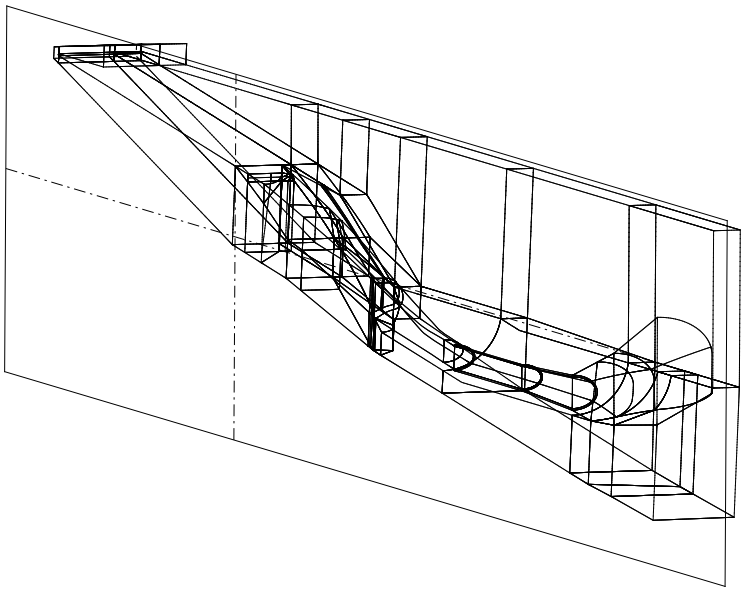

Figure 5.1 – Schematic of the computational domain for the M12REST engine. Flow is from left to right. The symmetry plane is shown and the x and y axes of the engine coordinate system are indicated by dashed lines.

Taking advantage of the symmetry of the engine geometry, only half of the experimental model was simulated. In total, the structured grid was composed of approximately 13.3 million cells divided amongst 56 blocks. The number of cells and the average cell density in both dimensional and non-dimensional form are provided in Table 5.1 for each region of the engine. The computational grid at selected cross-sections along the length of the engine is shown in Figure 5.2. Each cross-section is shown at the same relative scale. The stated axial location is relative to the engine coordinate system, as defined in Appendix E.

Examining Figure 5.2, it can be seen that a high density of cells is required to properly capture the shape transition of the inlet and the external inlet leading edge surfaces. Because the grid is structured, the inlet cell density propagates downstream into the combustor and external regions of the engine (cf. Figures 5.2d and 5.2e). Consequently, the external flow region accounts for slightly more than half the total number of cells in the computational domain and, due to the inherent compression of the

1 The terms fully-blunt and half-blunt leading edge were introduced in Section 3.4.1.

Table 5.1 – Computational Grid Dimensions for the M12REST Engine

Region	Number of cells (10^6)	Average Cell density (10^6 /unit-volume)	($1/mm^3$)
Forebody	1.777	0.420	5.4
Inlet	2.074	1.002	13.0
Combustor	1.290	4.545	58.8
Nozzle	0.507	0.474	6.1
External	7.693	1.817	23.5
Total	13.341	0.526	6.8

internal geometry, the largest cell density occurs within the combustor.

The simulation of the M12REST engine was performed using a uniform inflow of thermally perfect air at the nozzle exit conditions specified in Table 3.3a. No chemical reactions were considered and separate computations were completed for the high and low pressure test conditions. A no-slip, isothermal wall boundary condition was used at the engine surfaces with an assumed wall temperature of 300 K. This boundary condition is consistent with that used for the simulations of the facility nozzle flow (Section 3.3) and is considered appropriate for shock tunnel experiments with a test flow duration on the order of several milliseconds. The flow was assumed turbulent throughout the computational domain and was modelled using the 1998 Wilcox $k-\omega$ turbulence model with wall-matching functions (Baurle, 2012) for large values of y^+. For the simulation presented here the y^+ was less than 2.5 on the external surfaces (excluding the inlet leading edge surfaces), typically less than 60 in the inlet, less than 30 in the combustor and less than 10 in the nozzle. On the external inlet leading edge surfaces the y^+ was typically less than 15 with a peak value of 195 occuring at the cowl closure location of the inlet. This range of y^+ was considered adequate for the purposes of this thesis.

The convergence of the solution was determined by examining the error in mass flow rate across the inflow and outflow boundaries. The error in mass flow rate for the simulation presented here was 0.06 %. This level of convergence was deemed adequate for the purposes of assessing both the pressure distribution and forces on the flowpath. The simulation took approximately 30 h of wall-clock time to run in parallel on 24 processors (2.8 GHz Intel Xeon CPUs).

5.3 FLOW FIELD STRUCTURE

The flow field of the M12REST engine module is complex, being dominated by strong shock and expansion waves, and shock-shock and shock-

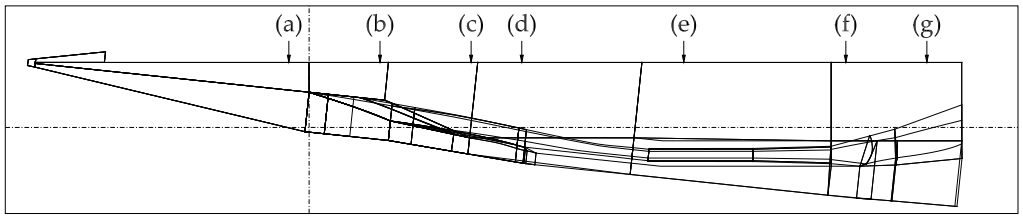

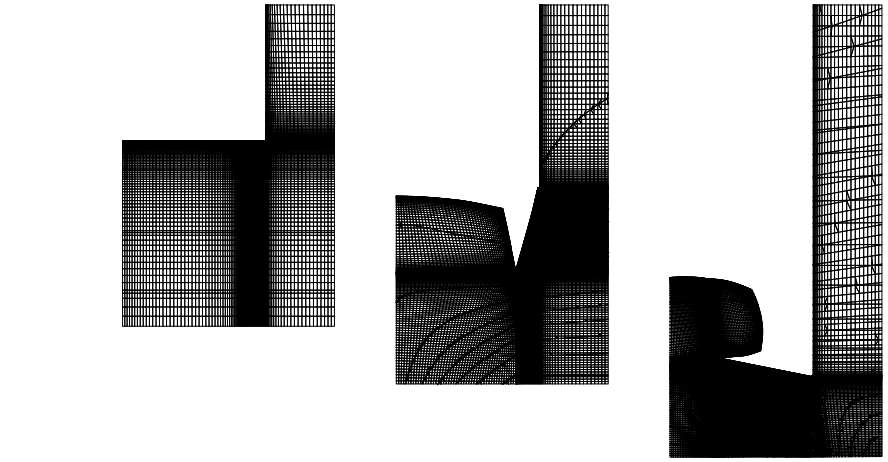

(a) $x = -20\,\text{mm}$ (b) $x = 70\,\text{mm}$ (c) $x = 160\,\text{mm}$

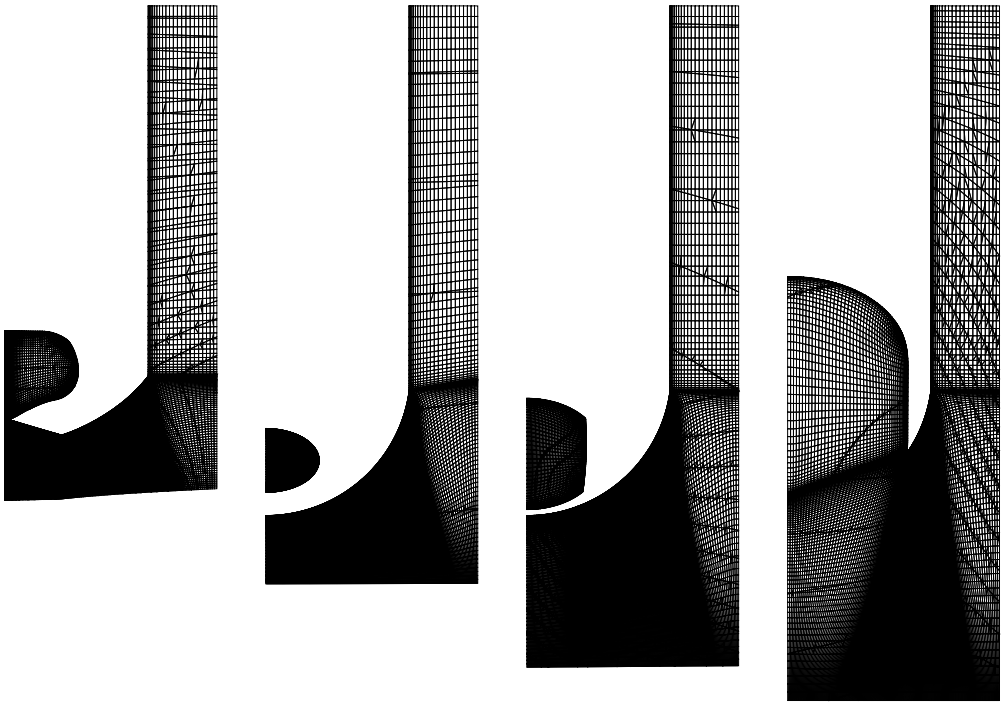

(d) $x = 210\,\text{mm}$ (e) $x = 370\,\text{mm}$ (f) $x = 530\,\text{mm}$ (g) $x = 610\,\text{mm}$

Figure 5.2 – Computational grid at selected cross-sections along the length of the engine

boundary layer interactions. This section provides a brief overview of the internal and external engine flow fields. Attention is focussed on those flow features that are pertinent to this thesis, that is, flow spillage from the forebody and the internal bodyside pressure distribution in the symmetry plane.

5.3.1 *External Flow Field*

The external flow field of the M12REST engine is visualised in Figure 5.3. Figure 5.3a shows Mach number contours on selected cross-sectional planes along the length of the engine while Figure 5.3b shows selected streamtraces in the left half of the engine. The results are for a simulation of the engine at the high pressure test condition.

The Mach number contours show the growth of the boundary layer along the forebody and the cross-sectional curvature of the forebody shock as a result of flow spillage from the sides of the forebody. The forebody flow spillage is clearly shown by the streamlines plotted in Figure 5.3b, as is the resulting 'roll-up' of the spilled flow as it travels along the side of the engine. Mass is also spilled past the sides of the inlet and past the inlet cowl closure location. This spillage is observable in Figure 5.3b. Further discussion of the mass capture performance of the engine at each test condition is provided in Section 5.4.

The bodyside and side-wall shocks that form within the inlet can be seen in Figure 5.3a along with the shocks formed by the external leading surfaces. Near the cowl closure of the inlet, the external leading edge shocks interact with the forebody shock resulting in localised heating on the order of $20\,MW/m^2$ and pressures on the order of 100 kPa for the high pressure test condition (the freestream static pressure is only 638 Pa). Finally, the flow along the side of the engine is distorted by the complex interactions of the spilled flow with the shock and expansions generated by the external leading edge surfaces. As a result, the wake flow behind the M12REST engine is highly non-uniform.

5.3.2 *Internal Flow Field*

The internal flow of the M12REST engine is visualised in Figure 5.4 with Figure 5.4a showing the normalised pressure distribution[2] along the internal bodyside surface for each test condition and Figure 5.4b showing contours of $\log_{10}(p)$ in the symmetry plane for the high pressure test condition. For completeness, a similar contour plot is provided in Appendix G

2 Consistent with Equation (3.10), the nominal forebody pressure given in Table 3.5 was used to normalise the numerical data. The nominal forebody pressure was computed using standard 2-D oblique shock relations (Ames Research Staff, 1953) and so represents an idealised situation.

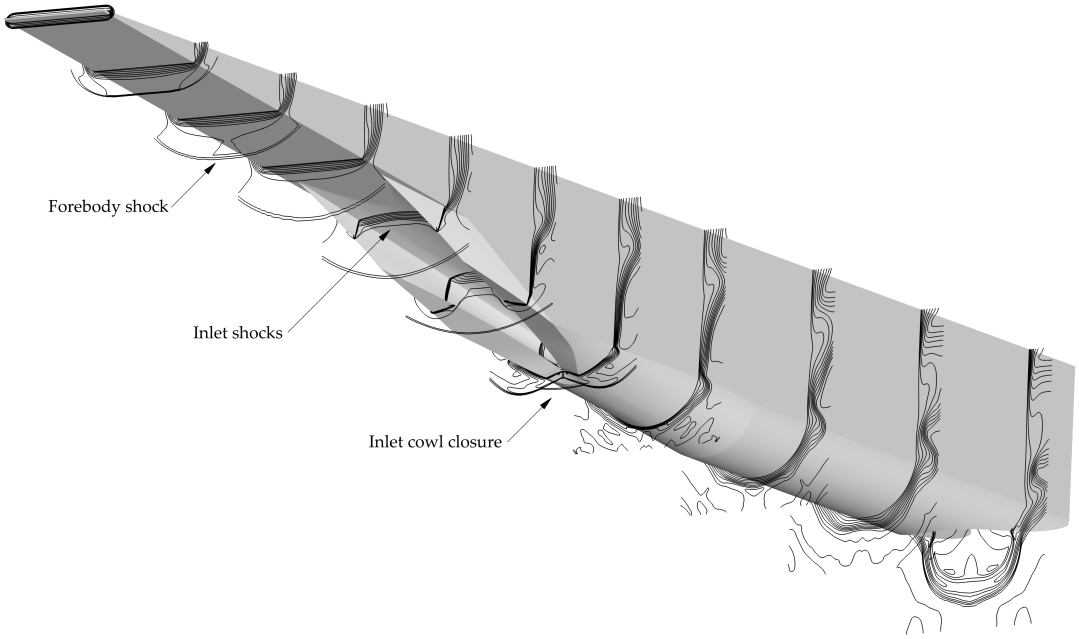

(a) Mach number contours on selected cross-sections along the length of the engine for the high pressure test condition. Contours are shown from $M = 1$ to 10 at intervals of $\Delta M = 1$. Cross-sections are shown from $x = -265$ to 295 mm at intervals of $\Delta x = 96$ mm and from $x = 295$ to 601 mm at intervals of $\Delta x = 102$ mm.

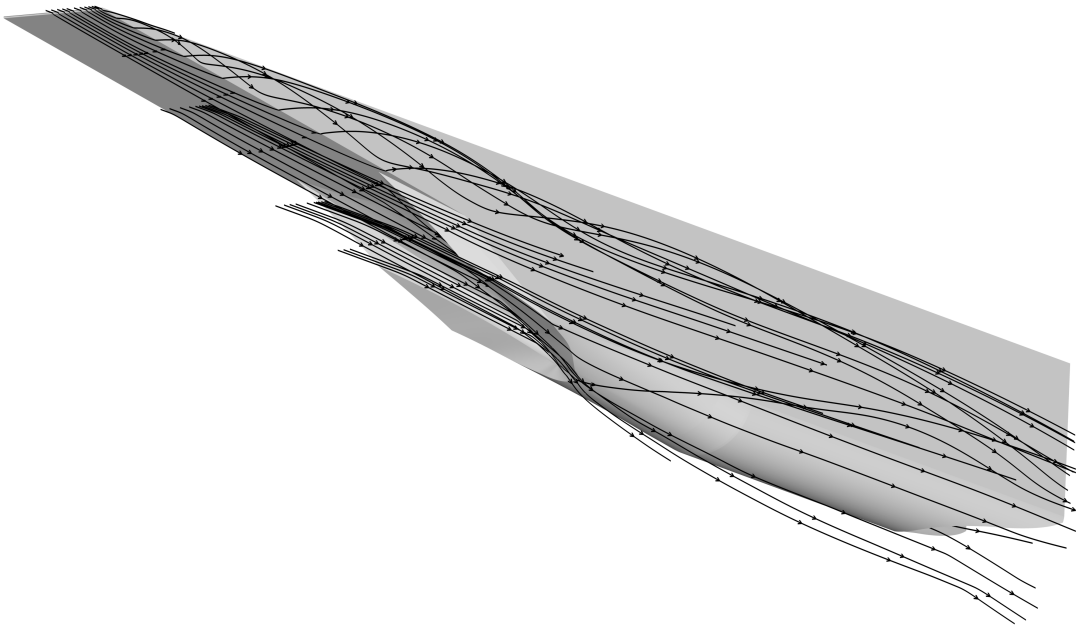

(b) Selected external streamlines of the M12REST engine at the high pressure test condition. For clarity only streamlines in the left half of the engine flow field have been plotted.

Figure 5.3 – External flow field of the M12REST engine at the high pressure test condition

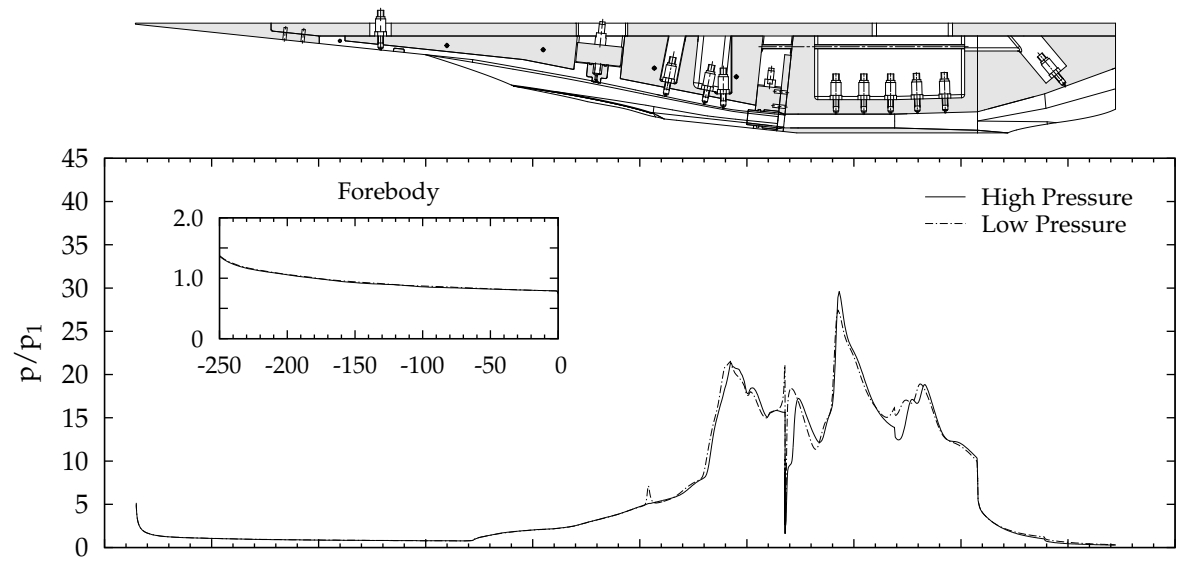

(a) Normalised pressure distribution along the symmetry plane bodyside of the engine at each test condition

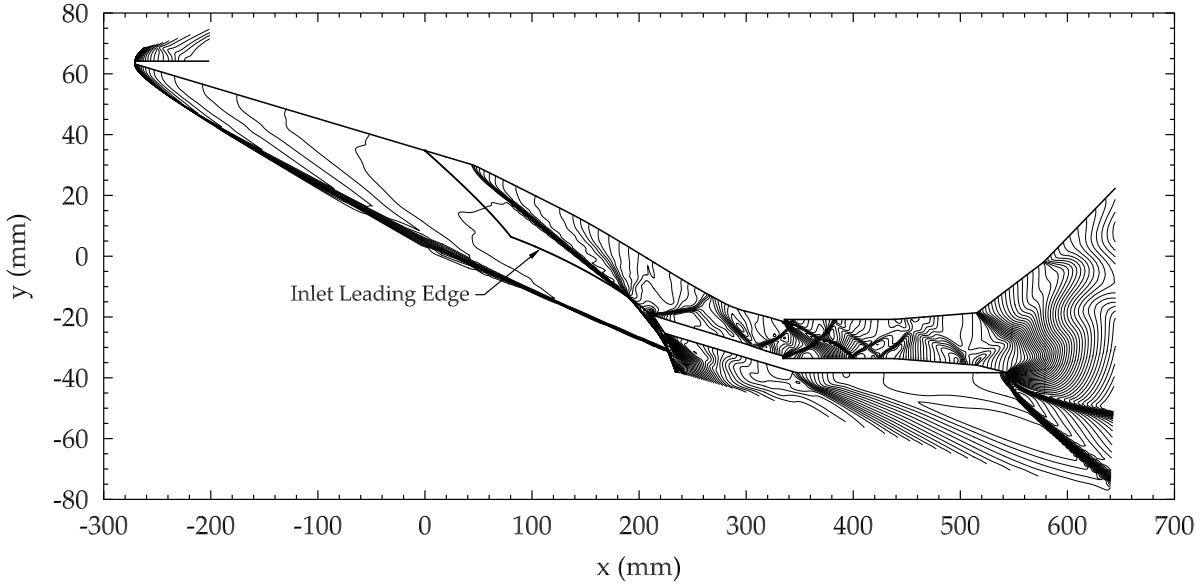

(b) Symmetry plane pressure contours of the M12REST engine at the high pressure test condition. Contours of $\log_{10}(p)$ are plotted over the range 2.5 to 5.5 at intervals of 0.04. To aid visualisation the scale of the vertical axis has been increased relative to that of the horizontal axis.

Figure 5.4 – Internal flow field of the small-scale M12REST engine for no fuel injection

for the low pressure test condition. The horizontal axes of Figures 5.4a and 5.4b are identical and, to aid intepretation, a cross-sectional drawing of the M12REST engine at the correct relative scale is provided. An enlarged view of the normalised pressure distribution along the forebody is provided in Figure 5.4a as an inset figure. Also note that to aid visualisation of the flow field, the vertical axis of Figure 5.4b is increased relative to the horizontal axis.

As seen in Figure 5.4a, the normalised pressure lies above unity near the forebody leading edge; a consequence of the forebody leading edge bluntness (0.5 mm) and viscous interaction (Anderson, 2006, Chapter 7). Moving downstream from the leading edge, the normalised forebody pressure decreases due to flow spillage (Figure 5.3), crossing unity at $x \approx 182$ mm. Within the inlet, the pressure increases to a peak pressure of $p/p_1 = 21$. In the combustor, the pressure distribution is highly non-uniform with a peak pressure of $p/p_1 = 30$ at $x = 396$ mm. Finally, in the engine nozzle the internal area ratio increases rapidly expanding the flow and causing a corresponding rapid decrease in pressure.

The shock dominated flow field indicated by the non-uniformity of the bodyside pressure distribution is clearly evident in the contour plot provided in Figure 5.4b. At this off-design condition both the forebody shock and primary inlet shock form upstream of the cowl closure point of the inlet. The internal cowl shock strikes the bodyside surface just upstream of the inlet throat, forming a shock-boundary layer interaction with the bodyside boundary layer. The subsequent return shock strikes the cowlside surface in the inlet isolator, upstream of the step. Expansion waves and recompression shocks formed at the step interact with the reflected cowl shock to produce a highly non-uniform flow field within the combustor. At the entrance to the nozzle a strong expansion fan originates from the bodyside corner while a weaker expansion originates at the cowlside corner. Due to an insufficient length, the bodyside expansion fan is not reflected by the cowlside wall and as a consequence there is a loss of thrust because of under-expansion of the gas and flow angularity. At the cowlside trailing edge of the nozzle, the interaction of the external flow with the expanding internal flow leads to a strong external recompression shock – typical for an under-expanded nozzle flow (Heiser and Pratt, 1994). For this engine, the recompression shock causes a small separation of the external boundary layer. These nozzle flow features demonstrate that further work is required to improve the nozzle flowpath. Since the design of three-dimensional, airframe integrated, single-expansion ramp nozzles for scramjet engines is a state-of-the-art research area, the design of an efficient nozzle for the M12REST engine was not within the scope of this thesis.

The symmetry plane contours plotted in Figure 5.4b are for the high pressure test condition. A corresponding plot for the low pressure test condition is provided in Figure G.1. Comparison of these two figures

shows that, as expected, the locations of the dominant flow structures within the M12REST engine are slightly different at the low pressure test condition compared to the high pressure test condition. This is a consequence of the slightly different freestream Mach number and unit Reynolds number of the two test conditions. Further discussion of the internal flow field of a REST engine, with particular focus on the inlet, may be found in Barth et al. (2012) and Turner (2010).

5.4 MASS CAPTURE PERFORMANCE

The mass capture ratio is an important performance parameter for hypersonic airbreathing vehicles as any air that flows through the projected frontal area but does not enter the engine(s) cannot be burnt, yet incurs a drag penalty that must be overcome by the propulsive system. Furthermore, the mass capture is directly related to the forebody and inlet designs and the integration of the two. Referring to Figure 5.5 the following areas are defined:

1. A_F: The projected frontal area of the vehicle. For the M12REST engine this is equal to $5552\,mm^2$.
2. A_1: The projected area of the inlet. For the M12REST engine this is equal to $3308\,mm^2$.
3. $A_2 = f(M)$: The theoretical capture area of the inlet for a given Mach number and an appropriate choice of representative forebody shock. For the M12REST engine a 2-D oblique shock originating from a virtual, perfectly sharp leading edge is used as the reference shock. Thus, at the design point, $A_2(12) = 3090\,mm^2$ while at the nominal test conditions $A_{2,HP}(10.4) = 2805\,mm^2$ and $A_{2,LP}(10.2) = 2780\,mm^2$.

Each of these areas may be used to calculate a mass capture ratio:

$$m_{c,i} = \frac{\dot{m}_{th}}{\rho u_x A_i} \tag{5.1}$$

where $\dot{m}_{th}$ is the mass flow through the throat of the inlet and ρ and u_x are freestream values. One-dimensional flow properties at the inlet throat are provided in Table 5.2 for each test condition. These properties were calculated from the numerical simulations by conserving the mass, momentum and energy fluxes (Baurle and Gaffney, 2008). Freestream values of ρ and u_x are taken from Table 3.3.

The requirements of the particular analysis dictate which area should be used in Equation (5.1). Defining the capture ratio with respect to the total frontal area of the vehicle, A_F, is appropriate when comparing different vehicle concepts. Obviously, the engine with the larger capture ratio has

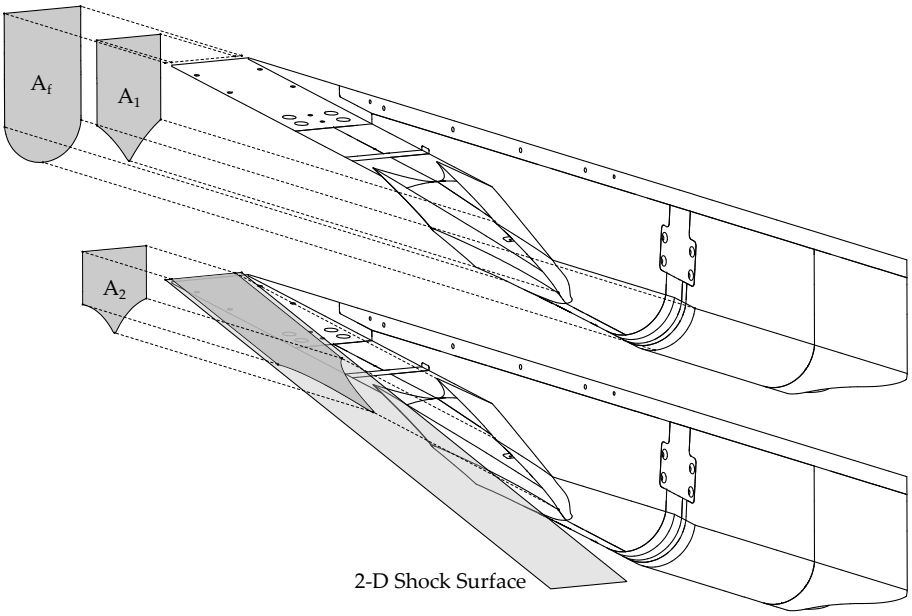

Figure 5.5 – Engine capture area definitions. Using a planar shock from the virtual sharp leading edge a number of capture areas may be defined and used to evaluate the influence of the forebody on the inlet.

Table 5.2 – Flux Averaged Inlet Throat Properties

	Units	Low Pressure	High Pressure
p	Pa	27 570	45 968
T	K	1238	1142
ρ	kg/m^3	0.077 59	0.140 22
u_{x_I}	m/s	2556	2578
u_{y_I}	m/s	−137	−114
u_{z_I}	m/s	−23	−28
M	–	3.74	3.91
$\dot{m}_{th}$	g/s	34.77	63.37
A_{th}	mm^2	174.4	

a greater thrust generation capability. The ratio A_1/A_F indicates what proportion of the frontal area of the vehicle is associated with the engine capture. For the current configuration this ratio is 59.6 %. Increasing this fraction towards 100 % without sacrificing vehicle operability is desirable, and is the goal of engine/airframe integration. Defining the capture ratio with respect to the projected inlet area A_1 is useful for vehicle-level studies of the engine performance and is the typical definition used for the analysis of gas turbine engines (Mattingly, 2006, Section 10.4.5). For mixed compression engines the presence of the vehicle forebody shock can be accounted for by calculating the capture ratio with respect to area A_2. This reference area is defined by projecting the inlet leading edges parallel to the forebody until they intersect with an idealised forebody shock surface and then projecting onto the freestream. Using area A_2 to define the capture ratio provides a value that is useful for comparison with isolated, non-integrated inlet tests.

It should be noted that area A_2 is a function of Mach number and that at shock-on-lip, A_2 will be equal to the projected area A_1 only if the leading edges lie on the ideal shock surface. This is not the case for the M12REST engine. For this inlet the leading edges that meet at the cowl closure location lie below the 2-D shock surface at shock-on-lip. This results in $A_2(12)/A_1 = 93.4\,\%$ at the design Mach number.

Using the data provided in Tables 3.3 and 5.2, the mass capture ratio of the M12REST engine with respect to A_2 is

$$m_{c,2} = \begin{cases} 71.7\,\% & \text{for the high pressure test condition} \\ 69.2\,\% & \text{for the low pressure test condition} \end{cases} \tag{5.2}$$

This capture performance is relatively high, particularly given the slenderness and length of the engine forebody. The mass capture ratio is smaller at the low pressure test condition than at the high pressure test condition. This result is expected since the Mach number of the low pressure test condition is smaller than that of the high pressure test condition. Being further from the design condition, the inlet spills more flow past the cowl closure point at the low pressure test condition than at the high pressure test condition.

Figure 5.6 provides a comparison of the mass capture ratios for the three different reference areas and clearly demonstrates the influence that the choice of reference area has on the calculated mass capture performance. With respect to the total frontal area, the capture ratio is approximately[3] $m_{c,F} = 35\,\%$. Discounting any frontal area that is not associated with the inlet increases the capture ratio to $m_{c,1} = 59\,\%$. Finally, accounting for the presence of the forebody shock increases the capture ratio by a further

3 The values quoted here are the average of the capture ratios for the high and low pressure test conditions. The actual ratios calculated for each test condition are provided in full in Appendix G.3.

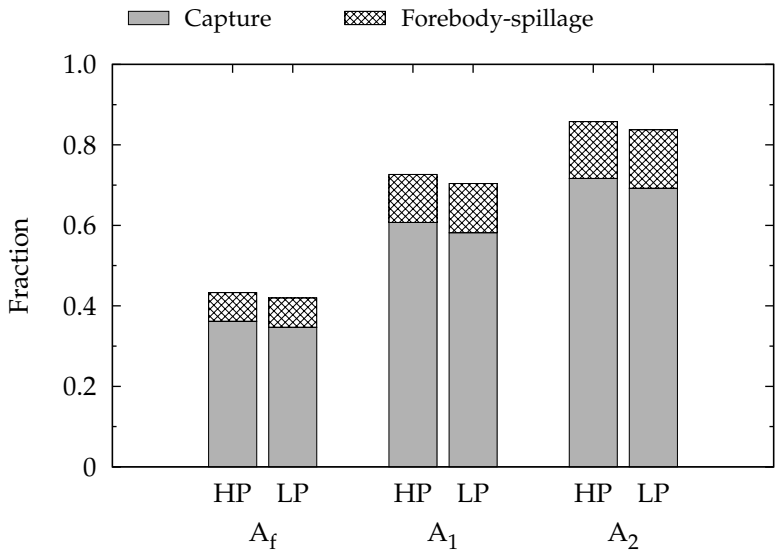

Figure 5.6 – Mass capture fractions for different reference areas.

11 % to $m_{c,2} = 70\,\%$.

In addition to the captured mass fraction, Figure 5.6 also shows the fraction of flow that is spilled from the sides of the forebody. Denoted by m_{sp}, the forebody spillage fraction is defined by

$$m_{sp,i} = \frac{2\dot{m}_{A_3}}{\rho u_x A_i} \tag{5.3}$$

where $\dot{m}_{A_3}$ is the mass flow that crosses reference area A_3, defined in Figure 5.7. Since any flow that lies outside the boundary of the projected inlet capture area A_1 can never enter the engine,[4] for the calculation of the forebody flow spillage fraction, the reference area A_3 was taken to be a vertical plane that extends forward from the start of the inlet and is offset from the engine symmetry plane by a distance equal to half the inlet capture width.

Examining Figure 5.6, it can be seen that the forebody flow spillage is small but non-negiligle compared to the captured mass. With respect to reference area A_2, any flow that is not captured or spilled from the forebody is spilled from the inlet. Integrating the product ρw over the reference area A_3 and including a factor of two, the forebody spillage fraction is calculated to be

$$\dot{m}_{A_3} = \begin{cases} 12.5\,\mathrm{g/s} & \text{for the high pressure test condition} \\ 7.3\,\mathrm{g/s} & \text{for the low pressure test condition} \end{cases} \tag{5.4}$$

4 Here 'never' is used in the context of an engine flying at 0° AOY, since, for the more general case, the capture areas defined in Figure 5.5 are no longer very meaningful.

These values correspond to 14.1 % and 14.5 % of the total flow through area A_2 for the high and low pressure test conditions respectively and are thus comparable with the fraction of flow spilled from the inlet. These results indicate that despite the simple design and narrow width, the performance of the wedge forebody was quite good. Furthermore, the length of the forebody was conservative (Section 3.4.2) and could be reduced by appropriately accounting for the effects of the boundary layer and blunted leading edge (Section 3.4.2). With a shorter forebody, the forebody spillage fraction would be reduced and the overall capture ratio increased.

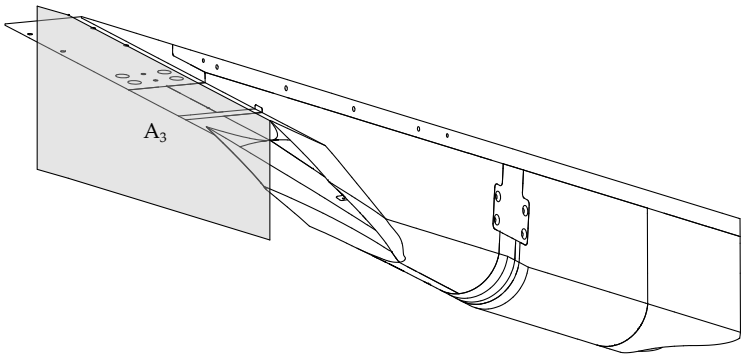

Figure 5.7 – Reference area used for calculation of the forebody flow spillage mass flow rate

5.5 ENGINE SURFACE FORCES

This section presents an analysis of the aerodynamic forces of the M12REST engine for each test condition. The data are presented in the form of force coefficients and the centre of force location. Corresponding absolute force data is provided in Appendix G. The drag, lift and moment coefficients are defined as follows:

$$C_D = \frac{F_D}{qA_f} \tag{5.5}$$

$$C_L = \frac{F_L}{qA_p} \tag{5.6}$$

$$C_{M,LE} = \frac{M_{LE}}{qA_pL} \tag{5.7}$$

where F_D is the drag force, F_L is the lift force and M_{LE} is the moment about the model leading edge[5] and q is the dynamic pressure of the test condition, as given in Table 3.3. The drag is normalised with respect to the projected frontal area A_f, the lift with respect to the projected planar

5 To be precise, a reference or idealised leading edge location is used. Explained in Appendix E, the reference leading edge gives a model length of exactly 0.915 m.

area $A_p = 52\,704 \times 10^{-6}\,m^2$ and the moment with respect to the projected planar area A_p and overall model length $L = 0.915\,m$.

Consistent with the methodology described in Section 4.7 for the experimental force data, the vertical position of the centre of force is chosen *a priori* to coincide with the top surface of the engine. The normalised horizontal position of the centre of force is then given by

$$CF = \frac{1}{L}\frac{M_{LE}}{F_L} \tag{5.8}$$

where the model length has been used as the normalising length. The centre of force location thus has a range 0 to 1 with $CF = 0$ corresponding to the engine leading edge and $CF = 1$ corresponding to the engine nozzle exit. This definition for the centre of force location is shown graphically in Figure 4.15. Further discussion regarding the centre of force calculation is provided in Appendix F.

The net force coefficients and centre of force location for the M12REST engine are plotted in Figure 5.8 with the contributions due to the surface pressure forces and surface viscous (skin friction) forces shown separately. In addition to the net force coefficients, which are of interest for comparison with experimental force data, the forces acting on three different regions or surface groupings of the engine are also plotted in Figure 5.8. Shown in Figure 5.9, these groups consisted of (1) the internal flowpath surfaces, (2) the external surfaces and (3) the forebody surfaces, which included the blunt leading edge.

The force data plotted in Figure 5.8 display some interesting results. With respect to the drag coefficient, the total drag contributed by the internal and external surfaces are comparable and approximately double that of the forebody. At the high pressure test condition the internal drag coefficient is 0.090 while the external drag coefficient is 0.093, marginally higher. Similarly, at the low pressure test condition both the internal and external drag coefficients are 0.102. At the high and low pressure test conditions the forebody drag coefficients are 0.037 and 0.039, respectively.

While the total values are similar, the division between the pressure and viscous components for the internal and external groups is very different. The total internal drag is dominated by the viscous component; a result that was expected and is a well established feature of hypersonic flows (Bowcutt et al., 1987; Paull et al., 1995a). This result is also because the engine nozzle and divergent portion of the combustor produce pressure thrust which counteracts the pressure drag of the inlet. In comparison, the pressure and viscous components contribute almost equally to the total external drag. The total drag of the forebody is approximately half that of the internal and external groups and is dominated by the pressure component. Finally, the viscous forces contribute 66 % of the net drag at the high pressure test condition and 71 % of the net drag at the low

pressure test condition. The complete set of absolute force data for the M12REST engine is provided in Appendix G.4.

Another interesting result from Figure 5.8 is the magnitude of drag on the forebody. Using the nominal forebody pressure from Table 3.5 and the dimensions of the forebody from Figure 3.8, the inviscid drag of the forebody wedge is expected to be 4.0 N at the high pressure test condition and 2.3 N at the low pressure test condition. These values correspond to a drag coefficient of 0.015 (at each test condition) and account for 56 % of the total inviscid drag on the forebody surface group. The remaining inviscid drag is contributed by the blunt leading edge. That is, blunting the forebody leading edge to a radius of 0.5 mm *doubled* the inviscid drag of the forebody surface group. In total, the blunt leading edge contributes 7 % of the net drag of the engine, a significant fraction.

The development of a blunt forebody leading edge for a hypersonic flight vehicle is a difficult design problem, the solution of which must satisfy a number of competing constraints, including aerodynamic, thermal and material temperature constraints. The forebody leading edge design is therefore highly dependent on both the vehicle configuration and flight trajectory to be flown. The numerical simulations presented here were not available when the current engine was being designed and so the leading edge radius was chosen to be slightly smaller than that used on previous REST engines (see, for example, Turner and Smart, 2010). Hirschel and Weiland (2009) state that the thermal load on the leading edge can be managed even with a leading edge radius on the order of $R/L_{ref} \approx 0.0001$ where L_{ref} is a vehicle reference length. For the NASA Hyper-X flight vehicle, the leading edge radius and total vehicle length were 0.8 mm (0.03 inch, Berry et al., 2001) and 3.66 m (12 feet, Figure 2.7), respectively giving $R/L = 0.0002$. For the current M12REST engine, the ratio of leading edge radius to engine length is $R/L = 0.0005$. This is 2.5 times larger than the Hyper-X leading edge and 5 times larger than that suggested by Hirschel and Weiland (2009), confirming that the 0.5 mm radius leading edge is too blunt for the current model.

Whilst the engine drag is dominated by the internal viscous forces, the lift, pitching moment and, through Equation (5.8), centre of force location are each dominated by the forebody and external pressure components, the viscous force component is negligible. For the lift, the external surfaces contribute 61 % of the total pressure component at the high pressure test condition. The forebody surfaces contribute 37 % and the internal engine surfaces contribute the remaining 2 %. Similar values are obtained for the low pressure test condition. For the pitching moment, the internal and forebody pressure components produce almost equal and opposite moments. The net pitching moment coefficient is therefore nearly equal to the contribution from the external surface group – the difference is 5 % of the net value at the high pressure test condition and just 2 % at the low pressure test condition. The internal viscous force produces a small

(a) Drag coefficient

(b) Lift coefficient

(c) Pitching moment coefficient about the leading edge

(d) Normalised centre of force location. Only the total value (pressure plus viscous) is shown for each region.

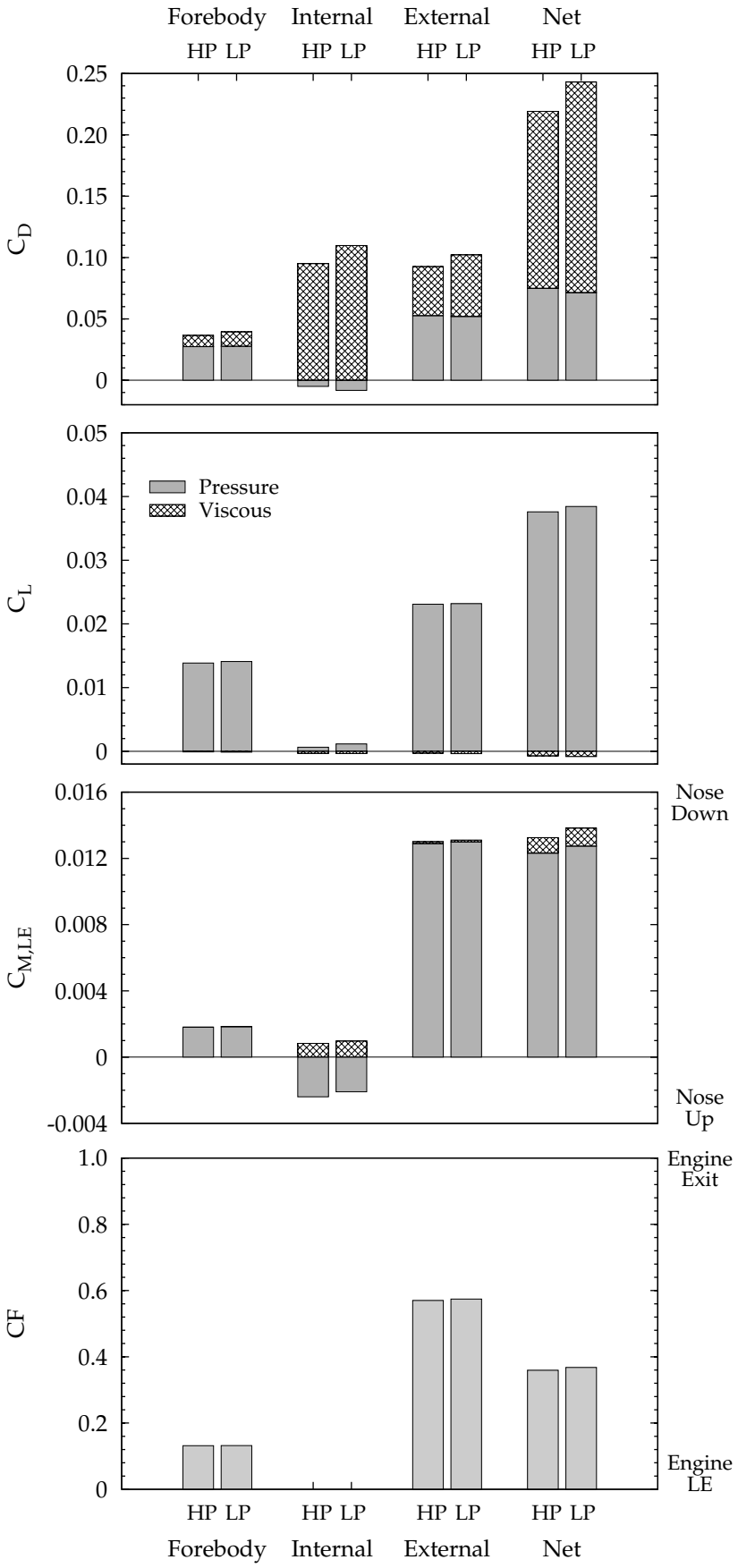

Figure 5.8 – Force coefficients and centre of force location for the M12REST engine at each test condition. Except for the centre of force data, each column is a cumulative bar graph of the pressure and viscous force components.

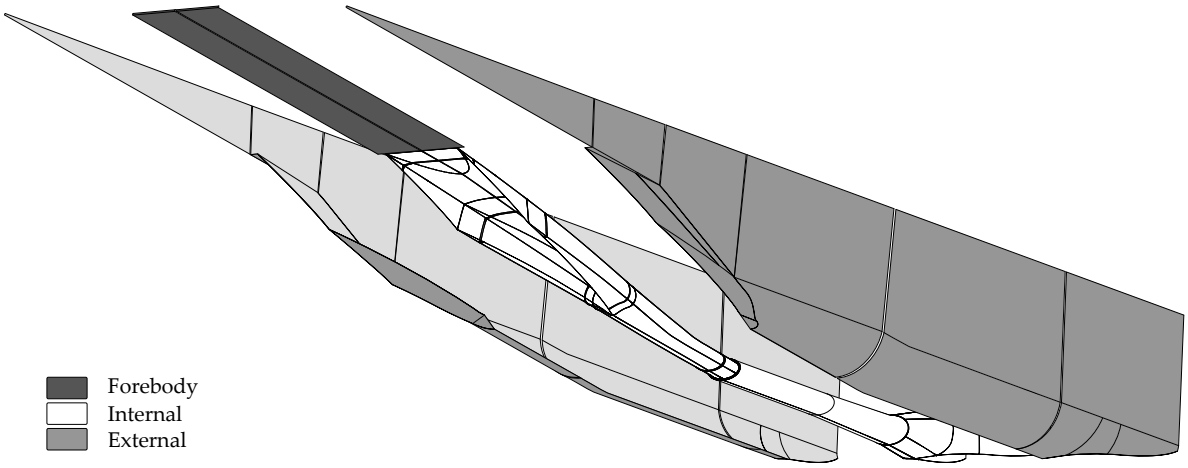

Figure 5.9 – Division of the M12REST engine surfaces into the internal, external and forebody surface groups

positive moment, a result that is a consequence of the height of the engine and the selection of the model leading edge as the reference location for calculating the momemt.

Care must be exercised when interpreting the pitching moment data as the values are influenced by the chosen reference location. It is therefore usual to combine the calculated moment with the net force vector to define the centre of force location (Appendix F). The normalised centre of force location is plotted in Figure 5.8d for the forebody, external and net engine surface groups. Only the total centre of force location is shown for each group and, because it lies well outside the bounds of the engine, the centre of force location for the internal surfaces is not shown.[6] Examining Figure 5.8d it can be seen the forebody centre of force is located at $CF = 0.13$. This is 120 mm from the leading edge or at $x = -151$ mm in the engine coordinate system. Being slightly less than half way along the length of the forebody (cf. Figure 3.8) this position is consistent with expectations. For the external surface group, the centre of force is located at $CF = 0.57$. This is 522 mm from the leading edge or at $x = 251$ mm in the engine coordinate system. Examining Figure 5.4b it can be seen that this location is downstream of the cowl closure location and so is consistent with expectations (the pressure is highest in the cowl closure region). Finally, the centre of force for the entire engine is located at $CF = 0.36$. This is 329 mm from the leading edge or at $x = 70$ mm in the

6 Equation (5.8) defines the axial location of the centre of force in terms of the lift while the vertical location of the centre of force is taken to correspond to the top surface of the engine. As a consequence of these definitions, and because the internal surfaces produce very little lift, the centre of force location for the internal surface group lies far outside the bounds of the M12REST engine. See Appendix F for further discussion.

engine coordinate system. The engine centre of force location and line of action of the net force are shown in Figure 5.10.

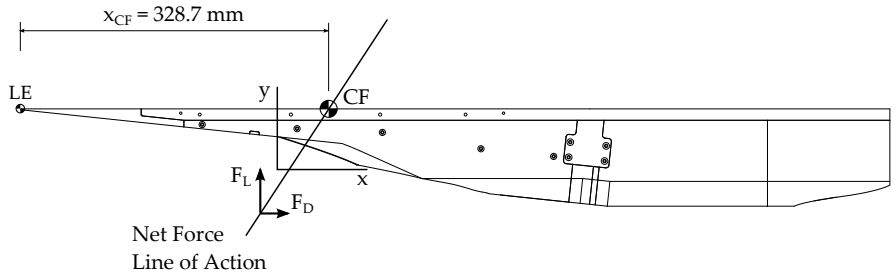

Figure 5.10 – Centre of force location for the M12REST engine at the high pressure test condition

Since airbreathing cruise and acceleration vehicles are drag sensitive (Hirschel and Weiland, 2009), two additional breakdowns of the engine drag force are of interest. These are (1) the breakdown of the internal drag into the contributions from the inlet, combustor and engine nozzle surfaces and (2) the breakdown of the external drag into the contributions from the lower and side surfaces of the engine. Drag coefficient data for these two breakdowns are provided in Figure 5.11 with the contributions due to the surface viscous and surface pressure forces shown separately for each subgroup. The complete set of force data, including the lift and moment forces, are provided in Appendix G.4.

The drag coefficient data presented in Figure 5.11 display several interesting results. Firstly, the viscous drag of the inlet is comparable with the viscous drag of the combustor. Specifically, the viscous drag of the inlet is only 8 % larger than that of the combustor at the high pressure condition and only 6 % larger at the low pressure test condition. This demonstrates that, at least for the case of no fuel injection, viscous drag reduction within the inlet is equally as important as viscous drag reduction within the combustor. Similarity of the inlet and combustor viscous drag components for the case of no fuel injection is not a new result. Turner (2010, Table 3.7) found that inlet viscous drag was approximately 34 % larger than combustor viscous drag for a REST scramjet engine designed for flight at Mach 8; Paull et al. (1995a) and Tanimizu et al. (2009) found that viscous drag on the inlet and cowl of a quasi-axisymmetric scramjet engine was comparable with combustor viscous drag for a Mach number range of 6 to 10, and Mitani et al. (1999) showed that inlet viscous drag was approximately 2.3 times larger than combustor viscous drag for a two-dimensional side-wall compression scramjet engine at Mach 4. The large variation of the results from literature indicates that the inlet-to-combustor viscous drag ratio is strongly dependent on the engine design.

Further insight may be gained for the M12REST engine by calculating

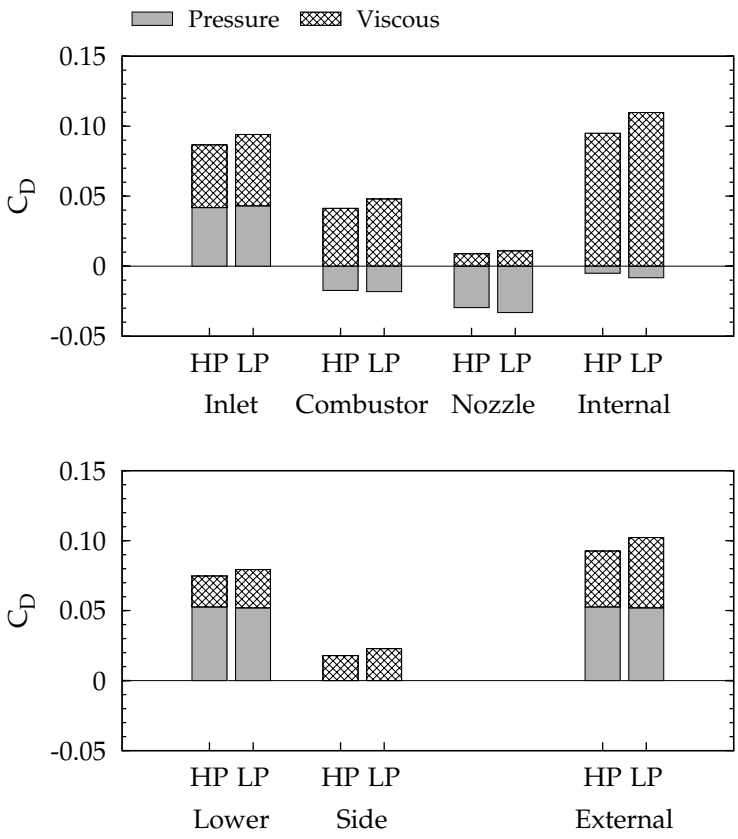

(a) Internal surface group

(b) External surface group

Figure 5.11 – Drag coefficient breakdown for the internal and external surface groups

the average axial wall shear stress. Denoted by $(\tau_w)_x$, the axial wall shear stress is defined by

$$(\tau_w)_x = \frac{(F_x)_v}{A_w} \tag{5.9}$$

where $(F_x)_v$ is the axial (drag) component of viscous force and A_w is the wetted surface area. The total wetted surface area is 22 100 mm^2 for the inlet and 10 431 mm^2 for the combustor. Using the absolute force data provided in Table G.3 for the high pressure test condition, the average axial shear stress is 540 Pa within the inlet and 1058 Pa within the combustor. Hence, similarity of inlet viscous drag with combustor viscous drag is a consequence of the larger surface area of the inlet.[7] Despite this result, it is worthwhile considering whether a significant reduction in inlet viscous drag could be achieved through localised reduction of the wall shear stress. Figure 5.12 plots the normalised cummulative summation of inlet wetted surface area and inlet viscous drag as functions of the local axial

7 The inverse interpretation is that combustor viscous drag is similar to inlet viscous drag because the wall shear stress is higher in the combustor than in the inlet.

wall shear stress. These results are for the high pressure test condition. Results for the low pressure test condition are provided in Appendix G.5. The distribution of axial wall shear stress within the inlet is provided in Figure 5.13 for the high pressure test condition. To aid visualisation, the left and right inlet halves are shown separate from one another.

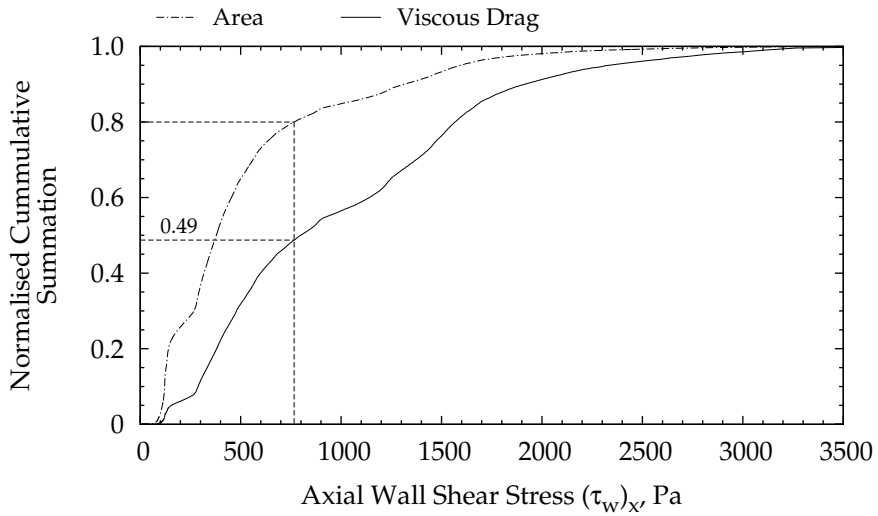

Figure 5.12 – Normalised cummulative summation of inlet wetted surface area and inlet viscous drag as functions of the local axial wall shear stress at the high pressure test condition

Figure 5.12 shows that 20 % of the inlet surface area has an axial wall shear stress greater than 766 Pa and accounts for just 51 % of the total inlet viscous drag. With reference to Figure 5.13, this result suggests that efforts to reduce inlet viscous drag should focus on the internal portion of the inlet, that is, the region downstream of the cowl closure location, since this is where the axial wall shear stress is larger than 766 Pa.

One technique for viscous drag reduction that has been studied extensively in the Centre for Hypersonics is boundary layer combustion of gaseous hydrogen fuel (see for e.g. Barth et al., 2013; Goyne et al., 2000; Kirchhartz et al., 2012; Stalker, 2005). Due to the risk of inlet unstart and increased drag resulting from higher pressures on the forward facing inlet surfaces, combustion of fuel within a scramjet inlet is undesirable however, viscous drag reduction by way of film cooling may also be possible. Recent numerical simulations by Pudsey et al. (2013) indicate that, relative to the case of no fuel injection, the near-field wall shear stress on a flat plate is reduced by more than 60 % when an array of 0.25 mm diameter porthole injectors, spaced 1 mm apart, is used to deliver hydrogen into a 10 mm thick boundary layer. Combustion was suppressed in the simulations leading Pudsey et al. (2013) to conclude that the viscous drag reduction was due to film-cooling. Achieving a similar reduction within the M12REST inlet for all regions with an axial wall shear stress larger than 1000 Pa

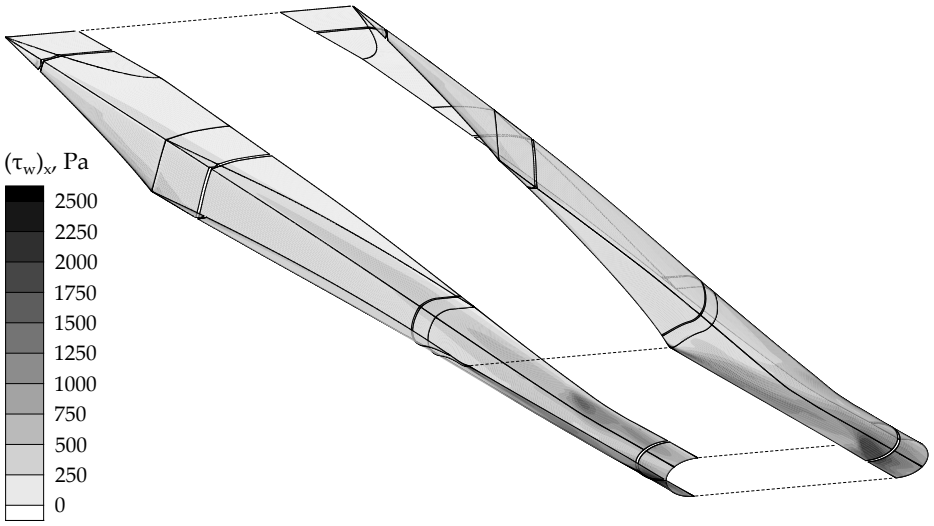

Figure 5.13 – Axial shear stress distribution within the M12REST inlet at the high pressure test condition. To aid visualisation, the left and right inlet halves are shown separate from one another.

would decrease the inlet viscous drag by 26 % (at the high pressure test condition). The corresponding reduction in total inlet drag and net engine drag would be 13 % and 5 %, respectively.

Injection of fuel within the isolator of the M12REST engine is currently under investigation (Barth et al., 2012, Section III.C), albeit with the goal of more effectively delivering fuel into the mainstream flow of the engine. Based on the data presented in Figure 5.11a, the results of Mitani et al. (1999), Tanimizu et al. (2009), and Turner (2010) and the preceding discussion, it is recommended here that some research effort be focussed on reducing inlet viscous drag, with particular emphasis on the suitability and performance of multiporthole injector arrays, similar to that studied by Pudsey et al. (2013).

Returning once again to Figure 5.11, the second interesting result to be discussed is that the pressure thrust generated by the combustor is 59 % of the pressure thrust generated by the nozzle surfaces at the high pressure test condition and 55 % of the nozzle pressure thrust at the low pressure test condition. Of the combustor pressure thrust, just 7 % is contributed by the step at the high pressure test condition, with the remaining fraction being contributed by the divergent portion of the combustor. Similarly, at the low pressure test condition, the step contributes just 8 % of the total combustor pressure thrust. Although divergence of the combustor cross-section is primarily used to prevent thermal choking of the flow in the lower portion of the design flight regime between Mach 6 and 8, the results of Figure 5.11a imply that at high Mach number flight conditions, the pressure thrust gained from a divergent combustor can be significant.

The third and final result to be discussed relates to the breakdown

of the external drag force shown in Figure 5.11b. The lower surfaces, which include the external inlet leading edge surfaces, contribute all of the pressure drag and 55 % of the total viscous drag of the external group. As expected, the side surfaces contribute only viscous drag, with the contribution representing 45 % of the total viscous drag of the external group or approximately 13 % of the net viscous drag of the engine (at each test condition). Although small, the viscous drag contribution of the side surfaces is not negligible and provides the motivation for using multiple engines in a side-by-side configuration. For each pair of engines the overall drag coefficient will be reduced relative to that of two individual engines by the side surface contribution, that is

$$C_{D,n} \approx nC_D - (n-1)C_{D,side} \tag{5.10}$$

where $C_{D,n}$ is the total drag coefficient for n engines stacked side-by-side, C_D is the drag coefficient of a single engine module and $C_{D,side}$ is the drag contribution of the side surfaces for a single engine module. An approximate sign is used in Equation (5.10) because other installation effects could result in an increase (or decrease) in drag that cannot be accounted for when analysing a single engine module. In addition to a drag reduction, flow spillage from the forebody is also decreased when engine are stacked side-by-side, thereby leading to greater thrust potential for a multi-engined vehicle compared with a single-engine vehicle, amongst other potential advantages.

5.6 How much drag is too much?

Accurate measurement or computation of the fuel-off drag of a complete scramjet engine is easier to achieve than the fuel-on drag. Accordingly, once fuel-off data are available it is worthwhile considering the potential for achieving a cruising or accelerating state with the vehicle configuration under investigation. From Figure 5.8, the net fuel-off drag coefficient for the M12REST engine is $C_D = 0.219$ at the high pressure test condition and $C_D = 0.243$ at the low pressure test condition. To be capable of achieving a cruising flight condition, the fuel-off drag must be overcome by the internal thrust produced by the engine. Alternatively the fuel-off drag power of an engine should be less than the input chemical energy of the injected fuel at a desired equivalence ratio; that is

$$D_t u_x \leqslant \dot{m}_{f,t} \Delta h_c \tag{5.11}$$

where D_t is the fuel-off (tare) drag, u_x is the flight velocity, $\dot{m}_{f,t}$ is the total mass flow of fuel and Δh_c is the heat of formation of the fuel (120 MJ/kg–H_2). Note that this equation is essentially the definition of the overall propulsive efficiency of an airbreathing engine (see Equation (7.2)

and Heiser and Pratt, 1994, Section 3.2.5). Using the definition of drag coefficient and equivalence ratio, Equation (5.11) can be rewritten as

$$\phi \geqslant \frac{C_{D,t} q A_f u_x}{\lambda \dot{m}_A \Delta h_c} \tag{5.12}$$

where q is the flight dynamic pressure, A_f is the frontal area, λ is the stoichiometric fuel-air ratio for hydrogen and $\dot{m}_A$ is the captured mass flow of air. Evaluating Equation (5.12) using the data from Figure 5.8a and Tables 3.3 and 5.2 gives $\phi \geqslant 0.95$ for the low pressure test condition and $\phi \geqslant 0.80$ for the high pressure test condition. Being less than one, these results imply that with *perfect conversion* of heat of combustion to thrust, the fuel contains sufficient chemical energy to overcome the fuel-off drag of the M12REST engine for the ingested air mass flow rate.

Further insight may be gained by using the definition of dynamic pressure and mass flow rate to rewrite Equation (5.12) as

$$C_D \frac{A_f}{A_c} \leqslant \frac{\lambda \Delta h_c}{u_x^2/2} \phi \tag{5.13}$$

where A_c is the freestream capture area of the engine. Equation (5.13) is a global performance constraint that applies to *any* airbreathing vehicle. The variation of the right-hand-side of Equation (5.13) with flight speed is plotted in Figure 5.14 assuming a fuel equivalence ratio of one.[8] The geometric capture ratio A_2/A_f for the M12REST engine is also provided and represents an upper limit for the actual capture performance of the engine (Section 5.4).

Examining Figure 5.14 it is clear that the ratio of chemical-to-kinetic energy rapidly drops as the flight speed increases, with the ratio reaching unity at $u_x = 2654\,\mathrm{m/s}$ or $M = 8.8$. At Mach 10 the ratio is 0.75 while at Mach 12, the design condition, the ratio is just 0.50. Coupled with the fact that the geometric capture-to-frontal area ratio is less than 0.55 for the M12REST engine, and that this value is typical for mixed-compression airframe integrated engines, Figure 5.14 places severe restrictions on the design of scramjet powered vehicles for high Mach number flight. Neglecting flow spillage from the forebody and inlet, Equation (5.13) requires that the fuel-off drag coefficient to be less than 0.37 at Mach 10 and less than 0.28 at Mach 12 for the M12REST engine. Accounting for flow spillage further reduces these values; for example, at the high pressure Mach 10 test condition, the mass capture A_c/A_f is calculated to be 0.36 (Figure 5.6) which is 28 % smaller than the geometric value A_2/A_f. With this capture ratio, Equation (5.13) requires that the fuel-off drag coefficient be smaller

8 Although scramjet engines are typically operated at fuel equivalence ratios less than one, within the context of the current discussion, the assumption of stoichiometric fuelling is appropriate because at this fuelling level, the *available* chemical energy is maximised. Stoichiometric fuelling therefore defines the upper limit of Equation (5.13).

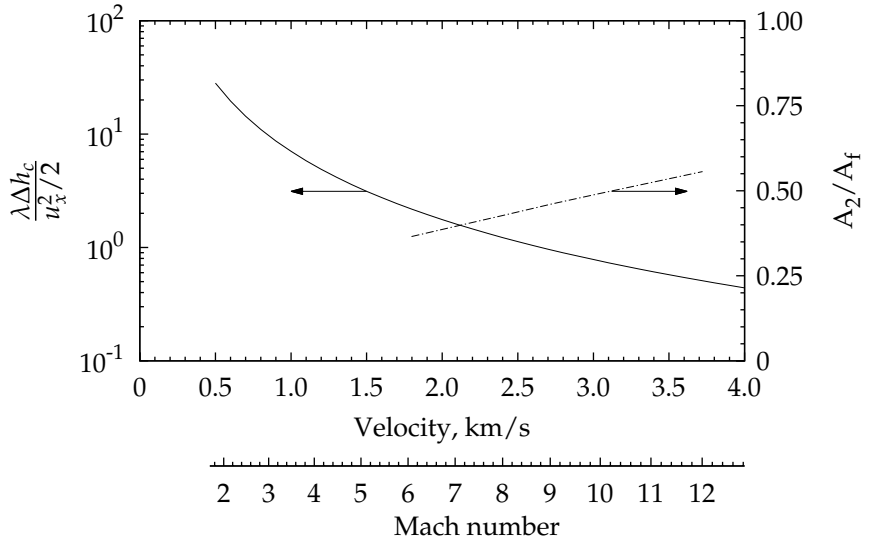

Figure 5.14 – Variation of fuel-chemical-to-engine-kinetic energy ratio and geometric engine capture ratio with flight speed. The Mach number axis corresponds to a 50 kPa dynamic pressure flight trajectory.

than 0.28.

These results immediately raise the question of how the fuel-off drag could be reduced. In general, complex interdependencies of the vehicle and engine make any reductions of the fuel-off drag of a complete vehicle difficult to achieve. However, for the M12REST engine developed in this work the engine nozzle does not utilise all the available area for expansion - the projected nozzle exit is only 51.7 % of the frontal area. The reduction in drag that could be achieved by increasing the nozzle expansion ratio can be estimated by calculating the theoretical thrust produced by an isentropic expansion of the combustor exit flow to a specified area ratio.[9] Using flux-averaged combustor exit conditions,[10] the theoretical thrust for the M12REST engine nozzle at the high pressure test condition is 12.7 N ($C_{T,NOZZLE} = 0.048$). Increasing the nozzle exit area to match the engine frontal area raises the theoretical thrust to 14.9 N ($C_{T,NOZZLE} = 0.056$). These theorectical values are significantly greater than the 5.5 N ($C_{T,NOZZLE} = 0.021$) of thrust actually produced by the current nozzle (Table G.3a) and suggest that greater improvement of the nozzle thrust would be achieved through using an appropriately designed nozzle rather than simply increasing the area ratio of the current geometry. Similar thrust coefficient values are obtained at the low pressure test condition.

Assuming that a nozzle geometry could be designed that uses the entire available area for expansion and produces thrust equal to the theoreti-

9 This calculation also assumes an ideal and callorically perfect gas.

10 These conditions were extracted from the fuel-off numerical simulation and are $p = 24\,713$ Pa, $T = 1150$ K, $u = 2432$ m/s, $M = 3.67$ at the high pressure test condition.

cal value, the fuel-off drag coefficient would be reduced from 0.219 to 0.184, which is approximately 50 % smaller than the limit imposed by Equation (5.13) (neglecting flow spillage). Two conclusions may be drawn from these results. Firstly, that the nozzle developed for this small-scale airframe integrated M12REST engine was not optimised for thrust, and secondly, that achieving a cruise condition at flight Mach numbers above ten is possible with a well designed vehicle.

Two caveats to the preceding discussion are that the formulation of Equation (5.11) does *not* account for the thrust gained from injection of fuel (in the absence of any chemistry) or for the reduction of drag through boundary-layer combustion[11] (Stalker, 2005). Referring to Figure 5.14, combustion and engine nozzle efficiencies less than unity drives the constraint curve towards the horizontal axis, while the thrust gained from fuel injection and drag reduction from boundary-layer combustion pushes the constraint curve away from the horizontal. The magnitudes of these counter-acting processes are dependent on the engine configuration and design. Given these two caveats, one may question the usefulness of the analysis encapsulated in Equation (5.13) and Figure 5.14. It is argued here that this analysis is useful for two reasons. Firstly, Equation (5.13) places an upper limit on the metric $C_D A_f / A_c$ and provides a direct, global method, for assessing the feasibility of achieving a cruising (or accelerating) state for a particular engine and flight velocity based solely on the available chemical energy. Secondly, and more importantly, the analysis highlights the change in operational principle required to achieve high Mach number flight. That is, for flight at low Mach numbers, sufficient thrust may be generated from conversion of the fuel chemical energy to heat. In comparison, for flight at high Mach numbers, the fuel contains insufficient chemical energy and so the engine thrust is generated primarily from injection of the fuel (Czysz, 1988) and internal viscous drag reduction via boundary layer combustion (Stalker, 2006b). With respect to the breakdown of the engine surfaces forces provided in Figure 5.8, this analysis highlights the importance of internal viscous drag reduction as an enabling technology for scramjet powered flight at high Mach numbers.

11 Equation (5.11) is a reformulation of the overall propulsive efficiency, defined by Equation (7.2) (see also Section 3.2.5 of Heiser and Pratt, 1994). The overall propulsive efficiency is in turn based on a thermodynamic evaluation of an airbreathing engine using the Brayton cycle (Builder, 1964; Czysz, 1988) and so implicitly assumes that the thrust or work output of the engine cycle is produced solely by an adiabatic expansion of the working fluid. Kirchhartz et al. (2012) and Chan (2012) (among others) have demonstrated that injection of fuel into the boundary layer of a constant area combustor produces a reduction in drag which is in accordance with the theory of Stalker (2005). This drag reduction does not require the working fluid to be expanded.

PRESSURE RESULTS

The sixth chapter, in which the M12REST *engine is shown to be somewhat insensitive to flight dynamic pressure, its performance is compared with a design-scale engine, and inlet-injected fuel is shown to act as a pilot for the step-injected fuel.*

6

6.1 INTRODUCTION

This chapter presents engine pressure data from the second test campaign. The primary goal of the campaign was to confirm operation of the engine at the Mach 10 test conditions. The streamlined, rigid mount detailed in Section 3.4.6 was used to ensure minimal blockage of the facility nozzle. Three types of shock tunnel tests were conducted: Fuel-off tests, for which no fuel was injected and the test gas was air; fuel-on tests, for which gaseous hydrogen fuel was injected and the test gas was air; and suppressed-combustion tests, for which gaseous hydrogen fuel was injected and the test gas was nitrogen. With respect to the fuel-off tests, fuel-on tests quantify the effects of combustion and suppressed-combustion tests quantify the effects of fuel mass addition.

Fuel-off engine data are presented in Section 6.2 and compared with available computations. Results demonstrating the effect of a boundary layer trip are also discussed. Fuel-on and suppressed-combustion results at each test condition for three distinct fuelling configurations are presented in subsequent sections. Section 6.3 discusses the inlet-only scheme, Section 6.4 the step-only scheme and Section 6.5 a combined injection scheme. In Section 6.6, the penultimate of the chapter, the influence of flight dynamic pressure on the engine performance is examined before Section 6.7 concludes the chapter with a comparison of the performance of the current, small-scale, engine to that of a design-scale engine previously tested by Suraweera and Smart (2009).

6.2 FUEL-OFF DATA

When compared with numerical simulation, fuel-off tests are useful for confirming, (1) the flow path geometry; (2) the correct assembly of the engine components; (3) the engine alignment with respect to the facility nozzle, and (4) the test flow condition. Repeatability, transient inlet starting and flow establishment characteristics are also evaluated using fuel-off shot data.

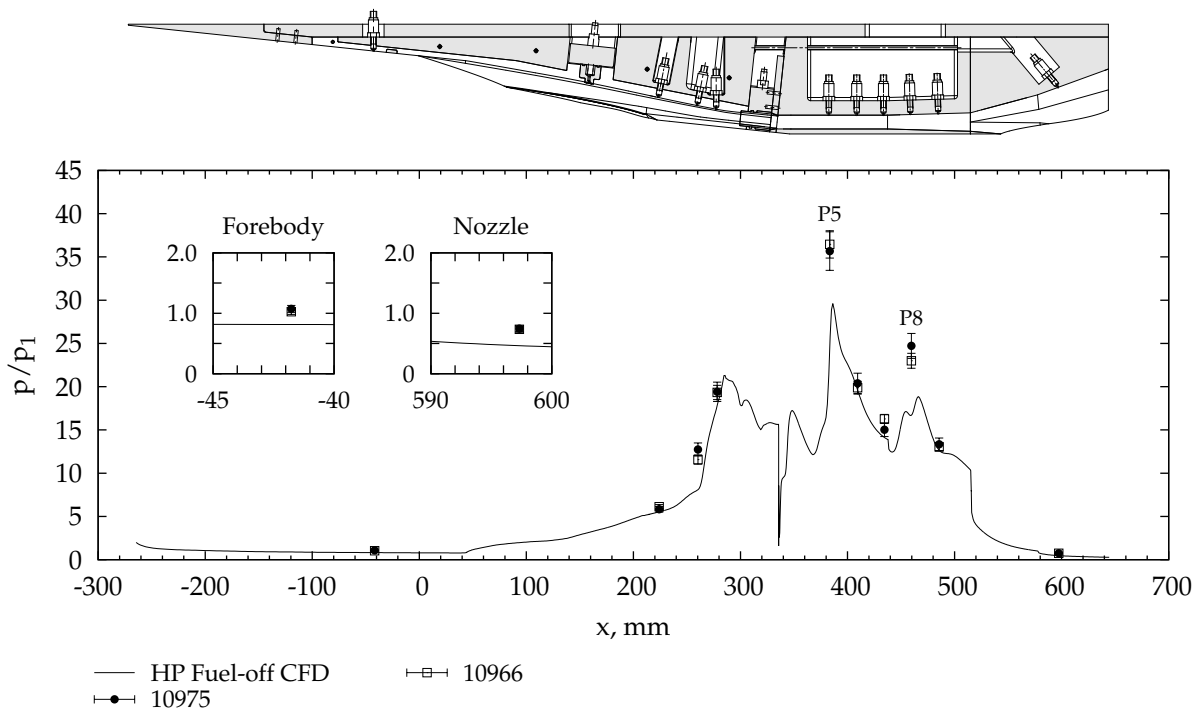

Figure 6.1 – Comparison of the experimental and numerical pressure distribution on the engine bodyside for no fuel injection at the high pressure test condition.

The experimental pressure distributions for two high pressure fuel-off shots are compared with a fuel-off numerical simulation in Figure 6.1. No boundary layer trip was fitted for these shots. The data are presented in the form of a pressure ratio relative to the nominal forebody pressure. Calculation of the normalised data is detailed in Section 3.5.2. To aid comparison inset figures that show enlarged views of the forebody and engine nozzle data are plotted. A cross-sectional view of the engine at the correct relative scale is also provided to aid intepretation of the pressure distribution. The error bars plotted in Figure 6.1 represent one standard deviation of the variation of the normalised pressure measurement during the test time. Based on the results and analysis presented in Appendices A and C the systematic uncertainty due to the calibration and nominal condition uncertainties is 5.5 %; this uncertainty is not explicitly indicated in Figure 6.1. The design and layout of Figure 6.1 is used consistently throughout this thesis for the presentation of the engine pressure data.

The experimental data show a steady increase in pressure within the inlet that is slightly upstream of the numerical simulation. Within the combustor the data show a distinct shock dominated structure that compares well with the numerical simulation. At locations P5 and P8, which correspond to shock impingement locations, the numerical simulation under-predicts the measured pressure. This result was obtained consis-

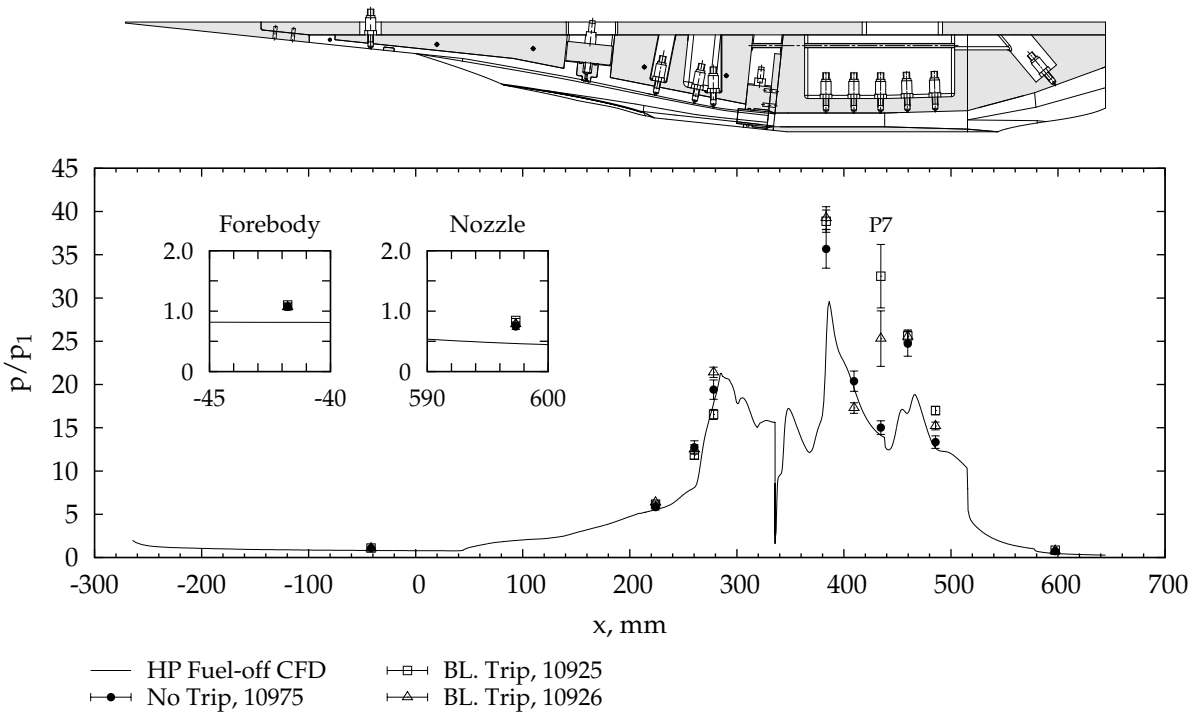

(a) High pressure condition.

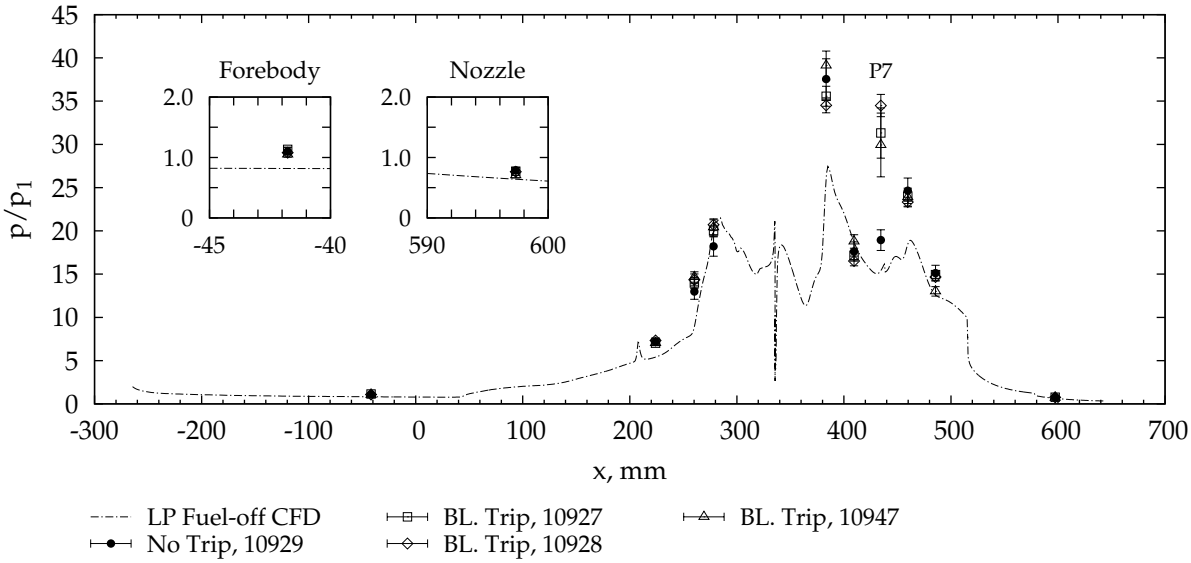

(b) Low pressure condition.

Figure 6.2 – Influence of the saw-tooth boundary layer trip on the measured pressure distribution for each test condition.

tently throughout both test campaigns and is expected to be related to the axial resolution of the computational grid at these locations.[1] On the forebody the numerical data lies below unity due to flow spillage from the forebody (Section 5.4). In comparison, the experimental forebody data lay equal to or slightly above unity, indicating that the test flow calculated using NENZFR under-predicts the experimental pressure. This under-prediction is expected to be related to the boundary layer transition location used for the NENZFR simulation of the nozzle flow (see Doherty, 2013a).

For several shots a saw-tooth boundary trip was fitted to the model. Measuring from the start of the inlet, the trip was located 20 mm upstream and featured triangular teeth that were approximately 3 mm in height (Figure 3.11). Normalised engine pressure data with the trip fitted are shown in Figure 6.2 for each test condition. For comparison, fuel-off data with no trip and the numerical results are also plotted. With the exception of location P7, there are no significant differences between the experimental data with and without the trip fitted. These results show that at each test condition the inlet flow was started independent of the presence of the boundary layer trip.

Although this data show that no boundary layer trip was necessary,[2] one was fitted for shots at the low presure condition as this ensured consistency with the engine configuration used during the force balance tests (Chapter 7). Unless otherwise stated, no trip was used for shots at the high pressure condition.

While the presence of the trip had little influence on inlet starting, a clear influence was observed at location P7. The magnitude of the measured pressure at this location was increased by approximately[3] 65 % and the transient data was less steady and less repeatable when the trip was fitted (as evidenced by the larger variation bars). The lack of observable effect of the trip elsewhere in the engine is expected to be due to the limited number of measurements.

In summary, the good match between the experimental data and numerical simulation throughout the engine indicates that the flow entering the engine was close to the nominal condition and that the inlet flow field was started. Taken together, Figures 6.1 and 6.2 also demonstrate good repeatability of the measurements. Additional fuel-off data examining the influence of chines fitted to the sides of the forebody are provided in Appendix H.2.

1 Prof. Michael Smart kindly provided the numerical simulation of the engine. All subsequent analysis was completed by the author. At the time of writing, a grid convergence study had not been completed.

2 Strictly, the results only apply for the test environment generated by the T4 Stalker Tube. See the review by Schneider (2008) for a discussion of the influence of test flow noise on boundary layer transition.

3 The stated value is for low pressure shot 10927 relative to shot 10929.

6.3 FUEL-ON DATA FOR INLET INJECTION

Normalised pressure data for injection from the inlet station are given in Figure 6.3 for a range of equivalence ratios at each test condition. Suppressed-combustion and fuel-off data are also provided. A vertical arrow on the x-axis indicates the location of fuel injection and, to assist visualisation, lines are drawn between consecutive transducers in the combustor; these lines should not be interpreted as depicting the pressure variation between these measurement locations.

The results exhibit similar trends at each test condition. The forebody data lay on top of one another demonstrating repeatability of the test flow. At each inlet tap, the pressure increases with fuel equivalence ratio. The inlet pressures for fuel-on tests are comparable with those measured for the suppressed-combustion tests, indicating that the increase in pressure within the inlet was caused by changes to the inlet flow field due to fuel mass addition of fuel and not combustion.

Combustion induced pressure rise was observed from location P6 onwards, independent of equivalence ratio and test condition. At either test condition the pressures within the combustor and engine nozzle increase as the fuel equivalence ratio increases, implying that, at least up to equivalence ratios of approximately 0.6, combustion was not mixing-limited for the inlet injection scheme.[4] At the high pressure test condition a peak normalised pressure of $p/p_1 = 56$ was measured at location P7. Similarly, at the low pressure test condition a peak normalised pressure of $p/p_1 = 46$ was measured at location P6. Due to the limited number of measurements, the axial resolution of the experimental data is coarse relative to the engine size. Consequently, the measured peak pressure at each test condition may not be the true maximum. The apparent upstream shift of the peak pressure location between the high and low pressure test conditions (cf. shots 10951 and 10944) may also be an artifact of the limited number of measurements.

At the highest fuel equivalence ratio tested, the normalised nozzle pressure was 100 % larger than the fuel-off value at the high pressure test condition and 70 % larger than the fuel-off value at the low pressure test condition. These results indicate that robust combustion of the fuel was achieved at either test condition with the inlet injection scheme. Additional fuel-on data showing repeatability and examining the influence of a sawtooth boundary trip on combustion for the inlet injection scheme are provided in Appendices H.4 and H.5 respectively.

4 In this thesis mixing-limited combustion is distinguished from mixing-controlled combustion. Mixing-limited combustion refers to the case where, for a particular cross-section, the combustion induced pressure rise does not increase with fuel equivalence ratio. Mixing-controlled combustion refers to the case where the distribution of combustion induced pressure rise along a duct is governed by the rate at which fuel and air are mixed.

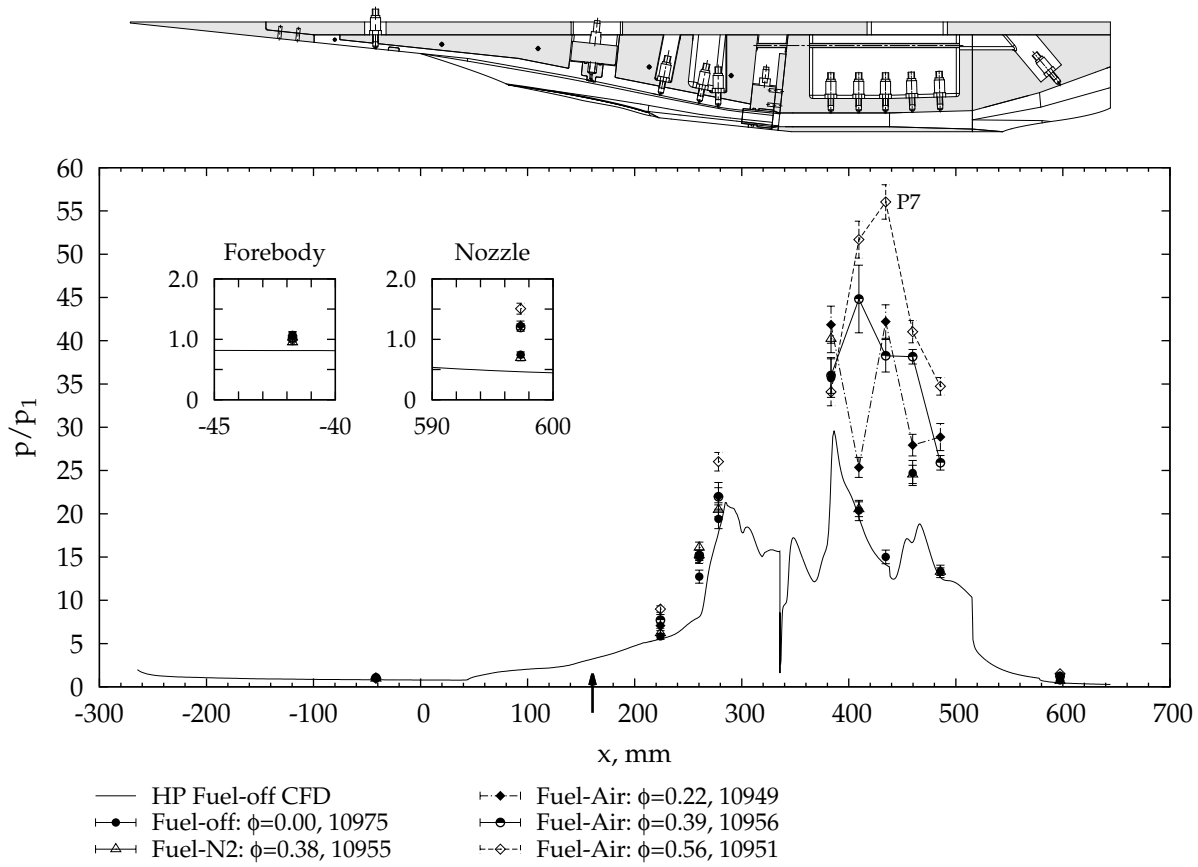

(a) High pressure condition. No boundary layer trip was fitted.

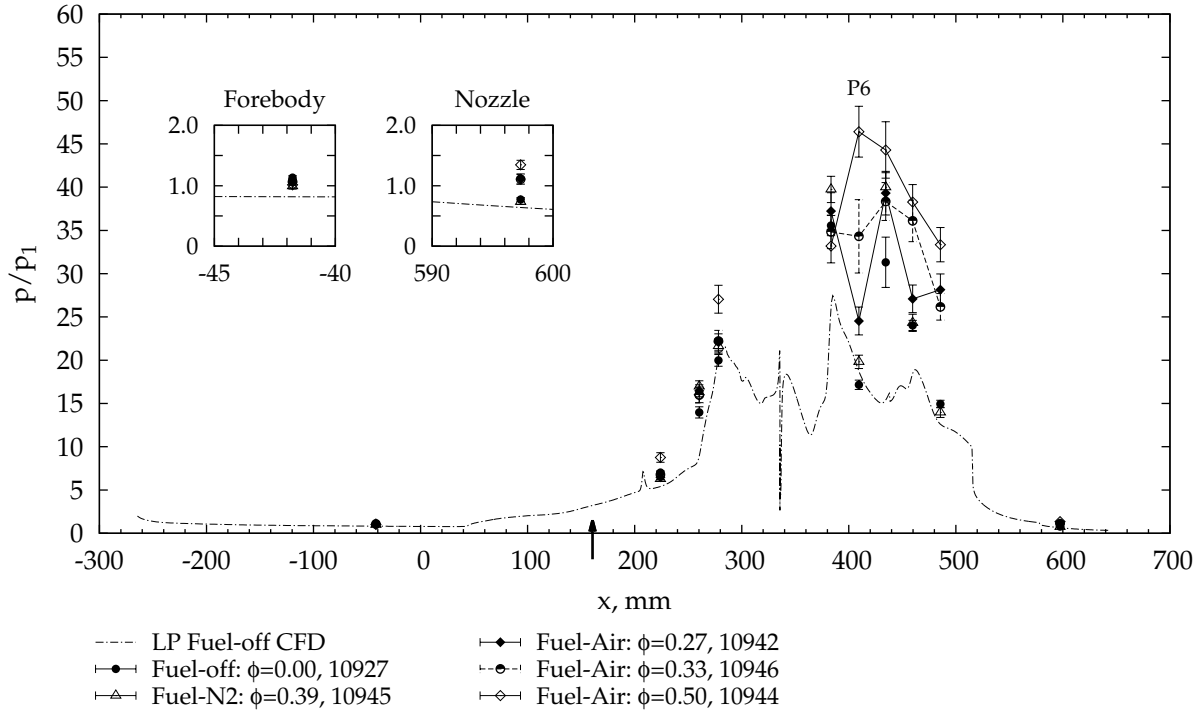

(b) Low pressure condition. A boundary layer trip was fitted.

Figure 6.3 – Engine bodyside pressure distribution for the inlet injection scheme at each test condition. The fuel injection location is indicated by an arrow.

6.4 FUEL-ON DATA FOR STEP INJECTION

Normalised pressure data for the step injection scheme are given in Figure 6.4 for a range of equivalence ratios at each test condition. Suppressed-combustion and fuel-off data are also plotted for comparison. To aid visualisation lines are again drawn between consecutive transducers in the combustor. The results plotted in Figure 6.4 show that fuel injection from the step produces only a small pressure rise in the combustor and engine nozzle at either test condition. The fuel-on data lay on top of the suppressed-combustion data[5] until location P9. At this location the fuel-on data are 16 % larger than the suppressed-combustion data at the high pressure test condition and 78 % larger at the low pressure test condition. Similarly, midway along the engine nozzle (location P10), the fuel-on data are 48 % larger than the suppressed-combustion data at the high pressure test condition and 57 % larger at the low pressure test condition. These results imply that some heat release due to combustion has occurred and that fuel injected from the step does not begin to burn until, or just downstream of, location P9.

Comparing the engine nozzle data (P10) in Figures 6.3 and 6.4, it can be seen that the fuel-on pressure increment per unit mass of fuel,

$$\Pi = \frac{1}{\phi_{\text{fuel-on}}} \left(\left(\frac{p_{10}}{p_1} \right)_{\text{fuel-on}} - \left(\frac{p_{10}}{p_1} \right)_{\text{fuel-N}_2} \right) \tag{6.1}$$

is in the range of 0.33 to 0.53 for the step injection scheme (at either test condition) and in the range of 1.13 to 2.45 for the inlet injection scheme (at either test condition). These values indicate that fuel injected from the inlet station was burnt more efficiently than fuel injected from the step station. This result is a consequence of the additional mixing and reaction length afforded by the inlet injection station and is consistent with previous experimental and cycle analysis results for a design-scale engine (Moule and Smart, 2013). Comparison of the engine data measured in this thesis with design-scale engine data is provided in Section 6.7.

One other interesting feature of the data plotted in Figure 6.4 is that the pressure increment at location P9 is larger at the low pressure test condition than at the high pressure test condition. This result is postulated to be due the saw-tooth boundary layer trip that was fitted to the model for tests at the low pressure test condition.[6]

Finally, repeatability of each test condition is again demonstrated by the collapse of the forebody pressure data and, as expected, the collapse of the inlet pressure data demonstrates that fuel injection from the step has no

5 Due to a small oversight, no suppressed-combustion test for the step injection scheme was completed at the low pressure test condition. For comparison, combined injection data are plotted in Figure 6.4b instead.

6 Further discussion of the influence of the trip on combustion is provided in Appendix H.5.

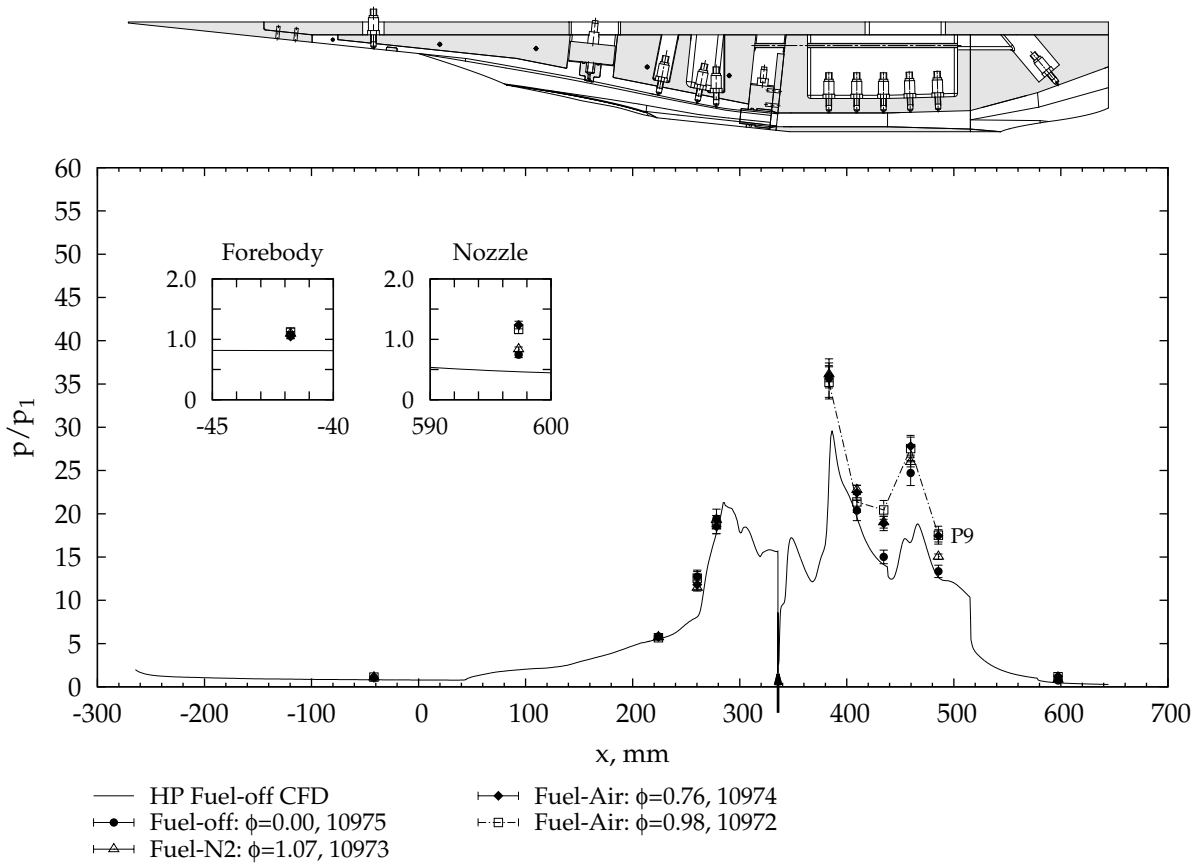

(a) High pressure condition. No boundary layer trip was fitted.

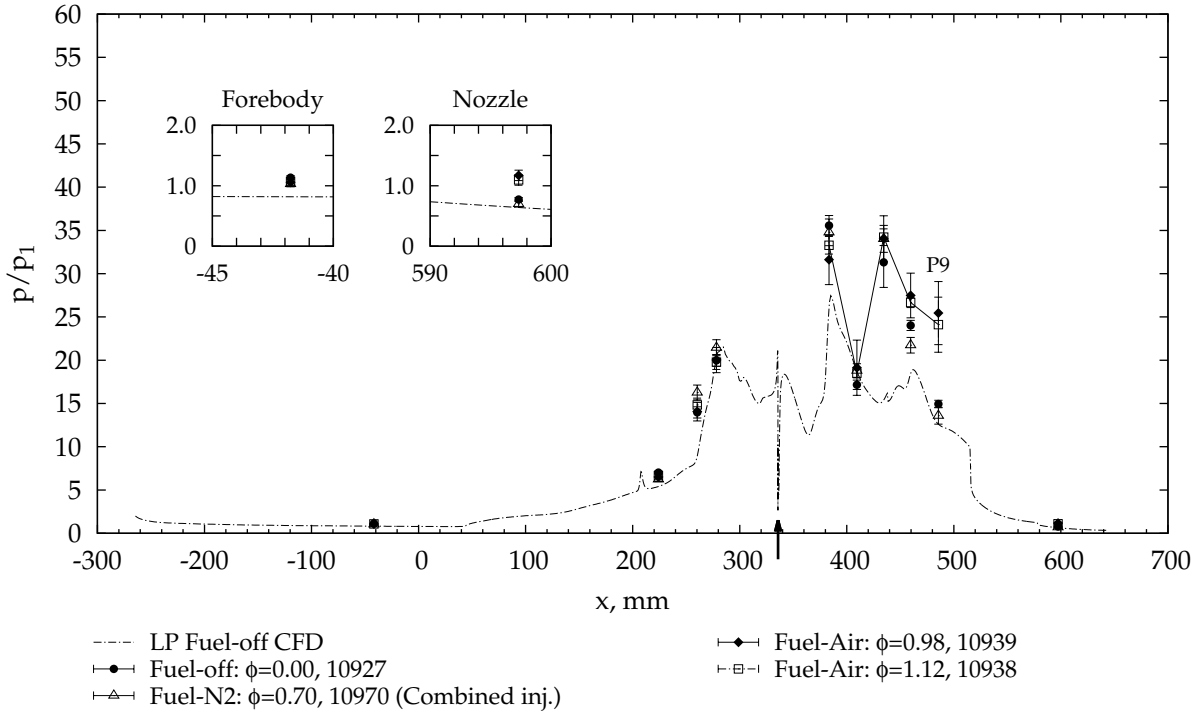

(b) Low pressure condition. A boundary layer trip was fitted.

Figure 6.4 – Engine bodyside pressure distribution for the step injection scheme at each test condition. The fuel injection location is indicated by an arrow.

influence on the inlet flow field. This was expected for two reasons, firstly, because the flow is hypersonic and secondly, because the Mach number of the current test condition is considered to be too high for dual-mode combustion to occur.[7]

6.5 FUEL-ON DATA FOR COMBINED INJECTION

Normalised pressure data for the combined injection scheme are given in Figure 6.5 for a range of equivalence ratios at each test condition. Lines drawn between consecutive transducers in the combustor are provided only to aid visualisation. For each combined injection test plotted in Figure 6.5, the fuel split parameter ξ, defined by Equation (3.7), was approximately[8] 0.68. Over the range of total equivalence ratios tested, this split corresponds to an inlet equivalence ratio between 0.19 and 0.42 and a step equivalence ratio between 0.46 and 0.90. These ranges are comparable with the inlet and step injection data presented in Sections 6.3 and 6.4.

In comparison with the inlet and step injection data presented in the previous sections, significant combustion induced pressure rise was obtained for the combined injection scheme. At the high pressure test condition, a peak pressure of $p/p_1 = 79$ was measured for shot 10964 at a total equivalence ratio of 1.32 ($\phi_{f,1} = 0.42$, $\phi_{f,2} = 0.90$); 75 % greater than that measured for the inlet injection scheme at $\phi = 0.39$ (shot 10956) and 40 % greater than the maximum pressure measured for the inlet injection scheme ($p/p_1 = 56$ for shot 10951). Similarly, at the low pressure condition, a peak pressure of $p/p_1 = 63$ was measured for shot 10969 at an equivalence ratio of 1.11 ($\phi_{f,1} = 0.37$, $\phi_{f,2} = 0.74$); 60 % greater than that measured for the corresponding inlet injection scheme test at $\phi = 0.35$ (shot 10943) and 35 % greater than the maximum measured pressure for the inlet injection scheme ($p/p_1 = 46$ for shot 10944).

Consider the following three observations based on the data presented in Figures 6.3 to 6.5:

1. No significant pressure rise was obtained with the step injection scheme.

2. The inlet injection scheme was not mixing-limited.

7 Dual-mode combustion refers to the case where the combustion pressure rise is sufficient to separate the boundary layers and cause the formation of an oblique shock-train upstream of the injection location. This combustion mode is typical of engines designed for flight Mach numbers less than 6 (Billig et al., 1990; Heiser and Pratt, 1994; Kobayashi et al., 2006; Waltrup and Billig, 1973). Turner and Smart (2013) recently documented the occurance of dual-mode combustion in a REST scramjet designed for flight at Mach 8.

8 The actual values for each shot are listed in the legend of Figure 6.5. Shown previously in Figure 3.15 the fuel split varied approximately linearly during the test time due to the late timing of fuel injection and the different filling rates of each plenum. Consequently, small shot-to-shot variations in the fuel injection timing lead to slight variations in the mean fuel split.

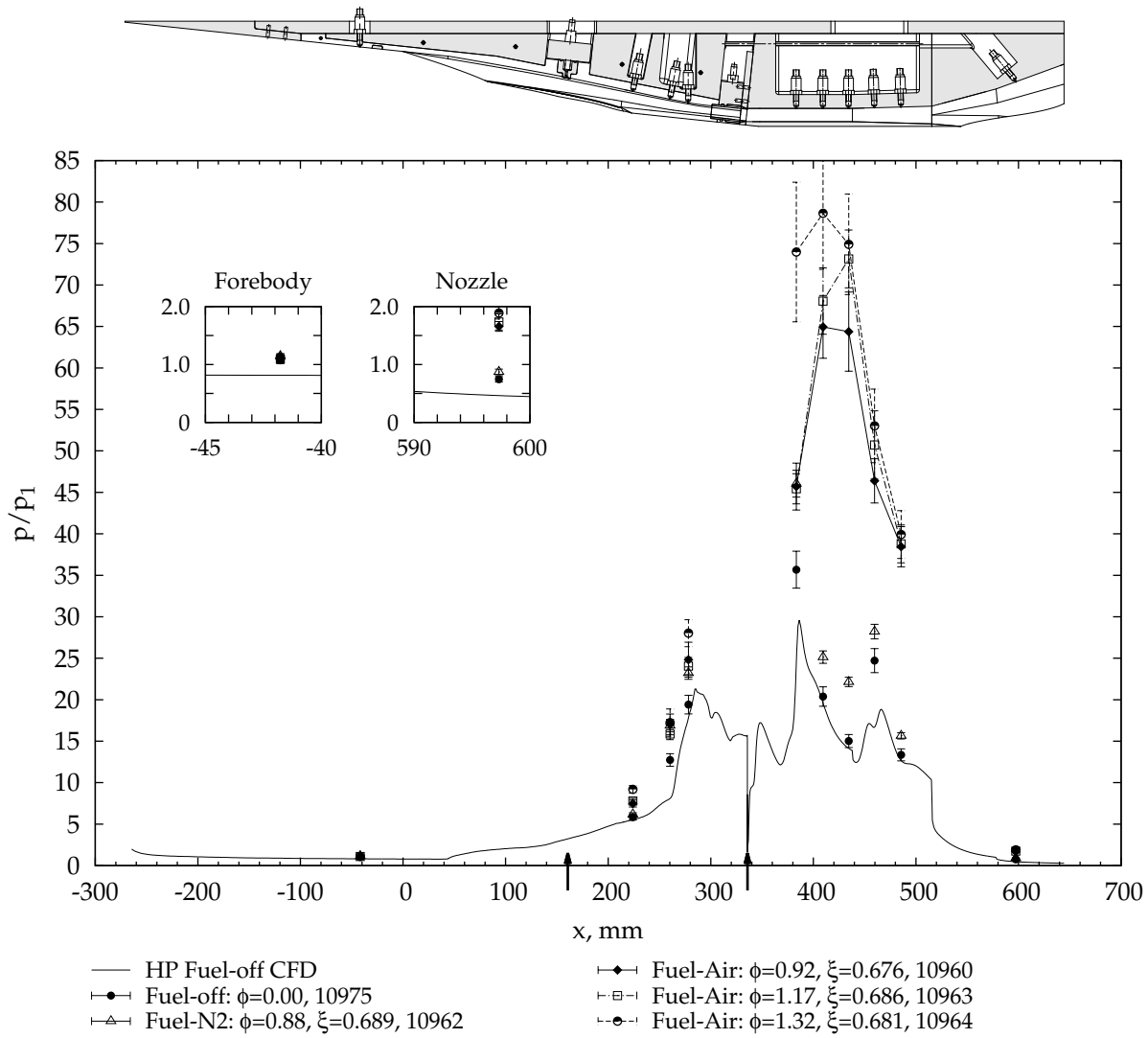

(a) High pressure condition.

Figure 6.5 – Engine bodyside pressure distribution for the combined injection scheme at each test condition. The fuel injection locations are indicated by arrows.

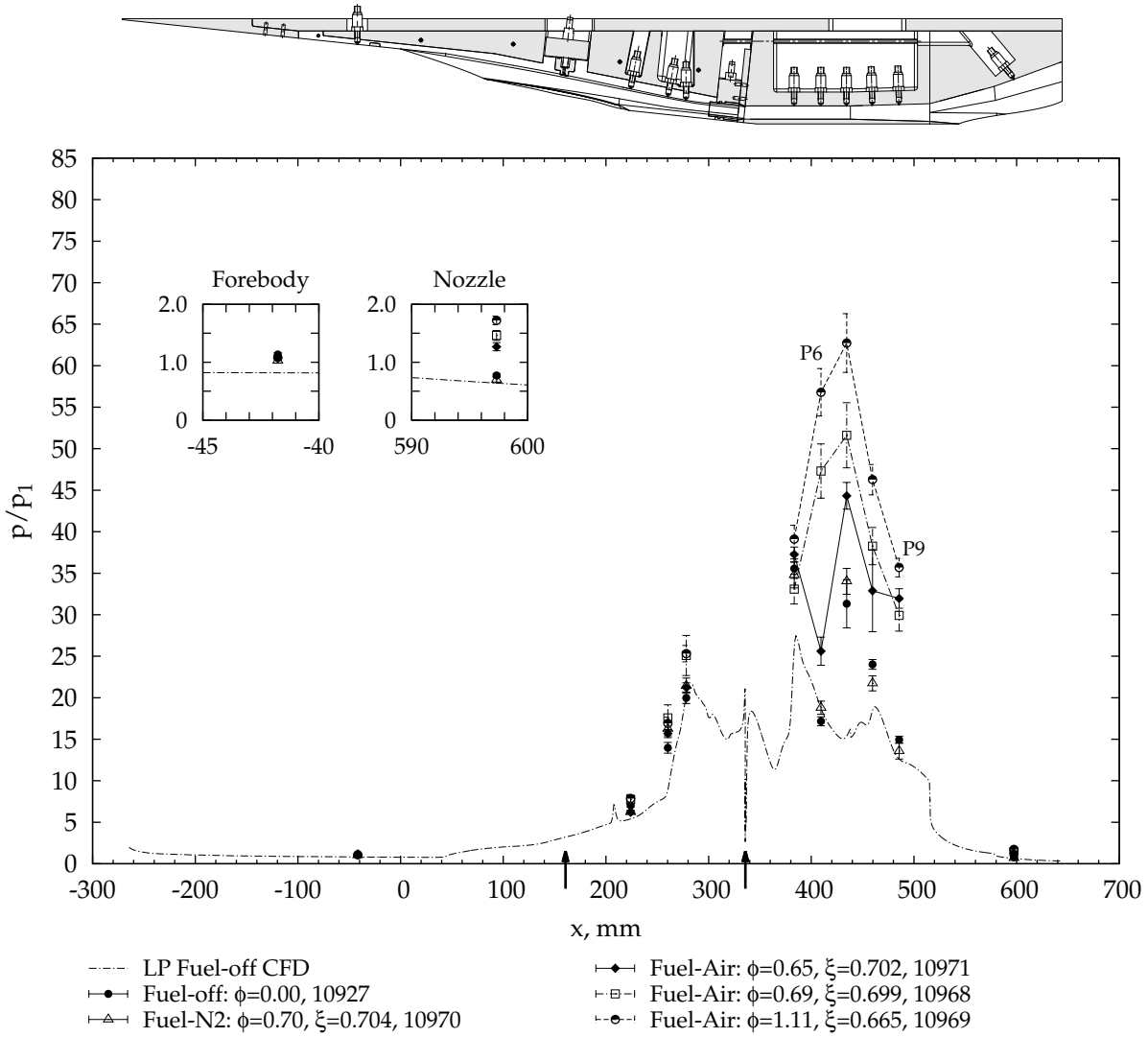

(b) Low pressure condition. A boundary layer trip was fitted.

Figure 6.5 – Continued.

3. The pressure rise measured for each combined injection shot was *greater* than that obtained for corresponding inlet injection shots.

Together, these observations imply that fuel injected from the step was burnt with greater efficiency for the combined injection scheme than for the step injection scheme. This improvement is theorised to be due to three mechanisms. Firstly, ignition and combustion of the inlet injected fuel upstream of the step produces free-radicals that accelerate ignition and reaction of the step injected fuel[9] (Han et al., 2004; Pellett et al., 2002). Secondly, combustion of the inlet injected fuel raises the average temperature and density within the combustor, decreasing the reaction time of the fuel injected at the step (see Rogers and Schexnayder, 1981, and Figure 6.8 of this thesis). Thirdly, interaction of the inlet fuel plumes with the cowl shock (and its reflections) changes the vorticity within the combustor leading to improved mixing of the step injected fuel (Buttsworth, 1996; Gehre et al., 2013; Schetz et al., 2010). Thus, in the context of the inlet and step injection scheme data, the combined injection scheme data unequivocally demonstrate the importance of inlet injection as a means of promoting combustion of fuel injected at the step.

There are several other features of the data plotted in Figure 6.5 that are worth discussing. Firstly, for the low pressure condition, the pressure measured at location P6 increases by 85 % as the fuel equivalence ratio is increased from $\phi = 0.65$ to $\phi = 0.69$ (shots 10971 and 10968). This sudden variation is hypothesised to be caused by the upstream movement of a shock impingement location, similar to that documented by Turner (2010, Section 5.3) for a Mach 8 REST scramjet. As a consequence of the limited number of measurement locations, the bodyside pressure distribution of the M12REST engine cannot be sufficiently characterised to confirm this hypothesis experimentally in this thesis.

Secondly, for the low pressure test condition the suppressed-combustion pressure is 10 % lower than the fuel-off pressure at location P8 and 9 % lower than the fuel-off pressure at location P9. Since the experimental uncertainty of the normalised pressure is ± 5.5 % (Section 3.5.2), these reductions in pressure are significant. Similar changes were observed by Suraweera and Smart (2009) for the design-scale M12REST engine and by Razzaqi and Smart (2011) for a two-dimensional scramjet engine. In each case, the axial resolution of the pressure measurements was sufficient to show that fuel mass addition altered the wave structure within each engine. A similar effect is expected to occur in the current experiments, causing the observed reduction in pressure at locations P8 and P9.

9 Although this mechanism cannot be experimentally confirmed in this thesis, simple one dimensional reacting gas calculations presented in Figure 6.8 and discussed in Section 6.6 indicate that the ignition length was approximately 40 mm at both test conditions. That is, similar to the distance between the throat and the step. Recent numerical simulations by Barth et al. (2014) for a half-design-scale inlet have also confirmed that the inlet injected fuel ignites and begins to burn slightly before the step.

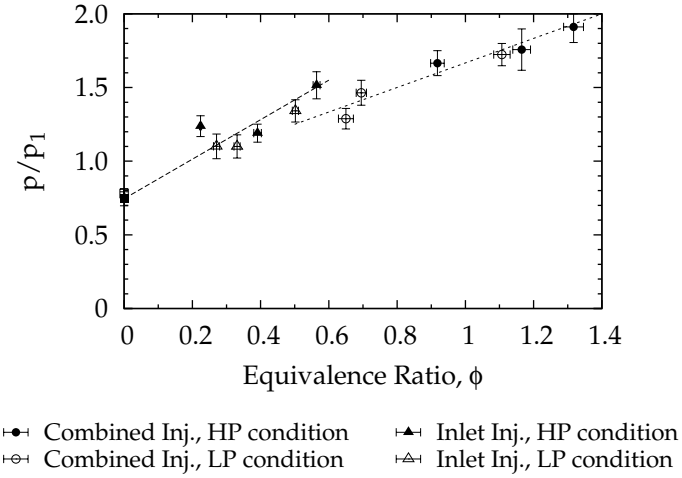

Figure 6.6 – Variation of normalised engine nozzle pressure with fuel equivalence ratio. Notional lines of best fit are shown.

The third interesting feature of the data plotted in Figure 6.5 is that the measured engine nozzle pressure increases linearly with fuel equivalence ratio. This is shown clearly by Figure 6.6 in which the normalised pressure ratio is plotted against the total equivalence ratio for both the inlet and combined injection schemes. Data at the high pressure test condition are represented by solid symbols, data at the low pressure test condition are represented by open symbols. Notional lines of best fit are also shown. While based on only a single measurement location in the engine nozzle, the approximately linear variation of pressure with equivalence ratio indicates that combustion is not mixing-limited for either injection scheme over the range of equivalence ratios examined. Noting also that thrust is proportional to the nozzle surface pressure distribution, then the trends established in Figure 6.6 are consistent with the thrust coefficient estimates made by Suraweera and Smart (2009) for the design-scale M12REST engine. These thrust estimates are reproduced in Figure 2.6.

Finally, the variation of inlet pressure with fuel equivalence ratio is consitent with that observed for the inlet injection scheme (cf. Figure 6.3 and Figure 6.5). At each test condition, the fuel-on inlet pressure data are comparable with the suppressed-combustion data, implying that fuel was not burning within the inlet and that the pressure rise was due to fuel mass addition. Repeatability of the test flow condition is indicated by the collapse of the forebody pressure data.

6.6 INFLUENCE OF FLIGHT DYNAMIC PRESSURE

This section discusses how the M12REST engine performance varies with flight dynamic pressure at nearly constant Mach number. Such a comparison is of interest because the flight corridor for airbreathing access-to-space

vehicles is generally taken to lie between constant dynamic pressure trajectories of 20 kPa and 100 kPa. The lower dynamic pressure limit is imposed by engine mass capture, net thrust and vehicle lift performance requirements, and by the requirement that the combustion chamber entrance pressure be sufficient for combustion to occur. The upper limit is imposed by airframe thermal and aerodynamic load contraints (Hirschel and Weiland, 2009; McRuer, 1991). For reference, these trajectories, along with lines of constant Mach number and the test conditions are plotted on a velocity-altitude map in Figure 3.7.

Normalised engine pressure data at the low and high pressure test conditions are compared in Figure 6.7 for the inlet and combined injection schemes. The step injection scheme is not considered as negligible combustion pressure rise was obtained for this scheme at each test condition (Figure 6.4). For comparison the fuel-off experimental data and pressure distribution from numerical simulations are also plotted in Figure 6.7. The inlet injection scheme data are for a fuel equivalence ratio near 0.55 and the combined injection data are for a total fuel equivalence ratio near 1.1. At the low pressure test condition the boundary layer trip shown in Figure 3.11 was fitted. No trip was fitted at the high pressure test condition data.

The numerical simulations show that the fuel-off engine pressure distribution is slightly altered by the change in test condition. Referring to Table 3.3, this change is caused by differences in the freestream unit-Reynolds number and Mach number, which alter the boundary layer development and shock angles within the engine, respectively. These differences however, are too small to be measured using the current instrumentation and hence, no influence of the test condition on the fuel-off engine pressures was observed experimentally.

For the fuel-on experimental data, the pressure increment measured at the low pressure test condition was smaller than that of the high pressure test condition by 10 to 20 %. This influence of the test condition was expected and is a consequence of the reduced pressure (or density) increasing the reaction length for combustion. A longer reaction length implies that proportionally less heat is released at the low pressure test condition than at the high pressure test condition, thereby resulting in a smaller pressure increment.

The influence of density and temperature on the ignition and reaction lengths is shown in Figure 6.8. The data in this figure were generated by solving the steady Euler equations for a chemically reacting gas along the length of a constant area streamtube. The reaction scheme of Rogers and Schexnayder (1981), which accounts for 16-species and 49-reactions was used. The inflow velocity was assumed to be 2567 m/s (Table 5.2 average) and the inflow species mass fractions were calculated from Table 3.3b by mixing air and pure hydrogen at constant volume assuming a fuel equivalence ratio of $\phi = 0.50$. Separate calculations were completed for

the low and high pressure test condition compositions with the inflow temperature and density varied as shown in Figure 6.8. A total length of 3 m was simulated and the ignition and reaction lengths were calculated using the temperature-based definitions[10] of Rogers and Schexnayder (1981).

As expected, the data in Figure 6.8 show that temperature influences the ignition length more strongly than the reaction length and that reaction length is strongly dependent on density. These trends are particularly noticeable when comparing the high and low pressure conditions, which are indicated by points in the relevant plots. The higher temperature (or total enthalpy, cf. Table 3.3) of the low pressure test condition reduces the ignition length to be comparable with the high pressure test condition, despite the almost factor two difference in density. In comparision, the reaction length of the high pressure test condition is 2.5 times smaller than that of the low pressure test condition, a reduction due to the increased density of the high pressure test condition. In summary, the fuel-air mixture is expected to ignite at a similar axial location for each test condition but at the exit of the combustor the reaction will be much less complete for the low pressure test condition compared with the high pressure test condition.

Figure 6.9 plots the pressure distributions along the first metre of the streamtube for both the low and high pressure test conditions. Similar to the presentation of experimental data, the computed distribution is presented as a pressure ratio relative to the nominal engine forebody pressure (Table 3.5). The ratio

$$\frac{p_{LP}}{p_{HP}} = \frac{(p_{LP}/p_{1,LP})}{(p_{HP}/p_{1,HP})} \tag{6.2}$$

has also been plotted to clearly show the difference between the two test conditions. Noting that the length of the M12REST combustor was 180 mm (Section 3.4) and that the streamtube computation was for a fully mixed inflow at fuel equivalence ratio of 0.50, the pressure distributions plotted in Figure 6.9 are consistent with the experimental inlet injection data plotted in Figures 6.3 and 6.7a. This implies that in the experiment the inlet injected fuel was well mixed by the end of the inlet and that the combustor length was insufficient for complete reaction of the fuel.

10 For completeness: the ignition temperature is defined as $T_{ig} = 0.05(T_{eq} - T_0) + T_0$ where T_{eq} is the equilibrium temperature and T_0 is the initial temperature. The *total* reaction temperature is defined as $T_{tr} = 0.95(T_{eq} - T_0) + T_0$. Using the computed temperature distribution along the streamtube, these ignition and total reaction temperatures are easily converted to lengths. Finally, the reaction length is defined as $L_r = L_{tr} - L_{ig}$.

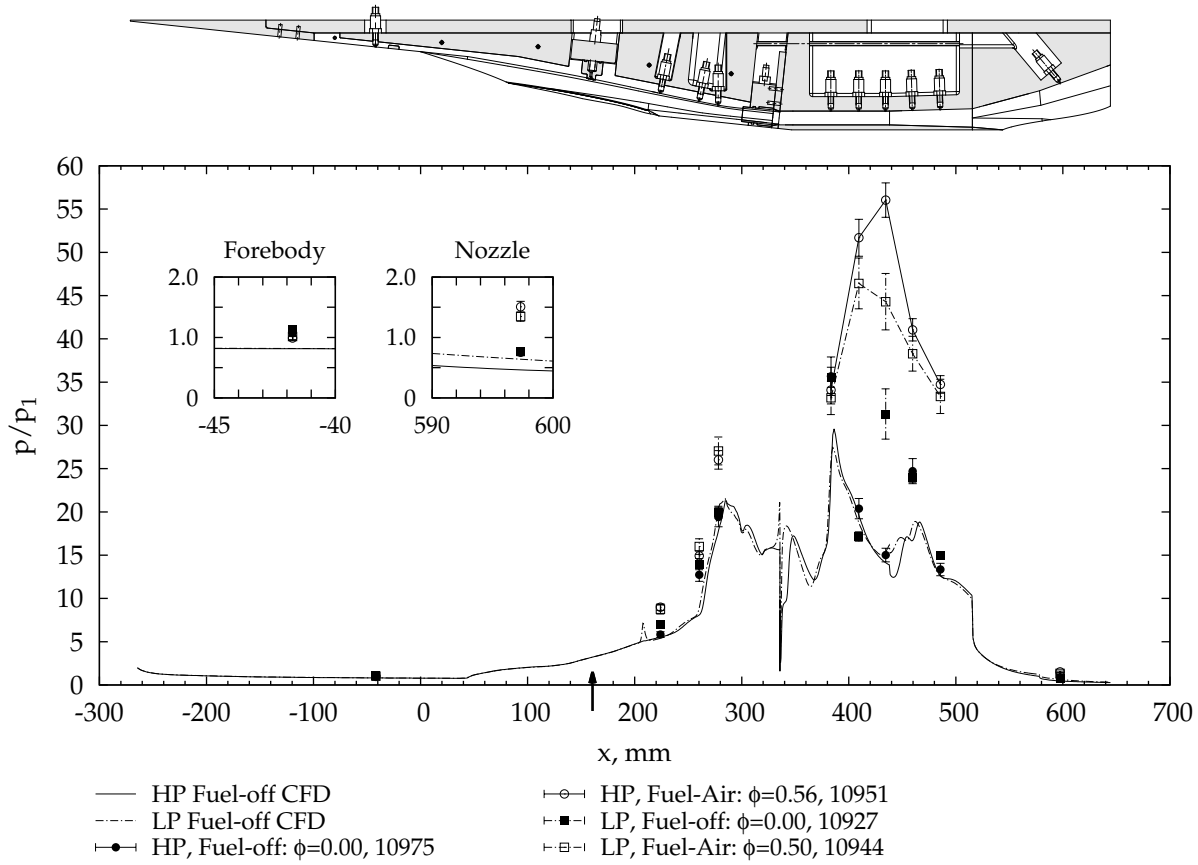

(a) Inlet injection scheme.

Figure 6.7 – Comparison of the engine bodyside pressure distribution at the low and high pressure test conditions. Fuel injection locations are indicated by arrows. A boundary layer trip was fitted for the low pressure data.

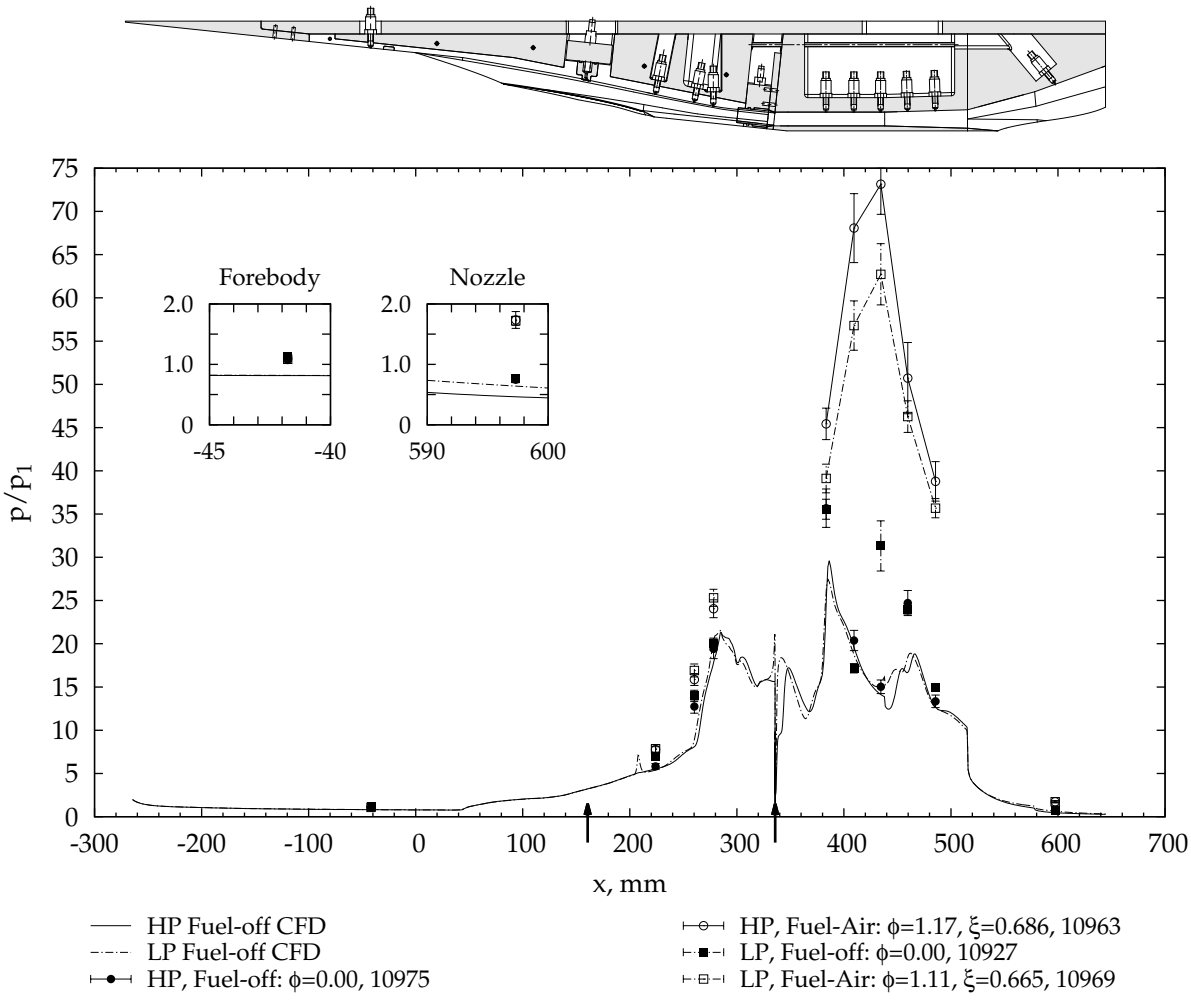

(b) Combined injection scheme.

Figure 6.7 – Continued.

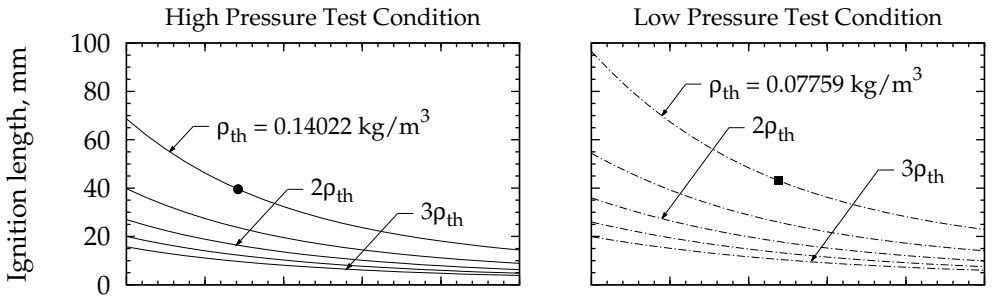

(a) Ignition length

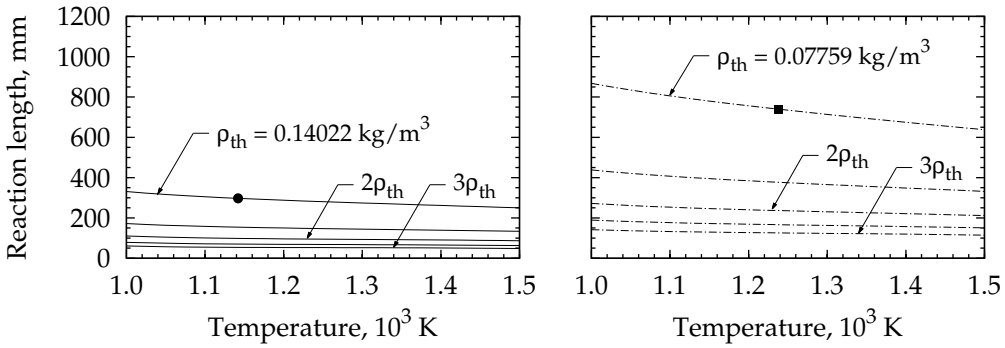

(b) Reaction length

Figure 6.8 – Variation of hydrogen ignition and reaction lengths with temperature and density. Lines of constant density are shown at intervals of $0.5\rho_{th}$ between ρ_{th} and $3\rho_{th}$ where ρ_{th} was taken from Table 5.2. The calculated ignition and reaction lengths for each test condition are indicated by solid points. Refer to the text for a description of the calculation method.

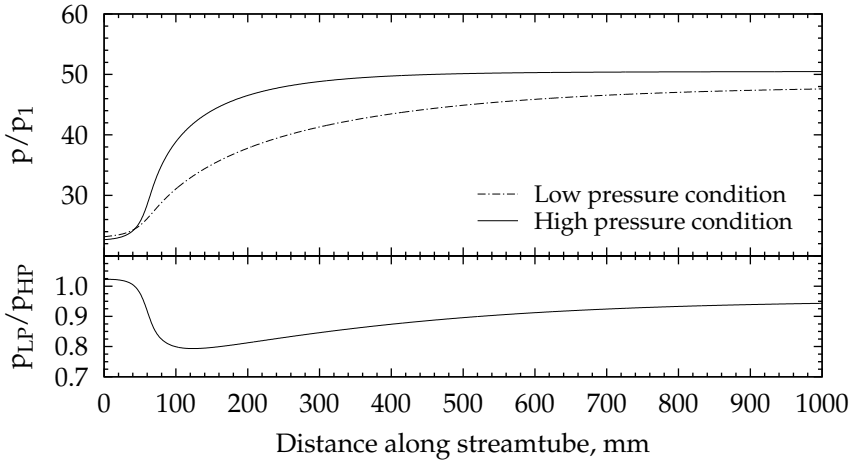

Figure 6.9 – Variation of pressure along a constant area streamtube for the low and high pressure test conditions. Refer to the text for a description of the calculation method.

6.7 COMPARISON WITH DESIGN-SCALE ENGINE DATA

This section provides a comparison of the engine pressure data measured in this thesis at the high pressure Mach 10 test condition, to that measured by Suraweera and Smart (2009) for the design-scale engine at a Mach 9 flight condition. The reason for using the off-design condition data of Suraweera and Smart (2009) for comparison is simply that no other data has been published for the design-scale engine.

As stated in Section 3.4, the M12REST engine developed in this thesis was a factor of 0.32 smaller than the design-scale engine. Sub-design-scale testing is standard practice in the field of hypersonics due to size constraints imposed by the available wind tunnel facilities. Typically, to achieve similitude of the flow field between a sub-scale wind tunnel experiment and full-scale flight article, some form of scaling of the flow condition is required (Bushnell, 2006; McGilvray et al., 2010). The predominant scaling method used for supersonic combustion experiments is the binary scaling method (Hornung, 1988; Stalker and Pulsonetti, 2004) for which the flow velocity, temperature and gas composition of the test condition are matched to flight while the density is adjusted such that the product of density and length remains constant.

Although the model used in this thesis was sub-design-scale, no scaling of the test condition was undertaken. This was not by choice but by neccessity; the high pressure Mach 10 test condition (Table 3.3) corresponds to the upper operational limit of the T4 Stalker Tube. A tripling of the nozzle supply pressure (and hence nozzle exit pressure) as required by the binary scaling method was not possible. In addition to the un-scaled test condition, the test methodology was also different between the current work and that of Suraweera and Smart (2009). Shown clearly in Figure 6.10, the design-scale engine was tested by Suraweera and Smart (2009) in semi-freejet mode with the facility nozzle flow replicating the conditions behind an assumed vehicle forebody shock. A Mach 8 facility nozzle was used and the engine featured a short forebody of length 150 mm. In comparison, the current engine was tested in freejet mode with the facility nozzle flow replicating a true flight condition. A Mach 10 facility nozzle was used and the engine features a 272 mm long forebody and streamlined external geometry. A comparison of the small and design-scale engine data is of interest because it allows the effects of the un-scaled test condition and the test methodology to be partially assessed. Section 6.7.1 presents a comparison of the fuel-off data while Sections 6.7.2 to 6.7.4 present comparisons of the fuel-on data for the inlet, step and combined injection schemes respectively.

Before comparing the small and design-scale engine data, three other differences that existed between the two engines should be noted. These are as follows: Firstly, the design-scale engine featured a fully enclosed conical thrust nozzle with area ratio of 8.0 relative to the engine throat. In

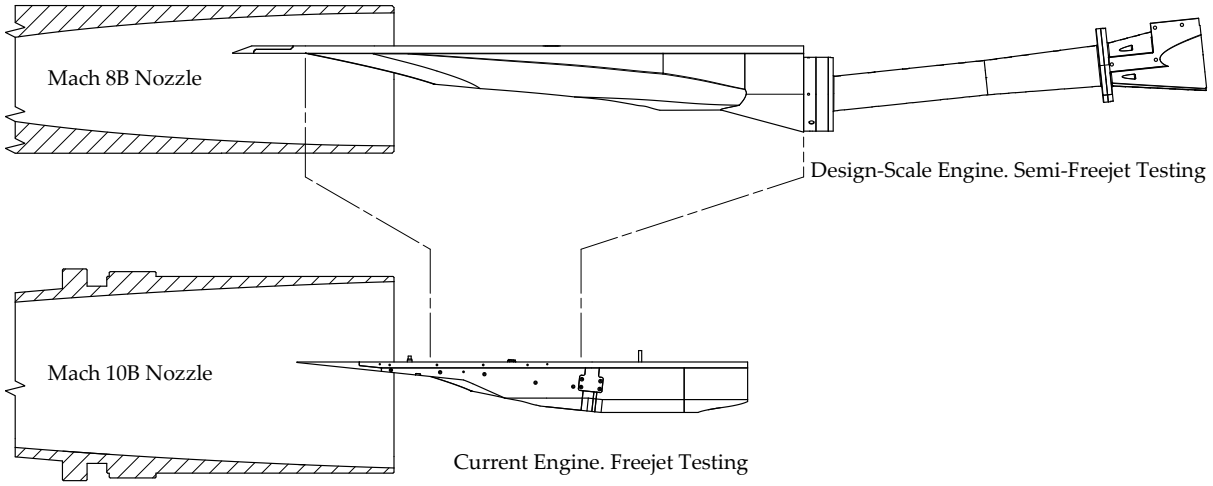

Figure 6.10 – Comparison of the small-scale airframe integrated engine and the design-scale engine tested by Suraweera and Smart (2009). The engines are shown at the same scale. The small-scale engine was tested in freejet mode with the T4 Mach 10B nozzle. The design-scale engine was tested in semi-freejet mode with the T4 Mach 8B nozzle.

Table 6.1 – Nominal Test Flows Computed using NENZFR

(a) Flow Properties

		Freestream		Forebody	
	Units	Design-scale, semi-freejet	Small-scale, freejet	Design-scale, semi-freejet	Small-scale, freejet
p	Pa	921	638	3012	2430
T	K	242	213	355	334
ρ	kg/m^3	0.013 20	0.010 37	0.0294	0.0252
u_x	m/s	2816	3044	2775	3003
M		9.02	10.38	7.3	8.2
q	kPa	52.4	48.0	113.4	113.8
Re_u	$10^6/m$	2.39	2.25	3.88	3.77

(b) Flow Composition

Species	Design-scale, semi-freejet	Small-scale, freejet
Y_{N2}	0.7429	0.7336
Y_{O2}	0.2044	0.1940
Y_N	0	0
Y_O	0.0008	0.0008
Y_{NO}	0.0519	0.0716

comparison, the current engine featured a partially open three-dimensional thrust nozzle with a projected area ratio of 16.1 relative to the engine throat. Secondly, at the step injection station, the design-scale engine featured 48 porthole injectors, each 1.5 mm in diameter and angled at 10° to the axis of the inlet. Mechanical design constraints precluded the injectors from being geometrically scaled (Doherty, 2013b) so the current engine featured 24 porthole injectors, each 0.65 mm in diameter and angled at 15° to the inlet axis. Thirdly, the leading edge radii of both the design-scale engine and current engine were 0.7 mm.

Table 6.1 summarises the freestream and forebody flow properties and flow composition for the small-scale freejet and design-scale semi-freejet engine experiments. Data for the Mach 10 nozzle are reproduced from Tables 3.3 and 3.5. To ensure consistency, the Mach 8 test condition was (re)computed with NENZFR using the models and assumptions that are described in Section 3.3.1. For each test condition the freestream and forebody flow conditions are related by an oblique shock calculation using a flow deflection angle of 6° and assuming a frozen composition.

6.7.1 *Fuel-off Data*

Normalised engine pressure data for the small and design-scale engines are compared with corresponding numerical simulations in Figure 6.11 for the case of no fuel injection. The axial distance along the engine is normalised by the engine inlet capture width (w_c) which is 48 mm for the small-scale engine and 150 mm for the design-scale engine. An enlarged view of the forebody pressure data is provided as an inset figure to aid comparison. Due to the differing geometries of the engine nozzles, experimental data are plotted only up to the end of the combustor. The design and layout of Figure 6.11 is used consistently throughout this section for the comparison of the small and design-scale engine pressure data.

As expected the experimental and numerical pressure distributions for the small-scale engine compare well with the design-scale engine distributions. On the forebody the numerical simulations clearly show the influence of flow spillage from the slender forebody of the small engine; the distribution lies below unity and is decreasing while that of the design-scale engine remains constant. Within the engine the numerical pressure distribution of the small engine lies slightly above that of the design-scale engine and the shock impingement locations lie slightly upstream, despite the design-scale engine being tested at a lower Mach number (Table 6.1). These differences, while too small to be resolved experimentally, result from the ingestion of a relatively thick forebody boundary layer by the small engine. On the symmetry plane, at the entrance to the inlet, the normalised thickness of the boundary layer was $\delta/w_c = 0.131$ for the

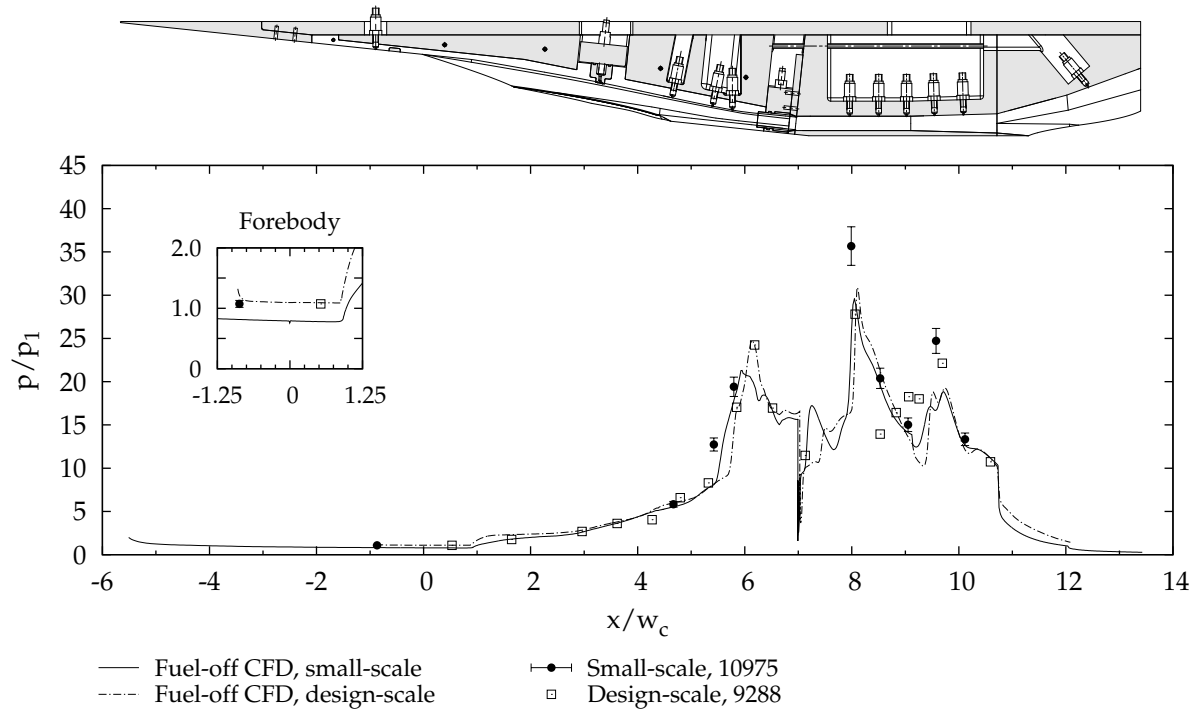

Figure 6.11 – Comparison of the bodyside pressure distributions of the small and design-scale engines for no fuel injection.

small engine but only $\delta/w_c = 0.018$ for the design-scale engine. Finally, the source of the discrepancy between the experimental data and numerical simulation around $x/w_c = 9$ for the design-scale engine was never identified by Suraweera and Smart (2009).

6.7.2 *Fuel-on Data for Inlet Injection*

Normalised pressure data from the small and design-scale engine tests are compared in Figure 6.12 for the inlet injection scheme at two different fuel equivalence ratios. To aid interpretation, suppressed-combustion data for the design-scale engine and the numerical fuel-off pressure distribution for each engine are also plotted. An inset figure that shows an enlarged view of the forebody pressure data is also drawn and the axial distance along the engine has been normalised by the inlet capture width. To assist visualisation, lines are drawn between consecutive transducers in the combustor; these lines should not be interpreted as depicting the pressure variation between these measurement locations.

At a fuel equivalence ratio of 0.30 (Figure 6.12a) the pressure data in the inlet are comparable for the small and design-scale engines, indicating that the influence of fuel mass addition in the inlet is similar in each engine. In the isolator of the inlet, that is $x/w_c \approx 6$ to 7, the data for the design-

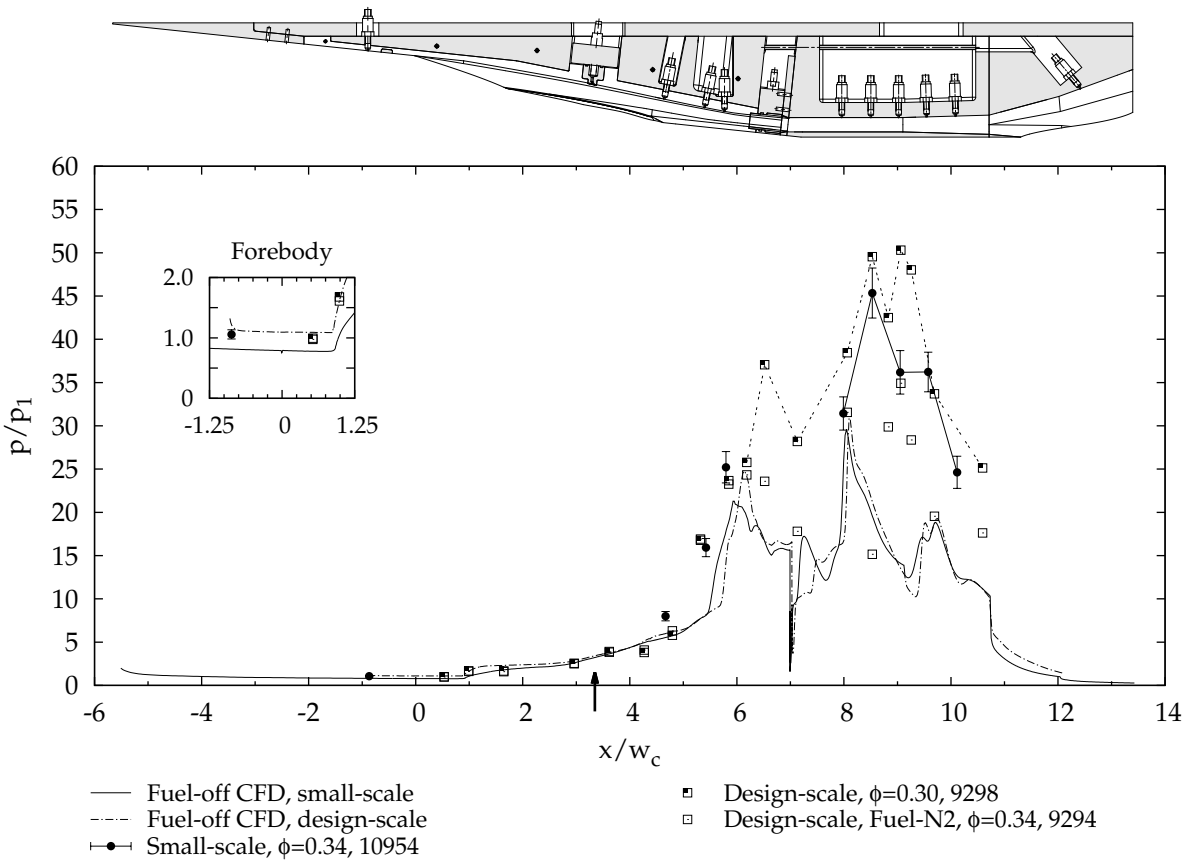

(a) $\phi = 0.30$

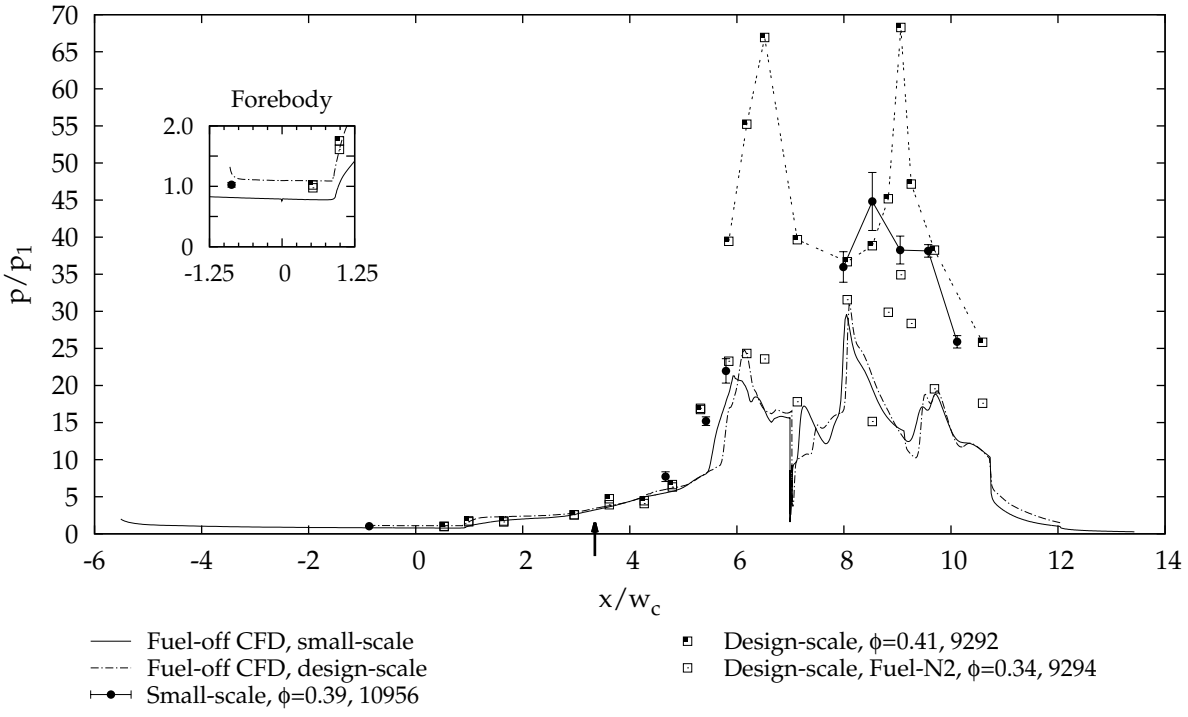

(b) $\phi = 0.40$

Figure 6.12 – Comparison of the bodyside pressure distributions of the small and design-scale engines for the inlet injection scheme. The fuel injection location is indicated by an arrow.

scale engine display a significant influence of combustion; the fuel-on pressure is approximately 58 % higher than the suppressed-combustion pressure (Figure 6.12a). This influence could not be measured in the small-scale engine because the model size and design of the step injector plenum prevented any pressure taps from being placed in the region $6 \leqslant x/w_c \leqslant 8$ (Doherty, 2013b). In the combustor, the small-scale engine data generally lie below the design-scale engine data within the constant area section of the combustor and are comparable with the design-scale engine data within the divergent section of the combustor. For example, at location $x/w_c = 9.1$, the pressure measured for the small-scale engine is 39 % smaller than that of the design-scale engine where as at location $x/w_c = 9.6$ the pressure measured for the small-scale engine is 7 % larger than that of the design-scale engine.

At a fuel equivalence ratio of 0.40 (Figure 6.12b), the pressure distributions of the small and design-scale engines are quite different from one another. In particular, for the design-scale engine the pressures within the isolator show a very significant influence of combustion; the peak pressure at $x/w_c = 6.5$ is $p/p_1 = 67$, only 2 % smaller than the peak pressure in the combustor. Compared with the data for an equivalence ratio of 0.30, the influence of combustion has moved further upstream for the design-scale engine. For the small-scale engine, the lack of pressure rise at $x/w_c = 5.9$ may indicate that the fuel does not burn as early as in the design-scale engine. This result is consistent with the ignition and reaction length calculations presented in Figure 6.8, but cannot be confirmed with the current model and instrumentation. Finally, with the exception of the peak pressure at $x/w_c = 9.1$, the small-scale engine data in the combustor are comparable with the design-scale engine data.

6.7.3 *Fuel-on Data for Step Injection*

Normalised pressure data for the small and design-scale engines are compared in Figure 6.13 for the step injection scheme at a fuel equivalence ratio of approximately 0.80. Again fuel-off numerical distributions for each engine are provided to aid interpretation, an inset figure shows an enlarged view of the forebody pressure data and lines are draw between consecutive transducers in the combustor.

In comparison with the inlet injection data plotted in Figure 6.12, the step injection data plotted in Figure 6.13 show a clear and significant influence of the lack of scaling of the test condition. Good combustion pressure rise was obtained for the design-scale engine, whilst negligible combustion pressure rise was obtained for the small engine. For both engines no influence of combustion was observed upstream of the injection location.

Based on the data presented and discussed in Sections 6.3 to 6.5, combustion of fuel injected from the step was kinetically limited for the small-scale

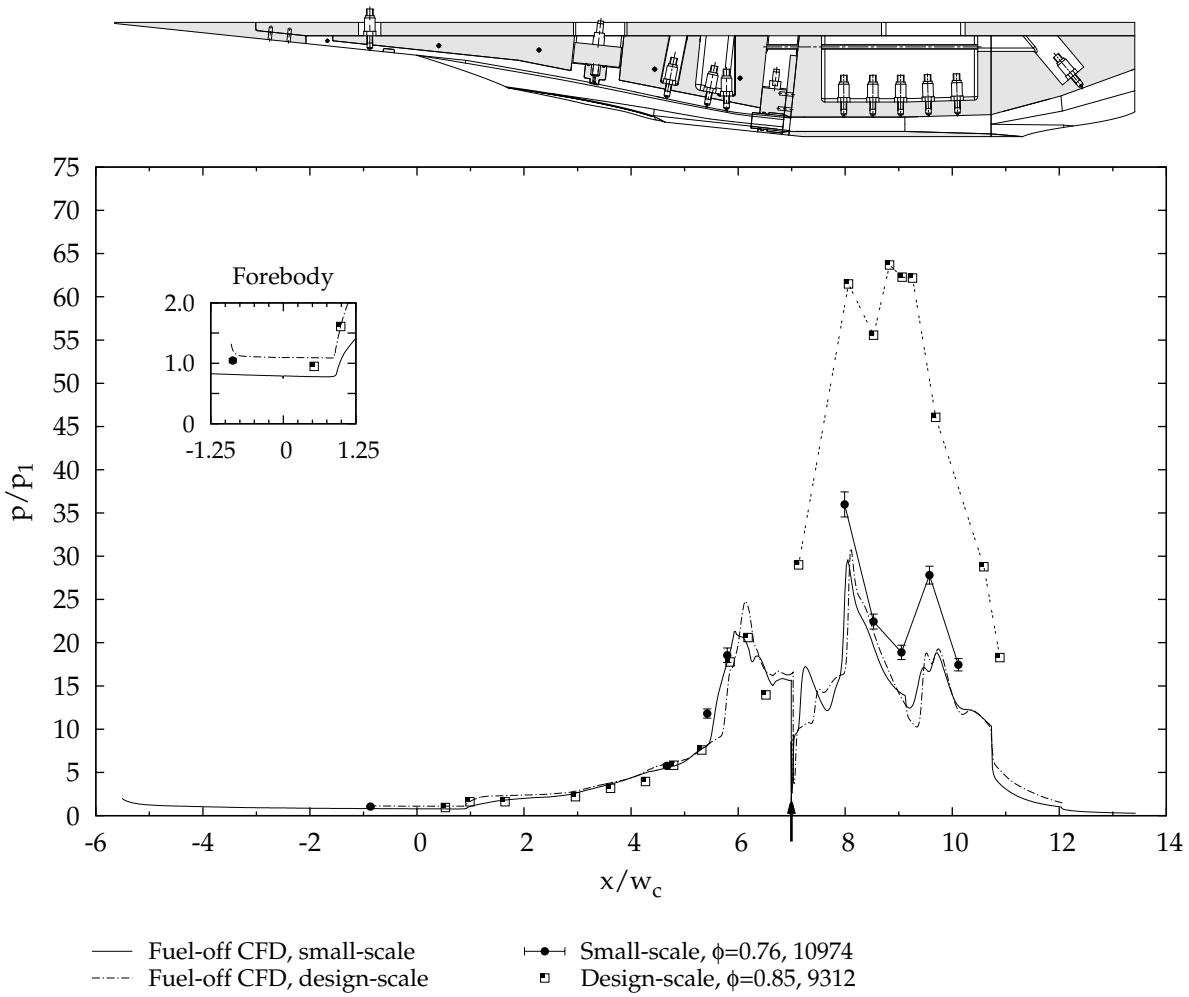

Figure 6.13 – Comparison of the bodyside pressure distributions of the small and design-scale engines for the step injection scheme. The fuel injection location is indicated by an arrow.

engine. The reduced static density of the test condition, relative to that required by the binary scaling method, increases the reaction length such that no significant pressure rise is obtained before the flow reaches the combustor exit. This conclusion is supported by reaction length data plotted in Figure 6.8b for a constant area streamtube. The calculated reaction length for the high pressure test condition is $L_r = 297\,\text{mm}$; significantly longer than the length of the combustor $L_c = 180\,\text{mm}$ of the small-scale M12REST engine. If the test condition was appropriately scaled, the density would be approximately tripled and, based on the data plotted in Figure 6.8b, the reaction length would reduce to 48 mm, approximately one-fifth of the combustor length. The lack of combustion achieved for the step injection scheme with the small-scale engine is a direct consequence of the test condition being unscaled. In comparison, the design-scale engine test was conducted at the design pressure,[11] for which the combustor was sufficiently long to allow the fuel to mix and burn before reaching the combustor exit. Finally, based on quasi-one-dimensional cycle analysis, Moule and Smart (2013) concluded that for the design-scale engine the step injection scheme was mixing-limited. This is very different from the kinetically limited combustion that was observed in this work for the small-scale engine and highlights the importance of appropriately scaling the test flow when testing sub-scale scramjet engines.

6.7.4 *Fuel-on Data for Combined Injection*

Normalised pressure data for the small and design-scale engines are compared in Figure 6.14 for the combined injection scheme at a total fuel equivalence ratio above 1.0. Once again, an inset figure that shows an enlarged view of the forebody pressure data is drawn and fuel-off numerical distributions for each engine are provided to aid interpretation. To assist visualisation, lines are again drawn between consecutive transducers in the combustor.

The data plotted in Figure 6.14 display similar trends to that presented in Section 6.7.2 for the inlet injection scheme. Within the inlet, the small and design-scale data are comparable with one another and are elevated above the fuel-off numerical value due to fuel mass addition. At the design-scale data, an influence of combustion is observed in the inlet isolator ($6 \leqslant x/w_c \leqslant 7$). Measurements in this region of the small-scale engine were not possible because of the model size. In the combustor, the small and design-scale engine data are comparable from location P6 onwards however, the design-scale engine data are for a lower fuel equivalance

11 The M12REST inlet and combustor geometries were designed for flight between Mach 6 and Mach 12 at a constant dynamic pressure of 50 kPa (Suraweera and Smart, 2009). The test condition used for the design-scale engine was marginally above the design dynamic pressure (Table 6.1).

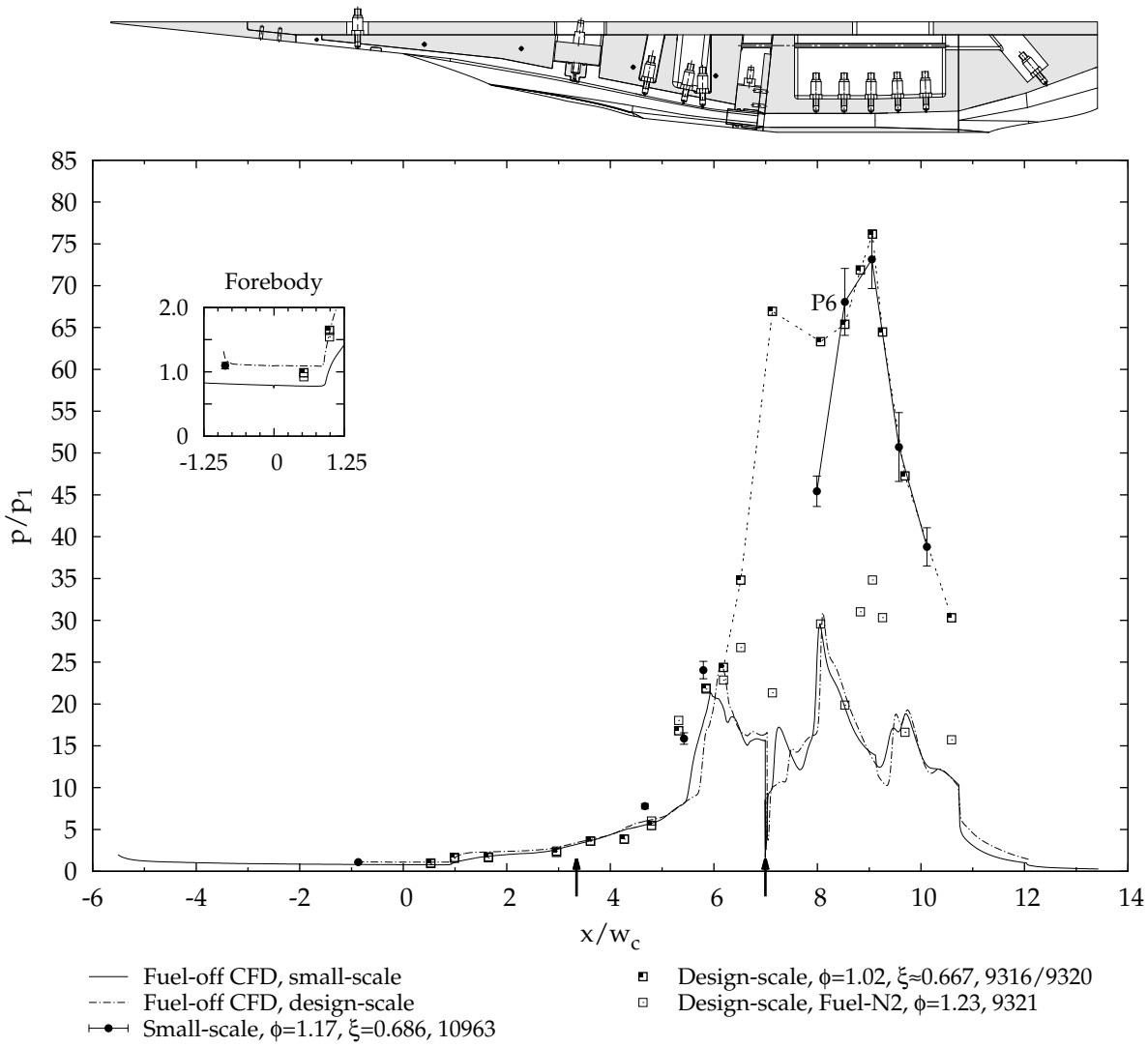

Figure 6.14 – Comparison of the bodyside pressure distributions of the small and design-scale engines for the combined injection scheme. The fuel injection locations are indicated by arrows.

ratio.[12] Similarity of the data therefore suggests that the design-scale test are more highly performing. Based on the data presented in Figures 6.11 to 6.14, the difference in performance of the small-scale engine compared with the design-scale engine is primarily related to the reduced scale and test condition. Nevertheless, good combustion pressure rise was obtained for the small-scale engine with both the inlet and combined injection schemes indicating that the small-scale engine is operable at the test conditions used in this thesis.

12 The total fuel equivalance ratios reported by Suraweera and Smart (2009) for the design-scale engine are believed to be between 15 and 30 % higher than reality. This is because the total fuel mass flow rate was calculated by Suraweera and Smart (2009) using a different method to that used in this thesis (see Appendix A.4.2, calibration constant α_C was introduced in this thesis).

FORCE BALANCE RESULTS

The seventh chapter, in which fuel-off engine force data are compared with numerical simulations, the force balance shielding is found to adversely influence the facility nozzle flow and engine performance metrics are calculated.

7

7.1 INTRODUCTION

This chapter presents engine force and pressure data from the first test campaign. The goal of the campaign was to measure the lift, drag and pitching moment of the M12REST engine at the Mach 10 test conditions for each injection scheme at a range of fuel equivalence ratios. Unfortunately three unforseen difficulties were encountered during the campaign that affected the quality of the measured force data. These difficulties and an overall summary of what occurred during the seven month test campaign are discussed in Section 7.2. Fuel-off data are presented in Section 7.3 and compared with numerical simulations. Fuel-on data for the inlet and combined injection schemes are presented in Sections 7.4 and 7.5 respectively. Using the experimental data, engine performance metrics including the specific thrust, specific impulse and overall thermodynamic efficiency are calculated and discussed in Section 7.6.

7.2 CAMPAIGN OVERVIEW

The purpose of this section is to provide an overview of what occurred during the force balance test campaign, to discuss the difficulties encountered and to justify the data selected for presentation in the remaining sections of this chapter. During the test campaign the quality of the measured force data was influenced by three main difficulties. These difficulties were that

1. the front half of the shielding was insufficiently stiff and made contact with the model during a test;
2. the force balance shielding created a significant blockage to the upper half of the Mach 10 nozzle, adversely affecting the test flow, and
3. the timing of fuel injection was too early.

Additionally, the measured Pitot-to-nozzle supply pressure ratio was lower than expected based on the nozzle survey data that was available at the time. This result was one of the motivations for the development of NENZFR (Section 3.3.1). With regards to these three difficulties, the

(a) Design A, initial shielding (b) Design D

Figure 7.1 – Comparison of the initial and final force balance shielding designs

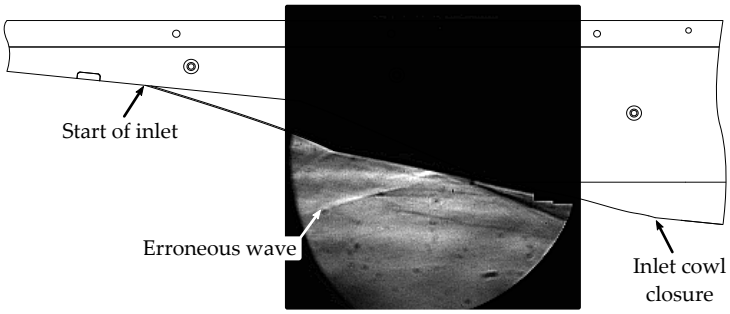

(a) Unstarted inlet. High pressure shot 10769, $t = 3.5$ ms after trigger of the nozzle supply pressure transducers (frame 56). For this shot the model was positioned 73 mm downstream from the nominal position (see Section 3.4.7) and shielding design C was fitted.

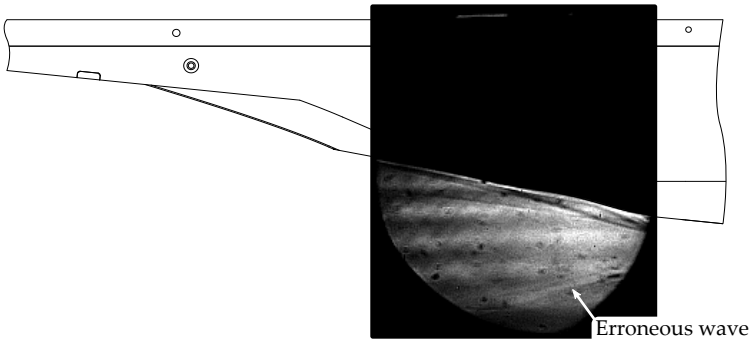

(b) Started inlet. High pressure shot 10771, $t = 2.6$ ms after trigger of the nozzle supply pressure transducers (frame 42). For this shot shielding design D was fitted.

Figure 7.2 – Interaction of a wave from the Mach 10 nozzle with the M12REST engine

first should have been identified and corrected prior to the experiments. The second was not anticipated because the upper portion of the force balance shielding was identical to that used by Robinson (2003d) during the development of the 3CFB. No adverse influence of the force balance shielding on the test flow produced by the Mach 6 nozzle was observed by Robinson (2003d). Finally, the third difficulty was not anticipated because no such influence of fuel injection timing had been observed by Suraweera and Smart (2009) during testing of the design-scale M12REST engine.

During the first half of the campaign, attention was focussed on stiffening the shielding and reducing its influence on the facility nozzle flow (items 1 and 2). The effect of early injection of fuel on the engine operation (item 3) was not identified as an issue until the second test campaign, during which a streamlined shielding design was used (Figure 4.1). Over the course of the first campaign a total of five iterations of the force balance shielding were used; from the initial design, design A, through to a 'double-wedge' design, design E. A photograph of each iteration is provided in Figure I.1 while designs A and D are compared in Figure 7.1. The force data presented in this chapter represent that recorded for shielding designs D and E. There are two reasons for choosing to present only this data. Firstly, of the different shielding iterations, the data set available for shielding design D was the most complete, covering all three injection schemes. Secondly, the engine pressure and force data exhibited the best quality time-history for fuel-off tests with these shielding designs.

Shielding designs B and C stiffened the front portion of the shielding however, after a period sufficient for flow establishment, the time-history of the recovered lift force did not follow that of the nozzle supply pressure as expected. Consequently, a schlieren optical system was setup to visualise the nozzle starting process and engine leading edge shock. The resulting images, although of low quality,[1] showed that the T4 Mach 10 nozzle was being adversely affected by the presence of the force balance shielding – an erroneous wave was observed that originated from within the facility nozzle and interacted with the engine.

Observation of this wave prompted the development of shielding designs D and E, each of which were designed to reduce the influence of the shielding through the use of a frontal wedge. The erroneous wave and its interaction with the M12REST engine is shown in Figure 7.2 for shots 10769 and 10771. A single frame extracted from the recorded high-speed video is shown for each shot. To aid interpretation, each frame is overlayed on a schematic of the engine. For shot 10769 shielding design C was fitted and, in an attempt to alleviate the blockage caused by the shielding, the model was positioned 73 mm downstream of the nominal position (Section 3.4.7). The erroneous wave is clearly visible in Figure 7.2a and, due to the posi-

1 Although the schlieren system was not optimized for the force balance campaign, the quality of the resulting images is considered sufficient for the purposes of this thesis.

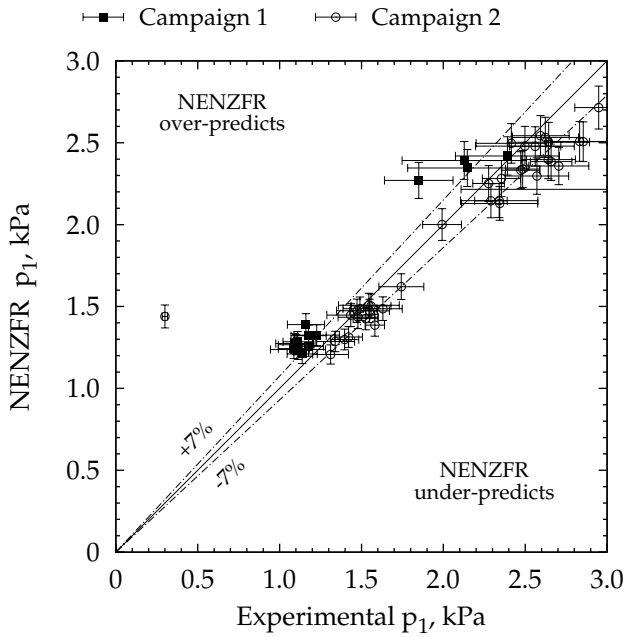

Figure 7.3 – Comparison of the experimental and NENZFR-predicted forebody pressure

tion of the model, is swallowed by the inlet, causing an inlet unstart. In comparison, for shot 10771 (Figure 7.2b), shielding design D was fitted and the model was located in the nominal position. The wave, while still present, appears weakened and iteracts with the engine downstream of the inlet cowl closure point.

In the high speed video, the wave was observed to move upstream during the nozzle starting process until approximately stabilising at the location shown in Figure 7.2b. The current hypothesis for the origin of the wave is that the force balance shielding sufficiently blocked the upper portion of the nozzle such that a stable[2] flow separation was formed inside the nozzle, slightly upstream of the nozzle exit plane. The observed wave is the shock formed at the upstream edge of the separation. Additional schlieren images for shielding designs C and D and from the second test campaign are provided in Appendix I.

Following the attachment of shield design D and the observation that the wave was still present, the decision was made to proceed with collecting data for each injection scheme. Shield design E, a double-wedge design, was a final attempt at improving the quality of the data and, when this did not appear to work very well, the testing was stopped and the campaign brought to an end.

2 Here stable means that the separation remained at a fixed axial location and did not continually move upstream nor get swept out of the nozzle during the test time.

Despite the difficulties encounted during the campaign and the presence of the erroneous wave, it is argued here that some data from the force balance campaign are reasonable and can be used for further analysis. Specifically, those force balance experiments for which either shielding design D or E was fitted exhibited the best quality time-history and so are presented in the remaining sections of this chapter. Furthermore, for tests in which the erroneous wave interacted with the model downstream of the inlet cowl closure point (Figure 7.2b), the measured internal pressure distribution was consistent with numerical simulations and with the pressure measurements from the second test campaign.[3] As shown in Figure 7.3, the measured pressure on the engine forebody compared well with that predicted from NENZFR – there is no significant difference between the data from campaign 1 and that from campaign 2. Thus, with the model in the nominal position relative to the facility nozzle exit, the wave is not swallowed by the inlet and the flow entering the engine is of sufficient quality to justify further analysis and presentation of the engine force data.

7.3 FUEL-OFF DATA

Experimental pressure distributions at the high and low pressure test conditions are compared with numerical simulation in Figure 7.4. Data from the second test campaign are also provided for comparison. The sawtooth boundary layer trip shown in Figure 3.11 was fitted for each force balance shot. For each test condition the measured pressures compare well with the distribution from the numerical simulation and with data from the second test campaign. The collapse of the forebody pressure data to a normalised value near unity gives confidence that the flow entering the engine was close to that predicted by NENZFR. This result also suggests that the wave observed in the schileren images and shown in Figure 7.2 does not alter the core flow properties significantly. The single data point in the inlet lies just upstream of the predicted distribution, a result that is consistent with the fuel-off data from the second test campaign (Section 6.2). The combustor pressure data are also consistent with data from the second test campaign, displaying a distinct shock dominated structure. At locations P5 and P8 (shock-impingement locations) the numerical simulation under-predicts the measured pressure. As noted in Section 6.2, this under-prediction is postulated to be related to the axial resolution of the computational grid at these locations. Finally, the force balance data exhibit slightly larger variation bars than the campaign 2 (rigid-mount) data. This is primarily a consequence of using a longer test time to process each force balance shot.[4] Further discussion on the requirement for a longer test time is provided in Section 3.5.1.

3 Engine pressure data from the second test campaign are presented in Chapter 6.
4 In the case of shot 10793, the flow was also atypically unsteady in the inlet and combustor.

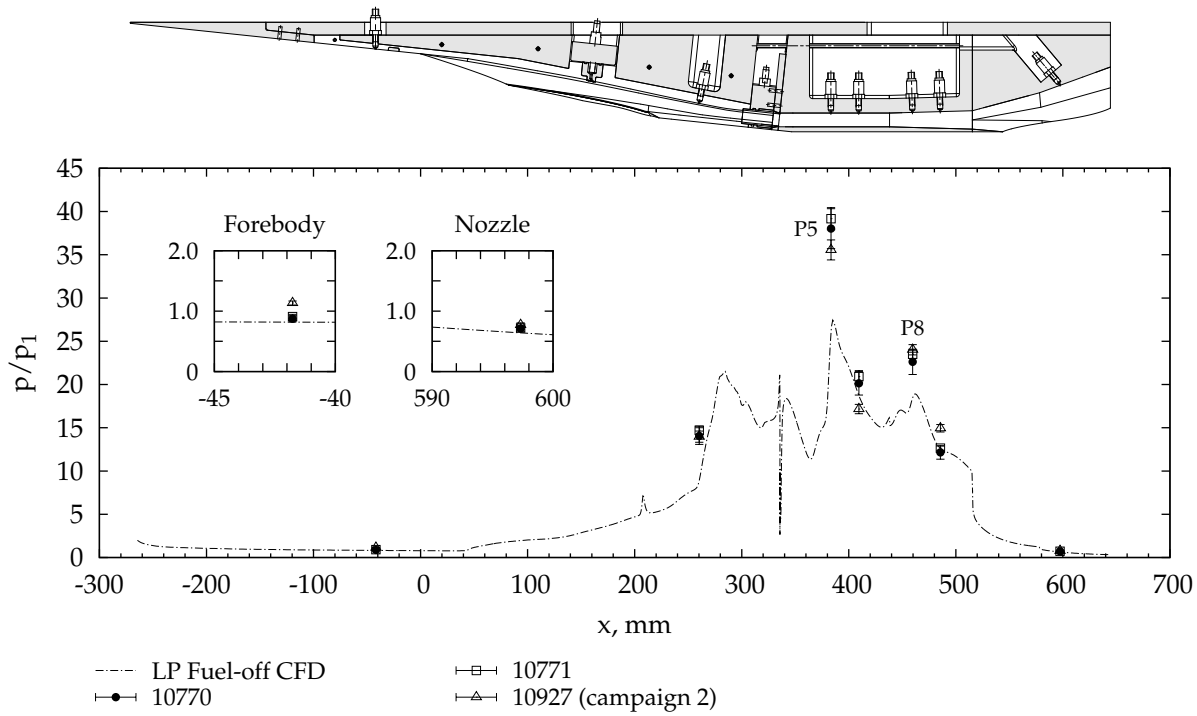

(a) Low pressure test condition. Shield design D. A boundary layer trip was fitted.

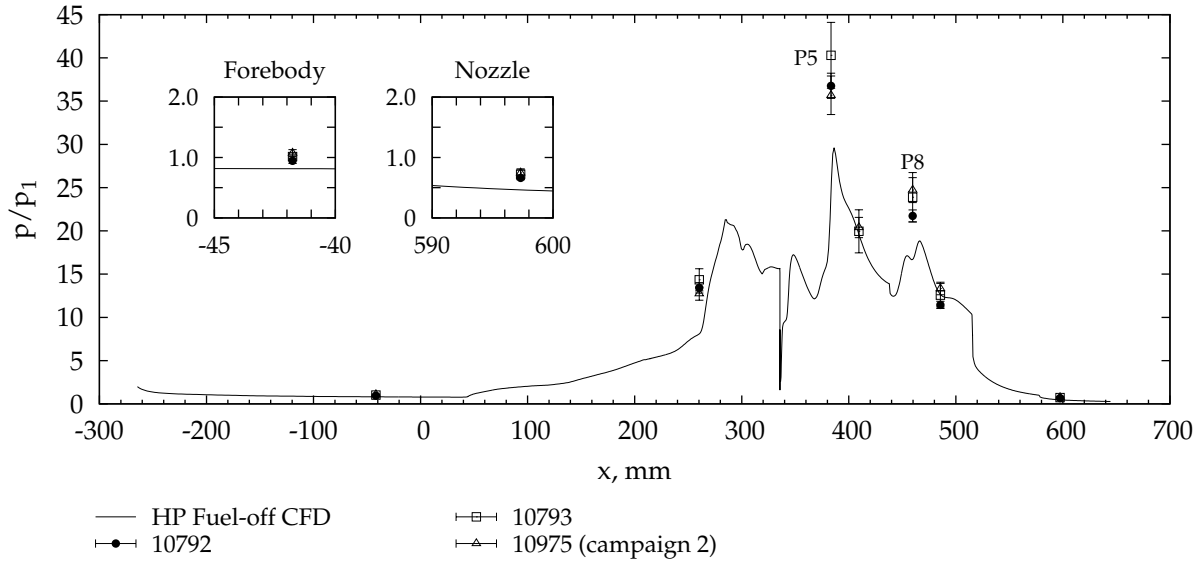

(b) High pressure test condition. Shield design E. A boundary layer trip was fitted.

Figure 7.4 – Comparison of the experimental and numerical pressure distribution on the engine bodyside for no fuel injection at each test condition.

Transient force data are plotted in Figure 7.5 for experiments at both the low and high pressure test conditions. Absolute force data are provided in the left column, force coefficients and the centre of force location are provided in the right column. Note that shielding design D was fitted for the low pressure experiments while shielding design E was fitted for the high pressure experiments. Engine nozzle pressure traces are also provided for comparison. In each figure the chosen test time is shown and the thick horizontal line indicates the value calculated from the steady-state numerical simulations presented in Chapter 5. The shaded region indicates the experimental uncertainty of the test time average for shots 10770 (Figure 7.5a) and 10792 (Figure 7.5b). A similar experimental uncertainty exists for shots 10771 and 10793 but for clarity is not shown. Calculation of this uncertainty is explained[5] in Section 4.8. Since flow arrival at the model leading edge does not occur until $t \approx 0.5$ ms (Figure 3.19), transient force coefficient data before this time are meaningless. The design and layout of Figure 7.5 is used consistently throughout this thesis for the presentation of engine force data.

Throughout the test campaign the recovered drag was observed to take longer to establish than the internal engine pressures, typically requiring a total establishment time of 3.5 ms, compared with an establishment time of 3 ms for the pressure data (cf. Figure 3.19). This increased establishment time is hypothesised to be related to the surface shear stress which was found by Jacobs et al. (1992) to take longer to establish than the surface pressure. To check that the balance was working correctly and that it was providing a realistic measure of the force establishment during a test, the force balance calibration data discussed in Chapter 4 was used to evaluate the ability of the balance to recover a distributed load for which the drag established slower than the lift. The evaluation followed a method similar to that described in Section 4.6, item 4. Presented in Appendix B.13, the results demonstrated that even when the time history of the input drag is different from the time history of the input lift, the input forces are recovered by the force balance. This provides confidence that the slow establishment of drag was physical. Finally, based on the results of the evaluation of the force balance calibration data (Section 4.6) a test time of 1 ms was typically used to process the campaign data.

On first examination the engine nozzle pressure, lift, drag and centre of force traces each display some degree of shot-to-shot repeatability. Irrespective of the oscillations, the time history of the recovered drag coefficient approximately follows that of the internal pressure measurements, being largest during startup (at $t \approx 1.5$ ms) before decreasing to a level that remains steady to within 18 % of the mean for shot 10770 and to within 16 % for shot 10771. Similar results are obtained for shots 10792 and 10793 with

5 Briefly, the experimental uncertainty includes contributions from the force balance calibration process and from the calculation of the facility nozzle flow.

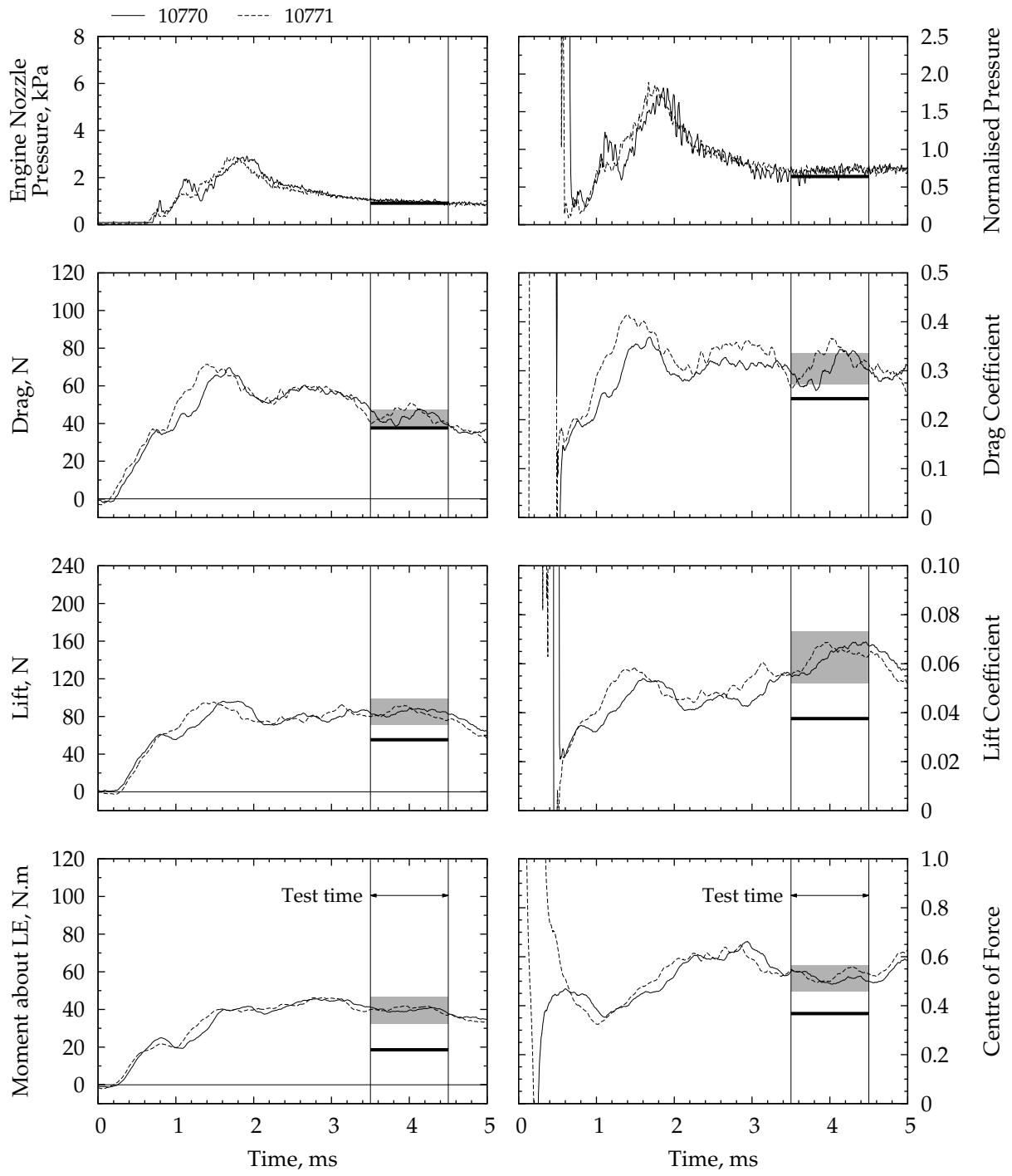

(a) Low pressure test condition. Shield design D. Boundary layer trip fitted. The shaded region indicates the experimental uncertainty of the mean for shot 10770.

Figure 7.5 – Transient fuel-off force data. Engine nozzle pressure traces have been provided for comparison. The force data were filtered using a 500 µs moving average; the pressure data by a 20 µs moving average. The solid horizontal line indicates the estimate from a steady-state CFD simulation. The time axis has been shifted so that zero corresponds to the trigger of the nozzle supply pressure.

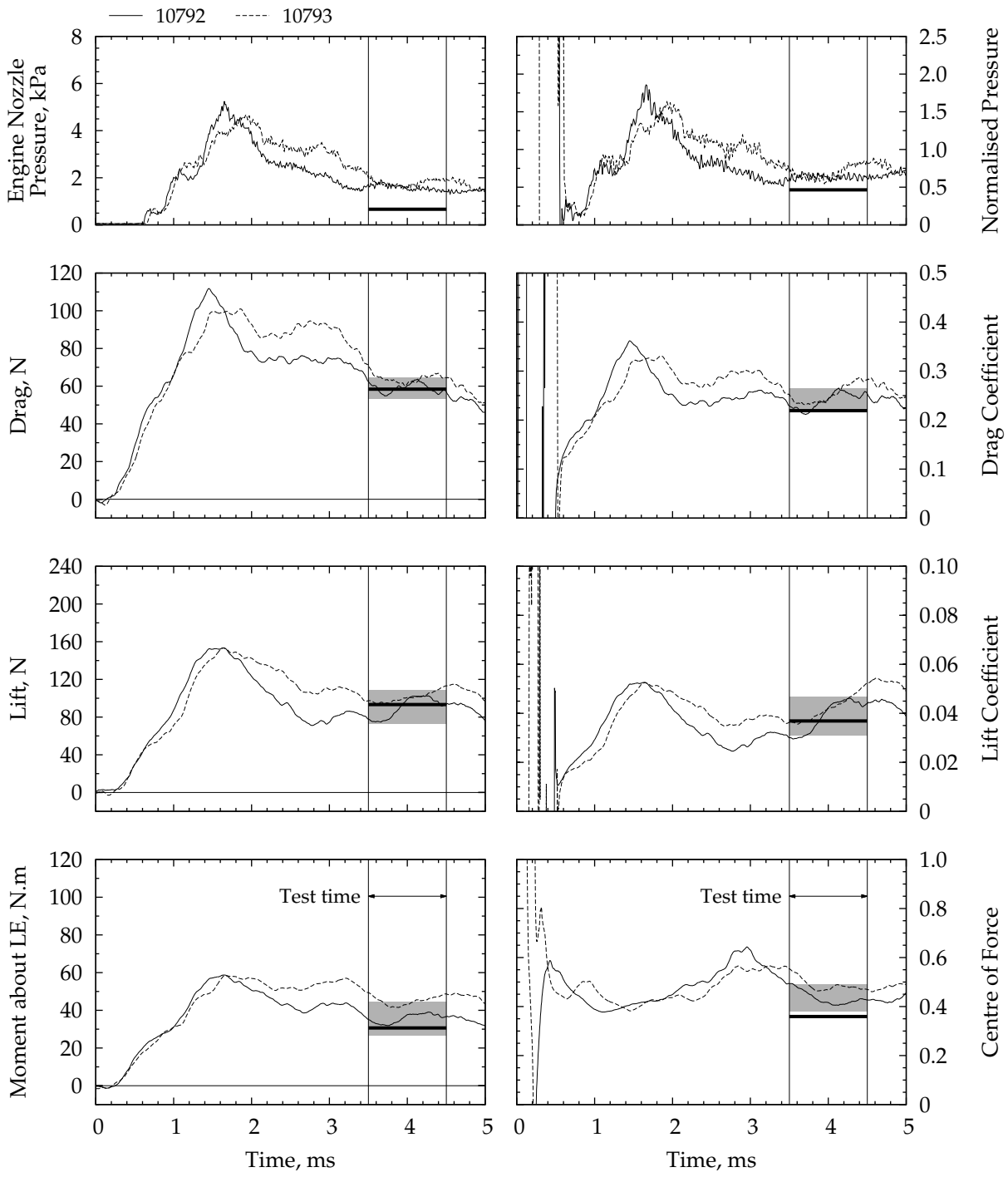

(b) High pressure test condition. Shield design E. Boundary layer trip fitted. The shaded region indicates the experimental uncertainty of the mean for shot 10792.

Figure 7.5 – Continued.

the recovered drag signal remaining steady to within 14 % and 15 % of the mean, respectively. At the low pressure test condition, the average[6] experimental drag coefficient is $C_{D,LP} = 0.312 \pm 0.032$. This value is 28 % greater than that from the numerical simulation; a difference that is larger than the experimental uncertainty. In comparison, the average experimental drag coefficient at the high pressure test condition is $C_{D,HP} = 0.246 \pm 0.025$. This value is 12 % greater than that from the numerical simulation; a difference that is slightly larger than the experimental uncertainty of 10 %.

In comparison with the recovered drag, the time history of the recovered lift force does not follow the facility nozzle supply pressure or internal engine pressure measurements as may be expected. At the low pressure test condition the lift rises during flow establishment, attains a slight peak at $t \approx 1.5$ ms and then stays approximately steady before eventually decreasing for $t \geqslant 4.5$ ms. As a consequence of this time history, the lift coefficient, which is calculated by normalising the recovered lift force with the nozzle supply pressure trace (Section 4.7), is not steady but consistently rises during the test time. A similar time history is obtained at the high pressure test condition with the exception that the peak lift attained during flow establishment is more dominant. During the test time the variation in lift coefficient is 16 % and 12 % of the mean for shots 10770 and 10771, respectively (low pressure test condition) and 32 % and 23 % of the mean for shots 10792 and 10793, respectively (high pressure test condition). At the low pressure test condition the average experimental lift coefficient is $C_{L,LP} = 0.0630 \pm 0.0108$. This value is 68 % greater than that from the numerical simulation; a difference much larger than the experimental uncertainty. A possible reason for this difference is discussed later in this section. Similarly, at the high pressure test condition the average lift coefficient is $C_{L,HP} = 0.0405 \pm 0.0078$. This value is only 10 % larger than that from the numerical simulation.

The final two forces to be discussed are the absolute moment about the leading edge[7] and the centre of force location. These are derived from the recovered lift, drag and moment about the balance centre according to Equations (4.27) and (4.28). As a consequence of a larger moment arm and force magnitude, the recovered lift dominates the leading edge moment. This is obvious when examining the traces plotted in Figure 7.5; at each test condition the time history of the leading edge moment closely follows that of the absolute lift. In comparison, the recovered centre of force is sensitive to small variations in the lift and leading edge moment with the overall time history resembling that obtained in Figures 4.12 and B.13 for recovery of a lower distributed load. Whether or not this time history is physical or an artifact of the force balance calibration is discussed below. The average experimental centre of force is $CF = 0.520 \pm 0.053$ at the

6 This is the average of both shots.
7 Also known as the leading edge moment.

low pressure test condition; 41 % greater than that calculated from the numerical simulation. At the high pressure test condition the average centre of force is $CF = 0.461 \pm 0.056$; 28 % greater than that calculated from the numerical simulation. During the test time the variation in centre of force is 7 % and 8 % of the mean for shots 10770 and 10771, respectively (low pressure test condition) and 12 % and 10 % of the mean for shots 10792 and 10793, respectively (high pressure test condition).

As noted above, the time history of the recovered centre of force resembles that obtained during the evaluation of the force balance calibration data and so may not be physical. However, for shots 10770 and 10771 a wave from the facility nozzle was present (Figure 7.2) and was observed to move upstream until reaching a quasi-stable position. Since the static pressure increases across a shock, we may expect that the upstream movement of the wave would cause a corresponding increase in the lift and shift the centre of force to the rear of the engine. While neither of these two behaviours is exhibited in Figure 7.5a, the interaction of the external engine flow field with the facility nozzle flow field is very complex. It is possible that other, unidentified, interactions exist that explain the transient behaviour of the recovered lift, leading edge moment and centre of force. Given that the recovered lift data do not exhibit the same large scale oscillations as obtained in Figure 4.12 for the evalution of the force balance calibration, it is argued here that the observed time history for the centre of force is physical and is not due to the apparent inability of the force balance to accurately recover a lower distributed load (Section 4.6.3).

Comparing Figures 7.5a and 7.5b it can be seen that at the high pressure test condition the experimental forces are comparable with the forces calculated from the numerical simulation of the engine, but that at the low pressure test condition the experimental forces are larger than the numerical value. With the exception of the test condition, the major difference between the experiments was the force balance shielding – shield design D was fitted for shots 10770 and 10771 while shield design E was fitted for shots 10792 and 10793. Analysis of the engine surface forces presented in Chapter 5 shows that the lift, moment and centre of force are dominated by the external flow, suggesting that the improved comparison with numerical simulation obtained for shield design E may be due to an improvement in the facility nozzle flow. That is, the observed wave from the facility nozzle may not be present with shield design E fitted. Additionally, because the wave from the facility nozzle interacted with the engine on the foward facing surfaces downstream of the inlet cowl closure location (Figure 7.2), the presence of this wave is also expected to affect the measured engine drag. Unfortunately, no schlieren images were recorded with shield design E fitted and so the absence of the facility nozzle wave cannot be confirmed for this shielding design.

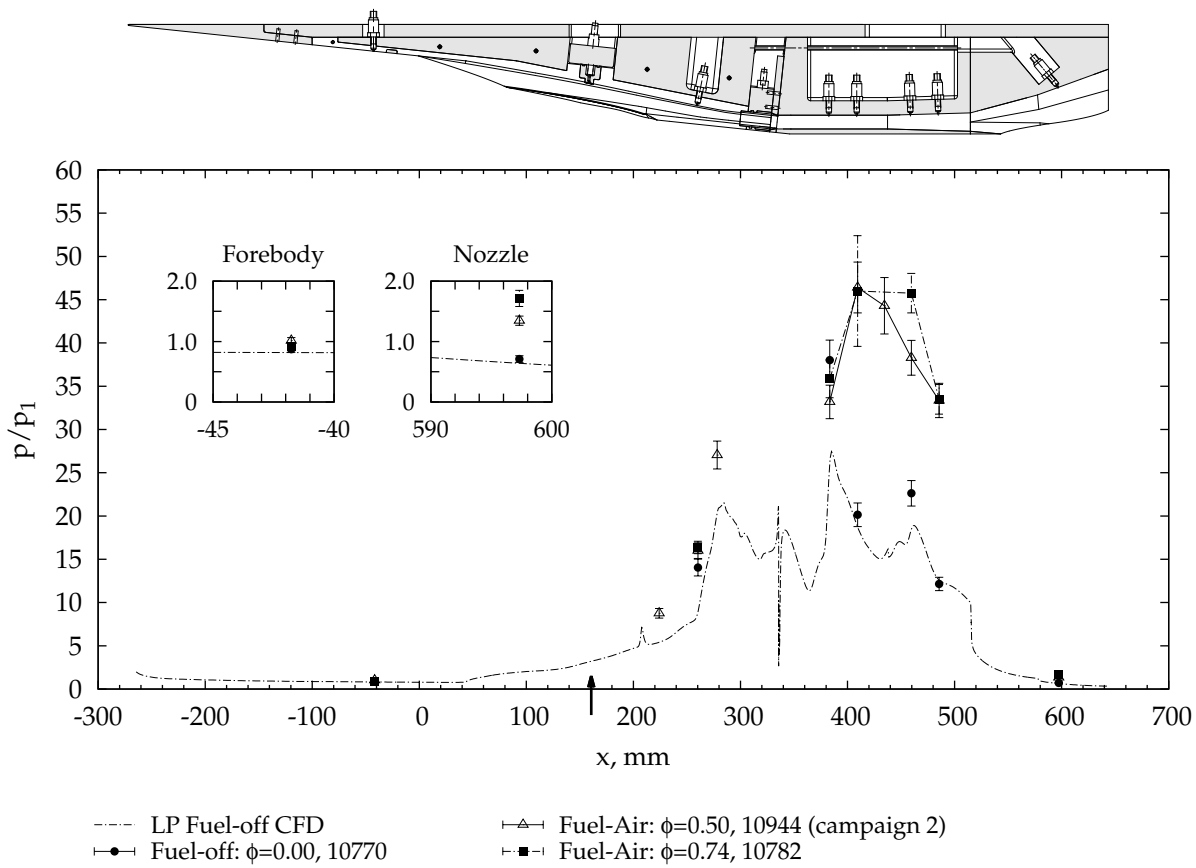

Figure 7.6 – Engine bodyside pressure distribution for the inlet injection scheme at the low pressure test condition. The fuel injection location is indicated by an arrow. A boundary layer trip was fitted.

7.4 FUEL-ON DATA FOR INLET INJECTION

During the force balance test campaign the engine did not start for many of the inlet injection shots that were conducted (Table L.6). As noted above and discussed in Appendix H.3, it wasn't until the second test campaign that early injection of fuel, relative to flow arrival at the model, was identified as being the primary cause for inlet unstart. Of the eight inlet injection shots conducted during the force balance campaign, only shot 10782 featured late injection of fuel and will be presented and discussed here.

Normalised engine pressure data for shot 10782 are given in Figure 7.6. This shot was conducted at the low pressure test condition. Fuel-off experimental data, discussed in Section 7.3, and fuel-on data from the second test campaign, discussed in Section 6.3, are also plotted for comparison. Examining the data for shot 10782 it can be seen that the normalised forebody data collapses to near unity indicating that the flow entering the

engine was close to the nominal condition. The pressure from the single measurement in the inlet is elevated above the fuel-off measurement due to fuel mass addition, consistent with that of shot 10944 and the other inlet injection data from the second test campaign (Section 6.3). Good combustion induced pressure rise is evident from location P6 onwards ($x \geqslant 409$ mm). Relative to the other data, the pressure at location P6 was unsteady, as evidenced by the large variation bars. At locations P8 and P10 the pressure measured for shot 10782 was greater than that measured for shot 10944; a result that is consistent with the increased fuel equivalence ratio of shot 10782.

The fuel equivalence ratio for shot 10782 was $\phi = 0.75$, the highest value of all the inlet injection shots across both test campaigns and test conditions (cf. Figure 6.3). The difference in fuel equivalence ratio for shots 10782 and 10944 is due to the chosen test times; a test time between 3.0 and 3.5 ms was used for shot 10944 whereas a test time between 3.7 and 4.5 ms was used for shot 10782.[8] Overall similarity of shot 10782 to shot 10944 is established by Figures 7.7 and 7.8 in which the transient Pitot pressure, fuel plenum pressure and engine inlet pressures are plotted. In Figure 7.7, the Pitot pressures to lie on top of one another. The fuel plenum pressures are also very similar. In Figure 7.8, with the exception of some difference during the nozzle starting and flow establishment processes, the absolute pressure traces from the second inlet tap lay on top of one another. Unfortunately no other inlet pressure data are available for shot 10782 however, the three traces for shot 10944 all exhibit similar structures and so the same is expected for shot 10782. Shots 10782 and 10944 are therefore very similar to one another. Hence, the difference in fuel equivalence ratio is primarily due to the chosen test time.

An inlet unstart is characterised by large scale oscillations of the inlet pressures caused by unsteady movement of the inlet shocks. This behaviour is exhibited by the data presented in Appendix H.3 but is not present in the traces plotted in Figure 7.8, leading to the conclusion that the inlet was started for both shot 10782 and shot 10944. Hence, these shots clearly demonstrate that at the low pressure Mach 10 test condition the small-scale airframe integrated M12REST inlet is able to support a significant mass flow of fuel from the inlet injection station without unstarting. In conjunction with the data presented in Appendix H.3, it can also be concluded that the restriction that early fuel injection places on the fuel equivalence ratio is an artifact of the transient testing environment and does not truly represent the performance capability of the M12REST engine.

Transient forces, force coefficients and the centre of force location are plotted in Figure 7.9 for shot 10782. Note that shielding design D was fitted. To provide a comparison, the average fuel-off transient forces from

8 See Sections 3.5.1 and 7.3 for further discussion of why different test times are used.

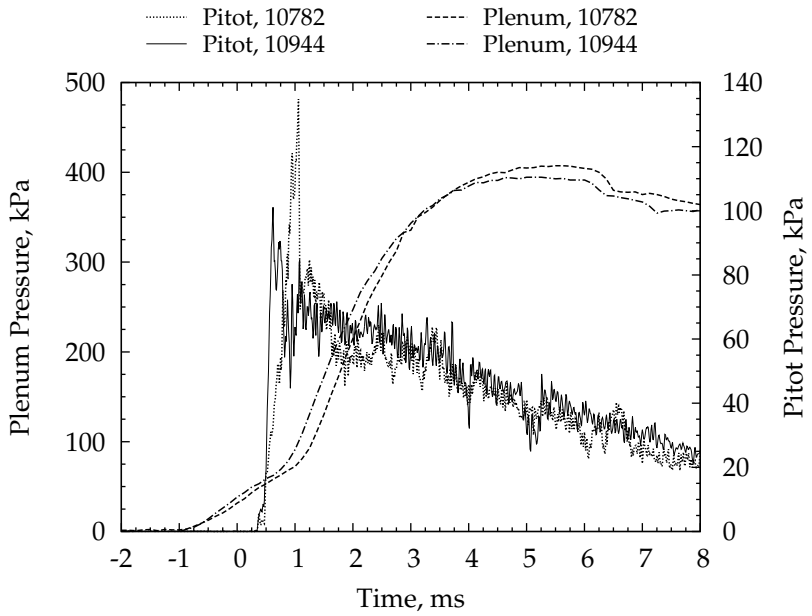

Figure 7.7 – Comparison of the inlet plenum and engine Pitot pressurs for shots 10782 and 10944. For clarity the Pitot pressure data were filtered using a 20 µs moving average and only every 25th data point of the unfiltered plenum pressure traces have been plotted.

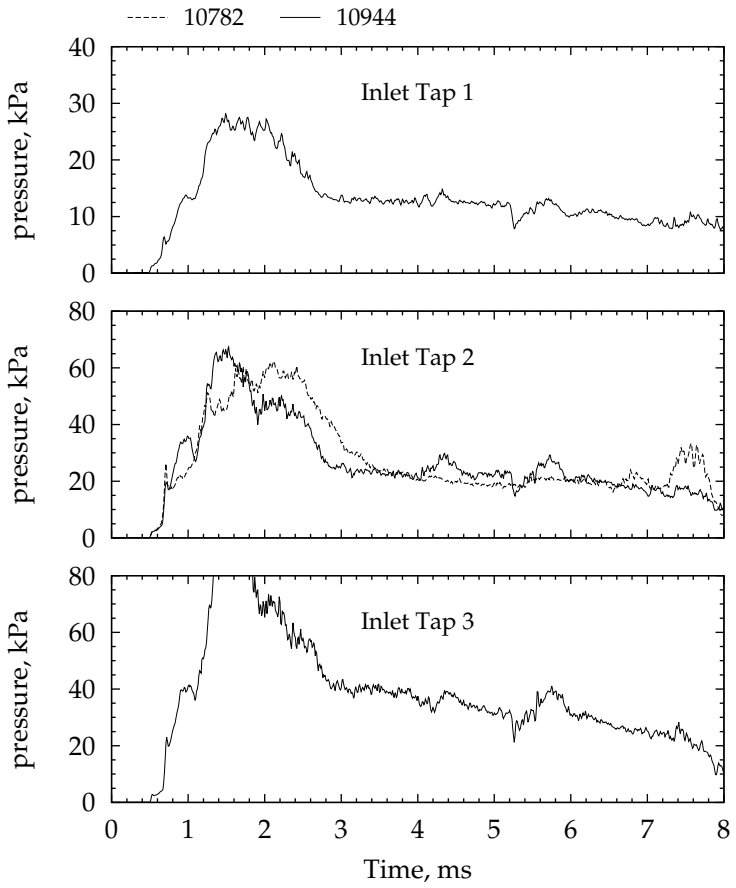

Figure 7.8 – Comparison of absolute inlet pressure data for shots 10782 and 10944. For clarity the data were filtered using a 20 µs moving average.

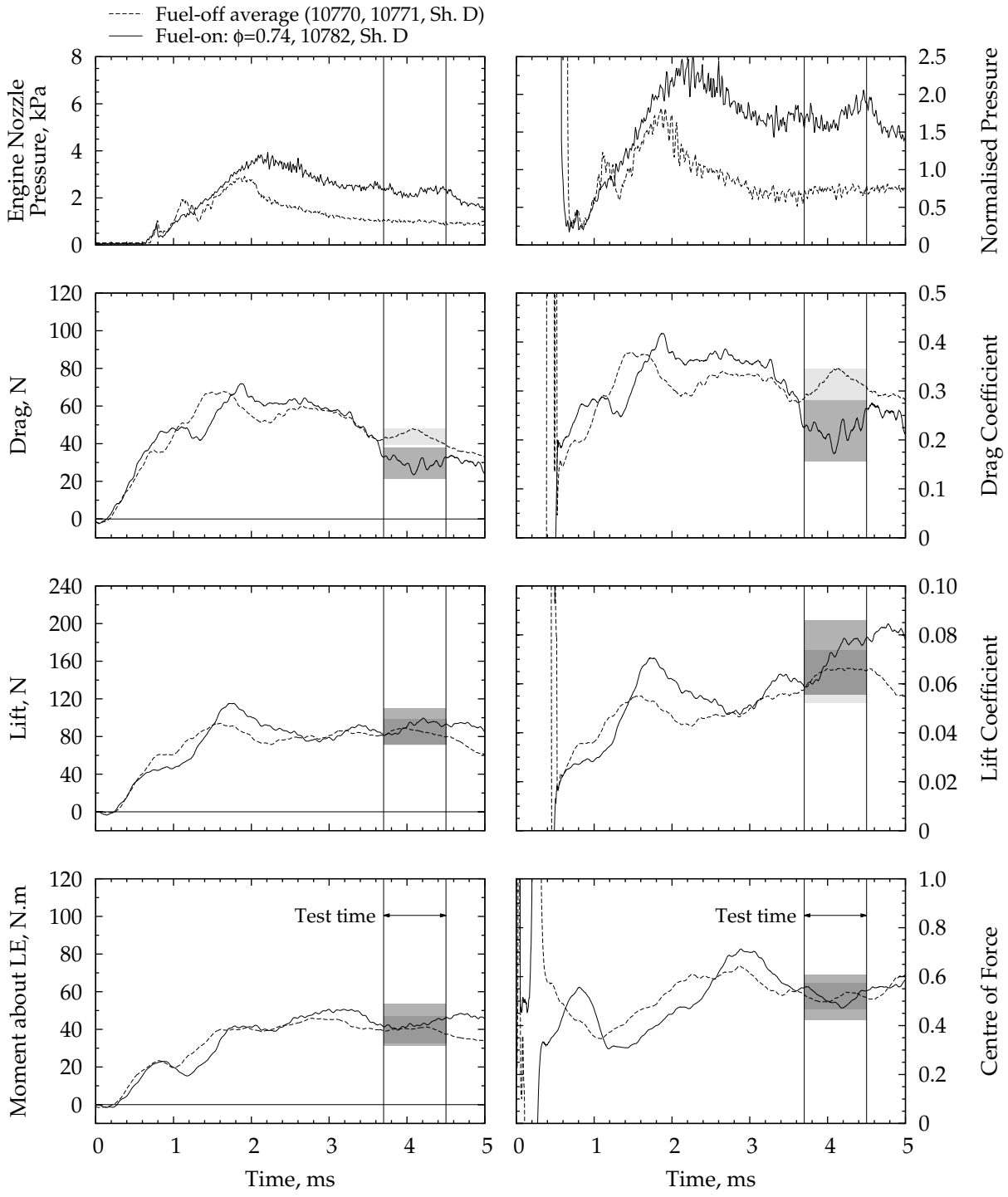

Figure 7.9 – Transient force coefficients for the inlet injection scheme at the low pressure test condition. Normalised engine nozzle pressure traces have also been provided for comparison. The force data were filtered using a 500 µs moving average; the pressure data by a 20 µs moving average. The time axis has been shifted so that zero corresponds to the trigger of the nozzle supply pressure.

Section 7.3 are also plotted. The recovered drag coefficient indicates that the engine flow field did not establish until approximately 3.7 ms after nozzle supply trigger. This is approximately 0.7 ms longer than the engine pressure data and is typical of the force data for fuel-on shots. During the test time the recovered drag coefficient was $C_D = 0.218 \pm 0.062$; this is 0.094 or 30 % smaller than the average fuel-off value. Global performance metrics for the engine are presented and discussed in Section 7.6.

The recovered fuel-on lift and leading edge moment signals are both very similar to the corresponding fuel-off signal. During flow establishment the fuel-on lift attains a slightly higher peak than the fuel-off signal before decreasing and remaining approximately steady. Once established, the fuel-on lift is identical to the fuel-off lift to within the experimental uncertainty. For $t \geqslant 4$ ms the fuel-on and fuel-off lift signals slowly begin to diverge, with the fuel-off lift decreasing while the fuel-on lift remains approximately steady. Due to a decreasing nozzle supply pressure, the lift coefficient consistently rises for $t \geqslant 3$ ms, varying 20 % during the test time for shot 10782. The average lift coefficient is $C_F = 0.0707 \pm 0.0151$. This value is only 12 % larger than the fuel-off average, a difference that is within the experimental uncertainty.

Similar to the lift, the transient structure of the recovered centre of force is comparable with the fuel-off average, albeit shifted in time. The average fuel-on centre of force is $CF = 0.514 \pm 0.092$, only 1 % smaller than the fuel-off value, i.e. negligible compared with the experimental uncertainty. During the test time the centre of force varied by 10 % of the mean value.

The data plotted in Figure 7.9 indicate that fuel injection in the inlet does not significantly affect the lift or centre of force. Two caveats for this result are that (1) it is based on a comparison of only two shots and that (2) the influence of the facility nozzle wave visualised in Figure 7.2b is difficult to quantify. However, if physical, this is an interesting result. Due to the engine nozzle geometry, it is expected that the centre of force would shift rearward and the lift would be greater for a fuel-on test relative to a fuel-off test. For the centre of force this expectation does not account for the increased pressure that occurs in the inlet due to mass addition of fuel. Referring to Figure 4.5, which plots the fuel-off load distribution for the engine, it is clear that for no fuel injection the majority of the lift is generated on the forebody and inlet surfaces. Therefore, for the inlet injection scheme, an increased pressure on the bodyside of the inlet produces a moment which counteracts the moment generated by the increased pressure on the rear surfaces of the nozzle. In this way, fuel injection on the inlet could help decouple the movement of the centre of force from combustion, potentially improving the controllability of a scramjet powered vehicle (Hirschel and Weiland, 2009, Section 4.4). Confirmation and investigation of this hypothesis remains a topic for future study.

7.5 FUEL-ON DATA FOR COMBINED INJECTION

Normalised engine pressure data for shot 10787 are provided in Figure 7.10. This high pressure shot was the only combined injection shot completed with shield design D for which fuel was injected late and the inlet started (Table L.6). For comparison, combined injection data from the second test campaign at a similar equivalence ratio are also plotted. Since no high pressure fuel-off shots were completed with shield design D, low pressure fuel-off data from Section 7.3 are shown.

The data for shot 10787 display the same trends that have been discussed previously in this thesis: the normalised forebody pressure is close to unity providing confidence in the freestream pressure and Mach number computed using NENZFR (Section 3.3.1); the inlet pressure data lay above the fuel-off data and numerical simulation due to fuel mass addition and significant combustion-induced pressure rise is measured within the combustor and engine nozzle. With the exception of location P5 the combustion pressure data for shot 10787 lay very close to that recorded for shot 10963; an expected result given the fuel equivalence ratios are the same (to within experimental uncertainty). The difference in pressure at location P5 is not unexpected as this tap coincides with a strong shock impingement and so small changes in the shock location can lead to large changes in the measured pressure.

Transient forces, force coefficients and the centre of force location are plotted in Figure 7.11 for shot 10787. Since no fuel-off data at the high pressure test condition were measured with shielding design D fitted, and because the influence of the shielding on the measured forces is difficult to quantify, two sets of average fuel-off data are provided for comparison. These sets are (1) high pressure fuel-off data with shield design E fitted and (2) low pressure fuel-off data with shield design D fitted. Note that only force coefficients for the low pressure test condition are plotted.

The recovered drag shows a clear influence of combustion with the signal being consistently lower than both fuel-off signals. Shortly before the start of the test time the drag for shot 10787 increases rapidly towards the fuel-off level and then, just as rapidly, settles back down to a steady level that is distinct from the fuel-off signals. As shown by the transient pressure data plotted in Figure 7.12, this sudden variation in drag coincides with an equivalent variation in the engine pressures. The disturbance in the pressure data first appears in the Pitot signal before propagating downstream. While the cause of the disturbance remains unkown, the fact that it was recovered by the force balance demonstrates the ability of the balance to measure the drag acting on the M12REST engine. The average drag coefficient during the test was $C_D = 0.118 \pm 0.034$. This is 0.128 or 52 % smaller than the average fuel-off value at the high pressure test condition and 0.194 or 62 % smaller than the average fuel-off value at the low pressure test condition. The variation in drag coefficient during

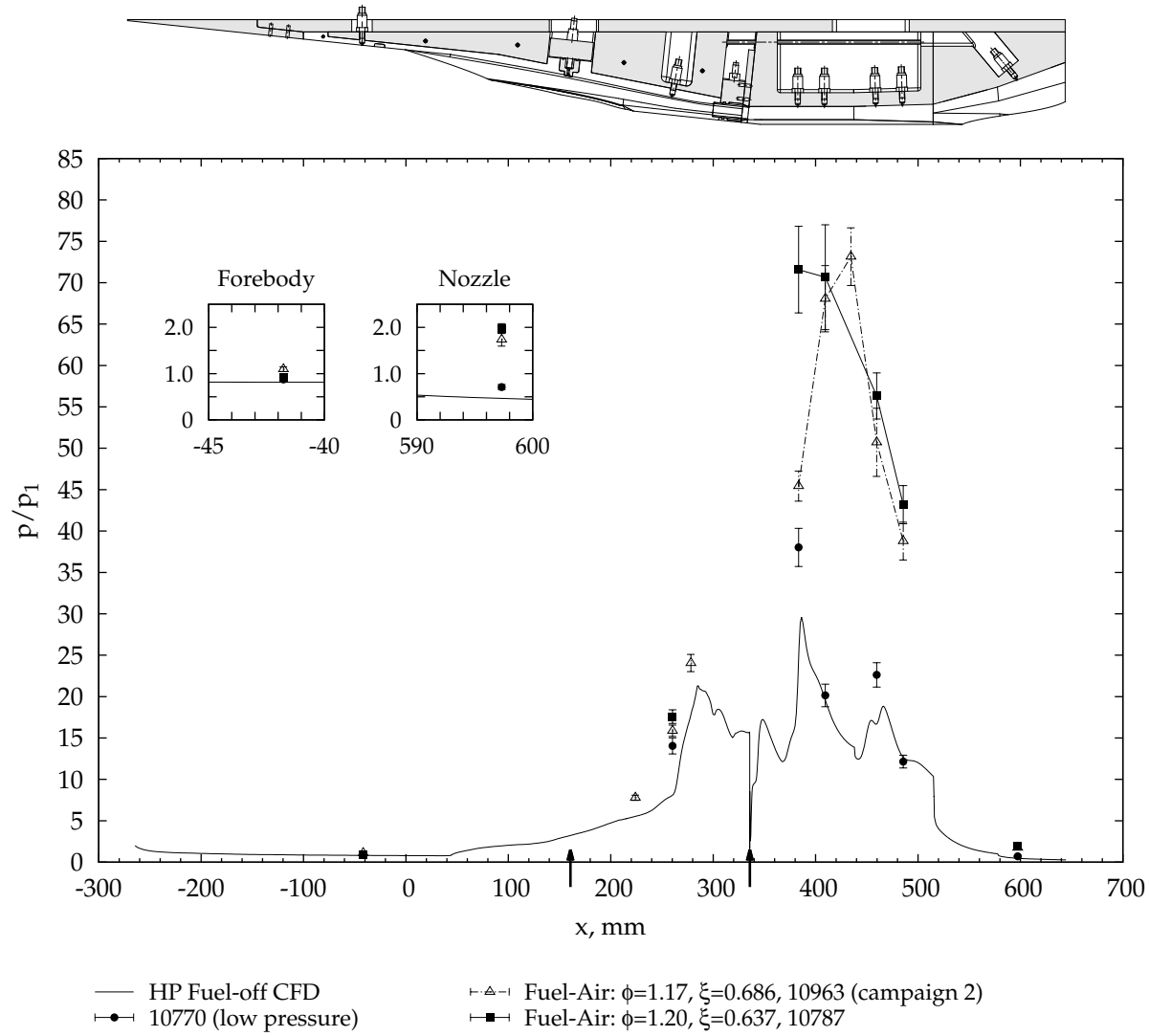

Figure 7.10 – Engine bodyside pressure distribution for the combined injection scheme at the high pressure test condition. The fuel injection locations are indicated by arrows. A boundary layer trip was fitted.

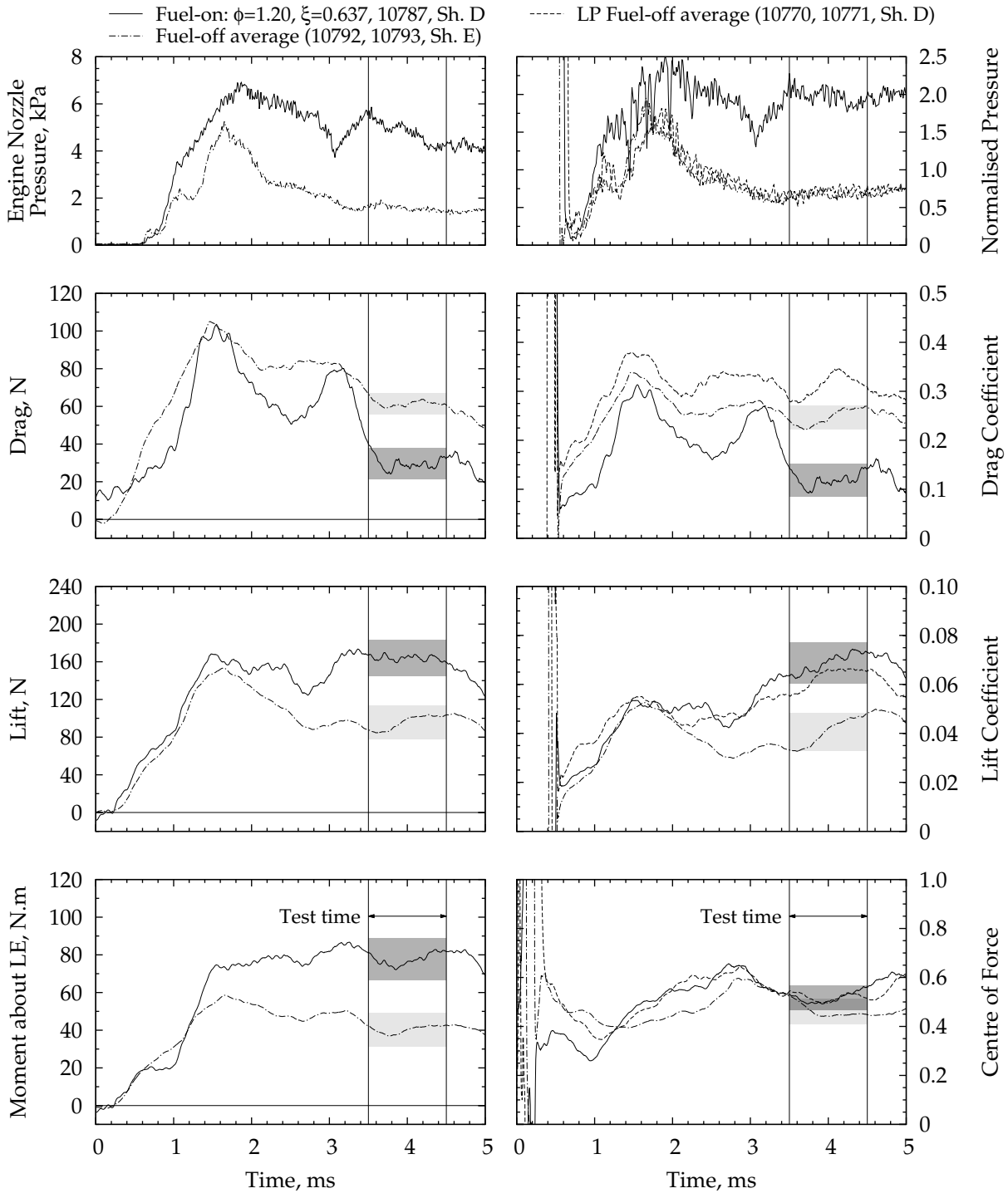

Figure 7.11 – Transient force coefficients for the combined injection scheme at the high pressure test condition. Normalised engine nozzle pressure traces have also been provided for comparison. The force data were filtered using a 500 µs moving average; the pressure data by a 20 µs moving average. The time axis has been shifted so that zero corresponds to the trigger of the nozzle supply pressure.

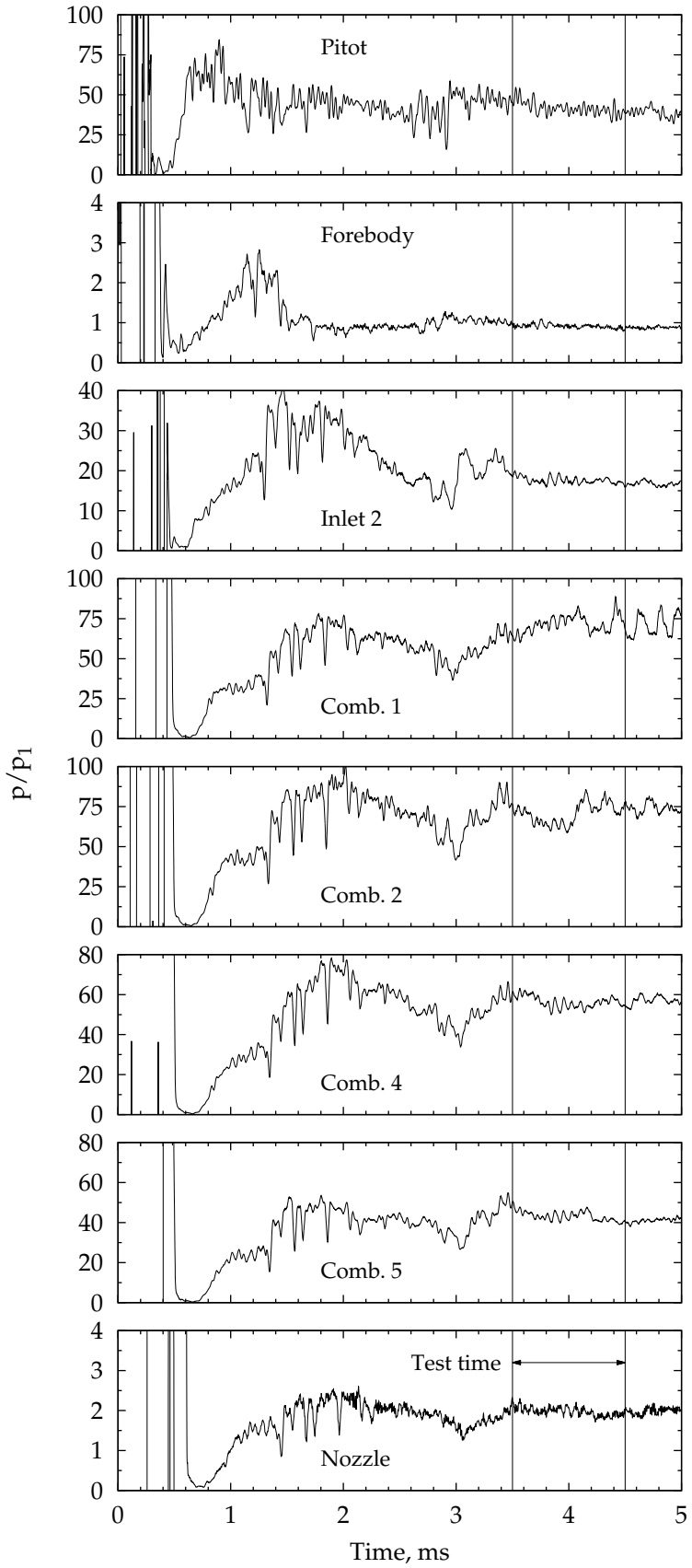

Figure 7.12 – Transient normalised pressure data for shot 10787. The data have been filtered using a 20 µs moving average and the time axis has been shifted so that zero corresponds to the trigger of the nozzle supply pressure.

the test time was 18 % of the mean.

Depending on which fuel-off data are used for comparison, the recovered lift for shot 10787 may or may not display an influence of fuel injection and combustion. It was surmised in Section 7.3 that the primary reason why the experimental fuel-off force data matched the numerical simulation at the high pressure test condition but not at the low pressure test condition was because of the difference in the force balance shielding. Noting also that the difference in lift coefficient at the two test conditions predicted by the numerical simulation is smaller than can be measured with the force balance (cf. Table 4.2 and Figure 5.8), it is argued here that the fuel-on lift coefficient for shot 10787 is most appropriately compared with the average low pressure fuel-off lift signal (which featured the same shielding design) and not with the average high pressure fuel-off lift signal (which featured a different shielding design). Based on this comparsion, the fuel-on lift coefficient does not display any measureable influence of fuel injection and combustion. For the recovered centre of force, no influence of fuel injection or combustion is apparent (regardless of which fuel-off data are used for comparison). This similarity of the fuel-on lift and centre of force to the fuel-off lift and centre of force is consistent with the results presented in Section 7.4 for the inlet injection scheme. Once again, further investigation and confirmation of these results remains a topic for future study. Finally, the average lift coefficient was $C_L = 0.0688 \pm 0.0084$ with a variation of 11 % during the test time. The average centre of force location was $CF = 0.518 \pm 0.051$ with a variation of 8 % during the test time. These average values are 9 % and 0.4 % different from the low-pressure fuel-off values, respectively.

7.6 ENGINE PERFORMANCE METRICS

The aim of this thesis was to investigate the performance of an airframe integrated three-dimensional scramjet engine. Thus, using the measured drag data from Sections 7.3 to 7.5, this section presents an analysis of the engine performance using four performance metrics: the specific impulse, the specific thrust, the overall thermodynamic efficiency and the corrected overall thermodynamic efficiency. Each of these are defined below. A summary of the measured force coefficients, centre of force location and associated fuelling data is given in Table 7.1. Values for the relevant normalising parameters are also provided. Although net thrust was not measured for the M12REST engine in the current work, the performance of the engine may be examined using the measured thrust increment. In terms of the measured drag coefficients, the thrust increment is given by

$$\Delta T = -\Delta C_D q A_f = (C_{D,FUEL-OFF} - C_{D,FUEL-ON}) q A_f \tag{7.1}$$

Table 7.1 – Summary of Force Balance Results

(a) Measured Fuel-off Force Coefficients. Mass flow unit – g/s

	Low Pressure		High Pressure	
	CFD	Exp.	CFD	Exp.
C_D	0.243	0.312 ± 0.032	0.219	0.246 ± 0.025
C_L	0.0376	0.0630 ± 0.0108	0.0369	0.0405 ± 0.0078
CF	0.368	0.520 ± 0.053	0.359	0.461 ± 0.056
$\dot{m}_A$	34.8	32.8 ± 2.1	63.4	61.1 ± 3.9
Shielding	D		E	

(b) Measured Fuel-on Force Coefficients and Fuelling Data. Mass flow unit – g/s

	Inlet Inj.	Combined Inj.
C_D	0.218 ± 0.062	0.118 ± 0.034
C_L	0.0707 ± 0.0151	0.0688 ± 0.0084
CF	0.514 ± 0.092	0.518 ± 0.051
ϕ	0.74 ± 0.11	1.20
$\dot{m}_f$	0.68 ± 0.09	2.14
$\dot{m}_A$	31.0 ± 2.0	61.3 ± 3.9
Condition	LP	HP
Shielding	D	D

(c) Reference values

	Units	Low Pressure		High Pressure	
A_f	$10^{-6}\,m^2$	5552	± 0	5552	± 0
u_x	m/s	3089	± 104	3044	± 100
q	kPa	27.9	± 1.1	48.0	± 1.9

The four performance metrics to be calculated are defined as follows where the superscript Δ is used to emphasise that each performance parameter is calculated using the increment in thrust rather than the total internal or net engine thrust.

1. *Overall efficiency*: Defined as the ratio of the engine thrust power to the fuel chemical energy.

$$\eta_o^\Delta = \frac{-\Delta C_D q A_f u_x}{\dot{m}_{f,t} \Delta h_c} \tag{7.2}$$

2. *Corrected overall efficiency*: Defined as the ratio of the engine thrust power to the chemical and sensible energy of the fuel.

$$\eta_{o,c}^\Delta = \frac{-\Delta C_D q A_f u_x}{\dot{m}_{f,t} (\Delta h_c + \psi_f)} \tag{7.3}$$

where ψ_f is the exergy (available energy) of the injected flow. This equation differs from Equation (7.2) by accounting for the potential thrust that may be extracted from the pressurised (and possibly heated) fuel. The fuel exergy is given by (Cengel and Boles, 2002, Section 7.4):

$$\begin{aligned} \psi_f &= (h_f - h_d) - T_d(s_f - s_d) + \frac{u_f^2}{2} \\ &= C_p(T_f - T_d) - T_d \left(C_p \ln \frac{T_f}{T_d} - R \ln \frac{p_f}{p_d} \right) + \frac{u_f^2}{2} \end{aligned} \tag{7.4}$$

where properties with subscript f are those of fuel at the location of injection and properties with subscript d are those of the 'dead-state', that is, the local atmospheric values. C_p and R are the specific heat at constant pressure and specific gas constant of the fuel,[9] respectively.

3. *Specific Impulse*: Defined as the thrust generated per unit mass of fuel and normalised by the acceleration of gravity at sea-level ($g = 9.81\,\mathrm{m/s^2}$).

$$I_{sp}^\Delta = \frac{-\Delta C_D q A_f}{\dot{m}_{f,t} g} \tag{7.5}$$

4. *Specific Thrust*: Defined as the thrust generated per unit mass of air flow through the engine.

$$T_{sp}^\Delta = \frac{-\Delta C_D q A_f}{\dot{m}_A} \tag{7.6}$$

9 $C_p = 14\,307\,\mathrm{J/(kg\,K)}$ and $R = 4124\,\mathrm{J/(kg\,K)}$ for hydrogen. For simplicity the specific heat is assumed constant. See Appendix J for further details.

Each performance metric was evaluated for the inlet and combined injection schemes. The results are provided in Table 7.2. Because no fuel-off drag data was available for the high pressure test condition with shield design D fitted, when calculating the performance metrics for the combined injection scheme, the following value for the fuel-off drag coefficient was used:

$$C_{D,HP,SH.D} \approx C_{D,HP,CFD} + \left(C_{D,LP,SH.D} - C_{D,LP,CFD}\right) = 0.288 \tag{7.7}$$

Equation (7.7) assumes that the difference between the experiment and numerical simulation at the low pressure test condition (with shield design D fitted) can be completely attributed to the influence of the force balance shielding on the facility nozzle flow and the subsequent iteraction of the erroneous facility wave with the model (Sections 7.2 and 7.3). It is then assumed that the same error in drag would occur at the high pressure test condition if shield design D was fitted. Using the fuel-off drag coefficient defined by Equation (7.7) for the combined injection scheme data ensures that the calculated thrust increment is for a consistent experimental configuration. Finally, the exergy of the fuel was calculated to be approximately 6.5 MJ/kg for each injection station assuming a fuel plenum temperature of 300 K. Full details are provided in Appendix J.

Table 7.2 – Engine Performance Metrics

	Units	Inlet Inj.	Combined Inj.
η_o^Δ		0.55	0.54
$\eta_{o,c}^\Delta$		0.52	0.51
I_{sp}^Δ	s	2177	2155
T_{sp}^Δ	m/s	469	739

Examining the data in Table 7.2, it can be seen that the overall efficiency and specific impulse of the inlet and combined injection schemes are equal but that the specific thrust produced by the combined injection scheme is 48 % larger than that produced by the inlet injection scheme. Combining Equations (7.5) and (7.6) and using the definition of fuel equivalence ratio, the specific thrust may be written as

$$T_{sp}^\Delta = \phi I_{sp}^\Delta \lambda g \tag{7.8}$$

where λ is the stoichiometric fuel-air ratio (Section 3.4.5). In this form it becomes clear that the improved specific thrust of the combined injection shot is directly related to an increased fuel equivalence ratio (cf. Table 7.1).

When justifying the use of an on-board fuel tank (Section 3.4.5), it was stated that including the thrust contribution of the fuel was important for force balance testing of complete scramjet engines. Given the experimental

data in Table 7.2, it is worthwhile considering what fraction of the performace may be attributed to just fuel injection. Subject to the assumption that the plenum temperature was 300 K, injection of fuel is estimated to contribute 6 % of both the specific impulse and specific thrust for the inlet injection scheme. For the combined injection scheme, injection of fuel is estimated to contribute 20 % of the specific impulse and 11 % of the specific thrust. These are non-negligble contributions, confirming the assertion that thrust gained from fuel must be included in force balance experiments, particularly at high Mach number test conditions. Full details of the calculation of these values is provided in Appendix J.

The similarity of the specific impulse for the two schemes is an interesting result and is due in part to the contribution from fuel injection. Subtracting this contribution, the specific impulse of the inlet injection scheme reduces to 2046 s and the specific impulse of the combined injection scheme reduces to 1724 s. These values are the fraction of specific impulse due to combustion heat release. The smaller value for the combined injection scheme indicates that, relative to the fuel mass flow rate, the measured thrust increment was not as large as it could be. This is not surprising given that the fuel equivalence ratio of this test was greater than 1; on a global scale the excess fuel cannot be used for combustion.

An estimate for the internal performance of the M12REST engine can be made by subtracting the specific impulse and specific thrust required to overcome the internal fuel-off drag from those values listed in Table 7.2. That is,

$$\eta_o^i = \eta_o^\Delta - \frac{F_{x,CFD}^i u_x}{\dot{m}_{f,t} \Delta h_c} \tag{7.9}$$

$$\eta_{o,c}^i = \eta_{o,c}^\Delta - \frac{F_{x,CFD}^i u_x}{\dot{m}_{f,t} (\Delta h_c + \psi_f)} \tag{7.10}$$

$$I_{sp}^i = I_{sp}^\Delta - \frac{F_{x,CFD}^i}{\dot{m}_{f,t} g} \tag{7.11}$$

$$T_{sp}^i = T_{sp}^\Delta - \frac{F_{x,CFD}^i}{\dot{m}_A} \tag{7.12}$$

where $F_{x,CFD}^i$ is the fuel-off drag of the internal flow path calculated from numerical simulation (Chapter 5). The superscript i is used to indicate that the above performance metrics are for the internal flow path. Using the data provided in Tables 7.1 and G.3, the above equations may be evaluated. The results are provided in Table 7.3 for two cases. For case 1, $F_{x,CFD}^i$ includes only the internal surface group shown in Figure 5.9 whereas for case 2, $F_{x,CFD}^i$ includes both the internal and forebody surface groups. In this way case 1 results are suitable for comparison with semi-freejet experimental data that do not feature a vehicle forebody and case 2 are

suitable for comparsion with freejet experiments or numerical simulation which include the vehicle forebody.

Negative values are obtained for the inlet injection scheme, indicating that the measured thrust increment was insufficient to overcome the internal drag of the engine. For the combined injection scheme the internal performance metrics are all positive. Accounting for the engine forebody (case 2), the internal specific impulse and specific thrust were 548 s and 189 m/s respectively for the combined injection scheme at a fuel equivalence ratio of 1.20.

Table 7.3 – Estimated Internal Engine Performance. Case 1 is for just the internal surface group, case 2 is for the internal and forebody surface groups; see Figure 5.9.

	Units	Inlet Inj.		Combined Inj.	
		Case 1	Case 2	Case 1	Case 2
η_o^i		−0.05	−0.28	0.26	0.14
$\eta_{o,c}^i$		−0.04	−0.25	0.24	0.13
I_{sp}^i	s	−181	−1095	1011	548
T_{sp}^i	m/s	−38	−235	348	189

Smart (2012) investigated the influence of inlet compression ratio on scramjet engine performance and, as a part of the study, made quite detailed estimates for scramjet specific impulse and overall efficiency across a range of flight Mach numbers. The results are reproduced in Figure 7.13 where the pressure ratio P_{rat} is the ratio of the static pressure at the inlet throat to the static pressure of the freestream. Key assumptions made by Smart (2012) include that the vehicle was flying on a constant dynamic pressure trajectory of 50 kPa, that the engine was fuelled with gaseous hydrogen at an equivalence ratio of 1.0, that the combustion efficiency was 80 %, that the engine featured a divergent combustor with area ratio of 2 and that, relative to the freestream capture area, the nozzle expansion ratio was 1.5 with a thrust efficiency[10] of 90 %.

For the M12REST engine studied in this thesis, the inlet compression ratio is $P_{rat} = 72$ (see Tables 3.3 and 5.2), the combustor has an area ratio of 2 (Section 3.4.1) and, relative to the freestream capture area,[11] the nozzle expansion ratio is 1.43 at the high pressure test condition. Hence, the M12REST engine is comparable with that analysed by Smart (2012). Based on the results plotted in Figure 7.13, at a Mach 10 flight condition an internal specific impulse of approximately 1500 s is predicted with an

10 Defined as the ratio of actual thrust produced by the nozzle expansion to that produced by an isentropic expansion of the flow to the same area ratio.

11 Combining the data in Tables 3.3 and 5.2, the freestream capture area is 2008 mm^2 at the high pressure test condition and 1924 m^2 at the low pressure test condition.

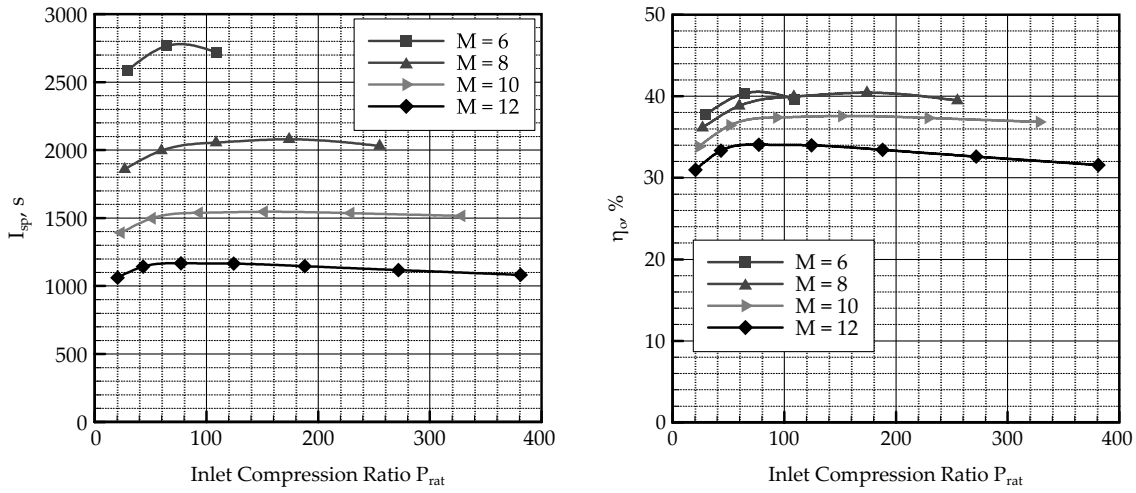

(a) Specific Impulse

(b) Overall Efficiency

Figure 7.13 – Theoretical internal scramjet engine performance as a function of inlet compression ratio for different flight Mach numbers. Reproduced from Smart (2012).

---

overall efficiency of 0.37. These values are approximately 2.7 times larger than those listed in Table 7.3. There are several possible reasons why the M12REST engine does not meet the performance estimates of Smart (2012). These are listed as follows.

1. A lower than assumed combustion efficiency: as noted above, Smart (2012) assumed an overall combustion efficiency of 80 %. Because of the small-scale of the current engine and an un-scaled test condition (Section 3.3.2) a combustion efficiency of 80 % may not have been achieved in the current experiments. Typically the experimental combustion efficiency is estimated by matching the measured pressure distribution using quasi-one dimensional cycle analysis (see for e.g. Moule and Smart, 2013). Due to the sparseness of the internal pressure measurements (Figure 3.9 and Section 3.4.4), such an analysis was not possible for the current work.

2. An inefficient engine nozzle design: as discussed in Section 5.6, the fuel-off thrust produced by the current engine nozzle was 5.5 N at the high pressure test condition. This corresponds to a nozzle thrust efficiency of just 43 %, significantly less than the value of 90 % assumed by Smart (2012). Possible reasons for the low efficiency include that the current nozzle is not a fully enclosed nozzle and that the inflow to the nozzle is highly non-uniform. If a more efficient nozzle was fitted to the engine, the internal specific impulse would increase by approximately 283 s.

3. Larger inviscid drag due to forebody leading edge bluntness: while the analysis of Smart (2012) included the vehicle forebody, it did not include the drag associated with a blunt leading edge. This drag was excluded because leading edge bluntness is highly dependent on the vehicle configuration and flight trajectory and the drag associated with leading edge bluntness may be attributed to the vehicle airframe or external surfaces, rather than to the internal engine flow path. For the current engine, the leading edge radius is 0.5 mm. As discussed in Section 5.5, the inviscid drag of this leading edge is 3.6 N and is comparable with the inviscid drag of the forebody wedge (3.7 N). Excluding this drag from the forebody surface group increases the internal engine specific impulse by 171 s.

4. The result is based on a single shot: A significant caveat for the results presented in Table 7.3 is that they are based solely on a single shot for each fuelling configuration. The variation of thrust increment with fuel equivalence cannot be determined from the experimental data recorded for this thesis and so it remains unknown whether or not the values given in Tables 7.2 and 7.3 are the highest achievable with the current engine.

Addressing items 2 and 3 would increase the internal specific impulse from 548 s to approximately 1002 s, an improvement of 83 %. Further improvement is expected to be achieved by increasing the engine scale without altering the test condition (item 1) and item 4 may be addressed by completing another test campaign. Unfortunately, time and resources did not permit a third campaign from being completed as a part of this thesis.

To conclude this chapter, it is worthwhile postulating the feasability of achieving a cruising state at Mach 10 with a modified version of the current M12REST engine. Using Equations (7.1) and (7.7) and the data in Table 7.1, a thrust increment of $\Delta T = 45.3$ N is estimated for the combined injection scheme at equivalence ratio of 1.20. Based on the numerical simulation of the engine presented in Chapter 5, the net fuel-off drag is 58.4 N at the high pressure test condition (Table G.2). Combining these two values gives a fuel-on drag of 13.1 N. This is the value of drag that is be expected to be measured for the M12REST engine in the absence of any adverse influences related to the force balance shielding and facility nozzle flow.

Now suppose that a sharp leading edge is used for the engine forebody. In this case, the fuel-off drag decreases from 58.4 N to 54.8 N and the fuel-on drag decreases from 13.1 N to 9.5 N. Further suppose that a more efficient nozzle is fitted to the engine and that this nozzle has an exit area equal to the frontal area of the M12REST engine and a thrust efficiency of 90 %. Such a nozzle would produce 13.4 N of thrust for fuel-off (Section 5.6), a value that is 7.9 N greater than the current nozzle. With this nozzle fitted, the fuel-off engine drag is further reduced to 46.9 N and the

fuel-on drag is reduced to just 1.6 N, that is, almost a cruising state. Further improvement could be gained by shortening the forebody which would decrease the fuel-off drag (by reducing the frontal area) while improving the mass capture performance of the engine (by reducing forebody flow spillage). Also note that in addition to reducing the fuel-off drag of the engine, an improved engine nozzle design is expected to increase the measured fuel-on thrust increment, thereby further descreasing the fuel-on drag.

While the preceeding calculation is quite approximate, it does indicate that achieving a cruise condition at Mach 10 should be possible with a modified version of the current M12REST engine. The results and discussion presented in this section and in Section 5.6 unequivocally demonstrate that the development of an efficient, shape-transitioning engine nozzle is critical to the achievement of net thrust at high Mach number flight conditions.

CONCLUSIONS AND RECOMMENDATIONS

The eighth and final chapter, in which the story is brought to a close and some recommendations are made for future areas of investigation.

8

8.1 THESIS SUMMARY

The aim of this thesis was to experimentally investigate the performance of an airframe integrated REST scramjet engine module at a true Mach 10 flight condition. The experiments were conducted using the T4 Stalker Tube at The University of Queensland and the engine performance was characterised through measurement of internal pressure and net lift, thrust and pitching moment using a three-component stress wave force balance.

An existing Mach 12 REST engine flowpath was integrated with a slender 6° wedge forebody, streamlined external geometry and three dimensional thrust nozzle. The scale of the engine module was chosen so that the entire engine fitted within the core-flow diamond produced by the Mach 10 nozzle of the test facility. Although the resulting engine was one-third of the design-scale, operational limits of the T4 Stalker Tube prevented the test conditions from being adjusted to satisfy the binary scaling principle $\rho L = \text{constant}$ (Hornung, 1988). Two true-flight test conditions were used, a low pressure condition simulating flight at a dynamic pressure 28 kPa and a high pressure condition simulating flight at a dynamic pressure 48 kPa.

Two experimental campaigns were conducted for this thesis. During the first campaign a three-component force balance was used and technical difficulties, caused by the design of the associated shielding, were encounted which adversely affected the quality of the test flow. During the second campaign the force balance was replaced by a streamlined rigid mount. The resulting internal pressure data demonstrated the operability of the engine at each test condition for a range of fuel equivalence ratios. Three fuel injection schemes were studied, inlet-only injection, step-only injection and a combined injection scheme for which the fuel split was approximately 68 % to the step and 32 % to the inlet. Good combustion pressure rise was recorded for both the inlet and combined injection schemes and the timing of fuel injection was found to influence flow establishment within the engine.

Despite the technical difficulties experienced, the results of this thesis indicate that it is possible to measure the net forces of a mechanically and geometrically complex, moderate scale, hydrogen fuelled, airframe

integrated scramjet engine module at high Mach number test conditions within an impulse facility. With continued improvement of the force balance technology, it will be possible to better quantify the net aerodynamic performance of the M12REST engine. Unfortunately time and resources did not permit a third test campaign to be completed as a part of this thesis.

The remaining two sections of this chapter detail the major findings of this thesis and the recommendations for future work. For clarity each section has been divided into two groups, scientific and technical. Scientific findings and recommendations are those that are directly related to the operation of the M12REST engine while the technical findings and recommendations focus on the experimental environment and apparatus, including the force balance technology.

8.2 THESIS FINDINGS

8.2.1 *Scientific*

SF1. REST*-based scramjet engines can be integrated with an airframe without adversely affecting engine operation.* This thesis has documented the first experimental data for an airframe integrated REST scramjet. The data also represents the first time that a REST scramjet has been tested in a freejet configuration. During the design of the model two aspects of the integration with a slender wedge forebody were of concern, these were that flow spillage from the forebody would be significant and that the thick boundary layer that develops along the forebody would affect the inlet. The experimental data presented in this thesis, in conjuction with fuel-off numerical simulations demonstrate that flow spillage was approximately 12 % of the flow through the projected inlet capture area and did not adversely affect the engine operation. The experimental data also demonstrate that no boundary layer trip was needed on the forebody at either test condition and that the thick forebody boundary layer ingested by the inlet did not affect engine operation.

SF2. *Inlet injected fuel acts as a pilot for the fuel injected at the step, significantly increasing the combustion induced pressure rise.* While very little combustion occured when fuel was injected only from the step, robust burning was observed for both the inlet and combined injection schemes. The measured increase in pressure was greater for the combined scheme than for the inlet scheme. Taken as a set the data unequivocally demonstrate that the inlet injected fuel acts as a pilot for the step injected fuel in the combined injection scheme. Three mechansims are hypothesised to be at work. Firstly, the interaction of the inlet fuel plumes with the engine cowl shock would increase vorticity within the combustor, thereby increasing the mixing of the step injected fuel (Buttsworth, 1996; Gehre et al., 2013). Secondly,

ignition and combustion of the inlet injected fuel creates free-radicals that would promote ignition of the step injected fuel and thirdly, combustion of the inlet injected fuel would increase the mean flow temperature and pressure, beneficially influencing the ignition and reaction lengths for the step injected fuel.

The operation of the M12REST *engine was demonstrated to be relatively insensitive to changes in flight dynamic pressure.* There are two aspects to this conclusion. Firstly, although the engine was one-third of the design-scale, no scaling of the test condition to satisfy ρL = constant was completed. Even so, good combustion induced pressure rise was measured at both test condition. Secondly, data for the low and high pressure test conditions were comparable for both the inlet and combined injection schemes. SF3.

Generation of net thrust at high flight Mach numbers is difficult. Although technical difficulties were encountered in this thesis, some net force data was measured for the M12REST engine at the Mach 10 test conditions. This data represents the first time that aerodynamic forces have been directly measured at such a high Mach number for an airframe integrated fuelled scramjet engine. The measured fuel-on thrust increment for both the inlet and combined injection schemes indicated that the specific impulse of the M12REST engine was approximately 2200 s with an overall efficiency of approximately 55 % (with respect to the fuel chemical energy). Despite the good performance, net thrust was not achieved, a result that was due in large part to an inefficient engine nozzle. Numerical force data presented in this thesis highlighted the challenge of thrust production at Mach numbers above ten. Based the measured thrust increment and numerical fuel-off drag, it was estimated that a cruising state, i.e. thrust equal drag, could be achieved with a modified version of the current engine. The necessary modifications included sharpening the forebody leading edge and developing an efficient three-dimensional thrust nozzle with exit area equal to frontal area of the engine (Section 7.6). Judicious use of thrust gained from fuel injection and maximising the internal drag reduction achieved through boundary layer combustion of the step injected fuel would help achieve net thrust. SF4.

8.2.2 *Technical*

Early timing of fuel injection relative to arrival of the test flow artifically influences the engine operation and combustion. Although the physical mechanisms are not well understood, the internal pressure data of the M12REST engine proved that early fuel injection for either the inlet or combined injection schemes prevented the inlet from properly starting. For the step-only injection scheme, early timing of fuel injection resulted in unsteady combustion with a larger pressure rise than was achieved with late timing of TF1.

fuel injection. This is not considered to be meaningful data and is due to an interaction with the facility starting process. Further to this, the influence of fuel injection timing on flow establishment does not apply to all model geometries (see, for example, Kirchhartz, 2010, Section 5.3) and so should be assessed experimentally for each (new) configuration tested within the T4 Stalker Tube.

TF2. *The T4 Mach 10 nozzle is susceptible to blockage from the model and/or the associated shielding.* Captured by high speed schlieren photography during the force balance campaign, an erroneous oblique shock wave was observed exiting the facility nozzle and interacting with the model flow field. This shock was hypothesised to originate from a localised flow separation near the exit of the facility nozzle. The ultimate cause for the flow separation remaining in the nozzle is hypothesised to be blockage of the facility nozzle by the force balance shielding. This blockage is also due to the facility nozzle exit diameter being comparable with the width of the test section.[1] An influence of this type has not previously been documented in the T4 Stalker Tube.

TF3. *The on-board fuel system based around a small fuel tank worked.* During the development of the M12REST engine the decision was made to place the fuel system on-board the experimental model so that forces due to fuel injection were included in the force measurement. The resulting fuel system utilised a small 150 cm^3 Swagelok® sample cylinder as the tank. This tank was found to be adequate for the current experiments, supplying a steady plenum pressure for a duration of approximately 2 ms. In addition, the thrust due to fuel injection was estimated to contribute 6 % of the specific impulse of the engine for the inlet injection scheme and 20 % for the combined injection. The use of an on-board fuel tank to permit inclusion of the fuel injection forces is thus important for force balance testing of scramjet engines at high Mach flight conditions.

TF4. *A comprehensive documentation of the calibration of a 3-component stress wave force balance.* A technical achievement rather than a technical finding, the explanation provided in Chapter 4 of the creation of a GIRF from a set of individual point-load calibrations represents the most comprehensive and detailed to date. Calculation of the GIRF weighting factors for the M12REST engine and evaluation of the GIRF were also explained. The documentation of the three-component force balance presented in this thesis will be useful for any researcher who is interested in conducting experiments with a multi-component stress wave force balance.

1 The T4 test section is 450 mm square while the exit diameter of the Mach 10 nozzle is 378 mm.

8.3 THESIS RECOMMENDATIONS

8.3.1 *Scientific*

SR1. *Investigate the state of the boundary layer on the forebody of the* M12REST *engine through measurement of heat flux.* Forced-transition to turbulence of a hypervelocity boundary layer is an area of ongoing research within the Centre for Hypersonics (see, for example, Wise and Smart, 2012). The experimental data presented in this thesis indicated that no boundary layer trip was required on the forebody of the M12REST engine at the investigated test conditions. Using the correlation of He and Morgan (1994), the boundary layer transition length was estimated in this theis to be comparable with the forebody length (Section 3.4.2). However, numerical simulations of the engine assumed fully turbulent boundary layers. Instrumentation of the forebody of the M12REST engine with heat flux gauges would allow the state of the boundary layer entering the engine to be characterised and would contribute to the limited experimental data that exists in the literature for boundary layer transition at high Mach numbers (see Technical Recommendation 6).

SR2. *Develop an efficient three-dimensional nozzle for the* M12REST *engine.* In conjuction with numerical simulation, the force data measured in this thesis showed that the engine nozzle was poorly designed and limited the thrust of the engine. While the literature contains many studies of (notionally) two-dimensional single expansion ramp nozzles (SERN), very little work has been completed examining how to design an efficient three-dimensional nozzle for airframe integrated REST-based scramjet engines. The modular design of the M12REST model developed for this thesis would permit the net, integrated performance of different nozzle designs to be evaluated experimentally.

SR3. *Investigate design alterations to the inlet to increase the projected engine capture-to-frontal area ratio.* Although the M12REST engine designed for this thesis featured streamlined external geometry, the projected engine capture-to-frontal area ratio was only $A_1/A_f = 60\,\%$. Increasing this fraction closer to 100 % without adversely affecting the internal performance improves the thrust generation potential of the engine. Recent computational work by Gollan and Ferlemann (2011) has suggested that for REST inlets, turning of the internal flow parallel to the nominal flight direction could be achieved gradually within the inlet rather than sharply at the inlet-combustor interface. Doing this would significantly reduce the projected area of the external cowlside surfaces of the inlet, thereby reducing the frontal area without affecting the inlet capture. The projected capture-to-frontal area ratio would subsequently increase. Hence it is recommended that the preliminary results of Gollan and Ferlemann (2011) be investigated further, both computationally and experimentally.

SR4. *Investigate the piloting effect that inlet-injected fuel has on step-injected fuel through numerical simulation.* While fuel-on numerical simulations would have aided the interpretation of the experimental data, such simulations were not considered within the scope of this thesis. It is therefore recommended that a numerical study of the M12REST engine be completed. This study should account for the effects of fuel injection and combustion. In particular the study should examine the changes to the internal flow field that result from injection of the fuel, compare the mixing and combustion performance of the three different injection schemes tested in this thesis and in particular investigate by what mechanism the inlet-injected fuel promotes combustion of the step-injected fuel.[2]

SR5. *Examine the use of stream-thrust probes to predict the internal thrust of an engine.* In this work the internal performance of the M12REST engine was estimated by comparing the net drag measured for a fuel-on test to that measured for a fuel-off test. The internal performance of the engine was estimated by subtracting the fuel-off drag calculated from numerical simulation from the experimental thrust increment. Demarcation of internal and external performance of the engine for a single experiment would be useful and possible through the measurement of stream-thrust at the engine nozzle exit (in addition to the force balance). This methodology has previously been proposed by Voland (1990) and more recently Hiers et al. (2005) have investigated the development of a suitable probe. Since it provides an independent method for the estimation of internal thrust, the measurement of the nozzle exit stream-thrust would also be of use during complete engine tests which do not use a force balance.

8.3.2 *Technical*

TR1. *Redesign the force balance top plate and additional inertial mass to reduce the frontal area of the associated shielding.* Before any further experiments with the M12REST engine and force balance are completed, the top plate and additional inertial mass of the force balance must be redesigned to reduce the frontal area of the associated shielding to be comparable with that of the streamlined shielding used during the second test campaign of this thesis (see Figure 4.1). Noting that in this work the force balance was mounted to the top of the test section using a tunnel attachment plate rather than the standard T4 attachment rails (see Figure 3.16), there is no reason for the balance top plate to be 211 mm wide. Minimising the frontal area of the force balance shielding will limit the influence of the shielding on the facility nozzle, subsequently improving the quality of the test flow and the force measurement.

2 At the time of writing this recommendation is being addressed through the work of Mr. James Barth, a PhD candidate within the CFH. See, for example, Barth et al. (2014, 2012).

Reduce the forebody length of the engine. In this work the forebody length was defined assuming that an inviscid 2-D shock formed from a sharp leading edge would intersect the inlet cowl closure location at the design condition. Viscous flow effects on the forebody and the blunt leading edge cause an increase in the forebody shock standoff, resulting in a conservative forebody length and increased flow spillage. It is recommended that fuel-off numerical simulations be completed across a range of Mach numbers and that the resulting data set be used to judiciously shorten the forebody of the engine. TR2.

Investigate the use of Loctite® 515™ as a suitable transmission medium for stress waves. During the development of the three-component force balance, Robinson (2003a, Section 5.4.3) discovered that repeatability and transmission of stress waves was improved when Molykote® 111 compound grease was applied to the interface of each model joint. Robinson also stated that the signal quality did not degrade when the model was left for several weeks. In this thesis, due to the lack of o-ring seals, Loctite® 515™ was used as a sealant at many of the major interfaces of the model (Doherty, 2013b) and it was assumed that this substance would be a suitable stress wave transmission medium. Given the change in calibration strain signals that occured between the pre- and post-campaign calibrations of the force balance, it is recommended that the suitability and long term stability of Loctite® 515™ as a stress wave transmission medium be investigated prior to any further experiments with the M12REST engine and three-component force balance. TR3.

Re-manufacture the stress bars. Towards the end of the force balance campaign the primary strain gauges were intermittenly faulty. Rather than re-instrument the current bars, which would be difficult to achieve without destroying the existing instrumentation,[3] it is recommended that each of the bars be remade. Remaking the bars also allows the design to be slightly altered such that each bar is machined as a single piece, rather than being a bolted assembly of three components. This would eliminate two unnecessary joints per bar.[4] Additionally, the dimensions of the piezo-electric film of the current stress bars were chosen by Robinson (2003d, Section 5.2.6) based on the expected force and strain magnitudes. Noting that the fuel-off lift and drag of the scramjet engine tested by Robinson were approximately 400 N and 100 N (respectively), while those of M12REST engine were approximately 100 N and 50 N (respectively), the smaller magnitude of the forces of the M12REST engine should be taken into account TR4.

3 Each bar was shielded using a PVC tube that was sealed and held in place by RTV silicone adhesive.

4 The design of the bars is detailed in Robinson (2003d). Recently the capabilities of the Mechanical Engineering Workshop at The University of Queensland have increased through the addition of a 5-axis CNC mill. Such a mill makes the creation of each bar as a single piece easy.

during (re)instrumentation of the stress bars. Is is expected that increasing the response of the gauges relative to the input force would improve the force recovery of the balance.

TR5. *Fit additional pressure transducers to the engine nozzle.* Typically, quasi-one dimensional cycle analysis of the internal pressure measurements is completed to estimate the combustion efficiency achieved during the experiment (see, for example, Moule and Smart, 2013). Due to the limited number of pressure taps within the engine combustor and particularly the engine nozzle, an anlysis of this type was unable to be completed for the small-scale M12REST engine data presented in this thesis. Increasing the number of pressure transducers within the engine nozzle to at least three would permit the variation of pressure on the bodyside to be partially resolved, thereby providing sufficient information to allow cycle analysis of future data to be completed.

TR6. *Instrument the engine forebody with thin-film heat flux gauges and additional pressure transducers.* Related to scientific recommendation 1, it is recommended that the forebody be instrumented with thin-film heat flux gauges in a manner similar to Wise and Smart (2012) so that the state of the boundary layer entering the engine can be better characterised. Furthermore, it is also recommended that the forebody be instrumented with additional pressure transducers as this would permit the pressure variation across the forebody to be partially resolved. Additional forebody pressure transducers would also provide extra data for comparison with the numerical simulations of the engine (Chapter 5) and with the calculated facility nozzle flow (Section 3.3 and Figure 7.3).

TR7. *Instrument each fuel plenum for measurement of the fuel temperature.* In this thesis the standard methodology[5] used for calculating the fuel mass flow rate for a single-plenum injection scheme was found to over-estimate the mass flow rate when applied to a combined injection scheme. This result was intimately related to the theoretical basis of the calibration method and was accounted for in this thesis through the introduction of an empirical calibration constant specifically for combined injection schemes. The theoretical basis for the combined injection calibration constant has not been well established. The introduction of the empirical calibration constant can be circumvented through measurement of the fuel plenum temperature (in addition to the fuel plenum pressure). The caveat is that the temperature measurement should have a similar transient response to the pressure measurement. It is recommended that further analysis and experimentation be conducted to improve the calibration methodologies for combined injection systems.

5 Here 'standard methodology' should be interpreted as meaning 'that which has been used within the Centre for Hypersonics for several years'.

Measure the facility recoil signal using a 5 µs *timebase (medium timebase).* Due to the observed sensitivity of flow establishment within the engine to the timing of fuel injection, it is recommended that for future experiments the facility recoil, which triggers the fuel system, be recorded using a 5 µs timebase rather than a 400 µs timebase as used in this thesis. A smaller recording timebase would greatly improve the repeatability and control of the fuel injection timing. TR8.

Investigate the benefits and feasibility of altering the stress bar arrangement to decrease force coupling. The current "M" arrangement of the force balance stress bars was chosen by Robinson (2003d) after an extensive finite-element study because it offered the best combination of force recovery and ease of shielding. This arrangement however, results in strong coupling between the output strain signals and force inputs, particularly when the centre of force of the scramjet engine does not coincide with the symmetry plane of the bars. It is therefore recommended that a finite element analysis similar to that completed by Robinson et al. (2004) be undertaken for the M12REST engine. The analysis should focus on developing a greater understanding of the response of the model to the calibration hits and to a distributed aerodynamic load, with the goal of improving the force recovery for the M12REST engine. The benefits of using of an internal drag bar in combination with two external lift bars should also be assessed during the study. TR9.

Record high speed schlieren video of the inlet cowl closure region. During the first test campaign, the use of high speed schlieren video was crucial for diagnosing the influence of the force balance shielding on the facility nozzle. It is therefore recommended that schlieren video be used for all future test campaigns with the small-scale M12REST engine. Specifically, the optics should attempt to visualise the inlet cowl closure location, thus allowing the starting processes of the inlet flow to be assessed based on the external cowl shock location. TR10.

Investigate transient flow establishment in complete scramjet flowpaths. During this thesis the timing of fuel injection relative to flow arrival at the model was observed to affect the establishment of the engine flow field. While flow establishment within scramjet combustors has previously been studied (see, for example, Jacobs et al., 1992), the data presented in this thesis imply that our knowledge of flow starting and establishment of complete scramjet engine tested within reflected shock tunnel facilities is incomplete. It is therefore recommended that transient numerical simulations of the facility nozzle and engine starting processes be conducted to provide a greater understanding of the physical mechanisms at work. TR11.

"One never notices what has been done; one can only see what remains to be done."

– Marie Curie, 1894

Abdel-Jawad, MM (2004). "Stability Assessment of Planetary Entry Vehicles in the X3 Superorbital Expansion Tube". PhD Thesis. Brisbane, Australia: The University of Queensland (cited on page 77).

Abdel-Jawad, MM, Mee, DJ, and Morgan, RG (2007). "New Calibration Technique for Multiple-Component Stress-Wave Force Balances". *Review of Scientific Instruments*, 78(065101), pages 1–7. DOI: 10.1063/1.2744235 (cited on pages 77, 84).

Abdel-Jawad, MM, Mee, DJ, Morgan, RG, Jacobs, PA, and Philpot, JA (2001). "Transient Force Measurements at Superorbital Speeds". In: *23rd International Symposium on Shock Waves*. Fort Worth, Texas, U.S.A, pages 565–571 (cited on page 77).

Ames Research Staff (1953). *Equations, Tables, and Charts for Compressible Flow*. Technical Report 1135. NACA (cited on page 119).

Anderson, JD (2000). *Hypersonic and High Temperature Gas Dynamics*. 1st edition. Virginia: American Institute of Aeronautics and Astronautics (cited on page 9).

– (2003). *Modern Compressible Flow with Historical Perspective*. 3rd edition. Sydney: McGraw Hill (cited on page 35).

– (2006). *Hypersonic and High Temperature Gas Dynamics*. 2nd edition. AIAA Education Series. Virginia: American Institute of Aeronautics and Astronautics. DOI: 10.2514/4.861956 (cited on pages 1, 52, 122).

Bakos, RJ, Tsai, CY, Rogers, RC, and Shih, AT (1999). "The Mach 10 Component of NASA's Hyper-X Ground Test Program". In: *14th International Symposium on Air-Breathing Engines*. Florence, Italy: ISABE-99-7216 (cited on pages 19, 21).

Barth, JE, Wheatley, V, and Smart, MK (2013). "Hypersonic Turbulen Boundary-Layer Fuel Injection and Combustion: Skin-Friction Reduction Mechanisms". AIAA *Journal*, 51(9), pages 2147–2157. DOI: 10.2514/1.J052041 (cited on page 134).

– (2014). "Inlet Fuel Injection in a Mach 12 Shape-Transitioning Scramjet". In: *52nd* AIAA *Aerospace Sciences Meeting*. National Harbor, Maryland, U.S.A: AIAA-2014-1159. DOI: 10.2514/6.2014-1159 (cited on pages 50, 152, 204).

Barth, JE, Wheatley, V, Smart, MK, Petty, DJ, and Basore, KD (2012). "Flow Physics Inside a Shape-Transitioning Scramjet Engine". In: *18th* AIAA/3AF *International Space Planes and Hypersonic Systems and*

Technologies Conference. Tours, France: AIAA-2012-5888. DOI: 10.2514/6.2012-5888 (cited on pages 123, 135, 204).

Barthelemy, R (1989). "The National Aero-Space Plane Program". In: AIAA/NASA *Symposium on the Maintainability of Aerospace Systems*. Anaheim, California, U.S.A.: AIAA-89-5053. DOI: 10.2514/6.1989-5053 (cited on page 3).

Baurle, RA (2012). VULCAN*: Viscous Upwind Algorithm for Complex Flow Analysis, User Manual*. NASA Langley Research Centre. URL: http://vulcan-cfd.larc.nasa.gov/ (cited on pages 115, 117).

Baurle, RA and Gaffney, RL (2008). "Extraction of One-Dimensional Flow Properties from Multidimensional Data Sets". *Journal of Propulsion and Power*, 24(4), pages 704–714. DOI: 10.2514/1.32074 (cited on pages 43, 123).

Beckel, SA, Garrett, JL, and Gettinger, CG (2006). "Technologies for Robust and Affordable Scramjet Propulsion". In: *14th* AIAA/AHI *International Space Planes and Hypersonics Systems and Technologies Conference*. Canberra, Australia: AIAA-2006-7980. DOI: 10.2514/6.2006-7980 (cited on pages 5, 9).

Bendat, JS and Piersol, AG (2010). *Random Data: Analysis and Measurement Procedures*. John Wiley & Sons, Inc. ISBN: 978-0-470-24877-5 (cited on page 282).

Ben-Yakar, A, Mungal, MG, and Hanson, RK (2006). "Time Evolution and Mixing Characteristics of Hydrogen and Ethylene Transverse Jets in Supersonic Crossflows". *Physics of Fluids*, 18(2), page 026101. DOI: 10.1063/1.2139684 (cited on page 4).

Berry, SA, Auslender, AH, Dilley, AD, and Calleja, JF (2001). "Hypersonic Boundary-Layer Trip Development for Hyper-X". *Journal of Spacecraft and Rockets*, 38(6), pages 853–864. DOI: 10.2514/2.3775 (cited on page 129).

Bilardo, VJ, Curran, FM, Hunt, JL, Lovell, NT, Maggio, G, Wilhite, AW, and McKinney, L (2003). "The Benefits of Hypersonic Airbreathing Launch Systems for Access to Space". In: *39th* AIAA/ASME/SAE/ASEE *Joint Propulsion Conference*. Huntsville, Alabama, U.S.A: AIAA-2003-5265. DOI: 10.2514/6.2003-5265 (cited on page 4).

Billig, FS (1995). "Supersonic Combustion Ramjet Missile". *Journal of Propulsion and Power*, 11(6). Compilation and indexing terms, Copyright 2006 Elsevier Inc. All rights reserved 95122949005 0748-4658 Supersonic combustion ramjet missile Fleet defense weapons Hypersonic inlets Mach number Angle of attack Injectors Borane Aluminum alkyls, pages 1139–1146 (cited on page 3).

Billig, FS, Corda, S, and Pandolfini, PP (1990). "Design Techniques for Dual Mode Ram-Scramjet Combustors". In: *Propulsion and Energetics Panel, 75th Symposium*. Volume 479. AGARD Conference Proceedings. Neuilly-sur-Seine, France: AGARD. ISBN: 0549-7191 (cited on pages 1, 2, 149).

Bowcutt, KG, Anderson, JD, and Capriotti, D (1987). "Viscous Optimized Hypersonic Waveriders". In: AIAA *25th Aerospace Sciences Meeting*. Reno, Nevada, U.S.A: AIAA-1987-0272. DOI: 10.2514/6.1987-272 (cited on pages 52, 128).

Bowcutt, KG, Gonda, M, Hollowell, S, and Ralston, T (2002). "Performance, Operational and Economic Drivers of Reusable Launch Vehicles". In: *38th* AIAA/ASME/SAE/ASEE *Joint Propulsion Conference & Exhibit*. Indanapolis, Indiana, U.S.A: AIAA-2002-3901. DOI: 10.2514/6.2002-3901 (cited on page 4).

Bowcutt, KG, Smith, TR, Kothari, AP, Raghavan, V, Tarpley, C, and Livingston, JW (2011). "The Hypersonic Space and Global Transportation System: A Concept for Routine and Affordable Access to Space". In: *17th* AIAA *International Space Planes and Hypersonic Systems and Technologies Conference*. San Francisco, California, U.S.A: AIAA-2011-2295. DOI: 10.2514/6.2011-2295 (cited on pages 3, 4).

Boyce, RR, Takahashi, M, and Stalker, RJ (2005a). "Mass Spectrometric Measurements of Driver Gas Arrival in the T4 Free-Piston Shock-Tunnel". *Shock Waves*, 14(5-6), pages 371–378. DOI: 10.1007/s00193-005-0276-3 (cited on pages 48, 69, 70).

– (2005b). "Mass Spectrometric Measurements of the Freestream Composition in the T4 Free-Piston Shock-Tunnel". *Shock Waves*, 14(5-6), pages 359–370. DOI: 10.1007/s00193-005-0275-4 (cited on page 45).

Bradford, J, Charania, A, Wallace, J, and Eklund, D (2004). "Quicksat: A Two-Stage-to-Orbit Reusable Launch Vehicle Utilizing Air-Breathing Propulsion for Responsive Space Access". In: *Space 2004 Conference and Exhibit*. San Diego, California, U.S.A: AIAA-2004-5950. DOI: 10.2514/6.2004-5950 (cited on page 3).

Builder, CH (1964). "On the Thermodynamic Spectrum of Airbreathing Propulsion". In: *1st* AIAA *Annual Meeting*. Washington, DC, U.S.A: AIAA-64-243. DOI: 10.2514/6.1964-243 (cited on pages 2, 139).

Burtschell, Y and Zeitoun, DE (2003). "Shock/Shock and Shock/Boundary Layer Interactions in an Axisymmetric Steady Laminar Flow". *Shock Waves*, 12(6), pages 487–495. DOI: 10.1007/s00193-003-0187-0 (cited on page 4).

Bushnell, DM (2006). "Scaling: Wind Tunnel to Flight". *Annual Review of Fluid Mechanics*, 38, pages 111–128. DOI: 10.1146/annurev.fluid.38.050304.092208 (cited on page 159).

Buttsworth, DR (1996). "Interaction of Oblique Shock Waves and Planar Mixing Regions". *Journal of Fluid Mechanics*, 306, pages 43–57. doi: 10.1017/S002211209600122X (cited on pages 152, 200).

Cengel, YA and Boles, MA (2002). *Thermodynamics An Engineering Approach*. 4th edition. Sydney: McGraw Hill (cited on pages 191, 354).

Chan, WYK (2012). "Effects of Flow Non-uniformities on the Drag Reduction by Boundary Layer Combustion". PhD Thesis. Brisbane, Australia: The University of Queensland (cited on pages 48, 70, 77, 106, 139, 258).

Chan, WYK, Jacobs, PA, and Mee, DJ (2012). "Suitability of the k-ω Turbulence Model for Scramjet Flowfield Simulations". *International Journal for Numerical Methods in Fluids*, 70(4), pages 493–514. doi: 10.1002/fld.2699 (cited on pages 42, 292).

Chan, WYK, Smart, MK, and Jacobs, PA (2013). *Flowpath Design of an Axisymmetric Mach 7.0 Nozzle for T4*. Research Report 2013/02. Brisbane, Australia: School of Mechanical and Mining Engineering, The University of Queensland (cited on page 294).

Cockrell, CE, Engelund, WC, Bittner, RD, Jentink, TN, Dilley, AD, and Frendi, A (2001). "Integrated Aeropropulsive Computational Fluid Dynamics Methodology for the Hyper-X Flight Experiment". *Journal of Spacecraft and Rockets*, 38(6), pages 836–843. doi: 10.2514/2.3773 (cited on pages 19, 20).

Coleman, HW and Steele, WG (1999). *Experimentation and Uncertainty Analysis for Engineers*. 2nd edition. Quoted doi is for the 3rd Edition. New York, u.s.a.: John Wiley & Sons, Inc. doi: 10.2514/2.3773 (cited on pages 110, 236, 237, 281–287, 306, 309).

Curran, ET (2001). "Scramjet Engines: The First Forty Years". *Journal of Propulsion and Power*, 17(6), pages 1138–1148 (cited on pages 3, 9).

Czysz, PA (1988). "Thermodynamic Spectrum of Airbreathing Propulsion". In: sae *Future Transportation Technology Conference and Exposition*. San Francisco, California, u.s.a: sae-881203 (cited on pages 2, 57, 139, 356).

Daniel, WJT and Mee, DJ (1995). "Finite Element Modelling of a Three-component Force Balance for Hypersonic Flows". *Computers and Structures*, 54(1), pages 35–48. doi: 10.1016/0045-7949(94)00309-Q (cited on page 76).

Dann, AG and Morgan, RG (2011). "Analytical Method of Prediction of Turbulent Boundary-Layer Separation in Hypersonic Flows". aiaa *Journal*, 49(9), pages 2068–2072. doi: 10.2514/1.J050673 (cited on pages 4, 52).

Davies, WR and Bernstein, L (1969). "Heat Transfer and Transition to Turbulence in the Shock-Induced Boundary Layer on a Semi-Infinite

Flat Plate". *Journal of Fluid Mechanics*, 36(1), pages 87–112. DOI: 10.1017/S0022112069001534 (cited on pages 47, 67).

Doherty, LJ (2009). *Guide to Creating* rest *Inlet Models in* catia. Research Report 2009/10. Brisbane, Australia: School of Mechanical and Mining Engineering, The University of Queensland.

– (2013a). *Simulation and Uncertainty Analysis of the T4 Mach 10 Nozzle Flow using* nenzfr. Research Report 2013/16. Brisbane, Australia: School of Mechanical and Mining Engineering, The University of Queensland (cited on pages 38, 42, 43, 64, 144, 293–296).

– (2013b). *Thesis Supplement I: Design and Assembly of the Mach 12* rest *Three-Component Force Balance Model*. Research Report 2013/14. Brisbane, Australia: School of Mechanical and Mining Engineering, The University of Queensland (cited on pages 50, 51, 55, 57, 64, 80, 98, 99, 161, 164, 205, 266, 315, 333).

– (2013c). *Thesis Supplement II: Three-Component Force Balance Calibration Data for the Mach 12* rest *Engine*. Research Report 2013/15. Brisbane, Australia: School of Mechanical and Mining Engineering, The University of Queensland (cited on pages 90, 92, 93, 251, 254, 266).

Doherty, LJ, Chan, WYK, Zander, F, Jacobs, PA, Gollan, RJ, and Kirchhartz, RM (2012). nenzfr*: Non-Equlibrium Nozzle Flow, Reloaded*. Research Report 2012/08. Brisbane, Australia: School of Mechanical and Mining Engineering, The University of Queensland (cited on pages 41, 43, 290, 293).

Doherty, LJ, Smart, MK, and Mee, DJ (2012). "Design of an Airframe Integrated 3-D Scramjet and Experimental Results at a Mach 10 Flight Condition". In: *18th* aiaa/3af *International Space Planes and Hypersonic Systems and Technologies Conference*. Tours, France: aiaa-2012-5910. DOI: 10.2514/6.2012-5910.

Doherty, LJ and Wise, DJ (2013). *Pitot Survey Data for the* t4 *Mach 10 Nozzle*. Research Report 2013/07. Brisbane, Australia: School of Mechanical and Mining Engineering, The University of Queensland (cited on pages 38, 39).

East, RA, Stalker, RJ, and Baird, JP (1980). "Measurements of Heat Transfer to a Flat Plate in a Dissociated High-enthalpy Laminar Air Flow". *Journal of Fluid Mechanics*, 97(4), pages 673–699. DOI: 10.1017/S0022112080002753 (cited on page 67).

Engelund, WC, Holland, SD, Cockrell, CE, and Bittner, RD (2001). "Aerodynamic Database Development for the Hyper-X Airframe Integrated Scramjet Propulsion Experiments". *Journal of Spacecraft and Rockets*, 38(6), pages 803–810. DOI: 10.2514/2.3768 (cited on pages 19, 20).

Ferlemann, PG (2005). "Comparison of Hyper-X Mach 10 Scramjet Preflight Predictions and Flight Data". In: *13th* aiaa/cira *International Space Planes and Hypersonic Systems and Technologies Conference*. Capua, Italy: aiaa-2005-3352. doi: 10.2514/6.2005-3438 (cited on pages 19, 21).

Ferlemann, SM, McClinton, CR, Rock, KE, and Voland, RT (2005). "Hyper-X Mach 7 Scramjet Design, Ground Test and Flight Results". In: aiaa/cira *13th International Space Planes and Hypersonics Systems and Technologies Conference*. Capua, Italy: aiaa-2005-3322. doi: 10.2514/6.2005-3322 (cited on page 21).

Ferri, A (1973). "Mixing-Controlled Supersonic Combustion". *Annual Review of Fluid Mechanics*, 5, pages 301–360. doi: 10.1146/annurev.fl.05.010173.001505 (cited on page 1).

Flaherty, KW, Andrews, KM, and Liston, GW (2010). "Operability Benefits of Airbreathing Hypersonic Propulsion for Flexible Access to Space". *Journal of Spacecraft and Rockets*, 47(2), pages 280–287. doi: 10.2514/1.43750 (cited on page 4).

Gangurde, DY (2007). "L1d Simulation of Ludwieg Tube Fuel System for T4". Masters Thesis. Brisbane, Australia: The University of Queensland (cited on page 60).

Gangurde, DY, Mee, DJ, and Jacobs, PA (2007). "Numerical Simulation of a Ludwieg-tube Fuel Delivery System for Scramjet Experiments in Shock Tunnels". In: *16th Australasian Fluid Mechanics Conference*. Gold Coast, Australia. url: http://www.afms.org.au/proceedings/16/Gangurde.pdf (cited on page 60).

Gardner, AD, Paull, A, and McIntyre, TJ (2002). "Upstream Porthole Injection in a 2-D Scramjet Model". *Shock Waves*, 11(5), pages 369–375. doi: 10.1007/s001930200120 (cited on page 13).

Gehre, R, Peterson, D, Wheatley, V, and Boyce, RR (2013). "Numerical Investigation of the Mixing Process in Inlet-Fuelled Scramjets". In: *29th International Symposium on Shock Waves*. Madison, Wisconsin, u.s.a (cited on pages 152, 200).

Gildfind, DE, Morgan, RG, McGilvray, M, Jacobs, PA, Stalker, RJ, and Eichmann, TN (2011). "Free-Piston Driver Optimisation for Simulation of High Mach Number Scramjet Flow Conditions". *Shock Waves*, 21(6), pages 559–572. doi: 10.1007/s00193-011-0336-9 (cited on pages 35, 36).

Gollan, RJ and Ferlemann, PG (2011). "Investigation of rest-Class Hypersonic Inlet Designs". In: *17th* aiaa *International Space Planes and Hypersonic Systems and Technologies Conference*. San Francisco, California, u.s.a: aiaa-2011-2254. doi: 10.2514/6.2011-2254 (cited on page 203).

Gollan, RJ and Jacobs, PA (2013). "About the Formulation, Verification and Validation of the Hypersonic Flow Solver Eilmer". *International Journal for Numerical Methods in Fluids*, 73(1), pages 19–57. doi: 10.1002/fld.3790 (cited on pages 4, 42).

Gollan, RJ and Smart, MK (2013). "Design of Modular Shape-Transition Inlets for a Conical Hypersonic Vehicle". *Journal of Propulsion and Power*, 29(4), pages 832–838. doi: 10.2514/1.B34672 (cited on page 5).

Goozée, RJ, Jacobs, PA, and Buttsworth, DR (2006). "Simulation of a Complete Reflected Shock Tunnel Showing a Vortex Mechanism for Flow Contamination". *Shock Waves*, 15(3-4), pages 165–176. doi: 10.1007/s00193-006-0015-4 (cited on page 35).

Goyne, CP, Stalker, RJ, Paull, A, and Brescianini (2000). "Hypervelocity Skin-Friction Reduction by Boundary-Layer Combustion of Hydrogen". *Journal of Spacecraft and Rockets*, 37(6), pages 740–746 (cited on pages 50, 134).

Gupta, R, Yos, J, Thompson, R, and Lee, KP (1990). *A Review of Reaction Rates and Thermodynamic and Transport Properties for an 11-Species Air Model for Chemical and Thermal Nonequilibrium Calculations to* 30 000 K. Reference Publication 1232. Hampton, Virginia, u.s.a.: nasa Langley Research Center (cited on page 42).

Han, B, Sung, CJ, and Nishioka, M (2004). "Effects of Vitiated Air on Hydrogen Ignition in a High-speed Laminar Mixing Layer". *Combustion Science and Technology*, 176(3), pages 305–330. doi: 10.1080/00102200490256018 (cited on pages 48, 152).

Haynes, WM, editor (2013). crc *Handbook of Chemistry and Physics*. 94th edition. 2013 - 2014. crc Press, Taylor & Francis Group (cited on pages 64, 263).

He, Y and Morgan, RG (1994). "Transition of Compressible High Enthalpy Boundary Layer Flow over a Flat Plate". *The Aeronautical Journal*, 98(972), pages 25–34 (cited on pages 53, 203).

Heiser, WH and Pratt, DT (1994). *Hypersonic Airbreathing Propulsion*. Edited by J Przemieniecki. aiaa Education Series. Washington, DC: American Institute of Aeronautics and Astronautics. doi: 10.2514/4.470356 (cited on pages 1, 2, 9, 122, 137, 139, 149).

Heppenheimer, TA (2007). *Facing the Heat Barrier: A History of Hypersonics*. The nasa History Series sp-2007-4232. Washington, DC, u.s.a.: National Aeronautics and Space Administration (cited on page 1).

Hess, S (2009). "A Low Enthalpy Test Condition for the T4 Shock Tunnel". Diploma Thesis. Brisbane, Australia: Centre for Hypersonics, Division of Mechanical Engineering, The University of Queensland (cited on page 36).

Hiers, RS, Sirbaugh, JR, McCann, CBT, Cummings, RM, Luft, CLS, and Grillos, CDP (2005). "Experimental Verification of the Aerodynamics of Stream Thrust Probes". In: *43rd* aiaa *Aerospace Sciences Meeting and Exhibit*. Reno, Nevada, u.s.a: aiaa-2005-1215. doi: 10.2514/6.2005-1215 (cited on page 204).

Hirschel, EH (2005). *Basics of Aerothermodynamics*. Springer-Verlag/aiaa. doi: 10.1007/b137734 (cited on page 52).

Hirschel, EH and Weiland, C (2009). *Selected Aerothermodynamic Design Problems of Hypersonic Flight Vehicles*. Springer-Verlag/aiaa. doi: 10.1007/978-3-540-89974-7 (cited on pages 3, 4, 52, 53, 129, 132, 154, 184, 323).

Hirschen, C, Gülhan, A, Beck, W, and Henne, U (2009). "Measurement of Flow Properties and Thrust on Scramjet Nozzle using Pressure-Sensitive Paint". *Journal of Propulsion and Power*, 25(2), pages 267–280. doi: 10.2514/1.37957 (cited on pages 4, 17).

Högenauer, E and Koelle, D (1989). "sänger The German Aerospace Vehicle Program". In: aiaa *First National Aero-Space Plane Conference*. Dayton, Ohio, u.s.a.: aiaa-89-5007. doi: 10.2514/6.1989-5007 (cited on page 3).

Holland, SD, Woods, WC, and Engelund, WC (2001). "Hyper-X Research Vehicle Experimental Aerodynamics Test Program Overview". *Journal of Spacecraft and Rockets*, 38(6), pages 828–835. doi: 10.2514/2.3772 (cited on page 19).

Hornung, H (1988). "28th Lanchester Memorial Lecture – Experimental Real-Gas Hypersonics". *Aeronautical Journal*, 92(920), pages 379–389 (cited on pages 43, 159, 199).

Hudson, S, Brown, K, Kammeyer, M, Cahill, D, Coleman, H, Steele, G, and McLain, S (2003). *Assessing Experimental Uncertainty - Supplement to* aiaa *s-071a-1999*. Guide g-045-2003. aiaa. doi: 10.2514/4.476648 (cited on pages 237, 281–285, 287).

Hunt, JL (1987). "Hypersonic Airbreathing Vehicle Design (Focus on Aero-Space Plane)". In: *Hypersonics Volume 1: Defining the Hypersonic Environment*. Edited by J Bertin, R Glowinski, and J Periaux. Volume 8. Progress in Scientific Computing. Birkhäuser. Chapter 5, pages 205–262 (cited on page 4).

Hunt, JL, Laruelle, G, and Wagner, A (1997). *Systems Challenges for Hypersonic Vehicles*. Technical Memorandum 112908. Hampton, Virginia, u.s.a.: nasa Langley Research Center (cited on page 4).

Itoh, K (2005). "Study on Scramjet Engine Characteristics under Mach 8 to 15 Conditions". In: *5th European Symposium on Aerothermodynamics for Space Vehicles*. Cologne, Germany: ESA-SP-563 (cited on page 22).

Jacobs, PA (1994). "Quasi-One-Dimensional Modelling of a Free-Piston Shock Tunnel". AIAA *Journal*, 32(1), pages 137–145 (cited on page 60).

– (1998). *Shock Tube Modelling with L1d*. Research Report 1998/13. Brisbane, Australia: Division of Mechanical Engineering, The University of Queensland (cited on page 60).

Jacobs, PA and Gollan, RJ (2008). *The Eilmer3 Code: User Guide and Example Book*. Research Report 2008/07. Brisbane, Australia: School of Mechanical and Mining Engineering, The University of Queensland (cited on page 42).

Jacobs, PA, Gollan, RJ, Denman, AW, O'Flaherty, BT, Potter, DF, Petrie-Repar, PJ, and Johnston, IA (2010). *Eilmer's Theory Book: Basic models for Gas Dynamics and Thermochemistry*. Department Report 2010/09. Brisbane, Australia: School of Mechanical and Mining Engineering, The University of Queensland (cited on page 42).

Jacobs, PA, Gollan, RJ, Potter, DF, Zander, F, Gildfind, DE, Blyton, P, Chan, WYK, and Doherty, LJ (2011). *Estimation of High-Enthalpy Flow Conditions for Simple Shock and Expansion Processes using the ESTCj Program and Library*. Research Report 2011/02. Brisbane, Australia: School of Mechanical and Mining Engineering, The University of Queensland. URL: https://espace.library.uq.edu.au/view/UQ:321755 (cited on pages 42, 367).

Jacobs, PA, Rogers, RC, Weidner, EH, and Bittner, RD (1992). "Flow Establishment in a Generic Scramjet Combustor". *Journal of Propulsion and Power*, 8(4), pages 890–899. DOI: 10.2514/3.23566 (cited on pages 67, 69, 70, 175, 207).

Jazra, T (2010). "Optimisation of Hypersonic Vehicles for Airbreathing Propulsion". PhD Thesis. Brisbane, Australia: The University of Queensland (cited on page 3).

Jazra, T, Preller, D, and Smart, MK (2013). "Design of an Airbreathing Second Stage for a Rocket-Scramjet-Rocket Launch Vehicle". *Journal of Spacecraft and Rockets*, 50(2), pages 411–422. DOI: 10.2514/1.A32381 (cited on pages 3–5, 17).

Johnson, HB, Alba, CR, Candler, GV, MacLean, M, Wadhams, TP, and Holden, MS (2008). "Boundary-Layer Stability Analysis of the Hypersonic International Flight Research Transition Experiments". *Journal of Spacecraft and Rockets*, 45(2), pages 228–236. DOI: 10.2514/1.31878 (cited on page 53).

Kanda, T, Sunami, T, Tomioka, S, Tani, K, and Mitani, T (2001). "Mach 8 Testing of a Scramjet Engine Model". *Journal of Propulsion and Power*, 17(1), pages 132–138. DOI: 10.2514/2.5718 (cited on pages 21, 23).

Kanda, T, Tani, K, Kobayashi, K, Saito, T, and Sunami, T (2002). "Mach 8 Testing of a Scramjet Engine with Ramp Compression". *Journal of Propulsion and Power*, 18(2), pages 417–423. doi: 10.2514/2.5950 (cited on page 21).

Kawai, S and Lele, SK (2010). "Large-Eddy Simulation of Jet Mixing in Supersonic Crossflows". aiaa *Journal*, 48(9), pages 2063–2083. doi: 10.2514/1.J050282 (cited on page 4).

Kirchhartz, RM (2010). "Upstream Wall Layer Effects on Drag Reduction with Boundary Layer Combustion". PhD Thesis. Brisbane, Australia: The University of Queensland (cited on pages 202, 232, 258, 288, 315, 334).

Kirchhartz, RM, Mee, DJ, and Stalker, RJ (2012). "Supersonic Skin-Friction Drag with Tangential Wall Slot Fuel Injection and Combustion". aiaa *Journal*, 50(2), pages 313–324. doi: 10.2514/1.J051073 (cited on pages 17, 77, 134, 139).

Kleine, H, Hiraki, K, Maruyama, H, Hayashida, T, Yonai, J, Kitamura, K, Kondo, Y, and Etoh, TG (2005). "High-Speed Time-Resolved Color Schlieren Visualization of Shock Wave Phenomena". *Shock Waves*, 14(5/6), pages 333–341. doi: 10.1007/s00193-005-0273-6 (cited on page 67).

Kobayashi, K, Tomioka, S, Kato, K, Murakami, A, and Kudo, K (2006). "Performance of a Dual-mode Combustor with Multistaged Fuel Injection". *Journal of Propulsion and Power*, 22(3), pages 518–526. doi: 10.2514/1.19294 (cited on pages 4, 149).

Lee, JY and Lewis, MJ (1993). "Numerical Study of the Flow Establishment Time in Hypersonic Shock Tunnels". *Journal of Spacecraft and Rockets*, 30(2), pages 152–163. doi: 10.2514/3.11523 (cited on page 67).

Lewis, MJ (2003). "Hypersonic Propulsion Airframe Integration Overview". In: *39th* aiaa/asme/sae/asee *Joint Propulsion Conference and Exhibit*. Huntsville, Alabama, u.s.a: aiaa-2003-4405. doi: 10.2514/6.2003-4405 (cited on pages 4, 5).

Lordi, JA, Mates, RE, and Moselle, JR (1966). *Computer Program for the Numerical Solution of Nonequilibrium Expansions of Reacting Gas Mixtures*. Contractor Report 472. nasa (cited on page 42).

Lorrain, P, Brieschenk, S, Capra, BR, and Boyce, RR (2012). "A Detailed Investigation of Nominally 2-D Radical-Farming Scramjet Combustion". In: *18th* aiaa/3af *International Space Planes and Hypersonic Systems and Technologies Conference*. Tours, France: aiaa-2012-5812. doi: 10.2514/6.2012-5812 (cited on page 359).

Lu, FK and Marren, DE (2002). "Principles of Hypersonic Test Facility Development". In: *Advanced Hypersonic Test Facilities*. Edited by FK Lu

and DE Marren. Volume 198. Progress in Astronautics and Aeronautics. Reston, Virginia: American Institute of Aeronautics and Astronautics. Chapter 2, pages 17–28 (cited on pages 34, 47).

Marren, D, Lewis, MJ, and Maurice, LQ (2001). "Experimention, Test, and Evaluation Requirements for Future Airbreathing Hypersonic Systems". *Journal of Propulsion and Power*, 17(6), pages 1361–1365 (cited on page 47).

Marshall, LA and Corpening, GP (2005). "A Chief Engineer's View of the nasa x-43a Scramjet Flight Test". In: *13th* aiaa/cira *International Space Planes and Hypersonics Systems and Technologies*. Capua, Italy: aiaa-2005-3332. doi: 10.2514/6.2005-3332 (cited on pages 18, 21).

Mattingly, JD (2006). *Elements of Propulsion: Gas Turbines and Rockets*. Edited by JA Schetz. aiaa Education Series. Washington, DC: American Institute of Aeronautics and Astronautics. doi: 10.2514/4.861789 (cited on page 125).

McBride, BJ, Zehe, MJ, and Gordon, S (2002). nasa *Glenn Coefficients for Calculating Thermodynamic Properties of Individual Species*. Technical Publication 2002-211556. Cleveland, Ohio, u.s.a.: nasa Glenn Research Center (cited on page 42).

McGilvray, M, Jacobs, PA, Morgan, RG, Gollan, RJ, and Jacobs, CM (2009). "Helmholtz Resonance of Pitot Pressure Measurements in Impulsive Hypersonic Text Facilities". aiaa *Journal*, 47(10), pages 2430–2439. doi: 10.2514/1.42543 (cited on pages 38, 56, 315).

McGilvray, M, Kirchhartz, RM, and Jazra, T (2010). "Comparison of Mach 10 Scramjet Measurements from Different Impulse Facilities". aiaa *Journal*, 48(8), pages 1647–1651. doi: 10.2514/1.J050025 (cited on page 159).

McGuire, JR (2007). "Ignition Enhancement for Scramjet Combustion". PhD Thesis. Sydney, Australia: The University of New South Wales (cited on page 246).

McRuer, D (1991). "Design and Modeling Issues for Integrated Airframe-Propulsion Control of Hypersonic Flight Vehicles". In: *American Control Conference*. Boston, Massachusetts, u.s.a (cited on pages 4, 154).

Mee, DJ (1993). *Uncertainty Analysis of Conditions in the Test Section of the T4 Shock Tunnel*. Research Report 1993/4. Brisbane, Australia: Division of Mechanical Engineering, The University of Queensland. url: https://espace.library.uq.edu.au/view/UQ:8434 (cited on page 291).

– (2002). *Dynamic Calibration of Force Balances*. Research Report 2002/6. Brisbane, Australia: Division of Mechanical Engineering, The Unversity of Queensland. url: https://espace.library.uq.edu.au/view/UQ:84101 (cited on pages 4, 77, 92, 252, 263).

Mee, DJ (2003). "Dynamic Calibration of Force Balances for Impulse Hypersonic Facilities". *Shock Waves*, 12, pages 443–455. DOI: 10.1007/s00193-003-0181-6 (cited on pages 75, 77, 80, 106, 258, 263).

– (2007). HYFORCE *Computer Program for Numerical Deconvolution. Version 1.6*. Technical report. Brisbane, Australia: Department of Mechanical Engineering, The University of Queensland (cited on pages 81, 84, 85, 252).

Mee, DJ, Daniel, WJT, and Simmons, JM (1992). "Three-component Aerodynamic Force Measurements in Hypervelocity Impulse Facilities". In: *11th Australasian Fluid Mechanics Conference*. Edited by MR Davis and GJ Walker. Volume 1. Hobart, Australia: The University of Tasmania, pages 55–58. ISBN: 0 85901 519 X (cited on page 76).

– (1996). "Three-Component Force Balance for Flows of Millisecond Duration". AIAA *Journal*, 34(3), pages 590–595. DOI: 10.2514/3.13108 (cited on pages 73, 76).

Mitani, T, Hiraiwa, T, Tarukawa, Y, and Masuya, G (2002). "Drag and Total Pressure Distributions in Scramjet Engines at Mach 8 Flight". *Journal of Propulsion and Power*, 18(4), pages 953–960. DOI: 10.2514/2.6022 (cited on pages 22, 23).

Mitani, T, Kanda, T, and Hiraiwa, T (1999). "Drags in Scramjet Engine Testing: Experimental and Computational Fluid Dynamics Studies". *Journal of Propulsion and Power*, 15(4), pages 578–583. DOI: 10.2514/2.5466 (cited on pages 22, 132, 135).

Mitani, T, Tomioka, S, Kanda, T, Chinzei, N, and Kouchi, T (2003). "Scramjet Performance Achieved in Engine Tests from M4 to M8 Flight Conditions". In: *12th* AIAA *International Space Planes and Hypersonic Systems and Technologies*. Norfolk, Virginia, U.S.A: AIAA-2003-7009. DOI: 10.2514/6.2003-7009 (cited on page 22).

Moule, Y and Smart, MK (2013). "Performance Analysis of a Mach 12 Scramjet at Off-Design Conditions". *Journal of Propulsion and Power*, 29(1), pages 282–285. DOI: 10.2514/1.B34563 (cited on pages 12, 15, 147, 166, 195, 206).

Murthy, SNB and Curran, ET, editors (2001). *Scramjet Propulsion*. Progress in Astronautics and Aeronautics 189. Reston, Virginia: AIAA. DOI: 10.2514/4.866609 (cited on page 9).

NASA (1976). *U.S. Standard Atmosphere 1976*. Technical Memorandum X-74335. NASA (cited on pages 45, 46).

NATO, AVT Working Group 10 (2006). *Technologies for Propelled Hypersonic Flight*. RTO Technical Report AVT-007-V2. North Atlantic Treaty Organisation (cited on page 5).

Oates, GC (1997). *Aerothermodynamics of Gas Turbine and Rocket Propulsion*. Edited by J Przemieniecki. Education Series. aiaa. doi: 10.2514/4.861345 (cited on pages 2, 71).

Odam, J (2004). "Scramjet Experiments using Radical Farming". PhD Thesis. Brisbane, Australia: The University of Queensland (cited on page 13).

Odam, J and Paull, A (2007). "Radical Farming in Scramjets". In: *New Results in Numerical and Experimental Fluid Mechanics VI. Contributions to the 15th* stab/dglr *Symposium*. Edited by C Tropea, S Jakirlic, HJ Heinemann, R Henke, and H H´onlinger. Notes on Numerical Fluid Mechanics and Multidisciplinary Design 96. Berlin: Springer-Verlag, pages 276–283. isbn: 978-3-540-74460-3 (cited on page 13).

Paull, A (1996). "A Simple Shock Tunnel Driver Gas Detector". *Shock Waves*, 6(5). Technical Note, pages 309–312. doi: 10.1007/PL00022719 (cited on page 69).

Paull, A, Stalker, RJ, and Mee, DJ (1995a). "Experiments on Supersonic Combustion Ramjet Propulsion in a Shock Tunnel". *Journal of Fluid Mechanics*, 296, pages 159–183. doi: 10.1017/S0022112095002096 (cited on pages 27–30, 74, 76, 128, 132).

– (1995b). "Scramjet Thrust Measurement in a Shock Tunnel". *The Aeronautical Journal*, 99(984), pages 161–163 (cited on pages 27, 57).

pcb Piezotronics Inc. (2013). *Introduction to Piezoelectric Pressure Sensors*. url: http://www.pcb.com/TechSupport/Tech_Pres (cited on pages 231, 246).

Pellett, GL, Bruno, C, and Chinitz, W (2002). "Review of Air Vitiation Effects on Scramjet Ignition and Flameholding Combustion Processes". In: *38th* aiaa/asme/sae/asee *Joint Propulsion Conference and Exhibit*. Indianapolis, IN, u.s.a: aiaa-2002-3880. doi: 10.2514/6.2002-3880 (cited on pages 48, 152).

Porter, LM, Paull, A, Mee, DJ, and Simmons, JM (1994). "Shock Tunnel Measurements of Hypervelocity Blunted Cone Drag". aiaa *Journal*, 32(12), pages 2476–2477. doi: 10.2514/3.12318 (cited on pages 27, 74, 76).

Prost, R and Goutte, R (1984). "Discrete Constrained Iterative Deconvolution Algorithms with Optimized Rate of Convergence". *Signal Processing*, 7(3), pages 209–230. doi: 10.1016/0165-1684(84)90001-X (cited on pages 81, 85, 252, 256).

Pudsey, AS, Boyce, RR, and Wheatley, V (2013). "Hypersonic Viscous Drag Reduction via Multiporthole Injector Arrays". *Journal of Propulsion and Power*, 29(5), pages 1087–1096. doi: 10.2514/1.B34782 (cited on pages 134, 135).

Pulsonetti, M (1995). *Experimental Methods for a Scramjet Scaling Study*. Research Report 1995/7. Brisbane, Australia: Mechanical Engineering Department, The University of Queensland (cited on page 246).

Rao, SS (2004). *Mechanical Vibrations*. 4th edition. Pearson Prentice Hall (cited on page 64).

Razzaqi, SA and Smart, MK (2011). "Hypervelocity Experiments on Oxygen Enrichment in a Hydrogen-Fueled Scramjet". aiaa *Journal*, 49(7), pages 1488–1497. doi: 10.2514/1.J050866 (cited on page 152).

Ridings, AN (2012). "uq's T4 Shock Tunnel Data Acquisition System". In: *National Instruments Technical Symposium 2012*. Brisbane, Queensland, Australia (cited on pages 41, 238).

Riedmüller, D (2008). "Determination of Boundary Layer Transition in a Reflected Shock Tunnel Nozzle". Master's thesis. Institut für Raumfahrtsysteme, Universität Stuttgart and Department of Mechanical Engineering, The University of Queensland (cited on pages 42, 292).

Robinson, MJ (2003a). *Calibration Techniques, Results and Supporting Documentation for the T4 Three-Component Force Balance*. Research Report 2003/2. Brisbane, Australia: Division of Mechanical Engineering, The University of Queensland (cited on pages 77, 80, 98, 99, 205, 260).

– (2003b). *Experimental Results and Supporting Documentation for the T4 Three-Component Force Balance*. Research Report 2003/4. Brisbane, Australia: Division of Mechanical Engineering, The University of Queensland (cited on pages 64, 77).

– (2003c). fea *of the* nasa/gasl pgu *and* t4 *Three-Component Force Balances*. Research Report 2003/5. Brisbane, Australia: Division of Mechanical Engineering, The University of Queensland (cited on page 77).

– (2003d). "Simultaneous Lift, Moment and Thrust Measurements on a Scramjet in Hypervelocity Flow". PhD Thesis. Brisbane, Australia: The University of Queensland (cited on pages 27, 30, 33, 57, 62, 73, 77, 78, 109, 171, 205, 207, 251, 263).

Robinson, MJ, Mee, DJ, and Paull, A (2006). "Scramjet Lift, Thrust and Pitching-Moment Characteristics Measured in a Shock Tunnel". *Journal of Propulsion and Power*, 22(1), pages 85–95. doi: 10.2514/1.15978 (cited on pages 6, 30, 31, 77).

Robinson, MJ, Mee, DJ, Tsai, CY, and Bakos, RJ (2004). "Three Component Force Measurements on a Large Scramjet in a Shock Tunnel". *Journal of Spacecraft and Rockets*, 41(3), pages 416–425. doi: 10.2514/1.10699 (cited on pages 77, 207).

Robinson, MJ, Rowan, SA, and Odam, J (2003). *T4 Free Piston Shock Tunnel Operator's Manual*. Research Report 2003/1. Updated June 2007 by Mee, D. J.; Hitchcock, K. W. and Malcolm, D. J. M. Brisbane, Australia:

Department of Mechanical Engineering, The University of Queensland (cited on page 243).

Robinson, MJ, Schramm, JM, and Hannemann, K (2007). "An Investigation into Internal and External Force Balance Configurations for Short Duration Wind Tunnels". In: *New Results in Numerical and Experimental Fluid Mechanics VI. Contributions to the 15th* stab/dglr *Symposium*. Edited by C Tropea, S Jakirlic, HJ Heinemann, R Henke, and H H´onlinger. Notes on Numerical Fluid Mechanics and Multidisciplinary Design 96. Berlin: Springer-Verlag, pages 129–136. isbn: 978-3-540-74460-3 (cited on pages 74, 75, 77).

– (2011). "Design and Implementation of an Internal Stress-Wave Force Balance in a Shock Tunnel". ceas *Space Journal*, 1, pages 45–57. doi: 10.1007/s12567-010-0003-5 (cited on pages 74, 75, 77).

Rogers, RC, Capriotti, DP, and Guy, RW (1998). "Experimental Supersonic Combustion Research at nasa Langley". In: *20th* aiaa *Advanced Measurement and Ground Testing Technology Conference*. Albuquerque, New Mexico, u.s.a: aiaa-98-2506. doi: 10.2514/6.1998-2506 (cited on pages 2, 3).

Rogers, RC and Schexnayder, CJ (1981). *Chemical Kinetic Analysis of Hydrogen-Air Ignition and Reaction Times*. Technical Paper 1856. Hampton, Virginia, u.s.a.: nasa Langley Research Center (cited on pages 152, 154, 155).

Rogers, RC, Shih, AT, and Hass, NE (2005). "Scramjet Development Tests Supporting the Mach 10 Flight of X-43". In: *13th* aiaa/cira *International Space Planes and Hypersonic Systems and Technologies Conference*. Capua, Italy: aiaa-2005-3351. doi: 10.2514/6.2005-3351 (cited on page 19).

Rogers, RC, Shih, AT, Tsai, CY, and Foelsche, RO (2001). "Scramjet Tests in a Shock Tunnel at Flight Mach 7, 10 and 15 Conditions". In: *37th* aiaa/asme/sae/asee *Joint Propulsion Conference and Exhibit*. Salt Lake City, Utah, u.s.a: aiaa-2001-3241. doi: 10.2514/6.2001-3241 (cited on pages 19, 21).

Rogers, RC and Weidner, EH (1993). "Scramjet Fuel-Air Mixing Establishment in a Pulse Facility". *Journal of Propulsion and Power*, 9(1), pages 127–133. doi: 10.2514/3.11494 (cited on pages 69, 334).

Rowan, SA and Paull, A (2006). "Performance of a Scramjet Combustor with Combined Normal and Tangential Fuel Injection". *Journal of Propulsion and Power*, 22(6), pages 1334–1338. doi: 10.2514/1.18744 (cited on page 77).

Rowan, SA, Takahashi, M, Sunami, T, Itoh, K, Komuro, T, and Sato, K (2005). "Viscous Drag Reduction in a Mach 12 Scramjet Engine". In: *13th* aiaa/cira *International Space Planes and Hypersonic Systems and*

Technologies Conference. Capua, Italy: AIAA-2005-3356. DOI: 10.2514/6.2005-3356 (cited on pages 22, 25, 26).

Sacher, P (2010). *Engineering Engine/Airframe Integration for Fully Reusable Space Transportation Systems*. RTO Educational Note AVT-185. AVT/VKI Lecture Series, von Karman Institute. NATO (cited on pages 3, 5).

Sahoo, N, Suryavamshi, K, Reddy, KPJ, and Mee, DJ (2005). "Dynamic Force Balances for Short-Duration Hypersonic Testing Facilities". *Experiments in Fluids*, 38(5), pages 606–614. DOI: 10.1007/s00348-005-0932-5 (cited on page 77).

Sanderson, SR and Simmons, JM (1991). "Drag Balance for Hypervelocity Impulse Facilities". AIAA *Journal*, 29(12), pages 2185–2191. DOI: 10.2514/3.10858 (cited on pages 27, 73, 76, 80, 97).

Schetz, JA, Maddalena, L, and Burger, SK (2010). "Molecular Weight and Shock-Wave Effects on Transverse Injection in Supersonic Flow". *Journal of Propulsion and Power*, 26(5), pages 1102–1113. DOI: 10.2514/1.49355 (cited on page 152).

Schneider, SP (2008). "Development of Hypersonic Quiet Tunnels". *Journal of Spacecraft and Rockets*, 45(4), pages 641–664. DOI: 10.2514/1.34489 (cited on page 144).

Shimura, T, Sakuranaka, N, Sunami, T, and Tani, K (2001). "Thrust, Lift, and Pitching Moment of a Scramjet Engine". *Journal of Propulsion and Power*, 17(3), pages 617–621. DOI: 10.2514/2.5786 (cited on pages 21–23).

Simeonides, G (2003). "Correlation of Laminar-Turbulent Transition Data over Flat Plates in Supersonic/Hypersonic Flow including Leading Edge Bluntness Effects". *Shock Waves*, 12(6), pages 497–508. DOI: 10.1007/s00193-003-0184-3 (cited on pages 4, 53).

Simmons, JM (1995). "Measurement Techniques in High-Enthalpy Hypersonic Facilities". *Experimental Thermal and Fluid Science*, 10(4), pages 454–469. DOI: 10.1016/0894-1777(94)00066-H (cited on page 47).

Simmons, JM, Daniel, WJT, Mee, DJ, and Tuttle, SL (1993). "Force Measurement in Hypervelocity Impulse Facilities". In: *New Trends in Instrumentation for Hypersonic Research*. Edited by A Boutier. NATO ASI Series E: Applied Sciences – Vol. 224. Dordrecht: Kluwer Academic Publishers, pages 285–294. DOI: 10.1007/978-94-011-1828-6 (cited on pages 6, 27, 76).

Skinner, KA (1994). "Mass Spectrometry in Shock Tunnel Experiments of Hypersonic Combustion". PhD Thesis. Brisbane, Australia: The University of Queensland (cited on pages 69, 70).

Smart, MK (1999). "Design of Three-Dimensional Hypersonic Inlets with Rectangular-to-Elliptical Shape Transition". *Journal of Propulsion and*

Power, 15(3), pages 408–416. DOI: 10.2514/2.5459 (cited on pages 5, 9, 10, 49, 52).
– (2001). "Experimental Testing of a Hypersonic Inlet with Rectangular-to-Elliptical Shape Transition". *Journal of Propulsion and Power*, 17(2), pages 276–283. DOI: 10.2514/2.5774 (cited on pages 5, 10, 12, 62).
– (2006). "Flight Data Analysis of the HyShot 2 Scramjet Flight Experiment". AIAA *Journal*, 44(10), pages 2366–2375 (cited on page 48).
– (2012). "How Much Compression Should a Scramjet Inlet Do?" AIAA *Journal*, 50(3)Jackson, T. Pages 610–619. DOI: 10.2514/1.J051281 (cited on pages 194–196).

SMART, MK and RUF, EG (2006). "Free-Jet Testing of a REST Scramjet at Off-Design Conditions". In: *25th* AIAA *Aerodynamic Measurement Technology and Ground Testing Conference*. San Francisco, California, U.S.A: AIAA-2006-2955. DOI: 10.2514/6.2006-2955 (cited on pages 12, 13).

SMART, MK and TETLOW, MR (2009). "Orbital Delivery of Small Payloads using Hypersonic Airbreathing Propulsion". *Journal of Spacecraft and Rockets*, 46(1), pages 117–125 (cited on page 3).

SMART, MK and TREXLER, CA (2004). "Mach 4 Performance of Hypersonic Inlet with Rectangular-to-Elliptical Shape Transition". *Journal of Propulsion and Power*, 20(2), pages 288–293. DOI: 10.2514/1.1296 (cited on pages 10, 12, 13).

SMITH, AL and MEE, DJ (1996a). "Drag Measurements in a Hypervelocity Expansion Tube". *Shock Waves*, 6, pages 161–166. DOI: 10.1007/s001930050033 (cited on pages 27, 76).
– (1996b). "Dynamic Strain Measurement using Piezoelectric Polymer Film". *Journal of Strain Analysis for Engineering Design*, 31(6), pages 463–465 (cited on page 76).

SMITH, AL, MEE, DJ, DANIEL, WJT, and SHIMODA, T (2001). "Design, Modelling and Analysis of a Six Component Force Balance for Hypervelocity Wind Tunnel Testing". *Computers and Structures*, 79, pages 1077–1088. DOI: 10.1016/S0045-7949(01)00005-0 (cited on pages 73, 76).

SMITH, EC (1966). "The Starting Process in a Hypersonic Nozzle". *Journal of Fluid Mechanics*, 24(4), pages 625–640. DOI: 10.1017/s0022112066000880 (cited on page 67).

STALKER, RJ (1966). "The Free-Piston Shock Tunnel". *The Aeronautical Quarterly*, 17, pages 351–370 (cited on pages 33, 35).
– (1967). "A Study of the Free-Piston Shock Tunnel". AIAA *Journal*, 5(12), pages 2160–2165. DOI: 10.2514/3.4402 (cited on pages 33, 35, 36).
– (1989). "Recent Developments with Free Piston Drivers". In: *17th International Symposium on Shock Waves and Shock Tubes*. Edited by YW KIM. Volume 208. American Institute of Physics Conference Proceed-

ings. Bethlehem, PA, U.S.A: American Institute of Physics, pages 96–105 (cited on pages 33, 35).

Stalker, RJ (2005). "Control of Hypersonic Turbulent Skin Friction by Boundary-Layer Combustion of Hydrogen". *Journal of Spacecraft and Rockets*, 42(4), pages 577–587. DOI: 10.2514/1.8699 (cited on pages 17, 50, 134, 139).

– (2006a). "Modern Developments in Hypersonic Wind Tunnels". *The Aeronautical Journal*, 110(1103), pages 21–39 (cited on page 35).

– (2006b). "Scramjets, Sub-orbital Flight and Skin Friction". In: *14th* AIAA/AHI *Space Planes and Hypersonic Systems and Technologies Conference*. Culpepper Memorial Lecture. Canberra, Australia: AIAA-2006-8156. DOI: 10.2514/6.2006-8156 (cited on pages 3, 24, 34, 139).

Stalker, RJ and Morgan, RG (1988). "The University of Queensland Free Piston Shock Tunnel T4– Initial Operation and Preliminary Calibration". In: *4th National Space Engineering Symposium*. Adelaide, SA, Australia (cited on pages 34, 291).

Stalker, RJ and Paull, A (1998). "Experiments on Cruise Propulsion with a Hydrogen Scramjet". *The Aeronautical Journal*, 102(1011), pages 37–43 (cited on pages 27, 29).

Stalker, RJ, Paull, A, Mee, DJ, Morgan, RG, and Jacobs, PA (2005). "Scramjets and Shock Tunnels – The Queensland Experience". *Progress in Aerospace Sciences*, 41, pages 471–513. DOI: 10.1016/j.paerosci.2005.08.002 (cited on pages 6, 17, 29, 30, 34, 47, 48).

Stalker, RJ and Pulsonetti, M (2004). *Experiments on Scaling of Supersonic Combustion*. Research Report 2004/13. Brisbane, Australia: Division of Mechanical Engineering, The University of Queensland (cited on pages 43, 159).

Suraweera, M (2006). "Reduction of Skin Friction Drag in Hypersonic Flow by Boundary Layer Combustion". PhD. Brisbane, Australia: The University of Queensland (cited on page 34).

Suraweera, M and Smart, MK (2008). "TZM Mach 10 Nozzle Insert Test in the T4 Shock Tunnel". Unpublished Technical Report, The University of Queensland. Brisbane, Australia (cited on page 38).

– (2009). "Shock Tunnel Experiments with a Mach 12 Rectangular-to-Elliptical Shape-Transition Scramjet at Off-Design Conditions". *Journal of Propulsion and Power*, 25(3), pages 555–564. DOI: 10.2514/1.37946 (cited on pages iii, 5, 12–17, 33, 49, 50, 141, 152, 153, 159, 160, 162, 166, 168, 171).

Takahashi, M, Komuro, T, Sato, K, Itoh, K, Tanno, H, and Ueda, S (1999). "Development of a New Force Measurement Method for Scramjet Testing". In: *9th* AIAA *International Space Planes and Hypersonic Systems*

and Technologies Conference. Norfolk, VA, U.S.A: AIAA-99-4961. DOI: 10.2514/6.1999-4961 (cited on pages 21, 22).

Takahashi, M, Komuro, T, Sato, K, Kodera, M, Tanno, H, and Itoh, K (2006). "Effect of Combustor Shape on Scramjet Characteristics at Hypervelocity Condition over Mach 10 Flight". In: *14th AIAA/AHI Space Planes and Hypersonic Systems and Technologies Conference*. Canberra, Australia: AIAA-2006-8024. DOI: 10.2514/6.2006-8024 (cited on pages 24–26).

Takahashi, M, Sunami, T, Hideyuki, T, Komuro, T, and Itoh, K (2005). "Performance Characteristics of a Scramjet Engine at Mach 10 to 15 Flight Condition". In: *13th AIAA/CIRA International Space Planes and Hypersonic Systems and Technologies Conference*. Capua, Italy: AIAA-2005-3350. DOI: 10.2514/6.2005-3350 (cited on page 22).

Tan, H, Li, LL, Wen, Y, and Zhang, Q (2011). "Experimental Investigation of the Unstart Process of a Generic Hypersonic Inlet". AIAA *Journal*, 49(2), pages 279–288. DOI: 10.2514/1.J050200 (cited on page 4).

Tanimizu, K (2008). "Nozzle Optimization Study and Measurements for a Quasi-Axisymmetric Scramjet Model". PhD Thesis. Brisbane, Australia: The University of Queensland (cited on page 30).

Tanimizu, K, Mee, DJ, Stalker, RJ, and Jacobs, PA (2009). "Drag Force on Quasi-Axisymmetric Scramjets at Various Flight Mach Numbers: Theory and Experiment". *Shock Waves*, 19(2), pages 83–93. DOI: 10.1007/s00193-009-0194-x (cited on pages 17, 27, 30–32, 77, 132, 135).

– (2011). "Thrust Nozzle Design Study for a Quasi-Axisymmetric Scramjet-Powered Vehicle". *Journal of Propulsion and Power*, 27(1), pages 40–49. DOI: 10.2514/1.48586 (cited on pages 4, 27, 30, 31).

Tanno, H, Kodera, M, Komuro, T, Sato, M, Takahashi, M, and Itoh, K (2005). "Aerodynamic Force Measurement on a Large-Scale Model in a Short Duration Test Facility". *Review of Scientific Instruments*, 76(3), pages 1–5. DOI: 10.1063/1.1865815 (cited on pages 22, 25).

Tanno, H, Paull, A, and Stalker, RJ (2001). "Skin-Friction Measurements in a Supersonic Combustor with Crossflow Fuel Injection". *Journal of Propulsion and Power*, 17(6), pages 1333–1338. DOI: 10.2514/2.5883 (cited on page 77).

Tomioka, S, Kobayashi, K, Kudo, K, Murakami, A, and Kanda, T (2006). "Performance of Supersonic Combustors with Fuel Injection in Diverging Section". *Journal of Propulsion and Power*, 22(1), pages 111–119. DOI: 10.2514/1.16041 (cited on page 4).

Turner, JC (2010). "An Experimental Investigation of Inlet Fuel Injection in a Three-Dimensional Scramjet Engine". PhD Thesis. Brisbane, Aus-

tralia: The University of Queensland (cited on pages 12, 57, 123, 132, 135, 152).

Turner, JC and Smart, MK (2008). "Application of Radical Farming to a 3-D Scramjet at Mach 8". In: *46th* aiaa *Aerospace Sciences Meeting and Exhibit*. Reno, Nevada, u.s.a: aiaa-2008-101. doi: 10.2514/6.2008-101 (cited on pages 10, 12, 13, 54).

– (2010). "Application of Inlet Injection to a Three-Dimensional Scramjet at Mach 8". aiaa *Journal*, 48(4), pages 829–838. doi: 10.2514/1.J050052 (cited on pages 5, 12, 13, 129).

– (2013). "Mode Change Characteristics of a Three-Dimensional Scramjet at Mach 8". *Journal of Propulsion and Power*, 29(4), pages 982–990. doi: 10.2514/1.B34569 (cited on pages 12, 149).

Tuttle, SL (1996). "Measuring Thrust and Drag in a Hypersonic Impulse Facility". PhD Thesis. Brisbane, Australia: The University of Queensland (cited on page 27).

Tuttle, SL, Mee, DJ, and Simmons, JM (1994). "Lift, Drag and Thrust Measurement in a Hypersonic Impulse Facility". In: *18th* aiaa *Aerospace Ground Testing Conference*. aiaa-94-2596. doi: 10.2514/6.1994-2596 (cited on pages 27, 76).

– (1995). "Drag Measurements at Mach 5 using a Stress Wave Force Balance". *Experiments in Fluids*, 19(5), pages 336–341. doi: 10.1007/BF00203418 (cited on pages 27, 76).

Tuttle, SL and Simmons, JM (1992). "Hypersonic Drag Measurement in Free Piston Shock Tunnels". In: *11th Australasian Fluid Mechanics Conference*. Edited by MR Davis and GJ Walker. Volume 1. Hobart, Australia: The University of Tasmania, pages 291–294. isbn: 0 85901 519 X (cited on page 76).

van Driest, ER (1956). "The Problem of Aerodynamic Heating". *Aeronautical Engineering Review*, 15, pages 26–41 (cited on page 52).

Vandenkerckhove, J and Barréré, M (1997). "Energy Management (in Hypersonic Propulsion Systems)". In: *The Synerjet Engine: Airbreathing/Rocket Combined-Cycle Propulsion for Tommorow's Space Transports*. Edited by WJD Escher. Volume pt-54. Progress in Technology aiaa-1996-4556. Society of Automotive Engineers, Inc. Chapter 16, pages 389–403 (cited on page 57).

Voland, RT (1990). "Methods for Determining the Internal Thrust of Scramjet Engine Modules from Experimental Data". In: *26th* aiaa/sae/asme/asee *Joint Propulsion Conference*. Orlando, Florida, u.s.a: aiaa-90-2340. doi: 10.2514/6.1990-2340 (cited on page 204).

Voland, RT, Huebner, LD, and McClinton, CR (2006). "x-43a Hypersonic Vehicle Technology Development". *Acta Astronautica*, 59(1-

5), pages 181–191. DOI: 10.1016/j.actaastro.2006.02.021 (cited on page 18).

Waltrup, PJ and Billig, FS (1973). "Structure of Shock Waves in Cylindrical Ducts". AIAA *Journal*, 11(10), pages 1404–1408 (cited on page 149).

White, JA and Morrison, JH (1999). "A Pseudo-Temporal Multi-Grid Relaxation Scheme for Solving the Parabolized Navier-Stokes Equations". In: *14th* AIAA *Computational Fluid Dynamics Conference*. Norfolk, VA, U.S.A: AIAA-1999-3360. DOI: 10.2514/6.1999-3360 (cited on page 115).

Wilcox, DC (1998). *Turbulence Modelling for* CFD. California, U.S.A: DCW Industries, Inc (cited on page 117).

– (2006). *Turbulence Modelling for* CFD. 3rd edition. California, U.S.A: DCW Industries, Inc (cited on pages 42, 290).

Williams, C (2010). "Redesign of the T4 Shock Tunnel Mach 10 Nozzle Throat". Master of Engineering. Brisbane, Australia: The University of Queensland (cited on pages 38, 294).

Wise, DJ and Smart, MK (2012). "Forced Transition of Hypervelocity Boundary Layers". In: *18th* AIAA/3AF *International Space Planes and Hypersonic Systems and Technologies Conference*. Tours, France: AIAA-2012-5866. DOI: 10.2514/6.2012-5866 (cited on pages 53, 203, 206).

Witte, DW, Huebner, LD, Trexler, CA, and Cabell, KF (2003). "Propulsion Airframe Integration Test Techniques for Hypersonic Airbreathing Configurations at NASA Langley Research Center". In: *39th* AIAA/ ASME/SAE/ASEE *Joint Propulsion Conference*. Huntsville, Alabama, U.S.A: AIAA-2003-4406. DOI: 10.2514/6.2003-4406 (cited on page 5).

Yatsuyanagi, N, Chinzei, N, Mitani, T, Wakamatsu, Y, Masuya, G, Iwagami, S, Endo, M, and Hanus, G (1998). "Ramjet Engine Test Facility (RJTF) in NAL-KRC, Japan". In: *8th* AIAA *International Space Planes and Hypersonic Systems and Technologies Conference*. Norfolk, Virginia, U.S.A: AIAA-1998-1511. DOI: 10.2514/6.1998-1511 (cited on page 21).

Zander, F and Morgan, RG (2009). "Composite Scramjet Combustor". In: *16th* AIAA/DLR/DGLR *International Space Planes and Hypersonics Systems and Technologies Conference*. Bremen, Germany: AIAA-2009-7354. DOI: 10.2514/6.2009-7354 (cited on page 55).

CALIBRATION METHODS

A.1 INTRODUCTION

A

This appendix presents the calibration methods used for the nozzle supply pressure transducers, the engine and fuel plenum pressure transducers and the engine fuel system. For each calibration the apparatus is shown, sample data are provided and the results are summarised. Uncertainty analysis for the nozzle supply, engine and fuel plenum pressure transducers is presented. The uncertainty analysis for the fuel system, being more complex, is presented in Appendix C.

A.2 NOZZLE SUPPLY TRANSDUCERS

Two PCB® piezo-electric transducers, model number 109M91, were used to measure the pressure in the nozzle supply region of the T4 Stalker Tube. Accurate measurement of this pressure is critical for determination of the test flow conditions (Section 3.3). This section describes the method used to calibrate the nozzle supply pressure transducers. Sample results are provided and calculation of the calibration uncertainty is detailed.

Labelled as SPA and SPB, the nozzle supply transducers were calibrated dynamically using the hydraulic rig shown in Figure A.1. Taking advantage of the incompressibility of oil, this rig permits pressures up to approximately 50 MPa to be (safely and easily) applied to the sensor face through the manual adjustment of a piston. The hydraulic rig is capable of generating a rapid pressure *decrease*, opposite to the pressure *increase* that actually occurs during an experiment in the T4 Stalker Tube. Because PCB® piezo-electric transducers exhibit a linear response and very low hysteresis, the difference between the hydraulic rig and experiment does not affect the validity of the calibration method.[1]

Each transducer is calibrated against a USG SOLFRUNT® model 1981 high pressure bourdon tube gauge of range 0 to 80 000 kPa. A manual ball valve separates a reservoir from the oil-filled tube to which the piston, transducer and reference gauge are connected. The initial state of the rig is such that the the piston is wound out, the reservoir is (nearly) empty

1 The voltage output of a piezo-electric transducer is proportional to the applied pressure. When the pressure is held constant, the output signal decays to zero at a rate that is governed by the time constant of the sensor (PCB Piezotronics Inc., 2013). If the applied pressure is removed once the output signal has decayed, the resulting negative voltage change is equal in magnitude to the positive voltage change that occured when the pressure was first applied.

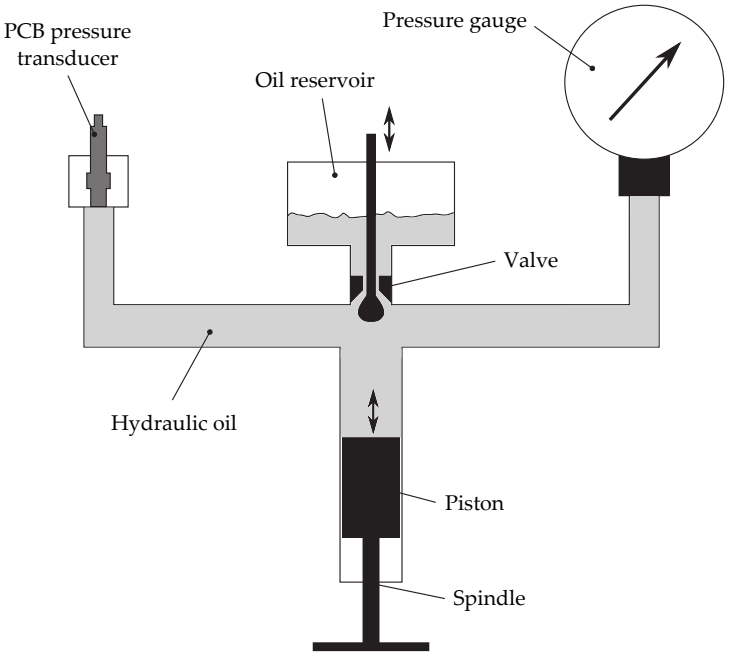

(a) Schematic, adapted from Kirchhartz (2010)

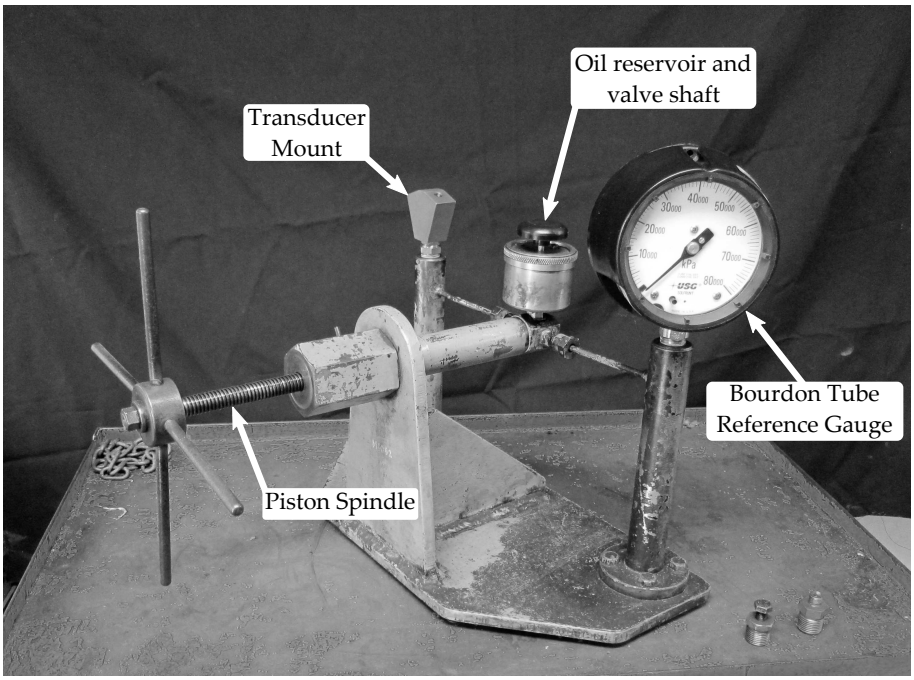

(b) Photograph. The transducer mount shown in this photograph is a recent modification (circa June 2012) that allows the two nozzle supply pressure transducers to be calibrated simultaneously.

Figure A.1 – Hydraulic rig used to calibrate the nozzle supply pressure transducers

and the manual ball valve is closed. The spindle is used to push the piston forward, compressing the oil in the main tube and causing an increase in pressure. Once the pressure measured by the reference gauge is at the desired value, the system is held until the voltage output from the piezoelectric transducer has sufficiently decayed. The shaft of the ball valve is then struck with a hammer, causing the valve to open and allowing oil to flow into the reservoir. Due to the incompressibility of hydraulic oil, a small change in the volume rapidly releases the pressure applied to the transducer.

Using the data acquisition system of the T4 Stalker Tube (see Section 3.2.3) the transducer output is recorded for a total duration of 120 ms at a sampling frequency of 1 MHz (1 µs timebase). A typical output signal for SPB at a calibration pressure of 41 MPa is provided in Figure A.2. The magnitude of the change in signal between the first 15 ms and the indicated averaging window is proportional to the change in pressure. Each transducer is calibrated over the range 16 to 46 MPa at intervals of 5 MPa. Typically three repeat calibrations are completed at each pressure level.

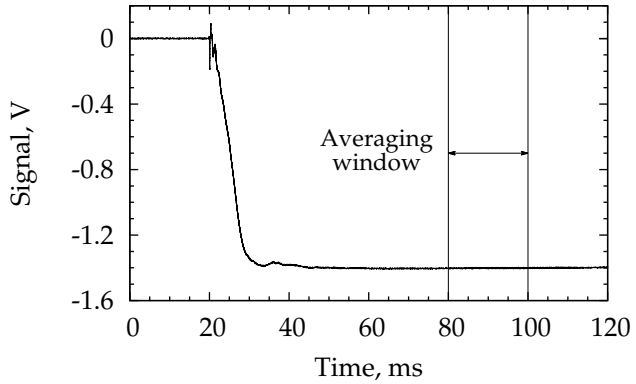

Figure A.2 – A typical transient voltage signal obtained using the oil calibration rig. The data are for gauge SPB at a nominal pressure of 41 MPa (calibration SPB_41000KPA_1).

Due to the importance of the nozzle supply pressure measurement for the accurate determination of the test flow conditions, SPA and SPB are calibrated prior to the start of each experimental campaign that is conducted in the T4 Stalker Tube. For this thesis, a total of five sets of calibration data were analysed to determine an overall sensitivity for each transducer. The five data sets represented all the available calibration data that was recorded between the first and second test campaigns conducted for this thesis. Three sets were recorded by the author and one set each was recorded by Dr. Wilson Chan and Mr. Dylan Wise.

Table A.1 – Calibration Summary for the Nozzle Supply Pressure Transducers

(a) Calibration results over a 12 month period

Person	Month	Year	Sensitivity (10^{-5} V/kPa) SPA	SPB	Notes
Luke Doherty	March	2011	3.5063	3.4482	Early in campaign 1
Wilson Chan	September		3.6858	3.4047	KARI campaign
Dylan Wise	October		3.6087	3.4514	Nozzle survey campaign
Luke Doherty	November		3.5732	3.4635	Pre-campaign 2
Luke Doherty	February	2012	3.6129	3.4303	Post-campaign 2

(b) Overall calibration results

Gauge	Model	S/N	Range (MPa)	Sensitivity (10^{-5} V/kPa)	Calibration Uncertainty (%)
SPA	109M91	5563	120	3.5795	±2.09
SPB		5564		3.4465	±1.97

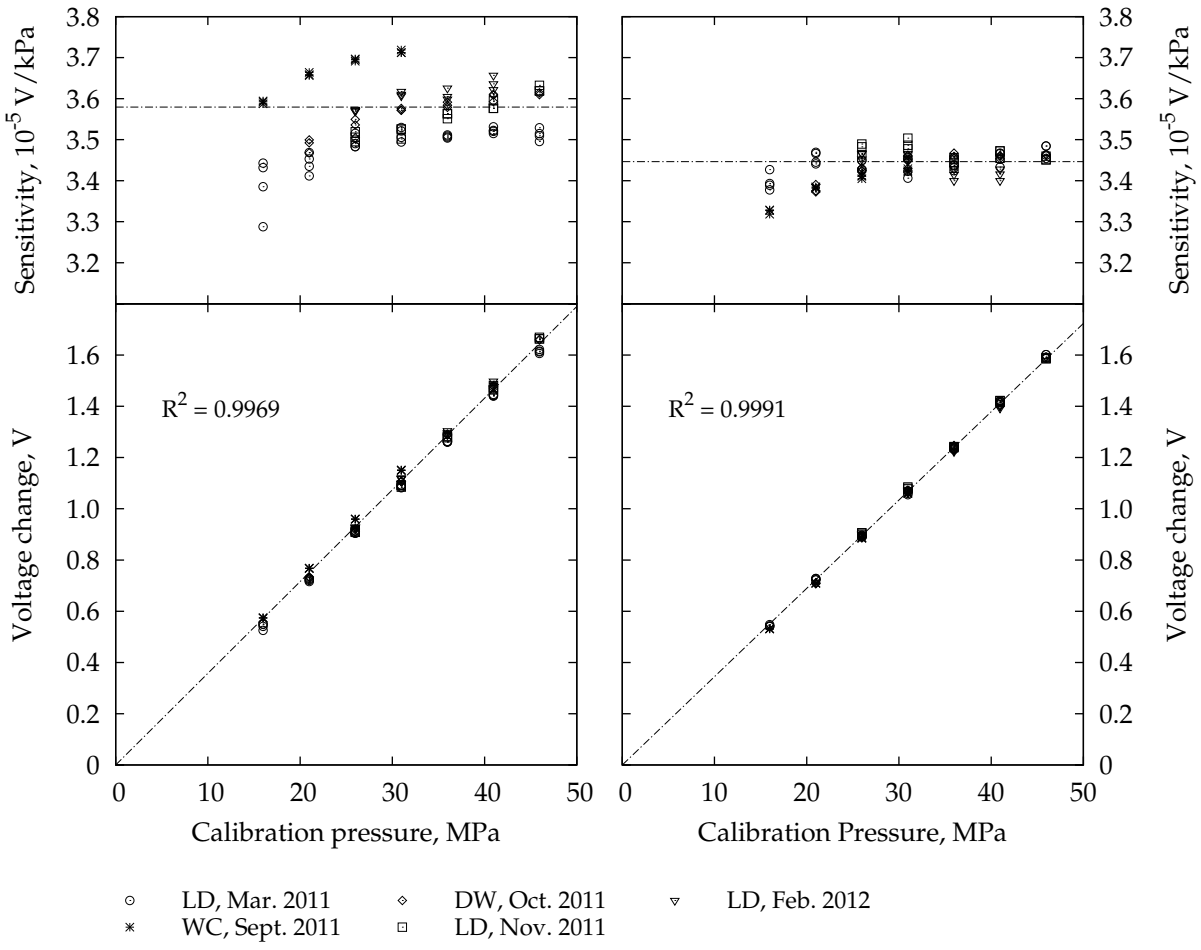

Figure A.3 – Calibration data for the nozzle supply pressure transducers. Data for SPA are given in the left column, data for SPB are given in the right column

The transducer sensitivity for each set of data is determined by plotting the magnitude of the measured voltage change[2] against the calibration pressure and finding the line of best fit that passes through the origin. Grouping the five sets of data together and applying the same method gives the overall sensitivity for each transducer. The results are summarised in Table A.1 and Figure A.3. In the lower half of Figure A.3 the measured change in voltage is plotted against the measured pressure for each calibration, while the individual sensitivities are provided in the upper half. These sensitivities are calculated by taking a straight-line fit between the origin and the data point of interest on the voltage-pressure graph. Each data set is represented by a different symbol. Data for SPA are given in the left column of Figure A.3 and data for SPB in the right column. The overall sensitivity of each gauge is indicated by a dashed line.

The sensitivities listed in Table A.1 for each data set do not display any significant trend with time and are to within $\pm 3\,\%$ of the overall sensitivity for SPA and to within $\pm 1.2\,\%$ for SPB. In Figure A.3, the measured voltages display good linearity with pressure and lie close to the line of best fit. The individual sensitivities computed for SPA exhibit greater variability than those computed for SPB. It is hypothesised that this increased variability is related to the damage to the ceramic coating on the head of SPA as shown in Figure 3.6. For this reason, only transducer SPB was used to process the experimental data for inclusion in this thesis.

Some variation with calibration pressure is exhibited by the individual sensitivities of each transducer. This variation is similar for each data set suggesting that it is caused by or related to the calibration rig. There are several difficulties associated with the hydraulic calibration rig. Firstly, because the oil pressure acts to hold the ball valve closed, achieving a rapid, clean opening of the valve is difficult and practically restricts the calibration pressure to be less than 50 MPa. Achieving three acceptable calibration signals typically requires on the order of 10 repeat hits, particularly at the higher calibration pressures.

Secondly, due to the design, the ball valve does not perfectly seal. The rate of leakage of oil past the valve and into the reservoir influences whether or not the calibration can be completed and the accuracy of the pressure recorded from the dial gauge (relative to the actual pressure applied to the transducer at the time the valve is opened). Leakage of oil also influences the decay of the transducer voltage output to zero.

Thirdly, the valve shaft has a diameter of only 6 mm and connects with the ball via a thin thread. This thread and the shaft are subject to damage from being repeatedly struck with a hammer during the calibration process. It is common for the rig to require maintenance after a set of calibrations has been completed.

2 To ensure consistency each set of data was (re)processed using the averaging window shown in Figure A.2.

The variation of the individual sensitivities with pressure that is observed in Figure A.3 is hypothesised to be primarily related to leakage of oil past the valve. Achieving a rapid opening of the valve may also influence the computed sensitivity. Despite this variation, the calibration data recorded using the hydraulic rig is considered of sufficient quality for use in this thesis. The uncertainty analysis for the overall sensitivity is presented in the next section.

A.2.1 *Calibration Uncertainty*

A concise summary of the uncertainty analysis for the hydraulic calibration rig is provided in this section. General details regarding experimental uncertainty analysis, as used in this thesis, are given in Appendix C.2. As described in the previous section, the overall sensitivity of each nozzle supply pressure transducer is calculated by fitting a linear equation of the form

$$V_t = S_t p \tag{A.1}$$

to the calibration data, where V_t is the output transducer voltage, p is the measured reference gauge pressure and S_t is the transducer sensitivity to be determined (i.e. the slope of a line of best fit). For this thesis the line of best fit was calculated using a weighted least squares method via. the MATLAB® function `robustfit`.

As discussed in Appendix C.2.3 the line of best fit is considered to be a data reduction equation for the calibration data. The sensitivity in Equation (A.1) is written as

$$S_t = f(V_{c,1}, V_{c,2}, \ldots, V_{c,N}, p_{c,1}, p_{c,2}, \ldots, p_{c,N}) \tag{A.2}$$

where $\{\{V_{c,i}, p_{c,i}\}\}_{i=1}^{N}$ is the set of calibration data. The form of function f depends on the method used to generate the line of best fit (and may not be able to be written analytically). The total systematic uncertainty is found by applying Equation (C.7) to Equation (A.2) to give[3]

$$\begin{aligned} B_{S_t}^2 = &\sum_{i=1}^{N}\left(\frac{\partial S_t}{\partial V_{c,i}}\right)B_{V_{c,i}}^2 + 2\sum_{i=1}^{N-1}\sum_{k=i+1}^{N}\left(\frac{\partial S_t}{\partial V_{c,i}}\right)\left(\frac{\partial S_t}{\partial V_{c,k}}\right)B_{V_{c,i}V_{c,k}} \\ &+ \sum_{i=1}^{N}\left(\frac{\partial S_t}{\partial p_{c,i}}\right)B_{p_{c,i}}^2 + 2\sum_{i=1}^{N-1}\sum_{k=i+1}^{N}\left(\frac{\partial S_t}{\partial p_{c,i}}\right)\left(\frac{\partial S_t}{\partial p_{c,k}}\right)B_{p_{c,i}p_{c,k}} \\ &+ 2\sum_{i=1}^{N}\sum_{k=i}^{N}\left(\frac{\partial S_t}{\partial V_{c,i}}\right)\left(\frac{\partial S_t}{\partial p_{c,k}}\right)B_{V_{c,i}p_{c,k}} \end{aligned} \tag{A.3}$$

3 This is Equation 7.27 from Coleman and Steele (1999) without the precision uncertainty terms.

where $B_{V_{c,i}}$ is the systematic uncertainty in transducer voltage, $B_{p_{c,i}}$ is the systematic uncertainty in pressure and $B_{V_{c,i}V_{c,k}}$, $B_{p_{c,i}p_{c,k}}$ and $B_{V_{c,i}p_{c,k}}$ are the covariance estimates for the correlated systematic uncertainties in different pairings of transducer voltage and pressure variables (Coleman and Steele, 1999, Section 4-2.3).

In this thesis the systematic uncertainty in transducer voltage was assumed to be $\pm 1\,\%$ of the measured value, due solely to installation effects in the calibration rig. The systematic uncertainty in the pressure measured using the bourdon gauge was assumed to consist of two elemental uncertainties: a constant uncertainty of $\pm 400\,\mathrm{kPa}$ for the gauge accuracy[4] and a constant uncertainty of $\pm 500\,\mathrm{kPa}$ for the gauge readability and leakage of oil past the valve.[5] The measurement of the transducer voltage and calibration pressure shared no elemental systematic uncertainties and so the covariance estimate $B_{V_{c,i}p_{c,k}} = 0$. The covariance estimate $B_{V_{c,i}V_{c,k}}$ for each pair of calibration transducer voltages was evaluated using Equation (C.10) under the assumption that the elemental systematic uncertainties were correlated across all five sets of calibration data. This assumption was considered reasonable since the same hydraulic rig was used for each data set. The same assumption was used when evaluating the covariance estimate $B_{p_{c,i}p_{c,k}}$ for each pair of calibration pressures.

Equation (A.3) was implemented in a MATLAB® script. The partial derivatives were estimated using finite difference and a perturbation of $\pm 0.01\,\%$ as recommended by Hudson et al. (2003, Section 7.2.4). The resulting total systematic uncertainty in the overall sensitivity for each transducer is

$$B_{S_t} = \begin{cases} \pm 1.71\,\% & \text{for SPA} \\ \pm 1.86\,\% & \text{for SPB} \end{cases} \tag{A.4}$$

Calculated using Equations (C.29) to (C.31), the precision uncertainty of the overall sensitivity is

$$P_{S_t} = \begin{cases} \pm 1.21\,\% & \text{for SPA} \\ \pm 0.65\,\% & \text{for SPB} \end{cases} \tag{A.5}$$

Based on the data plotted in Figure A.3 the larger precision uncertainty for SPA is not unexpected. Finally, the total calibration uncertainty for the

4 This corrsponds to $\pm 0.5\,\%$ of full-scale as stated by the supplier, Ross Brown Sales Pty. Ltd.

5 This corresponds to half of a single measurement division on the gauge. During a calibration the gauge was constantly monitored to ensure that the pressure did not noticeably decrease prior to the ball valve being opened. Thus uncertainty in pressure due to leakage past is grouped with the gauge readability error.

nozzle supply pressure transducers is

$$U_{S_t} = \sqrt{P_{S_t}^2 + B_{S_t}^2} = \begin{cases} \pm 2.09\,\% & \text{for SPA} \\ \pm 1.97\,\% & \text{for SPB} \end{cases} \tag{A.6}$$

Calculation of the experimental uncertainty is discussed in Appendix C.3.

A.3 ENGINE AND FUEL PLENUM PRESSURE TRANSDUCERS

This section describes the calibration method for the engine pressure transducers. Sample results are provided and the calculation of the calibration uncertainty is detailed. The engine Kulite® and fuel plenum PCB® pressure transducers were calibrated dynamically using the rig shown in Figure A.4. Two OMEGADYNE® pressure transducers of range 0 to 344.7 kPa (0 to 50 psi, low range) and 0 to 1379 kPa (0 to 200 psi, high range) were used as the reference gauges. The general calibration procedure is as follows: the entire system is isolated from the atmosphere and evacuated using the vacuum pump. Provided there are no leaks or that any present are sufficiently small the reservoir bottle is isolated from the transducer manifold and vacuum pump and filled to the desired pressure (which may be sub-atmospheric) based on the dial gauge. The transducer manifold is then isolated and the solenoid valve triggered, allowing the gas in the reservoir bottle to flow into the evactuated transducer manifold.

Data are recorded using National Instruments™ PXI-6133 14-bit cards connected to a PXI-8196 controller and employing BNC-2090A adapters for ease of use (Ridings, 2012). These are the same models as those used for the main data acquisition system of the T4 Stalker Tube (Section 3.2.3). A 1 MHz sampling rate (1 µs timebase) was used and the data were recorded for a duration of 150 ms.

Sample data are provided in Figure A.5 for Kulite® transducer S/N R65-39 at a nominal reservoir bottle pressure of 80 kPa. Two curves are plotted, the normalised signal for the transducer and the corresponding pressure signal of the reference gauge. The normalised signal is calculated by transiently normalising the measured voltage output of the transducer with the measured pressure output of the reference gauge. A slight time delay exists between the rise of the transducer and reference gauge due to their differing locations on the transducer manifold (Figure A.4b). This time delay is appropriately accounted for when calculating the normalised signal. The transducer sensitivity is then given by the average of the normalised signal over a designated averaging window as shown in Figure A.5.

The sensitivity of each transducer was determined for a range of reservoir bottle pressures. The 10 psi and 25 psi gauges were calibrated against the low range reference gauge at intervals of 20 kPa. The calibration range was 0 to 100 kPa for the 10 psi gauges and 0 to 180 kPa for the 25 psi

V0: Fill valve
V1: Gauge isolation valve
V2: Manifold isolation valve
V3: Manifold/Vacuum vent valve
V4: Vacumm isolation valve
V5: Reservoir bottle vent valve

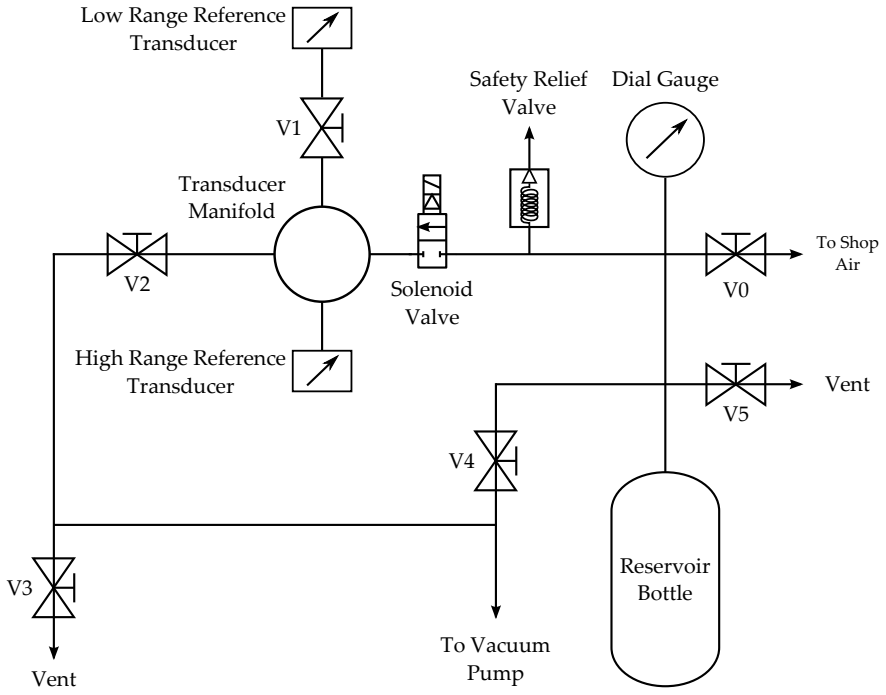

(a) Schematic

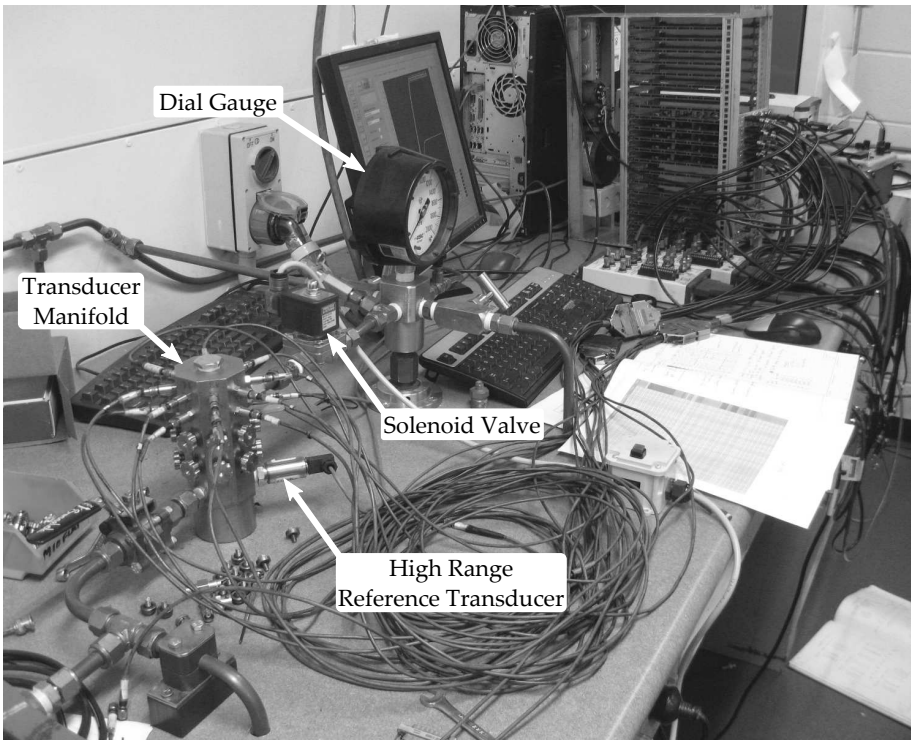

(b) Photograph

Figure A.4 – Pressure transducer calibration rig

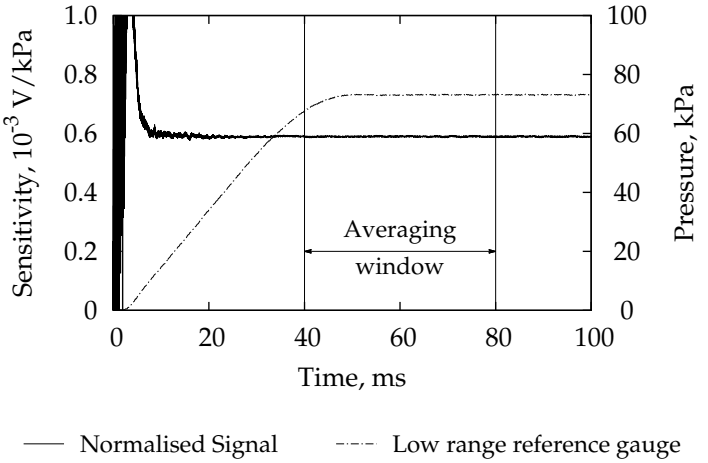

Figure A.5 – Sample pressure transducer calibration data. Data are for Kulite® transducer S/N R65-39 (25 psi range) and the low range reference gauge. The nominal fill pressure of the reservoir bottle was 80 kPa. The averaging window is indicated and for clarity the time axis is arbitarily shifted.

gauges. The 100 psi and 500 psi gauges were calibrated against the high range gauge at intervals of 100 kPa. The calibration range was 0 to 100 psi, being limited by the maximum system pressure of the calibration rig.[6]

Five repeat calibrations were completed at each reservoir bottle fill pressure and for each calibration the gauge sensitivity was determined as shown in Figure A.5. The overall average sensitivity was then computed and used during the experiments within the T4 Stalker Tube. Table A.2 provides a complete summary of the transducers used for each experimental campaign. Details of the reference gauges are also provided. For each engine pressure transducer the average sensitivity, the standard deviation (σ) as a percentage of the average and the number of calibrations completed (n_c) are given.

A.3.1 *Calibration Uncertainty*

A concise summary of the uncertainty analysis for the pressure calibration rig is provided in this section. General details regarding experimental uncertainty analysis, as used in this thesis, are given in Appendix C.2.

For each reservoir bottle fill pressure the transducer sensitivity is calculated using the following experession

$$S_t = \frac{V_t}{V_{ref}} S_{ref} \tag{A.7}$$

6 The solenoid valve used in the calibration rig was rated to a maximum pressure of 1 MPa.

Table A.2 – Calibration Summary for the Engine Pressure Transducers

(a) OMEGADYNE® Reference Transducers

Gauge	Model	S/N	Range (psi)	Sensitivity (V/kPa)	Accuracy[a] (%)
Low range	PX319-050A55	1101071190	50	1.4470×10^{-2}	±0.25
High range	PX319-200A55	0715071029	200	3.6140×10^{-3}	±0.25

a This is the manufacturer quoted value that includes linearity, hysterisis and repeatability. The value is as a percentage of full-scale for a best-straight-line (BSL) fit.

(b) Campaign 1 transducers

Location	Label	Type	S/N	Range (psi)	Sensitivity (V/kPa)	σ (%)	n_c	$X^B_{\overline{S}_t}$ (%)	$X^P_{\overline{S}_t}$ (%)	$X_{\overline{S}_t}$ (%)
Forebody	P1	Kulite®	V65-78	10	1.4215×10^{-3}	0.3	22	2.33	0.13	2.33
Inlet 1	P2		n/a							
Inlet 2	P3		R65-39	25	5.8777×10^{-4}	0.4	45	1.76	0.11	1.76
Inlet 3	P4		n/a							
Combustor 1	P5		J79-29	100	1.4718×10^{-4}	0.3	35	1.70	0.09	1.70
Combustor 2	P6		J79-30	100	1.4777×10^{-4}	0.3	35	1.70	0.09	1.70
Combustor 3	P7		n/a							
Combustor 4	P8		J79-31	100	1.4809×10^{-4}	0.3	34	1.71	0.09	1.72
Combustor 5	P9		J79-28	100	1.4754×10^{-4}	0.3	35	1.70	0.09	1.70
Nozzle	P10		R65-98	10	1.4473×10^{-3}	0.2	22	2.33	0.10	2.33
Inlet Fuel	F1	PCB®	12492	500	1.4284×10^{-3}	0.3	33	2.40	0.10	2.40
Step Fuel	F2		12491	500	1.4679×10^{-3}	0.2	33	2.39	0.06	2.39
Shielding 1	SH1	Kulite®	V65-55	10	1.4199×10^{-3}	0.3	19	2.34	0.15	2.35
Shielding 2	SH2		R65-97	10	1.3940×10^{-3}	0.5	20	2.35	0.23	2.36
Shielding 3	SH3		V65-85	25	5.7594×10^{-4}	0.3	45	1.76	0.09	1.76
Shielding 4	SH4		R65-37	25	5.8903×10^{-4}	0.3	45	1.76	0.09	1.76

(c) Campaign 2 transducers

Location	Label	Type	S/N	Range (psi)	Sensitivity (V/kPa)	σ (%)	n_c	$X^B_{\overline{S}_t}$ (%)	$X^P_{\overline{S}_t}$ (%)	$X_{\overline{S}_t}$ (%)
Forebody	P1	Kulite®	R65-98	10	1.4376×10^{-3}	0.2	20	2.51	0.11	2.51
Inlet 1	P2		V65-85	25	5.7530×10^{-4}	0.3	45	1.76	0.09	1.76
Inlet 2	P3		R65-39	25	5.8800×10^{-4}	0.3	45	1.76	0.08	1.76
Inlet 3	P4		R65-37	25	5.8960×10^{-4}	0.3	45	1.76	0.08	1.76
Combustor 1	P5		L77-94	100	1.5135×10^{-4}	0.3	36	1.74	0.08	1.74
Combustor 2	P6		L77-95	100	1.4699×10^{-4}	0.2	36	1.74	0.08	1.74
Combustor 3	P7		L77-97	100	1.4585×10^{-4}	0.2	36	1.74	0.08	1.74
Combustor 4	P8		J79-27	100	1.4747×10^{-4}	0.3	36	1.74	0.09	1.75
Combustor 5	P9		J79-29	100	1.4639×10^{-4}	0.3	36	1.74	0.09	1.75
Nozzle	P10		V65-55	10	1.4313×10^{-3}	0.1	20	2.51	0.07	2.51
Inlet Fuel	F1	PCB®	12492	500	1.3733×10^{-3}	0.3	35	2.42	0.11	2.43
Step Fuel	F2		12491	500	1.4668×10^{-3}	0.2	35	2.42	0.08	2.43

where S_t and V_t are the sensitivity and measured voltage output of the transducer, respectively. Similarly S_{ref} and V_{ref} are the sensitivity and measured voltage output of the reference gauge, respectively. The systematic uncertainty in measured voltage due to the National Instruments™ data acquisition system is assumed negligible in this thesis. Systematic uncertainties of ±1 %, ±2 % and ±0.5 % due to installation effects in the transducer manifold are assumed for the Kulite®, PCB® and reference transducer outputs, respectively. These uncertainties, along with the manufacturer specified accuracy for the reference gauge (Table A.2), are the elemental systematic uncertainties for the calculation of the transducer sensitivity from a single calibration. As the manufacturer accuracy is given as a percentage of full-scale, the uncertainty associated with the reference gauge is a constant that is equal to 0.862 kPa for the 50 psi reference gauge and equal to 3.447 kPa for the 200 psi reference gauge. Thus, for *each* calibration, the systematic uncertainty in the transducer sensitivity is

$$X^B_{S_t} = \begin{cases} \sqrt{1^2 + 0.5^2 + (86.2/P)^2} \leqslant \pm 4.45\,\% & \text{for 10 and 25 psi Kulites®} \\ \sqrt{1^2 + 0.5^2 + (344.7/P)^2} \leqslant \pm 1.41\,\% & \text{for 100 psi Kulites®} \\ \sqrt{2^2 + 0.5^2 + (344.7/P)^2} \leqslant \pm 2.23\,\% & \text{for PCBs®} \end{cases} \tag{A.8}$$

where P is the calibration pressure in units of kilopascal. The sensitivity listed in Table A.2 for each transducer represents the mean of a set of individual calibrations, $\overline{S}_t$. Since these individual calibrations were conducted with the same apparatus and against the same reference gauge, the elemental errors in each individual calibration are correlated with those of every other calibration included in the calculation of the mean. Thus, the total systematic uncertainty $X^B_{\overline{S}_t}$ of the mean sensitivity is calculated by applying Equations (C.7) and (C.10). This calcuation was achieved through the use of a MATLAB® script. The resulting values for $X^B_{\overline{S}_t}$ are provided in Table A.2 for each transducer.

The relative precision uncertainty, $X^P_{\overline{S}_t}$ of the mean sensitivity is calculated using Equation (C.17) to be

$$X^P_{\overline{S}_t} \leqslant \begin{cases} \pm 0.13\,\% & \text{for P1 through P10} \\ \pm 0.11\,\% & \text{for F1 and F2} \end{cases} \tag{A.9}$$

The calculated values of $X^P_{\overline{S}_t}$ for each transducer are listed in Table A.2. Finally, the total calibration uncertainty is

$$X_{\overline{S}_t} = \sqrt{\left(X^P_{\overline{S}_t}\right)^2 + \left(X^B_{\overline{S}_t}\right)^2} \leqslant \begin{cases} \pm 2.51\,\% & \text{for P1 and P10} \\ \pm 1.76\,\% & \text{for P2 through P9} \\ \pm 2.43\,\% & \text{for F1 and F2} \end{cases} \tag{A.10}$$

Calculation of the experimental uncertainty is discussed in Appendix C.3.

A.4 FUEL SYSTEM

In this section the theory and calibration methodology for the fuel delivery system are described and sample results are provided. Two different fuel systems are discussed: single-leg fuel systems, for which a single Ludwieg tube (or tank) supplies fuel to a single plenum chamber, and combined fuel systems, for which a single Ludwieg tube supplies fuel to multiple plenum chambers that cannot be considered identical. The theory provided here for single-leg systems follows the original work of Prof. David Mee and that reported in Robinson et al. (2003) while the theory presented for combined systems has not previously been documented.

A.4.1 *Single-leg systems*

A schematic of a generic single-leg fuel system is provided in Figure A.6. Assuming that the flow velocity within the plenum chamber behind the injectors is sufficiently slow, then we may write that $p_{p,0} \approx p_p$ and $T_{p,0} \approx T_p$. If the flow through the injectors is assumed choked then the mass flow rate is given by:

$$\dot{m}_f = C_d A \sqrt{\frac{\gamma}{R}\left(\frac{2}{\gamma+1}\right)^{\frac{\gamma+1}{\gamma-1}}} \frac{p_p}{\sqrt{T_p}} \tag{A.11}$$

where C_d is a discharge coefficient that accounts for viscous losses; A is the total area of the injector holes; and R and γ are the gas constant and specific heat ratio of the fuel, respectively. As only plenum pressure, p_p, and initial tank fill pressure, p_{Ti}, were measured during these experiments (Sections 3.4.4 and 3.4.5), several additional assumptions are required to provide an expression for T_p in Equation (A.11). Depicted in Figure A.6, the first of these assumptions is that the gas in the tank undergoes an intial isentropic expansion to some intermediate state, designated by subscript 0:

$$\left(\frac{T_{Ti}}{T_0}\right)^{\frac{\gamma}{\gamma-1}} = \frac{p_{Ti}}{p_0} \tag{A.12}$$

The second assumption is that the gas then flows adiabatically and with some loss in total pressure from the intermediate state to the plenum chamber. Thus, the conditions in plenum are related to state 0 by

$$T_p = T_0 \tag{A.13}$$

$$p_p = k p_0 \tag{A.14}$$

where k is some constant that is unique to the setup being considered (i.e. k is dependent on the solenoid valve and fittings used, the tubing lengths and bends). Combining Equations (A.12) to (A.14) the plenum temperature is given by

$$T_p = T_{Ti}\left(\frac{kp_{Ti}}{p_p}\right)^{\frac{\gamma-1}{\gamma}} \tag{A.15}$$

Substituting into Equation (A.11) gives:

$$\begin{aligned}\dot{m}_f &= C_d A\sqrt{\frac{\gamma k^{\frac{\gamma-1}{\gamma}}}{RT_{Ti}}\left(\frac{2}{\gamma+1}\right)^{\frac{\gamma+1}{\gamma-1}} p_{Ti}^{\frac{\gamma-1}{2\gamma}} p_p^{\frac{\gamma+1}{2\gamma}}} \\ &= \alpha p_{Ti}^{\frac{\gamma-1}{2\gamma}} p_p^{\frac{\gamma+1}{2\gamma}}\end{aligned} \tag{A.16}$$

where

$$\alpha = C_d A\sqrt{\frac{\gamma k^{\frac{\gamma-1}{\gamma}}}{RT_{Ti}}\left(\frac{2}{\gamma+1}\right)^{\frac{\gamma+1}{\gamma-1}}} \tag{A.17}$$

The constant α is determined experimentally by opening the solenoid valve for a short length of time (typically around 100 ms) and allowing fuel to be ejected from the system into a vacuum. Integrating Equation (A.16) over the period that the valve is open gives the total mass lost from the system

$$\Delta m = \alpha p_{Ti}^{\frac{\gamma-1}{2\gamma}} \int_{t_i}^{t_f} p_p^{\frac{\gamma+1}{2\gamma}}\, dt \tag{A.18}$$

With knowledge of the total volume (V_T) of the fuel system between the solenoid valve and manual isolation valve (Figure 3.13) and by recording the initial (p_{Ti}) and final (p_{Tf}) pressure in the tank, the total mass expelled from the system may also be calculated using

$$\Delta m = \frac{(p_{Ti} - p_{Tf})V_T}{RT_{Ti}} \tag{A.19}$$

where it has been assumed that $T_{Ti} = T_{Tf}$. Combining Equations (A.18) and (A.19) gives the following expression

$$\alpha = \frac{(p_{Ti} - p_{Tf})V_T}{RT_{Ti} p_{Ti}^{\frac{\gamma-1}{2\gamma}} \int_{t_i}^{t_f} p_p^{\frac{\gamma+1}{2\gamma}}\, dt} \tag{A.20}$$

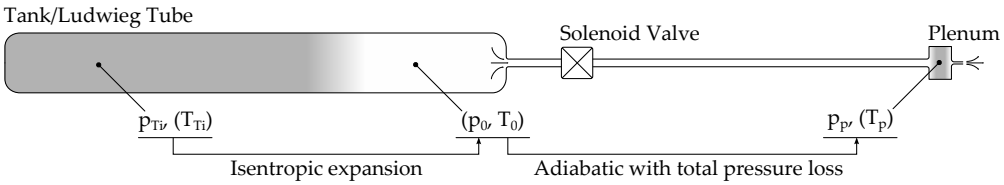

Figure A.6 – Schematic of a single-leg fuel system. Quantities in brackets were not experimentally measured.

A.4.2 *Combined systems*

For combined fuelling systems it is tempting to write that the total mass flow of fuel is the summation of the individual flows through each leg of the system, that is

$$\dot{m}_{f,t} = p_{Ti}^{\frac{\gamma-1}{2\gamma}} \left(\alpha_1 p_{p,1}^{\frac{\gamma+1}{2\gamma}} + \alpha_2 p_{p,2}^{\frac{\gamma+1}{2\gamma}} \right) \tag{A.21}$$

However, Equation (A.21) is incorrect and over-estimates the fuel flow rate. This is a consequence of the assumption represented by Equation (A.14) and the subsequent inclusion of the proportionality constants k_j into the calibration constants α_j (see Equation (A.20), $j = 1$ corresponds to the inlet plenum, $j = 2$ corresponds to the step plenum). For a single leg system, a causality exists between the tank fill pressure and plenum pressure. This causality is represented by Equation (A.14). The proportionality constant k_j subsequently becomes included into the calibration constant α_j (Equation (A.20)) implying that the calibration constant α_j is *specific* to the arrangement of the fuel system that is used during the calibration. When two single leg systems are combined and supplied fuel from the same tank, the causality between the tank fill pressure and measured plenum pressure changes. That is, the respective proportionality constant of each plenum is altered by the presence of the other plenum. This is seen in Figure A.7 in which typical calibration pressure traces are plotted for the inlet, step and combined schemes for a tank filling pressure of approximately 1100 kPa. Clearly the peak pressures attained in the inlet and step injector plenums are smaller for the combined scheme than for the individual schemes.

It is not possible to determine the change in proportionality constants based solely on measurement of the plenum pressure. Consequently, for this thesis, a third calibration constant α_C was introduced such that the

total mass flow of fuel for a combined system was given by

$$\dot{m}_{f,t} = \alpha_c p_{Ti}^{\frac{\gamma-1}{2\gamma}} \left(\alpha_1 p_{p,1}^{\frac{\gamma+1}{2\gamma}} + \alpha_2 p_{p,2}^{\frac{\gamma+1}{2\gamma}} \right) \tag{A.22}$$

This constant is determined experimentally using the same methodology as the individual calibration constants: the solenoid valve is opened for a period and initial and final tank pressure are noted. The total mass lost from the tank based on the change in tank pressure is equated to the integral of Equation (A.22) so that

$$\alpha_c = \frac{(p_{Ti} - p_{Tf})V_T}{RT_{Ti} p_{Ti}^{\frac{\gamma-1}{2\gamma}} \int_{t_i}^{t_f} \left(\alpha_1 p_{p,1}^{\frac{\gamma+1}{2\gamma}} + \alpha_2 p_{p,2}^{\frac{\gamma+1}{2\gamma}} \right) dt} \tag{A.23}$$

A.4.3 *Fuel System Volume*

For completeness the volume of each component of the fuel system between the manual isolation valve and solenoid valve (Figure 3.13) are provided in Table A.3.

Table A.3 – Fuel System Component Volumes

Component	Volume, cm^3		Calculation Method
	Campaign 1	Campaign 2	
Manual valve to Transducer	2.8	2.8	Theoretical
1/8 inch fill line	9.2	2.7	Theoretical
1/4 inch fill line	0	5.1	Theoretical
Tank	150	150	Manufacturer
Tank-to-Solenoid	2.2	2.2	Theoretical
Total	164.2	162.8	

A.4.4 *Plenum Pressure Correction*

Due to the relatively long time frame over which the calibration of the fuel system occurs, the pressure measured by the PCB® transducer returns to a negative value after the valve closes and the system has drained of gas. This is seen in Figure A.8 for the 'raw' signal and is a consequence of the discharge time constant of the piezo-electric crystals at the heart of the transducers (PCB Piezotronics Inc., 2013). Following Pulsonetti (1995) and McGuire (2007), each raw plenum signal was adjusted using a

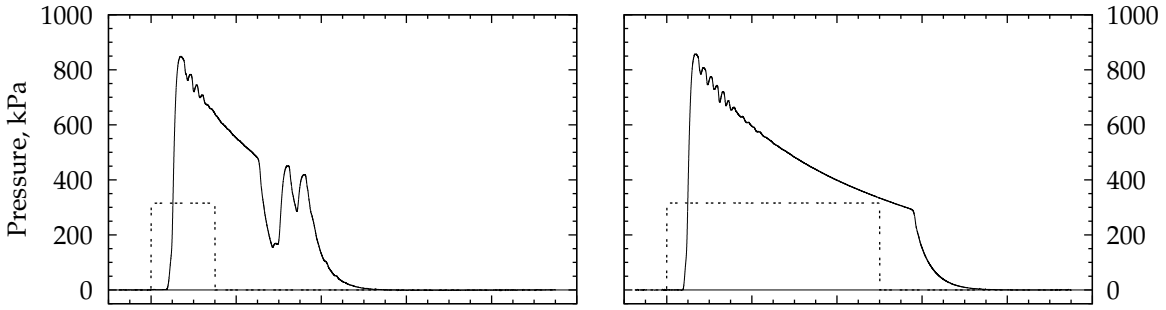

(a) Inlet injection scheme. The initial tank pressure was 1175 kPa for the campaign 1 calibration and 1115 kPa for the campaign 2 calibration.

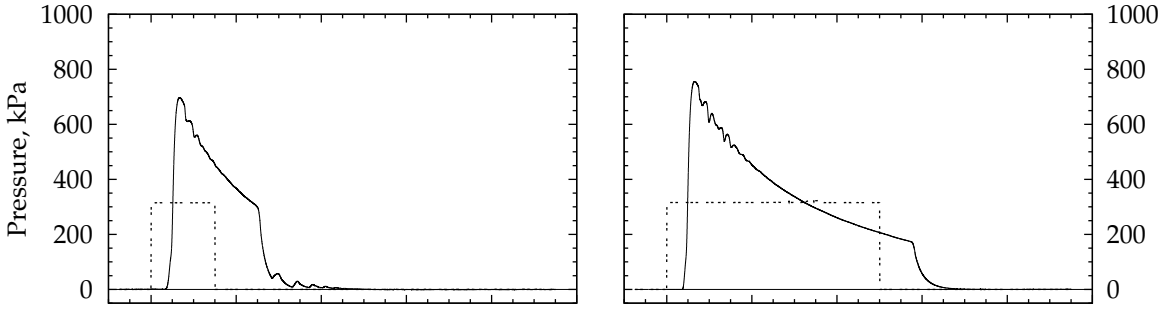

(b) Step injection scheme. The initial tank pressure was 1168 kPa for the campaign 1 calibration and 1102 kPa for the campaign 2 calibration.

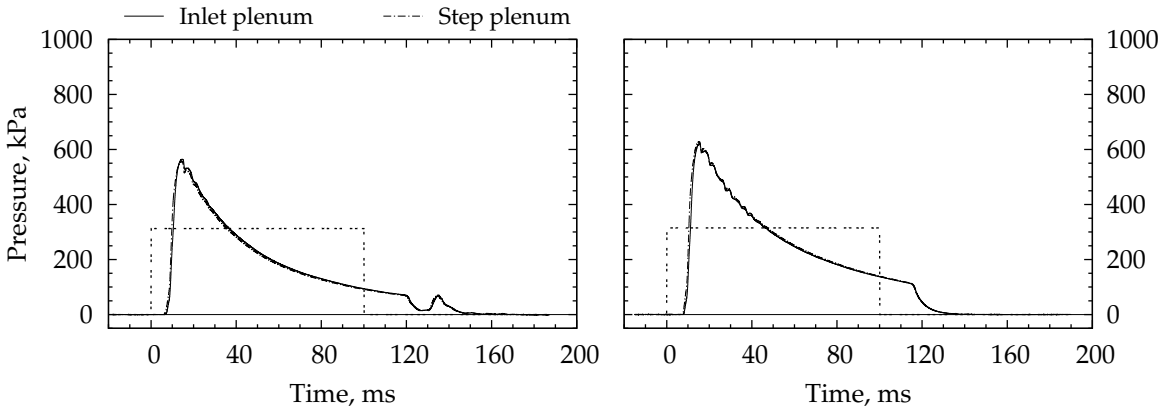

(c) Combined injection scheme. The initial tank pressure was 1098 kPa for both calibrations.

Figure A.7 – Typical calibration pressure traces recorded for the inlet, step and combined injection schemes. The initial fill pressure for the tank was approximately 1100 kPa for each calibration. Campaign 1 data is given on the left, campaign 2 data on the right. The data were filtered using a 0.5 ms moving average and the solenoid trigger signals has been provided for comparison (dotted line).

linear correction defined by points O and A. The rotated signal has been provided in Figure A.8 for comparison. The correction of the raw data was completed prior to evaluation of Equations (A.20) and (A.23).

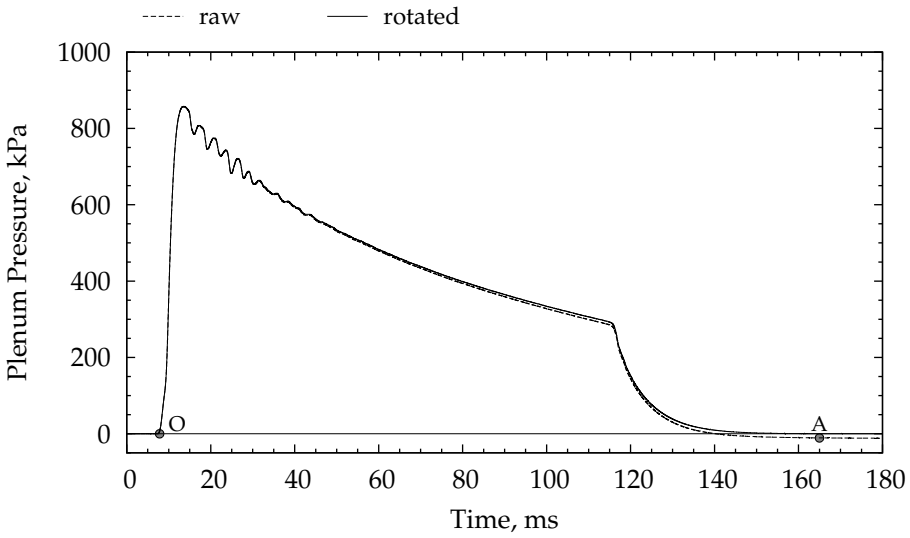

Figure A.8 – Correction of fuel plenum pressure using a linear offset. The data was filtered by a 0.5 ms moving average and the time axis has been shifted so that zero corresponds to fuel solenoid trigger. The data are from campaign 2 calibration F1-1000kPa-1.

A.4.5 *Calibration Results*

Equations (A.20) and (A.23) were evaluated for the inlet, step and combined injection schemes over a range of tank fill pressures. The resulting values for the respective calibration constants are plotted in Figure A.9. The mean values, summarised in Table A.4, are shown in each plot as a horizontal line. The total uncertainty in the mean calibration constant was approximately 10 % and is listed in Table A.4. The total uncertainty for each individual calibration was appoximately 6.5 % and is indicated in Figure A.9. The uncertainty analyses for a single calibration and for the mean calibration constant are provided in full in Appendix C.8.

The change in calibration constants between the first and second campaigns is believed to be a consequence of alterations made to the fuel solenoid valve for the second test campaign. A softer spring and a different plunger with improved sealing material on the plunger face were installed for the second campaign. These changes resulted in improved opening and closing transients (Figure A.7) and improved sealing of the valve. Since the combined fuel calibration constant is dependent on the individual calibration constants, a decrease in the individual constants α_1 and α_2 produce an increase in in the combined fuel constant α_C.

Table A.4 – Fuel System Calibration Results

	Campaign 1			Campaign 2		
Inj. Scheme	α	σ_α (%)	$X_{\overline{\alpha}}$ (%)	α	σ_α (%)	$X_{\overline{\alpha}}$ (%)
Inlet	1.662×10^{-9}	0.83	12.9	1.387×10^{-9}	0.31	9.0
Step	2.849×10^{-9}	1.99	11.1	2.122×10^{-9}	1.46	9.2
Combined	0.768	1.24		0.843	0.64	

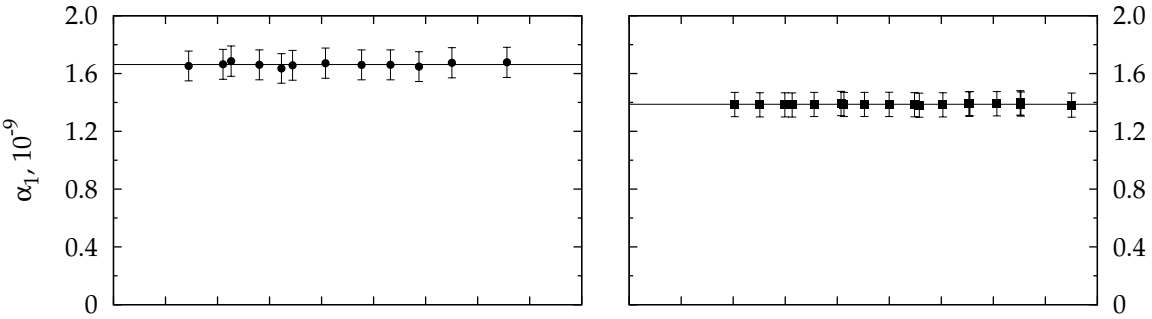

(a) Inlet injection scheme

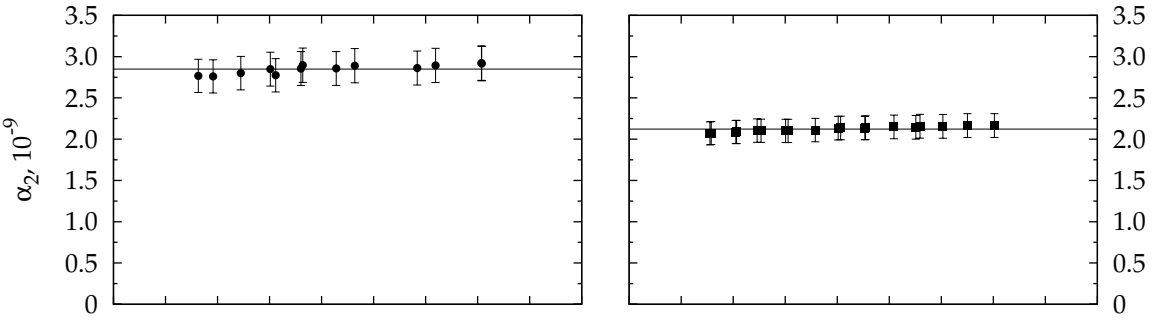

(b) Step injection scheme

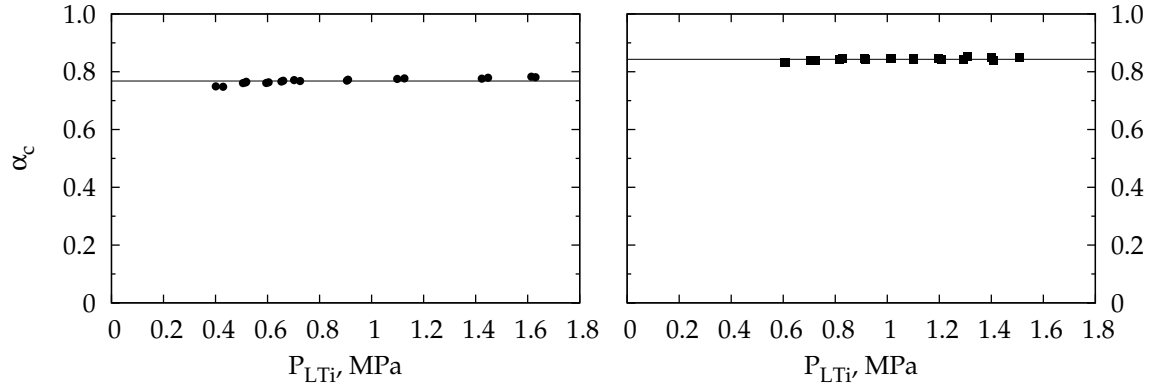

(c) Combined injection scheme

Figure A.9 – Fuel calibration constants for inlet, step and combined injection schemes. The averaged value is indicated by a horizontal line. Campaign 1 data is given on the left, campaign 2 data on the right.

3CFB SUPPLEMENTARY NOTES AND RESULTS

B

B.1 INTRODUCTION

This appendix presents supplementary notes and results for the calibration of the three-component stress wave force balance. These results are presented in support of the discussion of the calibration method that is given in Chapter 4. Further calibration results may also be found in Doherty (2013c).

B.2 CALIBRATION TEST MODEL AND HIT NAMING CONVENTION

Prior to the manufacture of the M12REST engine, the operation of the 3CFB gauges was confirmed using the test model shown in Figure B.1. This is the same test model used by Robinson (2003d) during the development of the balance. As stated in Section 4.2, each of the primary piezo-electric film gauges were found to be operational. With the exception of that on bar 1, the secondary piezo-resitive gauges were also found to be operational. Seven of eight operational gauges was considered sufficient for this thesis.

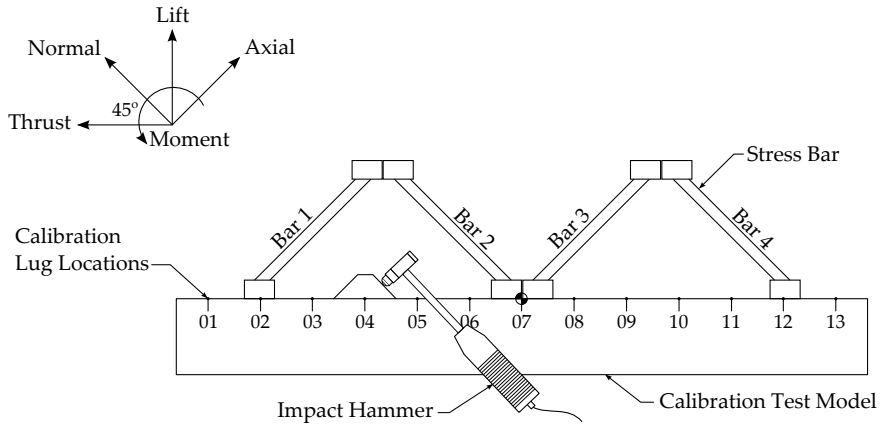

Figure B.1 – Schematic of the test model used to evaluate the force balance

The calibration of the test model was also used to develop the necessary data management and analysis code. The influence of the choice of calibration weighting factors on the quality of the GIRF was also investigated. The calibration of the M12REST engine involved more than 960 hammer hits and in order to efficiently deal with this quantity of data a naming convention, based on that established by Robinson (2003d, section 5.3.1),

was used to *uniquely* identify each calibration hit.

An acronym was used which specified on which side of the model the calibration lug was placed, the direction of the hammer hit, the axial station of the calibration lug and the repeat hit number. For example, LUA15_2 indicates that the calibration lug was positioned at station 15 on the *Left*, *Upper* side of the model, that the hit was in the *Axial* direction and that it was the *second* such hit at this location. The naming convention included an upper/lower surface designation so that a consistent convention could be used for both the test model (Figure B.1) and the M12REST engine (Figure 4.3).

B.3 SUMMARY OF DATA PROCESSING STEPS

Table B.1 summarises each data processing step required for the calibration of the three-component force balance. References to supporting documents or sections of this thesis are provided where appropriate. MATLAB® scripts written by the author handled the passing of data to and from HYFORCE. HYFORCE was used to complete the numerical convolution and deconvolution. The deconvolution algorithm implemented in HYFORCE was based on that reported in Prost and Goutte (1984).

Table B.1 – Data Processing Steps for the Force Balance Calibration

Step	Description
1	Invert the calibration strains (Appendix B.4).
2	Zero the hammer signal outside of the pulse (see Section 3.2.3 in Mee, 2002).
3	Trim the hammer and strain signals to 8000 data points as this is the most that the HYFORCE program can accept (Mee, 2007). For a recording timebase of 5 µs, the total duration of the timmed signal will be 40 ms which is sufficient for shock tunnel data.
4	Generate the individual IRF for each bar and calibration hit by deconvolving the measured calibration strains with the associated truncated hammer signals.
5	Convolve each individual IRF with a unit-input load to generate a set of expected unit-strain responses. For shock tunnel tests the time history of the unit-input load may either be a pure step, a tunnel-type load (Figure 4.6) or an SPA-type load (i.e. scaled from a measured nozzle supply pressure trace).
6	Cross-deconvolve the different 'sets' of calibration data (see Appendix A.3 in Mee, 2002).
7	Create a loading specification file based on a nominated reference load distribution and specified calibration locations. See Section 4.5 and Appendix B.6.

Table B.1 – Continued.

Step	Description
8	Define an output specification matrix that reduces coupling of the strain outputs and that appropriately accounts for the polarity of the different strain gauges. See Equations (4.13) to (4.16) and Appendix B.4.
9	Assemble the GIRF using the nominated loading specification and output specification files (see Section 4.4). Assembly of the GIRF is completed by HYFORCE. Scaling factors for the force components must also be specified, as discussed in Appendix B.6.
10	For each calibration hit, combine the unit-strain responses (generated in step 5) according to the output specification matrix. This produces point-load strain files.
11	Deconvolve each point-load strain file using the GIRF and plot the recovered forces. See item 3, page 92 and Appendix B.10.
12	Using the reference load distribution, specified calibration locations and output specification matrix, combine the unit-strain responses to form the expected distributed strain response. Deconvolve this distributed strain response using a nominated GIRF. See item 4, page 92 and Section 4.6.1.
13	Based on the net forces of the reference load distribution used in step 12, scale the unit-input load from step 5 to create a true-input load file. Convolve this load file with the GIRF to produce the convolved-expected strain reponse of the balance to the distributed load.
14	Generate plots comparing the true and deconvolved forces and expected and convolved strain responses of the balance.
15	Repeat steps 12 to 14 for a *fuel-off* distributed load. See item 5, page 93 and Section 4.6.2.
16	Repeat steps 12 to 14 for a distributed load formed from hits to the *lower* surfaces of the engine. See item 6, page 93, Section 4.6.3 and Appendix B.7.
17	Repeat step 12 for a distributed load formed from hits to the *side* surfaces of the engine. See item 7, page 93 and Appendix B.12.

B.4 SIGN OF INDIVIDUAL IRF AND STRAIN ASYMMETRY

When conducting a calibration hit like that depicted in Figure B.1, the instrumented impact hammer measures a *positive* force input. Simply deconvolving the hammer signal with the corresponding strain signal(s) produces an individual impulse response (G_k^{ij}) that is *inverted* relative to the correct response. This inversion is caused by the fact that in the $N-A$

coordinate system (Figure B.1) each calibration hit imparts a *negative* force to the model. To account for this difference each strain signal is inversed prior to deconvolution with the relevant hammer signal.

In addition to appropriately accounting for the direction of the hammer hits relative to the assumed coordinate system, the polarity of each strain gauge must also be considered. In this thesis this was achieved in the definition of the output specification matrix (A_o). Neglecting to account for the strain gauge polarity can lead to one (or more) of the combined strain signals being dominated by the others, reducing the ability of the GIRF to recover the associated force input.

Consider for example the calibration test model as shown in Figure B.1. The test model, being a solid rectangular block, and the stress bars are both symmetric about the seventh calibration location. This symmetry dictates that strains measured for hits in the normal and axial directions at corresponding locations should also be symmetric. Example strain data are plotted in Figure B.2 for calibration hits at locations N03 and A11. This data show clearly that bars 2 and 3 are asymmetric. Noting that the force balance could be reassembled with bar 2 (or 3) inverted or even swapped with one of the other bars, the asymmetry of bars 2 and 3 is an artifact of the wiring and installation of the particular gauges and does not represent the true 'sign' of the strain.

In this thesis the combined normal, axial and moment strain signals were formed using the following methodology: bars 1 and 3, being parallel to the axial coordinate were averaged to give the axial strain; bars 2 and 4, being parallel to the normal coordinate, were averaged to give the normal strain; and, the difference between bars 1 and 3 and between bars 2 and 4 were averaged to give the moment strain. That is,

$$\begin{aligned} y_N &= \frac{1}{2}(y_2 + y_4) \\ y_A &= \frac{1}{2}(y_1 + y_3) \\ y_M &= \frac{1}{4}(y_2 - y_4 + y_1 - y_3) \end{aligned}$$

If the asymmetric polarity of bars 2 and 3 was neglected then, based on the above equations, the axial strain signal for hit N03 would be significantly smaller than the normal strain signal, thus affecting the quality of the recovered forces.

A study was conducted for the M12REST engine to examine the effect that inverting each gauge had on the quality of the recovered forces for both the fuel-off and fuel-on distributed loads (see item 5 for the basic methodology). The results of this study are provided in full in Doherty (2013c) and showed that the best force recovery occured when bar 2 was inverted. The output specification matrix used in this thesis is given by Equation (4.16).

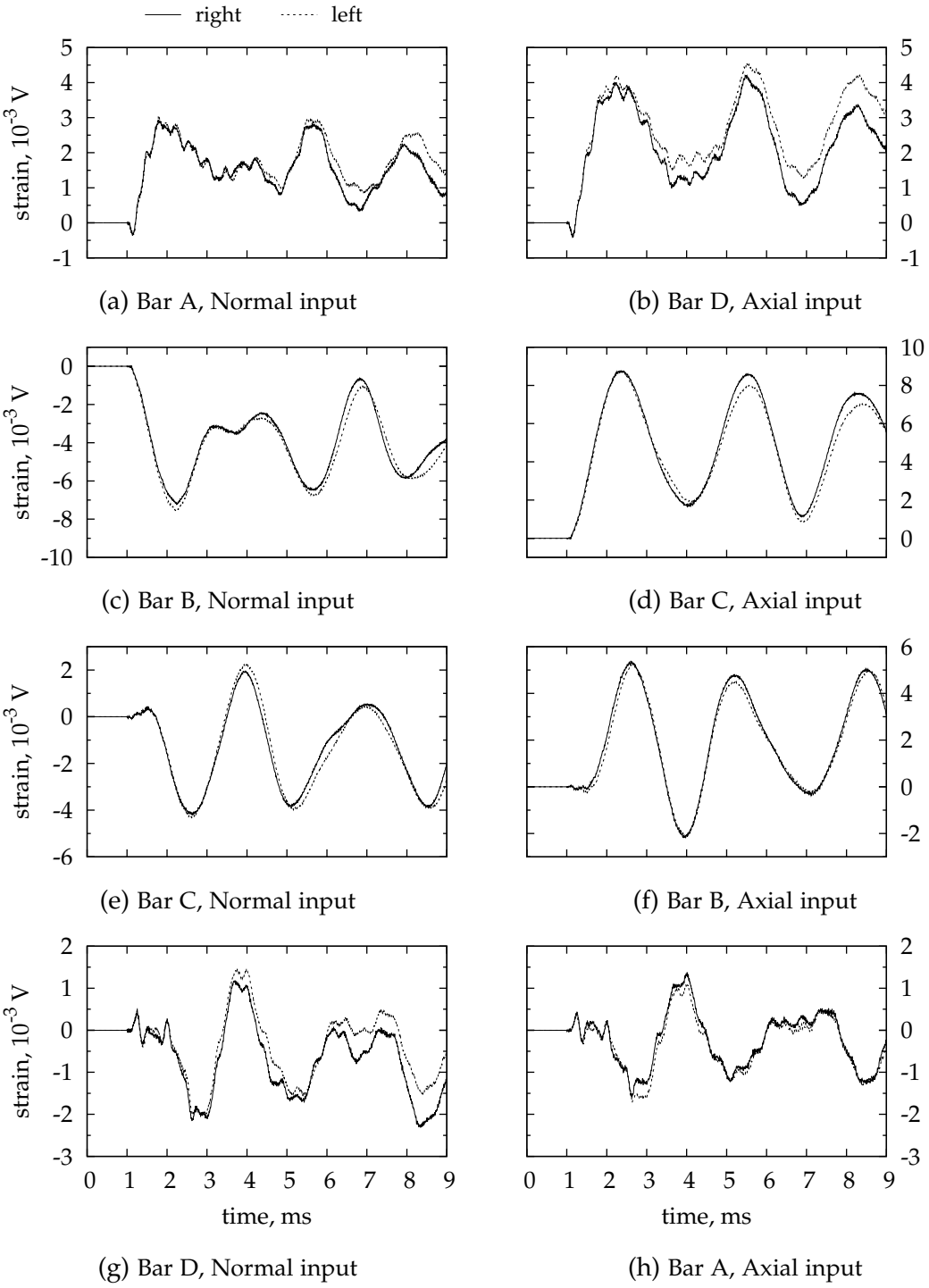

(a) Bar A, Normal input

(b) Bar D, Axial input

(c) Bar B, Normal input

(d) Bar C, Axial input

(e) Bar C, Normal input

(f) Bar B, Axial input

(g) Bar D, Normal input

(h) Bar A, Axial input

Figure B.2 – Unit-step responses of each stress bar due to an input at location N03 (left column) or location A11 (right column). Data are given for both the left-side and right-side locations of the calibration lug. The responses were generated by convolving the respective individual IRF (g_k^{ij}) with a unit-step.

B.5 INFLUENCE OF DECONVOLUTION ITERATIONS

The deconvolution algorithm implemented in the computer program HYFORCE is a constrained interative algorithm that was proposed by Prost and Goutte (1984). Given the iterative nature of the algorithm and the fact that no specific convergence criterion has been implemented within HYFORCE, it is useful to consider the influence that the number of iterations has on the quality of the impulse response function and recovered forces. The basic one-dimensional deconvolution integral on which the stress wave force measurement technique is based is

$$y(t) = \int_0^t g(t-\tau)u(\tau)d\tau \tag{B.1}$$

where $g(t)$ is the impulse response function (IRF) of the system, $u(t)$ is the input force and $y(t)$ is the measured strain response. Chapter 4 provides further discussion of the theory and underlying assumptions. In this section the above deconvolution integral will be written more concisely as

$$y(t) = (g * u)(t) \tag{B.2}$$

The inverse calculation, that is, the deconvolution of the response $y(t)$ with the IRF $g(t)$ will be written as

$$u(t) = (g * y)^{-1}(t) \tag{B.3}$$

Similarly deconvolution of the system response $y(t)$ with the input $u(t)$ to recover the IRF $g(t)$ of the system will be written as

$$g(t) = (u * y)^{-1}(t) \tag{B.4}$$

Throughout the remainder of this section the dependence on time of u, g and y is not explicity written. Furthermore, let a subscript number indicate the number of iterations that were used for deconvolution when deriving the system IRF from the measured input and output. Thus, g_{100} indicates that the 100 iterations were used when evaluating $(u * y)^{-1}$ and y_{100} indicates that g_{100} was used when evaluating $(g * u)^{-1}$. With this notation in place, it is possible to examine the influence of the number of iterations on the ability of an IRF to recover a known force input. The results are presented in Figures B.4 and B.4b.

Using the *pre*-campaign calibration data, the individual IRF of bar 1 for a hit at location RUA09 was computed using either 100 or 300 iterations. The individual IRF were then convolved with a unit-step input load to give the expected unit-strain response. The results for each IRF are compared in Figure B.4b. The magnitude and time history of the computed strain responses are essentially identical. Looking closely, the response computed

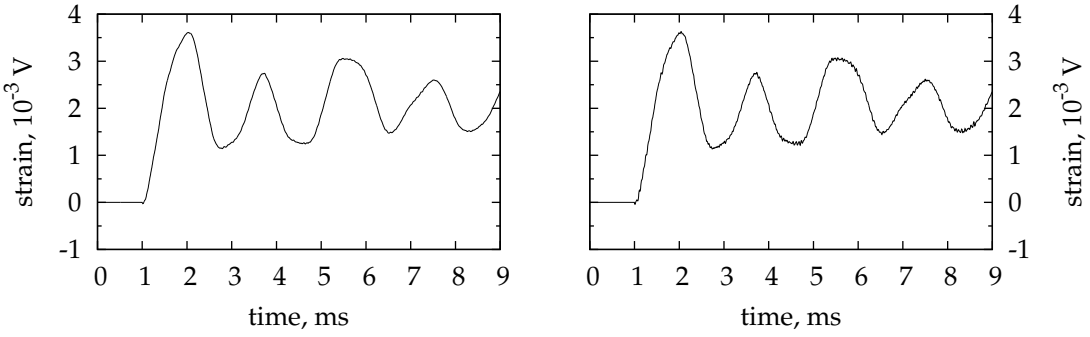

(a) $y_{s,100} = (g_{100} * u_{step})$ (b) $y_{s,300} = (g_{300} * u_{step})$

Figure B.3 – Computed response of Bar 1 to a unit-step input at RUA09 for two IRF, g_{100} and g_{300}, each derived from the measured hammer hit data using a different number of deconvolution iterations.

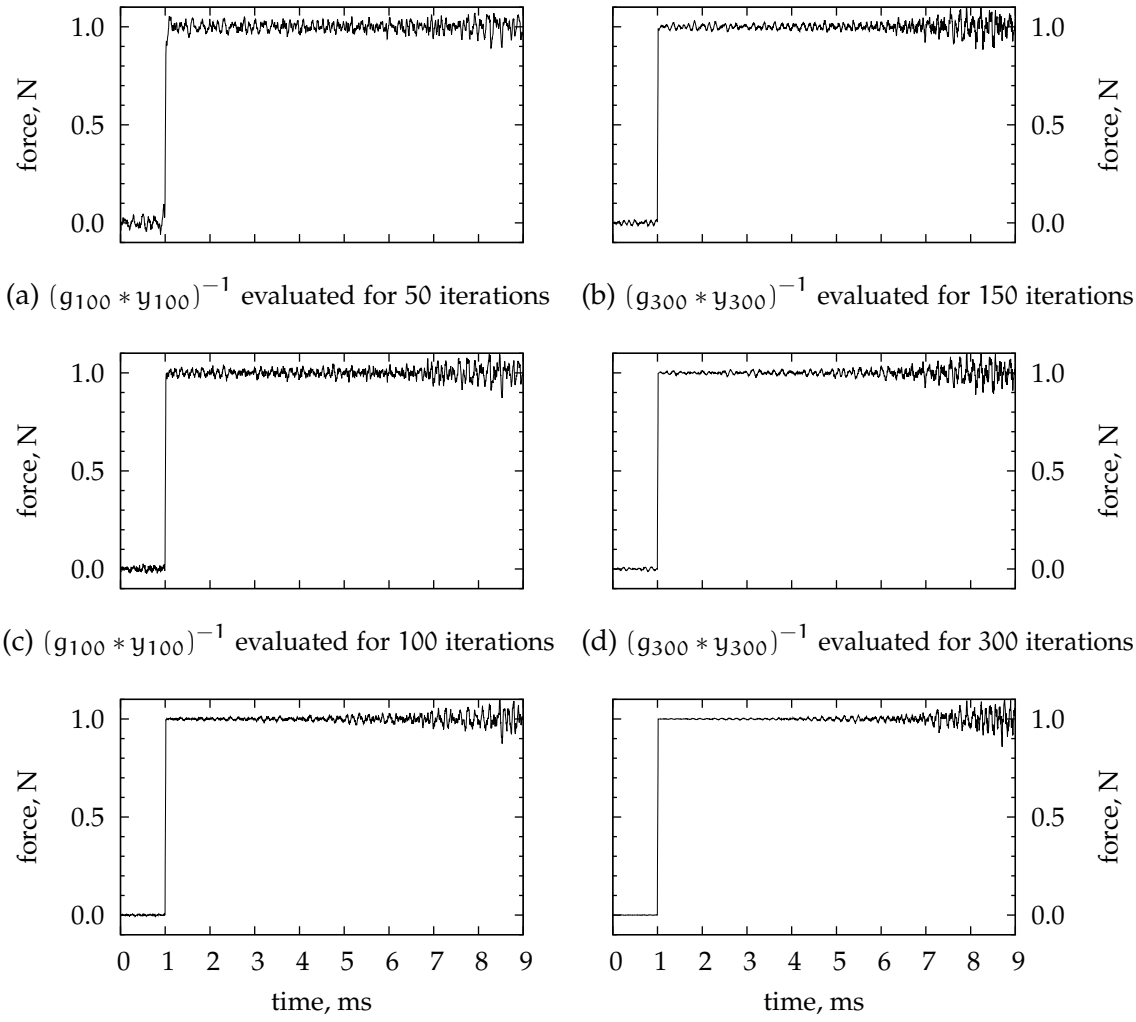

(a) $(g_{100} * y_{100})^{-1}$ evaluated for 50 iterations (b) $(g_{300} * y_{300})^{-1}$ evaluated for 150 iterations

(c) $(g_{100} * y_{100})^{-1}$ evaluated for 100 iterations (d) $(g_{300} * y_{300})^{-1}$ evaluated for 300 iterations

(e) $(g_{100} * y_{100})^{-1}$ evaluated for 500 iterations (f) $(g_{300} * y_{300})^{-1}$ evaluated for 1500 iterations

Figure B.4 – Effect of the number of deconvolution iterations on the quality of the recovered force signal for two IRF, g_{100} and g_{300}.

from g_{300} has slightly more high frequency content than the response computed from g_{100}.

The strain responses plotted in Figure B.4b were deconvolved with the corresponding IRF using three different values for the number of iterations. The values were chosen to be half, equal to or five times the number of iterations used when deconvolving the IRF from the experimental data. The recovered forces are plotted in Figure B.4. In each case the step response is well recovered. However, the magnitude of the high frequency content of the recovered force is influenced by which individual IRF was used and by the number of deconvolution iterations completed. For a given individual IRF the data show that increasing the number of deconvolution iterations improves the quality of the recovered signal. This is to be expected for a constrained iterative algorithm such as that implemented in HYFORCE. Similarly the data also show that an individual IRF derived using a larger number of deconvolution iterations from the measured hammer hit data produce highers quality recovered force signals.

Based on the results plotted in Figure B.4 it would be tempting using a very large number of deconvolution iterations when calculating the individual IRF from the calibration hammer hit data and when using the individual IRF to deconvolve a given strain signal. There are however, two practical limitations on the number of deconvolution iterations. Firstly, increasing the number of iterations increases the computational time required for the deconvolution algorithm. This time is significant when computing 960 individual IRF as was required for the calibration of the 3CFB in this thesis. Secondly, deconvolution increases any system inconsistent noise that may be present in the signals and can affect the quality of the recovered forces during an actual experiment. In this thesis 300 deconvolution iterations were used when generating the individual IRF from the calibration data; this value is consistent with previous researchers, see, for example, Chan (2012), Kirchhartz (2010), and Mee (2003). In comparison, when using the GIRF to deconvolve calibration or experimental data 1500 iterations were found to be necessary.

B.6 GIRF WEIGHTING FACTORS AND SCALING OF GIRF SUB-MATRICES

The complete set of calibration weighting factors used to form the GIRF are provided in Table B.2. These values were calculated using Equations (4.18) to (4.22) and the reference load distribution provided in Figure 4.4. This distribution approximates a fuel-on distribution for the M12REST engine at the high-pressure test condition. Note that due to difficulty in obtaining a single, clean hit at station 1, only calibration stations 2 through 20 were used to form the GIRF. Also, the weighting factors given in Table B.2 represent the *total* for each calibration station and direction. As depicted in Figure 4.3 and discussed in Section 4.4, the calibration lug was placed

Table B.2 – Individual IRF Weighting Factors used to form the Global Impulse Response Function of the balance.

Hit	Normal	Axial	Moment
UN02	0.066 542 79	0.000 000 00	−0.386 230 18
UA02	0.000 000 00	0.059 088 15	−0.293 626 62
UN03	0.057 123 45	0.000 000 00	−0.299 046 77
UA03	0.000 000 00	0.051 098 68	−0.207 252 96
UN04	0.055 383 48	0.000 000 00	−0.258 416 82
UA04	0.000 000 00	0.050 005 40	−0.157 145 66
UN05	0.052 277 51	0.000 000 00	−0.214 171 18
UA05	0.000 000 00	0.047 641 84	−0.106 203 77
UN06	0.049 517 02	0.000 000 00	−0.174 679 78
UA06	0.000 000 00	0.045 589 95	−0.059 989 54
UN07	0.057 948 12	0.000 000 00	−0.171 441 22
UA07	0.000 000 00	0.067 674 77	−0.027 238 31
UN08	0.086 450 09	0.000 000 00	−0.206 562 82
UA08	0.000 000 00	0.123 815 56	0.063 254 07
UN09	0.115 956 82	0.000 000 00	−0.211 069 97
UA09	0.000 000 00	0.164 554 86	0.234 364 82
UN10	0.166 779 09	0.000 000 00	−0.208 658 09
UA10	0.000 000 00	0.241 148 38	0.563 707 73
UN11	0.087 762 09	0.000 000 00	−0.059 850 49
UA11	0.000 000 00	0.270 910 64	0.880 719 36
UN12	−0.146 988 86	0.000 000 00	0.016 583 46
UA12	0.000 000 00	−0.005 358 81	−0.022 315 79
UN13	−0.097 380 01	0.000 000 00	−0.044 436 50
UA13	0.000 000 00	0.012 418 64	0.063 057 91
UN14	−0.300 173 20	0.000 000 00	−0.307 816 29
UA14	0.000 000 00	−0.136 625 46	−0.818 529 21
UN15	0.147 781 02	0.000 000 00	0.235 652 21
UA15	0.000 000 00	0.146 692 72	1.012 826 12
UN16	−0.083 303 30	0.000 000 00	−0.180 247 15
UA16	0.000 000 00	−0.117 202 43	−0.916 261 43
UN17	0.204 563 51	0.000 000 00	0.559 049 05
UA17	0.000 000 00	0.039 727 23	0.346 863 56
UN18	0.081 487 81	0.000 000 00	0.269 075 11
UA18	0.000 000 00	−0.089 643 81	−0.864 568 98
UN19	0.217 010 22	0.000 000 00	0.840 083 65
UA19	0.000 000 00	0.019 670 29	0.207 676 08
UN20	0.181 262 36	0.000 000 00	0.802 183 80
UA20	0.000 000 00	0.008 793 41	0.100 662 63

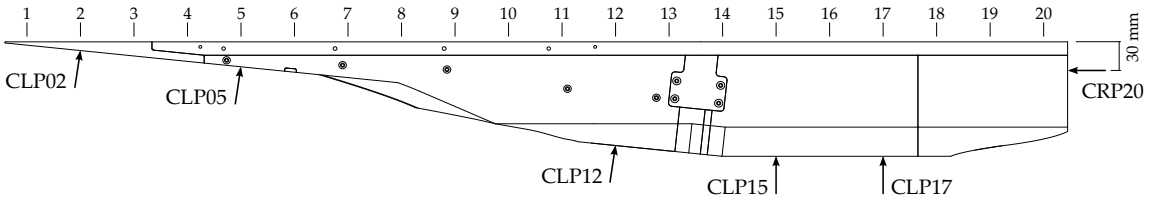

Figure B.5 – Lower calibration hit locations

on both the left and right hand sides of the model and two repeat hits in each direction for each lug position were completed. The weighting factors povided in Table B.2 were thus reduced by a factor of four when combining the individual IRF from hit sets 1 and 2 to form the GIRF.

In addition to defining the calibration weighting factors and output specification matrix, when assembling the GIRF HYFORCE also permits the user to specify scaling factors for each force component. These scaling factors are applied during the deconvolution process and can be used to prevent smaller magnitude signals from being dominated by larger magnitude signals (Robinson, 2003a). Studies by the author examining the influence of the scaling factors indicated that only the ratio of the scaling factors and not the absolute value is important and that the scaling factors act as amplifiers or filters for the recovered forces, affecting the magnitude of the signal oscillations without significantly affecting the mean value (for an appropriate averaging window). In this thesis a scaling factor of unity was used for each force component.

B.7 FORMATION OF A DISTRIBUTED LOWER LOAD

Recovered forces for a distributed load formed using calibration hits to both the lower and upper surfaces of the M12REST engine are presented and discussed in Section 4.6.3. This section provides additional details concerning the formation of the expected strain response for the lower distributed load.

A schematic of the lower calibration hit locations is provided in Figure B.5. Each hit location was marked on the experimental model using permanent ink and the aid of string guides as shown in Figure B.6. The coordinates of each hit location relative to the rear and top surfaces of the model[1] were measured using vernier calipers. The resulting values are provided in Table B.3 along with the theoretical coordinates extracted from a three-dimensional CAD model of the engine.

The general methodology used to combine the lower and upper calibration data was as follows. Using HYFORCE, individual IRF were generated

1 This is the force balance 1 or fb1 coordinate system as defined in Appendix E.

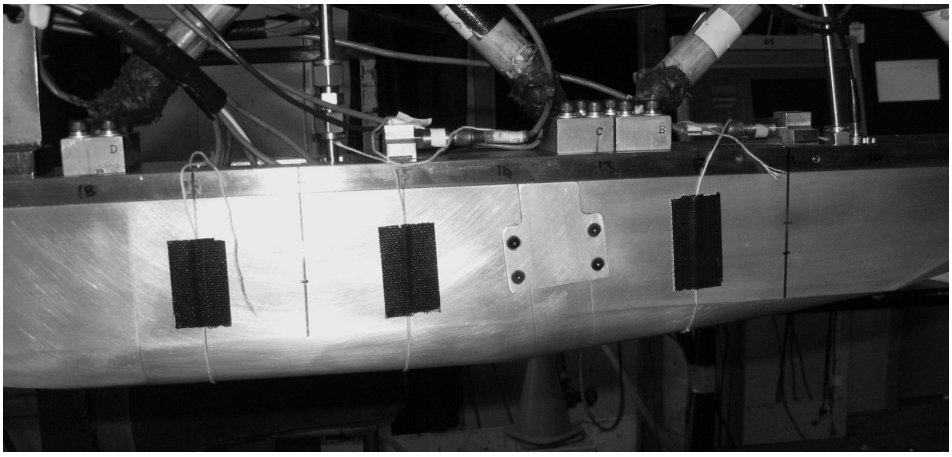

Figure B.6 – Marking the lower calibration hit locations using guide strings

Table B.3 – Lower Calibration Hit Coordinates

	Measured (mm)		Theorectical (mm)	
Label	x_{fb1}	y_{fb1}	x_{fb1}	y_{fb1}
CLP02	-844.0 ± 0.5	-8 ± 1	-844	-8.44
CLP05	-707.0 ± 0.5	-22 ± 1	-706.7	-22.9
CLP12	-387.0 ± 0.5	-93 ± 1	-386.5	-93.13
CLP15	-250.0 ± 0.5		-249.3	-102.47
CLP17	-158.0 ± 0.5		-157.8	-102.47
CRP20	0.0 ± 0.0	-30.0 ± 0.5	0.0	-30

for each bar and lower calibration hit from the measured hammer impulse and strain data. These individual IRF were then convolved with the unit-input load shown in Figure 4.6 to create a set of unit-strain responses. With reference to Figure 4.5, the unit-strain responses for the lower calibration locations were combined to simulate the lift distribution. The unit-strain responses for the upper calibration hits were similarly combined to simulate the drag distribution. The drag produced by the lower calibration hits at locations CLP02, CLP05 and CLP12 was taken into account when calculating the weightings for the upper calibration unit-strain responses. Defining $F_{x,j}$ and $F_{y,j}$ to be the drag and lift acting on the j-th slice of the engine as depicted in Figure 4.5, the weighting factors w for the lower unit-strain responses are defined by Equations (B.5) to (B.10) as follows:

$$w_{CLP02} = \frac{1}{\cos\theta} \sum_{j=1}^{3} F_{y,j} \tag{B.5}$$

$$w_{CLP05} = \frac{1}{\cos\theta} \left(\sum_{j=4}^{7} F_{y,j} + \frac{1}{2} F_{y,8} \right) \tag{B.6}$$

$$w_{CLP12} = \frac{1}{\cos\theta}\left(\frac{1}{2}F_{y,8} + \sum_{j=9}^{12} F_{y,j} + \frac{1}{2}F_{y,13}\right) \tag{B.7}$$

$$w_{CLP15} = \frac{1}{2}F_{y,13} + \sum_{j=14}^{15} F_{y,j} + \frac{1}{2}F_{y,16} \tag{B.8}$$

$$w_{CLP17} = \frac{1}{2}F_{y,16} + \sum_{j=17}^{20} F_{y,j} \tag{B.9}$$

$$w_{CRP20} = F_{x,20} \tag{B.10}$$

where $\theta = 6°$ is the angle of the forebody and external cowl surface relative to the x direction. Note that once formed the individual IRF for hit CRP20 was inverted so that it correctly corresponded to a force input in the positive x-direction. Consequently, no negative sign is required in Equation (B.10). The weighting factors for the upper unit-strain responses are similarly given by

$$w_j^k = \begin{cases} \dfrac{\delta_k^*}{\sqrt{2}}F_{x,j} & \forall j \in \{3,4,6-11,13-19\} \\ \dfrac{\delta_k^*}{\sqrt{2}}\left(F_{x,j} - F_{CLP,j}\sin\theta\right) & \forall j \in \{2,5,12\} \end{cases} \tag{B.11}$$

where $k \in \{N, A\}$ and

$$\delta_k^* = \begin{cases} -1 & \text{for } k = N \\ 1 & \text{for } k = A \end{cases}$$

The weighted summation of the individual unit-strain responses gives the total strain expected in each bar which was then combined according to the output specification matrix (Equation (4.16)) to give the expected strain response for the lower distributed load. Finally these strains were deconvolved using the GIRF. The resulting recovered forces are provided in Figure 4.12 and discussed in Section 4.6.3.

B.8 HAMMER HIT QUALITY

Typical hammer impulse signals from the pre- and post-campaign calibration sets are provided in Figure B.7 for location LUN08. Three repeat hits are shown for each calibration set and, for the purposes of visualisation, only the first millisecond has been plotted.[2] Raw hammer signals are provided in Figure B.7a, truncated hammer signals are provided in Figure B.7b and the result of convolution of the truncated hammer signal with a unit-step are provided in Figure B.7c.

2 The total recording time was 80 ms at a sampling interval of 5 µs.

Examining the raw hammer signals plotted in Figure B.7a, it can be seen that some noise is present outside of the pulse and that this noise is small relative to the peak signal value ($< 1\,\%$). As discussed by Mee (2002, Section 3.2.3) and Robinson (2003d, Section 3.4.6), this low magnitude noise adversely affects the quality of any IRF generated from the pulse signal. Consequently, and following both Mee (2002, 2003) and Robinson (2003d), each hammer signal was adjusted such that regions outside the pulse were exactly zero.[3] The resulting signals, known as truncated hammer signals, are provided in Figure B.7b.

Individual IRF are generated by deconvolving each strain signal with the associated truncated hammer signal (step 4, Table B.1). Furthermore, the quality of each truncated hammer signal was confirmed by convolving the signal with a unit-step. A perfect impulse (with area equal to one), when convolved with a unit-step returns a unit-step (Mee, 2003). Sample results of this convolution process are provided in Figure B.7c. The input unit-step signal is also plotted for comparison. As expected, each recovered step signal is shifted in time by half of the pulse width and the rise time is equal to the base width of the hammer pulse (approximately 240 µs for the example hits shown in Figure B.7b).

Figure B.8 provides a scatter plot of the peak force versus pulse width for the pre- and post-campaign data sets. Associated histograms with bin widths of 5 N and 5 µs are also provided. Given the large number of hits that were completed for each calibration set it is not surprising that significant scatter is present in Figure B.8. The peak force ranges between approximately 50 and 440 N while the pulse width ranges between approximately 150 and 380 µs. For the pre-campaign data set the average peak force is (176 ± 55) N and the average pulse width is (214 ± 38) µs, where the quoted uncertainty represents one standard deviation of the data set. Similarly, for the post-campaign data set the average peak force is (251 ± 63) N and the average pulse width is (198 ± 25) µs. These average pulse widths are comparable with the characteristic time of the system. The characteristic time is defined as the time taken for a stress wave to travel from one end of the model to the other and back and is approximately equal to[4] 285 µs. Mee (2002, 2003) investigated the influence of the pulse width on the resulting IRF and found that even when the pulse width cannot be considered short compared with the response of the system, an IRF determined via deconvolution of the hammer impulse with the strain response is almost indistinguishable from the true IRF. Hence, despite the similarity in period of the pulse width and system response and the

3 The criterion that was used in this thesis to define regions outside the pulse was any portion of the signal that is smaller than 1 % of the peak signal. Additionally, prior to setting regions outside the pulse to zero, the hammer signal was adjusted so that the mean of the noise was exactly zero.

4 Calculated using a model length of 915 mm and a sound speed in aluminium of 6420 m/s (Haynes, 2013, Section 14).

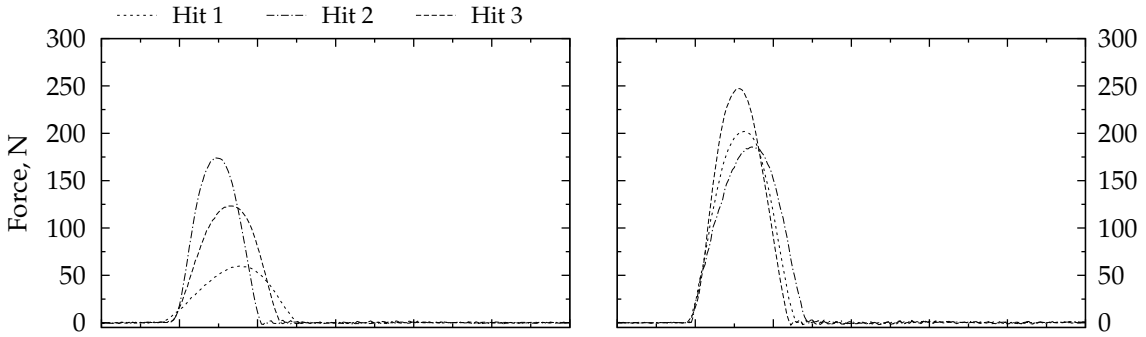

(a) Raw hammer signals. For visualisation purposes only the first 1 ms has been shown.

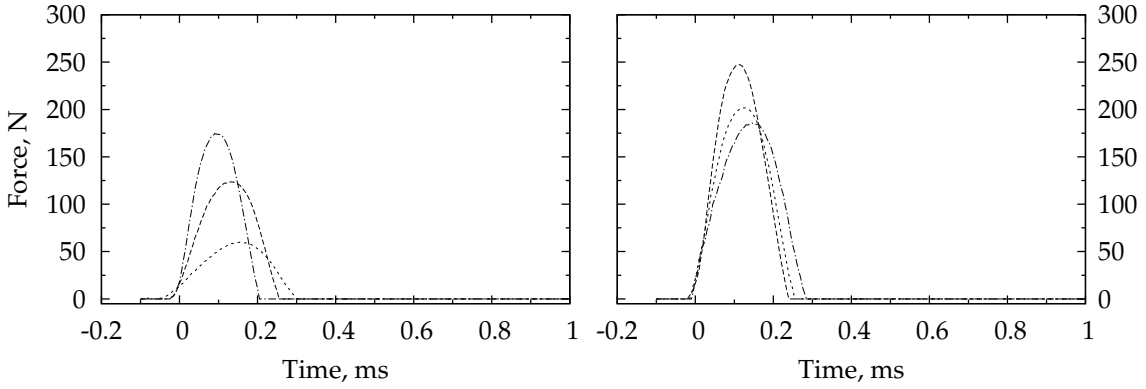

(b) Truncated hammer signals. For visualisation purposes only the first 1 ms has been shown.

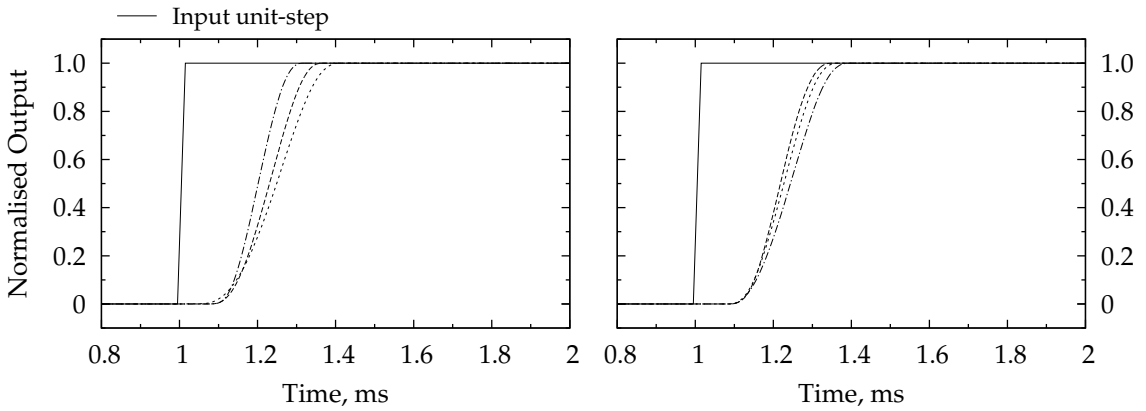

(c) Normalised step-convolution output. These signals were generated by convolving each truncated hammer signal with a unit-step and then normalising the output by the integral of the hammer signal.

Figure B.7 – Hammer hit data for location LUN08. Data given in the left hand column are from the *pre*-campaign calibration set, data given in the right hand column are from the *post*-campaign calibration set.

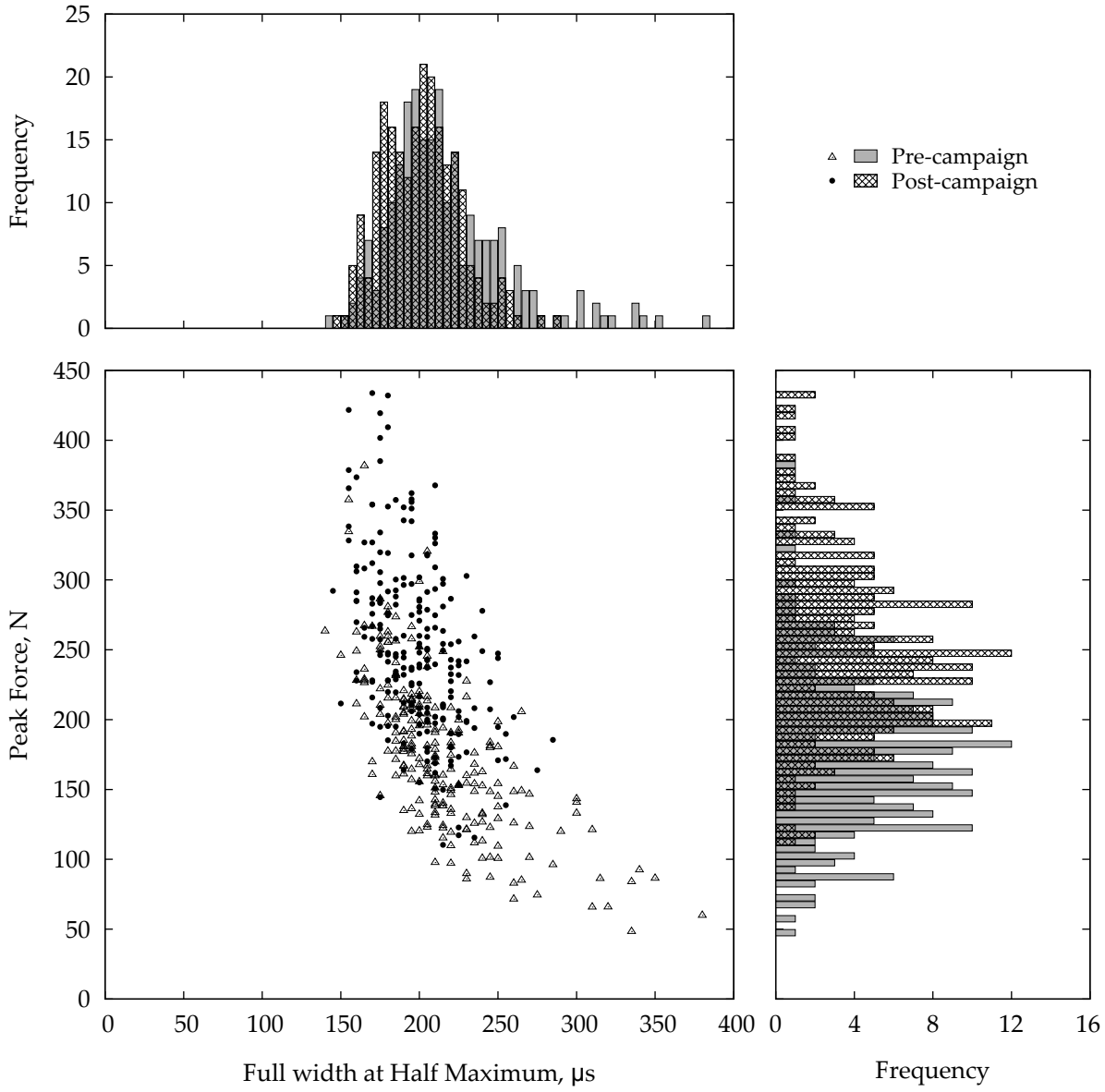

Figure B.8 – Scatter plot of peak force versus pulse width for every hammer hit. The bin width for the associated histograms is 5 N for the peak force and 5 µs for the pulse width.

scatter in the data, each hammer hit was considered to be of sufficient quality for purpose of calibrating the force balance for use in this thesis.[5] Techniques for improving the repeatability of the hammer impulse and reducing the scatter in Figure B.8 is a topic for future investigation. The full set of calibration hammer hits may be found in Doherty (2013c).

B.9 STRAIN REPEATABILITY AND SYMMETRY

Example unit-load strain responses for the primary gauge on each stress bar are provided in Figures B.9 and B.10 for the pre- and post-campaign calibration sets, respectively. Each row corresponds to a single stress bar while each pair of columns corresponds to hits on the left and right sides of the model. Data for three calibration locations are presented. These locations are a normal hit at station 08 (Figures B.9a and B.10a), an axial hit at station 11 (Figures B.9b and B.10b), and a normal hit at station 14 (Figures B.9c and B.10c). Each strain response was generated by convolving the associated individual IRF with the unit-load given in Figure 4.6.

Examining the results plotted in Figures B.9 and B.10, it can be seen that irrespective of which particular stress bar or calibration is examined, the strain responses from three repeat hits lie almost exactly on top of one another. Furthermore, comparing responses for hits on the left side of the model with those for hits on the right side of the model, it can be seen that the strains are slightly asymmetric. This asymmetry is not surprising since the internal mechanical structure of the M12REST engine is not perfectly symmetric (Doherty, 2013b). In this thesis, asymmetry of the strain responses was accounted for by always averaging the individual IRF formed from hits to the left and right sides of the model (Section 4.4).

Finally, careful comparison of the data plotted in Figure B.9 with that plotted in Figure B.10 reveals that the expected unit-load responses are slightly different for the pre-campaign calibration compared with the post-campaign calibration. Possible reasons for the change in calibration are discussed in Section 4.6.1. A full set of strain repeatability results may be found in Doherty (2013c).

B.10 RECOVERY OF CALIBRATION POINT LOADS

The ability of the GIRF to recover point loads at selected calibration stations along the length of the M12REST engine is shown in Figure B.11 for both the pre- and post-campaign calibration data. Each row represents a different calibration station according to the quoted j-index value (cf. Figure 4.3). The left hand column presents data for a normal hit; the right hand column

5 It should be noted that when conducting the hammer hits, only those which featured a single, well-formed pulse were kept and used for the calibration of the balance i.e. the three hits represent three good hits out of a larger set of hits.

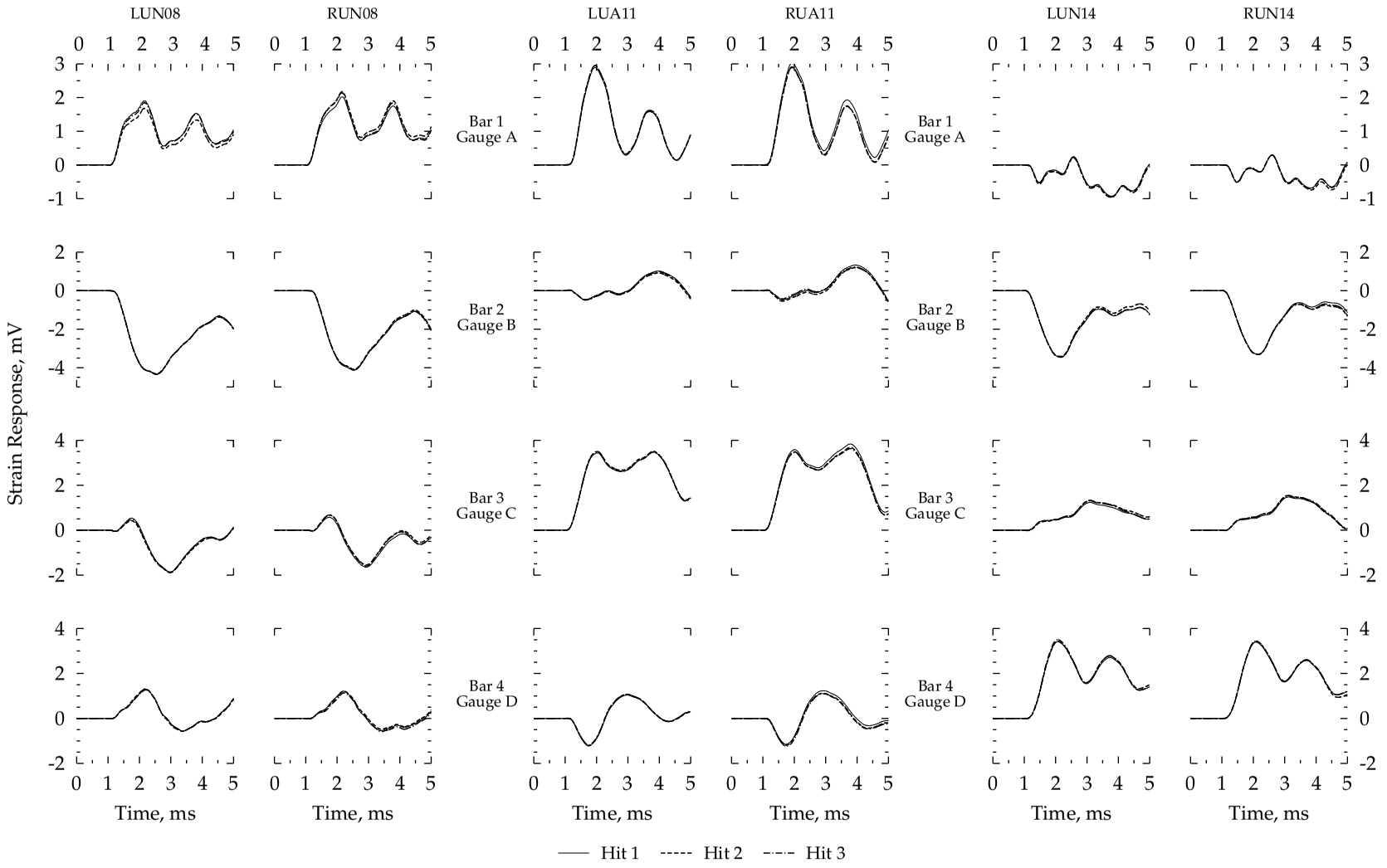

(a) Normal hit, station 08 (b) Axial hit, station 11 (c) Normal hit, station 14

Figure B.9 – Strain repeatability and symmetry for selected *pre*-campaign calibration hits

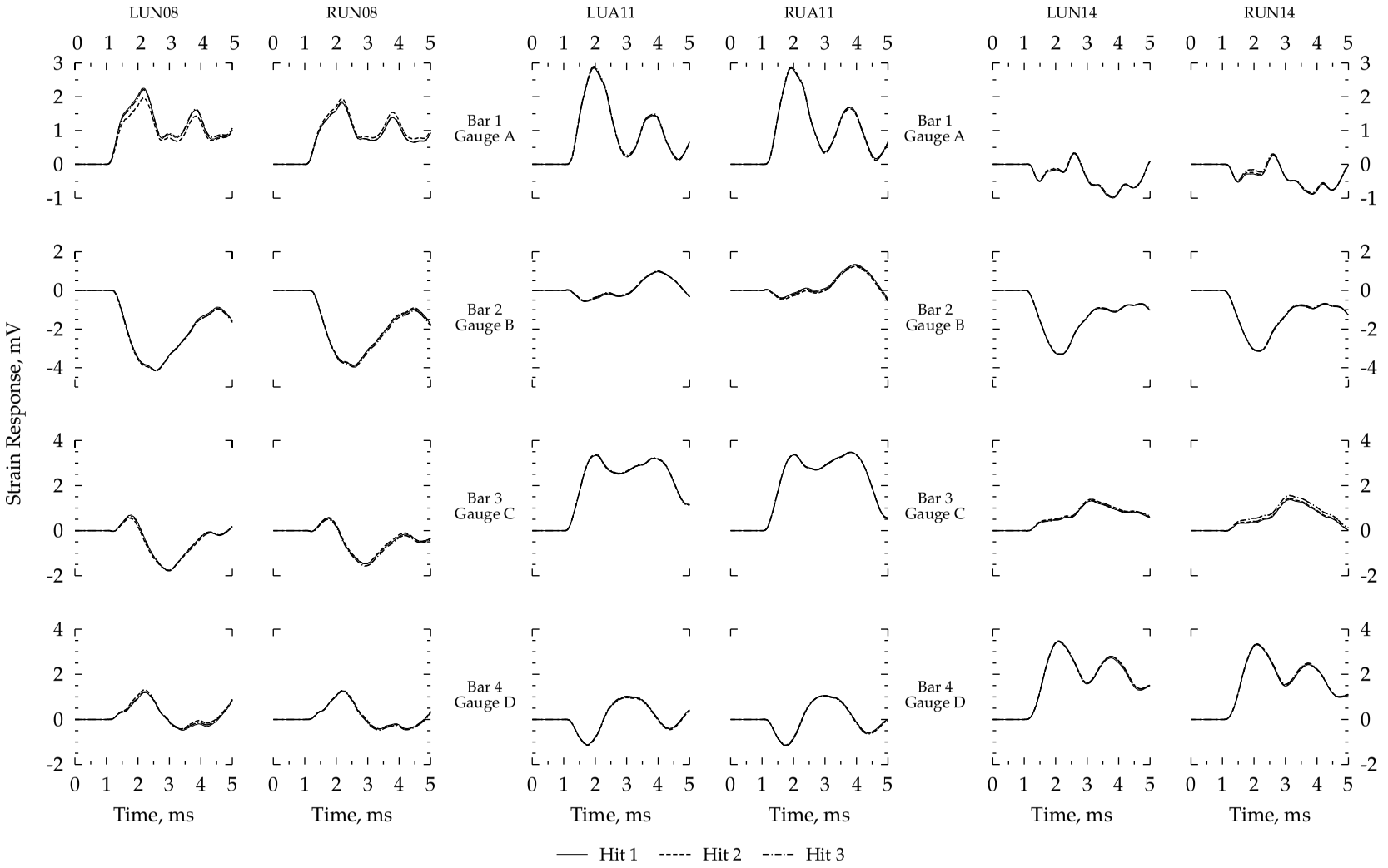

(a) Normal hit, station 08 (b) Axial hit, station 11 (c) Normal hit, station 14

Figure B.10 – Strain repeatability and symmetry for selected *post*-campaign calibration hits

presents data for an axial hit.

While the overall quality of the recovered forces is poor, there are some trends that are worth mentioning. Firstly, the dominant transient structures in the pre-campaign recovered forces are comparable those of post-campaign recovered forces. Secondly, the overall time history of the recovered forces for the two orthogonal hit directions (i.e. normal and axial) are generally different from each other at each calibration station and the quality of the recovered forces varies along the length of the engine. The quality of the recovered force signals is worse at the model extremities and better near the centre of the model. For stations $j = 5$ through to $j = 11$ a large scale, low frequency oscillation dominates the recovered forces for a normal input but is absent from the recovered forces for an axial input. Also at station $j = 11$ an axial input is recovered better than a normal input whereas the reverse occurs at station $j = 17$.

These results are each a consequence of the shape of the load distribution that was used to form the GIRF. Shown in Figure 4.4, the forces are greatest at calibration locations $j = 8$ through to $j = 11$, leading to these locations beign weighted more than the other during the formation of the GIRF. It is therefore expected that the GIRF would recover point loads at these locations better than elsewhere along the model. Similarly, the axial load is significantly greater than the normal load at station $j = 11$ resulting in an axial input being better recovered at this location than a normal input. Station $j = 17$ represents the opposite case. The inability of the GIRF to accurately recover a point load is not unexpected. The GIRF was created to recover a distributed load. The stress wave pattern induced within the model by a point load is significantly different from that induced by a distributed load of the same net force. As a consequence, the distributed-GIRF struggles to recover an applied point force.

B.11 CROSS-DECONVOLVED DISTRIBUTED LOAD RECOVERY

For completeness, cross-deconvolved recovered forces for the fuel-off and lower fuel-off distributed loads are provided in Figures B.12 and B.13 respectively. The cross-deconvolution was completed between the pre- and post-campaign calibration data. That is, the *pre*-campaign expected strain was deconvolved using the *post*-campaign GIRF. Similarly, the *post*-campaign expected strain was deconvolved using the *pre*-campaign GIRF. In conjuction with the recovered forces plotted in Figures 4.7, 4.8, 4.10 and 4.12, the data plotted in Figures B.12 and B.13 complete the set of evaluations of the GIRF for the three distributed loads examined in this thesis.

Comparing the fuel-off recovered force data plotted in Figure B.12 with that plotted in Figure 4.10 it is obvious that the forces recovered by cross-deconvolution are degraded with respect to those recovered

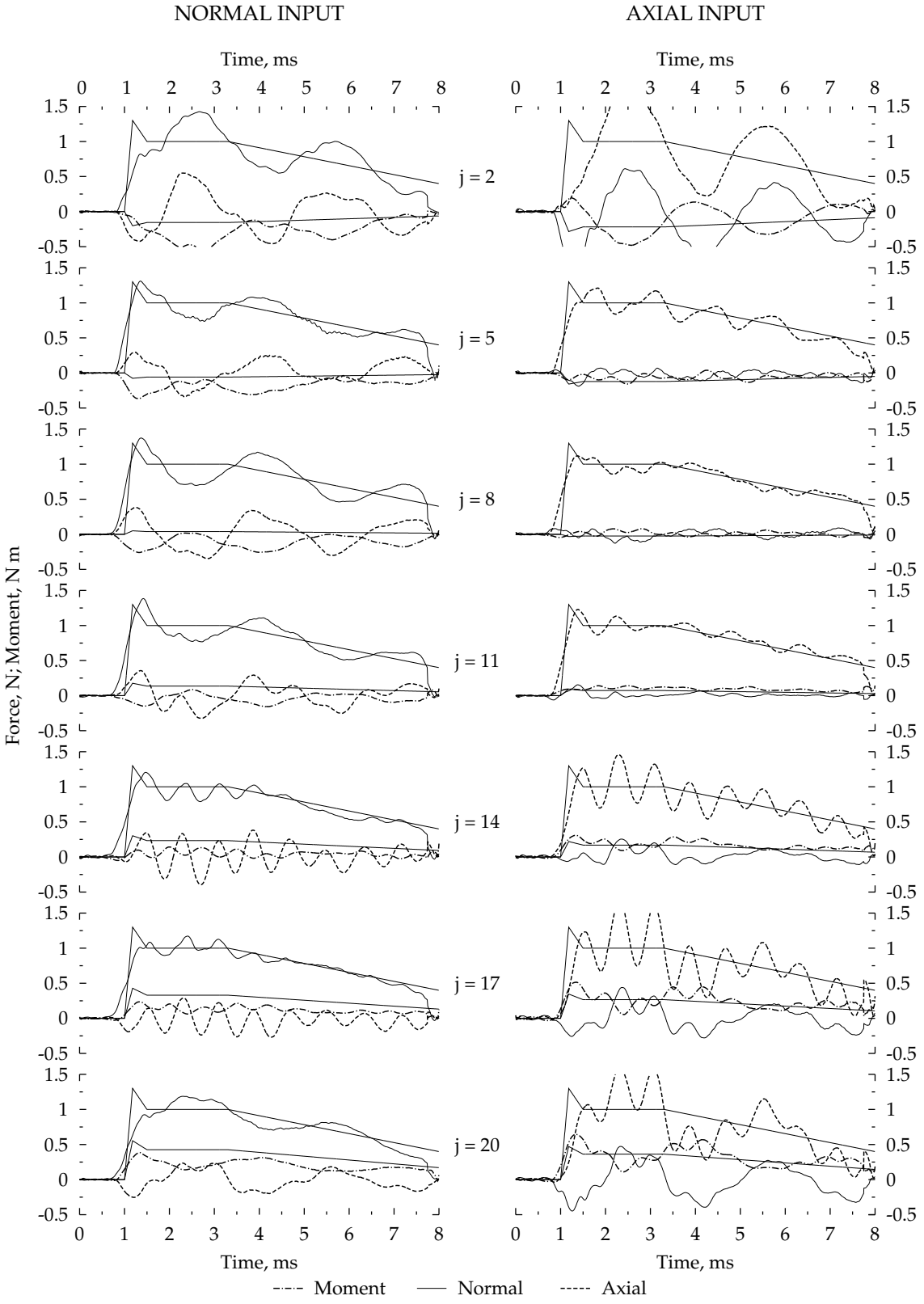

(a) *Pre*-campaign calibration

Figure B.11 – Recovery of tunnel-type point loads at selected calibration locations using the primary gauge calibration data and GIRF. The recovered forces have been filtered by a 500 µs moving average.

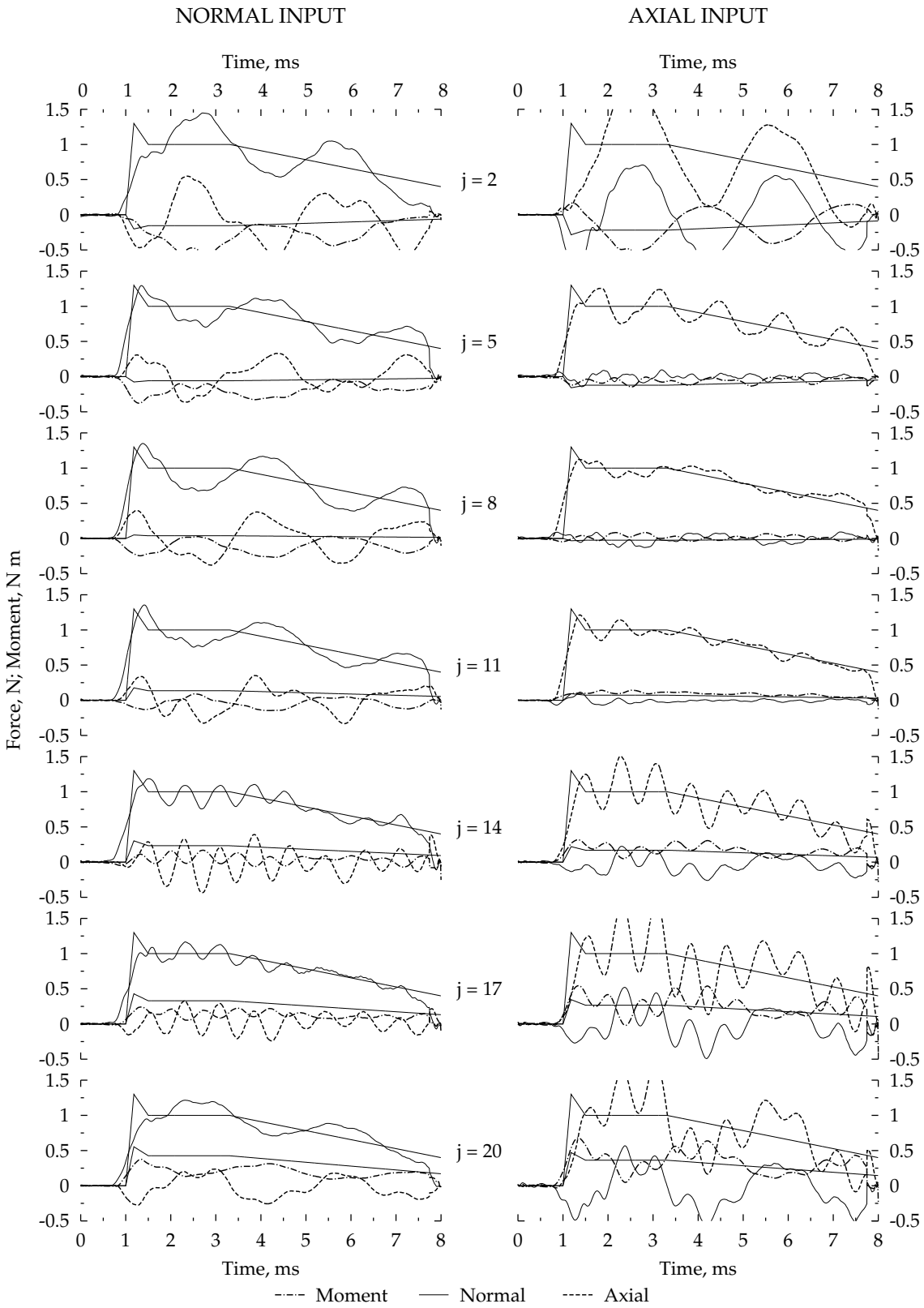

(b) *Post*-campaign calibration

Figure B.11 – Continued.

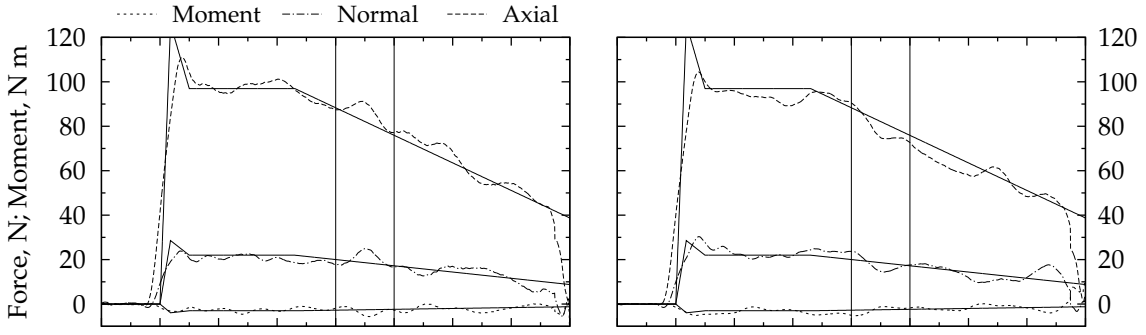

(a) Recovered Normal, Axial and Moment force components.

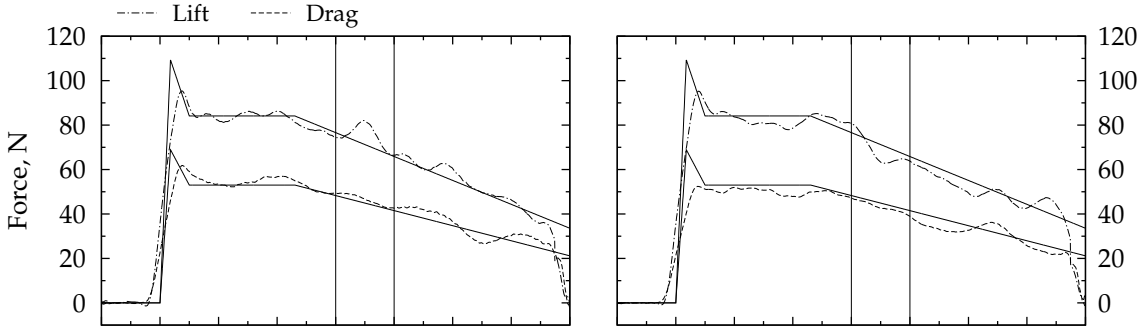

(b) Recovered Lift and Drag force components. These are computed via a coordinate transformation from the recovered Normal and Axial forces (Appendix E).

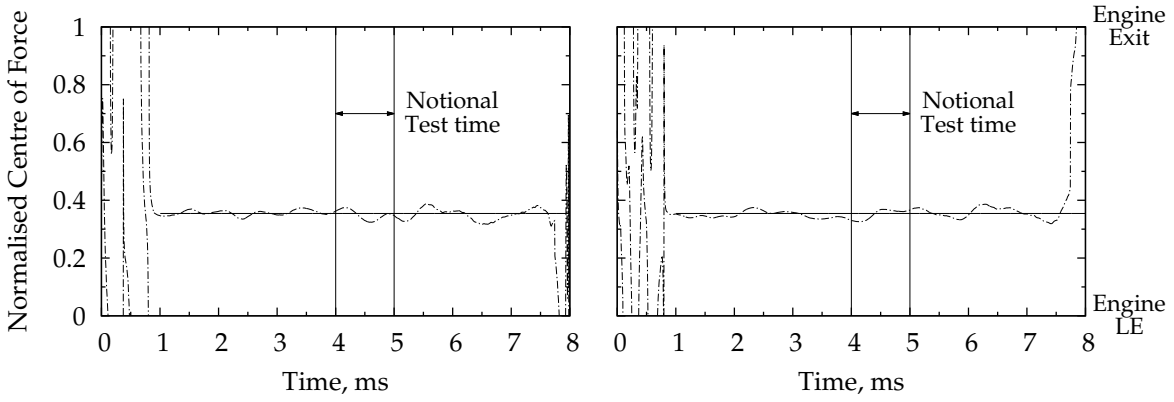

(c) Recovered Normalised Centre of Force. This is computed from the recovered lift, drag and moment using knowledge of the balance centre and leading edge locations (Section 4.7).

Figure B.12 – Cross-deconvolved recovered forces for the fuel-off distributed load formed from the *primary* gauges. *Pre*-campaign strain data deconvolved using the *post*-campaign GIRF is given in the left hand column, *post*-campaign strain data deconvolved using the *pre*-campaign GIRF is given in the right hand column. The recovered forces have been filtered by a 500 µs moving average.

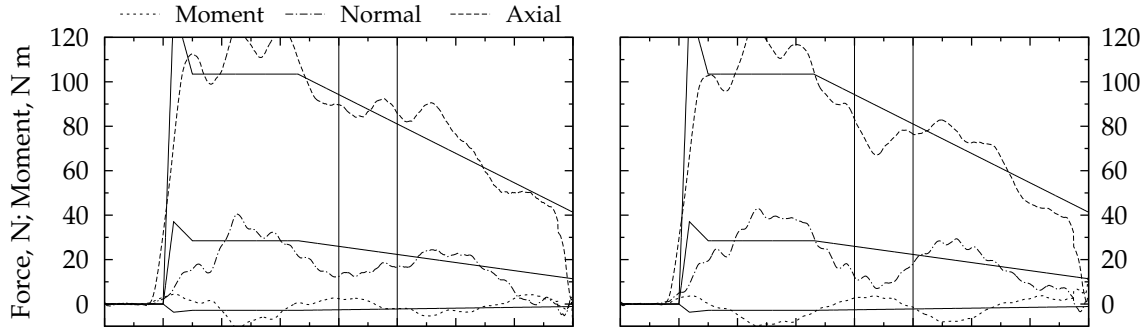

(a) Recovered Normal, Axial and Moment force components

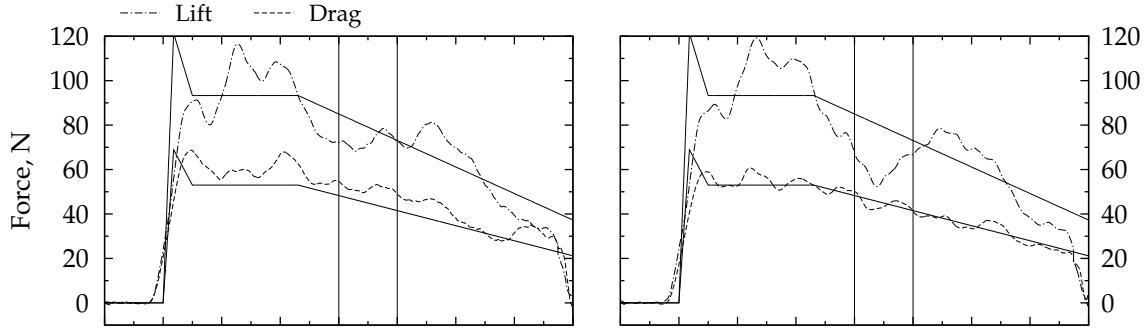

(b) Recovered Lift and Drag force components. These are computed via a coordinate transformation from the recovered Normal and Axial forces (Appendix E).

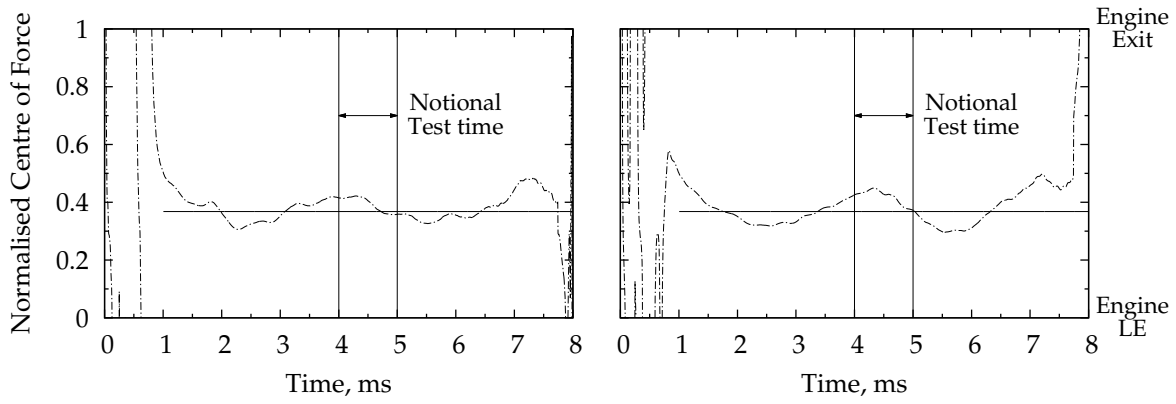

(c) Recovered Normalised Centre of Force. This is computed from the recovered lift, drag and moment using knowledge of the balance centre and leading edge locations (Section 4.7).

Figure B.13 – Cross-deconvolved recovered forces for the fuel-off distributed load formed from both the lower and upper calibration hits using the *primary* gauges. *Pre*-campaign strain data deconvolved using the *post*-campaign GIRF is given in the left hand column; *post*-campaign strain data deconvolved using the *pre*-campaign GIRF is given in the right hand column. The recovered forces have been filtered by a 500 µs moving average.

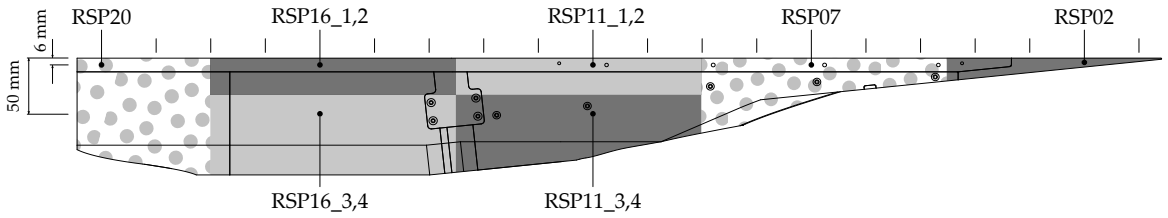

Figure B.14 – Location of, and area allocated to each side calibration hit

by self-deconvolution. Qualitatively, the overall 'level' of degradation is independent of the GIRF. These results imply that some change in the model occured between the pre- and post-campaign calibrations of the force balance. In comparison, the cross-deconvolved froces plotted in Figure B.13 for the lower fuel-off distributed load are comparable with the self-deconvolved forces plotted in Figure 4.12. Further discussion of these results is given in Sections 4.6.3 and 4.6.3.

B.12 RECOVERY OF A DISTRIBUTED SIDE LOAD

The force balance used in this thesis was designed to recover two in-plane force components and the in-plane moment, that is, the lift and drag forces and the pitching moment. The balance cannot recover out-of-plane forces and moments such as the yawying and rolling moments and side force. Nevertheless, these out-of-plane forces and moments may be present due to misalignment of the model with respect to the facility nozzle or asymmetric non-uniformities of the test flow. It is therefore important to assess the sensitivity of the balance to these out-of-plane forces. This assessment was accomplished by hitting the model from the side, calculating the corresponding individual IRF and unit-load strain responses and combining the unit-load strains to represent an applied, out-of-plane loading distribution. The combined strain signals were then deconvolved and the magnitude of the recovered forces compared to those expected for the in-plane forces. Details of this procedure are provided in this section.

Shown in Figure B.14, the M12REST engine was hit from the side at seven different locations. Two hits were conducted at each location. The side area allocated to each hit has been drawn in Figure B.14. These areas and corresponding weighting factor for each hit are summarised in Table B.4. The weighting factors were calculated by approximating the side of the M12REST engine as a flat plate and assuming a misalignment with the test flow of 0.2° angle-of-yaw. This misalignment angle is *twice* that of the uncertainty in the measured yaw alignment of the model (see Section 3.4.7). Assuming a Mach 10 freestream flow with static pressure 1000 Pa, the

Table B.4 – Area and weighting factors for the side calibration hits. Area unit – mm^2

Label	Hit	Area label	Area	Weighting
RSP02	1	A_2	1987.4	0.0994
	2		1987.4	0.0994
RSP07	1	A_7	8082.8	0.4041
	2		8082.8	0.4041
RSP11	1	$A_{11,1}$	6382.1	0.3191
	2		6382.1	0.3191
RSP11	3	$A_{11,2}$	11 374.3	0.5687
	4		11 374.3	0.5687
RSP16	1	$A_{16,1}$	6382.1	0.3191
	2		6382.1	0.3191
RSP16	3	$A_{16,2}$	14 692.8	0.7346
	4		14 692.8	0.7346
RSP20	1	A_{20}	10 420.3	0.5210
	2		10 420.3	0.5210

pressure differential between the two sides of a flat plate is approximately 100 Pa. On the windward side the flow is processed by an oblique shock, increasing the pressure to 1050 Pa and on the leeward side the flow is processed by a Prandtl-Meyer expansion, decreasing the pressure to 952 Pa. For both the oblique-shock and Prandtl-Meyer expansion calculations the specific heat ratio and gas constant were assumed to be 1.4 and 287 J/(kg K) respectively, i.e. nominal values for air. The weighting factors sum to a net side force of 5.9 N, equivalent to 13.1 % of the expected drag and 8.3 % of the expected lift for the M12REST engine with no fuel injection (see Table 4.1 and Chapter 5).

The total normal, axial and moment strains formed by the weighted summation of the individual unit-strain responses using the weighting factors given in Table B.4 are plotted in Figure B.15a for the pre- and post-campaign calibration data. The lift, drag and moment signals recovered by deconvolution are similarly provided in Figure B.15b. Comparing the strains plotted in Figure B.15a to those plotted in Figure 4.14 for a typical shot, it can be seen that the side force strains are approximately three orders of magnitude smaller than those measured during a shot. The recovered lift, drag and pitching moment plotted in Figure B.15b are each less than 1 further demonstrating that the balance is not very sensitive to an out-of-plane force. In this thesis an uncertainty of ± 1 N or ± 1 N m due to out-of-plane forces was considered acceptable.

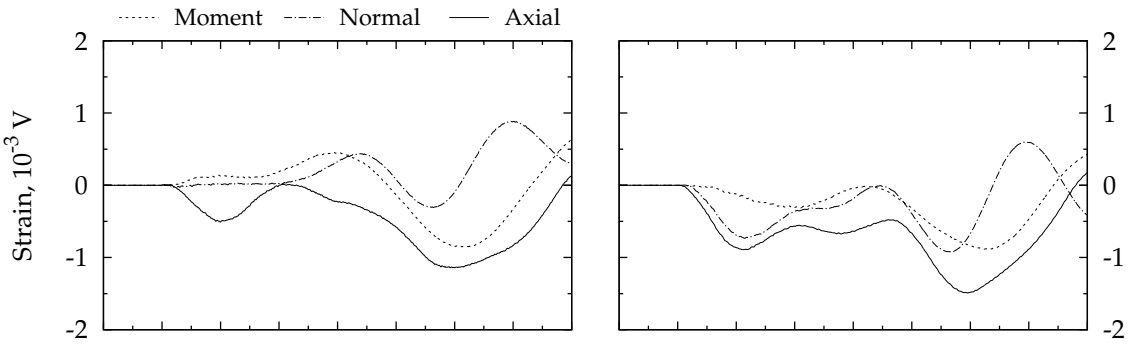

(a) Normal, Axial and Moment strains formed by a weighted summation of individual strain responses.

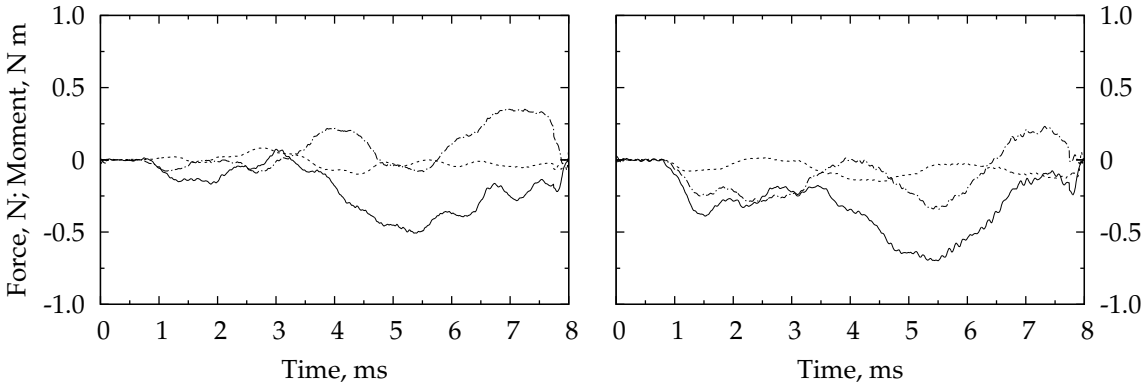

(b) Recovered Normal, Axial and Moment (about balance centre) forces.

Figure B.15 – Sensitivity of GIRF to uniform distributed side load using the *primary* gauges. *Pre*-campaign calibration data is given in the left hand column, *post*-campaign calibration data is given in the right hand column. The recovered forces have been filtered by a 500 µs moving average.

B.13 SENSITIVITY TO FORCE TIME HISTORY

It was noted in Chapter 7 that during the test campaign the engine drag was observed to establish more slowly than the internal pressure measurement. It was also found that the time histories of the recovered lift and drag signals were different from one another. To check that the balance was providing a realistic measurement during the experiment, the ability of the balance to recover a distributed load with drag time history different to the lift time history was investigated. The investigation followed a methodology similar to that described in Section 4.6 (items 4 and 5) but using two different unit-loads, one for lift and one for drag. These unit-loads are shown in Figure B.16.

The methodology was as follows: at each calibration station, the lift and drag unit-loads were scaled by the total lift and drag acting on the

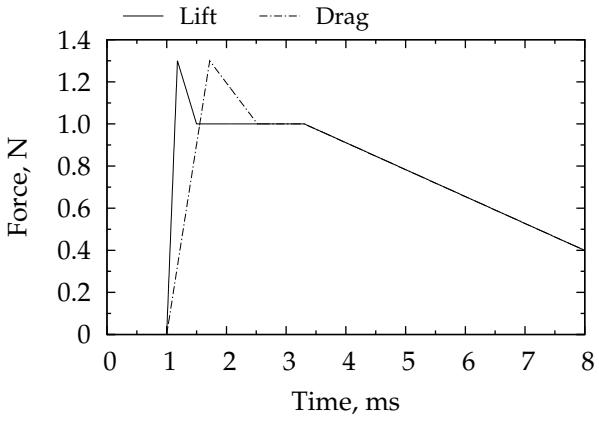

Figure B.16 – Time history of unit, tunnel-type input loads with different establishment transients

corresponding slice of the engine as given by either the reference or fuel-off load distribution (Figures 4.4 and 4.5 respectively). These lift and drag inputs were then transformed to give the normal and axial inputs at each calibration station. The normal and axial inputs were convolved with the individual IRF for each stress bar to give the expected strain response of each bar to an input load at each calibration station. For each bar, the set of strain responses were then added together to give to the total expected strain response. Finally, the responses of the four bars were combined according to Equation (4.14) to give the total expected normal, axial and moment strain response of the balance. This total expected strain response was then deconvolved with the GIRF and the recovered forces compared with the total input force. The results are provided in Figure B.17 for the reference load distribution (Figure 4.4) and in Figure B.18 for the fuel-off load distribution (Figure 4.5).

Examining the recovered forces plotted in Figure B.17 it is clear that both the time history and magnitude of the input load are reasonably well recovered by each GIRF (pre- and post-campaign). However, the recovered forces are degraded with respect to those plotted in Figure 4.7 for the same load distribution; an oscillation with period approximately 1 ms is present in Figure B.17 but absent from Figure 4.7. Similar results are obtained for the fuel-off load distribution results plotted in Figure B.18; the time history and magnitude of the recovered forces match the input loads reasonably well but the quality of the recovered forces are degraded with respect to the results plotted in Figure 4.10. A very low frequency oscillation is present in the recovered normal and axial forces for the fuel-off distributed load. This oscillation is similar to, but less dominant than, that which occured in the recovered forces for a lower distributed fuel-off load (Section 4.6.3). Due to the transformation to the lift-drag coordinate

system, this oscillation remains in the recovered lift and centre of force but is eliminated from the recovered drag.

Together with Figures 4.7 and 4.10, the results presented in Figures B.17 and B.18 indicate that the balance is slightly sensitive to the lift and drag having different time histories. That is, when the drag time history is different to the lift time history the recovered forces do not match the input loads as closely as the forces recovered for the case where the lift and drag time history are identical. This sensitivity of the balance to differences in the time history of the lift and drag is a consequence of cross-coupling between the force inputs and strain outputs of the balance. It is also a consequence of the lift and drag not being directly measured but being recovered via a coordinate transformation of the recovered normal and axial components.

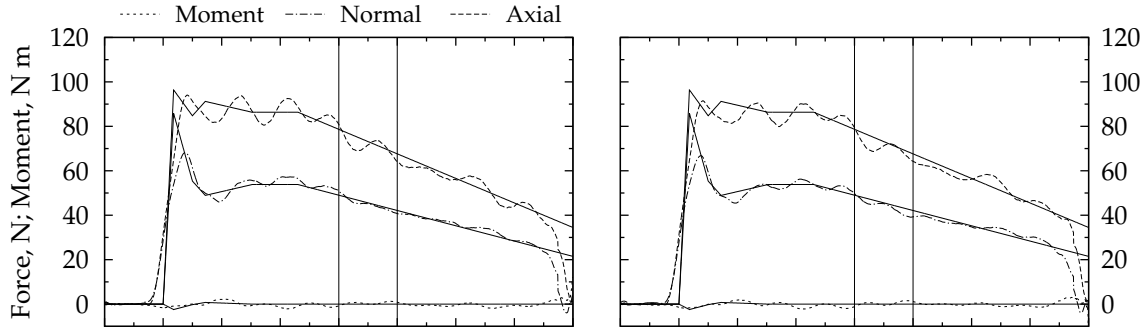

(a) Recovered Normal, Axial and Moment force components.

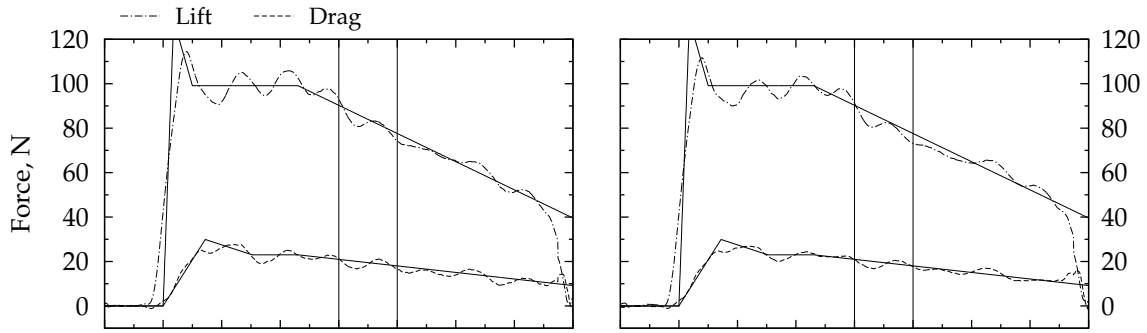

(b) Recovered Lift and Drag force components. These are computed via a coordinate transformation from the recovered Normal and Axial forces (Appendix E).

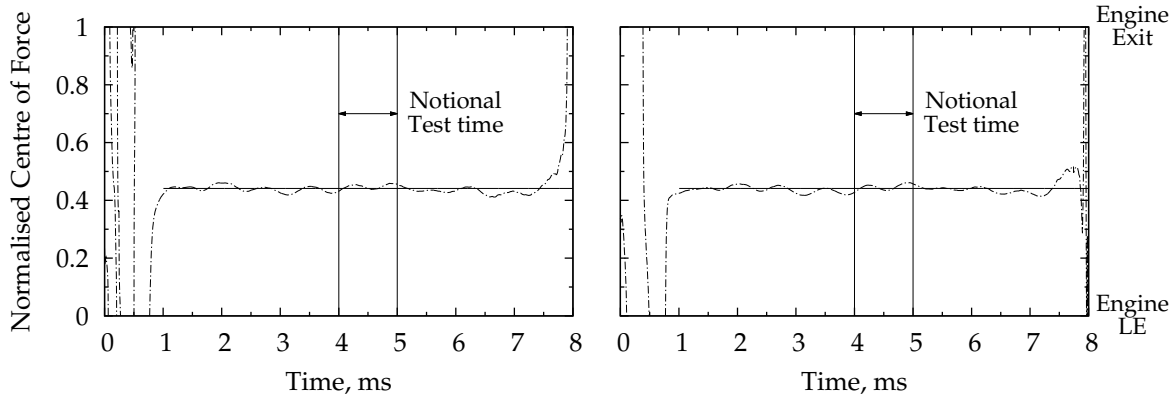

(c) Recovered Normalised Centre of Force. This is computed from the recovered lift, drag and moment using knowledge of the balance centre and leading edge locations (Section 4.7).

Figure B.17 – Recovery of the reference (fuel-on) distributed load with long drag establishment using the GIRF formed from the *primary* gauge signals. *Pre*-campaign calibration data is given in the left hand column, *post*-campaign calibration data is given in the right hand column. The recovered forces have been filtered by a 500 µs moving average.

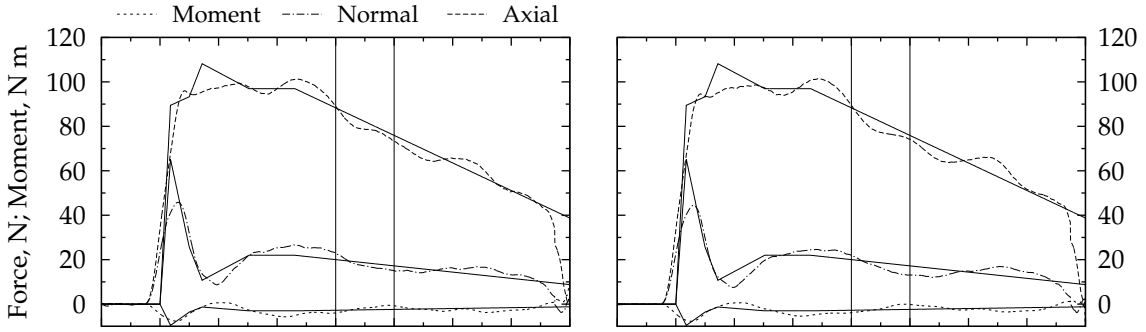

(a) Recovered Normal, Axial and Moment force components

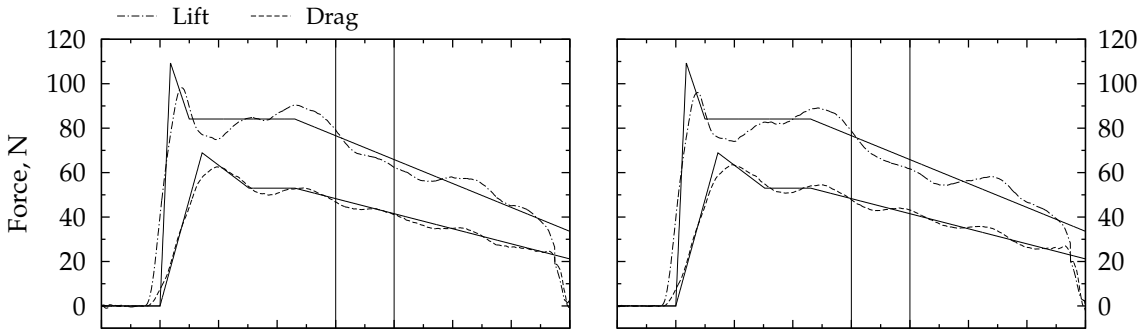

(b) Recovered Lift and Drag force components. These are computed via a coordinate transformation from the recovered Normal and Axial forces (Appendix E).

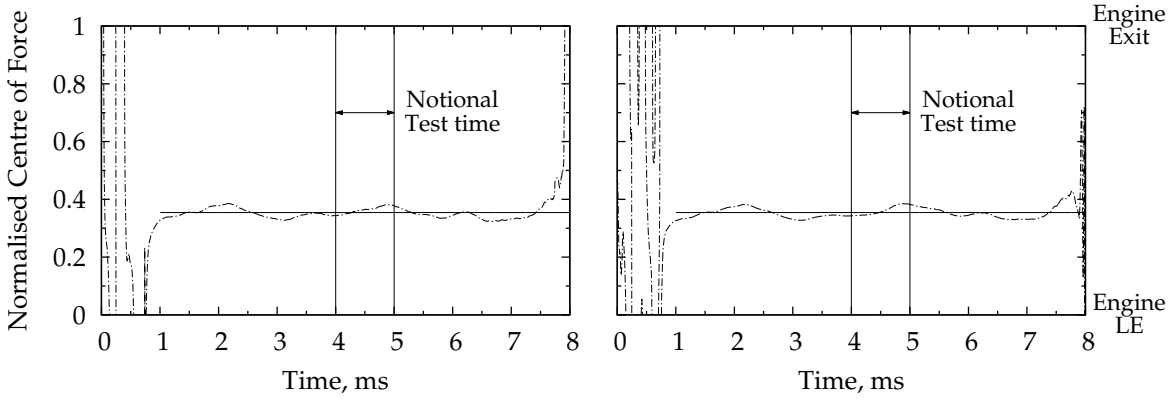

(c) Recovered Normalised Centre of Force. This is computed from the recovered lift, drag and moment using knowledge of the balance centre and leading edge locations (Section 4.7).

Figure B.18 – Recovery of the fuel-off distributed load with long drag establishment using the GIRF formed from the *primary* gauge signals. *Pre*-campaign calibration data is given in the left hand column, *post*-campaign calibration data is given in the right hand column. The recovered forces have been filtered by a 500 µs moving average.

UNCERTAINTY ANALYSIS

C.1 INTRODUCTION

C

This appendix presents the uncertainty analysis for the experimental results presented in this thesis. The appendix begins with a description of the general theory of uncertainty analysis as applied in this thesis. The theory description closely follows that presented in Coleman and Steele (1999) and Hudson et al. (2003), albeit more concisely. The appendix continues by outlining the experimental uncertainty for the nozzle supply, engine and fuel plenum pressure measurements in Appendix C.3. The analyses presented in these two sections build on that presented in Appendices A.2 and A.3, respectively. The uncertainty of the nozzle exit flow properties, calculated using NENZFR, are provided in Appendix C.4. This is followed by a presentation of the uncertainties for the nominal engine forebody conditions in Appendix C.5. Throughout this thesis the experimental engine pressure data are presented in the form of a ratio relative to the nominal engine forebody pressure. The uncertainty analysis for this derived quantity is provided in Appendix C.6 and a similar analysis for the engine force coefficients is presented in Appendix C.7. The penultimate and final sections of this appendix are concerned with the fuel system. Appendix C.8 presents the uncertainty analysis for the fuel system calibration while Appendix C.9 presents the uncertainty analysis for the experimental fuel and air mass flow rates and the fuel equivalence ratio.

C.1.1 *A Comment on the Treatment of the Test Time Average*

Care must be exercised when applying the theory outlined in the following sections to shock tunnel data. Due to the transient testing environment generated by impulse facilities such as the T4 Stalker Tube, it is not appropriate to treat the selection of the test time and the test time averaging process as a data reduction equation (or algorithm). In this thesis, the test time is chosen for each shot and once chosen is considered fixed. The average during the test time is then taken to be a single, fundamental measurement rather than an average of a large number of samples.[1] For shock tunnel data, the precision uncertainty of a single measurement (which is the average during the test time) should be estimated from a

1 For a half millisecond test time as used in this thesis and sampling rate of 1 MHz, the mean pressure during the test time is the average of 500 samples.

set of repeat shots and not from the variation during the test time. See Coleman and Steele (1999, Section 4-3.1) and Bendat and Piersol (2010) for further discussion.

C.2 THEORY

Based extensively on the descriptions, explanations and equations that appear in Coleman and Steele (1999) and Hudson et al. (2003), the purpose of this section is to provide a succinct summary of the general theory of uncertainty analysis, with particular focus on those aspects that have been applied and used in this thesis. Consider a general data reduction equation

$$F = F(\psi_1, \psi_2, \ldots, \psi_n) \tag{C.1}$$

that is some function of n fundamental measurements ψ_i. The term *fundamental* is used here to emphasise that the data reduction equation should be written in terms of the experimental quantities that are (actually) measured. At its most general, the data reduction equation does not need to be able to be written as an analytical expression, it can be any "black box" that takes a set of inputs $\{\psi_i\}_{i=1}^{n}$ and returns an output F. For such a case, the partial derivatives that appear in the following equations must be calculated numerical using a finite difference scheme (or equivalent). A specific example of such a "black box" is the computer program NENZFR that is used in this thesis to calculate the nozzle exit flow properties (see Section 3.3 and Appendix C.4).

The general expression[2] for the total absolute uncertainty U_F in computed result F is

$$U_F^2 = \sum_{i=1}^{n} \left(\frac{\partial F}{\partial \psi_i} \right)^2 U_{\psi_i}^2 + 2 \sum_{i=1}^{n-1} \sum_{k=i+1}^{n} \left(\frac{\partial F}{\partial \psi_i} \right) \left(\frac{\partial F}{\partial \psi_k} \right) U_{ik} \tag{C.2}$$

where U_{ψ_i} is the total uncertainty in input ψ_i and U_{ik} is the covariance estimate that accounts for the uncertainties in ψ_i and ψ_k being correlated. At its most general, experimental uncertainty analysis consists entirely of the evaluation of Equation (C.2). This evaluation however, may be simplified by considering the systematic or bias uncertainties separately to the precision or random uncertianties. For any quantity, the total uncertainty can be written as

$$U^2 = P^2 + B^2 \tag{C.3}$$

where P is the random uncertainty component and B is the systematic

2 This expression is the 95 % confidence interval of the uncertainty based on the so-called *large-sample* assumption. See Appendix B in Coleman and Steele (1999) for further details.

uncertainty component. Similarly, the total covariance estimate for the correlated uncertainty between two quantities may be written as

$$U_{ik} = P_{ik} + B_{ik} \tag{C.4}$$

where P_{ik} and B_{ik} are the covariance estimates for the correlated precision and bias uncertainty components, respectively. Subsitution of Equations (C.3) and (C.4) into Equation (C.2) yields

$$U_F^2 = P_F^2 + B_F^2 \tag{C.5}$$

with

$$P_F^2 = \sum_{i=1}^{n} \left(\frac{\partial F}{\partial \psi_i} \right)^2 P_{\psi_i}^2 + 2 \sum_{i=1}^{n-1} \sum_{k=i+1}^{n} \left(\frac{\partial F}{\partial \psi_i} \right) \left(\frac{\partial F}{\partial \psi_k} \right) P_{ik} \tag{C.6}$$

and

$$B_F^2 = \sum_{i=1}^{n} \left(\frac{\partial F}{\partial \psi_i} \right)^2 B_{\psi_i}^2 + 2 \sum_{i=1}^{n-1} \sum_{k=i+1}^{n} \left(\frac{\partial F}{\partial \psi_i} \right) \left(\frac{\partial F}{\partial \psi_k} \right) B_{ik} \tag{C.7}$$

where P_{ψ_i} and B_{ψ_i} are the random and systematic uncertainty components for each fundamental input ψ_i, respectively. Usually, by their very nature, the random uncertainties of the fundamental inputs are not correlated with one another and so $P_{ik} = 0 \, \forall \, i, k$ and Equation (C.6) reduces to the root-sum-square of the fundamental precision uncertainties. Hudson et al. (2003, Section 6.2) discuss one example in which the precision uncertainties of two variables were correlated.

The uncertainty in each fundamental measurement is considered to be due to a number of elemental uncertainty sources. Examples of such sources are calibration, data acquisition, installation and modelling or conceptual uncertainties.[3] Each elemental uncertainty source is assumed to be uncorrelated with the other elemental sources for a particular fundamental measurement. Thus, assuming that measurement ψ_J contains m_J elemental sources, the random and bias uncertainties for this measurement are

$$P_{\psi_J}^2 = \sum_{e=1}^{m_J} \left(P_{\psi_J} \right)_e^2 \tag{C.8}$$

$$B_{\psi_J}^2 = \sum_{e=1}^{m_J} \left(B_{\psi_J} \right)_e^2 \tag{C.9}$$

Although the elemental uncertainties are uncorrelated with each other for

3 Further examples and discussion may be found in Sections 4-2.1 and 4-2.4 of Coleman and Steele (1999) and in Chapter 5 of Hudson et al. (2003).

a particular measurement they can be correlated across multiple fundamental measurements. When this is the case, the covariance estimate B_{ik} in Equation (C.7) is non-zero and, following Coleman and Steele (1999, Section 4-2.3), is approximated in this thesis by

$$B_{ik} = \sum_{e=1}^{L} (B_i)_e (B_k)_e \tag{C.10}$$

where measurements ψ_i and ψ_k share L elemental uncertainties. A typical example of correlated elemental bias uncertainties is that which occurs when a set of transducers are calibrated against the same reference gauge. The resulting calibration uncertainty for each gauge includes an elemental contribution due to the reference gauge accuracy. This elemental uncertainty is correlated across the set of transducers and should be taken into account in any data reduction equation that uses measurements from more than one transducer in the set. Further explanation and discussion of the effect of correlated elemental uncertainties may be found in Section 4–2 of Coleman and Steele (1999).

C.2.1 *Some additional nomenclature*

This section defines additional nomenclature that is useful in subsequent sections of this appendix. By definition $(U_F)_{\psi_i}$ denotes the absolute uncertainty in output F due to absolute uncertainty in input ψ_i and is given by

$$(U_F)_{\psi_i} = \left(\frac{\partial F}{\partial \psi_i}\right) U_{\psi_i} \tag{C.11}$$

where U_{ψ_i} is the absolute uncertainty in input ψ_i and the derivative $\partial F/\partial \psi_i$ is the absolute sensitivity of output F to input ψ_i. Multiplying both sides of Equation (C.11) by $1/F$ and multiplying the right hand side by ψ_i/ψ_i gives

$$(X_F)_{X_{\psi_i}} = \left(\frac{\partial X_F}{\partial X_{\psi_i}}\right) X_{\psi_i} \tag{C.12}$$

where $X_F = U_F/F$ and $X_{\psi_i} = U_{\psi_i}/\psi_i$ are the relative (total) uncertainties and

$$\frac{\partial X_F}{\partial X_{\psi_i}} = \left(\frac{\partial F}{\partial \psi_i}\right) \frac{\psi_i}{F} \tag{C.13}$$

is the relative sensitivity of the output F to input ψ_i. In Coleman and Steele (1999) and Hudson et al. (2003) the relative sensitivity $\partial X_F/\partial X_{\psi_i}$ is known as the 'uncertainty magnification factor'. Finally, the relative bias

and precision uncertainties of a value are denoted by

$$X_F^B = \frac{B_F}{F} \tag{C.14}$$

$$X_F^P = \frac{P_F}{F} \tag{C.15}$$

C.2.2 *Uncertainty of a Mean Value*

Note that the theory given in this section is only used in this thesis for the analysis of the calibration data that is presented in Appendix A. The theory does not apply to the average during the test time. Following Coleman and Steele (1999, Section 4-3.1), the test time average is treated in this thesis as a single measurement rather than the average of a set of measurements.

When the data reduction equation is the calculation of the mean of m repeat measurements

$$F = \overline{\psi} = \frac{1}{m}\sum_{k=1}^{m}\psi_k \tag{C.16}$$

then the precision uncertainty of the average $P_F \equiv P_{\overline{\psi}}$ does not need to be evaluated using Equation (C.6), rather, it may be calculated more easily from the standard deviation of the measurements as follows

$$P_{\overline{\psi}} = \frac{2\sigma_{\psi_k}}{\sqrt{m}} \tag{C.17}$$

where

$$\sigma_{\psi_k}^2 = \frac{1}{m-1}\sum_{k=1}^{m}\left(\psi_k - \overline{\psi}\right)^2 \tag{C.18}$$

is the standard deviation and m is assumed $\geqslant 10$ (Coleman and Steele, 1999, Appendix B). Similarly, the precision uncertainty of a *single* measurement is given by

$$P_{\psi_k} = 2\sigma_{\psi_k} \tag{C.19}$$

The above method corresponds to that presented and discussed by Hudson et al. (2003, Section 2) and Coleman and Steele (1999, Section 4-3.3 and Appendix B).

No simplified equations exist for the bias uncertainty of the mean $B_{\overline{\psi}}$ which must be calculated using Equation (C.7). Calibration of the engine and fuel plenum pressure transducers is one example of this type of calculation (see Appendix A.3). As discussed by Hudson et al. (2003,

Section 6), a significant benefit of using Equation (C.17) to determine the precision uncertainty is that it implicity accounts for any correlation of the random uncertainty between the input measurements.

A more general case for the uncertainty in the mean occurs when the quantities to be averaged cannot be considered as fundamental measurements but are themselves derived using a data reduction equation. This case may be written as

$$\overline{F} = \frac{1}{m} \sum_{k=1}^{m} F_k \tag{C.20}$$

where F_k is as per Equation (C.1). For this case the precision uncertainty of the average result $P_{\overline{F}}$ is again calculated from the standard deviation of the individual results

$$P_{\overline{F}} = \frac{2\sigma_{\overline{F}}}{\sqrt{m}} \tag{C.21}$$

$$\sigma_{\overline{F}}^2 = \frac{1}{m-1} \sum_{k=1}^{m} \left(F_k - \overline{F}\right)^2 \tag{C.22}$$

while the bias uncertainty $B_{\overline{F}}$ is calculated through careful application of Equations (C.7) and (C.10) to Equation (C.20). The calibration of the M12REST engine fuel system that is presented in Appendix A.4 is an example of this type of calculation.

Coleman and Steele (1999) state in Section 4–3.3 that the bias uncertainty of the mean is simply equal to that of a single result, that is $B_{\overline{F}} = B_F$. This equality however, is only true for the special case when each F_k has been calculated for the *same* nominal values of the inputs.[4] When this is not the case, such as during the calibration of the M12REST engine fuel system, the bias uncertainty of the average result should be determined from Equations (C.7) and (C.10).

C.2.3 *Uncertainty of a Linear Regression*

Consider a set of calibration data $\{x_i, y_i\}_{i=1}^{n}$ to which a linear model of the form

$$y = mx + c \tag{C.23}$$

is fitted. As explained by Coleman and Steele (1999, Chapter 7), the coefficients m and c should each be considered as data reduction equations

4 This constraint can be shown by applying Equation (C.7) to $F = 1/2(f(x_1, y_1) + f(x_2, y_2))$, where f is a function. The resulting expression for $B_{\overline{F}}$ reduces to that for B_F only when $\partial F/\partial x|_{x_1} = \partial F/\partial x|_{x_2}$, $\partial F/\partial y|_{y_1} = \partial F/\partial y|_{y_2}$ and B_x, B_y, B_{xy} are each constant with x, y.

that are functions of the fitted data, that is

$$m = m(x_1, x_2, \ldots, x_n, y_1, y_2, \ldots, y_n) = m(\{x_i, y_i\}_{i=1}^n) \tag{C.24}$$

$$c = c(x_1, x_2, \ldots, x_n, y_1, y_2, \ldots, y_n) = c(\{x_i, y_i\}_{i=1}^n) \tag{C.25}$$

The total uncertainty for each coefficient is calculated by application of Equations (C.6) and (C.7) to the above. In general however, calculation of the individual uncertainty for each coefficient is of limited use. During an experiment, a new value x_{new} is recorded and substituted into the computed linear model to determine the corresponding y_{new}. When written as

$$y_{new} = m(\{x_i, y_i\}_{i=1}^n)x_{new} + c(\{x_i, y_i\}_{i=1}^n) \tag{C.26}$$

it is clear that the calculation of the total uncertainty of y_{new} must account for the uncertainty correlation that exists between the coefficients m and c (via. the calibration data) and which may also exist between x_{new} and each x_i and y_i measurement. Generally, the total uncertainty in y_{new} cannot be written explicitly in terms of the individual uncertainties of m, c and x_{new} but must be calculated by applying Equations (C.6) and (C.7) to Equation (C.26). Strategies for dealing with and presenting the total uncertainty of a regression are described by Hudson et al. (2003, Sections 7.1.2 and 7.2.2) and Coleman and Steele (1999, Section 7-5).

For the special case in which no constant is included in the linear model and the elemental systematic uncertainties of x_{new} are not correlated with the elemental uncertainties of the x_i and y_i data, then it can be shown that the total uncertainty in the computed value y_{new} reduces to

$$\left(\frac{U_{y_{new}}}{y_{new}}\right)^2 = \left(\frac{U_m}{m}\right)^2 + \left(\frac{B_{x_{new}}}{x_{new}}\right)^2 + \left(\frac{P_{x_{new}}}{x_{new}}\right)^2 \tag{C.27}$$

or

$$X_{y_{new}}^2 = X_m^2 + X_{x_{new}}^2 \tag{C.28}$$

where U_m is the total uncertainty in coefficient m and $B_{x_{new}}$ and $P_{x_{new}}$ are the bias and precision uncertainties of x_{new}, respectively.

One further simplification is made in this thesis. Rather than calculate the precision uncertainty of coefficient m using Equation (C.6), this thesis follows Hudson et al. (2003, Section 7.1.1) by assuming that the random uncertainty of the calibration measurements $\{x_i\}_{i=1}^n$ are transported and captured in the random uncertainty of the corresponding $\{y_i\}_{i=1}^n$. This assumption permits the precision uncertainty of coefficient m to be easily

calculated using

$$P_m = 2\sqrt{\frac{e_Y^2}{e_{XX}}} \tag{C.29}$$

where

$$e_Y^2 = \frac{1}{n-2}\sum_{i=1}^{n}(y_i - mx_i)^2 \tag{C.30}$$

$$e_{XX} = \sum_{i=1}^{n} x_i^2 - \frac{1}{n}\left(\sum_{i=1}^{n} x_i\right) \tag{C.31}$$

C.3 EXPERIMENTAL PRESSURE MEASUREMENT

This section presents the calculation of the total experimental uncertainty for the nozzle supply, engine and fuel plenum pressure transducers. During a shot, the measured pressure is calculated using

$$p(t) = \frac{V(t) - V_0}{S} \tag{C.32}$$

where $V(t)$ is the measured output signal of the transducer of interest, V_0 is the measured output signal just prior to the experiment[5] and S is the transducer sensitivity that was determined from a calibration. The calibration methods used for the different transducers are described in Appendices A.2 and A.3.

Equation (C.32) has the form of a linear equation with an intercept of V_0/S and a slope of $1/S$. For simplicity and because it gives a conservative estimate, the uncertainty in the difference $V(t) - V_0$ is taken to be equal to the uncertainty in $V(t)$. Since calibration of each transducer was completed in an apparatus that was different and separate from the experimental model, the elemental uncertainties of $V(t)$ measured during a shot are *not* correlated with those measured during calibration.[6] Hence, for each transducer the total experimental uncertainty is given by Equation (C.28) with $X_{y_{new}} \equiv X_{p(t)}$, $X_m \equiv X_S$ and $X_{x_{new}} \equiv X_{V(t)}$. The calibration uncertainty for each gauge is known and are reported in Tables A.1b and A.2. The values used for the transducer output uncertainty $X_{V(t)}$ are discussed below for each transducer type.

Nozzle Supply Transducers: Following Kirchhartz (2010), a experimental uncertainty of $X_{V(t)} = 3\,\%$ is assumed in this thesis for the measured voltage output of the nozzle supply pressure transducers. This

5 i.e. with the model under a stable vacuum and before flow arrival.

6 The exception here is that the same data acquisition system was used during both the calibration and experiment. In this thesis however, systematic errors introduced by the data acquisition system are assumed negligible.

uncertainty accounts for the mounting used during the experiments and for possible thermal effects due to the intense temperatures to which the nozzle supply transducers are subjected during a shot.[7]

Engine Kulite® Transducers: An experimental uncertainty of $X_{V(t)} = 1\,\%$ is assumed in this thesis for the measured voltage output of the engine Kulite® pressure transducers. This uncertainty accounts for the mounting used during the experiment (which was similar to that used during calibration) and for possible thermal effects. To provide some thermal protection o-ring grease and a thin piece of cellophane were applied to the sensor face of each transducer during installation of the gauges into the M12REST model.

Fuel Plenum PCB® Transducers: In this thesis an experimental uncertainty of $X_{V(t)} = 2\,\%$ is assumed for the voltage output measured from the fuel plenum PCB® pressure transducers. This uncertainty accounts for the vibration isolation mounting used during the experiment (which was very different to that used during calibration) and for possible thermal effects. Consistent with the installation of the engine Kulite® transducers, o-ring grease and a piece of cellophane were also applied to the face of the fuel plenum transducers.

Using the above experimental uncertainties for the measured voltage output during an experiment and the total calibration uncertainty, the total experimental can be calculated. The results for the nozzle supply, engine and fuel plenum pressure transducers are summarised in Table C.1. Note that due to damage to the ceramic coating of nozzle supply transducer SPA, only transducer SPB was used to process the experimental data that is presented in this thesis.

Table C.1 – Measurement Uncertainty for the Nozzle Supply, Engine and Fuel Plenum Pressure Transducers

Transducer	Calibration X_S (%)	Exp. Voltage $X_{V(t)}$ (%)	Exp. Pressure $X_{p(t)}$ (%)
Nozzle supply SPA	2.09	3.00	3.66
Nozzle supply SPB	1.97	3.00	3.59
Engine P1 and P10	2.51	1.00	2.70
Engine P2 through P9	1.76	1.00	2.02
Fuel Plenum F1 and F2	2.43	2.00	3.15

7 As shown in Figure 3.6, the sensor face of each transducer featured a ceramic thermal barrier coating. To further thermally protect the gauge face the small volume in front of each transducer is filled with o-ring grease prior to each shot. This grease was not used during calibration of the transducers.

C.4 NOZZLE EXIT FLOW PROPERTIES

This section summarises the uncertainty calculation and results for the nozzle exit flow properties. As described in Section 3.3.1, the nozzle exit flow properties were calculated in this thesis using the program NENZFR (Doherty, Chan, et al., 2012). This program couples a one-dimensional, equilibrium gas, reflected shock calculation for the nozzle supply conditions with an axisymmetric, viscous, chemically reacting RANS simulation of the nozzle flow. One-dimensionalised nozzle exit flow properties are computed by conserving the mass, momentum and energy fluxes over a nominated core-flow radius.

NENZFR takes a total of nine inputs that govern the calculation of the exit flow properties. These inputs consist of four experimental inputs, the initial temperature ($T_{ST,f}$) and pressure ($p_{ST,f}$) of gas in the shock tube, the incident shock speed (u_{ss}) and the nozzle supply pressure (p_s) and five numerical inputs, the nozzle wall temperature (T_w), the boundary layer transition location within the nozzle (x_t), the turbulent-to-laminar viscosity ratio (μ_t/μ) and turbulence intensity[8] (I_t) at the nozzle throat and the normalised core flow radius ($\tilde{r}_c$). The relative uncertainty for each input is provided in Table C.2 and discussed below. Corresponding nominal values for the numerical inputs are also provided. Nominal values for the experimental inputs are given in Tables 3.1 and 3.2.

Table C.2 – Relative Uncertainty of each NENZFR Input Variable

(a) Experimental Inputs

ψ_i	X_{ψ_i} (%)
$p_{ST,f}$	1.5
$T_{ST,f}$	2
u_{ss}	5
p_s	3.6

(b) Numerical Inputs

ψ_i	Units	Nominal	X_{ψ_i} (%)
T_w	K	300	4
x_t	mm	100	100
μ_t/μ		100	100
I_t	%	5	80
$\tilde{r}_c$		0.317 46	5

Shock Tube Filling Temperature: The temperature of the test gas in the shock tube is not measured. Since the shock tube is the first section of the T4 Stalker Tube to be filled in preparation for an experiment and the remainder of the filling process takes approximately 20 min, it is reasonable to assume that the initial temperature of the test gas in the shock tube is equal to the ambient conditions in the laboratory. These conditions are taken to be 300 K with an uncertainty of $\pm 2\,\%$ or ± 6 K.

8 Defined as the ratio of the root-mean-square of the turbulent velocity fluctuations to the mean velocity (Wilcox, 2006).

Shock Tube Filling Pressure: The initial pressure of the test gas in the shock tube was measured using a USG SOLFRUNT® bourdon tube dial gauge of range 0 to 200 kPa (gauge). The manufacturer stated accuracy of the gauge is ±0.5 % of full-scale, equivalent to an absolute uncertainty of ±1 kPa. The divisions of the gauge are 2 kPa so a gauge readability uncertainty of ±1 kPa is assumed. Finally, since the measurement is a gauge pressure measurement, a conservative uncertainty of ±2 kPa is included to account for variations of the local ambient pressure. Taking the root-sum-square of these elemental uncertainties, the total measurement uncertainty for the shock tube fill pressure is ±2.4 kPa, equivalent to ±1.5 % for the nominal fill pressure of the low pressure test condition and ±0.96 % for the high pressure test condition (cf. Table 3.1).

Incident Shock Speed: Following Mee (1993), the uncertainty of the shock speed was assumed to be ±5 % with the major elemental component being due to attenuation of the speed as the shock traverses the length of the tube. In this thesis the 2nd and 3rd timing stations were used to calculate the incident shock speed. Justification for using these timing stations is based on the argument that the gas sitting between the 3rd timing station and the end of the shock tube flows through the nozzle and over the model during the nozzle starting and flow establishment periods, while the gas that sits between the 2nd and 3rd timing stations flows over the model during the test time. This justification was originally provided by Stalker and Morgan (1988, Section 2) and was repeated by Mee (1993, Section 6).

Although usage of the 2nd and 3rd timing stations for the calculation of the incident shock speed is the usual practice when processing data from the T4 Stalker Tube, the validity of the method and the accuracy of the computed nozzle supply enthalpy have recently been questioned. Due to attenuation, the speed of the shock calculated using the 2nd and 3rd timing stations is larger than the speed at shock reflection. Consequently, the strength of the reflected shock is calculated to be greater than that which occurs in the experiment. This results in an over-estimation of the nozzle supply pressure relative to the peak value measured in the experiment. This difference is accounted for by isentropically expanding the calculated nozzle supply conditions to match the experimental pressure measured over the nominated test time.

Mr. Philippe Lorrain, a PhD candidate within the CfH, has found that the predicted nozzle supply pressure closely matches the peak pressure measured during the experiment when an extrapolated value for the incident shock speed is used for the reflected shock calculation. This extrapolated value is determined by using all three shock timing stations and the nozzle supply pressure transducer to

define three incident shock speeds along the length of the shock tube. A linear fit through the three shock speeds and extrapolation to the end of the shock tube provides an estimate for the incident shock speed at shock reflection. In addition to providing a better match to the measured peak pressure, usage of the extrapolated shock speed also reduces the predicted nozzle supply enthalpy. This in turn decreases the temperature of the nozzle exit flow and improves a comparison between experimental fuel-on scramjet engine data and numerical simulations that account for both fuel injection and combustion.

At the time of writing the appropriateness of using the extrapolated incident shock speed is under investigation by Mr. Philippe Lorrain. For this thesis, in which no reacting computational simulations of the engine are presented, the standard method for calculating the nozzle supply conditions was considered adequate and the uncertainty of the shock speed was taken to be $\pm 5\,\%$.

Nozzle Supply Pressure: Calculation of the uncertainty in the measured nozzle supply pressure is presented in Appendix C.3.

Nozzle Wall Temperature: An isothermal wall boundary condition with temperature 300 K was used in this thesis. This was considered a reasonable assumption given the short flow duration (approximately 5 ms). The uncertainty was assumed to be $\pm 4\,\%$ or $\pm 12\,\mathrm{K}$.

Boundary Layer Transition Location: Although the transition location of a boundary layer may be determined from heat flux measurements, no such data exist for the Mach 10 nozzle that was used in this thesis. Heat flux measurements recorded by Riedmüller (2008) for the T4 Stalker Tube Mach 6 nozzle indicated that the boundary layer was fully turbulent 200 mm downstream of the nozzle throat. Thus, a transition location of 100 mm was assumed for the Mach 10 nozzle with an uncertainty of $\pm 100\,\%$.

Turbulent Parameters: Noting that the flow produced by the T4 Stalker Tube is noisy, the nominal values selected for the turbulent-to-laminar viscosity ratio and the turbulence intensity were chosen from the upper end of the ranges recommended by Chan et al. (2012) with an assumed uncertainty of $\pm 100\,\%$ for the turbulent-to-laminar viscosity ratio and an uncertainty of $\pm 80\,\%$ for the turbulence intensity.

Core Flow Radius: The core flow radius over which the nozzle exit flow properties were averaged was chosen to be 60 mm based on the position and size of the M12REST engine in the test section (see Figure 3.18). An uncertainty of $X_{\tilde{r}_c} = \pm 5\,\%$, which corresponds

to ± 3 mm, was considered reasonable based on the uncertainty in model position (Section 3.4.7).

Each nozzle exit flow property computed by NENZFR may be considered to be a "black box" data reduction equation of the form of Equation (C.1). The nine NENZFR inputs are the fundamental variables on which each exit flow property is dependent. The uncertainties of the nine NENZFR inputs are independent of one another and so the total uncertainty in each freestream property may be found by evaluating Equation (C.2) with $U_{ik} = 0 \, \forall \, i, k$. This evaluation was completed numerically using finite difference[9] to calculate the sensitivity derivatives $\partial F / \partial \psi_i$. Further details, including the full set of relative sensitivities[10] may be found in Doherty (2013a) and Doherty, Chan, et al. (2012).

The results of the uncertainty analysis are provided in Table C.3 for the high pressure test condition and in Table C.4 for the low pressure test condition. The data are presented in the form of the relative component uncertainties $(X_F)_{\psi_i}$ as defined by Equation (C.12). Also provided are the results of a grid convergence study, the spatial variation of the exit flow properties over the core and the error associated with using the response surface rather than completing a full NENZFR calculation. Note that the response surface error was not calculated using the method described in Appendix C.2.3 but was calculated simply as the root-sum-square of the difference between a true NENZFR output and that predicted by the fitted response surface for a number of test cases. Further details of these additional studies are provided in Doherty (2013a).

Examining the data in Tables C.3 and C.4 it can be seen that the uncertainties for each test condition are similar to one another and that the total uncertainty is dominated primarily by the incident shock speed uncertainty component $(X_F)_{u_{ss}}$ and secondly by the nozzle supply pressure uncertainty component $(X_F)_{p_s}$. Noting that the incident shock speed is used mainly to infer the nozzle supply conditions and in particular the nozzle supply temperature, these results clearly demonstrate that to reduce the nozzle exit flow uncertainties further attention should be focussed on improving our knowledge of the nozzle supply temperature. This may be achieved either through direct measurement of the nozzle supply temperature or through improving the method by which the supply temperature is calculated using the incident shock speed (cf. the discussion above regarding the shock speed uncertainty). To be worthwhile, a direct measurement of the nozzle supply temperature would need to have a measurement uncertainty and response time similar to those of the nozzle supply pressure transducers.

Other notable results from Tables C.3 and C.4 are that

9 Each NENZFR input was perturbed by $\pm 2.5\,\%$.
10 Defined by Equation (C.13).

1. the flow properties of interest[11] vary by less than 0.5 % over the nominated core radius,
2. the flow properties are typically within 1 % of those predicted from the grid convergence study,
3. the influence of the inflow turbulent parameters (μ_t/μ and I_t) is small,
4. the exit flow properties do not seem strongly dependent on the chosen boundary layer transition location[12] and,
5. the uncertainty component due to the assumed nozzle wall temperature is negligible.[13]

C.5 FOREBODY FLOW PROPERTIES

The uncertainty analysis presented in Appendix C.4 for the nozzle exit conditions was extended to include the predicted engine forebody flow conditions by coupling NENZFR with an oblique shock calculation. The results are presented in Table C.5 for the high pressure test condition and in Table C.6 for the low pressure test condition. The forebody angle $\theta = 6°$ was included in the analysis with an assumed uncertainty of $\pm 0.1°$ or ± 0.0167 %, consistent with the uncertainty in model alignment (Section 3.4.7). The data exhibit trends that are similar to the nozzle exit uncertainty data: the uncertainties are similar at each test condition and the total uncertainty is dominated by the shock speed and nozzle supply pressure components, $(X_F)_{u_{ss}}$ and $(X_F)_{p_s}$ respectively.

C.6 NORMALISED PRESSURE

Explained in Section 3.5.2, engine pressure data are presented in this thesis in the form of a pressure ratio relative to the nominal forebody pressure.

11 That is, the static pressure, temperature and density, the flow velocity, the Mach number, the dynamic pressure, the unit Reynolds number and the mass flux.

12 This result is consistent with the data of Chan et al. (2013) and Doherty (2013a) who demonstrated that the influence of the boundary layer transition location is approximately asymptotic for $x_t \geqslant 50$ mm. As a consequence, the influence of the chosen transition location is underestimated by this analysis. See Doherty (2013a) for futher discussion.

13 One caveat exits for this result. The current simulations assumed that the wall temperature was constant along the length of the nozzle. However, the results of a transient thermal-structural finite element analysis by Williams (2010) indicate that the wall temperature in the throat region is approximately 2200 K and rapidly decreases downstream of the throat. As analysis simulated a total duration of 5 ms assuming a steady state surface heat flux, the predicted temperatures are expected to be conservative. Nevertheless, the influence of a high localised wall temperature on the nozzle flow exit properties requires further investigation.

Table C.3 – Summary of the Relative Uncertainty in each Nozzle Exit Flow Property for the Nominal High Pressure Air Test Condition

	$(X_F)_{\psi_i}$														
ψ_i	$p_{ST,f}$	$T_{ST,f}$	u_{SS}	p_s	T_w	x_t	μ_t/μ	I_t	$\tilde{r}_c$	Total 1[(a)]	FNU[(b)]	GC[(b)]	RSA[(b)]	Total 1[(c)]	Total 2[(d)]
F \ X_{ψ_i}	0.96	2	5	3.59	4	100	100	80	5						
ρ_s	0.17	−0.46	−5.37	2.94	0	0	0	0	0	6.14	0	0	0	6.14	6.14
T_s	−0.16	0.43	5.06	0.63	0	0	0	0	0	5.11	0	0	0	5.12	5.12
H_s	−0.22	0.61	7.19	0.84	0	0	0	0	0	7.27	0	0	0	7.27	7.27
p	−0.12	0.34	4.06	3.85	−0.06	−0.63	0.03	0.05	0.03	5.64	0.53	−1.05	0.08	5.76	5.76
$T[0]$	−0.29	0.80	9.38	1.06	−0.02	−0.56	0.09	−0.75	0	9.52	0.10	−0.29	0.07	9.53	9.53
ρ	0.17	−0.46	−5.35	2.80	−0.04	−0.19	0	0.77	0.02	6.11	0.46	−0.76	0.04	6.17	6.17
u_x	−0.10	0.28	3.25	0.39	0	0	0	0.05	0	3.29	0	−0.01	0.02	3.29	3.29
u_y															
a	−0.15	0.40	4.70	0.53	−0.01	−0.27	0	−0.38	0	4.78	0.05	−0.15	0.04	4.78	4.77
M	0.05	−0.12	−1.44	−0.14	0.01	0.19	−0.19	0.46	0	1.55	0.05	0.15	0.03	1.56	1.56
Pitot	−0.04	0.10	1.17	3.57	−0.03	−0.11	0.02	0.96	0.03	3.88	0.46	−0.77	0.07	3.98	3.98
p_t	0.18	−0.50	−5.77	2.91	0.01	1.25	−0.11	3.09	0.03	7.29	0.35	−0.10	0.17	7.30	7.30
H_t	−0.22	0.61	7.18	0.84	0	0	0	0.10	0	7.26	0	−0.02	0.03	7.26	7.26
q	−0.04	0.10	1.16	3.58	−0.04	−0.19	0	0.88	0.02	3.87	0.46	−0.77	0.07	3.98	3.97
ρu_x	0.07	−0.18	−2.10	3.19	−0.04	−0.19	0	0.82	0.02	3.91	0.46	−0.77	0.05	4.02	4.02
Re_u	0.32	−0.87	−10.16	2.29	−0.02	0.23	−0.14	1.51	0.02	10.56	0.43	−0.51	1.74	10.73	10.59
p/q	−0.09	0.25	2.90	0.27	−0.02	−0.43	0.03	−0.83	0.01	3.07	0.10	−0.28	0.04	3.09	3.09
μ	−0.25	0.69	8.05	0.90	−0.02	−0.43	0.14	−0.68	0	8.18	0.05	−0.26	1.79	8.37	8.18
$k[0]$	−0.27	0.75	8.73	0.98	−0.02	−0.51	0	−0.73	0	8.87	0.05	−0.28	1.99	9.09	8.87
$e[0]$	−1.33	3.66	43.04	4.12	−0.03	−0.99	0.07	−1.27	0.01	43.44	0.57	0.48	1.75	43.48	43.45
Y_{N2}	0.01	−0.03	−0.34	−0.04	0	0	0	0	0	0.35	0	−0.02	0.03	0.35	0.35
Y_{O2}	0.05	−0.14	−1.63	−0.16	0	0	0	0	0	1.64	0.01	−0.07	0.12	1.65	1.65
Y_N															
Y_O	−1.24	3.40	40	0.03	0	0	0	−0.52	0.03	40.16	0.15	−0.06	1.13	40.18	40.17
Y_{NO}	−0.23	0.63	7.47	0.82	0	0	0	0.09	0	7.54	0.06	0.40	0.58	7.58	7.56
μ_t	−0.18	0.49	5.82	−0.42	−0.04	53.10	125.49	−39.90	−0.06	142.10	0.47	0.23	0.08	142.11	142.11
k_t	−0.18	0.49	5.84	−0.42	−0.04	53.09	125.51	−39.85	−0.05	142.11	0.51	0.23	0.07	142.11	142.11
tke	−0.44	1.21	14.16	−2.88	0.02	72.51	125.12	−39.54	−0.46	150.62	1.90	−0.94	0.33	150.64	150.64
ω	−0.09	0.25	2.99	0.34	0.02	19.25	−0.45	1.16	−0.38	19.53	1.59	−1.92	0.03	19.69	19.69

[(a)] Root-sum-square total uncertainty due to the NENZFR inputs.
[(b)] FNU: Flow Non-uniformity; GC: Grid convergence error; RSA: Error resulting from usage of a response surface approximation. See Doherty (2013a) for details.
[(c)] Root-sum-square total uncertainty when using a response surface approximation.
[(d)] Root-sum-square total uncertainty for a NENZFR output. This total excludes the response surface error.

Table C.4 – Summary of the Relative Uncertainty in each Nozzle Exit Flow Property for the Nominal Low Pressure Air Test Condition.

	$(X_F)_{\psi_i}$														
ψ_i	$p_{ST,f}$	$T_{ST,f}$	u_{SS}	p_s	T_w	x_t	μ_t/μ	I_t	$\tilde{r}_c$	Total 1[a]	FNU[b]	GC[b]	RSA[b]	Total 1[c]	Total 2[d]
$F \setminus X_{\psi_i}$	1.50	2	5	3.59	4	100	100	80	5						
ρ_s	0.25	−0.44	−5.38	2.95	0	0	0	0	0	6.16	0	0	0	6.16	6.16
T_s	−0.23	0.40	4.94	0.60	0	0	0	0	0	5	0	0	0	5	5
H_s	−0.34	0.60	7.37	0.83	0	0	0	0	0	7.45	0	0	0	7.45	7.45
p	−0.19	0.33	4.05	3.80	0.09	0.53	−0.05	0.13	−0.11	5.60	0.43	−1.05	0.08	5.71	5.71
$T[0]$	−0.44	0.77	9.52	1.05	0.02	−0.18	−0.09	−0.78	−0.03	9.65	0.18	−0.29	0.07	9.66	9.66
ρ	0.26	−0.45	−5.53	2.75	0.07	0.79	0	0.85	−0.08	6.31	0.30	−0.76	0.04	6.36	6.36
u_x	−0.15	0.27	3.32	0.39	0	0	0	0.05	0	3.35	0	−0.01	0.02	3.36	3.36
u_y															
a	−0.22	0.39	4.80	0.52	0.01	−0.13	−0.07	−0.37	−0.01	4.86	0.09	−0.15	0.04	4.87	4.87
M	0.07	−0.12	−1.47	−0.13	−0.01	0.20	0.20	0.47	0.02	1.58	0.09	0.15	0.03	1.59	1.59
Pitot	−0.05	0.09	1.11	3.52	0.07	0.78	0.04	1.02	−0.08	3.92	0.29	−0.77	0.07	4	4
p_t	0.28	−0.49	−6.05	2.88	0.01	1.25	0.21	3.08	0	7.50	0.32	−0.10	0.17	7.51	7.51
H_t	−0.34	0.60	7.37	0.83	0	0	0	0.13	0	7.45	0	−0.02	0.03	7.45	7.45
q	−0.05	0.09	1.10	3.52	0.07	0.79	0	0.95	−0.08	3.89	0.29	−0.77	0.07	3.98	3.98
ρu_x	0.11	−0.18	−2.21	3.14	0.07	0.79	0	0.90	−0.08	4.03	0.29	−0.77	0.05	4.11	4.11
Re_u	0.48	−0.83	−10.30	2.26	0.05	1.06	0	1.44	−0.06	10.74	0.25	−0.51	1.74	10.89	10.75
p/q	−0.14	0.24	2.95	0.28	0.03	−0.26	−0.05	−0.83	−0.03	3.10	0.19	−0.28	0.04	3.12	3.12
μ	−0.38	0.66	8.08	0.88	0.02	−0.27	0	−0.54	−0.02	8.18	0.12	−0.26	1.79	8.38	8.19
$k[0]$	−0.40	0.70	8.66	0.94	0.02	−0.19	−0.10	−0.70	−0.03	8.78	0.13	−0.28	1.99	9.01	8.78
$e[0]$	−1.64	2.85	35.41	2.79	0.03	−0.34	−0.17	−0.94	−0.03	35.68	0.41	0.48	1.75	35.74	35.69
Y_{N2}	0.01	−0.02	−0.31	−0.03	0	0	0	−0.02	0	0.31	0	−0.02	0.03	0.32	0.31
Y_{O2}	0.08	−0.14	−1.73	−0.15	0	0	0	0	0	1.74	0.01	−0.07	0.12	1.75	1.75
Y_N															
Y_O	−1.83	3.17	39.30	0.17	0	0	0	−0.40	0.02	39.48	0.13	−0.06	1.13	39.49	39.47
Y_{NO}	−0.29	0.51	6.39	0.69	0	0	0	0.06	0	6.46	0.05	0.40	0.58	6.49	6.47
μ_t	−0.26	0.46	5.69	−0.54	0.09	53.90	126.50	−41.43	−0.20	143.73	0.68	0.23	0.08	143.73	143.73
k_t	−0.26	0.46	5.72	−0.54	0.09	53.93	126.49	−41.44	−0.20	143.73	0.65	0.23	0.07	143.73	143.73
tke	−0.66	1.15	14.22	−2.96	0.07	72.78	125.78	−40.61	−0.54	151.59	2.16	−0.94	0.33	151.61	151.61
ω	−0.14	0.24	3	0.34	0.04	19.63	−0.71	1.71	−0.41	19.95	1.73	−1.92	0.03	20.12	20.12

[a] Root-sum-square total uncertainty due to the NENZFR inputs.
[b] FNU: Flow Non-uniformity; GC: Grid-convergence error; RSA: Error resulting from usage of a response surface approximation. See Doherty (2013a) for details.
[c] Root-sum-square total uncertainty when using a response surface approximation.
[d] Root-sum-square total uncertainty for a NENZFR output. This total excludes the response surface error.

Table C.5 – Summary of the Relative Uncertainty in each Engine Forebody Flow Property for the Nominal High Pressure Air Test Condition.

	$(X_F)_{\psi_i}$										X_F
ψ_i	$p_{s_{T,f}}$	$T_{s_{T,f}}$	u_{ss}	p_s	T_w	x_t	μ_t/μ	I_t	$\tilde{r}_c$	θ	Total 1
$F \setminus X_{\psi_i}$	0.96	2	5	3.59	4	100	100	80	5	1.67	
p	−0.07	0.20	2.41	3.69	−0.04	−0.31	−0.02	0.54	0.03	1.90	4.84
$T[0]$	−0.27	0.74	8.65	0.99	−0.02	−0.42	0.07	−0.54	0	0.81	8.80
ρ	0.20	−0.54	−6.27	2.70	−0.03	0.12	−0.09	1.08	0.03	1.08	7.02
u_x	−0.10	0.28	3.24	0.39	0	0	0	0.06	0	−0.05	3.28
u_y	−0.10	0.28	3.24	0.39	0	0	0	0.06	0	1.63	3.66
a	−0.13	0.37	4.30	0.49	−0.01	−0.21	0.04	−0.27	0	0.40	4.38
M	0.03	−0.09	−1.06	−0.10	0.01	0.21	−0.04	0.32	0	−0.43	1.22
Pitot	−0.01	0.02	0.27	3.49	−0.03	0.12	−0.09	1.18	0.03	1.03	3.84
p_t	0.01	−0.03	−0.25	3.56	0.01	1.08	−0.25	2.72	0.03	−0.96	4.72
H_t	−0.22	0.61	7.18	0.84	0	−0.03	0	0.07	0	0	7.26
q	−0.01	0.01	0.22	3.48	−0.03	0.12	−0.09	1.19	0.03	1.02	3.83
$\rho u_{\parallel}$	0.09	−0.26	−3.02	3.09	−0.03	0.12	−0.09	1.13	0.03	1.05	4.61
Re_u	0.30	−0.82	−9.60	2.35	−0.01	0.44	−0.15	1.54	0.03	0.44	10.06
p/q	−0.07	0.19	2.19	0.21	−0.02	−0.43	0.07	−0.65	0	0.87	2.50
μ	−0.20	0.56	6.57	0.75	−0.01	−0.32	0.05	−0.41	0	0.61	6.69
$k[0]$	−0.21	0.58	6.84	0.77	−0.01	−0.33	0.06	−0.43	0	0.64	6.97
β	−0.02	0.06	0.66	0.06	−0.01	−0.13	0.02	−0.20	0	0.92	1.16

Table C.6 – Summary of the Relative Uncertainty in each Engine Forebody Flow Property for the Nominal Low Pressure Air Test Condition.

	$(X_F)_{\psi_i}$										X_F
ψ_i	$p_{s_{T,f}}$	$T_{s_{T,f}}$	u_{ss}	p_s	T_w	x_t	μ_t/μ	I_t	$\tilde{r}_c$	θ	Total 1
$F \setminus X_{\psi_i}$	1.50	2	5	3.59	4	100	100	80	5	1.67	
p	−0.11	0.19	2.39	3.64	0.08	0.63	0	0.62	−0.09	1.88	4.83
$T[0]$	−0.41	0.71	8.78	0.98	0.02	−0.13	−0.07	−0.57	−0.02	0.80	8.93
ρ	0.30	−0.52	−6.46	2.66	0.06	0.76	0.06	1.19	−0.07	1.08	7.24
u_x	−0.15	0.27	3.30	0.38	0	0	0	0.06	0	−0.05	3.34
u_y	−0.15	0.27	3.30	0.38	0	0	0	0.06	0	1.63	3.72
a	−0.20	0.36	4.38	0.48	0.01	−0.07	−0.03	−0.28	−0.01	0.39	4.46
M	0.05	−0.09	−1.08	−0.10	−0.01	0.07	0.03	0.34	0.01	−0.43	1.22
Pitot	−0.01	0.02	0.20	3.44	0.06	0.76	0.06	1.30	−0.07	1.03	3.90
p_t	0.03	−0.04	−0.53	3.51	0.02	1.06	0.22	2.90	−0.02	−0.93	4.80
H_t	−0.34	0.60	7.37	0.82	0	−0.01	0	0.06	0	0	7.44
q	0	0.01	0.15	3.43	0.06	0.76	0.07	1.30	−0.07	1.02	3.89
$\rho u_{\parallel}$	0.15	−0.26	−3.16	3.05	0.06	0.76	0.07	1.25	−0.07	1.05	4.75
Re_u	0.46	−0.79	−9.81	2.32	0.05	0.86	0.12	1.67	−0.05	0.45	10.30
p/q	−0.10	0.18	2.24	0.21	0.02	−0.14	−0.07	−0.68	−0.02	0.86	2.52
μ	−0.31	0.54	6.64	0.73	0.01	−0.10	−0.05	−0.42	−0.02	0.60	6.75
$k[0]$	−0.32	0.56	6.95	0.76	0.01	−0.10	−0.05	−0.44	−0.02	0.62	7.07
β	−0.03	0.05	0.68	0.06	0.01	−0.04	−0.02	−0.21	−0.01	0.91	1.16

This ratio is calculated using

$$\frac{p}{p_1} = \frac{p(t)}{p_s(t-\tau)}\left(\frac{p_s}{p_1}\right)_{nom} \tag{C.33}$$

Noting that the nominal forebody pressure $p_{1,nom}$ is itself a derived quantity, then the normalised pressure may be written generally as[14]

$$\frac{p}{p_1} = f(p, p_s, p_{s,nom}, u_{ss}, p_{ST,f}, T_{ST,f}, T_w, x_t, \mu_t/\mu, I_t, \tilde{r}_c, \theta) \tag{C.34}$$

where p_s and $p_{s,nom}$ are taken to be two separate measurements whose uncertainties are correlated. The total relative uncertainty X_{p/p_1} is found by applying Equation (C.2) to Equation (C.34) and normalising by p/p_1. The resulting uncertainty expression is

$$X^2_{p/p_1} = X^2_p + X^2_{p_s} + X^2_{p_{s,nom}} + X^2_{p_{1,nom}} - 2X_{p_s p_{s,nom}} + 2\frac{\partial X_{p_{1,nom}}}{\partial X_{p_{s,nom}}}\left(X_{p_s p_{s,nom}} - X^2_{p_{s,nom}}\right) \tag{C.35}$$

where

$$X_{p_s p_{s,nom}} = \left(\frac{1}{p_s}\right)\left(\frac{1}{p_{s,nom}}\right)\sum_{e=1}^{L}(u_{p_s})(u_{p_{s,nom}}) \tag{C.36}$$

is the relative covariance estimate for the correlated uncertainties of p_s and $p_{s,nom}$ (cf. Equation (C.10)). Assuming that all the elemental uncertainties of p_s and $p_{s,nom}$ are correlated then

$$X_{p_s p_{s,nom}} = X^2_{p_s} = X^2_{p_{s,nom}} \tag{C.37}$$

and Equation (C.35) reduces to

$$X^2_{p/p_1} = X^2_p + X^2_{p_{1,nom}} \tag{C.38}$$

Substituting in values from Tables C.1, C.5 and C.6, the total uncertainty in the normalised engine pressure data is

$$X_{p/p_1} = \pm 5.5\,\% \tag{C.39}$$

14 For simplicity the time shift value τ is assumed to have no uncertainty.

C.7 FORCE COEFFICIENTS AND INNER SHIELDING PRESSURE

C.7.1 *Drag Coefficient*

The experimental drag coefficient is calculated using

$$C_D(t) = \frac{1}{A_f}\frac{F_D(t)}{p_s(t-\tau_{PP})}\left(\frac{p_s}{q}\right)_{nom} \tag{C.40}$$

Noting that the nominal dynamic pressure q_{nom} is itself a derived quantity, then the drag coefficient may be written generally as[15]

$$C_D = f(A_f, F_D, p_s, p_{s,nom}, u_{ss}, p_{ST,f}, T_{ST,f}, T_w, \chi_t, \mu_t/\mu, I_t, \tilde{r}_c) \tag{C.41}$$

where p_s and $p_{s,nom}$ are taken to be two separate measurements whose uncertainties are correlated. In this thesis the frontal area A_f is taken to be a fixed reference value and so has no uncertainty. Equations (C.40) and (C.41) have the same form as Equations (C.33) and (C.34) with p/p_1 replaced with C_D, p replaced with F_D, and $p_{1,nom}$ replaced with q_{nom}. Hence, the total relative uncertainty X_{C_D} is given by

$$X_{C_D}^2 = X_{F_D}^2 + X_{p_s}^2 + X_{p_{s,nom}}^2 + X_{q_{nom}}^2 - 2X_{p_s p_{s,nom}} + 2\frac{\partial X_{q_{nom}}}{\partial X_{p_{s,nom}}}\left(X_{p_s p_{s,nom}} - X_{p_{s,nom}}^2\right) \tag{C.42}$$

where $X_{p_s p_{s,nom}}$ is the relative covariance estimate for the correlated uncertainties of p_s and $p_{s,nom}$ as given by Equation (C.36). Assuming that all the elemental uncertainties of p_s and $p_{s,nom}$ are correlated, then Equation (C.37) holds and Equation (C.42) reduces to

$$X_{C_D}^2 = X_{F_D}^2 + X_{q_{nom}}^2 \tag{C.43}$$

The elemental sources of uncertainty for the recovered drag force are discussed in Section 4.8. The uncertainty in the nominal freestream dynamic pressure is taken from either Table C.3 or Table C.4 depending on the test condition.

C.7.2 *Lift Coefficient*

The experimental lift coefficient is calculated using

$$C_L(t) = \frac{1}{A_p}\frac{F_{L,c}(t)}{p_s(t-\tau_{PP})}\left(\frac{p_s}{q}\right)_{nom} \tag{C.44}$$

15 For simplicity the time shift value τ_{PP} is assumed to have no uncertainty.

where $F_{L,c}$ is the corrected lift force that accounts for pressure build-up within the force balance shielding cavity (see Section 4.7) and is given by

$$F_{L,c}(t) = F_L(t) + A_p p_{sh}(t) \tag{C.45}$$

where $p_{sh}(t)$ is the average pressure recorded by four inner shielding pressure transducers (Figure 4.2). Noting that F_L and p_{sh} share no elemental sources of uncertainty with each other or any other term in Equation (C.44) then, following the method described in the previous section for the drag coefficient and in Appendix C.6 for the normalised pressure ratio, the total relative uncertainty of the lift coefficient is given by

$$X_{C_D}^2 = X_{F_{L,c}}^2 + X_{p_s}^2 + X_{p_{s,nom}}^2 + X_{q_{nom}}^2 - 2X_{p_s p_{s,nom}} + 2\frac{\partial X_{q_{nom}}}{\partial X_{p_{s,nom}}}\left(X_{p_s p_{s,nom}} - X_{p_{s,nom}}^2\right) \tag{C.46}$$

where $X_{p_s p_{s,nom}}$ is the relative covariance estimate of p_s and $p_{s,nom}$ as defined by Equation (C.36) and $X_{F_{L,c}}$ is the relative uncertainty in the corrected lift, that is

$$X_{F_{L,c}}^2 = \left(\frac{1}{F_{L,c}}\right)^2 (U_{F_L}^2 + A_p^2 U_{p_{sh}}^2) \tag{C.47}$$

Once again, assuming that all the elemental uncertainties of p_s and $p_{s,nom}$ are correlated, then Equation (C.37) holds and Equation (C.46) reduces to

$$X_{C_{L,c}}^2 = X_{F_{L,c}}^2 + X_{q_{nom}}^2 \tag{C.48}$$

The uncertainty in the recovered lift is discussed in Section 4.8. The uncertainty of the inner shielding pressure measurement $U_{p_{sh}}$ is discussed in Appendix C.7.5 and the uncertainty in the nominal dynamic pressure is taken from either Table C.3 or Table C.4 depending on the test condition.

C.7.3 *Moment about Model Leading Edge*

The corrected moment about the model leading edge is

$$M_{LE,c}(t) = M_{BC,c}(t) + F_{L,c}(t)(x_{BC} - x_{LE}) - F_D(t)(y_{BC} - y_{LE}) \tag{C.49}$$

where (x_{BC}, y_{BC}) and (x_{LE}, y_{LE}) are the coordinates of the balance centre and model leading edge respectively, F_D is the recovered drag force, $F_{L,c}$ is the corrected lift force (Equation (C.45)) and $M_{BC,c}$ is the corrected moment about the balance centre, defined as follows

$$M_{BC,c}(t) = M_{BC}(t) - \left((x_{BC} - x_{LE})^2 \frac{w}{2} p_{sh}(t)\right.$$

$$- (L - (x_{BC} - x_{LE}))^2 \frac{w}{2} p_{sh}(t)\Bigg) \quad \text{(C.50)}$$

where w is the model width, L is the model length and $p_{sh}(t)$ is the average inner shielding pressure. Substituting Equations (C.45) and (C.50) into Equation (C.49) and simplifying gives

$$M_{LE,c}(t) = M_{BC}(t) + F_L(t)(x_{BC} - x_{LE}) - F_D(t)(y_{BC} - y_{LE}) + \frac{L}{2} A_p p_{sh}(t) \quad \text{(C.51)}$$

In this thesis the model length, planar area and locations of the balance centre and model leading edge are each taken to be reference values with no uncertainty.[16] Applying Equation (C.2) to Equation (C.51), the total uncertainty is

$$u^2_{M_{LE,c}} = u^2_{M_{BC}} + (x_{BC} - x_{LE})^2 u^2_{F_L} + (y_{BC} - y_{LE})^2 u^2_{F_D} + \left(\frac{L}{2} A_p\right)^2 u^2_{p_{sh}} \quad \text{(C.52)}$$

The uncertainties in the recovered lift, drag and moment about the balance centre are discussed and defined in Section 4.8. Calculation of the uncertainty in the average inner shielding pressure is presented in Appendix C.7.5.

C.7.4 *Centre of Force Location*

The normalised centre of force location is defined by

$$CF(t) = \frac{M_{LE,c}}{LF_{L,c}} = \frac{M_{BC} + F_L(x_{BC} - x_{LE}) - F_D(y_{BC} - y_{LE}) + \frac{L}{2} A_p p_{sh}}{L(F_L + p_{sh} A_p)} \quad \text{(C.53)}$$

As stated in the previous sections, in this thesis, the balance centre location, leading edge location, planar area of the model and model length are each taken to be reference values with no uncertainty. The total uncertainty in centre of force is found by applying Equation (C.2) to Equation (C.53) to give

$$u^2_{CF} = \left(\frac{\partial CF}{\partial M_{BC}}\right)^2 u^2_{M_{BC}} + \left(\frac{\partial CF}{\partial F_D}\right)^2 u^2_{F_D} + \left(\frac{\partial CF}{\partial F_L}\right)^2 u^2_{F_L} + \left(\frac{\partial CF}{\partial p_{sh}}\right)^2 u^2_{p_{sh}} \quad \text{(C.54)}$$

16 Stated more precisely, it is assumed that the uncertainty in these quantities is sufficiently small as to be negligible compared with the uncertainty in the recovered forces and inner shielding pressure.

Evaluating the partial derivatives gives

$$\frac{\partial CF}{\partial M_{BC}} = \frac{1}{L}(F_L + p_{sh}A_p) \tag{C.55}$$

$$\frac{\partial CF}{\partial F_D} = -\frac{1}{L}\left(\frac{y_{BC} - y_{LE}}{F_L + p_{sh}A_p}\right) \tag{C.56}$$

$$\frac{\partial CF}{\partial F_L} = \frac{1}{L}\left(\frac{x_{BC} - x_{LE}}{L} - CF\right) \tag{C.57}$$

$$\frac{\partial CF}{\partial p_{sh}} = \frac{A_p}{F_{L,c}}\left(\frac{1}{2} - CF\right) \tag{C.58}$$

Finally, substituting Equations (C.55) to (C.58) into Equation (C.54) and using Equation (4.35), the total uncertainty in centre of force is

$$U_{CF}^2 = \frac{1}{(LF_{L,c})^2}\left(U_{M_{LE,c}}^2 + L^2 CF\left(CF - \frac{2(x_{BC} - x_{LE})}{L}\right)U_{F_L}^2 + (LA_p)^2(CF^2 - CF)U_{p_{sh}}^2\right) \tag{C.59}$$

C.7.5 *Inner Shielding Pressure*

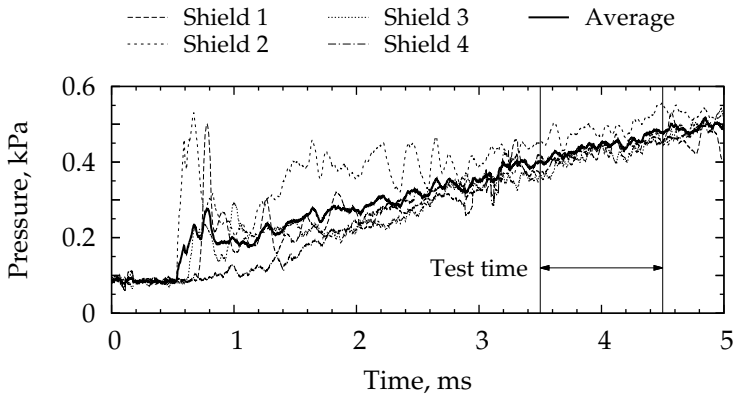

Figure C.1 – Typical inner shielding pressure for a shot at the lower pressure test condition. These data are for shot 10770 and have been filtered by a 60 µs moving average. The time axis has been shifted so that zero corresponds to the trigger of the nozzle supply pressure.

As described in Section 4.2, the pressure within the force balance shielding cavity was measured using four Kulite® pressure transducers. Two were mounted on the M12REST model and two were mounted on the force balance top plate (Figure 4.2). To correct the recovered lift and pitching moment for the pressure build-up within the shielding, the average pressure measured by the four transducers was assumed to act uniformly on the top

surface of the M12REST engine. For convenience, the typical inner shielding pressure traces provided in Figure 4.16 are reproduced in Figure C.1. Although reasonable agreement between the four pressure measurements is observed in Figure C.1, the variation that does exist affects the validity of the assumption that the average pressure acts uniformly on the top surface of the engine. Quantifying the effect of a non-uniform pressure on the calculated lift and moment correction is difficult so, as a first approximation, the variation between the four pressure measurements is used in this thesis to define the uncertainty in the average pressure as follows: at each instance in time the standard deviation, $\sigma_{sh}(t)$, of the four pressure measurements is calculated. A typical result is provided in Figure C.2. The standard deviation is then averaged over the test time to give the inner shielding pressure uncertainty $U_{p_{sh}}$, that is

$$U_{p_{sh}} = \langle \sigma_{sh}(t) \rangle_{t_{start}}^{t_{end}} \tag{C.60}$$

where t_{start} and t_{end} are the start and end of test time. Equation (C.60) is evaluated for each shot. The results are summarised in Table C.7 for the shots presented in this thesis.

Table C.7 – Summary of Inner Shielding Pressure Uncertainty

Shot	Condition	p_{sh}, Pa	$U_{p_{sh}}$, Pa	$X_{p_{sh}}$, %
10756	LP	770.8	116.67	15.1
10761	HP	1333.3	221.84	16.6
10770	LP	442.5	32.94	7.4
10771	LP	383.6	40.55	10.6
10782	LP	387.3	69.58	18.0
10787	HP	671.1	62.38	9.3
10790	LP	337.5	37.87	11.2
10792	HP	475.2	48.22	10.1
10793	HP	495.2	53.68	10.8

C.8 FUEL SYSTEM CALIBRATION

With reference to Appendix A.4 this section presents the uncertainty analysis for the fuel system calibration. The corresponding uncertainty analysis for the experimental fuel mass flow rate and fuel equivalence ratio is provided in Appendix C.9.

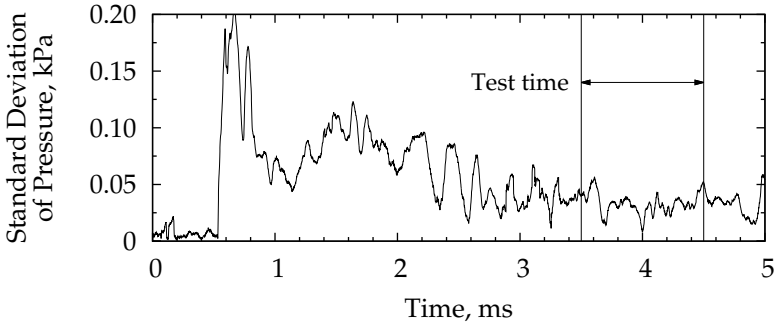

Figure C.2 – Typical time variation of the standard deviation of the inner shielding pressure measurements. The data corresponds to the inner shielding pressures presented in Figure C.1, that is, for shot 10770. The time axis has been shifted so that zero corresponds to the trigger of the nozzle supply pressure.

C.8.1 *Calibration Uncertainty for a Single Leg System*

This section summarises the uncertainty analysis for the calibration constant α calculated from a *single* calibration of a single leg fuel system. The uncertainty analysis for the *mean* value of α from a set of calibrations is presented next in Appendix C.8.2.

Derived in Appendix A.4, the expression for the fuel calibration constant α is (cf. Equation (A.20))

$$\alpha = \frac{(p_{Ti} - p_{Tf})\, V_T}{R T_{Ti} p_{Ti}^{\frac{\gamma-1}{2\gamma}}\, I} = f(p_{Ti}, p_{Tf}, V_T, T_{Ti}, P_p, \gamma, R, t_i, t_f) \tag{C.61}$$

with

$$I = \int_{t_i}^{t_f} p_p^{\frac{\gamma+1}{2\gamma}}\, dt \tag{C.62}$$

In this thesis the gas constant R and specific heat ratio γ are assumed to have negligible uncertainty. The integration limits t_i and t_f are also considered to have negligible uncertainty. Since the initial p_{Ti} and the final pressure p_{Ti} of the fuel tank were measured using the same transducer, the systematic uncertainties of these two measurements are correlated. All other inputs are independent of one another and share no elemental sources of error. The uncertainties used in this thesis for the input variables are as follows:

Volume of Fuel Tank: As explained in Appendix A.4.3, the volume of the fuel tank was not directly measured. An uncertainty of $\pm 5\,\%$ was

assumed.

Initial Fuel Temperature: Consistent with the input used for NENZFR (Appendix C.4) the initial temperature of the fuel in the tank was assumed to be 300 K with an uncertainty of ±2 % or ±6 K.

Plenum Pressure Measurement: A total measurement uncertainty of ±3.2 % was used for the plenum pressure. Calculation of this value is explained in Appendix C.3.

Initial and Final Fuel Tank Pressure: As stated in Section 3.4.5 the fuel tank pressure was recorded using a GE® Druck pressure transmitter (model PTX7517-3257). This gauge has a range of 0 to 10 MPa and a manufacturer quoted accuracy of ±0.3 % of full-scale output. This uncertainty equates to a constant absolute uncertainty of 30 kPa.

The total systematic uncertainty in α is calculated by applying Equation (C.7) to Equation (C.61) to give

$$\begin{aligned} B_\alpha^2 = &\left(\frac{\partial\alpha}{\partial V_T}\right)^2 B_{V_T}^2 + \left(\frac{\partial\alpha}{\partial T_{Ti}}\right)^2 B_{T_{Ti}}^2 + \left(\frac{\partial\alpha}{\partial p_p}\right)^2 B_{p_p}^2 \\ &+ \left(\frac{\partial\alpha}{\partial p_{Ti}}\right)^2 B_{p_{Ti}}^2 + \left(\frac{\partial\alpha}{\partial p_{Tf}}\right)^2 B_{p_{Tf}}^2 \\ &+ 2\left(\frac{\partial\alpha}{\partial p_{Ti}}\right)\left(\frac{\partial\alpha}{\partial p_{Tf}}\right) B_{p_{Ti}p_{Tf}} \end{aligned} \tag{C.63}$$

where the last term accounts for the correlation of p_{Ti} and p_{Tf}. Evaluating the partial derivatives gives

$$\frac{\partial\alpha}{\partial V_T} = \frac{\alpha}{V_T} \tag{C.64}$$

$$\frac{\partial\alpha}{\partial T_{Ti}} = -\frac{\alpha}{T_{Ti}} \tag{C.65}$$

$$\frac{\partial\alpha}{\partial p_{Tf}} = -\frac{\alpha}{p_{Ti} - p_{Tf}} \tag{C.66}$$

$$\frac{\partial\alpha}{\partial p_p} = -\frac{\alpha}{I}\frac{\partial I}{\partial p_p} \tag{C.67}$$

$$\frac{\partial\alpha}{\partial p_{Ti}} = \frac{\alpha}{2\gamma p_{Ti}}\left(\frac{(\gamma+1)p_{Ti} + (\gamma-1)p_{Tf}}{p_{Ti} - p_{Tf}}\right) \tag{C.68}$$

Substituting Equations (C.64) to (C.68) into Equation (C.63), dividing through by α and setting[17]

$$B_{p_{Ti}p_{Tf}} = B_{p_{Ti}} B_{p_{Tf}} \tag{C.69}$$

17 For simplicity the only elemental source of error considered is that due to the gauge accuracy. Equation (C.10) thus reduces to $B_{ik} = B_i B_k$.

the relative systematic uncertainty in α is

$$\begin{aligned}(X_\alpha^B)^2 = (X_{V_T}^B)^2 + (X_{T_{Ti}}^B)^2 + \left(\frac{\partial X_I}{\partial X_{p_p}}\right)^2 \left(X_{p_p}^B\right)^2 + \left(\frac{1}{\frac{p_{Ti}}{p_{Tf}} - 1}\right)^2 (X_{p_{Tf}}^B)^2 \\ + \frac{1}{4}\left(\frac{(\gamma+1)p_{Ti} + (\gamma-1)p_{Tf}}{\gamma(p_{Ti} - p_{Tf})}\right)^2 (X_{p_{Ti}}^B)^2 \\ - \frac{1}{\gamma}\frac{(\gamma+1)p_{Ti} + (\gamma-1)p_{Tf}}{\left(\frac{p_{Ti}}{p_{Tf}} - 1\right)(p_{Ti} - p_{Tf})} X_{p_{Ti}}^B X_{p_{Tf}}^B\end{aligned} \tag{C.70}$$

where $X_{\psi_i}^B = B_{\psi_i}/\psi_i$ is the relative bias uncertainty in variable ψ_i and $\partial X_I/\partial X_{p_p}$ is a relative sensitivity, as defined by Equation (C.13), and must be calculated numerically. It is clear from Equation (C.70) that accounting for the correlated systematic uncertainties of p_{Ti} and p_{Tf} reduces the total systematic uncertainty in α. Furthermore, the systematic uncertainty of a single calibration is reduced when $p_{Tf} \ll p_{Ti}$, indicating that when completing a calibration the fuel valve should be opened for sufficient time as to allow the gas in the Ludweig tube or tank to completely vent through the fuel injectors being calibrated.

Once a set of calibrations at a range of tank fill pressure are completed, the relative precision uncertainty of each individual calibration is calculated using

$$X_\alpha^P = \frac{2\sigma_\alpha}{\alpha} \tag{C.71}$$

where σ_α is the standard deviation of the calibration set. Values of σ_α as a percentage of the mean value are given in Table A.4. Further discussion of this method for calculating the precision uncertainty may be found in Coleman and Steele (1999, Section 4-3.3) and Appendix C.2.2 of this thesis. Finally, the total uncertainty of each calibration is

$$X_\alpha = \sqrt{(X_\alpha^P)^2 + (X_\alpha^B)^2} \tag{C.72}$$

Values for X_α along with the calibration results are plotted in Figure A.9 for the inlet and step injection schemes. The systematic uncertainty X_α^B was 6 % for each experiment while the precision uncertainty X_α^P was between 0.5 and 4 % depending on the injectors and campaign (see Table A.4).

C.8.2 *Calibration Uncertainty of the Mean for a Single Leg System*

During an experiment the average calibration constant from a set of individual calibrations is used for the calculation of the fuel mass flow rate

(Equation (3.2)). This section presents an analysis of the uncertainty in the mean calibration constant that accounts for the correlated systematic uncertainties of the individual calibration constants. The average calibration constant is simply

$$\overline{\alpha} = \frac{1}{m}\sum_{k=1}^{m} \alpha_k \tag{C.73}$$

Noting that each α_k is a derived quantity, then the complete functional dependency of $\overline{\alpha}$ is

$$\overline{\alpha} = f(V_T, \{p_{Ti}\}_{k=1}^{m}, \{p_{Tf}\}_{k=1}^{m}, T_{Ti}, \{p_p\}_{k=1}^{m}) \tag{C.74}$$

where $\{p_{Ti}\}_{k=1}^{m}$ is the complete set of initial tank pressures measured across all the individual calibrations. Similarly, $\{p_{Tf}\}_{k=1}^{m}$ is the set of final tank pressures and $\{p_p\}_{k=1}^{m}$ is the set of plenum pressures. The total systematic uncertainty in the mean calibration constant is calculated by applying Equation (C.7) to Equation (C.74) to give

$$\begin{aligned}
B_{\overline{\alpha}}^2 = {} & \left(\frac{\partial\overline{\alpha}}{\partial V_T}\right)^2 B_{V_T}^2 + \left(\frac{\partial\overline{\alpha}}{\partial T_{Ti}}\right)^2 B_{T_{Ti}}^2 + \sum_{k=1}^{m}\left(\frac{\partial\overline{\alpha}}{\partial (p_{Tf})_k}\right)^2 B_{(p_{Tf})_k}^2 \\
& + \sum_{k=1}^{m}\left(\frac{\partial\overline{\alpha}}{\partial (p_p)_k}\right)^2 B_{(p_p)_k}^2 + \sum_{k=1}^{m}\left(\frac{\partial\overline{\alpha}}{\partial (p_{Ti})_k}\right)^2 B_{(p_{Ti})_k}^2 \\
& + 2\sum_{k=1}^{m-1}\sum_{l=k+1}^{m}\left(\frac{\partial\overline{\alpha}}{\partial (p_{Tf})_k}\right)\left(\frac{\partial\overline{\alpha}}{\partial (p_{Tf})_l}\right) B_{(p_{Tf})_k (p_{Tf})_l} \\
& + 2\sum_{k=1}^{m-1}\sum_{l=k+1}^{m}\left(\frac{\partial\overline{\alpha}}{\partial (p_{Ti})_k}\right)\left(\frac{\partial\overline{\alpha}}{\partial (p_{Ti})_l}\right) B_{(p_{Ti})_k (p_{Ti})_l} \\
& + 2\sum_{k=1}^{m-1}\sum_{l=k+1}^{m}\left(\frac{\partial\overline{\alpha}}{\partial (p_p)_k}\right)\left(\frac{\partial\overline{\alpha}}{\partial (p_p)_l}\right) B_{(p_p)_k (p_p)_l} \\
& + 2\sum_{k=1}^{m}\sum_{l=1}^{m}\left(\frac{\partial\overline{\alpha}}{\partial (p_{Ti})_k}\right)\left(\frac{\partial\overline{\alpha}}{\partial (p_{Tf})_l}\right) B_{(p_{Ti})_k (p_{Tf})_l}
\end{aligned} \tag{C.75}$$

Evaluating the partial derivatives,[18] dividing through by $\overline{\alpha}$ and setting

$$B_{(p_{Tf})_k (p_{Tf})_l} = B_{(p_{Tf})_k} B_{(p_{Tf})_l} \tag{C.76}$$

$$B_{(p_{Ti})_k (p_{Ti})_l} = B_{(p_{Ti})_k} B_{(p_{Ti})_l} \tag{C.77}$$

$$B_{(p_p)_k (p_p)_l} = B_{(p_p)_k} B_{(p_p)_l} \tag{C.78}$$

$$B_{(p_{Ti})_k (p_{Tf})_l} = B_{(p_{Ti})_k} B_{(p_{Tf})_l} \tag{C.79}$$

18 see Equations (C.64) to (C.68)

then Equation (C.75) becomes

$$
\begin{aligned}
\left(X^B_{\overline{\alpha}}\right)^2 = {} & \left(X^B_{V_T}\right)^2 + \left(X^B_{T_{Ti}}\right)^2 + \left(\frac{1}{m}\right)^2 \sum_{k=1}^{m} \left(\frac{\alpha_k}{\overline{\alpha}}\right)^2 \left(\frac{1}{\frac{p_{Ti}}{p_{Tf}} - 1}\right)_k^2 \left(X^B_{p_{Tf}}\right)_k^2 \\
& + \left(\frac{1}{m}\right)^2 \sum_{k=1}^{m} \left(\frac{\alpha_k}{\overline{\alpha}}\right)^2 \left(\frac{\partial X_I}{\partial X_{p_p}}\right)_k^2 \left(X^B_{p_p}\right)_k^2 \\
& + \frac{1}{4}\left(\frac{1}{m}\right)^2 \sum_{k=1}^{m} \left(\frac{\alpha_k}{\overline{\alpha}}\right)^2 \zeta_k^2 \left(X^B_{p_{Ti}}\right)_k^2 \\
& + 2\left(\frac{1}{m}\right)^2 \sum_{k=1}^{m-1} \sum_{l=k+1}^{m} \frac{\alpha_k}{\overline{\alpha}} \frac{\alpha_l}{\overline{\alpha}} \xi_k \xi_l \left(X^B_{p_{Tf}}\right)_k \left(X^B_{p_{Tf}}\right)_l \\
& + \frac{1}{2}\left(\frac{1}{m}\right)^2 \sum_{k=1}^{m-1} \sum_{l=k+1}^{m} \frac{\alpha_k}{\overline{\alpha}} \frac{\alpha_l}{\overline{\alpha}} \zeta_k \zeta_l \left(X^B_{p_{Ti}}\right)_k \left(X^B_{p_{Ti}}\right)_l \\
& + 2\left(\frac{1}{m}\right)^2 \sum_{k=1}^{m-1} \sum_{l=k+1}^{m} \frac{\alpha_k}{\overline{\alpha}} \frac{\alpha_l}{\overline{\alpha}} \left(\frac{\partial X_I}{\partial X_{p_p}}\right)_k \left(\frac{\partial X_I}{\partial X_{p_p}}\right)_l \left(X^B_{p_p}\right)_k \left(X^B_{p_p}\right)_l \\
& - \left(\frac{1}{m}\right)^2 \sum_{k=1}^{m} \sum_{l=1}^{m} \frac{\alpha_k}{\overline{\alpha}} \frac{\alpha_l}{\overline{\alpha}} \zeta_k \xi_l \left(X^B_{p_{Ti}}\right)_k \left(X^B_{p_{Tf}}\right)_l
\end{aligned}
\tag{C.80}
$$

where

$$\zeta = \frac{(\gamma+1)p_{Ti} + (\gamma-1)p_{Tf}}{\gamma(p_{Ti} - p_{Tf})} \tag{C.81}$$

$$\xi = \frac{1}{\frac{p_{Ti}}{p_{Tf}} - 1} \tag{C.82}$$

The first five terms in Equation (C.80) account for the uncertainties in the tank volume (V_T), the initial tank temperature (T_{T_i}), the final tank pressure measurements ($\{p_{Tf}\}_k$), the initial tank pressure measurements ($\{p_{Ti}\}_k$) and the plenum pressure measurements ($\{p_p\}_k$) respectively. The sixth term accounts for correlation between the final tank pressure measurements. This correlation is present because the same transducer is used for each calibration. Similarly, the seventh and eighth terms account for correlation between the initial tank pressure measurements and between the plenum pressure measurements, respectively. Finally, the ninth term accounts for correlation between each possible combination of the initial and final tank pressure measurements.

Table C.8 summarises the values calcuated for each term in Equation (C.80) for the campaign 1 and campaign 2 calibrations of the inlet

and step injectors. These results show that the 6th, 7th and 9th terms of Equation (C.80) all have a similar magnitude and are much larger than the other terms of the equation. It is clear from Equation (C.80) and Table C.8 that properly accounting for the correlated systematic uncertainties increases the uncertainty in the mean. Neglecting to account for the correlated systematic uncertainties would result in the uncertainty of the mean calibration constant being significantly underestimated. Consistent with the result for a single calibration (Equation (C.70)), the uncertainty in the mean calibration constant is reduced when $p_{Tf} \ll p_{Ti}$.

Taking advantage of the fact that a set of calibrations are completed, the precision uncertainty of the mean is calculated using

$$X_{\overline{\alpha}}^{P} = \frac{2\sigma_{\alpha}}{\overline{\alpha}\sqrt{m}} \tag{C.83}$$

where σ_{α} is the standard deviation of m individual calibrations. Further discussion of this method for calculating the precision uncertainty may be found in Coleman and Steele (1999, Section 4-3.3) and Appendix C.2.2 of this thesis. Finally, the total uncertainty of the mean is

$$X_{\overline{\alpha}} = \sqrt{\left(X_{\overline{\alpha}}^{P}\right)^2 + \left(X_{\overline{\alpha}}^{B}\right)^2} \tag{C.84}$$

Table C.9 summarises the systematic, precision and total uncertainty for the mean calibration constant of the inlet and step injection stations. Note that the uncertainties were slightly reduced for the campaign 2 calibration because the fuel solenoid valve was held open for longer (Figure A.7), resulting in a larger difference between the initial and final tank pressures.

Table C.8 – Component Systematic Uncertainties of the Mean Fuel Calibration Constant

	Campaign 1		Campaign 2	
Term in Equation (C.80)	Inlet Inj. 10^{-3}	Step Inj. 10^{-3}	Inlet Inj. 10^{-3}	Step Inj. 10^{-3}
1	2.50	2.50	2.50	2.50
2	0.40	0.40	0.40	0.40
3	1.24	0.77	0.29	0.32
4	0.05	0.06	0.03	0.04
5	1.10	0.66	0.25	0.26
6	11.28	7.55	4.22	4.55
7	9.98	6.54	3.54	3.71
8	0.65	0.67	0.70	0.69
9	−10.57	−7.02	−3.87	−4.12
$\left(X_{\overline{\alpha}}^{B}\right)^2$	16.57	12.12	8.81	8.35

Table C.9 – Total Uncertainty in Mean Calibration Constant for Single-leg Fuel System

	Campaign 1		Campaign 2	
	Inlet Inj. %	Step Inj. %	Inlet Inj. %	Step Inj. %
$X^P_{\overline{\alpha}}$	0.5	1.1	0.1	0.7
$X^B_{\overline{\alpha}}$	12.9	11.0	9.0	9.1
$X_{\overline{\alpha}}$	12.9	11.1	9.0	9.2

C.9 FUEL MASS FLOW AND EQUIVALENCE RATIO

This section presents the uncertainty analysis for the experimental fuel and air mass flow rates and the fuel equivalence ratio.

C.9.1 *Fuel Flow Rate for Single-leg Systems*

Derived in Appendix A.4 the fuel mass flow rate for a single-leg system is calculated using

$$\dot{m}_f = \overline{\alpha} p_{Ti}^{\frac{\gamma-1}{2\gamma}} p_p^{\frac{\gamma+1}{2\gamma}} \tag{C.85}$$

where p_{Ti} and p_p are the initial tank pressure and fuel plenum pressure measured during the experiment and $\overline{\alpha}$ is a constant determined from a set of calibrations. Since the same experimental apparatus is identical to that used during calibration, the experimental tank and fuel plenum pressure measurements are correlated with the calibration measurements. The complete functional dependency of the fuel mass flow rate is thus

$$\dot{m}_f = f((p_{Ti})_e, (p_p)_e, V_T, \{p_{Ti}\}_{k=1}^s, \{p_{Tf}\}_{k=1}^s, T_{T_i}, \{p_p\}_{k=1}^s) \tag{C.86}$$

where the subscript e is used to distinguish experimental measurements from those made during a calibration. The total systematic uncertainty in the fuel mass flow rate is found by applying Equation (C.7) to Equation (C.86) to give

$$\begin{aligned}(X^B_{\dot{m}})^2 = &\left(\frac{\gamma+1}{2\gamma}\right)^2 \left(X^B_{p_p}\right)_e^2 + \left(\frac{\gamma-1}{2\gamma}\right)^2 (X^B_{p_{Ti}})_e^2 + X^2_{\overline{\alpha}} \\ &- \left(\frac{2}{s}\right)\left(\frac{\gamma+1}{2\gamma}\right) \sum_{k=1}^{s} \left(\frac{\alpha_k}{\overline{\alpha}}\right)\left(\frac{\partial X_I}{\partial X_{p_p}}\right)_k (X_{p_p})_e (X_{p_p})_k\end{aligned}$$

$$+\left(\frac{1}{s}\right)\left(\frac{\gamma-1}{2\gamma}\right)\sum_{k=1}^{s}\left(\frac{\alpha_k}{\overline{\alpha}}\right)\zeta_k\left(X^B_{p_{Ti}}\right)_e\left(X^B_{p_{Ti}}\right)_k$$

$$-\left(\frac{2}{s}\right)\left(\frac{\gamma-1}{2\gamma}\right)\sum_{k=1}^{s}\left(\frac{\alpha_k}{\overline{\alpha}}\right)\left(\frac{1}{\frac{p_{Ti}}{p_{Tf}}-1}\right)_k\left(X^B_{p_{Ti}}\right)_e\left(X^B_{p_{Tf}}\right)_k \quad \text{(C.87)}$$

where

$$\zeta = \frac{(\gamma+1)p_{Ti}+(\gamma-1)p_{Tf}}{\gamma(p_{Ti}-p_{Tf})} \quad \text{(C.88)}$$

and Equation (C.80) and relations similar to Equations (C.76) to (C.79) have been used. The first two terms in Equation (C.87) account for the uncertainties in the experimental measurement of the initial tank pressure and plenum pressure, respectively, while the third term accounts for the uncertainty in the calibration constant. The fourth term accounts for correlation between the experimental and calibration measurements of the plenum pressure (the same transducer is used). Similarly, the fifth term accounts for correlation between the experimental and calibration measurements of the inital tank pressure. Finally, the sixth term accounts for correlation between the experimental measurement of the initial tank pressure and the calibration measurement of the final tank pressure.

Using the uncertainty values from Appendices C.3 and C.8, Equation (C.87) was evaluated for each fuel-on experiment. The general results were as follows:

1. The fifth and sixth terms in Equation (C.87) are approximately equal in magnitude and so cancel each other out. The fifth term lies between 0.009 and 0.0017. The magnitude of the sixth term is approximately 0.0001 larger than the fifth term.

2. The second term is negligible being equal to or less than 0.0003.

3. The fourth term is approximately -0.0014 and is approximately double that of the first term.

4. The third term is the dominate term.

Consequently, it was found that across both test campaigns, the uncertainty in fuel mass flow rate for the inlet and step injection schemes could be written approximately as

$$X_{\dot{m}} \approx X_{\overline{\alpha}} - 0.5\,\% \quad \text{(C.89)}$$

where $X_{\overline{\alpha}}$ is the calibration uncertainty for the mean calibration constant as given in Table C.9.

C.9.2 *Air Flow Rate*

The mass flow rate of captured air is calculated in this thesis using

$$\dot{m}_A = m_{c,1} A_1 \rho u_x \tag{C.90}$$

The mass capture ratio $m_{c,1}$ is calculated from the numerical simulations of the engine that are presented in Chapter 5 while the shot-specific density and velocity are calculated using a NENZFR response surface as described in Section 3.3. For simplicity, the projected frontal area of the inlet is taken to be a reference constant and so has no uncertainty associated with it. Referring to the mass capture data given in Table G.1, the capture ratio at the nominal high pressure test condition is 4.3 % larger than that at the nominal low pressure test condition. Assuming that this difference is mostly due to changes in the freestream Mach number, and noting that the difference in Mach number between the two test conditions is 1.4 %, which is comparable to the uncertainty in Mach number (Tables C.3 and C.4), an uncertainty of 5 % is used in this thesis for the mass capture ratio.

The static density and axial velocity of the nozzle exit flow are each derived properties that share fundamental error sources. For this reason the product ρu_x was included in the NENZFR uncertainty analysis that is presented in Appendix C.4. Considering the uncertainties in the capture ratio and mass flux to be independent,[19] the overall uncertainty in the mass flow rate of captured air is

$$X_{\dot{m}_A} = \sqrt{X^2_{m_{c,1}} + X^2_{\rho u_x}} = \begin{cases} 6.4\,\% & \text{for the HP test condition} \\ 6.5\,\% & \text{for the LP test condition} \end{cases} \tag{C.91}$$

For simplicity, an uncertainty of 6.5 % is used for both test conditions in all subsequent analysis.

C.9.3 *Equivalence Ratio*

The fuel equivalence ratio is

$$\phi = \frac{1}{\lambda} \frac{\dot{m}_f}{\dot{m}_A} \tag{C.92}$$

Noting that there is no uncertainty associated with the stoichiometric fuel-air ratio and that the fuel and air mass flow rates share no fundamental or elemental sources of error, then the uncertainty in the fuel equivalence

19 Strictly they are not independent as the numerical simulations of the M12REST engine were completed at the nominal test conditions. The nominal test condition uncertainties could not be propagated into the engine simulations.

ratio is simply

$$X_\phi = \sqrt{X_{\dot{m}_f}^2 + X_{\dot{m}_A}^2} \tag{C.93}$$

Using data from Appendices C.8, C.9.1 and C.9.2 the uncertainty in fuel equivalence ratio for the inlet and step injection schemes can be found. The results are given in Table C.10.

Table C.10 – Relative Uncertainty in Fuel Equivalence Ratio

	X_ϕ (%)	
Inj. Scheme	Campaign 1	Campaign 2
Inlet	14.0	10.7
Step	12.4	10.9

PRESSSURE TRANSDUCER MOUNTING

D

D.1 INTRODUCTION

This appendix details the mounting methods used for the Pitot, engine and fuel plenum pressure transducers. Further details regarding the design and development of the M12REST engine, including a full set of technical drawings, may be found in Doherty (2013b).

D.2 PITOT PROBE MOUNT

The Pitot probe used in this thesis is shown in Figure D.1. The probe was designed by McGilvray et al. (2009) and fits a single PCB® transducer. This probe design has a narrower profile than the standard Pitot probe mount used in the T4 Stalker Tube (see, for example Kirchhartz, 2010, Appendix A) which allowed the probe to be positioned in the core flow of the Mach 10B nozzle near the leading edge of the M12REST engine. See Doherty (2013b) for further information and technical drawings.

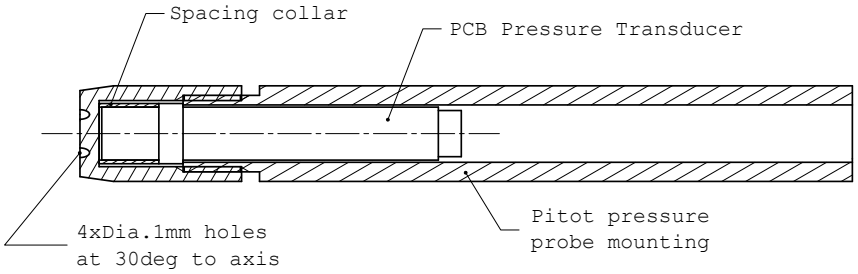

Figure D.1 – Mounting arrangement for Pitot probe transducers developed by McGilvray et al. (2009). Not to scale.

D.3 ENGINE PRESSURE TRANSDUCERS

Kulite® pressure transducers were used to measure the pressure distribution along the bodyside symmetry plane of the M12REST engine (Figure 3.9). The mounting hole for these transducers is shown in Figure D.2.

D.4 FUEL PLENUM TRANSDUCERS

With reference to Section 3.4.4, PCB® pressure transducers were used to measure the fuel plenum pressure. These were mounted using the vibration isolation mounting system shown in Figure D.3. This is the standard mounting method used for PCB® transducers within the CfH.

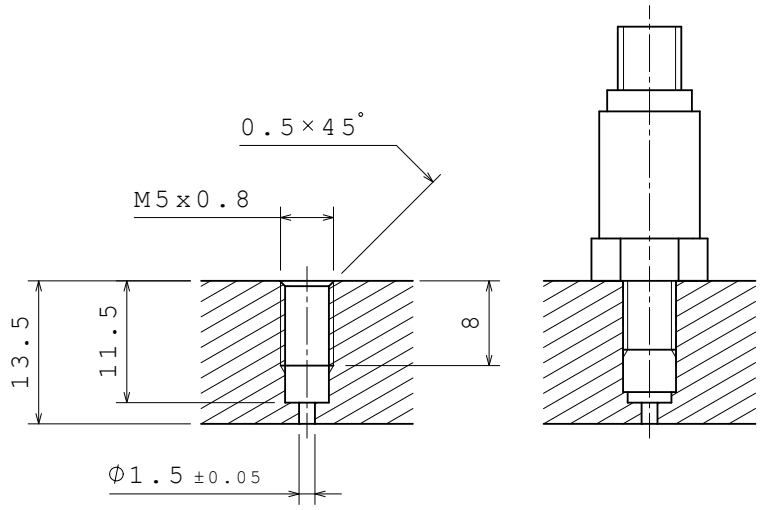

Figure D.2 – Mounting for Kulite® pressure transducers. Dimensions in millimetres. Not to scale.

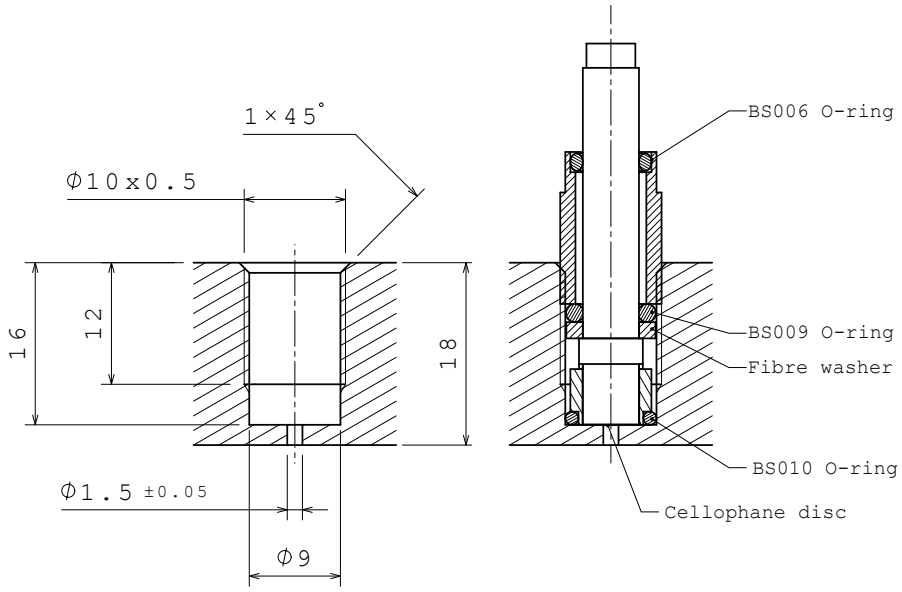

Figure D.3 – Vibration isolation mounting system for PCB® pressure transducers. Dimensions in millimetres. Not to scale.

COORDINATE SYSTEMS

E

E.1 INTRODUCTION

Several coordinate systems are used throughout this thesis. Each system and the relevant transformations are detailed here. The coordinates for each engine pressure tap and force balance calibration location are also provided in this Appendix in the relevant coordinate frames. Note that dimensions given in this Appendix are theoretical values extracted from the CATIA® CAD model of the engine. The manufacturing tolerance of the engine was specified as follows: angular, $\pm 0.5°$; linear with no or one decimal place, ± 0.10 mm; linear with two decimal places, ± 0.05 mm and geometry, as per ISO 2768-fh.

E.2 INLET COORDINATE SYSTEM

Shown in Figure E.1 and designated by (x_I, y_I, z_I), the inlet coordinate system is orientated such that x_I is parallel to the forebody surface, $x_I = 0$ corresponds to the start of the inlet and the symmetry plane of the engine lies in the $z_I = 0$ plane. The surfaces defining the inlet geometry were generated by the REST design tools in this coordinate system (hence its name). The grid used for the numerical simulation of the engine (presented Chapter 5) was also created in this frame.

E.3 ENGINE COORDINATE SYSTEM

The primary coordinate system used in this thesis is the engine coordinate system. Shown in Figure E.2 and designated by (x, y, z), this system is defined with respect to the inlet coordinates by the following transformation:

$$\begin{pmatrix} x \\ y \\ z \end{pmatrix} = \begin{pmatrix} \cos\theta & \sin\theta & 0 \\ -\sin\theta & \cos\theta & 0 \\ 0 & 0 & 1 \end{pmatrix} \begin{pmatrix} x_I \\ y_I \\ z_I \end{pmatrix} - \begin{pmatrix} 3.65\,\text{mm} \\ 0 \\ 0 \end{pmatrix} \tag{E.1}$$

where $\theta = 6°$ is the wedge angle of the forebody. This coordinate system has been rotated with respect to the inlet coordinate frame and shifted dowstream such that the x axis is parallel to the top surface of the engine and $x = 0$ corresponds to the start of the inlet. Unless otherwise stated, all data in this thesis are presented using the engine coordinate frame. The locations of the engine transducers in both the inlet and engine coordinate

systems are provided in Table E.1.

Table E.1 – Transducer Locations in the Inlet and Engine Coordinate Systems. Dimensions are millimetres.

	Inlet		Engine	
Location	x_I	y_I	x	y
P1	−42	34.94	−41.77	39.14
P2	226.95	19.59	224.10	−4.24
P3	263.77	15.91	260.34	−11.75
P4	281.92	14.35	278.22	−15.20
P5	387.16	19.77	383.46	−20.81
P6	413.02	22.49	409.46	−20.81
P7	437.89	25.10	434.46	−20.81
P8	462.80	28.32	459.57	−20.21
P9	488.57	31.76	485.56	−19.48
P10	597.14	67.90	597.32	5.11

E.4 FORCE BALANCE COORDINATE SYSTEM

For convenience two coordinate systems are defined for the force balance; both are shown in Figure E.3. The first, designated by (x_{fb1}, y_{fb1}) is defined to be parallel to the engine coordinate system with its origin located on the upper surface of the engine in the nozzle exit plane. This coordinate system is used to define the calibration locations of the force balance (Figure 4.3). A reference leading edge location is also defined with respect to this coordinate system. such that the overall length of the engine is exactly 0.915 m, slightly longer than the actual model length (when measuring to the centre of the forebody leading edge radius, cf. Figure 3.8). In the engine coordinate system, the location of the reference leading edge is

$$x_{LE} = -270.55\,\text{mm}$$
$$y_{LE} = \quad 64.16\,\text{mm}$$

The calibration locations, associated integration intervals and reference leading edge location are provided in Table E.2.

The primary force balance coordinate system, designated by (x_{fb}, y_{fb}), is defined to be parallel to the engine coordinate system with the origin coinciding with the balance centre. Referring to Section 4.5, the balance centre is defined to be located at centre of force of the reference load distribution that is used to form the global impulse response of the balance. As different loading distributions may be used to form the GIRF, the location

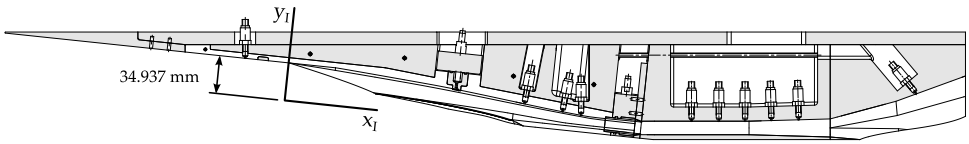

Figure E.1 – Inlet coordinate system

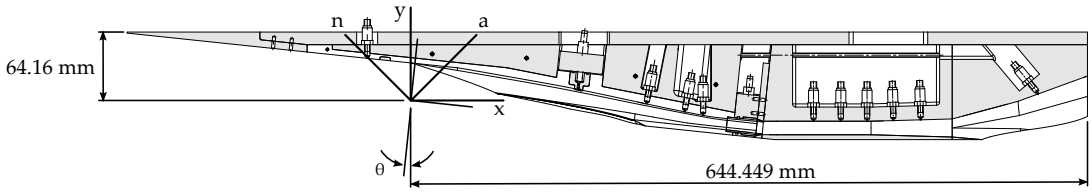

Figure E.2 – Engine coordinate system

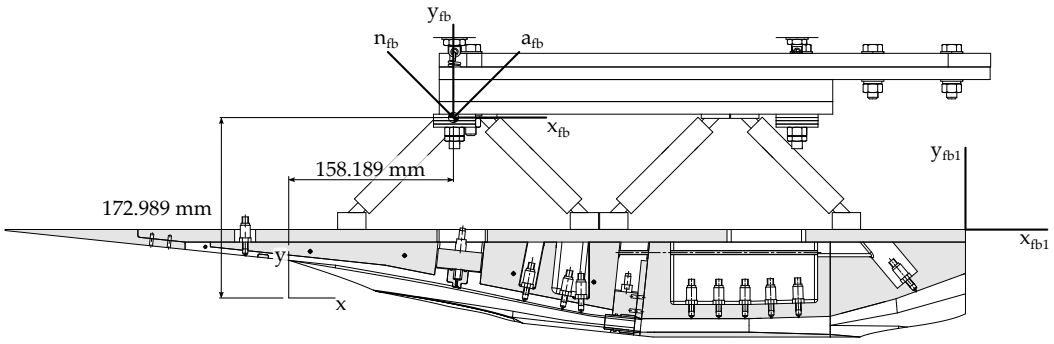

Figure E.3 – Force balance coordinate system

of the balance centre is not strictly unique. The reference distribution used in this thesis is given in Figure 4.4. Due to difficulty in obtaining a single clean hit at calibration station 1, only calibration stations 2 to 20 were used to form the GIRF (Appendix B.6). For the reduced load distribution, the location of the balance centre in the engine coordinate system is

$$x_{BC} = 158.19\,\text{mm}$$
$$y_{BC} = 172.99\,\text{mm}$$

This location is shown in Figure E.3.

E.5 NORMAL-AXIAL COORDINATE SYSTEMS

For both the engine and force balance coordinate systems, corresponding normal-axial coordinate systems are defined. Although all force data are presented in the lift-drag coordinate system, due to the orientation of the force balance stress bars and direction of the calibration hits, it is more convenient to use the normal-axial coordinate system for the force balance theory and calibration. The two coordinates systems are related by the following transformations:

$$\begin{pmatrix} A \\ N \end{pmatrix} = \frac{\sqrt{2}}{2} \begin{pmatrix} 1 & 1 \\ -1 & 1 \end{pmatrix} \begin{pmatrix} D \\ L \end{pmatrix} \tag{E.2}$$

$$\begin{pmatrix} D \\ L \end{pmatrix} = \frac{\sqrt{2}}{2} \begin{pmatrix} 1 & -1 \\ 1 & 1 \end{pmatrix} \begin{pmatrix} A \\ N \end{pmatrix} \tag{E.3}$$

Table E.2 – Force Balance Calibration Locations. Dimensions are millimetres.

Location	x_{fbl}	x	Integration Interval		
			x_{low}	x_{high}	Δx
"LE"	−915	−270.55			
1	−889.75	−245.30	−270.55	−222.43	48.13
2	−844	−199.55	−222.43	−176.68	45.75
3	−798.25	−153.80	−176.68	−130.93	
4	−752.50	−108.05	−130.93	−85.18	
5	−706.75	−62.30	−85.18	−39.43	
6	−661	−16.55	−39.43	6.32	
7	−615.25	29.20	6.32	52.07	
8	−569.50	74.95	52.07	97.82	
9	−523.75	120.70	97.82	143.57	
10	−478	166.45	143.57	189.32	
11	−432.25	212.20	189.32	235.07	
12	−386.50	257.95	235.07	280.82	
13	−340.75	303.70	280.82	326.57	
14	−295	349.45	326.57	372.32	
15	−249.25	395.20	372.32	418.07	
16	−203.50	440.95	418.07	463.82	
17	−157.75	486.70	463.82	509.57	
18	−112	532.45	509.57	555.32	
19	−66.25	578.20	555.32	601.07	
20	−20.50	623.95	601.07	644.45	43.38
Exit	0	644.45			

CENTRE OF FORCE CALCULATION

F.1 INTRODUCTION

F

This appendix details the equations used to calculate the centre of force from 3-D numerical simulations. Whether or not the centre of force is unique and well-defined is also discussed.

The force imparted to a body as it moves through a fluid has only two components: that due to the surface pressure and that due to the surface shear stress. Referring to Figure F.1 the net force-per-area is defined by

$$\mathbf{f} = -(p\hat{\mathbf{n}} + \tau_w \hat{\mathbf{v}}) \tag{F.1}$$

where p is the surface pressure, τ_w the wall shear stress, $\hat{\mathbf{n}}$ the (outward) unit normal vector and $\hat{\mathbf{v}}$ the unit tangent vector that is parallel to the local flow velocity. Integrating Equation (F.1) over the entire wetted surface of the body gives the total aerodynamic force

$$\mathbf{F}_{\text{aero}} = \iint_S \mathbf{f}\, dS \tag{F.2}$$

It is only after a reference coordinate system and origin are specified that the aerodynamic moments may be defined.

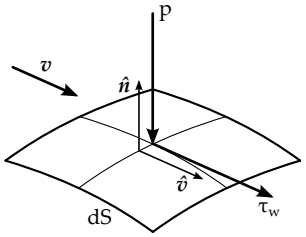

Figure F.1 – Fluid forces acting on a differential area element.

F.2 GENERAL FORMULATION

The derivation provided here closely follows that presented in Chapter 7 of Hirschel and Weiland (2009). Let the centre of force[1] ($\hat{\mathbf{r}}_{CF}$) be defined as any point about which the total aerodynamic force $\mathbf{F}_{\text{aero}}$ generates no net

1 In this thesis the centre of force, which includes contributions from both surface pressure and viscous forces, is distinguished from the centre of pressure and centre of skin friction, which include contributions from only the surface pressure forces and from the surface viscous forces respectively.

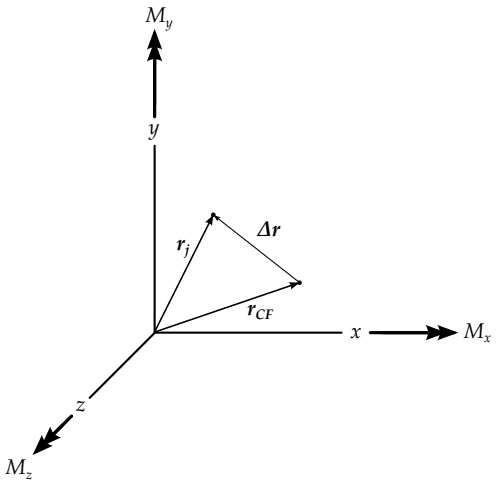

Figure F.2 – Centre of force defined relative to a specified coordinate system

moment.

$$\mathbf{M}_{CF} = \mathbf{M}_j + \Delta\mathbf{r} \times \mathbf{F}_{aero} = 0 \tag{F.3}$$

where

$$\Delta\mathbf{r} = \mathbf{r}_j - \mathbf{r}_{CF} = \begin{pmatrix} x_j - x_{CF} \\ y_j - y_{CF} \\ z_j - z_{CF} \end{pmatrix}, \quad \mathbf{F}_{aero} = \begin{pmatrix} F_x \\ F_y \\ F_z \end{pmatrix}, \quad \mathbf{M}_j = \begin{pmatrix} M_x|_j \\ M_y|_j \\ M_z|_j \end{pmatrix}$$

Subsituting the above into Equation (F.3) and evaluating the cross-product gives

$$\begin{pmatrix} M_x|_j \\ M_y|_j \\ M_z|_j \end{pmatrix} + \begin{pmatrix} F_z(y_j - y_{CF}) - F_y(z_j - z_{CF}) \\ -F_z(x_j - x_{CF}) + F_x(z_j - z_{CF}) \\ F_y(x_j - x_{CF}) - F_x(y_j - y_{CF}) \end{pmatrix} = 0 \tag{F.4}$$

Setting $\mathbf{r}_j = \mathbf{r}_0 = 0$ so that moments are calculated with respect to the origin of the coordinate system, then Equation (F.4) reduces to

$$\begin{pmatrix} M_x|_0 \\ M_y|_0 \\ M_z|_0 \end{pmatrix} + \begin{pmatrix} -F_z y_{CF} + F_y z_{CF} \\ F_z x_{CF} - F_x z_{CF} \\ -F_y x_{CF} + F_x y_{CF} \end{pmatrix} = 0$$

Alternatively,

$$\begin{pmatrix} M_x|_0^{zy} + M_x|_0^{yz} \\ M_y|_0^{zx} + M_y|_0^{xz} \\ M_z|_0^{yx} + M_z|_0^{xy} \end{pmatrix} = \begin{pmatrix} F_z y_{CF} - F_y z_{CF} \\ -F_z x_{CF} + F_x z_{CF} \\ F_y x_{CF} - F_x y_{CF} \end{pmatrix} \tag{F.5}$$

where $M_x|_0^{zy}$ is the x-component of the moment (about the origin) due to a force in direction-z with moment arm in direction-y (similarly for the other components). The moment components are defined below.

$$M_x|_0^{zy} = \iint_s f_z y \, dS \quad \text{(F.6)} \qquad M_x|_0^{yz} = -\iint_s f_y z \, dS \quad \text{(F.9)}$$

$$M_y|_0^{xz} = \iint_s f_x z \, dS \quad \text{(F.7)} \qquad M_y|_0^{zx} = -\iint_s f_z x \, dS \quad \text{(F.10)}$$

$$M_z|_0^{yx} = \iint_s f_y x \, dS \quad \text{(F.8)} \qquad M_z|_0^{xy} = -\iint_s f_x y \, dS \quad \text{(F.11)}$$

where $f_s = \mathbf{f} \cdot \hat{\mathbf{s}}$ is the net force-per-area acting in direction $s \in \{i, j, k\}$.

F.3 SYMMETRIC BODIES

For a vehicle that is symmetric about the $x - y$ plane and flying at 0° AOY the following conditions hold

$$F_z = M_x|_0^{zy} = M_x|_0^{yz} = M_y|_0^{zx} = M_y|_0^{xz} = z_{CF} = 0$$

Consequently, Equation (F.5) reduces to

$$M_z|_0^{yx} + M_z|_0^{xy} = F_y x_{CF} - F_x y_{CF} \quad \text{(F.12)}$$

The separate calculation of $M_z|_0^{yx}$ and $M_z|_0^{xy}$ is trivial for numerical data and so a "unique" centre of force location can be defined by

$$x_{CF} = \frac{M_z|_0^{yx}}{F_y} \quad \text{(F.13)}$$

$$y_{CF} = \frac{M_z|_0^{xy}}{F_x} \quad \text{(F.14)}$$

For experimental data it is not possible to separate the contributions of the x-direction and y-direction forces to the net moment; $M_z|_0^{yx}$ and $M_z|_0^{xy}$ cannot be individually determined as only the net moment $M_z|_0$ is measured. In this case, Equation (F.12) defines a line-of-action for the aerodynamic force and the centre of force can only be defined relative to some other reference location (typically the centre of mass), that is

$$x_{CF} = \frac{M_z + F_x y_{CF}}{F_y} \quad \text{(F.15)}$$

where y_{CF} is specified *a priori*.

F.4 IS THE CENTRE OF FORCE UNIQUE AND WELL-DEFINED?

In general a unique centre of force location may not exist nor may it be well-defined. These two facts are somewhat counter-intuitive to the general understanding of the centre of force location. The non-uniqueness of the centre of force is apparent on study of Equations (F.6) to (F.11). Each of these six equations, when equated to the corresponding element on the right-hand-side of Equation (F.5), defines one of the coordinates of the centre of force location. As there are six equations but only three unkowns (x_{CF}, y_{CF}, z_{CF}) the system is over-defined and in general cannot be uniquely solved. The second fact to be considered is that the centre of force may not be well-defined. To understand how this may occur, consider a body that is symmetric about the $x-y$ plane, for which there is no drag distribution and for which the lift distribution produces a pure moment and no net lift. Then, according to Equation (F.13) the centre of force is located at $x = \infty$ and so cannot be considered well-defined.

SUPPLEMENTARY ENGINE FLOW FIELD RESULTS

G.1 INTRODUCTION

G

This appendix presents additional data from the fuel-off numerical simulations of the M12REST engine. The engine flow field at the low pressure test condition is presented in Appendix G.2. The calculated engine mass capture and forebody flow spillage fractions at each test condition are provided in Appendix G.3. Appendix G.4 provides absolute force data for different surface groups of the engine. Finally, Appendix G.6 lists the calculated pressure at each tap along the bodyside symmetry plane of the engine.

G.2 FLOW FIELD STRUCTURE

Contours of $\log_{10}(p)$ on the engine symmetry plane are plotted in Figure G.1 for the low pressure test condition. A similar plot for the high pressure test condition is provided in Figure 5.4b. Comparing Figures 5.4b and G.1, it can be seen that the flow fields are almost identical with the dominant flow structures slightly shifted for the low pressure simulation relative to the high pressure simulation. The slight shift in location of the flow structures is expected since the Mach number and unit Reynolds number are slightly different for low pressure test compared to that of the high pressure test condition (Table 3.3) and these properties influence the wave angles and boundary layer thicknesses, respectively.

Slightly concerning is the presence of a small separation on the engine bodyside at $x \approx 205\,\text{mm}$ for the low pressure simulation. This separation was not present for the high pressure simulation and occurs at the same axial position as the cowl closure point of the inlet leading edges. The grid in this region is very complex and collapses to a singularity line; consequently, the separation is believed to be an artifact of the grid.

G.3 MASS CAPTURE PERFORMANCE

Engine mass capture and forebody flow spillage fractions at both test conditions are provided in Table G.1. Fractions are provided for each reference area defined in Figure 5.5. The data given in Table G.1 were used to generate Figure 5.6.

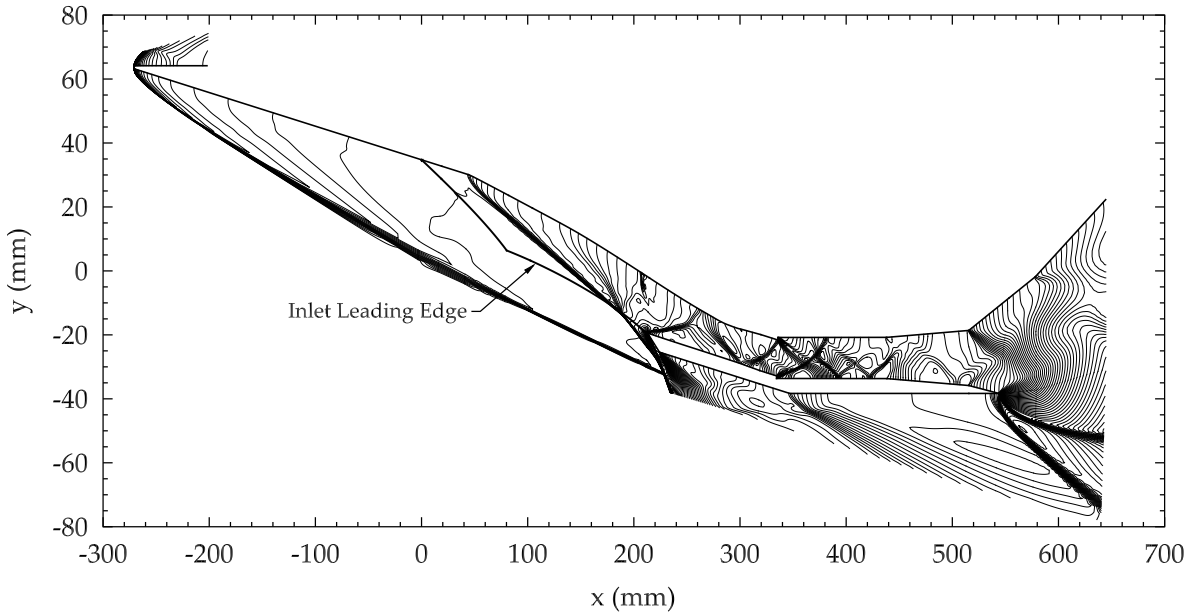

Figure G.1 – Symmetry plane pressure contours of the M12REST engine at the low pressure test condition. Contours of $\log_{10}(p)$ are plotted over the range 2 to 5.5 at intervals of 0.04. To aid visualisation the scale of the vertical axis has been increased relative to that of the horizontal axis.

G.4 ABSOLUTE ENGINE SURFACE FORCES

Absolute engine forces for each test condition are provided in Table G.2 and plotted in Figure G.2. With reference to Figure 5.9 the forces are divided into four groups of surfaces – the internal surfaces, the external surfaces, the forebody surfaces and finally, the entire engine group. For each group the contributions of the surface pressure and viscous forces are provided separately. The internal surface group can be further divided into the inlet, combustor and nozzle surface sub-groups. Force data for these sub-groups are given in Table G.3. Similarly, Table G.4 presents absolute force data for the breakdown of the external surface group into the side and lower surface sub-groups.

G.5 CUMMULATIVE SUMMATION OF INLET WALL SHEAR STRESS

Figure G.3 plots the normalised cummulative summation of inlet wetted surface area and inlet viscous drag as functions of the local axial wall shear stress for the low pressure test condition. Corresponding data for the high pressure test condition are plotted in Figure 5.12 and discussed in Section 5.5.

Table G.1 – Mass Capture and Forebody Flow Spillage

Reference Area		Low Pressure		High Pressure	
mm^2		$m_{sp,i}$	$m_{c,i}$	$m_{sp,i}$	$m_{c,i}$
A_F	5552	0.073	0.347	0.071	0.362
A_1	3308	0.122	0.582	0.119	0.607
$A_{2,HP}$	2803	n/a	n/a	0.141	0.717
$A_{2,LP}$	2780	0.146	0.692	n/a	n/a

Table G.2 – Absolute Force Data for the M12REST Engine at each Test Condition for No Fuel Injection. Data are given relative to the engine coordinate system. Force unit – N; Moment unit – N m

(a) High Pressure Test Condition

	Pressure			Viscous			Total (Pressure + Viscous)		
	F_x	F_y	M_z	F_x	F_y	M_z	F_x	F_y	M_z
Forebody	7.29	35.07	−5.76	2.44	−0.25	−0.09	9.73	34.82	−5.85
Internal	−1.34	1.62	−5.90	25.34	−0.81	0.51	24.00	0.81	−5.39
External	14.02	58.43	13.14	10.65	−0.74	−0.23	24.67	57.70	12.91
Net	19.97	95.12	1.48	38.43	−1.80	0.20	58.40	93.33	1.68

(b) Low Pressure Test Condition

	Pressure			Viscous			Total (Pressure + Viscous)		
	F_x	F_y	M_z	F_x	F_y	M_z	F_x	F_y	M_z
Forebody	4.29	20.72	−3.40	1.81	−0.18	−0.07	6.10	20.54	−3.47
Internal	−1.28	1.71	−3.20	17.00	−0.51	0.36	15.73	1.20	−2.85
External	8.04	34.09	7.74	7.78	−0.53	−0.20	15.82	33.56	7.54
Net	11.05	56.52	1.14	26.59	−1.22	0.09	37.65	55.30	1.23

(a) Drag

(b) Lift

(c) Pitching moment about the leading edge

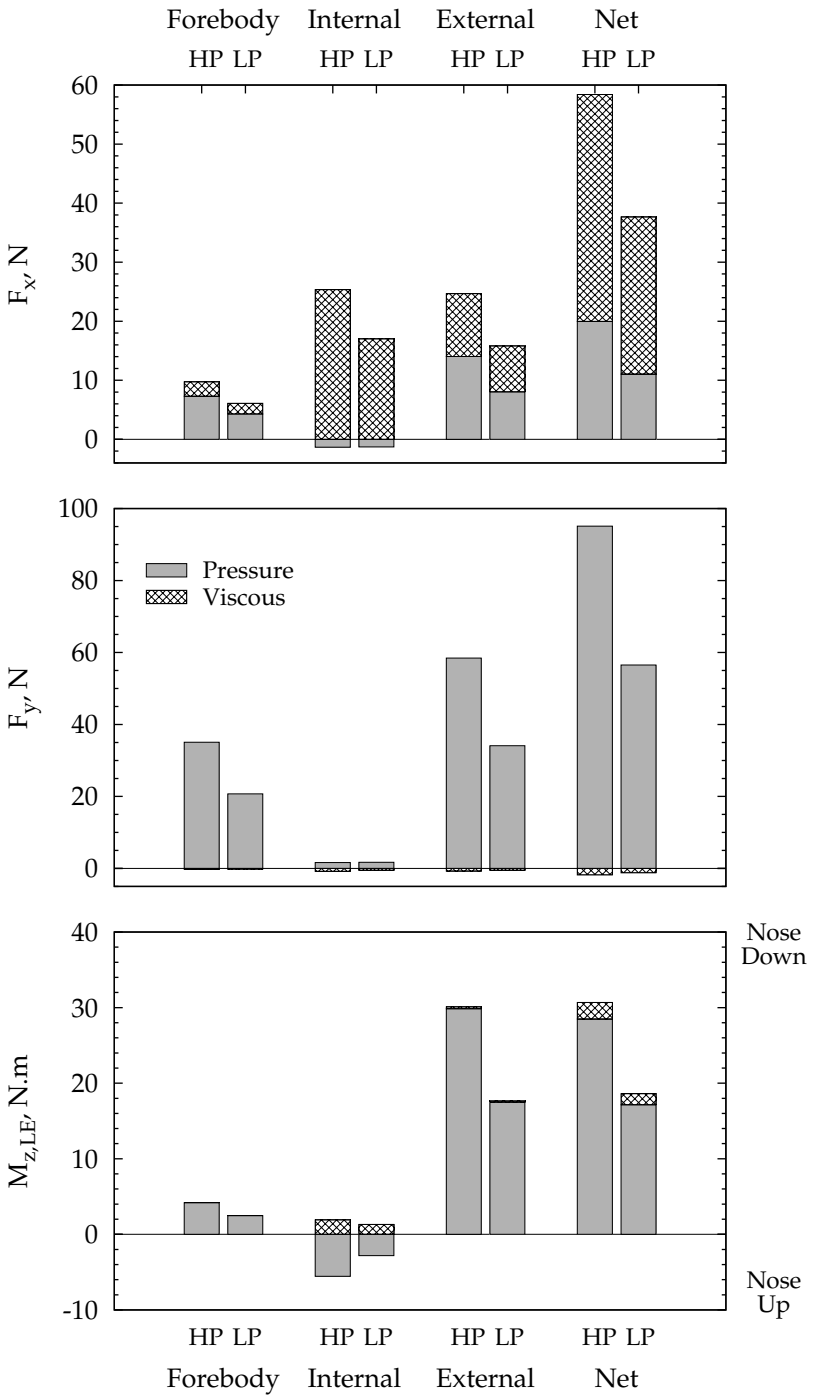

Figure G.2 – Absolute force data for the M12REST engine at each nominal test condition for no fuel injection. Each column is a cumulative bar graph of the pressure and viscous force components.

Table G.3 – Absolute Force Data for the *Internal* Engine Surfaces at each Test Condition. Data are given relative to the engine coordinate system. Force unit – N; Moment unit – N m

(a) High Pressure Test Condition

	Pressure			Viscous			Total (Pressure + Viscous)		
	F_x	F_y	M_z	F_x	F_y	M_z	F_x	F_y	M_z
Inlet	11.16	13.68	−2.19	11.93	−1.54	−0.20	23.08	12.14	−2.39
Combustor	−4.61	−9.71	−2.70	11.04	0.35	0.45	6.42	−9.36	−2.25
Nozzle	−7.88	−2.35	−1.01	2.37	0.37	0.27	−5.50	−1.98	−0.75
Internal	−1.34	1.62	−5.90	25.34	−0.81	0.51	24.00	0.81	−5.39

(b) Low Pressure Test Condition

	Pressure			Viscous			Total (Pressure + Viscous)		
	F_x	F_y	M_z	F_x	F_y	M_z	F_x	F_y	M_z
Inlet	6.68	7.94	−1.28	7.89	−1.01	−0.13	14.57	6.93	−1.41
Combustor	−2.82	−5.83	−1.90	7.43	0.22	0.29	4.61	−5.61	−1.60
Nozzle	−5.14	−0.40	−0.02	1.68	0.28	0.19	−3.45	−0.12	0.17
Internal	−1.28	1.71	−3.20	17.00	−0.51	0.36	15.73	1.20	−2.85

Table G.4 – Absolute Force Data for the *External* Engine Surfaces at each Test Condition. Data are given relative to the engine coordinate system. Force unit – N; Moment unit – N m

(a) High Pressure Test Condition

	Pressure			Viscous			Total (Pressure + Viscous)		
	F_x	F_y	M_z	F_x	F_y	M_z	F_x	F_y	M_z
Lower	14.02	58.43	13.14	5.90	−0.69	−0.04	19.92	57.75	13.10
Side	0.00	0.00	0.00	4.75	−0.05	−0.19	4.75	−0.05	−0.19
External	14.02	58.43	13.14	10.65	−0.74	−0.23	24.67	57.70	12.91

(b) Low Pressure Test Condition

	Pressure			Viscous			Total (Pressure + Viscous)		
	F_x	F_y	M_z	F_x	F_y	M_z	F_x	F_y	M_z
Lower	8.04	34.09	7.74	4.25	−0.47	−0.03	12.29	33.62	7.71
Side	0.00	0.00	0.00	3.53	−0.06	−0.17	3.53	−0.06	−0.17
External	8.04	34.09	7.74	7.78	−0.53	−0.20	15.82	33.56	7.54

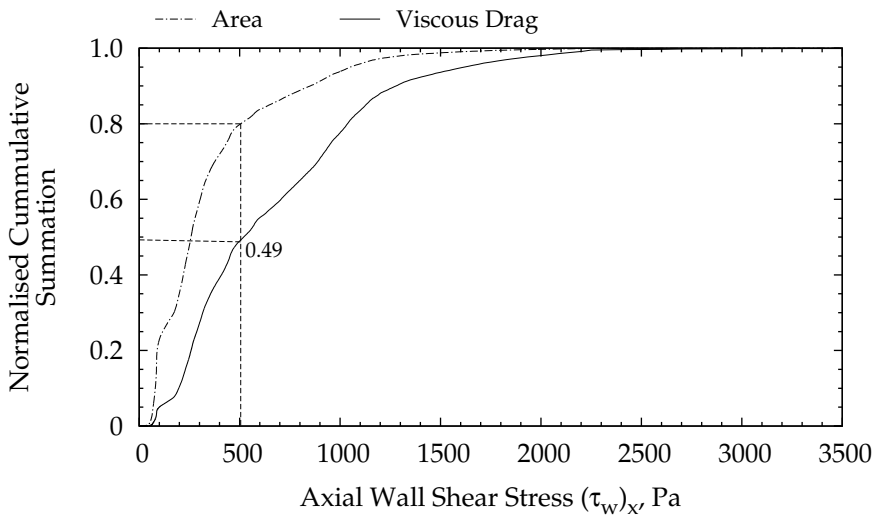

Figure G.3 – Normalised cummulative summation of inlet wetted surface area and inlet viscous drag as functions of the local axial wall shear stress at the low pressure test condition

G.6 ENGINE PRESSURES

For completeness, the absolute and normalised engine pressures at each tap location along the bodyside of the M12REST engine are listed in Table G.5. Values are given for each test condition and were calculated by averaging the numerical pressure over an interval of ± 1 mm around each nominal tap. The coordinate locations of each pressure tap are provided in Appendix E.

Table G.5 – Numerical Body Side Engine Pressures at each Tap Location. An averaging interval of ± 1 mm was used for each location.

	Low Pressure		High Pressure	
Location	p(kPa)	$p/p_{1,nom}$	p(kPa)	$p/p_{1,nom}$
P1	1.17	0.82	1.98	0.82
P2	7.70	5.40	13.40	5.52
P3	12.47	8.74	19.57	8.06
P4	28.77	20.16	42.95	17.69
P5	36.39	26.50	57.29	23.59
P6	26.71	18.71	47.55	19.58
P7	21.97	15.39	34.32	14.13
P8	26.50	18.56	40.67	16.75
P9	17.94	12.57	30.65	12.62
P10	0.91	0.64	1.13	0.46

SUPPLEMENTARY PRESSURE RESULTS

H.1 INTRODUCTION

H

This appendix presents and discusses supplementary engine pressure data that were recorded during the second test campaign. Appendix H.2 discusses the influence of forebody chines that were designed to reduce flow spillage from the forebody. Appendix H.3 discusses the influence that timing of fuel injection was found to have on the engine operation. Additional fuel-on data for the inlet injection scheme which demonstrate repeatablity of the measurements are provided in Appendix H.4. The last section of the appendix, Appendix H.5, discusses the influence of a saw-tooth boundary layer trip on the measured combustion pressures for the step and inlet injection schemes.

H.2 INFLUENCE OF FOREBODY CHINES

During the development of the airframe integrated M12REST engine, concerns were raised regarding the possible adverse influence of flow spillage from the forebody on the engine operation. In an effort to reduce flow spillage, additional pieces that attach to the sides of the forebody were designed. These pieces are known as chines. Shown fitted to the engine in Figure H.1, the width of each chine was 10 % of the engine capture width and the cross-sectional shape was inspired by the forebody of the NASA X43 flight vehicle. To help mitigate the additional frontal drag induced by fitting the chines, the rear half of the chines were designed to be symmetric with the front half. Technical drawings for the chines are provided in Doherty (2013b).

Normalised engine pressure data comparing the bodyside pressure distributions with and without the chines fitted are provided in Figure H.2 for no fuel injection at the high pressure test condition. The numerical data provided for comparison did not include the chines but did account for flow spillage from the forebody (see Chapter 5). The data do not indicate any influence of the chines at any measurement location.

H.3 INFLUENCE OF FUEL INJECTION TIMING

When conducting fuelled engine experiments within impulse facilities it is important to determine whether the timing of fuel injection has any influence on the establishment of steady flow for the particular engine

Figure H.1 – Photograph of the left-hand side forebody chine. The design was inspired by that used on the x43 flight vehicle.

and test condition under consideration. As explained in Section 3.4.5, the short test time of impulse facilities requires that the supply of fuel to the injectors be initiated prior to flow arrival at the model. Dependent on the trigger delay, early injection can result in a signficant mass of fuel being injected prior to arrival of the test flow at the model. Previous experimental and numerical studies, such as those of Kirchhartz (2010, Figure 5.22) and Rogers and Weidner (1993), have indicated that early injection of fuel does not significantly affect the establishment of steady combustion within shock tunnel facilities. This was not the case for the current configuration and test condition.

Figure H.3 presents transient normalised data for the high pressure test condition. Each row represents a different engine pressure tap. Data for the step injection scheme are given in the left hand column; data for the inlet injection scheme are given in the right hand column. Three different shots are shown for each data set: a baseline fuel-off shot, a shot for which fuel was injected early and a shot for which fuel was injected late. Corresponding fuel plenum traces are compared with a typical Pitot pressure trace in Figure H.4.

Two effects of fuel injection timing are seen in Figure H.3 depending on the injection scheme:

1. The inlet does not start;

2. An unsteady combustion mode (or false-positive).

Case 1 occurs for the inlet and combined injection schemes and is obvious and easy to detect. With reference to the right-hand column of Figure H.3, when fuel is injected early the inlet pressures oscillate significantly and

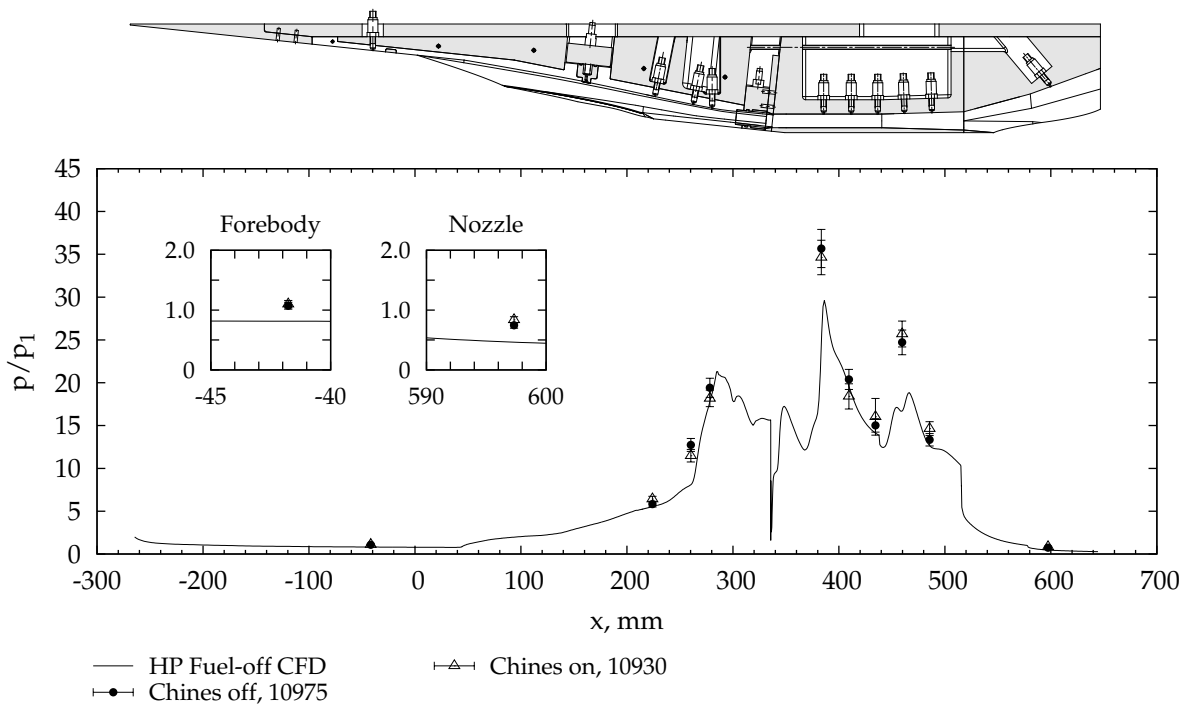

Figure H.2 – Influence of the forebody chines on the engine pressure distribution for no fuel injection at the high pressure test condition

never[1] attain a steady value. For this example shot (10950) the influence of the inlet unstart was observed at the forebody pressure tap, 40 mm upstream of the start of the inlet. Pressures within the combustor are also unsteady and comparable or lower in magnitude than the steady fuel-off values. In comparison, when the fuel is injected late relative to test flow arrival the inlet pressures attain a quasi-steady level that are elevated above the fuel-off data due to mass addition. The inlet pressures slowly increase with time because the rising fuel plenum pressure and falling nozzle supply pressure lead to increasing fuel equivalence ratio (cf. Figures 3.19 and H.4b). Steady pressures are attained within the combustor and engine nozzle, with a distinct pressure increment (relative to fuel-off) occurring at each transducer downstream of combustor tap 2, aka transducer P5.

Case 2, an unsteady combustion mode, occurs for the step injection scheme and is not as obvious as case 1. With reference to the left-hand column of Figure H.3, flow establishment within the inlet is unaffected by injection from the step regardless of the fuel timing. In the combustor, the starting shock is stronger and pressures remain elevated for longer with early fuel injection than with late fuel injection. Comparing data for shot

1 Here 'never' should be interpreted as 'not within the available flow duration'. It is entirely possible that, given sufficient test time, the starting transients would decay and the would inlet self-start.

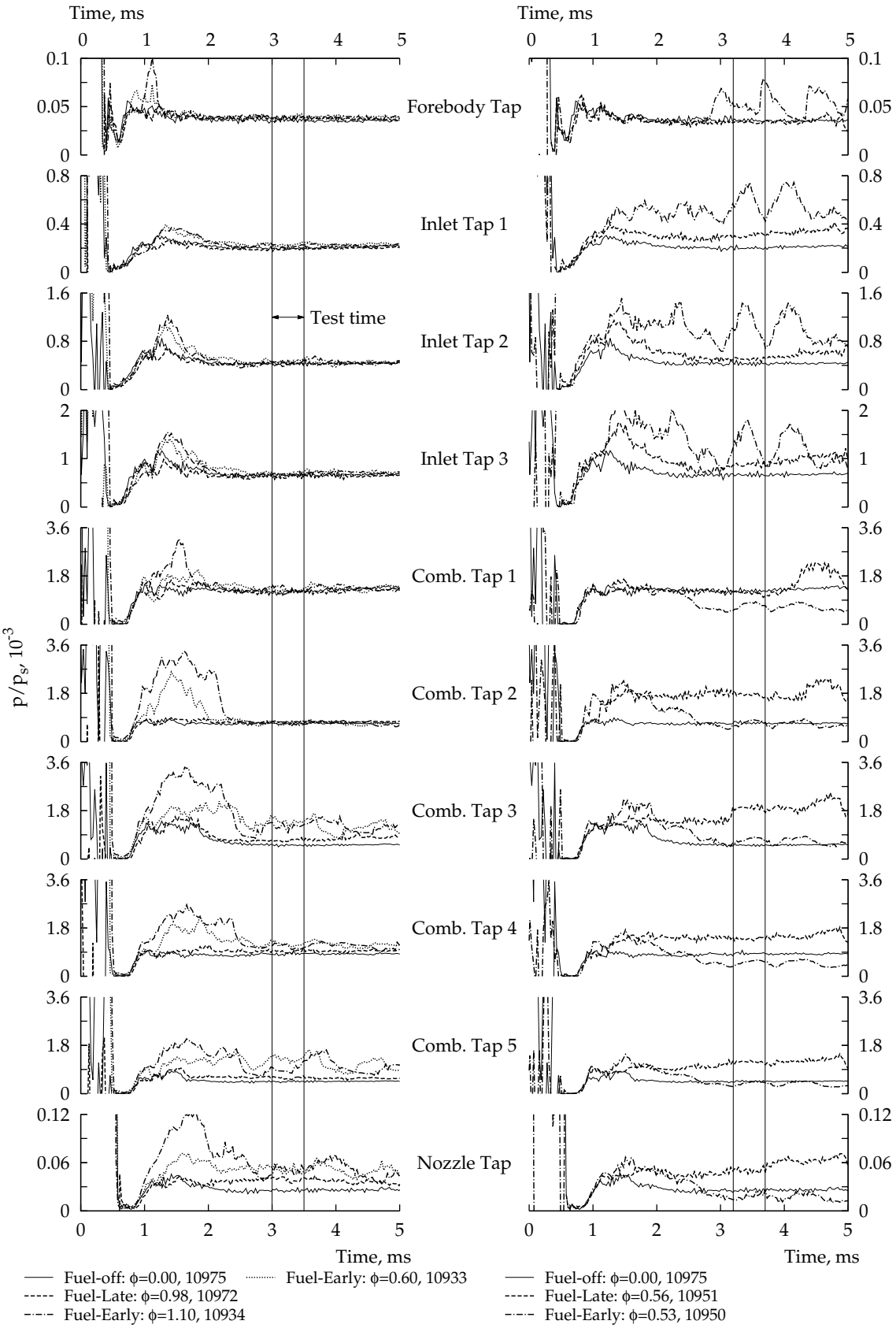

Figure H.3 – Normalised engine pressure traces examining the influence of fuel-injection timing on flow establishment. The left column is for step-only fuelling, the right column is for inlet-only fuelling. The data were filtered using a 20 μs moving average.

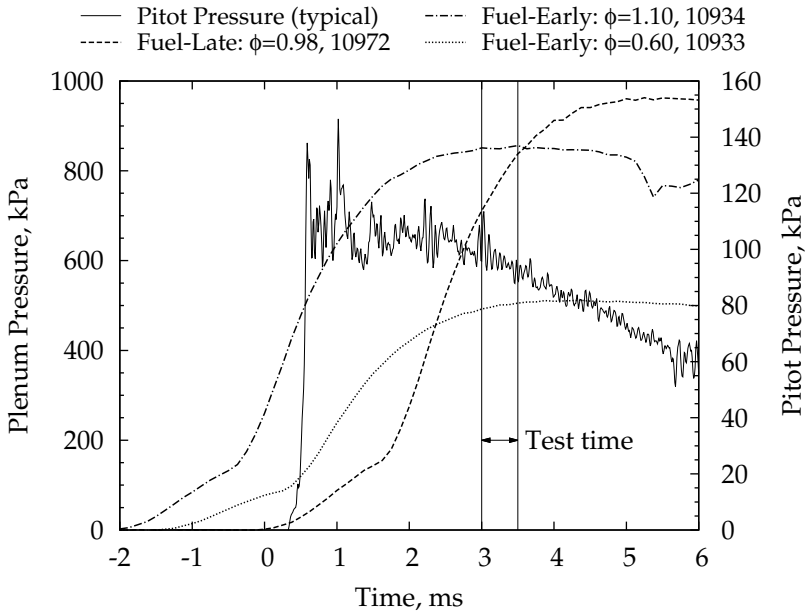

(a) Step Plenum

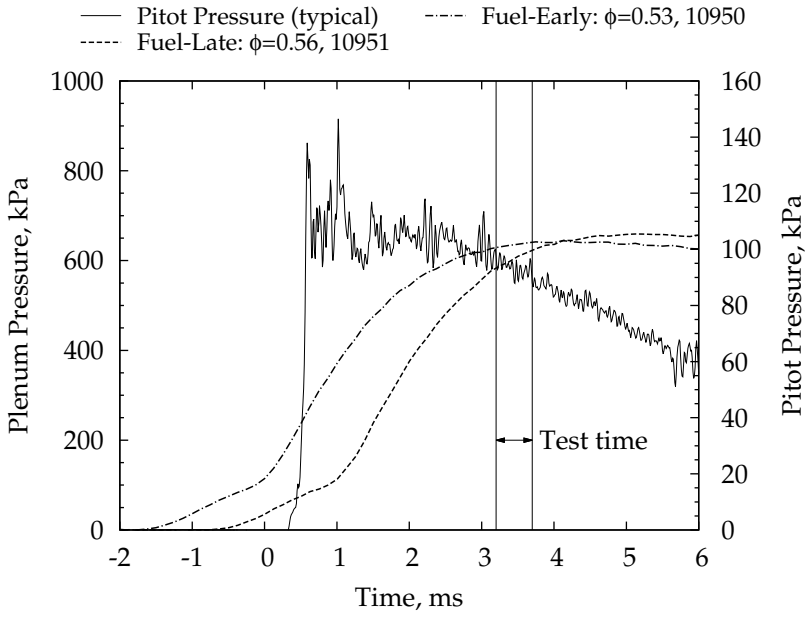

(b) Inlet Plenum

Figure H.4 – Comparison of a typical Pitot pressure trace with fuel plenum pressure traces for early and late fuel injection timing. The Pitot pressure trace was filtered using a 20 µs moving average.

10933 and shot 10934, the persistence of the starting slug of gas within the engine may be dependent on the fuel equivalence ratio. Once the unsteady expansion of the starting flow has past, the combustor pressures remain unsteady and elevated for the two early injection shots that are plotted, indicating that the occurrence of this unsteady combustion mode is independent of fuel equivalence ratio. For late injection the combustor and nozzle pressures are steady and, with the exception of the engine nozzle data, no combustion-induced pressure rise is discernable.

With respect to engine performance testing, the observed effect of fuel injection timing is an unwanted artifact of the transient test environment produced by the T4 Stalker Tube. During flight, the flow field within a scramjet engine would be established prior to initiation of fuel injection. Neither case has been observed during previous testing of either the M12REST engine or REST-based engines in general. It is currently hypothesised that the observed effects are primarily related to the low freestream static pressure of the test conditions and the small scale of the engine. Within the context of this thesis, further study of the transient starting of the M12REST engine was not possible however, improved understanding of the driving mechanisms would be useful for guiding future experiments.

A consequence of injecting fuel late relative to flow arrival at the model is that the fuel plenum pressures are rising while the Pitot pressure is decreasing, meaning that the fuel equivalence ratio is also increasing with time. The effect of this on the engine pressure data is shown in Figure H.5, in which transient absolute and normalised engine pressure data are plotted for shot 10960. Absolute pressure data are given in the left hand column; normalised data are given in the right hand column. This shot was a combined injection shot at a fuel equivalence ratio of 0.92. The fuel plenum pressures have been provided for comparison. The corresponding pressure distribution along the length of the engine is given in Figure 6.5a.

Examining Figure H.5 it can be seen that, as expected, the absolute Pitot pressure and forebody pressure signals both decrease with time. When normalised by the nozzle supply pressure these pressures are constant. The second inlet tap indicates that the inlet flow field was not established until $t \approx 2.8\,\text{ms}$. After flow establishment, the normalised inlet pressure trace plateaus before then slowly increasing for $t \geqslant 3.8\,\text{ms}$; an increase that is due to the increasing fuel equivalence ratio and eventually leads to an inlet unstart well after the test time. In comparison with the inlet pressure trace, the absolute pressure traces in the engine combustor and nozzle remain relatively constant after flow establishment. The sudden change in slope at $t \approx 4\,\text{ms}$ for the first combustor pressure tap is hypothesised to be related to the movement of the strong shock impingement location (cf. Figure 6.5a). Assuming constant combustion efficiency, plateauing of the absolute pressures in the combustor and engine nozzle suggests that the rising fuel mass flow rate was compensating for the decreasing captured air mass flow rate. When normalised by the nozzle supply pressure trace,

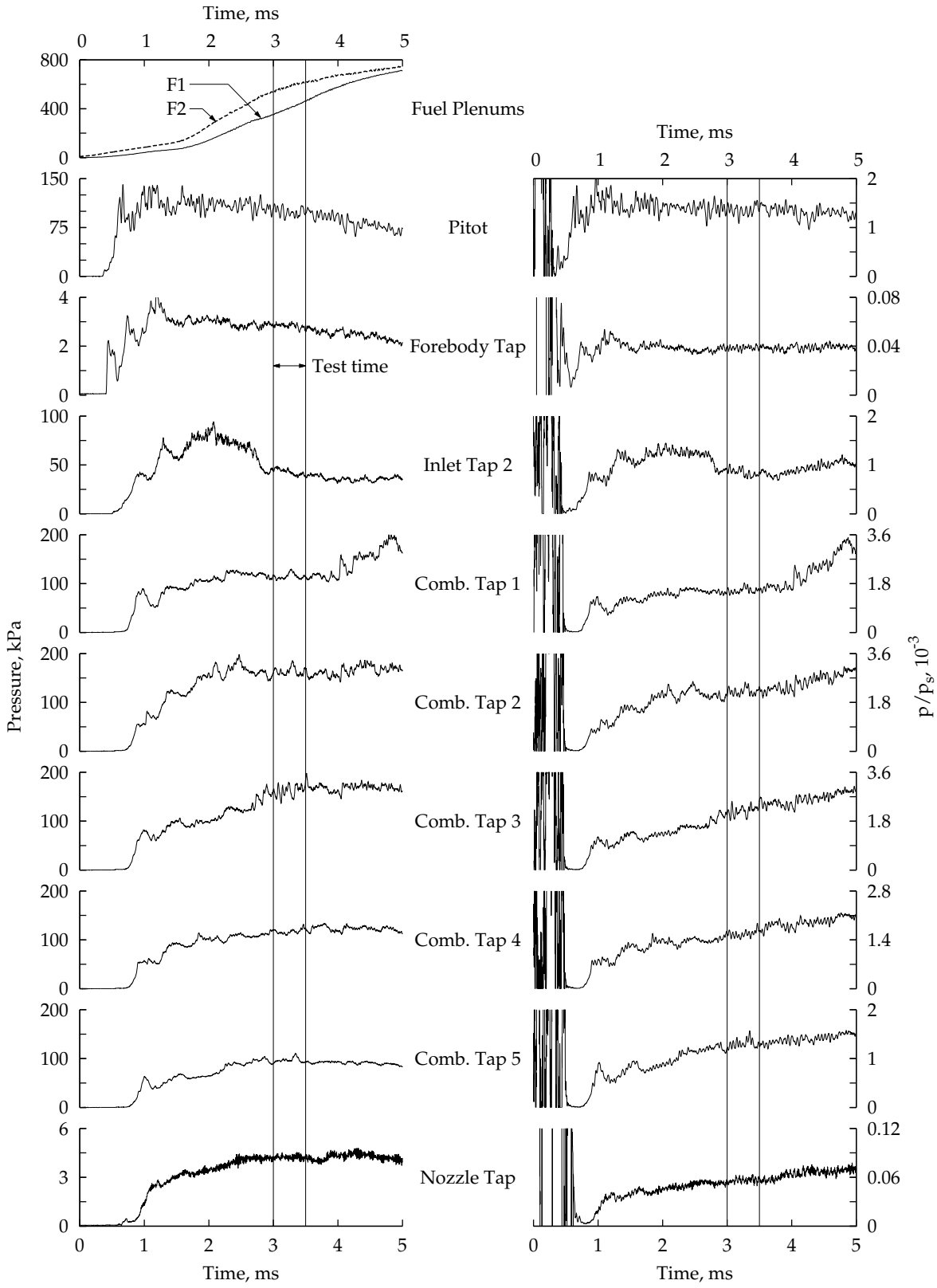

Figure H.5 – Absolute and normalised engine pressures for combined injection shot 10960. Fuel plenum pressure traces have been provided for comparison. The fuel equivalence ratio was 0.92. The data were filtered using a 20 µs moving average.

the combustor and engine nozzle pressures each increase steadily with time. The results plotted in Figure H.5 suggest that although the fuel plenum pressure rises and Pitot pressure decreases during a shot, the internal engine flow field varies in a quasi-steady way.

H.4 Repeatability of fuel-on data for inlet injection

Additional normalised engine pressure data for the inlet injection scheme are plotted in Figure H.6. The data were measured for fuel equivalence ratios close to $\phi = 0.35$ and demonstrate good repeatability at each engine measurement location.

H.5 Influence of a boundary layer trip on combustion

Section 6.2 briefly discussed the influence of a saw-tooth boundary layer trip on the measured fuel-off pressure distribution. This section presents a similar discussion for the fuel-on tests. The saw-tooth boundary layer trip is shown in Figure 3.11. Normalised engine pressure data for the step and inlet injection schemes with and with-out a boundary layer trip fitted are plotted in Figure H.7. Corresponding fuel-off data are also plotted for comparison, as is the numerical fuel-off pressure distribution. Inset figures that show enlarged views of the forebody and engine nozzle data are provided to aid interpretation. Note that the step injection data was recorded at the high pressure test condition and the inlet injection data at the low pressure test condition.

Based on the results plotted in Figure H.7a, the boundary layer trip has no significant influence on the pressure distribution for the step injection scheme. Although the fuel-on pressure at location P7 ($x = 434\,\text{mm}$) is significantly higher with the trip fitted, the pressure increment relative to fuel-off at this location is approximately independent of the presence of the trip. Since the engine nozzle pressure data (P10) are also similar for trip/no-trip tests, these results suggest that the saw-tooth trip used in this thesis has no influence on combustion for the step injection scheme.

Results for the inlet injection scheme are plotted in Figure H.7b and indicate that the presence of the boundary layer trip influences the measured combustion pressures. Relative to the fuel-off data, the pressure rise at locations P6 ($x = 409\,\text{mm}$) and P8 ($x = 460\,\text{mm}$) through to P10 ($x = 597\,\text{mm}$) is greater when the trip is fitted. The pressure increment at location P7 ($x = 434\,\text{mm}$) is unaffected by the presence of the trip. This result is surprising given that measurement P7 was the only measurement to show any influence of the trip for fuel-off tests (Figure 6.2). Within the engine nozzle the pressure increment (relative to fuel-off) was almost doubled when the trip was fitted, although a fraction of this improvement may be attributed to the higher equivalence ratio for the trip-on shot com-

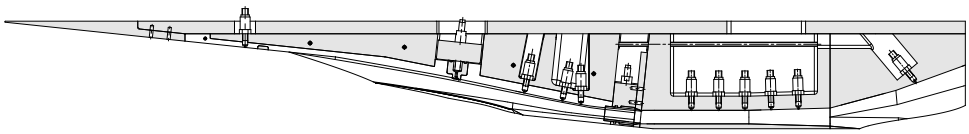

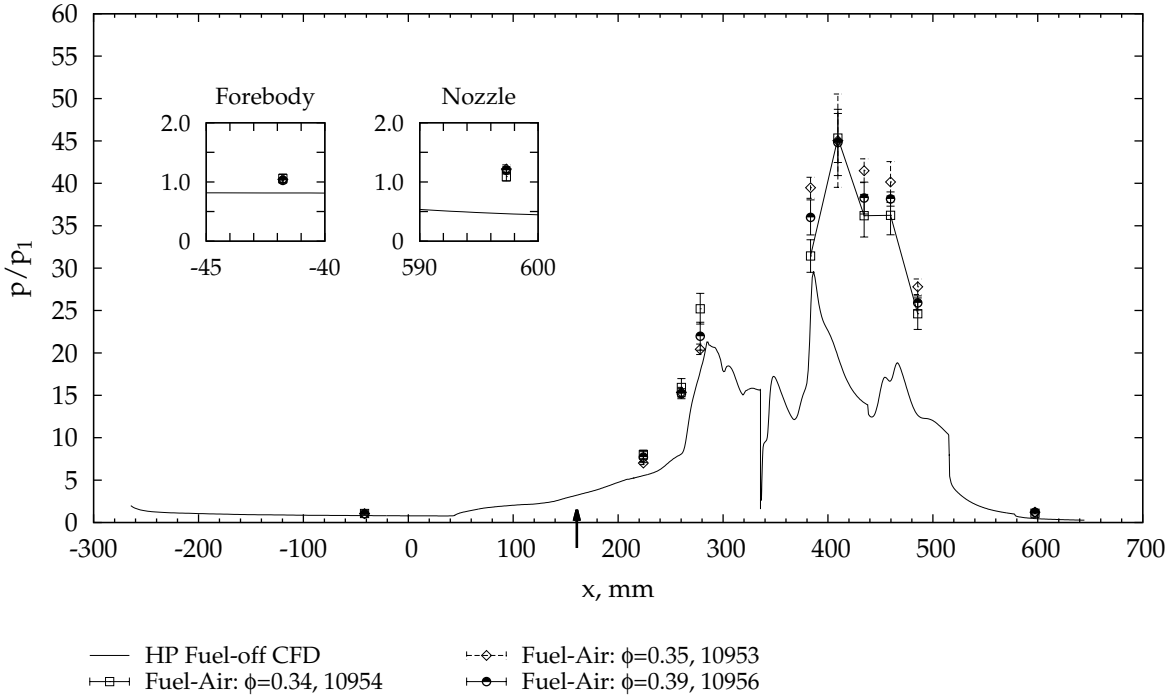

(a) High pressure condition

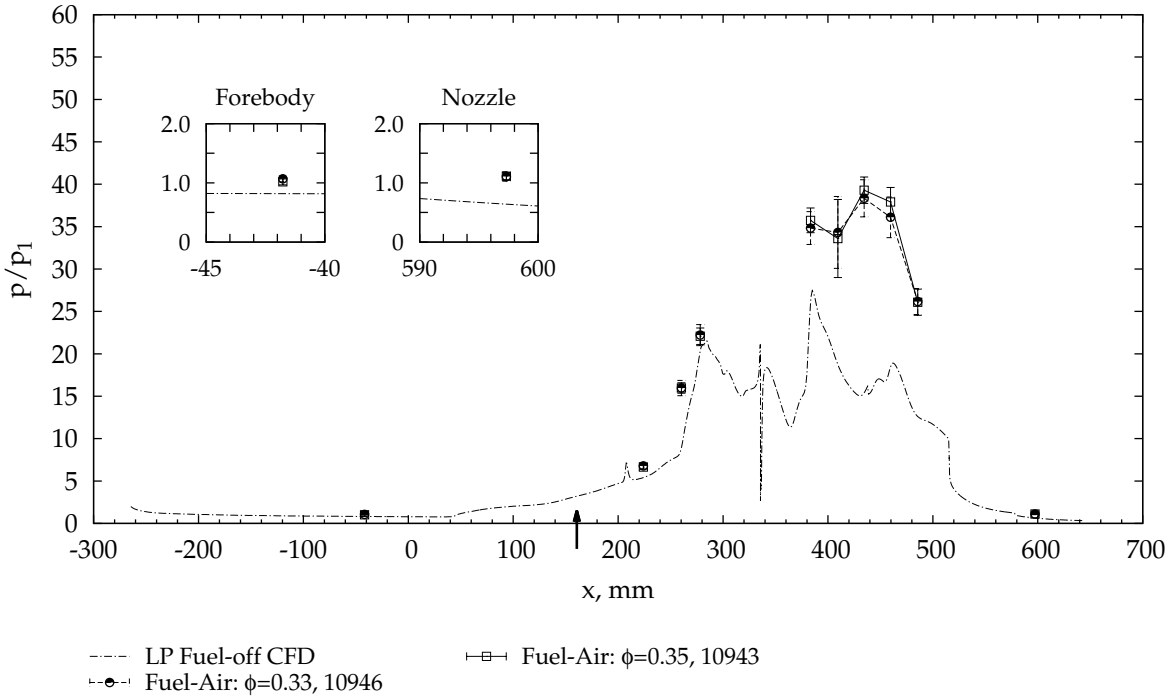

(b) Low pressure condition. Boundary layer trip fitted.

Figure H.6 – Engine bodyside pressure distribution for the inlet injection scheme. The fuel injection location is indicated by an arrow.

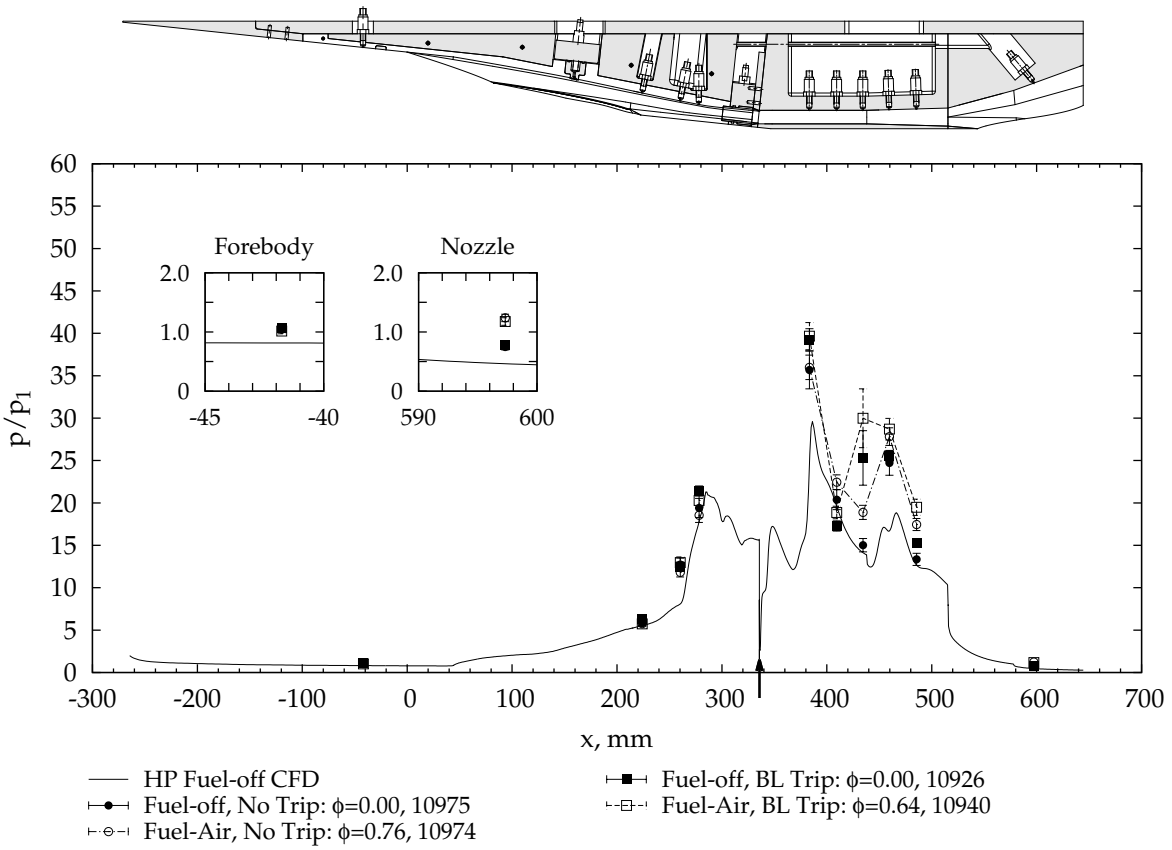

(a) Step injection scheme. High pressure test condition.

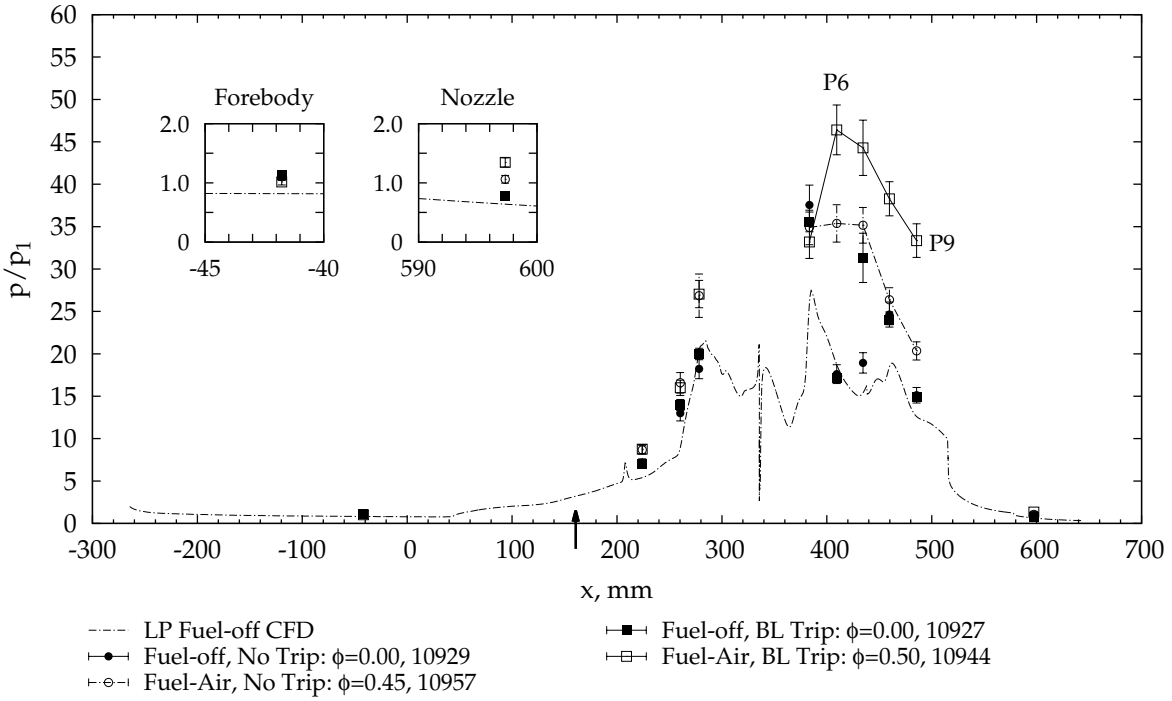

(b) Inlet injection scheme. Low pressure test condition.

Figure H.7 – Influence of the saw-tooth boundary layer trip on measured pressure distribution for fuel-on tests. The fuel injection location is indicated by an arrow.

pared with the trip-off shot. The improvement in combustion is expected to be related to alterations to the flow structure within the engine due to the shocks, expansions and vortices generated by the boundary layer trip. Detailed numerical simulations, which are considered beyond the scope of the current work, would be required to investigate this data further.

SUPPLEMENTARY FORCE BALANCE RESULTS

I

I.1 INTRODUCTION

This short appendix presents supplementary engine force data that were recorded during the first test campaign for the case of no fuel injection. Appendix I.2 presents the five force balance shielding iterations that were used. Appendix I.3 provides a summary of which GIRF were used to process each force balance shot presented in this thesis. Finally, Appendix I.4 presents engine pressure and force data for shield designs C and E at each test condition.

I.2 SHIELDING ITERATIONS

Photographs of the force balance shielding iterations used during the first experimental campaign are provided in Figure I.1. For comparison, a photograph of the streamlined shielding used during the second test campaign with a rigid tunnel mount is also provided.

The front portion of the shielding design A was not sufficiently rigid and so, during a shot, would flex downwards, touching the model and affecting the force measurement. Shielding designs B and C sought to increase the rigidity of the shielding through the addition of stiffening ribs and a strut. In order to reduce any possible interactions with the flow entering the engine, the shielding leading edge and location of the Pitot probe were also changed for shield design C. A frontal wedge was added to shield design C; the result was shield design D. The intention of adding the wedge was to reduce the influence of the shielding on the facility nozzle flow by deflecting flow around the sides of the upper shielding box. The final design iteration, shield design E, extended the wedge concept further by adding in a lower wedge. In comparison with the streamlined shielding shown in Figure I.1f, the upper half of the force balance shielding clearly created a significant blockage to the test flow.

I.3 GIRF USED FOR SHOT PROCESSING

For completeness, Table I.1 provides a summary of which GIRF were used to process each force balance shot presented in this thesis. In total four GIRF were formed from the calibration data. These were (1) the pre-campaign primary strain GIRF, (2) the post-campaign primary strain GIRF, (3) the pre-campaign secondary strain GIRF, and (4) the post-campaign

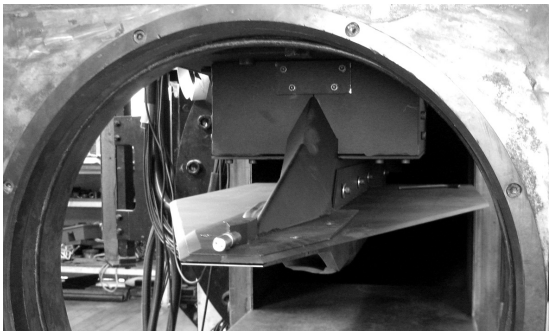

(a) Design A. Initial design.

(b) Design B. Stiffening ribs added to the 'wings'.

(c) Design C. Struts added, shielding leading edge trimmed back by 20 mm, the Pitot probe was moved back, raised and shifted off the symmetry plane.

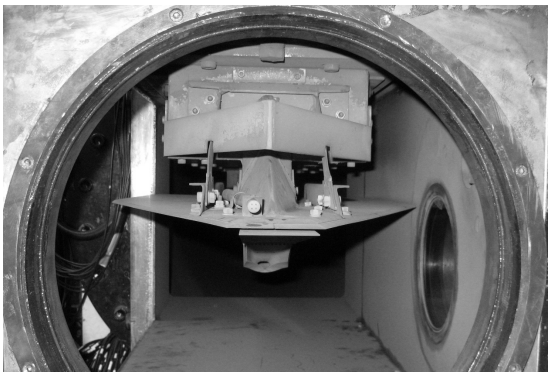

(d) Design D. Frontal wedged added.

(e) Design E. Double wedge design. The Pitot probe was placed in a similar location as for Designs C and D.

(f) Streamlined shielding used during the second test campaign with a rigid tunnel mount (see Figure 3.16).

Figure I.1 – Iterations of the force balance shielding during the first test campaign. For comparison, the streamlined shielding used during the second test campaign (with a rigid mount) is also provided.

secondary strain GIRF. Dependent on the quality of the strain signals measured during an experiment, one of three combinations of the GIRF were used to give the average transient force signals. These combinations were

1. The primary strain GIRF
2. The secondary strain GIRF
3. All four GIRF

A comparison of the uncorrected forces recovered using each GIRF is provided in Figure I.2 for shot 10761. In general, it was found that the time-history and magnitude of the forces recovered using the *pre-* and *post*-campaign GIRF (either primary or secondary) were always comparable with one another. It was also found that when both the primary and secondary strain signals were usable, the forces recovered from all four GIRF were comparable to one another. This gives confidence in the recovered forces for shots for which only the primary GIRF or only the secondary GIRF were used.

Table I.1 – Summary of which GIRF were used to Process each Force Balance Shot (1: used, 0: not used).

	Pre-campaign calibration		Post-campaign calibration	
Shot	Primary	Secondary	Primary	Secondary
10756	1	0	1	0
10761	1	1	1	1
10770	1	0	1	0
10771	1	0	1	0
10782	0	1	0	1
10787	0	1	0	1
10790	0	1	0	1
10792	0	1	0	1
10793	0	1	0	1

I.4 FUEL-OFF DATA FOR SHIELD DESIGNS C AND E

Fuel-off engine pressure data at the high pressure test condition with shield design C fitted and at the low pressure test condition with shield designs C and E fitted are provided in Figure I.3. Engine pressure data from the second test campaign have also been provided for comparision. The corresponding engine force data are plotted in Figures I.4 and I.5. The following observations can be made regarding the engine pressure and force data:

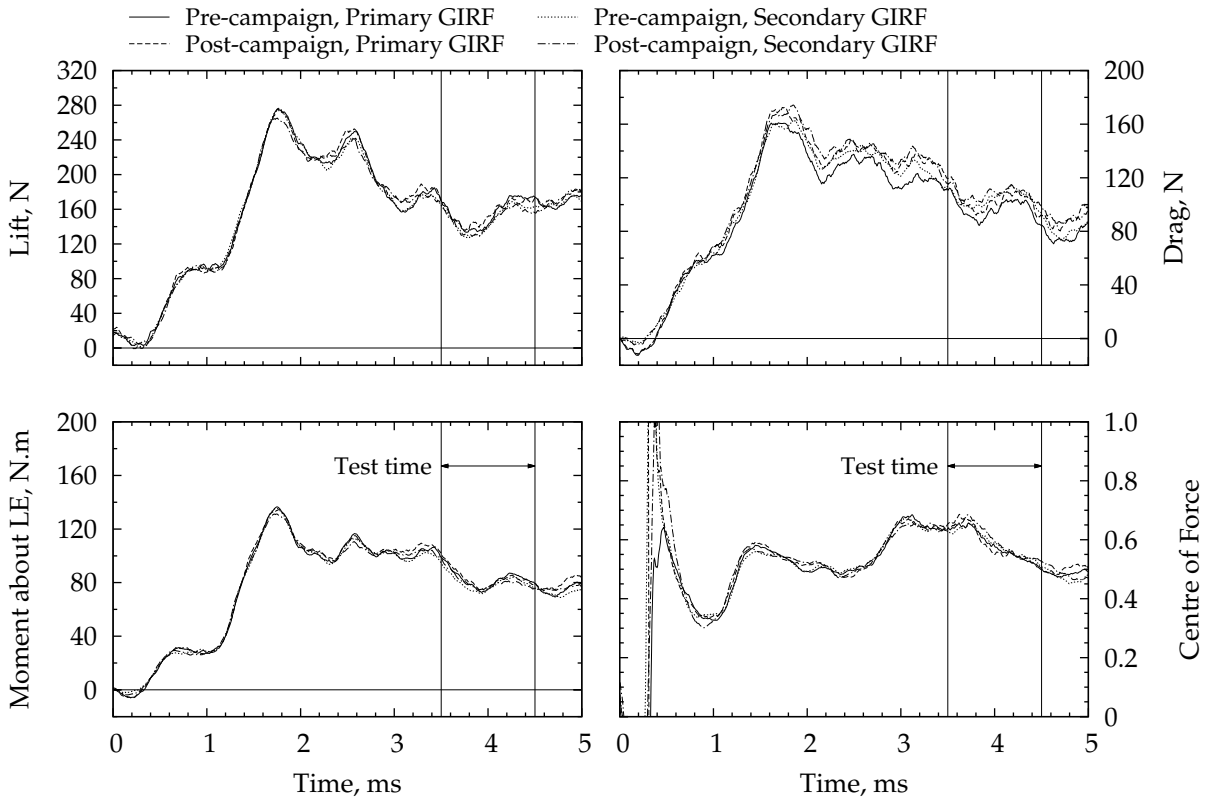

Figure I.2 – Comparison of uncorrected forces recovered using different GIRF for shot 10761 (high pressure test condition, shield design C). The data were filtered using a 500 µs moving average. The time axis has been shifted so that zero corresponds to the trigger of the nozzle supply pressure.

1. At each test condition the engine pressure data for shield design C are consistent with the numerical simulation and with the data from the second test campaign.

2. The engine forces measured with shield design C fitted are significantly different from that predicted from the numerical simulation. The recovered drag for shot 10761 is very unsteady while for shot 10756 the recovered drag does not establish until approximately 4.2 ms, significantly longer than the engine pressure data.

3. Engine pressure data for shot 10790 are not consistent with the numerical simulation or with data from the second test campaign. Within the inlet and combustor the measured pressures are significantly higher than expected. Based on the transient pressure data recorded for this shot, flow establishment within the engine was slower than expected for a fuel-off test.

4. The time-history of the recovered drag for shot 10790 with shield design E fitted is reasonable. The magnitude of the recovered drag is higher than that predicted from numerical simulation. However, the increased drag is expected based on the engine pressure data recorded for this shot.

In summary, and in the context of the data presented in Chapter 7 and Appendix K, the fuel-off data presented in Figures I.3 to I.5 demonstrate that the force balance shielding influenced the quality of the test flow and in-turn affected the quality of the engine pressure and force measurements.

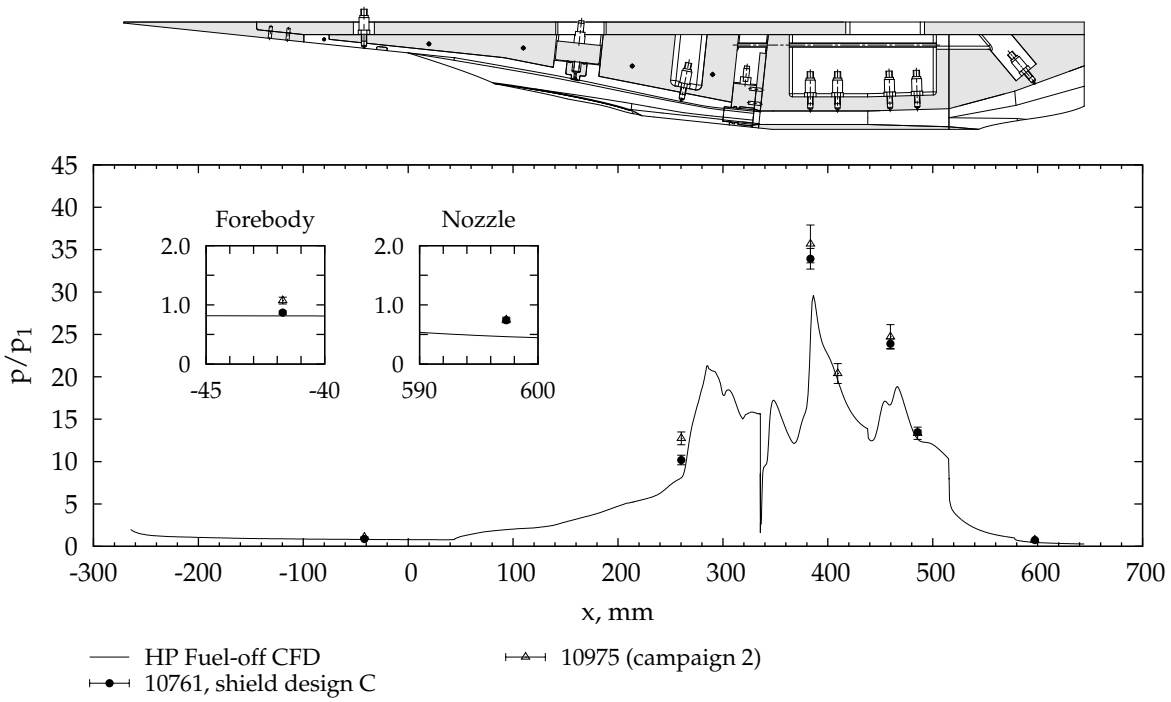

(a) High pressure condition. Shield design C. Boundary layer trip fitted.

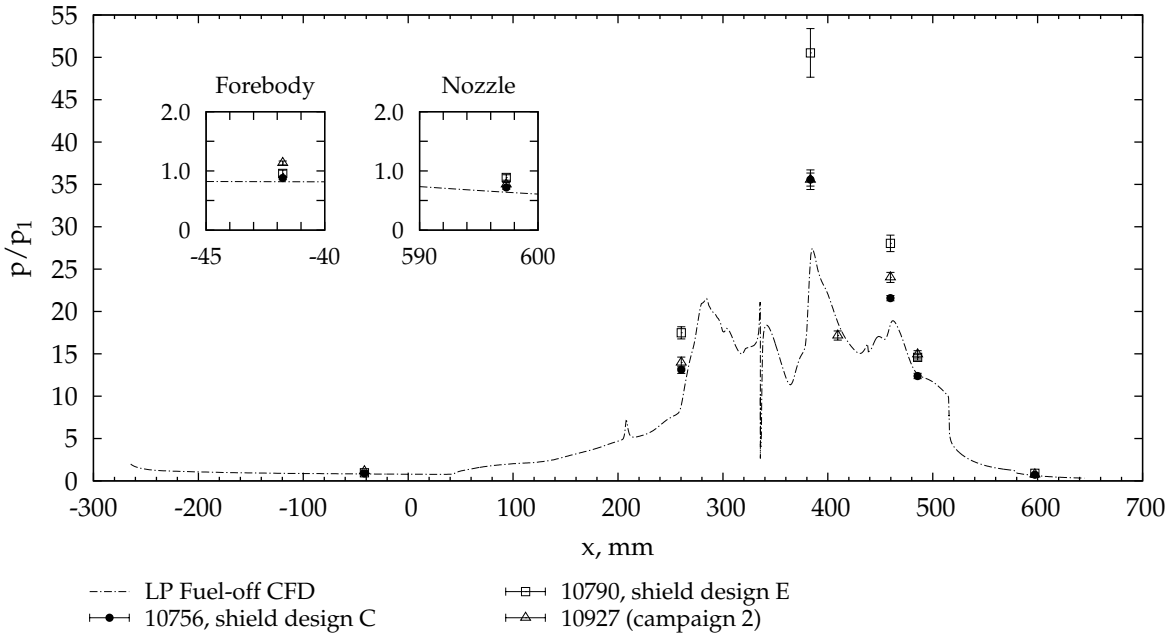

(b) Low pressure condition. Boundary layer trip fitted.

Figure I.3 – Comparison of the experimental and numerical pressure distribution on the engine bodyside for no fuel injection with shield designs C and E.

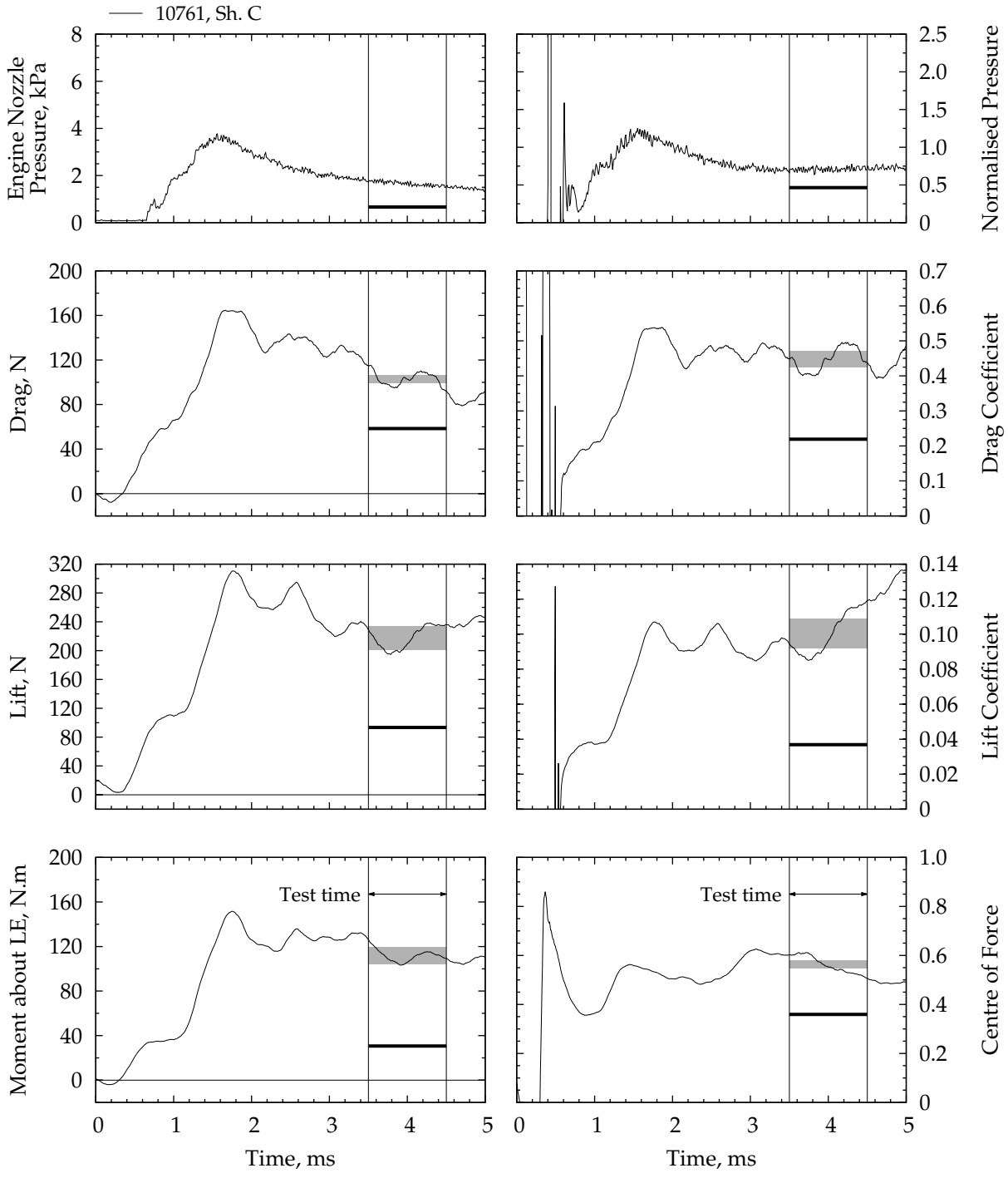

Figure I.4 – Transient fuel-off force coefficients at the high pressure test condition with shield design C. Normalised engine nozzle pressure traces have also been provided for comparison. The time axis has been shifted so that zero corresponds to the trigger of the nozzle supply pressure.

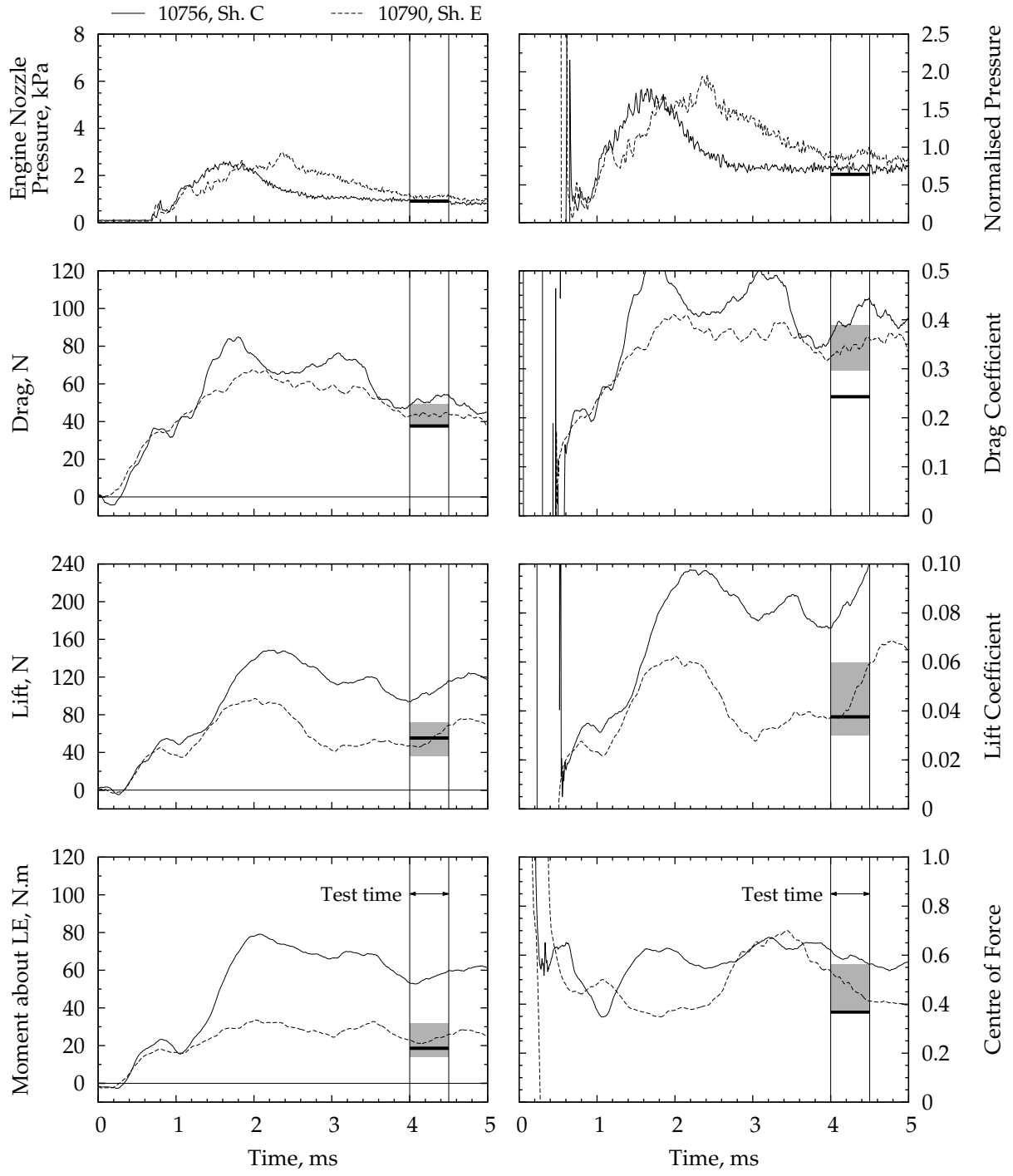

Figure I.5 – Transient fuel-off force coefficients at the low pressure test condition with shield designs C and E. Normalised engine nozzle pressure traces have also been provided for comparison. The time axis has been shifted so that zero corresponds to the trigger of the nozzle supply pressure.

STREAM THRUST AND EXERGY OF INJECTED FUEL

J

This appendix details the calculation of the fuel stream thrust and exergy. Since the fuel plenum temperature was not measured during the experiments, and cannot be extracted from the calibration data (Appendix A.4), the following analysis assumes the fuel mass flow to be fixed according to the particular shot under investigation. This permits the variation of exergy and stream thrust with plenum pressure to be examined assuming different fuel injector discharge coefficients.

J.1 STREAM THRUST

By definition the stream thrust of a fluid moving at velocity u through a duct of cross-sectional area A is

$$St = \dot{m}u + pA \tag{J.1}$$

where $\dot{m}$ is the mass flow rate and p is the static pressure of the fluid. Stream thrust is a vectorial quantity that is parallel to the fluid velocity vector. For a set of n injectors, each at an angle θ_k to the flight direction the total stream thrust is

$$St_t = \sum_{k=1}^{k=n} St_k \cos(\theta_k) \tag{J.2}$$

Assuming that each injector has the same cross-section and originates from the same plenum chamber, then Equation (J.2) can be written as

$$St_t = St_k \sum_{k=1}^{k=n} \cos(\theta_k) \tag{J.3}$$

where

$$St_k = \frac{\dot{m}}{n}u + pA_k \tag{J.4}$$

is the stream thrust contribution of each injector. In Equation (J.4) A_k is the cross-sectional area of a single injector and $\dot{m}$ is the total mass flow of fuel exiting the plenum chamber. The injector angles for the step and inlet stations of the M12REST engine are provided in Table J.1. Assuming

1. a calorically perfect gas,

2. isentropic flow, and

3. sonic injection

then the total mass flow rate $\dot{m}$ and temperature T, pressure p and velocity u at the exit of each injector are related to the plenum conditions (T_p, p_p) by

$$\dot{m} = nC_d A_k \sqrt{\frac{\gamma}{R}\left(\frac{2}{\gamma+1}\right)^{\frac{\gamma+1}{\gamma-1}}} \frac{p_p}{\sqrt{T_p}} \tag{J.5}$$

$$T = T_p\left(\frac{2}{\gamma+1}\right) \tag{J.6}$$

$$p = p_p\left(\frac{2}{\gamma+1}\right)^{\frac{\gamma}{\gamma-1}} \tag{J.7}$$

$$u = a = \sqrt{\gamma RT} \tag{J.8}$$

where C_d is the discharge coefficient of the injectors. Fixing the mass flow rate at that calculated for a particular shot, and assuming a value for the discharge coefficient allows the plenum temperature to be determined as a function of the plenum pressure. In turn the injector pressure, temperature, velocity and stream thrust also become functions of only plenum pressure. Such an analysis was completed for both an inlet injection scheme shot and a combined injection scheme shot. The results are presented below in Appendix J.3.

J.2 EXERGY

By definition[1] the exergy or available energy of a flow stream is given by

$$\begin{aligned}\psi &= (h - h_d) - T_d(s - s_d) + \frac{u^2}{2} \\ &= C_p(T - T_d) - T_d\left(C_p \ln\frac{T}{T_d} - R\ln\frac{p}{p_d}\right) + \frac{u^2}{2}\end{aligned} \tag{J.9}$$

where properties with subscript d are those of the local 'dead-state' which, for fuel injection into a scramjet engine, corresponds to the local *atmospheric* conditions and in this work are taken from Table 3.3. Using the same assumptions as in the previous section the temperature, pressure and velocity of the injected gas are given by Equations (J.6) to (J.8), respectively and, for fixed fuel mass flow and specified discharge coefficient, are functions of only the plenum pressure.

1 See Cengel and Boles (Section 7.4 of 2002)

Table J.1 – Angle of Injectors Relative to Engine Coordinate System X-Axis

Injector		Angle (°)	Notes
Step Plenum, 0.65 mm diameter injectors			
1		9	Cowlside symmetry plane
2	24	9.6	
3	23	10.9	
4	22	12.3	
5	21	13.7	
6	20	14.9	
7	19	16.1	
8	18	17.3	
9	17	18.3	
10	16	19.2	
11	15	20.1	
12	14	20.7	
13		21	Bodyside symmetry plane
Inlet Plenum, 1.30 mm diameter injectors			
1		57	
2		57	
3		57	

J.3 RESULTS

The results of the analysis outlined in the preceeding sections are provided in Figure J.1 for shot 10782 and in Figure J.2 for shot 10787. Shot 10782 was an inlet injection test at an equivalence ratio of 0.70 while shot 10787 was a combined injection test with total equivalence ratio 1.09. The engine pressure and force balance data for each of these shots are discussed in Sections 7.4 and 7.5 respectively.

The analysis of shots 10782 and 10787 was completed assuming the fuel mass flow was fixed. This methodology is useful as the fuel mass flow is dictated by the engine capture performance and required equivalence ratio, whereas the plenum conditions are able to be varied and the discharge coefficient is defined primarily by the geometry of the injectors. Consequently, in the context of designing fuel systems for high Mach number flight conditions, two important trends are established by the data plotted in Figures J.1 and J.2:

1. For a fixed discharge coefficient (i.e. injector geometry), increasing the fuel plenum pressure requires an increase in plenum temperature to maintain a fixed fuel mass flow. An increased plenum temperature and pressure in turn increase the stream thrust contributed by the fuel and the fuel exergy.

2. For a fixed plenum pressure, improving the discharge coefficient requires a significant increase in plenum temperature to maintain a fixed fuel mass flow. For plenum pressures above approximately 400 kPa, the fuel exergy is strongly dependent on the discharge coefficient.

These trends suggest that in order to increase the fuel stream thrust and exergy the injectors should be designed to have a discharge coefficient close to one and that the plenum temperature and pressure should be as large as possible (subject to any mechanical and thermal constraints). The requirement of large plenum temperature is useful given the expectation that the fuel would be used or even required to actively cool the scramjet airframe during an actual flight. Furthermore, the kinetic energy of the injected fuel also increases as the plenum temperature and pressure are raised. A thermodynamic analysis by Czysz (1988), which included the contribution of the fuel, demonstrated the importance of energetic injection of the fuel and the sensitivity of thrust to changes in the flow velocity through the engine.

For the experimental data the plenum temperature was expected to be approximately equal to the temperature of the fuel in the tank prior to injection, that is around 300 K. Based on the data in Figures J.1 and J.2, for the experimental plenum pressures, a plenum temperature of 300 K requires that the discharge coefficient was in the range 0.58 to 0.71 for the inlet injectors and approximately 0.50 for the step injectors. These values are considered reasonable given the small diameter of the injector holes (0.65 mm for the step, 1.3 mm for the inlet).

Table J.2 summarises the exergy, stream thrust, specific impulse and specific thrust of the fuel for each shot[2] assuming a plenum temperature of 300 K. Comparing these results to those given in Table 7.2 for the engine, the specific impulse and specific thrust of the fuel represent 6 % of the engine values for the inlet injection scheme data and 20 % and 11 % respectively for the combined injection scheme data. These are non-negligble contributions that would increase further with larger fuel total temperature.

2 Corresponding fuel and air mass flow data may be found in Table L.4.

Table J.2 – Fuel Stream Thrust and Exergy assuming a Plenum Temperature of 300 K

	Units	Shot 10782 Inlet Inj.	Shot 10787 Inlet Inj.	Shot 10787 Step Inj.
C_d		0.71	0.58	0.50
St	N	0.89	1.13	3.84
ψ	MJ/kg	7.0	6.5	6.5
I_{sp}	s	133	148	286
T_{sp}	N s/kg	29	18	63

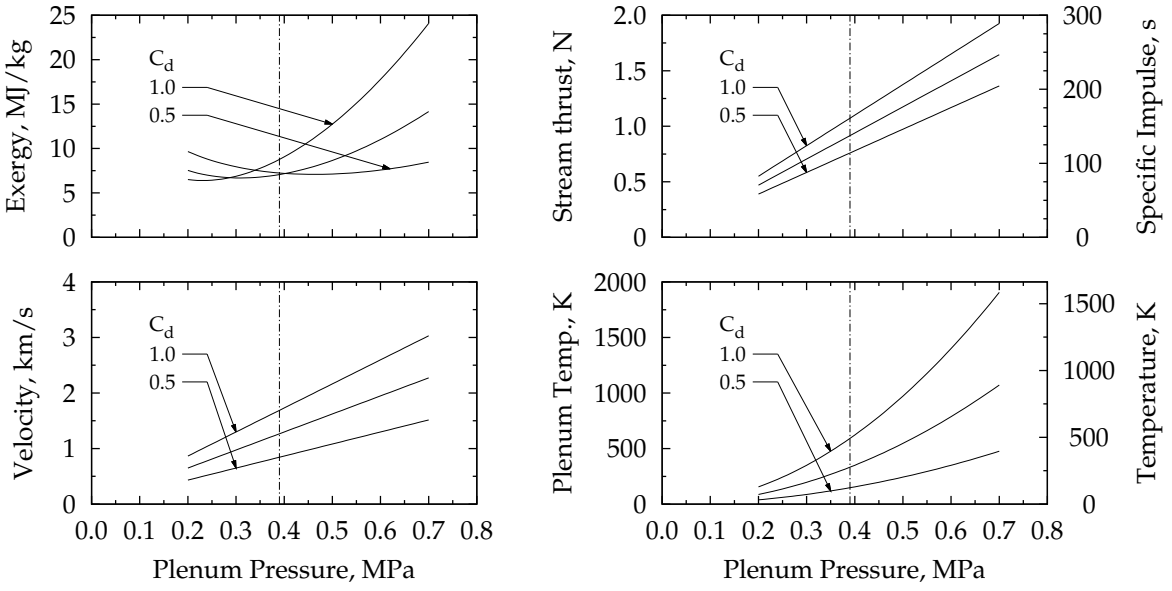

Figure J.1 – Variation of fuel stream thrust and exergy assuming a fixed mass flow of 0.68 g/s from the inlet injectors. The mass flow rate matches that of low pressure shot 10782 and corresponds to $\phi = 0.75$. Curves are shown for assumed fuel discharge coefficients in the range 0.5 to 1.0 with increments of 0.25. The experimental plenum pressure is indicated in each plot by a vertical dashed line.

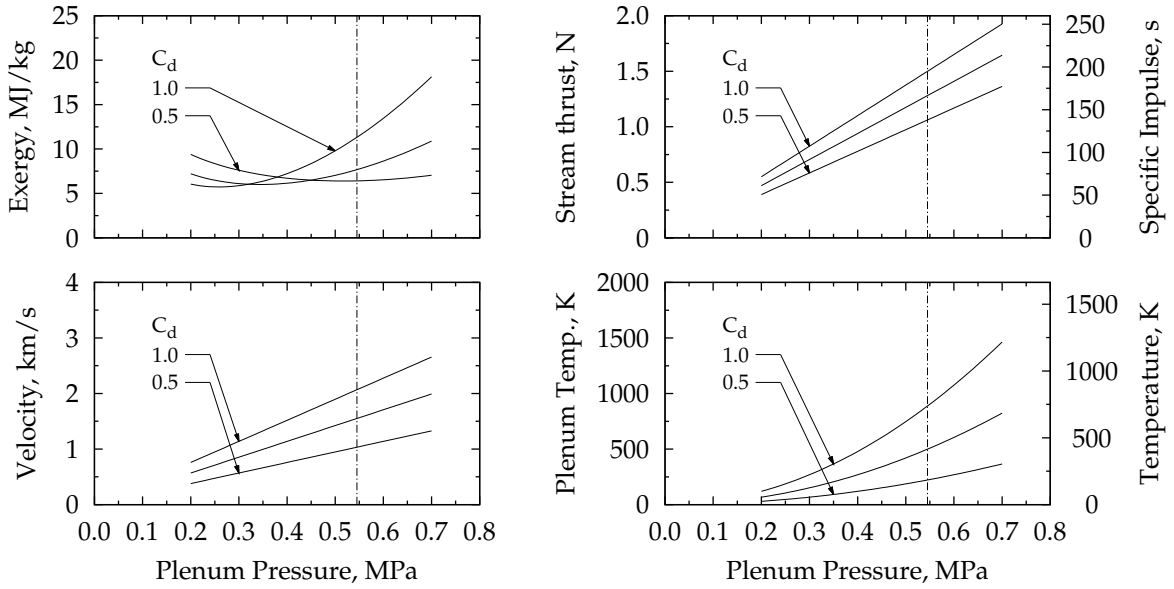

(a) Inlet injector plenum data. The fuel mass flow rate was fixed at 0.78 g/s.

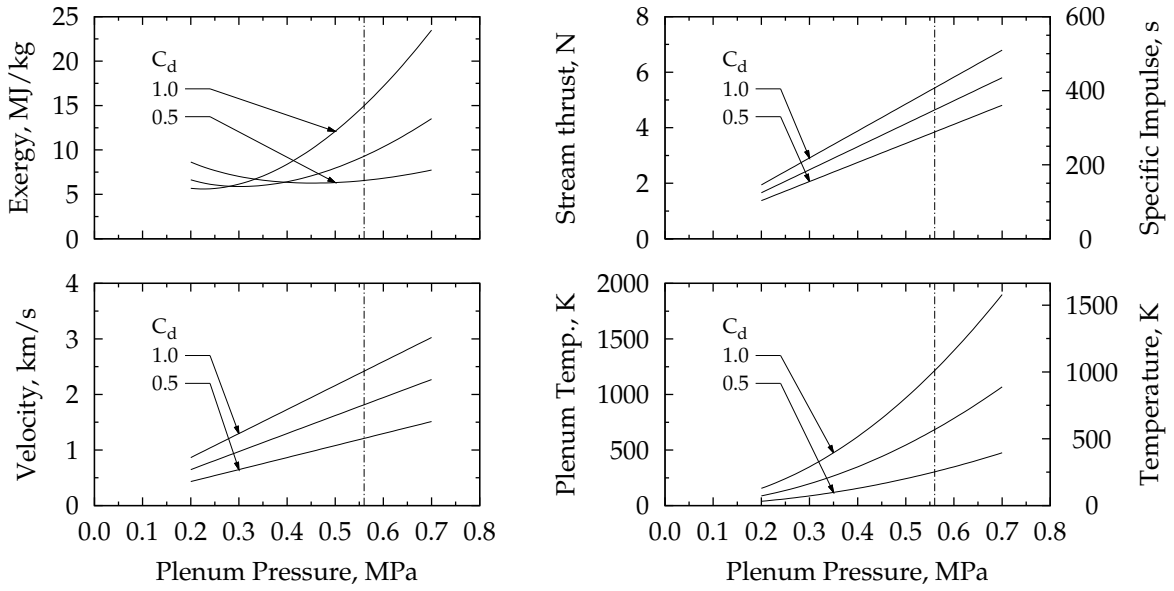

(b) Step injector plenum data. The fuel mass flow rate was fixed at 1.37 g/s.

Figure J.2 – Variation of fuel stream thrust and exergy for the combined injection scheme assuming fixed mass flow rate. The fixed mass flow rates for the inlet and step injectors match that of high pressure shot 10787 and correspond to a total fuel equivalence ratio of $\phi_t = 1.20$. Curves are shown for fuel discharge coefficients in the range 0.5 to 1.0 in increments of 0.25. The experimental plenum pressure is indicated in each plot by a vertical dashed line.

SCHLIEREN PHOTOGRAPHY

K.1 INTRODUCTION

K

During the first test campaign, in which the three-component force balance was used, the T4 Schlieren photography system was set up in an attempt to better understand the unexpected results that were being recorded. Not having planned to complete any optical diagnostics, on a short time frame and with the T4 Schlieren having been previously dismantled, the system established during campaign 1 was far from optimal (despite the help of Dr. Timothy McIntyre). Nevertheless, a picture is worth 1000 words and the, albeit low quality, images helped diagnose that the force balance shielding appeared to adversely influence the starting process of the facility nozzle. Prior to the second campaign, and with the help of Dr. Stefan Brieschenk, the Schlieren system was re-configured and the quality of the images was significantly improved. Improvement of the system has continued such that high quality schlieren images like those presented by Lorrain et al. (2012) are now possible.

The schlieren images shown in Figures K.1 to K.7 of this appendix were recorded using a Shimadzu HPV-1 camera. The frame-rate was set to 64 µs with an integration time of 32 µs. The camera was triggered 1 µs after the T4 facility nozzle supply pressure transducers such that frame 1 corresponds to $t = 1$ µs. For each set of images the flow is from left to right. A schematic of the engine showing the approximate location of the viewing window is also provided. Selected frames have been annotated.

Three shots from the first test campaign and four shots from the second test campaign sare shown. For shot 10768 (Figure K.1) a wave exiting the facility nozzle can be seen[1] interacting with the model just downstream of the cowl closure point. When the model is moved downstream, as it was for shot 10769 (Figure K.2), the wave is swallowed by the inlet causing an inlet unstart. The strong unstart shock can be seen clearly in the images for shot 10769. Shown in Figure K.3, shot 10771 featured shield design D and was positioned in the nominal position relative to the nozzle exit plane (Figure 3.18). The wave interacts downstream of the inlet cowl closure location and may be weakened compared with shot 10768 which featured shield design C. Photographs of the different shielding designs are provided in Figure I.1.

For the second test campaign (Figures K.4 to K.7) the forebody and inlet shocks are visible and, with the exception of shot 10950 (Figure K.6) the

1 Due to the poor quality, the images are best viewed digitally.

inlet was started. For shot 10950 fuel was injected early from teh inlet injection station, leading to engine unstart. The strong unstart shock can clearly been seen moving upstream in the images. Further discussion of the influence of fuel injection timing is provided in Appendix H.3.

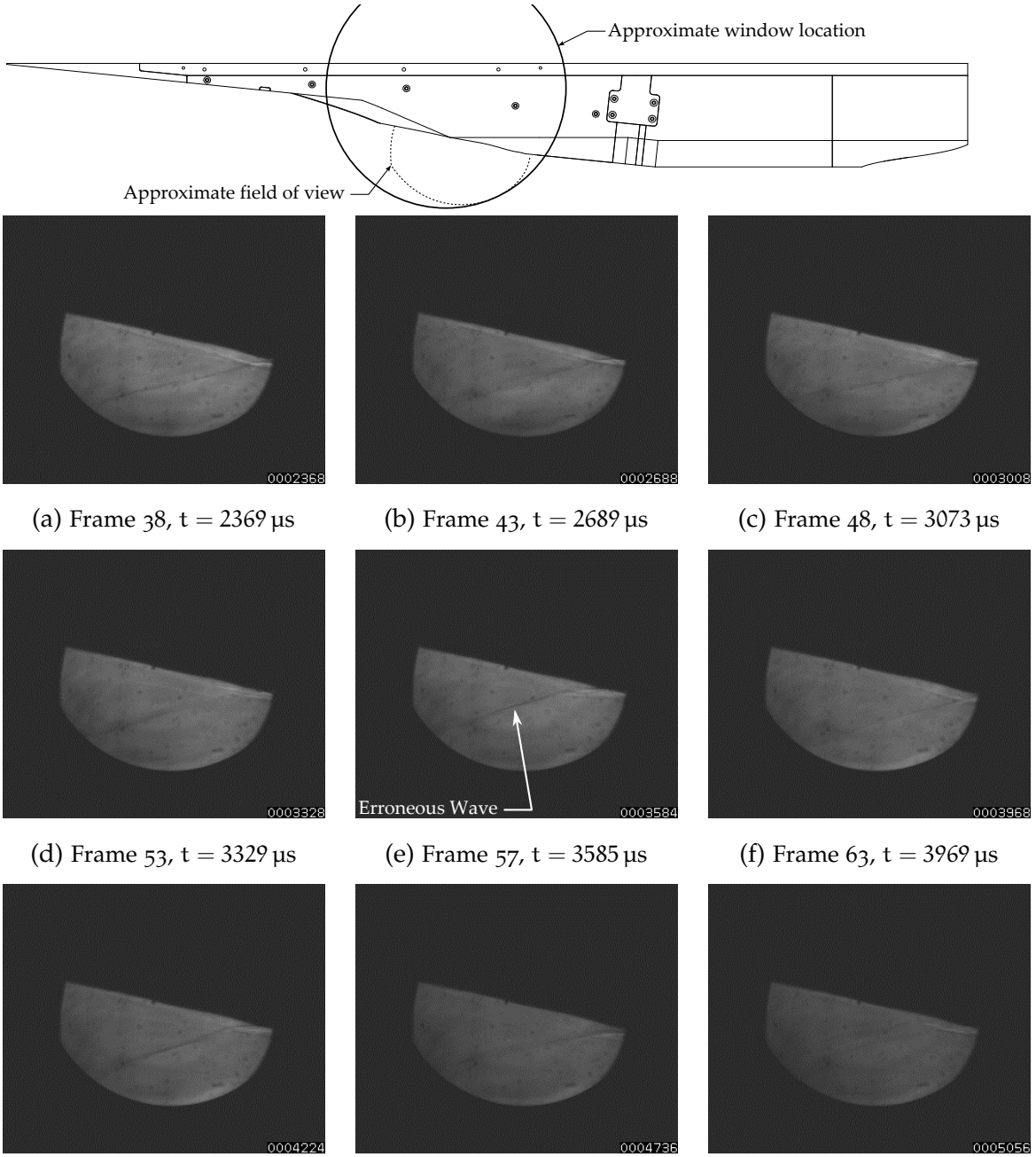

(a) Frame 38, t = 2369 µs (b) Frame 43, t = 2689 µs (c) Frame 48, t = 3073 µs

(d) Frame 53, t = 3329 µs (e) Frame 57, t = 3585 µs (f) Frame 63, t = 3969 µs

(g) Frame 67, t = 4225 µs (h) Frame 75, t = 4736 µs (i) Frame 80, t = 5057 µs

Figure K.1 – Shot 10768, campaign 1, shield design C. A wave from the facility nozzle is present and interacts with the engine.

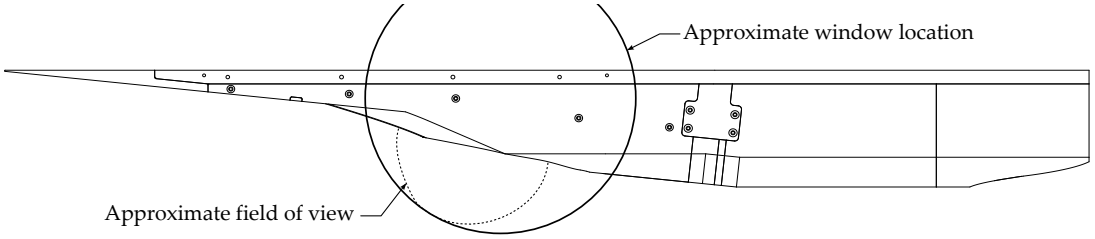

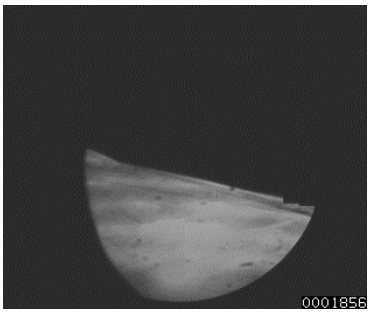

(a) Frame 30, t = 1857 µs

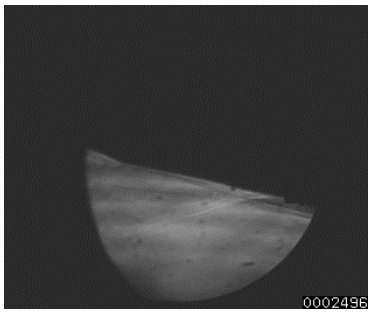

(b) Frame 40, t = 2497 µs

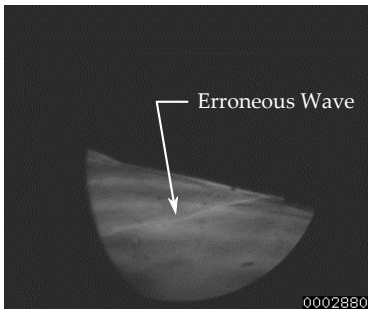

(c) Frame 46, t = 2881 µs

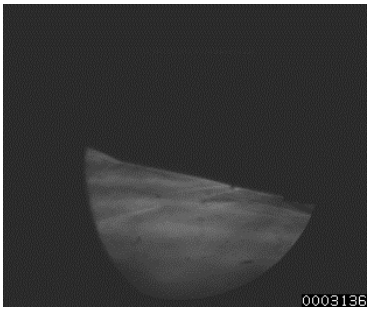

(d) Frame 50, t = 3137 µs

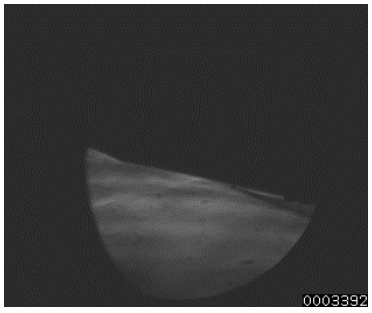

(e) Frame 54, t = 3393 µs

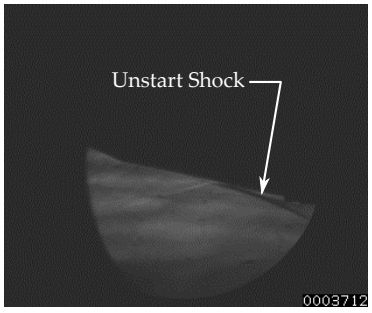

(f) Frame 59, t = 3713 µs

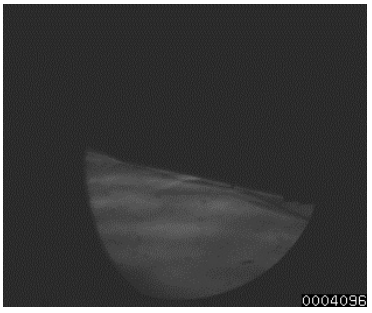

(g) Frame 65, t = 4097 µs

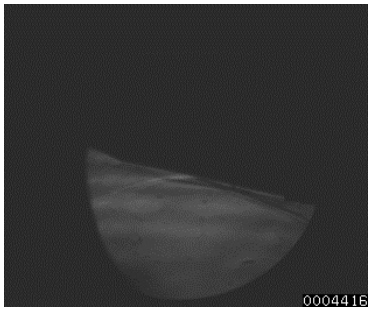

(h) Frame 70, t = 4417 µs

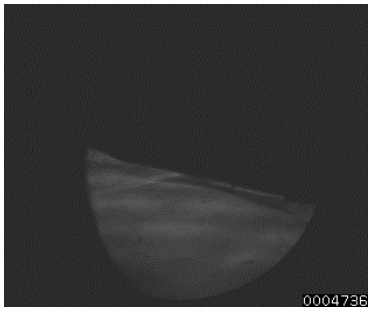

(i) Frame 75, t = 4737 µs

Figure K.2 – Shot 10769, campaign 1, shield design C. A wave from facility nozzle is present and causes an inlet unstart. For this shot the model was positioned 73 mm downstream of the nominal position.

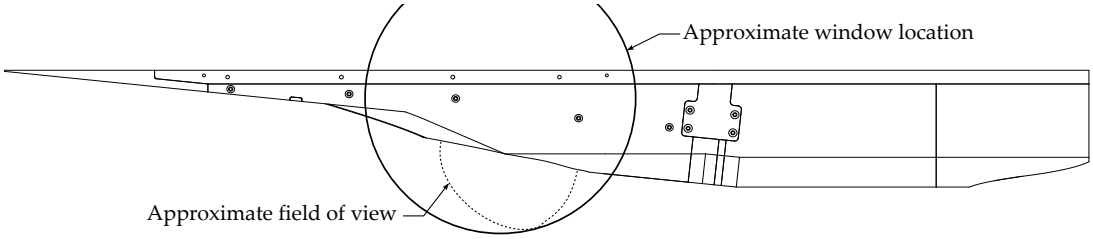

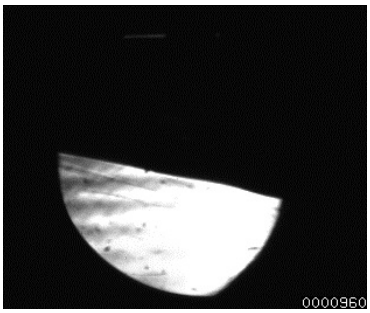

(a) Frame 16, t = 961 µs

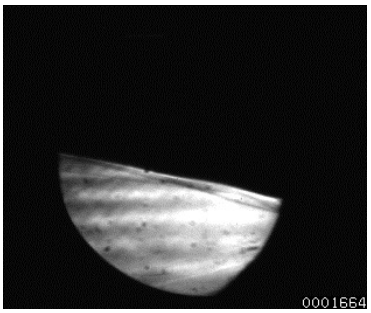

(b) Frame 27, t = 1665 µs

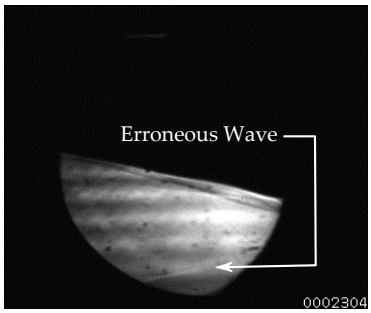

(c) Frame 37, t = 2305 µs

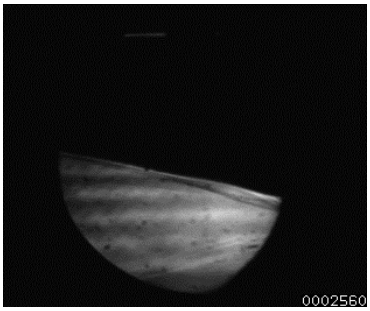

(d) Frame 41, t = 2561 µs

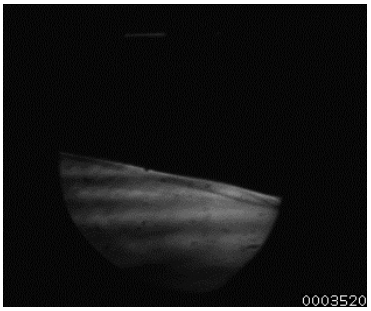

(e) Frame 56, t = 3521 µs. Approximate start of test time.

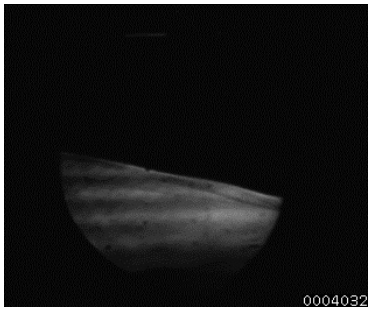

(f) Frame 64, t = 4033 µs

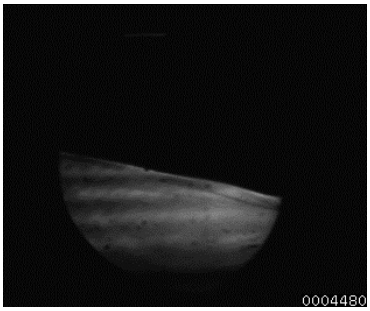

(g) Frame 71, t = 4481 µs. Approximate end of test time.

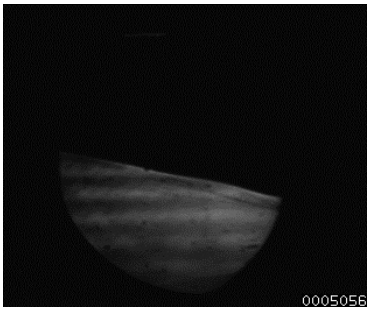

(h) Frame 80, t = 5057 µs

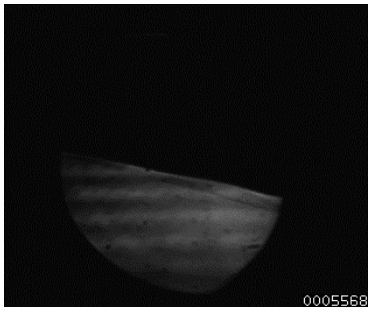

(i) Frame 88, t = 5569 µs

Figure K.3 – Shot 10771, campaign 1, shield design D. No fuel injection. A wave from the facility nozzle is present and interacts with engine downstream of cowl closure location.

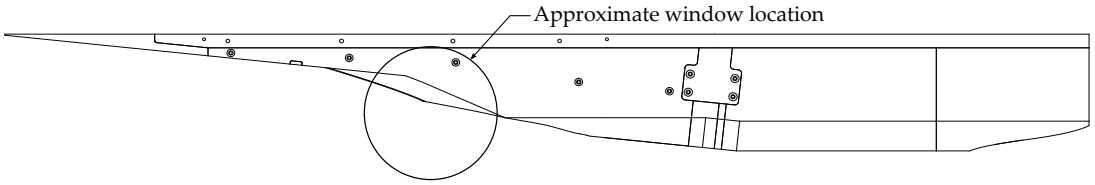

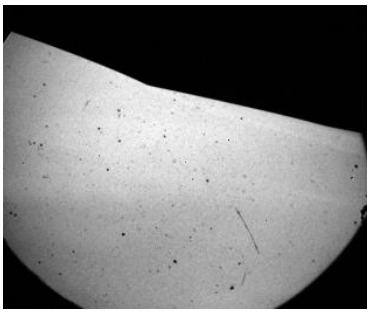

(a) Frame 16, t = 961 µs

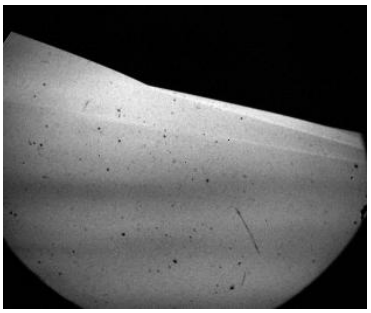

(b) Frame 26, t = 1061 µs

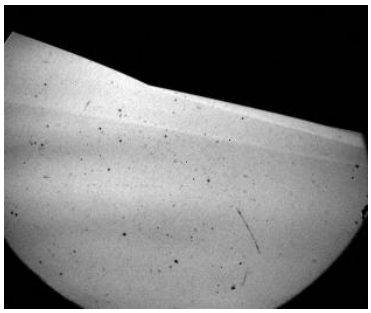

(c) Frame 38, t = 2369 µs

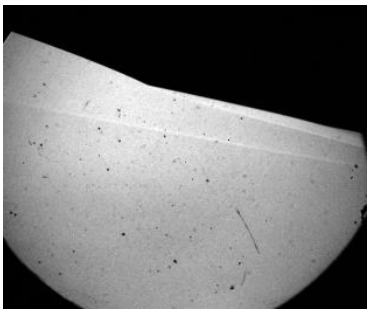

(d) Frame 48, t = 3009 µs. Start of test time.

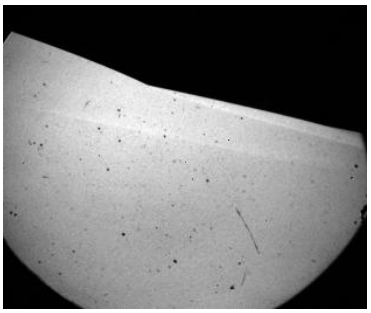

(e) Frame 52, t = 3265 µs

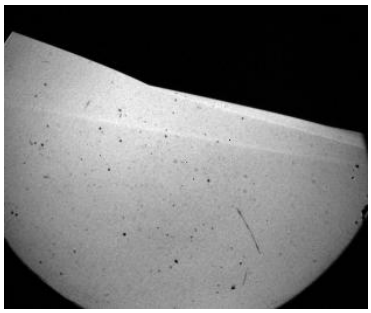

(f) Frame 56, t = 3521 µs. End of test time.

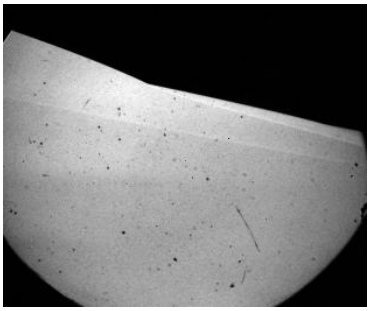

(g) Frame 66, t = 4161 µs

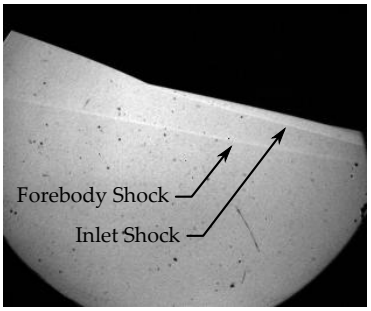

(h) Frame 76, t = 4801 µs

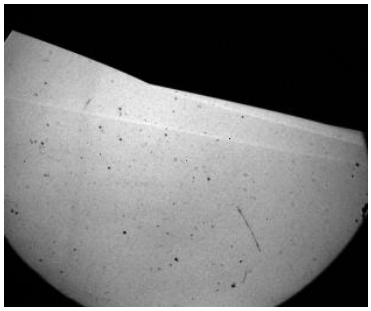

(i) Frame 86, t = 5441 µs

Figure K.4 – Shot 10929, campaign 2. No fuel injection.

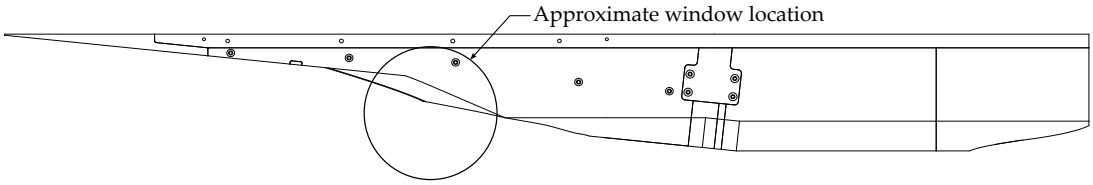

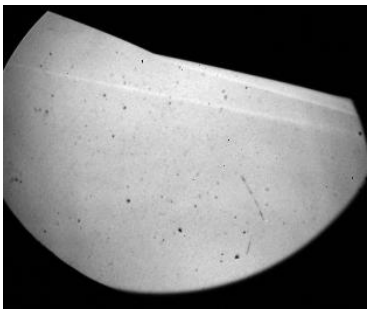

(a) Frame 16, t = 961 µs

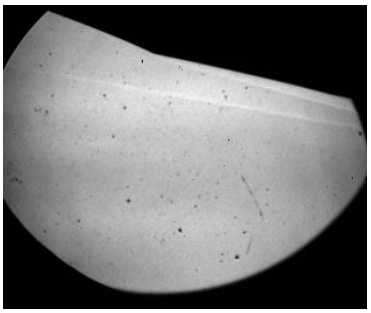

(b) Frame 26, t = 1601 µs

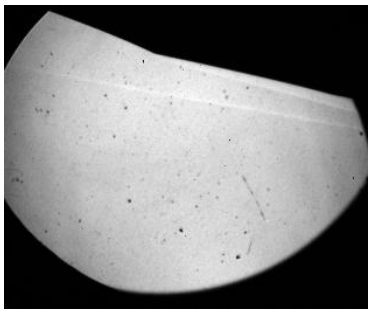

(c) Frame 38, t = 2369 µs

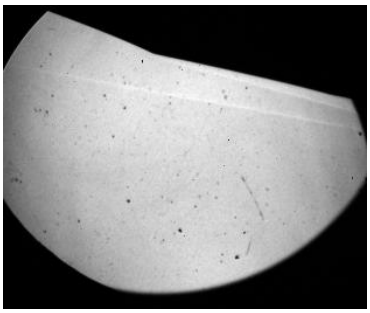

(d) Frame 51, t = 3201 µs. Start of test time.

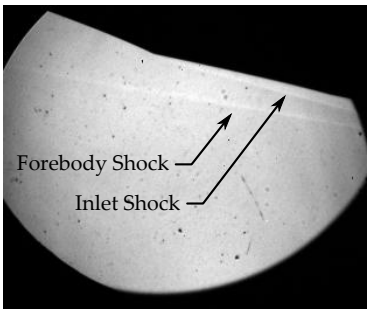

(e) Frame 55, t = 3457 µs

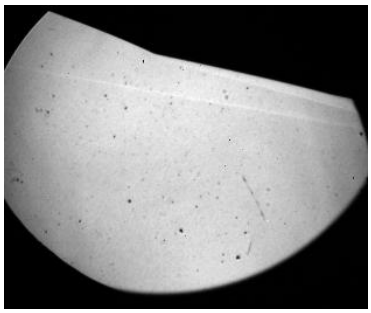

(f) Frame 59 t = 3713 µs. End of test time.

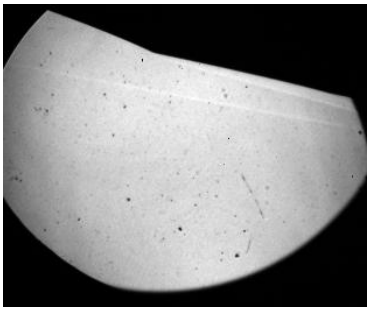

(g) Frame 66, t = 4161 µs

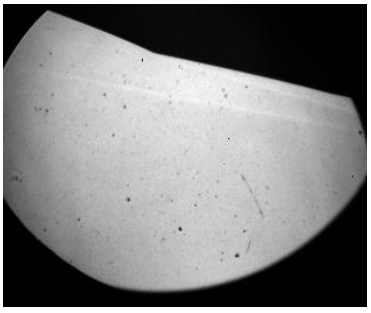

(h) Frame 76, t = 4801 µs

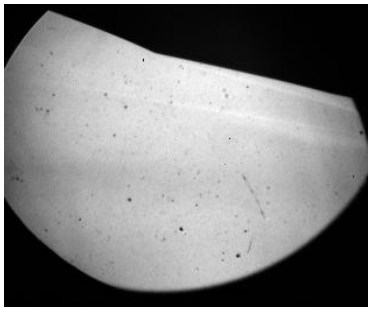

(i) Frame 86, t = 5441 µs

Figure K.5 – Shot 10951, campaign 2. Inlet injection scheme with $\phi = 0.56$. Inlet was started.

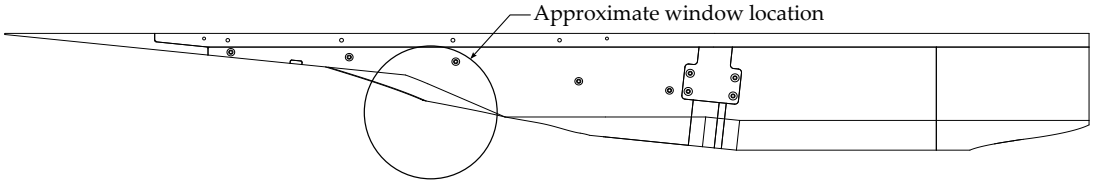

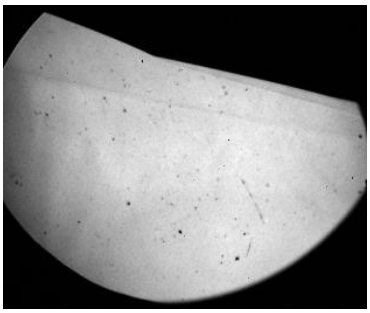

(a) Frame 16, t = 961 µs

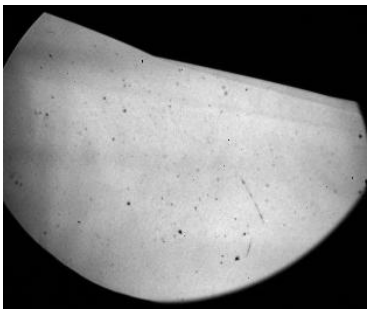

(b) Frame 26, t = 1601 µs

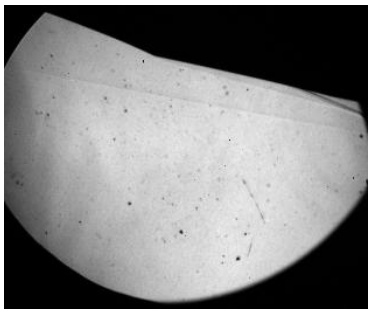

(c) Frame 35, t = 2177 µs. Unstart progressing upstream.

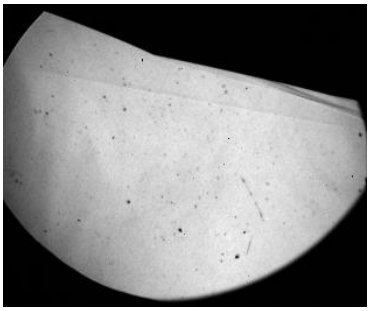

(d) Frame 37, t = 2305 µs. Unstart progressing upstream.

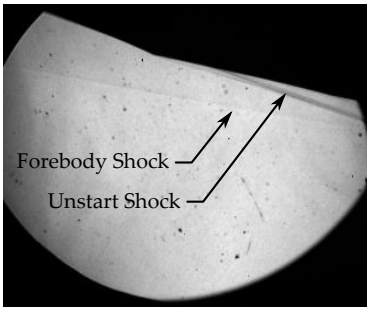

(e) Frame 39, t = 2433 µs. Unstart progressing upstream.

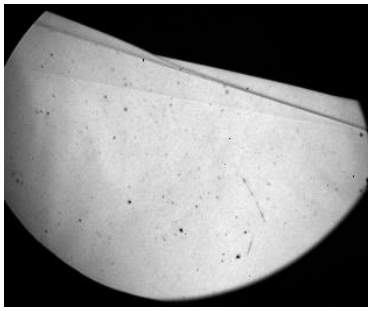

(f) Frame 41, t = 2561 µs. Unstart progressing upstream.

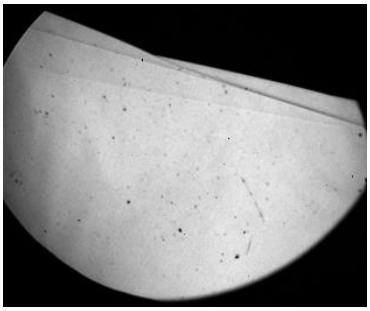

(g) Frame 46, t = 2881 µs. Unstart progressing upstream.

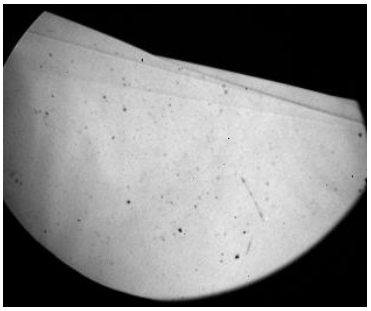

(h) Frame 50, t = 3137 µs. Approximate start of test time.

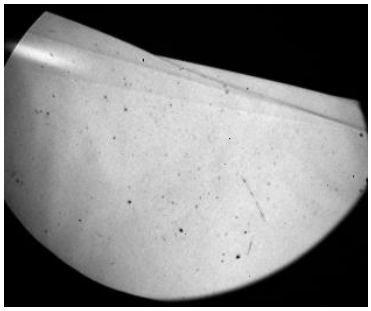

(i) Frame 58, t = 3649 µs. Approximate end of test time.

Figure K.6 – Shot 10950, campaign 2. Inlet injection with scheme with $\phi = 0.53$. Inlet was unstarted.

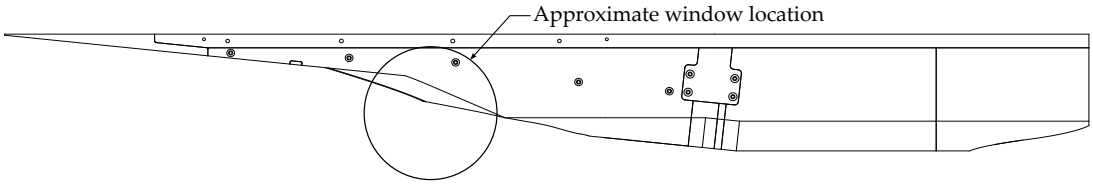

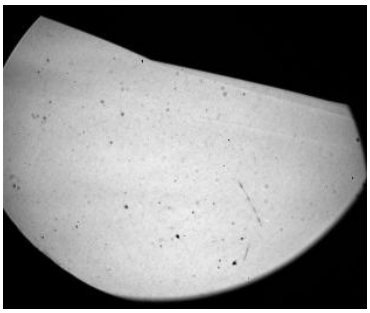

(a) Frame 16, t = 961 µs

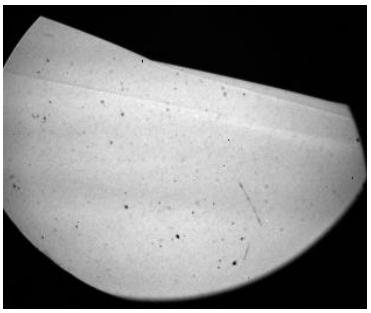

(b) Frame 26, t = 1601 µs

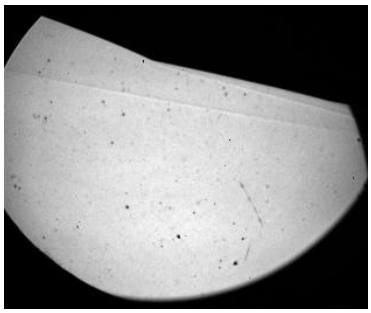

(c) Frame 38, t = 2369 µs

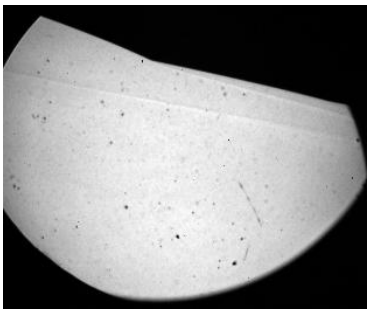

(d) Frame 47, t = 2945 µs. Start of test time.

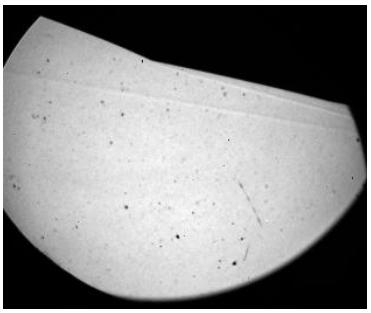

(e) Frame 51, t = 3201 µs

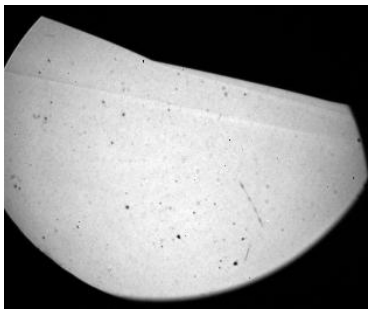

(f) Frame 55, t = 3456 µs. End of test time.

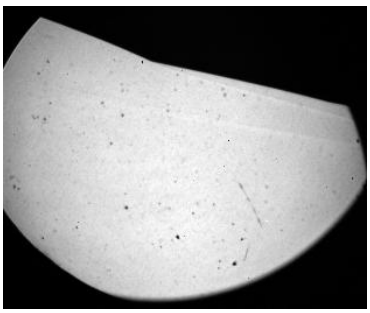

(g) Frame 66, t = 4161 µs

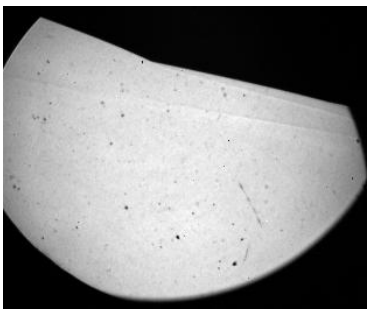

(h) Frame 76, t = 4801 µs

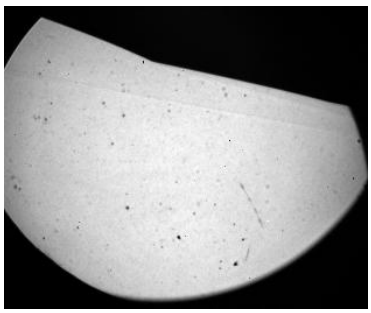

(i) Frame 86, t = 5441 µs

Figure K.7 – Shot 10960, campaign 2. Combined injection with $\phi = 0.92$.

INDIVIDUAL SHOT SUMMARIES

L

This appendix provides a set of tables which detail the operating, nozzle supply, nozzle exit, fuelling and forebody conditions for each shot conducted in the T4 Stalker Tube for this thesis. Tables defining the experimental configuration for each shot in both test campaigns are also provided. The tables contained in this appendix are as follows:

Table L.1 - Tunnel Operating and Nozzle Supply Conditions

Table L.2 - Nozzle Exit Flow Properties

Table L.3 - Nozzle Exit Composition and Turbulent Properties

Table L.4 - Fuel Flow Properties

Table L.5 - Forebody Flow Properties

Table L.6 - Campaign 1 Experimental Configuration

Table L.7 - Campaign 2 Experimental Configuration

The nozzle supply conditions listed in Table L.1 were calculated using ESTCj (Jacobs et al., 2011) as described in Section 3.3. The nozzle exit flow properties and species mass fractions listed in Tables L.2 and L.3 were calculated using NENZFR response surfaces as described in Section 3.3. Note that the nozzle supply temperature and enthalpy listed in Table L.2 were also calculated using NENZFR response surfaces. The forebody flow properties listed in Table L.5 were calculated from the nozzle exit flow properties (Table L.2) using oblique shock relations and assuming a fixed (frozen) composition.

The abbreviations used in Table L.1 are listed below. All other symbols may be found in the Nomenclature.

Res.	Reservior
C.T.	Compression Tube
S.T.	Shock Tube
Argon Frac.	Volume fraction of Argon gas in the compression tube. Helium was used for the remainder.
Diaph.	Primary diaphram thickness
O.R.	Over-run

Table L.1 – Tunnel Operating and Nozzle Supply Conditions for each Shot

	Res.	c.t.		s.t.							Nozzle Supply Conditions				
Shot	p_f	p_f	Argon	p_f	T_f	Test	Diaph.	Recoil	o.r.	u_{ss}	p_s	T_s	ρ_s	H_s	Pitot/p_s
-	MPa	kPa	Frac. %	kPa	K	Gas	mm	mm	mm	m/s	MPa	K	kg/m^3	MJ/kg	10^{-3}
10742	5.6	80.5	70	210	300	Air	6	−132	1	2138	40.4	3495	40.1	4.18	0.005
10743	5.6	80.5	70	210	300	Air	6	−130	1	2179	36.8	3506	36.4	4.20	−0.022
10744	6.5	80.5	70	210	300	Air	6	−131	1	2179	37.5	3518	37.0	4.22	0.844
10745	5.6	80.5	70	190	300	Air	6	−131	1	2213	36.9	3624	35.2	4.41	0.971
10746	5.6	80.5	70	190	300	Air	6	−131	1	2162	34.6	3500	34.3	4.19	1.666
10747	5.6	80.5	70	190	300	Air	6	−132	1	2196	35.8	3577	34.7	4.33	1.290
10748	5.6	80.5	70	190	300	Air	6	−131	1	2204	35.9	3592	34.6	4.35	1.266
10749	5.6	80.5	70	190	300	Air	6	−131	1	2154	34.5	3483	34.3	4.17	1.259
10750	5.6	80.5	70	190	300	Air	6	−130	1	2204	36.0	3594	34.7	4.35	1.209
10753	5.6	80.5	50	190	300	Air	6	−131	1	2331	33.7	3763	30.9	4.66	1.357
10754	5.6	80.5	50	170	300	Air	6	−131	1	2410	34.0	3965	29.5	5.04	1.165
10755	5.6	80.5	60	160	300	Air	6	−131	1	2284	35.4	3819	31.9	4.76	1.185
10756	5.6	80.5	60	160	300	Air	6	−131	1	2312	35.5	3867	31.6	4.85	1.312
10757	5.6	80.5	60	160	300	Air	6	−129	1	2312	34.4	3846	30.8	4.81	1.255
10758	5.6	80.5	60	160	300	N_2	6	−129	1	2331	34.2	4227	27.3	4.95	1.118
10761	12.0	156.0	38	250	300	Air	6	−159	1	2410	63.9	4156	52.8	5.33	1.299
10762	12.0	156.0	45	258	300	Air	6	−158	1	2221	67.8	3847	60.9	4.76	1.299
10763	5.6	80.5	60	160	300	Air	6	−130	1	2293	35.0	3827	31.5	4.78	1.394
10764	5.6	80.5	60	160	300	Air	6	−131	1	2321	35.3	3879	31.3	4.87	1.371
10765	5.6	80.5	60	160	300	Air	6	−130	1	2284	34.9	3809	31.6	4.74	1.350
10766	5.6	80.5	60	160	300	Air	6	−131	1	2196	32.6	3620	31.2	4.41	1.215
10767	5.8	80.5	60	160	300	Air	6	−131	1	2221	35.7	3720	33.2	4.58	1.162
10768	6.0	80.5	60	160	300	Air	6	−133	1	2331	38.2	3946	33.3	4.99	1.423
10769	6.0	80.5	60	160	300	Air	6	−132	1	2312	39.3	3933	34.4	4.96	1.298
10770	6.0	80.5	60	160	300	Air	6	−133	1	2340	38.7	3971	33.5	5.04	1.257

Table L.1 – continued

Shot	Res.	c.t.		s.t.			Diaph.	Recoil	o.r.	u_{ss}	Nozzle Supply Conditions				Pitot/p_s
-	p_f MPa	p_f kPa	Argon Frac. %	p_f kPa	T_f K	Test Gas	mm	mm	mm	m/s	p_s MPa	T_s K	ρ_s kg/m^3	H_s MJ/kg	10^{-3}
10771	6.0	80.5	60	160	300	Air	6	−132	1	2331	36.9	3924	32.4	4.95	1.299
10772	6.0	80.5	60	160	300	Air	6	−131	1	2275	35.8	3811	32.4	4.74	1.294
10773	5.9	80.5	60	160	300	Air	6	−132	1	2321	36.9	3908	32.5	4.92	1.267
10774	5.9	80.5	60	160	300	N_2	6	−132	1	2312	41.1	4355	31.8	5.12	1.180
10775	5.9	80.5	60	160	300	Air	6	−132	1	2284	39.9	3897	35.3	4.89	1.326
10776	5.9	80.5	60	160	300	Air	6	−132	1	2275	38.2	3852	34.1	4.82	1.305
10777	5.9	80.5	60	160	300	Air	6	−132	1	2284	35.0	3812	31.7	4.75	1.302
10778	5.9	80.5	60	160	300	Air	6	−133	1	2340	45.3	4077	38.1	5.22	1.253
10779	6.0	80.5	60	160	300	Air	6	−133	1	2321	41.3	3983	35.7	5.05	1.385
10780	6.0	80.5	60	160	300	Air	6	−134	1	2350	39.3	3997	33.7	5.09	1.505
10781	6.0	80.5	60	160	300	Air	6	−132	1	2312	40.7	3957	35.4	5.01	1.438
10782	5.9	80.5	60	160	300	Air	6	−132	1	2312	36.2	3880	32.1	4.87	1.280
10783	5.9	80.5	60	160	300	N_2	6	−132	1	2321	36.3	4259	28.7	4.99	1.192
10784	5.9	80.5	60	160	300	Air	6	−132	1	2340	36.9	3940	32.2	4.98	1.390
10785	5.9	80.5	60	160	300	Air	6	−132	1	2275	34.9	3795	31.8	4.72	1.411
10786	5.9	80.5	60	160	300	Air	6	−132	1	2302	36.1	3862	32.2	4.84	1.252
10787	12.0	156.0	45	250	300	Air	6	−161	1	2248	69.7	3932	61.1	4.91	1.411
10788	5.9	80.5	60	160	300	Air	6	−133	1	2293	40.5	3923	35.6	4.94	1.102
10789	5.9	80.5	60	160	300	Air	6	−123	1	2293	39.4	3905	34.8	4.91	1.162
10790	5.9	80.5	60	160	300	Air	6	−123	1	2302	34.0	3824	30.6	4.77	1.422
10792	12.0	156.0	45	250	300	Air	6	−150	1	2257	68.2	3934	59.9	4.91	1.306
10793	12.0	156.0	45	250	300	Air	6	−161	1	2239	70.6	3925	62.1	4.89	1.414
10794	12.0	156.0	45	250	300	Air	6	−153	0	2248	81.0	4035	69.2	5.08	1.406
10795	12.0	156.0	45	250	300	Air	6	−160	0	2239	81.3	4022	69.7	5.06	1.206
10796	12.0	156.0	45	250	300	Air	6	−156	1	2170	71.1	3809	64.6	4.69	1.327

Table L.1 – continued

Shot	Res.	c.t.		s.t.			Diaph.	Recoil	o.r.	u_{ss}	Nozzle Supply Conditions				Pitot/p_s
-	p_f MPa	p_f kPa	Argon Frac. %	p_f kPa	T_f K	Test Gas	mm	mm	mm	m/s	p_s MPa	T_s K	ρ_s kg/m^3	H_s MJ/kg	10^{-3}
10797	5.9	80.5	60	160	300	Air	6	−132	1	2312	40.5	3954	35.2	5.00	1.279
10798	5.9	80.5	60	160	300	Air	6	−131	0	2293	37.7	3875	33.5	4.86	1.185
10799	5.9	80.5	60	160	300	Air	6	−132	1	2302	41.3	3951	36.0	4.99	1.286
10925	12.0	156.0	45	250	300	Air	6	−161	14	2340	66.8	4066	56.6	5.16	1.299
10926	12.0	156.0	45	250	300	Air	6	−162	12	2162	63.8	3723	59.3	4.55	1.276
10927	5.9	80.5	60	160	300	Air	6	−136	13	2257	39.3	3840	35.2	4.79	1.395
10928	6.2	80.5	60	160	300	Air	6	−136	13	2204	34.5	3670	32.5	4.49	1.338
10929	6.5	80.5	60	160	300	Air	6	−138	13	2350	44.9	4088	37.7	5.24	1.392
10930	12.5	156.0	45	250	300	Air	6	−164	14	2221	79.2	3973	68.8	4.97	1.289
10931	12.5	156.0	45	250	300	Air	6	−162	14	2230	74.2	3943	64.9	4.92	1.332
10932	12.5	156.0	45	250	300	Air	6	−164	13	2239	74.0	3957	64.5	4.95	1.409
10933	12.5	156.0	45	250	300	Air	6	−163	14	2213	73.5	3906	65.0	4.86	1.427
10934	12.5	156.0	45	250	300	Air	6	−161	13	2239	67.1	3891	59.6	4.84	1.285
10935	12.5	156.0	45	250	300	Air	6	−162	14	2196	72.2	3863	64.6	4.78	1.369
10936	12.5	156.0	45	250	300	N_2	6	−162	14	2187	70.1	4147	57.0	4.84	1.213
10937	12.5	156.0	45	282	300	Air	6	−162	14	2179	69.5	3733	64.5	4.56	1.358
10938	6.4	80.5	60	160	300	Air	6	−136	14	2248	36.9	3785	33.6	4.69	1.373
10939	6.5	80.5	60	160	300	Air	6	−138	14	2331	42.0	4010	36.0	5.10	1.238
10940	12.5	156.0	45	250	300	Air	6	−161	14	2179	66.7	3781	61.0	4.64	1.304
10941	6.5	80.5	60	160	300	Air	6	−136	14	2312	38.9	3928	34.1	4.95	1.425
10942	6.5	80.5	60	160	300	Air	6	−137	14	2340	41.8	4023	35.7	5.13	1.404
10943	6.5	80.5	60	160	300	Air	6	−136	14	2312	41.3	3966	35.8	5.02	1.371
10944	6.5	80.5	60	160	300	Air	6	−137	14	2312	41.6	3971	36.0	5.03	1.397
10945	6.5	80.5	60	160	300	N_2	6	−138	12	2350	41.1	4444	31.1	5.24	1.245
10946	6.5	80.5	60	160	300	Air	6	−137	13	2331	41.1	3995	35.3	5.08	1.397

Table L.1 – continued

Shot	Res.	c.t.		s.t.			Diaph.	Recoil	o.r.	u_{ss}	Nozzle Supply Conditions				Pitot/p_s
-	p_f MPa	p_f kPa	Argon Frac. %	p_f kPa	T_f K	Test Gas	mm	mm	mm	m/s	p_s MPa	T_s K	ρ_s kg/m^3	H_s MJ/kg	10^{-3}
10947	6.5	80.5	60	160	300	Air	6	−137	14	2340	39.9	3992	34.4	5.07	1.375
10948	6.5	80.5	60	160	300	Air	6	−137	14	2340	42.0	4025	35.8	5.13	1.431
10949	12.5	156.0	45	250	300	Air	6	−162	12	2179	69.0	3803	62.7	4.68	1.361
10950	12.5	156.0	45	250	300	Air	6	−162	12	2170	65.7	3757	60.5	4.60	1.364
10951	12.5	156.0	45	250	300	Air	6	−156	13	2187	59.2	3718	55.1	4.54	1.316
10952	12.5	156.0	45	250	300	Air	6	−161	14	2170	63.3	3732	58.7	4.56	1.351
10953	12.5	156.0	45	250	300	Air	6	−162	14	2204	67.2	3830	60.6	4.73	1.340
10954	12.5	156.0	45	250	300	Air	6	−163	13	2221	74.1	3927	65.1	4.89	1.365
10955	12.5	156.0	45	250	300	N_2	6	−164	13	2213	74.5	4263	58.9	5.00	1.284
10956	12.5	156.0	45	250	300	Air	6	−163	13	2213	72.7	3899	64.4	4.85	1.321
10957	6.5	80.5	60	160	300	Air	6	−137	13	2321	41.5	3986	35.8	5.06	1.422
10958	12.5	156.0	45	250	300	Air	6	−162	14	2154	68.3	3753	63.0	4.59	1.473
10959	12.5	156.0	45	250	300	Air	6	−163	11	2162	75.8	3837	68.3	4.73	1.323
10960	12.5	156.0	45	250	300	Air	6	−163	13	2170	74.2	3837	66.8	4.74	1.357
10961	12.5	156.0	45	250	300	Air	6	−163	13	2170	67.1	3771	61.6	4.63	1.404
10962	12.5	156.0	45	250	300	N_2	6	−162	14	2179	70.8	4137	57.7	4.82	1.377
10963	12.5	156.0	45	250	300	Air	6	−160	14	2146	64.0	3696	60.0	4.50	1.312
10964	12.5	156.0	45	250	300	Air	6	−160	12	2154	63.4	3704	59.3	4.51	1.362
10965	12.5	156.0	45	250	300	Air	6	−163	14	2138	72.6	3765	66.7	4.61	1.200
10966	12.5	156.0	45	250	300	Air	6	−162	13	2170	75.2	3846	67.6	4.75	1.279
10967	6.5	80.5	60	160	300	Air	6	−137	13	2284	38.9	3880	34.5	4.86	1.366
10968	6.5	80.5	60	160	300	Air	6	−137	14	2293	40.5	3921	35.5	4.94	1.304
10969	6.5	80.5	60	160	300	Air	6	−138	12	2293	40.1	3916	35.2	4.93	1.257
10970	6.5	80.5	60	160	300	N_2	6	−136	14	2266	36.9	4149	30.0	4.84	0.493
10971	6.5	80.5	60	160	300	Air	6	−135	13	2221	37.5	3751	34.5	4.63	1.330

Table L.1 – continued

	Res.	c.t.		s.t.							Nozzle Supply Conditions				
Shot	p_f	p_f	Argon	p_f	T_f	Test	Diaph.	Recoil	o.r.	u_{ss}	p_s	T_s	ρ_s	H_s	Pitot/p_s
-	MPa	kPa	Frac. %	kPa	K	Gas	mm	mm	mm	m/s	MPa	K	kg/m^3	MJ/kg	10^{-3}
10972	12.5	156.0	45	250	300	Air	6	−160	14	2187	70.4	3832	63.5	4.73	1.377
10973	12.5	156.0	45	250	300	N_2	6	−163	14	2204	71.7	4207	57.4	4.92	1.168
10974	12.5	156.0	45	250	300	Air	6	−163	14	2179	73.2	3843	65.8	4.75	1.362
10975	12.5	156.0	45	250	300	Air	6	−163	14	2196	73.6	3877	65.6	4.81	1.350

Table L.2 – Nozzle Exit Flow Properties for each Shot

Shot	p	T[0]	ρ	u_x	a	M	Pitot	p_t	H_t	μ	k[0]	e[0]	T_s	H_s
-	Pa	K	g/m^3	m/s	m/s	-	kPa	MPa	MJ/kg	μs Pa	mW/(m^2 K)	kJ/kg	K	MJ/kg
10742	363.2	197.8	6.368	2950	282.5	10.45	51.2	21.0	4.47	13.3	18.5	56.8	3641	4.47
10743	334.0	199.3	5.810	2956	283.6	10.43	46.9	19.0	4.49	13.4	18.7	61.7	3650	4.49
10744	341.1	200.4	5.900	2963	284.4	10.42	47.8	19.4	4.51	13.5	18.7	64.2	3663	4.51
10745	339.0	205	5.730	2987	287.7	10.38	47.2	18.8	4.59	13.7	19.1	76.0	3710	4.59
10746	312.5	193.5	5.597	2923	279.4	10.46	44.1	18.2	4.38	13.2	18.4	47.3	3585	4.37
10747	327.1	200.6	5.651	2963	284.5	10.41	45.8	18.5	4.51	13.5	18.8	65.5	3662	4.51
10748	328.3	202.0	5.631	2970	285.5	10.40	45.9	18.4	4.54	13.6	18.9	69.1	3677	4.54
10749	310.2	192.0	5.600	2915	278.3	10.48	43.9	18.2	4.35	13.2	18.3	43.2	3568	4.35
10750	329.3	202.2	5.644	2971	285.7	10.40	46.0	18.5	4.54	13.6	18.9	69.5	3679	4.54
10753	321.0	219.9	5.053	3060	298.1	10.27	43.7	16.5	4.86	14.5	20.3	113.6	3849	4.86
10754	332.5	235.0	4.897	3132	308.2	10.16	44.3	15.9	5.12	15.3	21.5	145.4	3984	5.12
10755	332.1	214.6	5.360	3035	294.4	10.31	45.6	17.5	4.77	14.2	19.9	99.9	3802	4.76
10756	336.5	219.7	5.303	3060	297.9	10.27	45.8	17.3	4.86	14.4	20.2	111.4	3850	4.86
10757	325.0	217.7	5.170	3049	296.5	10.28	44.4	16.9	4.82	14.4	20.1	107.9	3829	4.82

Table L.2 – continued

Shot	p	T[0]	ρ	u_x	a	M	Pitot	p_t	H_t	μ	k[0]	e[0]	T_s	H_s
-	Pa	K	g/m^3	m/s	m/s	-	kPa	MPa	MJ/kg	μs Pa	$mW/(m^2\,K)$	kJ/kg	K	MJ/kg
10758	315.1	223	4.759	3172	304.4	10.42	44.2	17.6	4.95	14.2	20.6	−143.7	4227	4.95
10761	613.0	247.9	8.568	3202	316.3	10.12	81.0	28.6	5.34	16.0	22.6	138.9	4137	5.34
10762	608.8	215.0	9.817	3050	294.5	10.36	84.3	33.3	4.80	14.1	19.7	86.5	3849	4.80
10763	329.4	215.5	5.292	3039	295.0	10.30	45.1	17.3	4.78	14.2	19.9	102.4	3810	4.78
10764	335.5	221.0	5.254	3066	298.8	10.26	45.6	17.2	4.88	14.5	20.4	114.5	3862	4.88
10765	327.3	213.7	5.302	3030	293.8	10.31	44.9	17.3	4.75	14.2	19.8	98.3	3793	4.75
10766	297.2	195.6	5.266	2934	281.0	10.44	41.8	17.1	4.41	13.4	18.6	54.1	3604	4.41
10767	328.6	204.6	5.565	2984	287.4	10.38	45.7	18.2	4.59	13.7	19.1	75.6	3703	4.58
10768	365.5	227.9	5.553	3101	303.4	10.22	49.3	18.2	5.00	14.8	20.8	126.0	3929	5.00
10769	374.0	226.2	5.726	3093	302.2	10.23	50.6	18.8	4.97	14.7	20.7	121.6	3916	4.97
10770	371.9	230.6	5.584	3114	305.2	10.20	50.0	18.3	5.04	15.0	21.0	130.9	3954	5.04
10771	352.8	225.7	5.413	3090	301.9	10.23	47.7	17.7	4.96	14.7	20.7	122.7	3907	4.96
10772	335.3	213.7	5.433	3031	293.8	10.32	46.1	17.8	4.75	14.1	19.8	97.5	3794	4.75
10773	351.3	223.9	5.434	3081	300.7	10.25	47.6	17.8	4.93	14.6	20.5	118.9	3890	4.93
10774	377.3	231.7	5.487	3224	310.3	10.39	52.6	20.7	5.13	14.5	21.1	−137.0	4355	5.12
10775	376.9	222.1	5.877	3074	299.5	10.26	51.3	19.3	4.90	14.5	20.3	112.7	3880	4.90
10776	358.3	217.6	5.702	3051	296.4	10.29	49.0	18.7	4.82	14.3	20.0	104.4	3835	4.82
10777	328.7	214	5.320	3032	294.0	10.31	45.1	17.4	4.76	14.2	19.8	98.8	3795	4.75
10778	439.4	241.6	6.300	3167	312.3	10.14	58.3	20.8	5.23	15.6	21.9	144.8	4059	5.23
10779	395.8	231.4	5.925	3119	305.7	10.20	53.2	19.5	5.06	15.0	21.0	130.0	3965	5.06
10780	379.1	233.4	5.623	3127	307.1	10.18	50.8	18.4	5.09	15.1	21.2	136.0	3980	5.09
10781	388.5	228.6	5.886	3105	303.8	10.22	52.4	19.4	5.01	14.8	20.8	125.1	3940	5.01
10782	343.6	221.0	5.383	3067	298.7	10.26	46.7	17.6	4.88	14.5	20.3	113.4	3863	4.88
10783	333.0	225.0	4.983	3185	305.8	10.42	46.7	18.6	5.00	14.2	20.7	−142.1	4258	4.99
10784	353.9	227.4	5.388	3098	303.1	10.22	47.7	17.6	4.99	14.8	20.8	126.4	3923	4.99
10785	326.8	212.3	5.332	3023	292.8	10.32	45.0	17.4	4.72	14.1	19.7	94.8	3778	4.72

Table L.2 – continued

Shot -	p Pa	T[0] K	ρ g/m³	u_x m/s	a m/s	M -	Pitot kPa	p_t MPa	H_t MJ/kg	μ μs Pa	k[0] mW/(m² K)	e[0] kJ/kg	T_s K	H_s MJ/kg
10786	341.1	219.1	5.392	3057	297.4	10.28	46.5	17.6	4.85	14.4	20.2	109.3	3845	4.84
10787	632.5	221.6	9.895	3083	298.9	10.31	86.8	33.6	4.91	14.4	20.2	97.7	3913	4.91
10788	384.0	224.8	5.917	3087	301.3	10.25	52.0	19.5	4.95	14.6	20.5	117.6	3905	4.95
10789	373.2	223.0	5.796	3078	300.1	10.26	50.7	19.1	4.92	14.6	20.4	114.9	3887	4.92
10790	320.5	215.4	5.153	3038	295.0	10.30	43.9	16.8	4.78	14.3	20.0	103.0	3807	4.78
10792	620.8	221.9	9.697	3084	299.2	10.31	85.2	32.9	4.92	14.5	20.2	98.7	3915	4.92
10793	639.4	220.8	10.041	3079	298.4	10.32	87.9	34.1	4.90	14.4	20.1	96.1	3907	4.90
10794	744.1	231.9	11.128	3134	305.8	10.25	100.9	37.9	5.09	14.9	21.0	110.7	4016	5.09
10795	744.4	230.3	11.207	3127	304.8	10.26	101.1	38.2	5.06	14.8	20.8	108.4	4003	5.06
10796	628.3	208.7	10.438	3020	290.1	10.41	87.9	35.5	4.69	13.8	19.3	74.0	3791	4.69
10797	386.5	228.3	5.864	3104	303.6	10.22	52.1	19.3	5.01	14.8	20.8	124.6	3937	5.01
10798	355.7	220.1	5.596	3063	298.1	10.27	48.5	18.4	4.86	14.4	20.2	110.2	3857	4.86
10799	393.4	227.8	5.981	3102	303.3	10.23	53.1	19.7	5.00	14.8	20.8	123.1	3934	5.00
10925	626.4	236.8	9.166	3153	309.1	10.20	84.1	30.9	5.16	15.3	21.5	122.5	4047	5.16
10926	558.5	200.9	9.635	2978	284.7	10.46	78.9	32.6	4.55	13.6	18.9	59.1	3705	4.55
10927	366.8	216.2	5.878	3045	295.4	10.31	50.3	19.3	4.80	14.2	19.9	100.4	3823	4.80
10928	315.7	199.9	5.472	2958	284.1	10.41	44.2	17.9	4.50	13.5	18.8	64.6	3653	4.50
10929	437.3	243.0	6.234	3173	313.3	10.13	57.9	20.5	5.25	15.6	22.0	147.6	4070	5.25
10930	719.3	225.1	11.080	3102	301.3	10.30	98.4	37.8	4.98	14.6	20.4	101.1	3954	4.98
10931	672.3	222.4	10.482	3088	299.5	10.31	92.2	35.6	4.93	14.5	20.2	97.9	3925	4.93
10932	672.9	223.9	10.418	3095	300.5	10.30	92.1	35.4	4.96	14.5	20.4	100.5	3939	4.95
10933	661.0	218.5	10.490	3069	296.8	10.34	91.2	35.7	4.86	14.3	19.9	91.5	3888	4.86
10934	605.8	217.5	9.654	3063	296.2	10.34	83.6	32.7	4.84	14.2	19.9	91.3	3873	4.84
10935	644.4	214.2	10.432	3048	293.9	10.37	89.4	35.5	4.79	14.1	19.7	84.1	3845	4.79
10936	601.5	213.2	9.505	3141	297.6	10.55	86.5	36.6	4.84	13.6	19.7	−151.3	4147	4.84
10937	615.5	208.9	10.218	3020	290.2	10.41	86.0	34.7	4.70	13.8	19.3	74.5	3791	4.70

Table L.2 – continued

Shot	p	T[0]	ρ	u_x	a	M	Pitot	p_t	H_t	μ	k[0]	e[0]	T_s	H_s
-	Pa	K	g/m^3	m/s	m/s	-	kPa	MPa	MJ/kg	μs Pa	$mW/(m^2\,K)$	kJ/kg	K	MJ/kg
10938	342.5	210.8	5.628	3016	291.7	10.34	47.3	18.4	4.70	14.0	19.5	89.9	3768	4.70
10939	404.4	234.4	5.976	3133	307.7	10.18	54.1	19.7	5.11	15.1	21.3	135.0	3993	5.11
10940	588.4	206.3	9.888	3007	288.5	10.42	82.5	33.5	4.65	13.7	19.2	70.0	3763	4.65
10941	370.8	225.7	5.690	3090	301.9	10.24	50.2	18.7	4.96	14.7	20.6	120.8	3910	4.96
10942	403.8	235.9	5.928	3140	308.7	10.17	53.9	19.5	5.14	15.2	21.4	138.1	4006	5.13
10943	394.0	229.5	5.946	3110	304.4	10.22	53.1	19.6	5.03	14.9	20.9	126.4	3949	5.03
10944	397.4	230.0	5.984	3112	304.8	10.21	53.5	19.7	5.04	14.9	20.9	127.2	3954	5.04
10945	380.9	238.6	5.378	3259	314.9	10.35	52.7	20.4	5.25	14.9	21.7	−131.6	4444	5.24
10946	394.8	232.8	5.873	3125	306.6	10.19	52.9	19.3	5.08	15.1	21.2	133.0	3977	5.08
10947	384.5	232.7	5.721	3124	306.6	10.19	51.5	18.8	5.08	15.1	21.2	133.9	3975	5.08
10948	405.3	236.1	5.943	3141	308.8	10.17	54.1	19.5	5.14	15.2	21.4	138.4	4008	5.14
10949	610.3	208.4	10.155	3018	289.9	10.41	85.4	34.5	4.69	13.8	19.3	73.7	3785	4.69
10950	578.1	204.1	9.821	2995	286.9	10.44	81.3	33.3	4.61	13.7	19.1	65.5	3739	4.61
10951	520.9	200.9	8.989	2977	284.7	10.46	73.5	30.3	4.55	13.5	18.9	60.0	3701	4.55
10952	555.6	201.9	9.540	2983	285.4	10.45	78.4	32.3	4.57	13.6	18.9	61.3	3714	4.57
10953	598.6	211.2	9.824	3032	291.9	10.39	83.4	33.3	4.74	13.9	19.5	79.6	3812	4.74
10954	669.0	220.6	10.514	3080	298.3	10.32	92.0	35.8	4.90	14.4	20.1	95.0	3909	4.90
10955	645.9	221.7	9.819	3187	303.5	10.50	92.0	38.1	5.00	14.0	20.3	−144.9	4263	5.00
10956	653.6	217.8	10.405	3065	296.4	10.34	90.2	35.4	4.85	14.2	19.9	90.5	3881	4.85
10957	398.0	231.7	5.949	3120	305.9	10.20	53.5	19.6	5.07	15	21.1	130.5	3969	5.06
10958	598.4	203.5	10.197	2993	286.5	10.45	84.3	34.6	4.60	13.6	19.0	63.8	3735	4.60
10959	670.9	211.2	11.017	3034	291.8	10.40	93.6	37.6	4.74	13.9	19.4	78.0	3819	4.74
10960	657.5	211.3	10.789	3034	291.9	10.39	91.7	36.8	4.74	13.9	19.4	78.5	3819	4.74
10961	591.3	205.3	9.985	3002	287.8	10.43	83.0	33.9	4.63	13.7	19.1	67.8	3753	4.63
10962	606.5	212.4	9.620	3137	297.1	10.56	87.3	37.0	4.83	13.6	19.7	−151.9	4137	4.83
10963	557.4	198.4	9.739	2965	282.9	10.48	79.0	33.0	4.51	13.5	18.8	53.4	3679	4.50

Table L.2 – continued

Shot -	p Pa	T[0] K	ρ g/m³	u_x m/s	a m/s	M -	Pitot kPa	p_t MPa	H_t MJ/kg	μ μs Pa	k[0] mW/(m² K)	e[0] kJ/kg	T_s K	H_s MJ/kg
10 964	553.4	199.2	9.630	2969	283.5	10.47	78.4	32.6	4.52	13.5	18.8	55.4	3687	4.52
10 965	634.8	204.3	10.779	2998	287	10.45	89.4	36.7	4.62	13.7	19.0	64.9	3747	4.62
10 966	666.9	212.2	10.902	3038	292.5	10.39	92.9	37.2	4.76	14.0	19.5	79.9	3828	4.76
10 967	366.5	220.4	5.759	3065	298.3	10.27	49.9	18.9	4.87	14.4	20.2	109.9	3863	4.87
10 968	383.3	224.7	5.910	3087	301.2	10.25	52.0	19.4	4.95	14.6	20.5	117.5	3904	4.94
10 969	379.8	224.1	5.870	3084	300.8	10.25	51.5	19.3	4.94	14.6	20.5	116.6	3898	4.93
10 970	334.2	216.6	5.197	3141	300	10.47	47.3	19.3	4.85	13.8	20.0	−148.6	4149	4.84
10 971	345.5	207.3	5.773	2999	289.3	10.37	47.9	18.9	4.64	13.8	19.3	81.3	3734	4.64
10 972	625.5	211.1	10.274	3032	291.8	10.39	87.2	34.9	4.74	13.9	19.5	78.7	3814	4.73
10 973	618.8	217.6	9.581	3165	300.7	10.53	88.5	37.0	4.92	13.8	20.0	−147.9	4207	4.92
10 974	649.9	212.0	10.632	3037	292.4	10.39	90.5	36.2	4.75	14.0	19.5	79.9	3825	4.75
10 975	658.4	215.5	10.597	3054	294.8	10.36	91.2	36.1	4.81	14.1	19.7	86.1	3859	4.81

Table L.3 – Nozzle Exit Flow Composition and Turbulent Properties for each Shot

	Species Mass Fractions					Turbulent Parameters			
Shot -	N_2 kg/kg	O_2 kg/kg	N kg/kg	O kg/kg	NO kg/kg	$μ_t$ μs Pa	k_t μW/(m² K)	tke J/kg	ω 1/s
10 742	0.736 720 0	0.197 130 0	0	0.001 141 5	0.065 007 0	0.226	257	0.760	21 497
10 743	0.736 520 0	0.196 730 0	0	0.001 299 5	0.065 446 0	0.234	267	0.868	21 548
10 744	0.736 260 0	0.196 440 0	0	0.001 301 2	0.065 993 0	0.233	266	0.853	21 587
10 745	0.735 340 0	0.195 240 0	0	0.001 462 2	0.067 954 0	0.238	271	0.904	21 747
10 746	0.737 920 0	0.198 400 0	0	0.001 223 3	0.062 460 0	0.234	267	0.893	21 339
10 747	0.736 260 0	0.196 360 0	0	0.001 374 8	0.066 001 0	0.237	270	0.907	21 593

Table L.3 – continued

Shot	Species Mass Fractions					Turbulent Parameters			
	N_2	O_2	N	O	NO	μ_t	k_t	tke	ω
-	kg/kg	kg/kg	kg/kg	kg/kg	kg/kg	µs Pa	$\mu W/(m^2\,K)$	J/kg	1/s
10 748	0.735 960 0	0.195 980 0	0	0.001 416 3	0.066 640 0	0.238	271	0.916	21 643
10 749	0.738 300 0	0.198 860 0	0	0.001 190 0	0.061 645 0	0.233	266	0.887	21 284
10 750	0.735 920 0	0.195 940 0	0	0.001 416 6	0.066 719 0	0.238	271	0.914	21 649
10 753	0.732 970 0	0.191 810 0	0	0.002 199 1	0.073 024 0	0.256	292	1.129	22 239
10 754	0.731 320 0	0.189 290 0	0	0.002 858 4	0.076 534 0	0.266	303	1.233	22 708
10 755	0.733 720 0	0.192 980 0	0	0.001 874 3	0.071 429 0	0.249	283	1.025	22 068
10 756	0.732 980 0	0.191 950 0	0	0.002 065 8	0.073 005 0	0.252	287	1.058	22 235
10 757	0.733 280 0	0.192 290 0	0	0.002 062 1	0.072 371 0	0.253	289	1.087	22 167
10 758	0.999 990 0		0.000 018 1			0.262	306	1.273	23 142
10 761	0.730 900 0	0.190 010 0	0	0.001 662 9	0.077 430 0	0.224	255	0.603	23 076
10 762	0.733 440 0	0.193 680 0	0	0.000 881 6	0.071 993 0	0.202	230	0.455	22 074
10 763	0.733 580 0	0.192 760 0	0	0.001 934 6	0.071 727 0	0.250	285	1.046	22 099
10 764	0.732 810 0	0.191 690 0	0	0.002 133 5	0.073 368 0	0.253	289	1.076	22 276
10 765	0.733 860 0	0.193 140 0	0	0.001 872 8	0.071 136 0	0.249	284	1.037	22 040
10 766	0.737 430 0	0.197 700 0	0	0.001 365 4	0.063 506 0	0.241	274	0.979	21 414
10 767	0.735 450 0	0.195 320 0	0	0.001 504 2	0.067 729 0	0.241	274	0.940	21 731
10 768	0.731 980 0	0.190 670 0	0	0.002 212 5	0.075 141 0	0.252	287	1.020	22 493
10 769	0.732 150 0	0.191 000 0	0	0.002 075 9	0.074 776 0	0.248	283	0.973	22 441
10 770	0.731 700 0	0.190 280 0	0	0.002 287 1	0.075 738 0	0.252	288	1.021	22 576
10 771	0.732 230 0	0.190 960 0	0	0.002 209 1	0.074 600 0	0.253	288	1.049	22 423
10 772	0.733 850 0	0.193 180 0	0	0.001 816 3	0.071 157 0	0.247	282	1.004	22 040
10 773	0.732 440 0	0.191 270 0	0	0.002 138 2	0.074 148 0	0.252	287	1.038	22 366
10 774	0.999 970 0		0.000 026 0			0.254	297	1.085	23 456
10 775	0.732 620 0	0.191 720 0	0	0.001 885 9	0.073 775 0	0.244	278	0.927	22 314
10 776	0.733 240 0	0.192 490 0	0	0.001 822 5	0.072 452 0	0.245	279	0.952	22 168

Table L.3 – continued

	Species Mass Fractions					Turbulent Parameters			
Shot	N_2	O_2	N	O	NO	μ_t	k_t	tke	ω
-	kg/kg	kg/kg	kg/kg	kg/kg	kg/kg	µs Pa	$\mu W/(m^2\,K)$	J/kg	1/s
10 777	0.733 810 0	0.193 090 0	0	0.001 873 3	0.071 225 0	0.249	284	1.034	22 048
10 778	0.730 820 0	0.189 260 0	0	0.002 299 5	0.077 628 0	0.246	281	0.895	22 907
10 779	0.731 610 0	0.190 310 0	0	0.002 148 8	0.075 939 0	0.247	282	0.943	22 602
10 780	0.731 430 0	0.189 890 0	0	0.002 364 4	0.076 319 0	0.253	288	1.021	22 664
10 781	0.731 880 0	0.190 690 0	0	0.002 079 1	0.075 348 0	0.247	281	0.944	22 516
10 782	0.732 810 0	0.191 760 0	0	0.002 068 0	0.073 370 0	0.251	286	1.041	22 275
10 783	0.999 980 0		0.000 019 9			0.258	302	1.206	23 216
10 784	0.732 040 0	0.190 670 0	0	0.002 282 3	0.075 018 0	0.254	290	1.062	22 478
10 785	0.734 090 0	0.193 470 0	0	0.001 813 7	0.070 631 0	0.248	283	1.024	21 991
10 786	0.733 070 0	0.192 120 0	0	0.002 001 5	0.072 820 0	0.250	285	1.033	22 213
10 787	0.732 660 0	0.192 710 0	0	0.000 970 4	0.073 660 0	0.204	233	0.461	22 286
10 788	0.732 300 0	0.191 300 0	0	0.001 948 6	0.074 461 0	0.245	279	0.926	22 397
10 789	0.732 520 0	0.191 550 0	0	0.001 946 4	0.073 994 0	0.246	280	0.947	22 342
10 790	0.733 610 0	0.192 740 0	0	0.001 995 0	0.071 661 0	0.253	288	1.084	22 093
10 792	0.732 630 0	0.192 640 0	0	0.001 001 8	0.073 732 0	0.206	234	0.474	22 297
10 793	0.732 750 0	0.192 830 0	0	0.000 940 0	0.073 480 0	0.203	231	0.451	22 260
10 794	0.731 810 0	0.191 740 0	0	0.000 970 8	0.075 485 0	0.201	229	0.407	22 601
10 795	0.731 920 0	0.191 890 0	0	0.000 940 2	0.075 247 0	0.200	228	0.402	22 555
10 796	0.734 310 0	0.194 810 0	0	0.000 730 1	0.070 147 0	0.196	223	0.410	21 867
10 797	0.731 920 0	0.190 730 0	0	0.002 078 6	0.075 273 0	0.247	282	0.948	22 506
10 798	0.732 910 0	0.192 000 0	0	0.001 942 1	0.073 156 0	0.247	282	0.985	22 247
10 799	0.731 960 0	0.190 840 0	0	0.002 014 1	0.075 190 0	0.245	279	0.921	22 492
10 925	0.731 400 0	0.190 920 0	0	0.001 334 8	0.076 346 0	0.215	245	0.535	22 754
10 926	0.735 680 0	0.196 400 0	0	0.000 707 3	0.067 213 0	0.197	225	0.443	21 603
10 927	0.733 430 0	0.192 820 0	0	0.001 712 7	0.072 046 0	0.241	275	0.908	22 121

Table L.3 – continued

Shot	Species Mass Fractions					Turbulent Parameters			
	N_2	O_2	N	O	NO	μ_t	k_t	tke	ω
-	kg/kg	kg/kg	kg/kg	kg/kg	kg/kg	µs Pa	$\mu W/(m^2\,K)$	J/kg	1/s
10 928	0.736 420 0	0.196 510 0	0	0.001 412 6	0.065 658 0	0.240	273	0.945	21 569
10 929	0.730 730 0	0.189 080 0	0	0.002 375 1	0.077 819 0	0.248	282	0.911	22 949
10 930	0.732 330 0	0.192 420 0	0	0.000 882 1	0.074 373 0	0.199	226	0.401	22 395
10 931	0.732 570 0	0.192 670 0	0	0.000 910 7	0.073 843 0	0.201	229	0.428	22 311
10 932	0.732 420 0	0.192 470 0	0	0.000 940 2	0.074 167 0	0.202	230	0.433	22 359
10 933	0.733 000 0	0.193 210 0	0	0.000 854 5	0.072 938 0	0.199	227	0.422	22 186
10 934	0.733 130 0	0.193 270 0	0	0.000 939 6	0.072 666 0	0.204	233	0.470	22 157
10 935	0.733 530 0	0.193 860 0	0	0.000 802 0	0.071 805 0	0.198	226	0.418	22 047
10 936	0.999 990 0		0.000 008 7			0.201	235	0.482	22 809
10 937	0.734 300 0	0.194 780 0	0	0.000 753 1	0.070 169 0	0.197	224	0.422	21 872
10 938	0.734 300 0	0.193 870 0	0	0.001 654 1	0.070 181 0	0.243	276	0.947	21 944
10 939	0.731 330 0	0.189 930 0	0	0.002 221 0	0.076 519 0	0.248	283	0.941	22 693
10 940	0.734 720 0	0.195 250 0	0	0.000 752 9	0.069 275 0	0.198	226	0.437	21 787
10 941	0.732 210 0	0.191 070 0	0	0.002 075 2	0.074 639 0	0.249	283	0.980	22 424
10 942	0.731 210 0	0.189 710 0	0	0.002 294 1	0.076 791 0	0.249	284	0.956	22 740
10 943	0.731 790 0	0.190 590 0	0	0.002 080 1	0.075 548 0	0.246	281	0.933	22 544
10 944	0.731 730 0	0.190 520 0	0	0.002 080 8	0.075 671 0	0.246	280	0.927	22 561
10 945	0.999 970 0		0.000 034 5			0.260	304	1.146	23 692
10 946	0.731 480 0	0.190 090 0	0	0.002 219 2	0.076 218 0	0.249	284	0.959	22 645
10 947	0.731 490 0	0.190 040 0	0	0.002 290 1	0.076 189 0	0.251	286	0.994	22 642
10 948	0.731 190 0	0.189 690 0	0	0.002 294 3	0.076 832 0	0.249	284	0.953	22 747
10 949	0.734 370 0	0.194 870 0	0	0.000 753 1	0.070 004 0	0.197	225	0.425	21 856
10 950	0.735 110 0	0.195 720 0	0	0.000 729 7	0.068 447 0	0.198	225	0.437	21 710
10 951	0.735 710 0	0.196 340 0	0	0.000 775 7	0.067 176 0	0.202	230	0.485	21 605
10 952	0.735 510 0	0.196 170 0	0	0.000 729 4	0.067 589 0	0.198	226	0.451	21 637

Table L.3 – continued

	Species Mass Fractions					Turbulent Parameters			
Shot	N_2	O_2	N	O	NO	μ_t	k_t	tke	ω
-	kg/kg	kg/kg	kg/kg	kg/kg	kg/kg	µs Pa	$\mu W/(m^2\,K)$	J/kg	1/s
10 953	0.733 960 0	0.194 320 0	0	0.000 827 4	0.070 900 0	0.201	229	0.449	21 952
10 954	0.732 760 0	0.192 910 0	0	0.000 882 1	0.073 453 0	0.200	228	0.423	22 255
10 955	0.999 990 0		0.000 012 2			0.203	238	0.479	23 119
10 956	0.733 080 0	0.193 300 0	0	0.000 854 4	0.072 768 0	0.200	227	0.425	22 165
10 957	0.731 570 0	0.190 270 0	0	0.002 149 2	0.076 013 0	0.247	282	0.939	22 613
10 958	0.735 190 0	0.195 860 0	0	0.000 686 3	0.068 260 0	0.195	222	0.415	21 689
10 959	0.733 920 0	0.194 400 0	0	0.000 707 9	0.070 971 0	0.193	220	0.385	21 948
10 960	0.733 910 0	0.194 360 0	0	0.000 730 2	0.070 997 0	0.195	222	0.396	21 953
10 961	0.734 880 0	0.195 470 0	0	0.000 729 8	0.068 923 0	0.197	224	0.430	21 753
10 962	0.999 990 0		0.000 008 3			0.199	233	0.472	22 779
10 963	0.736 180 0	0.196 990 0	0	0.000 665 3	0.066 165 0	0.196	223	0.432	21 515
10 964	0.736 020 0	0.196 790 0	0	0.000 685 8	0.066 507 0	0.197	224	0.440	21 544
10 965	0.735 020 0	0.195 710 0	0	0.000 646 1	0.068 631 0	0.192	218	0.386	21 715
10 966	0.733 790 0	0.194 230 0	0	0.000 730 2	0.071 253 0	0.194	221	0.391	21 980
10 967	0.732 850 0	0.191 990 0	0	0.001 883 5	0.073 284 0	0.245	279	0.948	22 259
10 968	0.732 310 0	0.191 310 0	0	0.001 948 5	0.074 434 0	0.245	279	0.927	22 394
10 969	0.732 380 0	0.191 390 0	0	0.001 947 8	0.074 284 0	0.245	279	0.934	22 376
10 970	0.999 990 0		0.000 012 6			0.249	291	1.099	22 917
10 971	0.734 900 0	0.194 690 0	0	0.001 508 7	0.068 907 0	0.239	272	0.903	21 827
10 972	0.733 960 0	0.194 370 0	0	0.000 777 1	0.070 887 0	0.198	225	0.422	21 946
10 973	0.999 990 0		0.000 010 5			0.203	237	0.486	22 971
10 974	0.733 820 0	0.194 240 0	0	0.000 753 3	0.071 183 0	0.196	223	0.405	21 975
10 975	0.733 360 0	0.193 670 0	0	0.000 802 1	0.072 164 0	0.198	225	0.411	22 089

Table L.4 – Fuel Flow Properties for each Shot

Shot -	A_c $10^{-3}m^2$	$\dot{m}_{AIR}$ g/s	p_{Ti} kPa	$p_{p,1}$ kPa	$p_{p,2}$ kPa	α_1 10^{-9}	α_2 10^{-9}	$\dot{m}_{f,1}$ g/s	$\dot{m}_{f,2}$ g/s	ϕ_1 -	ϕ_2 -	ϕ_t -
10 742	1.9245	36.16										
10 743	1.9245	33.05										
10 744	1.9245	33.64										
10 745	1.9245	32.93										
10 746	1.9245	31.49										
10 747	1.9245	32.22										
10 748	1.9245	32.19										
10 749	1.9245	31.42	1413.2		764.6	1.662 30	2.849 32		2.3822		2.604	2.604
10 750	1.9245	32.27	763.1		407.2	1.662 30	2.849 32		1.2712		1.353	1.353
10 753	1.9245	29.76										
10 754	1.9245	29.52										
10 755	1.9245	31.30	522.2		294.1	1.662 30	2.849 32		0.9108		0.999	0.999
10 756	1.9245	31.23										
10 757	1.9245	30.34	695.3		413.7	1.662 30	2.849 32		1.2712		1.439	1.439
10 758	1.9245	29.05	702.4		416.9	1.662 30	2.849 32		1.2816		1.515	1.515
10 761	2.0085	55.10										
10 762	2.0085	60.14	715.4		391.8	1.662 30	2.849 32		1.2184		0.696	0.696
10 763	1.9245	30.95	725.9		391.0	1.662 30	2.849 32		1.2187		1.352	1.352
10 764	1.9245	31.01										
10 765	1.9245	30.92										
10 766	1.9245	29.73										
10 767	1.9245	31.95										
10 768	1.9245	33.13	741.6		420.1	1.662 30	2.849 32		1.3001		1.348	1.348
10 769	1.9245	34.09	726.8		410.6	1.662 30	2.849 32		1.2713		1.281	1.281
10 770	1.9245	33.46										
10 771	1.9245	32.18										

Table L.4 – continued

Shot -	A_c $10^{-3}m^2$	$\dot{m}_{AIR}$ g/s	p_{Ti} kPa	$p_{p,1}$ kPa	$p_{p,2}$ kPa	α_1 10^{-9}	α_2 10^{-9}	$\dot{m}_{f,1}$ g/s	$\dot{m}_{f,2}$ g/s	ϕ_1 -	ϕ_2 -	ϕ_t -
10 772	1.9245	31.69	730.4		466.0	1.662 30	2.849 32		1.4175		1.536	1.536
10 773	1.9245	32.22	425.1		235.5	1.662 30	2.849 32		0.7312		0.780	0.780
10 774	1.9245	34.04	748.5		469.0	1.662 30	2.849 32		1.4302		1.443	1.443
10 775	1.9245	34.77	1253.9		784.8	1.662 30	2.849 32		2.3937		2.365	2.365
10 776	1.9245	33.48	406.3		228.3	1.662 30	2.849 32		0.7073		0.726	0.726
10 777	1.9245	31.03	363.4	234.7		1.662 30	2.849 32	0.4157		0.460		0.460
10 778	1.9245	38.39	739.3	544.8		1.662 30	2.849 32	0.9467		0.847		0.847
10 779	1.9245	35.56	729.7	537.7		1.662 30	2.849 32	0.9344		0.902		0.902
10 780	1.9245	33.84	234.1	157.3		1.662 30	2.849 32	0.2770		0.281		0.281
10 781	1.9245	35.17	553.8	364.3		1.662 30	2.849 32	0.6436		0.628		0.628
10 782	1.9245	31.77	549.2	390.2		1.662 30	2.849 32	0.6816		0.737		0.737
10 783	1.9245	30.54	364.3	248.8		1.662 30	2.849 32	0.4371		0.492		0.492
10 784	1.9245	32.12	361.9	245.9		1.662 30	2.849 32	0.4324		0.462		0.462
10 785	1.9245	31.01	517.8	246.5	244.0	1.662 30	2.849 32	0.3506	0.5958	0.388	0.660	1.048
10 786	1.9245	31.72	619.0	306.8	301.2	1.662 30	2.849 32	0.4339	0.7320	0.470	0.793	1.262
10 787	2.0085	61.27	1171.2	544.9	560.5	1.662 30	2.849 32	0.7777	1.3657	0.436	0.766	1.202
10 788	1.9245	35.15										
10 789	1.9245	34.33										
10 790	1.9245	30.13										
10 792	2.0085	60.07										
10 793	2.0085	62.10										
10 794	2.0085	70.04	1419.1	75.6	120.6	1.662 30	2.849 32	0.1478	0.3775	0.072	0.185	0.258
10 795	2.0085	70.38	1337.7	538.9	590.2	1.662 30	2.849 32	0.7853	1.4550	0.383	0.710	1.093
10 796	2.0085	63.31	1514.5	639.8	685.0	1.662 30	2.849 32	0.9260	1.6827	0.502	0.913	1.415
10 797	1.9245	35.02	638.5	316.9	318.4	1.662 30	2.849 32	0.4481	0.7711	0.439	0.756	1.196
10 798	1.9245	32.99										

Table L.4 – continued

Shot -	A_c $10^{-3}m^2$	$\dot{m}_{AIR}$ g/s	p_{Ti} kPa	$p_{p,1}$ kPa	$p_{p,2}$ kPa	α_1 10^{-9}	α_2 10^{-9}	$\dot{m}_{f,1}$ g/s	$\dot{m}_{f,2}$ g/s	ϕ_1 -	ϕ_2 -	ϕ_t -
10 799	1.9245	35.70	604.5	68.8	115.5	1.662 30	2.849 32	0.1203	0.3212	0.116	0.309	0.425
10 925	2.0085	58.05										
10 926	2.0085	57.63										
10 927	1.9245	34.44										
10 928	1.9245	31.15										
10 929	1.9245	38.06										
10 930	2.0085	69.03										
10 931	2.0085	65.01	710.6		422.2	1.386 57	2.121 63		0.9662		0.510	0.510
10 932	2.0085	64.76	644.5		432.3	1.386 57	2.121 63		0.9720		0.515	0.515
10 933	2.0085	64.66	744.8		500.0	1.386 57	2.121 63		1.1241		0.597	0.597
10 934	2.0085	59.38	1230.0		851.2	1.386 57	2.121 63		1.9053		1.102	1.102
10 935	2.0085	63.85	1244.0		856.8	1.386 57	2.121 63		1.9191		1.032	1.032
10 936	2.0085	59.96	1276.7		881.2	1.386 57	2.121 63		1.9731		1.130	1.130
10 937	2.0085	61.98	1000.7		691.9	1.386 57	2.121 63		1.5488		0.858	0.858
10 938	1.9245	32.67	691.8		473.2	1.386 57	2.121 63		1.0609		1.115	1.115
10 939	1.9245	36.03	668.4		457.0	1.386 57	2.121 63		1.0247		0.977	0.977
10 940	2.0085	59.71	722.0		496.4	1.386 57	2.121 63		1.1121		0.640	0.640
10 941	1.9245	33.84	304.9	195.1		1.386 57	2.121 63	0.2886		0.293		0.293
10 942	1.9245	35.82	323.9	188.6		1.386 57	2.121 63	0.2829		0.271		0.271
10 943	1.9245	35.58	405.1	239.1		1.386 57	2.121 63	0.3579		0.346		0.346
10 944	1.9245	35.84	522.1	357.4		1.386 57	2.121 63	0.5236		0.502		0.502
10 945	1.9245	33.73	379.4	263.2		1.386 57	2.121 63	0.3848		0.392		0.392
10 946	1.9245	35.32	360.0	229.7		1.386 57	2.121 63	0.3400		0.331		0.331
10 947	1.9245	34.40										
10 948	1.9245	35.92	751.1	559.7		1.386 57	2.121 63	0.8100		0.774		0.774
10 949	2.0085	61.55	399.1	274.3		1.386 57	2.121 63	0.4016		0.224		0.224

Table L.4 – continued

Shot -	A_c $10^{-3}m^2$	$\dot{m}_{AIR}$ g/s	p_{Ti} kPa	$p_{p,1}$ kPa	$p_{p,2}$ kPa	α_1 10^{-9}	α_2 10^{-9}	$\dot{m}_{f,1}$ g/s	$\dot{m}_{f,2}$ g/s	ϕ_1 -	ϕ_2 -	ϕ_t -
10 950	2.0085	59.07	844.4	634.7		1.386 57	2.121 63	0.9173		0.533		0.533
10 951	2.0085	53.74	865.1	603.5		1.386 57	2.121 63	0.8817		0.564		0.564
10 952	2.0085	57.15	599.0	386.0		1.386 57	2.121 63	0.5705		0.343		0.343
10 953	2.0085	59.82	602.8	420.0		1.386 57	2.121 63	0.6138		0.352		0.352
10 954	2.0085	65.03	716.6	432.5		1.386 57	2.121 63	0.6453		0.341		0.341
10 955	2.0085	62.86	720.6	474.4		1.386 57	2.121 63	0.6989		0.382		0.382
10 956	2.0085	64.06	754.3	494.0		1.386 57	2.121 63	0.7284		0.391		0.391
10 957	1.9245	35.72	449.3	320.3		1.386 57	2.121 63	0.4665		0.449		0.449
10 958	2.0085	61.29	1136.8	391.3	506.5	1.386 57	2.121 63	0.5340	1.0192	0.299	0.571	0.870
10 959	2.0085	67.13	1394.1	469.4	613.5	1.386 57	2.121 63	0.6426	1.2366	0.329	0.633	0.962
10 960	2.0085	65.74	1407.1	407.0	583.9	1.386 57	2.121 63	0.5697	1.1869	0.298	0.620	0.918
10 961	2.0085	60.19	895.5	319.1	403.7	1.386 57	2.121 63	0.4333	0.8108	0.247	0.463	0.710
10 962	2.0085	60.60	1405.6	337.4	518.9	1.386 57	2.121 63	0.4853	1.0727	0.275	0.608	0.883
10 963	2.0085	58.00	1694.2	434.3	657.3	1.386 57	2.121 63	0.6187	1.3493	0.366	0.799	1.165
10 964	2.0085	57.43	1820.4	498.2	734.2	1.386 57	2.121 63	0.7030	1.4986	0.420	0.896	1.317
10 965	2.0085	64.90	1765.1	526.3	741.3	1.386 57	2.121 63	0.7334	1.5044	0.388	0.796	1.184
10 966	2.0085	66.53										
10 967	1.9245	33.97	632.3	217.6	282.1	1.386 57	2.121 63	0.2969	0.5675	0.300	0.574	0.874
10 968	1.9245	35.10	655.1	147.4	239.7	1.386 57	2.121 63	0.2140	0.4962	0.209	0.486	0.695
10 969	1.9245	34.83	852.5	272.7	369.7	1.386 57	2.121 63	0.3762	0.7468	0.371	0.736	1.107
10 970	1.9245	31.41	866.5	121.6	203.0	1.386 57	2.121 63	0.1888	0.4481	0.206	0.490	0.696
10 971	1.9245	33.32	735.7	124.5	205.6	1.386 57	2.121 63	0.1883	0.4423	0.194	0.456	0.650
10 972	2.0085	62.56	1308.5		776.0	1.386 57	2.121 63		1.7760		0.975	0.975
10 973	2.0085	60.90	1315.1		840.2	1.386 57	2.121 63		1.9025		1.073	1.073
10 974	2.0085	64.85	983.9		632.2	1.386 57	2.121 63		1.4303		0.757	0.757
10 975	2.0085	65.00										

Table L.5 – Forebody Flow Properties for each Shot

Shot	p	T	ρ	$u_{\parallel}$	M	q	μ	Re_u	θ	β
-	Pa	K	g/m^3	m/s	-	kPa	μs Pa	$10^6/m$	°	°
10 742	1394	310.6	15.57	2912	8.23	66.0	18.97	2.389	6.0	10.22
10 743	1279	312.5	14.18	2917	8.22	60.4	19.06	2.171	6.0	10.23
10 744	1305	314.1	14.40	2923	8.21	61.5	19.13	2.200	6.0	10.23
10 745	1292	320.8	13.95	2947	8.19	60.6	19.44	2.115	6.0	10.25
10 746	1201	303.9	13.70	2885	8.24	57.0	18.65	2.119	6.0	10.21
10 747	1251	314.3	13.79	2924	8.21	58.9	19.14	2.106	6.0	10.23
10 748	1254	316.4	13.73	2931	8.20	59.0	19.24	2.092	6.0	10.24
10 749	1194	301.7	13.72	2877	8.25	56.8	18.55	2.127	6.0	10.20
10 750	1257	316.6	13.76	2932	8.20	59.1	19.25	2.096	6.0	10.24
10 753	1208	342.3	12.22	3019	8.12	55.7	20.41	1.807	6.0	10.30
10 754	1237	364.2	11.76	3090	8.06	56.1	21.37	1.701	6.0	10.35
10 755	1255	334.6	12.99	2994	8.15	58.2	20.07	1.938	6.0	10.28
10 756	1267	342.1	12.82	3019	8.12	58.5	20.40	1.898	6.0	10.30
10 757	1225	339.1	12.51	3008	8.13	56.6	20.27	1.857	6.0	10.29
10 758	1206	349.9	11.61	3130	8.21	56.9	20.07	1.811	6.0	10.23
10 761	2270	383.2	20.52	3159	8.03	102.4	22.17	2.923	6.0	10.37
10 762	2313	335.9	23.87	3010	8.18	108.2	20.12	3.571	6.0	10.26
10 763	1244	336.0	12.82	2999	8.14	57.6	20.13	1.910	6.0	10.28
10 764	1261	343.9	12.70	3025	8.12	58.1	20.48	1.876	6.0	10.30
10 765	1238	333.4	12.86	2990	8.15	57.5	20.01	1.921	6.0	10.28
10 766	1140	306.9	12.87	2895	8.23	53.9	18.79	1.983	6.0	10.22
10 767	1252	320.1	13.55	2944	8.19	58.7	19.41	2.055	6.0	10.25
10 768	1368	353.8	13.39	3059	8.09	62.6	20.92	1.958	6.0	10.32
10 769	1402	351.5	13.81	3052	8.10	64.3	20.82	2.025	6.0	10.31
10 770	1389	357.7	13.45	3072	8.08	63.4	21.09	1.959	6.0	10.33
10 771	1322	350.6	13.06	3048	8.10	60.7	20.78	1.916	6.0	10.31
10 772	1268	333.4	13.18	2990	8.15	58.9	20.01	1.969	6.0	10.28
10 773	1319	348.0	13.12	3040	8.11	60.6	20.66	1.930	6.0	10.31
10 774	1440	363.2	13.36	3181	8.19	67.6	20.62	2.060	6.0	10.25
10 775	1418	345.7	14.21	3033	8.12	65.3	20.56	2.095	6.0	10.30
10 776	1352	339.1	13.81	3011	8.14	62.6	20.27	2.051	6.0	10.29
10 777	1243	333.8	12.90	2991	8.15	57.7	20.03	1.926	6.0	10.28
10 778	1631	373.8	15.11	3125	8.04	73.7	21.78	2.167	6.0	10.36
10 779	1479	359.1	14.27	3077	8.08	67.5	21.14	2.076	6.0	10.33
10 780	1413	361.8	13.52	3085	8.07	64.4	21.27	1.962	6.0	10.34
10 781	1454	355.0	14.19	3064	8.09	66.6	20.97	2.073	6.0	10.32
10 782	1292	343.8	13.01	3025	8.12	59.6	20.48	1.922	6.0	10.30
10 783	1274	353.0	12.16	3143	8.21	60.0	20.20	1.891	6.0	10.23

Table L.5 – continued

Shot	p	T	ρ	$u_{\parallel}$	M	q	μ	Re_u	θ	β
-	Pa	K	g/m^3	m/s	-	kPa	μs Pa	$10^6/m$	°	°
10 784	1325	353.2	12.99	3057	8.09	60.7	20.89	1.900	6.0	10.32
10 785	1237	331.2	12.94	2982	8.15	57.5	19.91	1.937	6.0	10.27
10 786	1285	341.1	13.04	3016	8.13	59.3	20.35	1.933	6.0	10.29
10 787	2391	345.4	23.99	3042	8.15	111.0	20.55	3.552	6.0	10.28
10 788	1442	349.6	14.29	3046	8.11	66.3	20.73	2.099	6.0	10.31
10 789	1403	347.0	14.00	3037	8.11	64.6	20.62	2.063	6.0	10.30
10 790	1210	335.8	12.48	2997	8.14	56.1	20.12	1.859	6.0	10.28
10 792	2346	345.9	23.51	3043	8.15	108.8	20.57	3.478	6.0	10.28
10 793	2420	344.4	24.36	3039	8.15	112.4	20.50	3.610	6.0	10.27
10 794	2794	360.6	26.87	3092	8.11	128.5	21.21	3.918	6.0	10.31
10 795	2799	358.3	27.08	3085	8.12	128.9	21.11	3.957	6.0	10.30
10 796	2401	327.0	25.46	2980	8.21	113.1	19.72	3.848	6.0	10.23
10 797	1447	354.6	14.14	3062	8.09	66.3	20.95	2.066	6.0	10.32
10 798	1339	342.6	13.54	3022	8.13	61.8	20.42	2.003	6.0	10.30
10 799	1474	354.0	14.42	3060	8.10	67.5	20.92	2.110	6.0	10.32
10 925	2340	367.3	22.07	3111	8.08	106.8	21.50	3.194	6.0	10.33
10 926	2146	315.5	23.58	2939	8.24	101.8	19.20	3.610	6.0	10.21
10 927	1386	337.1	14.24	3004	8.14	64.3	20.18	2.121	6.0	10.28
10 928	1207	313.3	13.35	2919	8.21	56.9	19.09	2.041	6.0	10.23
10 929	1621	375.8	14.94	3131	8.04	73.2	21.86	2.139	6.0	10.36
10 930	2715	350.9	26.84	3061	8.14	125.7	20.79	3.952	6.0	10.29
10 931	2542	346.8	25.41	3047	8.15	118.0	20.61	3.757	6.0	10.28
10 932	2540	349.0	25.24	3054	8.14	117.7	20.70	3.723	6.0	10.28
10 933	2506	341.1	25.48	3028	8.16	116.8	20.36	3.790	6.0	10.27
10 934	2297	339.5	23.45	3022	8.17	107.1	20.28	3.493	6.0	10.26
10 935	2452	334.9	25.38	3007	8.18	114.8	20.08	3.802	6.0	10.25
10 936	2337	336.8	23.38	3100	8.29	112.3	19.51	3.714	6.0	10.17
10 937	2351	327.1	24.92	2980	8.21	110.7	19.73	3.765	6.0	10.23
10 938	1299	329.2	13.67	2976	8.16	60.5	19.82	2.052	6.0	10.27
10 939	1508	363.4	14.37	3091	8.07	68.6	21.33	2.082	6.0	10.34
10 940	2252	323.4	24.14	2967	8.22	106.2	19.56	3.662	6.0	10.23
10 941	1391	350.7	13.73	3049	8.10	63.8	20.78	2.015	6.0	10.31
10 942	1504	365.6	14.24	3098	8.06	68.3	21.43	2.059	6.0	10.34
10 943	1474	356.3	14.33	3068	8.09	67.4	21.03	2.091	6.0	10.32
10 944	1487	357.2	14.42	3071	8.09	68.0	21.06	2.102	6.0	10.33
10 945	1448	373.3	13.06	3216	8.16	67.5	21.04	1.997	6.0	10.26
10 946	1473	361.1	14.13	3083	8.07	67.2	21.23	2.052	6.0	10.33
10 947	1435	360.9	13.76	3082	8.07	65.4	21.22	1.999	6.0	10.33
10 948	1509	365.9	14.28	3099	8.06	68.6	21.44	2.064	6.0	10.34

Table L.5 – continued

Shot	p	T	ρ	$u_{\parallel}$	M	q	μ	Re_u	θ	β
-	Pa	K	g/m^3	m/s	-	kPa	μs Pa	$10^6/m$	°	°
10 949	2332	326.4	24.77	2978	8.21	109.8	19.70	3.745	6.0	10.23
10 950	2216	320.1	24.00	2955	8.23	104.8	19.41	3.655	6.0	10.22
10 951	2001	315.5	21.99	2937	8.23	94.8	19.19	3.365	6.0	10.21
10 952	2133	316.8	23.33	2944	8.23	101.1	19.26	3.567	6.0	10.21
10 953	2282	330.5	23.93	2992	8.19	107.1	19.88	3.601	6.0	10.24
10 954	2533	344.3	25.51	3039	8.16	117.8	20.50	3.782	6.0	10.27
10 955	2496	349.4	24.07	3145	8.26	119.1	20.05	3.777	6.0	10.20
10 956	2480	340.1	25.28	3025	8.17	115.6	20.31	3.764	6.0	10.26
10 957	1487	359.6	14.32	3078	8.08	67.9	21.17	2.083	6.0	10.33
10 958	2296	319.3	24.93	2953	8.23	108.7	19.37	3.801	6.0	10.22
10 959	2560	330.7	26.85	2994	8.20	120.3	19.89	4.041	6.0	10.24
10 960	2508	330.8	26.29	2994	8.20	117.8	19.90	3.956	6.0	10.24
10 961	2265	321.9	24.39	2962	8.22	107.0	19.49	3.706	6.0	10.22
10 962	2358	335.6	23.67	3095	8.29	113.4	19.46	3.764	6.0	10.17
10 963	2146	311.8	23.86	2926	8.25	102.1	19.02	3.670	6.0	10.20
10 964	2130	313.0	23.59	2930	8.25	101.2	19.08	3.622	6.0	10.20
10 965	2436	320.6	26.35	2958	8.23	115.3	19.43	4.012	6.0	10.22
10 966	2543	332.1	26.56	2998	8.19	119.4	19.95	3.991	6.0	10.24
10 967	1380	343.2	13.93	3024	8.12	63.7	20.45	2.060	6.0	10.30
10 968	1439	349.4	14.27	3045	8.11	66.2	20.72	2.097	6.0	10.31
10 969	1427	348.6	14.18	3042	8.11	65.6	20.69	2.085	6.0	10.31
10 970	1286	340.7	12.72	3099	8.24	61.1	19.68	2.003	6.0	10.21
10 971	1314	324.2	14.04	2959	8.18	61.5	19.60	2.121	6.0	10.25
10 972	2385	330.4	25.03	2992	8.20	112.0	19.88	3.768	6.0	10.24
10 973	2397	343.3	23.53	3123	8.27	114.7	19.79	3.713	6.0	10.18
10 974	2478	331.8	25.90	2997	8.19	116.3	19.94	3.892	6.0	10.24
10 975	2503	336.8	25.77	3014	8.18	117.0	20.16	3.852	6.0	10.25

Legend for Table L.6

Column	Data	Color	Key
1	Shielding	white	Design A (initial)
			Design B (stiffening ribs added)
			Design C (struts added, Pitot shifted)
			Design D (wedge added)
			Design E (double wedge)
2	Boundary Layer	white	Not Fitted
	Trip		Fitted
3	Pitot	white	Cone-blank fitted
			Pitot probe fitted
4	Fuel	white	Fuel-off
			Fuel-N_2
			Fuel-Air
5	Injection Location		Step injection scheme
			Inlet injection scheme
			Combined injection scheme
6	Condition	white	Low-pressure condition fine-tuning
			Final Low-pressure condition (Table 3.3)
			High-pressure condition fine-tuning
			Final High-pressure condition (Table 3.3)
			Standard 6 mm dia. 3 MJ/kg condition
7	Nozzle		T4 Mach 10 nozzle
			T4 Mach 8 nozzle
8	Nozzle Location		Nominal pre-recoil position. Measured from inside front face of test section.
9	Shielding Gap	n/a	Units are millimetres
10	Dump Tank Vacuum	n/a	Units are 1 torr = 133 Pa
11	Schileren	white	No optics
			Shimadzu HPV-1 camera and flash lamp
			PointGrey still camera and LED light source
12	Thesis Figure	n/a	
13	Comments	n/a	

Table L.6 – Campaign 1 Experiment Configuration

Shot	1	2	3	4	5	6	7	8	9	10	11	12	13
10741								205	?	0.7			
10742								205	?	0.8			
10743								205	?	?			
10744								205	?	0.55			
10745								205	>2?	?			
10746								205	2	0.7			
10747								205	2	0.75			
10748								205	5	0.6			
10749								205	5	0.6			
10750								205	5	0.6			
10751								205	5	0.65			
10752								205	5	0.75			
10753								205	4	0.75			
10754								205	4	0.75			
10755								205	4	0.8			
10756								205	4	0.75			
10757								142	4	0.7			
10758								142	4	0.65			
10759								142	4	0.7			
10760								142	2	0.7			
10761								176	2	0.65			
10762								176	2	0.7			
10763								176	2	0.6			
10764								176	2	0.6			Camera flash didn't trigger
10765								176	2	0.6			Alignment heat gun left on and obscured Schlieren
10766								176	2	0.6			
10767								176	2	0.7			
10768								176	2	0.7			
10769								132	2	0.7			
10770								205	2	0.65		Figures 7.4a and 7.5a	
10771								205	2	0.4		Figures 7.4a and 7.5a	
10772								205	2	0.5			Fuel early
10773								205	2	0.6			
10774								205	2	0.7			
10775								205	2	0.8			
10776								205	2	0.8			
10777								205	2	0.75			
10778								205	2	0.7			Forebody strange, inlet didn't start
10779								205	2	0.7			Forebody strange, inlet didn't start, SPB noisy
10780								205	2	0.45			Fuel early, inlet didn't start
10781								205	2	0.55			Fuel early, inlet didn't start, forebody strange
10782								205	2	0.5			Fuel late, inlet started, SPA/SPB noisy
10783								205	2	0.45			Fuel early but inlet started (N_2 shot)

Table L.6 – Continued.

Shot	1	2	3	4	5	6	7	8	9	10	11	12	13
10784								205	2	0.45			Fuel early but inlet may have started, drag oscillatory, SPA/SPB noisy
10785								205	2	0.4			Fuel early but inlet may have started, very large pressure rise
10786								205	2	0.55			Fuel early but inlet started, combustor pressures are oscillatory
10787								205	2	0.35			Fuel later than usual for campaign 1
10788								205	2	0.42			Primary strains faulty, combustor pressures low
10789								205	3	0.5			Forebody, combustor signals strange
10790								205	3	0.47			Inlet slow to start
10791								205	3	?			Piston pre-launch, no data
10792								161	3	0.4			
10793								205	3	0.4			
10794								205	3	0.5			Fuel late, forebody strange, inlet didn't start
10795								205	3	0.8			Fuel late, inlet didn't start. Pitot/forebody transients were unusual
10796								205	3	0.8			Fuel late, inlet didn't start. Pitot/forebody transients were unusual
10797								205	3	0.5			SPA/SPB noisy, Pitot strange, inlet didn't start
10798								205	3	0.5			Pitot strange, engine pressures unsteady
10799								205	3	0.5			Inlet didn't start
10800								205	3	0.4			
10801								120	3	0.8			
10802								132	3	0.65			
10803								132	3	0.7			

Legend for Table L.7

Column	Data	Color	Key
1	Shielding		Streamlined, no fuel cover pieces
			Streamlined with fuel cover pieces
2	Boundary Layer Trip	white	Not Fitted
			Fitted
3	Forebody Chines	white	Not Fitted
			Fitted
4	Fuel	white	Fuel-off
			Fuel-N_2
			Fuel-Air
5	Injection Location		Step injection scheme
			Inlet injection scheme
			Combined injection scheme
6	Condition		Final Low-pressure condition (Table 3.3)
			Final High-pressure condition (Table 3.3)
7	Nozzle Location		Nominal pre-recoil position. Measured from inside front face of test section.
8	Dump Tank Vacuum	n/a	Units are 1 torr = 133 Pa
9	Schileren	white	No optics
			Shimadzu HPV-1 camera and LED light source
10	Thesis Figure Number	n/a	
11	Comments	n/a	

Table L.7 – Campaign 2 Experiment Configuration

Shot	1	2	3	4	5	6	7	8	9	10	11
10925							205	0.35		Figure 6.2	
10926							205	0.30		Figures 6.2 and H.7a	
10927							205	0.35		Figures 6.2, 6.7 and H.7b	
10928							179	0.40		Figure 6.2	
10929							205	0.40		Figures 6.2 and H.7b	
10930							205	0.32		Figure H.2	
10931							205	0.40			Inlet didn't start
10932							205	0.50			Inlet slow to start
10933							205	0.40			Combustor traces unsteady
10934							205	0.45		Figure H.3	Combustor traces unsteady
10935							205	0.45			Repeat last shot, fuel unintentionally late
10936							205	0.45			Repeat into N_2
10937							205	0.45			Shock tube was over-filled
10938							205	0.40		Figure 6.4b	Fuel was slightly early
10939							205	0.45		Figure 6.4b	Fuel was slightly early
10940							205	0.45		Figure H.7a	Fuel was slightly early
10941							205	0.40			Inlet didn't start, forebody trace strange
10942							205	0.45		Figure 6.3b	
10943							205	0.45		Figure H.6b	
10944							205	0.45		Figures 6.3b, 6.7a and H.7b	Inlet pressure high but traces and optics look good
10945							205	0.40		Figure 6.3b	
10946							205	0.45		Figures 6.3b and H.6b	
10947							205	0.35		Figure 6.2	
10948							205	0.40			Deliberate unstart by early fuel inj.
10949							205	0.40		Figure 6.3a	
10950							205	0.40		Figure H.3	Inlet didn't start
10951							205	0.40		Figures 6.3a, 6.7a and H.3	
10952							205	0.40			Inlet didn't start, seen in optics and pressure
10953							205	0.37		Figure H.6a	P6 and P8 look strange
10954							205	0.35		Figures 6.12a and H.6a	
10955							205	0.40		Figure 6.3a	
10956							205	0.50		Figures 6.3a, 6.12b and H.6a	Inlet slow to start
10957							205	0.45		Figure H.7b	
10958							205	0.40			Unsteady combustor data, fuel was slightly early
10959							205	0.45			Unsteady inlet data though mean values are ok
10960							205	0.40		Figure 6.5a	
10961							205	0.40			Forebody data strange
10962							205	0.40		Figure 6.5a	
10963							205	0.80		Figures 6.5a and 6.7b	
10964							205	0.80		Figure 6.5a	

Table L.7 – Concluded.

Shot	1	2	3	4	5	6	7	8	9	10	11
10965							205	0.45			Inlet didn't start
10966							205	0.35		Figure 6.1	
10967							205	0.40			Forebody trace strange, inlet may not have started
10968							205	0.35		Figure 6.5b	No forebody data
10969							205	0.45		Figures 6.5b and 6.7b	
10970							205	0.45		Figures 6.4b and 6.5b	
10971							205	0.45		Figure 6.5b	
10972							205	0.40		Figures 6.4a, 6.13 and H.3	
10973							205	0.45		Figure 6.4a	
10974							205	0.45		Figures 6.4a and H.7a	
10975							205	0.35		Figures 6.1, 6.7, 6.11 and H.3	

THE END.

The last page.

For the final word consider Ecclesiastes 3:1-8 (NIV) –

> "There is a time for everything, and a season for every activity under heaven:
> a time to be born and a time to die,
> a time to plant and a time to uproot,
> a time to kill and a time to heal,
> a time to tear down and a time to build,
> a time to weep and a time to laugh,
> a time to mourn and a time to dance,
> a time to scatter stones and a time to gather them,
> a time to embrace and a time to refrain,
> a time to search and a time to give up,
> a time to keep and a time to throw away,
> a time to tear and a time to mend,
> a time to be silent and a time to speak,
> a time to love and a time to hate,
> a time for war and a time for peace."

To which I will add –

> *There is a time to study and a time to play.*

and for now, I am finished with the former…